EPR Spectroscopic Characterization of Solution Dynamics of Albumins and Albumin-inspired, Self-organizing Compounds

Dissertation

zur Erlangung des Doktorgrades der Naturwissenschaften

(Dr. rer. nat.)

der

Naturwissenschaftlichen Fakultät II

Chemie, Physik und Mathematik

der Martin-Luther-Universität

Halle-Wittenberg

vorgelegt von

Herrn Dipl. Biophys. Jörg Reichenwallner

geb. am 26. Dezember 1981 in Stuttgart-Bad Cannstatt

Gutachter:

    1. Prof. Dr. Dariush Hinderberger

    2. Prof. Dr. Gunnar Jeschke

Tag der Verteidigung: 15. November 2018

"Thus, the task is, not so much to see what no one else has yet seen, but to think what nobody has yet thought, about what everybody sees."

Freely adapted from Arthur Schopenhauer (1788–1860)
and Albert Szent-Györgyi (1893–1986).

To my parents

Contents I

II

IV

Physical Constants

Notation	Quantity	Numerical value[a]	SI Unit
Da	atomic mass unit (u) = $(1/12) \cdot m(^{12}C)$	$1.660538921(73) \cdot 10^{-27}$	kg
e	elementary charge	$1.602176565(35) \cdot 10^{-19}$	C
g_S	Landé factor of free electron	$-2.00231930436153(53)$	–
$\hbar$	reduced Planck constant ($= h/2\pi$)	$1.054571726(47) \cdot 10^{-34}$	J s
k_B	Boltzmann constant	$1.3806488(13) \cdot 10^{-23}$	J K^{-1}
m_e	electron mass	$9.10938291(40) \cdot 10^{-31}$	kg
N_A	Avogadro's number	$6.02214129(27) \cdot 10^{23}$	mol^{-1}
R	universal gas constant ($= N_A \cdot k_B$)	$8.3144621(75)$	J mol^{-1} K^{-1}
γ_S	gyromagnetic ratio of free electron	$28.02495266(62)$	GHz T^{-1}
ε_0	vacuum permittivity	$8.854187817\ldots \cdot 10^{-12}$	C V^{-1} m^{-1}
μ_0	magnetic constant	$1.2566370614\ldots \cdot 10^{-7}$	N A^{-2}
μ_B	Bohr magneton	$-9.28476430(21) \cdot 10^{-24}$	J T^{-1}
μ_N	nuclear magneton	$5.05078353(11) \cdot 10^{-27}$	J T^{-1}

[a]based on CODATA recommended values of the fundamental constants of physics and chemistry,

given in the 2010 adjustment.

Acronyms and Abbreviations

aa	amino acid
AD	apolar dehydration
ADME	absorption, distribution, metabolism and excretion
AGE	advanced glycation endproducts
AH	apolar hydration
ALP	albumin lot purity
A.M.	arithmetic mean
AMBER	assisted model building with energy refinement
AMW	albumin molecular weight
ANS	8-anilinonaphthalene-1-sulfonic acid
APT	approximate Pake transformation
ATRP	atom transfer radical polymerization
BCA	bicinchoninic acid
BCG	bromocresol green
BLASTP	basic local alignment tool for proteins
BSA	bovine serum albumin
CBBG	Coomassie brilliant blue G-250
CD	circular dichroism
CE	conformational entropy
cHSA	polycationic HSA
CMC	critical micelle concentration
cmPALS	continuously monitored phase-analysis light scattering
CRC	chemical rubber company
CS	crystal structure
CW	continuous wave
Da	Dalton
DEER	double electron-electron resonance
DHAT	dynamic hydrophobic aggregation temperature
DHSA	dendronized HSA
DI	double integral
DL	double layer
DLC	Diplom-Lebensmittelchemiker
DLS	dynamic light scattering
DMS	doxyl methyl stearic acid

DNA	deoxyribonucleic acid
DOX	doxorubicin
DOXYL	4,4-dimethyl-oxazolidine-1-oxyl
DP	degree of polymerization
DPBS	Dulbecco's phosphate buffered saline
DPT	double-photon transition
DQC	double quantum coherence
DQT	double quantum transition
DRO	dynamic regime occupation
DSA	doxyl stearic acid
DSC	differential scanning calorimetry
DTA	differential thermal analysis
DTNB	5,5'-dithiobis(2-nitrobenzoic acid)
DTBN	di-t-butyl nitroxide
DTT	dithiothreitol
ED EPR	echo-detected EPR
EDTA	ethylenediamine-tetraacetic acid
EEC	entropy-enthalpy compensation
EFG	electric field gradient
ELISA	enzyme-linked immunosorbent assay
ELP	elastin-like polypeptides
ELS	electrophoretic light scattering
EM	electron microscopy
ENDOR	electron nuclear double resonance
EP	equilibrium partition (method)
EPR	electron paramagnetic resonance
eq	molar equivalents
ESA	equine serum albumin
ESE	electron spin echo
ESEEM	ESE envelope modulation
FA	fatty acid
FFA	free fatty acid
FCR	Folin-Ciocalteu reagent
FCS	fluorescence correlation spectroscopy
FD ESE	field-detected ESE
FG	functional group
FID	free induction decay
FITC	fluorescein isothiocyanate

FRET	Förster resonance energy transfer	LiCl	lithium chloride
FSA	(cat) feline serum albumin	*lin*PPG	linear α-alkoxy-ω-propargyl PG
FT	Fourier transform	MA	modulation amplitude
FWHM	full width at half maximum	MALDI	matrix-assisted LASER desorption/ionization
GFP	green fluorescent protein	MD	molecular dynamics
GHz	gigahertz = 10^9 Hz	Me	methyl group ($-CH_3$)
GLX	glyoxal	MG	molten globule
GSA	goat serum albumin	MHP	molecular hydrophobicity potential
HCl	hydrogen chloride		
HCT	hydrophilic collapse temperature	MHz	megahertz = 10^6 Hz
HEC	Heisenberg exchange coupling	MISS-DEER	mixed isotopologues for spectral separation DEER
HeNe	helium/neon		
HI	hydropathy index	MLU	Martin Luther University of Halle-Wittenberg
HIC	hydrophobic interaction chromatography	MM	macromonomer
HPLC	high-performance liquid chromatography	MOMD	microscopic order-macroscopic disorder
HPPS	high performance particle sizer	MPIP	Max Planck Institute for Polymer Research in Mainz
HSA	human serum albumin		
HYSCORE	hyperfine sublevel correlation spectroscopy	MPT	multi-photon transition
		MQT	multi-quantum transition
IAA	iodoacetamide (SL)	MS	mass spectrometry
IC	interconversion	MSL	maleimido proxyl SL
IC_{50}	half maximal inhibitory concentration	MTSSL	methanethiosulfonate SL
		MUSTANG	multiple structural alignment algorithm
IDP	intrinsically disordered protein		
IL	ionic liquid, interleukin	MW	molecular weight, microwave
IMTSL	methanethiosulfonic acid S-(1-oxyl-2,2,3,5,5-pentamethyl-imidazolidin-4-ylmethyl) ester	MWCO	molecular-weight cutoff
		NaCl	sodium chloride
		NaOH	sodium hydroxide
IR	infrared	N.A.	not available
ITC	isothermal titration calorimetry	N.C.	non-cooperative (binding site)
JGU	Johannes Gutenberg University Mainz	NMR	nuclear magnetic resonance
		NMRD	NMR dispersion
KCl	potassium chloride	NO	nitroxide
KOH	potassium hydroxide	NOE(SY)	nuclear Overhauser effect (spectroscopy)
krpm	kilorevolutions per minute		
LASER	light amplification by stimulated emission of radiation	OEGMA	oligo(ethylene glycol) methyl ether methacrylate
LCAO	linear combination of atomic orbitals	OTP-d_{14}	perdeuterated *ortho*-terphenyl
LCFA	long-chain fatty acid	PAGE	polyacrylamide gel electrophoresis
LCW	Lum-Chandler-Weeks		
LDV	LASER Doppler velocimetry	PAMAM	poly(amido amine)

PC	personal computer	SL	spin label
PDB ID	protein data bank identifier	SLE	stochastic Liouville equation
PEG	polyethylene glycol (= PEO)	SLI	scattered light intensity
(P)ELDOR	(pulsed) electron-electron double resonance	SLP	spin-labeled pharmaceuticals
PDI	polydispersity index	SNR	signal-to-noise ratio
PG	polyglycerol	SP	slipping plane
pH	pondus hydrogenii, potential of hydrogen	SPT	single-photon transition
		SQT	single-quantum transition
pI	isoelectric point	SRT	shot repetition time
pK_a	acid dissociation constant	SSA	sheep serum albumin
PME	particle mesh Ewald	ST EPR	saturation transfer EPR
PMMA	poly(methyl methacrylate)	TCEP	tris(2-carboxyethyl)phosphine
PPE	*para*-phenylene-ethynylene	TEM	transmission EM
PSD	phase-sensitive detector	TEMPO	2,2,6,6-tetramethylpiperidine-1-oxyl
PSMA	prostate specific membrane antigen		
		THz	terahertz $= 10^{12}$ Hz
PTE	1,2-dipalmitoyl-*sn*-glycero-3-phosphothioethanol	TNF	tumor necrosis factor
		TOF	time-of-flight
PTFE	polytetrafluoroethylene	TPT	triple-photon transition
PTM	posttranslational modification	TWT	travelling-wave tube
QD	quadrature detector, quantum dot	UV	ultraviolet
r-DSA	reduced DSA	Vis	visible
RAGE	receptors for AGEs	VPT	volume phase transition
RF	radio frequency	% v/v	volume percent
RMSD	root-mean-square deviation	wt %	weight percent
RODEO	rotationally decoupled domains	WW II	world war II
ROE	rotating-frame Overhauser effect	XRD	X-ray diffraction
RP-HPLC	reversed-phase HPLC	XSA	comparable serum albumin
RRM	resonant recognition model	XSA-N	native XSA
RSA	rabbit serum albumin	YASARA	yet another scientific artificial reality application
SA	squaric acid		
SANS	small-angle neutron scattering	ZQT	zero quantum transition
SAXS	small-angle X-ray scattering	3D	3-dimensional
SBS	surveillance benchmark spin		
S.D.	standard deviation		
SDS	sodium dodecyl sulfate		
SDSL	site-directed spin labeling		
SEDOR	spin echo double resonance		
SH	sulfhydryl		
SIFTER	single-frequency technique for refocusing		

Symbols

a	micellar component of $S(B)$, parameter, hydrodynamic radius ($= R_H$)
a_B	steepness of magnetic sweep
a_{iso}	isotropic hyperfine coupling constant
A_{ii}	tensor components of $\boldsymbol{A}$ ($i \in x,y,z$)
A_λ	absorption at wavelength λ [nm]
$A_{//}$	outer extrema separation of $S(B)$
$A_\perp$	intermediate extrema separation of $S(B)$
$\boldsymbol{A}$	hyperfine coupling tensor
Å	Angström
b	bound component (b_i) of $S(B)$, parameter
b_1	bound ligand with Brownian diffusion
b_2	bound ligand with free diffusion
$b_s(t)$	time-dependent factor in $\boldsymbol{\sigma}(t)$
$\boldsymbol{B}$	magnetic field vector (B_x, B_y, B_z)
$B(t)$	background factor in DEER time trace
$B_{r.m.s.}$	DEER background fit root mean square
$\boldsymbol{B}_s$	base operators
$\Delta B_{0,pp}$	(center-field) peak-to-peak linewidth
B_0	center-field (or $B_{z,0}$) in $S(B)$
B_1	MW field strength
$\boldsymbol{B}_1(t)$	oscillating MW field vector
B_2	reorientational model parameter
B_{22}	second osmotic virial coefficient
$B(x_i)$	magnetic field readout values
dB_z	modulation amplitude
$\boldsymbol{B}_z(t)$	time-dependent magnetic field
c	concentration
c_{BCA}	protein concentration from BCA test
c_{corr}	corrected concentration
c_{nom}	nominal concentration
c_{ny}	LCAO coefficient of $2p_y$ orbital
c_{opt}	optimum spin concentration for DEER
c_P	total (core-shell) polymer concentration
c_r	real concentration
c_{SH}	SH concentration from Ellman's test
C	capacitance of MW resonator, spin concentration, viscometer constant
C_{DI}	spectrometer constant in DI procedures
$C_{k,p}$	binding site cooperativity of sample k and Scatchard phase p
C_n	alkylene chain with n segments
ΔC°_P	standard molar heat capacity change
$\Delta C^\circ_{P,IC}$	standard molar heat capacity change of ligand interconversion
d	loss factor of MW resonator, diameter
$d^l_{m,m}(\beta)$	Wigner rotation matrices
$\boldsymbol{d}^{(j,k)}$	nuclear dipolar coupling tensor
d_{Pn}	polymer shell thickness
D	fractal DEER background dimensionality
DI_0	maximum value of double integral (DI)
$D^l_{m,m'}(\Omega)$	Wigner rotation matrix elements
D_M	magnetization diffusion
D_T	translational diffusion constant
$\boldsymbol{D}$	dipolar coupling tensor between electron spins
$\boldsymbol{D}_0$	zero-field interaction tensor
$\boldsymbol{D}_r$	rotational diffusion tensor
E	total energy of electron
E_0	electronic ground state energy
E_a	Arrhenius activation energy
E_B	potential energy of electron in magnetic field $\boldsymbol{B}$
$E(R)$	electric field in distance $d = R - a$ from surface of charged sphere of radius a
E_x	effective electric field along NO bond
$\Delta E_{n \to \pi^*}$	lone-pair excitation energy
f	free component of $S(B)$, function $f(x)$
f_m	relative weight of $P_m(r)$
FAi	fatty acid identifier i
$F_i(B)$	subspectrum of $i \in a, b_1, b_2, f, g$ in $S(B)$
$F_{SF}(\kappa a)$	Henry's function
$F(t)$	form factor in DEER time trace
g	gel-like component of $S(B)$
$g_2(t)$	DLS exponential for smooth distribution
g_{ii}	tensor components of $\boldsymbol{g}_J$ ($i \in x,y,z$)
g_{iso}	isotropic Landé factor
$\boldsymbol{g}_J$	anisotropic Landé factor of the bound electron
g_N	nuclear g factor
$G(r)$	spin-spin pair correlation function
ΔG°_A	standard free energy change of ligand association
$\Delta G^\circ_{A,int}$	intrinsic ΔG°_A
ΔG_{el}	electrostatic free energy change
ΔG_f	free energy change of protein folding
ΔG°_{IC}	standard free energy change of ligand interconversion
$\hat{\boldsymbol{G}}$	smoothness differential operator
h_i	line height ($i \in -1, 0, +1, \perp, C, M,$)
$\hat{\boldsymbol{H}}_0$	static Hamilton operator of the electron
$\hat{\boldsymbol{H}}_i$	individual components of $\hat{\boldsymbol{H}}_0$
$\hat{\boldsymbol{H}}_1(t)$	time-dependent Hamilton operator
$\hat{\boldsymbol{H}}_2(\Omega)$	orientational Hamilton operator
$\hat{\boldsymbol{H}}^Z$	Hamiltonian commutation superoperator
ΔH°_A	standard molar enthalpy change of ligand association
ΔH°_{IC}	standard molar enthalpy change of ligand interconversion
$\Delta H_{v.H.}$	van't Hoff enthalpy
i	index, complex number
I	nuclear spin, ionic strength

I_{abf}	empirical parameter for analyzing $S(B)$		$N_{c,k}$	number of uncompensated charges in sample k (N_c = averaged value)
I_i	intensity of spectral features in ϕ_i		N_E	number of equivalent binding sites
I_{rel}	relative signal intensity		N_{FA}	number of fatty acids
$\boldsymbol{I}$	nuclear spin vector (I_x, I_y, I_z)		N_i	number of quantity i
$\hat{\boldsymbol{I}}$	nuclear spin vector operator		N_L	number of bound ligands
j	index, temperature [°C]		N_{max}	number of recorded data points
J	total angular momentum of electron, axial ratio of protein shape (a/b)		$N_{P(r)}$	number of FA as derived from $P(r)$
			$N_{r,m}$	number of interspin distances ($m \in$ FA, SBS)
J_{AB}	isotropic exchange integral			
k_e	spin exchange constant		N_S	number of strong binding sites ($= N_1$)
k_i	forward rate constant (k_a = assoc.)		N_{SBS}	number of spins in MTSSL XSA
k_{-i}	backward rate constant (k_d = dissoc.)		N_t	number of time steps in DEER time trace
k_j	temperature-specific rate constant		N_T	number of total ligand binding sites
k_L	correlation constant for simulation-free construction of Scatchard plots		$N_{T,int}$	integer number of N_T
			N_W	number of weak binding sites ($= N_2$)
$k_{p,i}$	reduction rate constant of order p		$N(x)$	no of polypeptide chain positions $x = N_{aa}$
k_Q	coefficient for predicting modification-dependent N_c of BSA from ζ potential		N_Δ	number of FA as derived from Δ
			p	pressure, coherence order, Scatchard phase
k_{SW}	sweep width correction factor			
k_{TD}	temperature equivalent of each 16-DSA		pH_{EA}	pH of electrostatic activation of 16-DSA spin probe ($\approx$ pI)
k_ζ	coefficient for predicting ζ potential from the degree of BSA's modification		pH_i	specific pH value of feature i
			pH_{opt}	pH of optimum HSA stability
K_A	association constant for ligand binding		$pK_{a,Lys}$	mean collective lysine pK_a
$K_{A,int}$	intrinsic K_A		P	probability
K_D	dissociation constant for ligand binding		P_0	MW power ($= P_{MW}$)
K_{IC}	interconversion constant ($b_1 \leftrightarrow b_2$)		$P_{AB}(r)$	DEER-derived peak ratio in $P(r)$ of 16-DSA-probed HSA
$K(t,r)$	Kernel function for dipolar interactions			
l	angular momentum of electron		P_{ALP}	value of albumin lot purity (≥ 0.95)
L	orbital angular momentum, inductivity of MW resonator		$[P]_f$	concentration of free receptors on protein
			$[PL]$	concentration of protein-ligand complex
$[L]_{af}$	$= [L]_a + [L]_f$		$P_m(r)$	interspin system contribution to $P(r)$ ($m =$ FA, SBS)
$[L]_b$	$= [L]_{b1} + [L]_{b2}$			
$[L]_i$	ligand concentration occurring in the components $i \in a, b_1, b_2, f, g$		$P_{max}(r)$	maximum probability density in $P(r)$
			$P_{MD}(r)$	calculated $P(r)$ from MD simulation
$[L]_t$	total ligand concentration		$P(r)$	probability density of distance r, full interspin system
m_I	spin projection quantum number of nucleus			
			$P(R_H)$	distribution function of R_H in DLS
m_p	photon spin state		$P(t)$	decay function of MW power dissipation
m_S	spin projection quantum number of electron		q	number of analytical coherent data points
			Q	total charge, quality factor of resonator
m/z	MALDI-TOF mass-to-charge ratio		Q_M	nuclear quadrupole moment
$M_{z,0}$	equilibrium magnetization		r	radius
$\boldsymbol{M}(t)$	time-dependent macroscopic ensemble magnetization		$\langle r \rangle$	first moment of $P(r)$, mean distance
			$\langle r^2 \rangle$	diffusion distance, mean squared particle displacement
n	refractive index, DP			
n_i	number of i		r_{cut}	cutoff radius for MD simulation
$\langle n \rangle$	average number of spins per cluster		r_{DI}	signal strength normalization factor for double integration
n_L	matrix element number in Liouville space			
			r_{ij}	distance between i and j
n_{pq}	Hilbert space dimension		$r_{max,\langle r \rangle}$	maximum valid DEER distance
N	amount, DP			
N_{aa}	polypeptide chain length			

$r_{max,\sigma}$	maximum valid DEER distribution width
r_{NO}	nitroxide bond length
R	resistance of MW resonator, radius, universal gas constant
R^+	contact radius in Percus-Yevick approximation ($= d^+/2$)
R	correlation coefficient = Pearson's R
$[R]_f$	free receptor concentration
$[RL]$	concentration of receptor-ligand complex
$[R]_t$	total receptor concentration
R^2	correlation coefficient
R_G	radius of gyration
R_H	hydrodynamic radius
$\boldsymbol{R}$	rotation operator
$\boldsymbol{R}_{\alpha\alpha'\alpha\alpha'}$	rotation matrix
S	electron spin, order parameter
$S(B)$	experimental EPR spectrum
$S(B)_{sim}$	simulated EPR spectrum
SLI_{min}	minimum scattered light intensity
S_m	polyglycerol chain with m segments
S_{max}	pH of maximum ligand order ($= \gamma_{min}$)
$\boldsymbol{S}$	electron spin vector (S_x, S_y, S_z)
$\hat{\boldsymbol{S}}$	electron spin vector operator
$\hat{\boldsymbol{S}}^+$	raising ladder operator for m_S
$\hat{\boldsymbol{S}}^-$	lowering ladder operator for m_S
S_G	electron group spin tensor
$\Delta S°_A$	standard molar entropy change of ligand association
ΔS_{CE}	molar change in conformational entropy
$\Delta S°_{IC}$	standard molar entropy change of ligand interconversion
t	time
t_0	time of pump pulse onset in DEER
$t_{0.95}$	time after 95% of signal has vanished
$t_{1/2}$	half-life
t_{BG}	onset time of background correction for DEER time traces
t_{cut}	cutoff-time in DEER time trace
t_d	resonator dead-time
t_{DEER}	duration of DEER experiment
t_E	evolution time of spin ensemble
t_f	viscometer flow time
t_{max}	accessible dipolar evolution time
t_{MD}	MD simulation runtime
Δt	length of timestep in DEER time trace
Δt_{MD}	length of timestep in MD simulation
t_p	duration of MW irradiation ($= t_{on}$)
t_r	ringdown-time of MW resonator
t_{SRT}	shot repetition time
t_X	time for one scan in DEER experiment
T	temperature
T_1	longitudinal relaxation time constant
T_2	transversal relaxation time constant

T_{AD}	apolar dehydration temperature
T_{AH}	apolar hydration temperature
T_D	melting/denaturation temperature
T_H	enthalpy compensation temperatures
T_m	phase memory time ($= T_{ID}$), midpoint or melting temperature
T_P	performance temperature
$\boldsymbol{T}$	dipolar coupling tensor for hyperfine interactions
u	parameter, function $u(x)$
U	voltage
U_{ij}	magnetic dipole interaction energy
$\boldsymbol{U}(t)$	propagator, exponential operator
v	parameter, function $v(x)$
V	volume
V_E	spin echo amplitude
V_H	hydrodynamic volume
V_{out}	receiver gain of EPR spectrometer
$V(R)$	potential in distance $d = R - a$ from surface of charged sphere of radius a
$V(t)$	time-dependent echo decay in DEER
$\boldsymbol{V}$	nuclear quadrupole tensor
$W(r)$	density function
$\hat{\boldsymbol{W}}$	identity operator
x	variable, inverse temperature (T^{-1}), SA equivalents on BSA from MALDI-TOF
X	number of scans in DEER experiments
Y	doxyl position index in stearic acid
$Y_{l,m}$	Legendre polynomials
$Y^{\pm Z}$	multivalent ions of charge z_i
z_i	charge number of ion i
Z	charge number of protein
Z_i	nominal equivalents of sample composition
$\hat{\boldsymbol{Z}}_L$	stochastic Liouville superoperator
α	1st Euler angle, regularization parameter, Nelder parameter
α_z	thermodynamic fit parameter ($1 < z < 5$)
β	2nd Euler angle, tilt angle of diffusion axis ($\boldsymbol{D}$) and magnetic parameters ($\boldsymbol{g},\boldsymbol{A}$)
β_i	Nelder parameters ($i \in 0, 1, 2$)
γ	3rd Euler angle, wobbling angle
γ_i	gyromagnetic ratio of i
γ_{min}	pH of minimum wobbling angle ($= S_{max}$)
Γ	quality parameter of DEER time traces
$\boldsymbol{\Gamma}_\Omega$	rotational diffusion operator
$\boldsymbol{\Gamma}_\Omega^D$	diffusion superoperator
δ	change, flip angle
δ_1	partial specific volume of solvent
δ	Dirac delta function
δ_{ij}	Kronecker symbol

Δ — modulation depth, difference, error

Δ_{max} — limiting value of Δ for maximally occupied 16-DSA-probed HSA

$\Delta\Delta$ — modulation depth uncertainty

ε — loss angle

$\varepsilon_{eff,Pn}$ — effective dielectric constant of solvent-pervaded polymer shell

ε_r — relative permittivity, dielectric constant

ζ — Zeta potential

η — dynamic viscosity ($= \eta_{dyn}$), stretching factor

$[\eta]$ — intrinsic viscosity

η_0 — dynamic viscosity of pure solvent

η_N — nuclear asymmetry parameter

η_r — relative/specific viscosity ($= \eta_{sp}$)

η_{red} — Y-DSA reduction efficiency

θ — magic angle, thermodynamic quantities

θ_{ij} — angle between magnetic moments i and j

Θ — Heavyside step function

κ — inverse Debye length λ_D^{-1}

κ_{el} — conductivity of a solution

κ_M — magnetization constant

κ_y — thermodynamic fit parameter ($1 < y < 8$)

λ — wavelength, modulation depth parameter

λ_D — Debye length

λ_{jm} — eigenvalues of the diffusion equation

λ_{SO} — spin-orbit coupling constant

Λ — out-of-equilibrium density

$\boldsymbol{\mu}_i$ — magnetic moment of i

μ_e — electrophoretic mobility

μ_r — relative permittivity

ν — frequency, Scatchard equilibrium

$\nu_\perp$ — $= (\omega_{dd}(\theta_{AB} = \pi/2)/(2\pi))$ in Pake pattern

ν_{FWHM} — width of resonator dip

$\nu_{NL \to 0}$ — y-axis intercept in Scatchard plot

ν_{obs} — $= \omega_A/2\pi$

ν_{pump} — $= \omega_B/2\pi$

$\Delta\nu_{EPR}$ — width of EPR spectrum

$\Delta\nu_{FWHM}$ — excitation bandwidth of MW pulse

ν_S — Simha parameter

ξ_{PRS} — maximum number of observable spin echoes from an applied pulse sequence

ρ — solution density

ρ_k — molecular density of sample k

$\rho_{N,\pi}$ — spin density on nitrogen nucleus

$\rho_{O,\pi}$ — spin density on oxygen nucleus

ρ_Q — charge density

$\boldsymbol{\rho}_{eq}$ — equilibrium density operator

$\boldsymbol{\rho}(t)$ — density matrix

σ — Gaussian broadening of individual distances in $P_{MD}(r)$, standard deviation, screened fraction of surface charges

σ_{MG} — width of MG state

$\boldsymbol{\sigma}_{eq}$ — reduced equilibrium density operator

$\boldsymbol{\sigma}(t)$ — reduced density matrix

τ — free spin evolution time ($= \tau_1$)

τ_2 — experimental dipolar evolution time

τ_c — rotational correlation time

τ_{jm} — time constant of diffusion equation

τ_r — residence time of ligand in substrate

$\phi(c)$ — excess volume fraction of protein

ϕ_ζ — fraction of ζ potentials (ζ_1/ζ_2)

ϕ_i — fraction of EPR spectrum $S(B)$, ($i \in a, b_1, b_2, f, g$)

$\phi_{SH,DEER}$ — DEER-derived labeling efficiency

$\phi_{SH,Ellman}$ — c_{SH}/c_{BCA} = labeling efficiency, accessible thiols per albumin

$\Phi(N_L)$ — arbitrary function for the description of binding site interaction

χ — magnetic susceptibility

$\chi(\omega)$ — dynamic magnetic susceptibility

ψ — electronic wave function, arbitrary molecular rotation angle in free diffusion

ω — angular frequency ($\omega = 2\pi\nu$)

ω_1 — MW field strength

ω_A — DEER observer frequency

ω_B — DEER pump frequency

ω_{dd} — dipolar coupling frequency ($= 2\pi\nu_{dd}$)

ω_{ee} — angular dependent electron-electron coupling frequency

ω_{eff} — effective MW field

ω_{kl} — transition frequencies

ω_L — Larmor frequency

ω_{mod} — modulation frequency

ω_{mw} — angular frequency of MW field

ω_S — resonance frequency

Ω — solid angle

$\Delta\Omega_k$ — comparative excess sum hydropathy according to hydropathy scale k

Ω_S — resonance offset of electron spins

Ω_Z — Zeeman frequency

Ω_x — sum hydropathy

Mathematical Expressions and Operations

d	infinitesimal difference
∂	differentiation operator
$\exp(x)$	exponential function ($= e^x$)
$f'(x)$	$= \mathrm{d}f(x)/\mathrm{d}x$, differentiation of function $f(x)$
$[A,B]$	interval between $A \leq x \leq B$
$\lvert A \rvert$	absolute value of A
$\lVert \boldsymbol{A} \rVert$	absolute value of vector $\boldsymbol{A}$
$\perp, \parallel$	principal values of an axial tensor
$Tr(\boldsymbol{A})$	trace of matrix $\boldsymbol{A}$
$\ln x$	natural logarithm ($\log_e(x)$)
$\log x$	decadic logarithm ($\log_{10}(x)$)
$\max\{f(x)\}$	maximum of function $f(x)$
$\min\{f(x)\}$	minimum of function $f(x)$
sgn	sign function
∞	infinity
$A \propto B$	A is proportional to B
$\boldsymbol{I}_3$	unity matrix (1_{xx}, 1_{yy}, 1_{zz})
$\forall_i$	valid for all i
$A \in B$	A is an element of B
$\boldsymbol{A}^{\mathrm{T}}$	transposed matrix $\boldsymbol{A}$
$\overline{\mathrm{AB}}$	line segment length from A to B
$\hat{\boldsymbol{A}}$	vector/matrix operator of A

1 | Motivation

In the last two decades, electron paramagnetic resonance (EPR) spectroscopy has rapidly evolved towards an exceptionally promising tool in the realm of magnetic resonance for structural and dynamic investigations in soft matter sciences. This comprises applications for polymers,[1–6] proteins,[7–11] or even more complex, self-organizing supramolecular systems.[12–16]

The main reason for this recent methodological proliferation in EPR is its intriguing ability to observe highly complex nano-objects in terms of their structural and spatial alignment, their transport properties, their intrinsic dynamics ranging from pico- to microsecond timescales,[9] as well as sensing the inherent chemical environment from distinct regions in these nanostructures.[2,17–21] This is either achieved by using intrinsic EPR-active paramagnetic species, or by introducing them artificially in order to generate covalent modifications, or non-covalent self-assemblies with appropriate radical-bearing guest species. In this regard, the meanwhile broad specialist field of EPR spectroscopy and its general applicability is widely covered in the notable Biological Magnetic Resonance Volumes, chiefly edited by Prof. Dr. L. J. Berliner.

Particularly, besides continuous wave (CW) EPR spectroscopy and many pulsed EPR and ENDOR applications,[22] the 4-pulse DEER technique[23,24] has evolved towards an exceptionally compelling tool for the routined extraction of distances and distance distributions from biomacromolecules in the range of 1.8 to 6.0 nm.[25] Additionally, the relatively small size of paramagnetic species[8] facilitates reduction of structural and dynamic impairments of the substrate molecule in comparison to e.g. fluorescent probes in Förster resonance energy transfer (FRET) studies,[26] altogether yielding sharper and narrower distance distributions.[27] This allows for tracing slight structural changes and conformational transitions in macromolecules with high accuracy.[8]

Furthermore, significant improvements in instrumentation are continuously advanced, as the extension towards quasi-optical THz-frequencies,[28,29] the development of ever faster electronic devices,[22] a 5-pulse DEER sequence with improved sensitivity,[30] high performance low-noise components (HiPER),[31–33] as well as the increasing availability of appropriate software packages and extensions for complex dynamic and structural EPR data evaluation.[34–45] This also justifies the resurgence of EPR spectroscopy from a specialist application to a more accessible popular method without losing its essential intellectual content. Therefore, EPR constitutes a powerful spectroscopic alternative to X-ray diffraction (XRD) and nuclear magnetic resonance (NMR) that facilitates to generally supplement established experimental techniques in structural biology and biophysical chemistry.[11,25] Particularly, the limitations of these mainstream methods are often based on molecular size, or ensemble disorder of the investigated nano-objects that may finally lead to the inaccessibility of structural components. In this regard, it could be already shown that spatial constraints from EPR spectroscopy may help to overcome these limitations.[46,47]

In this thesis, EPR spectroscopy is applied to several albumins and albumin-inspired model systems that are nowadays deliberately used in biochemistry, protein biophysics and polymer chemistry for

tracing changes in their structural and/or dynamic properties. The central theme throughout this thesis is dedicated to utilize these model systems in order to apply and derive strategies that should reveal further insights into the inherent functionality of albumins.

Being highly conserved major transport proteins, albumins are found in blood plasmas throughout the animal kingdom ranging from fish, reptiles, to mammals.[48] Intense effort has been deployed during World War II on the production of a blood plasma substitute for battlefield treatment of wounded soldiers. This was mainly achieved during the American Red Cross Blood fractionation program at Harvard Medical school in the group of Edwin Cohn.[49] Since then, albumin can be purified in large quantities and is commercially distributed in a multi-ton scale with an annual turnover of billions of dollars.[50] This generous availability has made albumin to a favorite model compound gaining wide attention in protein research since the 1940s. It is therefore also found as a reference compound in many biochemical applications as e.g. SDS PAGE,[51,52] ELISA,[53] Bradford tests,[54] or BCA tests,[55,56] not least due to its extraordinary stability and its well-known physicochemical properties.[57]

For a long time these so-called albumin *colloids* were considered as of minor functional importance apart from their passive role in creating oncotic pressure that represents the physical origin for blood volume maintenance.[50] Over time, it turned out that albumins additionally exhibit an overwhelming capability to bind a vast diversity of small molecules.[50,58–60] Consequently, this intrinsic functional adaptability and their physiological role as integral constituents for absorption, distribution, metabolism and excretion (ADME) of pharmacological ingredients ultimately established albumins as effective screening substrates for drug delivery studies[61] throughout various scientific disciplines.

Currently, 80 ligands have been co-crystallized with human serum albumin (HSA) alone that are stored in the protein data bank (PDB, accessed Jun 5, 2018).[62] Apart from two specific binding sites for anionic drugs, named the Sudlow sites,[50,59] the complex nature of fatty acid binding and the reasons for albumins' high structural adaptability still remains strongly elusive,[50] although a plethora of solid studies is available in this regard.

Albumins have been made accessible to EPR spectroscopy for the first time during the 1960s by the pioneering group of Prof. Harden McConnell at Stanford University.[63,64] Since then these proteins were thoroughly investigated by several EPR groups that came across this subject aiming to further unravel the intricate solution dynamics of this intriguing research object. Yet, mainly due to the lack of appropriate EPR spectroscopic methods and accessible evaluation tools in the 1970s and 1980s, several functional and dynamic features of albumins are still awaiting some scientific attention since then. Truly, in recent years albumin research was markedly resurrected in EPR spectroscopy.[65–69] However, for a better understanding of the underlying mechanistic and dynamic principles that govern the inner working of albumins, a modern and revisited approach is required that should transcend established biophysical strategies.

This hypothetical approach should be able to shed new light on several rudimentary functional aspects that persist to date and will certainly also persist beyond this thesis.

A significant step forward was successfully made in previous studies by utilizing the combination of CW EPR and in particular 4-pulse DEER.[65,66,70–73] This approach utilizes the mutual self-assembling properties of paramagnetic fatty acid ligands and albumins in order to extract meaningful distance distributions. These fatty acid-derived distributions furthermore provide indirect structural and dynamic features of albumin itself. The obtained results are then discussed from the perspective of bound fatty acids that can be correlated to the structural scaffolding of albumin, based on a readily available and appropriate crystal structure.[74] Despite these promising results, several physicochemical aspects, as well as spectroscopic strategies have to be traced, complemented, refined, developed, rationalized and consolidated in order to achieve a strong new functional picture of albumin. Beyond that, a conclusive and expandable research platform should be rationalized that provides general guidance for approaching this long-term objective. This subject can be regarded as the major impetus for this thesis.

The contents of this manuscript are organized in mainly five parts. The first part in **Chapter 2** is dedicated to theoretical aspects of CW EPR and DEER spectroscopy as it is deliberately used for all studies. Several concepts that are needed to understand shape and appearance of EPR spectroscopic data, as well as some basic principles behind data analyses are provided thoroughly. The second part in **Chapter 3** emphasizes a short historic survey of what is known about the structural and dynamic properties of albumins, while emphasizing previous findings from EPR spectroscopy. This comprises spin probing studies with e.g. paramagnetic fatty acids, as well as some spin labeling strategies that were applied so far. Additionally, some clues are given about the superordinate physiological context of fatty acids bound to albumin.

The third part ranges from **Chapter 4** to **Chapter 9** where several different concepts and ideas were tested. More precisely, the influence of albumin sequence homologies on internal fatty acid alignments is investigated for several species throughout **Chapter 4** and **Chapter 6**. In **Chapter 5**, the established experimental EPR-active albumin sample system[65,66] is subjected to a rigorous discussion for figuring out its practicability. Ultimately, experimental parameters are optimized in terms of comparability, reproducibility and significance of achievable data sets. These findings are then subsequently applied wherever they are suitable, or needed. The influence of posttranslational modifications (PTMs) on the functionality of albumins is investigated in **Chapter 7**. Therefore, several albumins with different chemical alterations were provided. Some further investigations are made beyond EPR spectroscopy in order to retrieve the physical origins of the observed functional responses. In **Chapter 8**, the influence that protein net charge exerts on the spectral shape from EPR-active albumin samples is examined in the range from about $1 < pH < 13$.

A proof-of-principle study that facilitates a completely different approach for observing bound fatty acids is presented in **Chapter 9**. It is illustrated how the well-known, fatty acid-based and DEER-derived distance distributions[65,70] change when a localized and covalently attached spin label is introduced to the system.

The fourth part generally aims for stripping down the complexity of albumin-fatty acid interactions to a least attainable minimum. Therefore, several albumin-analogue amphiphilic polymers are provided, that have been synthesized from click-coupled macromonomers, consisting of linear polyglycerol chains attached to alkylene methacrylate. These polymeric, brush-like structures aim to mimic a protein-like core-shell structure with a hydrophobic core and a hydrophilic shell, each with variable size. The corresponding findings from these polymers are rationalized in **Chapter 10**. As it is known that such core-shell structures facilitate ligand binding[75,76] and may also act as effective drug transporters with potential medical applications,[77] it will be tested to which extent this model system may contribute to a better understanding of the self-organizing properties of fatty acids and albumin. A situational thermodynamic model, based on CW EPR spectroscopic data, is developed from these polymers just in case they are susceptible for albumin-analogous fatty acid interactions. Subsequently, this thermodynamic model is tested on HSA in **Chapter 11**. Therein, several findings and strategies that were established in the course of this thesis are largely adopted and integrated. Thus, the result section concludes with a study that is only accessible when several established methods that are presented throughout this manuscript are ultimately combined. Naturally, this chapter then builds most bridges to previous sections in a synergistic fashion. It mainly goes along without many additional explicit theories allowing to mainly focus on functional aspects of the investigated protein. In case scientific contributions from cooperation partners or assistants are used, they are indicated conscientiously in an acknowledgment section at the end of a corresponding chapter.

Finally, the fifth part in **Chapter 12** comprises a conclusion and an outlook concerning the obtained results. This section corroborates the concept of an expandable EPR spectroscopic albumin research platform. Emphasis is placed on the general significance of this research platform for further studies that may also trespass the scope of EPR spectroscopy. The outlook also points constructively towards some critical issues from the results and furthermore indicates possible directions for the development of novel albumin paradigms. The content of this work partially ranges at the interface of protein and polymer science. Where appropriate, some analytic strategies are therefore tested for their transferability in between these disciplines as e.g. in **Chapter 7** and **Chapter 10**, as well as **Chapter 10** and **Chapter 11**. This thesis is written in a way, so that individual chapters may stand alone when according crosslinks are taken into account. The analytic complexity may vary strongly depending on feasibility and individual requirements. However, at decisive sections the different chapters and appendices are interlocked for preventing overflowing redundancy and for eventually pointing at alternative routes of analyses. Chapter introductions may appear repetitive, but decisive contents and related references are recapitulated independently and carefully according to the topics. All references are given in a secluded section at the end of this thesis, being sorted according to their appearance in individual chapters as it was done e.g. by Schweiger and Jeschke.[22] Supporting calculations, simulations, tables and reference experiments are placed in appropriate appendices.

2 | Theoretical Aspects of Electron Paramagnetic Resonance Spectroscopy

For a better understanding of the underlying physical principles of EPR spectroscopy, this chapter will elucidate some basic principles and scientific context comprising continuous wave (CW) and pulsed EPR in magnetic resonance as it is used in this work throughout.

Retrospectively, magnetic resonance can be seen as technically being an epiphenomenon of World War II and was a direct consequence of preceding achievements in physical sciences and engineering, in the latter case mainly aiming for radar development.[1] Since then magnetic resonance was subjected to an unpredictably creative and rapid development in an inconceivably wide range of applications, especially in biological sciences.

Since the value of the magnetic moment of an electron was experimentally identified by Procopiu[2] in accordance to the predicted value from Niels Bohr's atomic model,[3] a precise method for measuring and manipulating the orientation of magnetic moments was first described by Isidor I. Rabi from experiments on molecular beams of LiCl.[4] In 1940 L. Alvarez and F. Bloch were able to measure also the magnetic moment of the neutron.[5] Thus, it could be shown that atomic nuclei as well as nucleons also possess a magnetic moment. It was only a matter of time that it could be independently shown by E. K. Zavoisky and B. Bleaney that the investigation of paramagnetic resonance phenomena originating from magnetic moments of electrons in complex samples as solids are feasible.[6,7] Simultaneously, a more determined approach was established as "nuclear induction" by F. Bloch,[8] commonly referred to as NMR. This method expanded Rabi's findings from the molecular beam towards liquid and solid systems, and was soon spread in many laboratories for sample characterization due to its high intrinsic resolution. Similarly, EPR spectroscopic investigations in subsequent years also lead to a rapid exploitment of paramagnetic resonance phenomena after 1946.[9,10] In order to evolve a conclusive theoretical fundament for the studies herein, the physical properties of the electron are used as a starting point for a stepwise development towards interpretation of experimental findings from complex self-organized systems that are encountered throughout this work.

2.1 | The Electron Spin

The electron is an elementary particle falling into the scope of charged leptons. Therefore, as a fermion it bears a half-integer spin ($S = 1/2$), a negative elementary electric charge ($Q = -e$) and it has a distinct mass m_e, whereas its size is still not precisely known. Most probably it is a point-like particle[11] with a spherical shape[12] and a radius of $r < 2 \cdot 10^{-18}$ m or less.[13,14] After P. Zeeman demonstrated that the angular momentum l of electrons in cadmium ions interact with external magnetic fields,[15] W. Gerlach and O. Stern found that silver atoms have an additional magnetic moment as they experience a space quantization although its ground state is characterized by $L = 0$.[16,17] S. A. Goudsmit and G. E. Uhlenbeck therefore advanced a hypothesis accrediting this property to an intrinsic angular momentum s of the spinning electron that should be connected to a

magnetic moment μ_S.[18,19] They called this intrinsic spin angular momentum the electron spin S, as rotating charges generate magnetic vector potentials. For a free electron μ_S and S are connected via the relation:

$$\mu_S = -\frac{g_S \mu_B}{\hbar} \cdot S = -\gamma_S \cdot S \tag{2.1}$$

whereas the factor $\gamma_S = -g_S \mu_B / \hbar = 1.7609 \cdot 10^{11}$ rad T^{-1} s^{-1} gives the mutual relation between magnetic moment and electron spin. This factor is called the *gyromagnetic ratio* and it is composed of the Bohr magneton μ_B, the reduced Planck constant $\hbar$ and the Landé factor $g_S \approx 2.00232$ of the free electron.

2.1.1 | The Electron Spin in Magnetic Fields – Zeeman Effect

In case the free electron is exposed to an external static magnetic field $B = [0,0,B_z]$, the magnetic moment μ_S and therefore also S experience a spatial quantization as the electron can only adopt orientations $S_z = m_S \cdot \hbar = \pm (1/2)\hbar$ with $m_S = \pm 1/2$ being the spin projection quantum number. Those two spatial adjustments may be parallel (α) or antiparallel (β) to the magnetic field B_z. In a vectorial picture, quantization gives the magnitude of the spin angular momentum that is defined as:

$$|S| = \hbar\sqrt{S(S+1)} = \hbar\sqrt{\tfrac{3}{4}} \tag{2.2}$$

Comparing the magnitudes of S and S_z the angle between the magnetic field axis and spin orientation can be determined. Its value is defined as $\theta = \arccos((1/3)^{-1/2})$ and it is called the *magic angle* of spin precession ($\theta = 54.74°$).[20,21] The corresponding projected value of the magnetic moment $\mu_z = \mu_B m_S$ can be written as:

$$\mu_z = -\gamma S_z = -g_S \mu_B m_S \quad . \tag{2.3}$$

Being a magnetic dipole[22] the electron experiences a torque ($\mu \times B$) from the magnetic field with a resulting potential energy E_B of the size:

$$E_B = -\mu_S B = -\mu_z B_z \quad . \tag{2.4}$$

With respect to the electronic ground state energy E_0 the total energy E can be written as:

$$E = E_0 + E_B = E_0 + g_S \mu_B m_S B_z \qquad . \tag{2.5}$$

2.1.2 | The Paramagnetic Resonance Phenomenon

Upon electromagnetic irradiation the electron spin quantum state can be perturbed to change its orientation from parallel (α) to antiparallel (β) with respect to the external magnetic field B_z (**Figure 2.1**). This artificially induced electronic transition is facilitated by absorption of the oscillating magnetic field component B_1 of the incident electromagnetic wave. Therefore, the difference in

potential energy $\Delta E_B = E_\beta - E_\alpha$ between state β and α has to be absorbed by the electron by choice of an appropriate frequency ν obeying the resonance condition:

$$\Delta E_B = E_\beta - E_\alpha = 2E_B = g_S\mu_B B_z = h\nu = \hbar\omega \qquad , \qquad (2.6)$$

where the relation $\omega = 2\pi\nu$ holds for a transformation from frequency to angular frequency units. In EPR spectroscopy this resonance condition is usually fulfilled in the microwave frequency range from 1 – 360 GHz and at magnetic field values ranging from 0.03 – 12.80 T.[23] This work exclusively focuses on X-band frequencies in the range of 9.1 – 9.8 GHz corresponding to magnetic fields of $B_z =$ 0.33 – 0.35 T, whereas 1 Tesla = 10^4 Gauss.
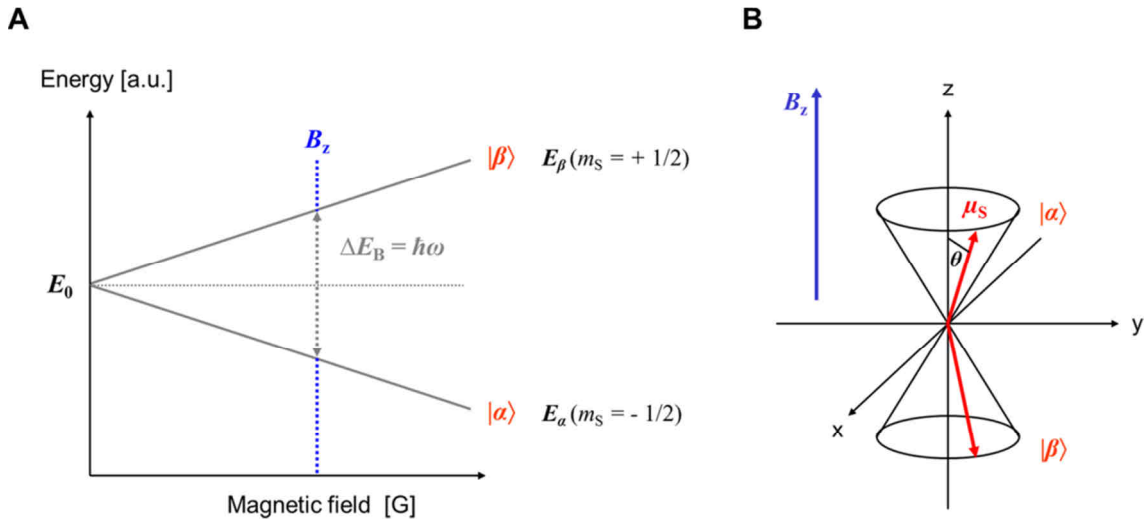
Figure 2.1 | An individual electron spin and its behavior in an external magnetic field B_z. (**A**) Energy scheme for a magnetic field-dependent energy splitting of eigenstates $|\alpha\rangle$ and $|\beta\rangle$ in terms of the resonance condition in equation 2.6. (**B**) Spatial quantization of the electron spin orientation with magic angle θ and corresponding precession cone.

2.2 | Electron Spin Ensembles

As we encounter large numbers of electron spins in an EPR sample, we will term them as a statistical spin ensemble as the occupation of the energy states E_α and E_β exhibits a Boltzmann-type behavior. This orientational spin polarization is strongly temperature-dependent occupying the energetically lower state α preferentially following the law:

$$\frac{N_\alpha}{N_\beta} = e^{\Delta E_B / k_B T} \qquad (2.7)$$

whereas N_i is the number of spins in each eigenstate $|\alpha\rangle$ and $|\beta\rangle$. From equation 2.7 it is also obvious that absorption will be much stronger for lower temperatures. Therefore this relationship is also called *spin temperature*.[10] At X-band microwave frequencies of $\nu = 9.4$ GHz and magnetic fields of $B = 0.34$ T the excess parallel spin fraction leading to a detectable signal is only 0.151% for 298 K but 3.052% at 150 K.[24]

2.2.1 | Ensemble Magnetization

According to Curie's law[25] the individual magnetic moments $\boldsymbol{\mu}_{z,i}$ of the spin ensemble resemble an equilibrium magnetization $\boldsymbol{M}_{z,0}$ per unit volume V in direction of the external magnetic field B_z:[26]

$$\boldsymbol{M}_{z,0} = \frac{1}{V}\sum_i \boldsymbol{\mu}_{z,i} = \frac{N \cdot g_S^2 \cdot \mu_B^2 \cdot S(S+1) \cdot B_z}{3k_B T} \qquad . \qquad (2.8)$$

The spin ensembles therefore sum up to a macroscopic magnetization that can be detected by an EPR spectrometer. As the time-dependent orientation of an individual spin S with its magnetic moment $\boldsymbol{\mu}$ generates a torque in a static magnetic field $\boldsymbol{B}_z$ an equation of motion can be defined:[27]

$$\hbar\frac{\mathrm{d}S}{\mathrm{d}t} = \boldsymbol{\mu} \times \boldsymbol{B}_z(t) \qquad (2.9)$$

with the corresponding ensemble denotation for multiple electron spins:

$$\hbar\frac{\mathrm{d}M}{\mathrm{d}t} = \boldsymbol{M} \times -\frac{g_S\mu_B\boldsymbol{B}_z}{\hbar} \qquad (2.10)$$

and $\boldsymbol{M}$ representing the macroscopic ensemble magnetization. All perturbations of the ensemble magnetization relative to its equilibrium by this torque cause a permanent precession on a cone around the z-axis with the Larmor frequency:

$$\omega_L = -\gamma_S B_z = g_S\mu_B B_z / \hbar \qquad (2.11)$$

and is tilted by the magic angle θ.

2.2.2 | Ensemble Magnetization Relaxation Processes in External Magnetic Fields

Without an external magnetic field B_z, the individual magnetic moments are randomly oriented in space. By switching the magnetic field on, the macroscopic magnetization $\boldsymbol{M}$ will emerge (**Figure 2.2A**). This magnetization equilibrium in z-direction is not established instantaneously but follows a well-defined time-dependence. For a complete description of this process two time constants are introduced: (*i*) the longitudinal or spin-lattice relaxation time constant T_1 that depends on the environment of the spin system and (*ii*) the transversal or spin-spin relaxation time constant T_2 that describes mutual interactions of spins in the system during the time t. Those two time constants obey the empirical differential equations:[10]

$$\frac{\mathrm{d}M_x}{\mathrm{d}t} = -\omega_L M_y - \frac{M_x}{T_2} \qquad (2.12)$$

$$\frac{\mathrm{d}M_y}{\mathrm{d}t} = +\omega_L M_x - \frac{M_y}{T_2} \qquad (2.13)$$

$$\frac{\mathrm{d}M_z}{\mathrm{d}t} = -\frac{\left(M_z - M_{z,0}\right)}{T_1} \qquad (2.14)$$

also termed as the Bloch equations[8] with M_i being the spatial components of $\mathbf{M}$. The solutions of equations 2.12 – 2.14 describe the exponential rise and decay of the equilibrium ensemble magnetization components $M_{i,0}$ until they reach equilibrium:[28]

$$\mathbf{M}(t) = \begin{pmatrix} [M_{x,0}\cos(\omega_L t) - M_{y,0}\sin(\omega_L t)]\cdot e^{-t/T_2} \\ [M_{y,0}\cos(\omega_L t) - M_{x,0}\sin(\omega_L t)]\cdot e^{-t/T_2} \\ M_{z,0} + [M_{z,\infty} - M_{z,0}]\cdot e^{-t/T_1} \end{pmatrix} \tag{2.15}$$

2.2.3 | The Effect of Continuous Microwave Irradiation $B_1(t)$

In case of continuous resonant irradiation, electromagnetic waves facilitate the induction of differences in electronic energy level occupation and the ensemble magnetization will inherently change its preferential group orientation from equilibrium as induced by the external magnetic field. Applying an oscillating monochromatic circular polarized microwave field $\mathbf{B}_1(t) = (B_1\cos(\omega_{mw}t)$, $B_1\sin(\omega_{mw}t),0)$ with a corresponding angular frequency ω_{mw} to B_z the field has to propagate in x-direction for tilting the magnetization $\mathbf{M}$ from z-direction. The result is a nutation around a so-called effective field ω_{eff} and an additional precession ω_1 in x-direction of the incident microwave (**Figure 2.2B**). Conveniently, a more illustrative representation is chosen where the coordinate system rotates with ω_{mw} while the magnetization rotates on a precession cone with an off-resonant Zeeman frequency $\Omega_Z = \omega_L - \omega_{mw}$ (**Figure 2.2A**). The magnetization $d\mathbf{M}/dt$ in the so-called *rotating frame* is accordingly described by a set of modified Bloch equations:

$$\frac{d\mathbf{M}}{dt} = \begin{pmatrix} -(\omega_L - \omega_{mw})M_y - \dfrac{M_x}{T_2} \\ -(\omega_L - \omega_{mw})M_x + \gamma_S B_1 M_z - \dfrac{M_y}{T_2} \\ -\gamma_S B_1 M_y - \dfrac{(M_z - M_{z,0})}{T_1} \end{pmatrix} = \begin{pmatrix} -\Omega_Z M_y - \dfrac{M_x}{T_2} \\ \Omega_Z M_x - \omega_1 M_z - \dfrac{M_y}{T_2} \\ -\omega_1 M_y - \dfrac{(M_z - M_{z,0})}{T_1} \end{pmatrix} \tag{2.16}$$

Upon additional consideration of magnetization diffusion D_M as caused by e.g. inhomogeneities in B_z, affecting relaxation rates and initial magnetization, the Bloch-Torrey equation applies:[29]

$$\frac{d\mathbf{M}}{dt} = \gamma_S(\mathbf{M} \times \mathbf{B}_z) - (\mathbf{M} - \mathbf{M}_0)\mathbf{R}_T + \nabla \cdot D_M \nabla(\mathbf{M} - \mathbf{M}_0) \tag{2.17}$$

with $\mathbf{R}_T$ describing the relaxation tensor. In the resonant case the effective field will equal the microwave frequency ($\omega_{eff} = \omega_1$) so that the Zeeman frequency contribution vanishes ($\Omega_Z = 0$) as shown in **Figure 2.2C**. Therefore, after sufficiently long irradiation times, a stationary magnetization state is established and time derivatives of the ensemble magnetization vector disappear ($d\mathbf{M}/dt = 0$). The termination of microwave irradiation after a time t_{on} will cause the system to pursue the adjustment of a recurrent equilibrium in $\mathbf{B}_z$-direction in the exponential time course of T_1 and T_2 according to equation 2.15.
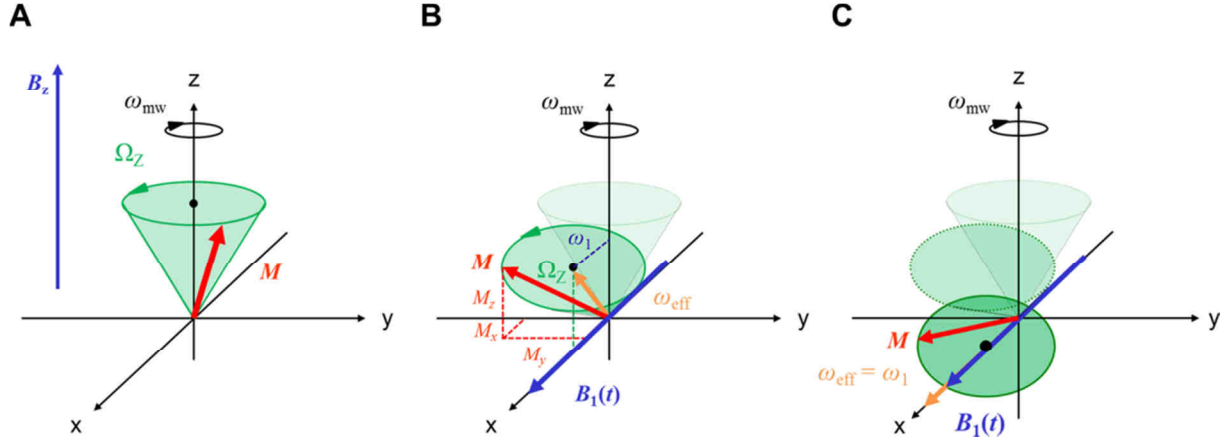
Figure 2.2 | Ensemble magnetization M exposed to microwave irradiation $B_1(t)$ in an external magnetic field B_z. (**A**) Ensemble magnetization in thermal equilibrium. (**B**) Off-resonant nutation of magnetization M along an effective field $\omega_{eff} \neq \omega_1$. (**C**) On-resonant precession of magnetization M with $\omega_{eff} = \omega_1$.

2.2.4 | Detection of an EPR Signal

The transverse magnetization components M_x and M_y are crucial for the detection of an EPR signal. For describing the uptake of microwave power in terms of the systems magnetization it affords to employ the complex notation of the dynamic magnetic susceptibility $\chi(\omega)$:[10]

$$\chi(\omega) = \chi'(\omega) + i\chi''(\omega) \tag{2.18}$$

as it is linked to magnetization by the relation $\chi = \mu_0 \mu_r M/B$ with μ_0 representing the magnetic constant and μ_r being the relative permeability.[26] Here, $\chi''(\omega)$ is an imaginary phasor describing the magnetization amplitude and $\chi'(\omega)$ is the phasor representing the real part of the dynamic magnetic susceptibility.[30] Hence, the loss tangent $\tan \varepsilon = \chi''(\omega)/\chi'(\omega)$ can be applied to determine the ratio of stored to lost power by the loss angle ε in the complex plane. This complex notation also facilitates the separation of the magnetic susceptibility in an in-phase ($\chi'(\omega)$) and 90°-out-of-phase ($\chi''(\omega)$) part relative to the microwave phase:[25]

$$M_x(t) = B_1[\chi'(\omega)\cos(\omega_{mw}t) + \chi''(\omega)\sin(\omega_{mw}t)] \tag{2.19}$$

With this relationship it can be shown that $\chi''(\omega)$ determines the lineshape of the absorption (**Figure 2.3A**) and $\chi'(\omega)$ its amplitude.[10] Both components can be measured simultaneously in a phase sensitive detector (PSD) or quadrature detector (QD) setup. In case of a two-level system as depicted in **Figure 2.1A**, the transversal relaxation processes lead to an absorption curve that can be expressed as a Lorentz function:

$$\chi''(\omega) = \frac{\omega_1 \chi_0 T_2}{2 + 2T_2^2(\omega - \omega_1)} \tag{2.20}$$

with the static susceptibility χ_0. Particularly, for paramagnetic species the magnetic susceptibility is $\chi > 0$. In a common experimental setup the sample is irradiated by linearly polarized electromagnetic

waves $\boldsymbol{B}_1(t) = (2B_1\cos(\omega_{mw}t), 0, 0)$ until the stationary state ($d\boldsymbol{M}/dt = 0$) is achieved.[10] With this constraint the Bloch formulation can be rearranged in a system of linear equations:

$$\boldsymbol{M}_\infty = \begin{pmatrix} M_x \\ M_y \\ M_z \end{pmatrix} = \begin{pmatrix} -\omega_1\Omega_Z T_2^2 \kappa_M^{-1} \\ \omega_1 T_2 \kappa_M^{-1} \\ (1+\Omega_Z^2 T_2^2)\kappa_M^{-1} \end{pmatrix} \tag{2.21}$$

with the magnetization constant $\kappa_M = M_{z,0}/(1+ \Omega_Z^2 T_2^2 + \omega_1^2 T_1 T_2)$ giving the Lorentzian lineshape of the absorption. The real (M_x) and imaginary (M_y) magnetization components are thus separated by a factor $M_x/M_y = \Omega_Z T_2$ and additionally comprise an intrinsic constant magnetization factor $M_{z,0}\omega_1$ (**Figure 2.3A**) giving the maximum signal amplitude of the real part (M_x). For low microwave powers following the relation $\omega_1^2 T_1 T_2 << 1$ the magnetization constant reduces to $\kappa_{red} = M_{z,0}/(1+ \Omega_Z^2 T_2^2)$.

In a typical CW EPR experiment (**Figure 2.3B**) the resonant microwave absorption process is realized by retaining the microwave frequency constant while the magnetic field $\boldsymbol{B}_z(t)$ is changed in order to detect the complete signal. This is typically done from lower to higher field-values with the steepness $a_B \cdot t$ in a magnetic field sweep embracing the sweep width $B_{max} - B_{min}$.[24] Furthermore, this external magnetic field determines the orientation of the lab coordinate system. For an additional amplification of the absorption signal from the paramagnetic sample, induction coils are used to modulate the B_z field of the magnet with an additional modulation amplitude dB_z and a corresponding modulation frequency $\omega_{mod} = 100$ kHz. The absorption curve (χ'') is therefore displayed as its derivative (χ') and constitutes a typical continuous wave (CW) EPR spectral shape (**Figure 2.3A**, red trace).
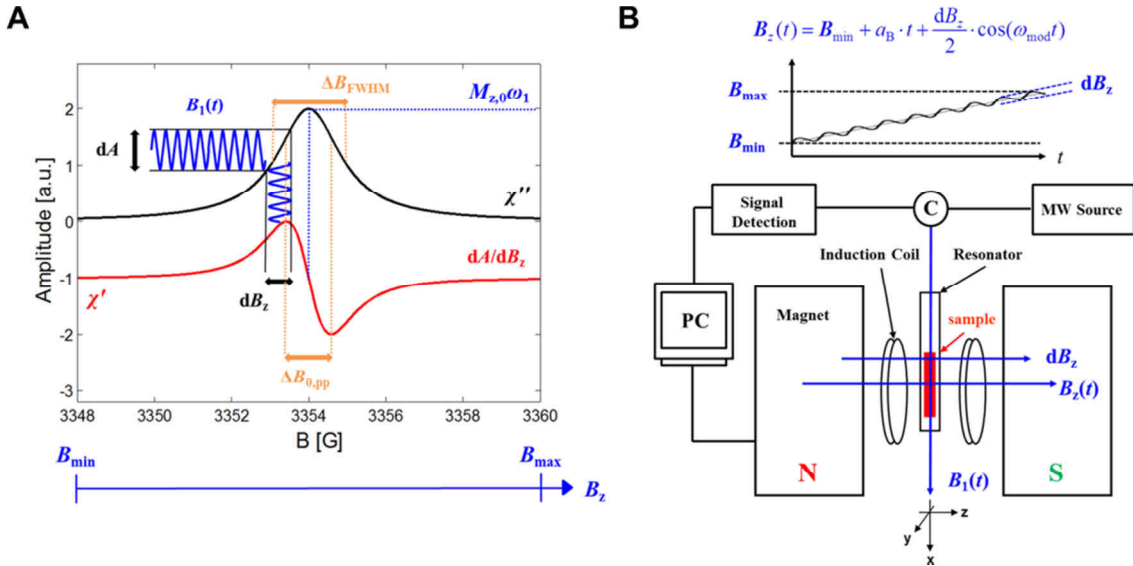
Figure 2.3 | Schematic representation of the signal detection in a CW EPR experiment. (**A**) The microwave absorption (black) was calculated with a Lorentzian function similar to equation 2.20 for a system at a X-band frequency of 9.4 GHz, g_S = 2.0023, $\Delta B_{FWHM} = 1.0$ G, sweep width = 12 G = 1.2 mT and a resulting resonant magnetic field at a value of $B_{z,0} = 3354$ G. (**B**) Experimental setup of a CW EPR experiment with all essential components as described in the text. The field sweep from B_{min} to B_{max} is visualized in a schematic graph of how the applied magnetic field $B_z(t)$ changes with time.[24]

The microwave travels from its source to the circulator where it is deflected towards the resonator bearing the sample. The resonators quality (Q) factor determines the amount of absorbed microwave energy. In case of resonance the signal is entering the detector upon repeated passage of the circulator and can be recorded with appropriate software on a PC. The parameters of a derivative absorption spectrum (χ') are mainly characterized by the g-value of the electron and therefore the position of the resonance line and its according peak-to-peak width $\Delta B_{0,\mathrm{pp}}$ that is defined as:[10,31]

$$\Delta B_{0,\mathrm{pp}} = \frac{2\sqrt{1 + \omega_1 T_1 T_2}}{\gamma_\mathrm{S} T_2 \sqrt{3}} \approx \frac{2}{\gamma_\mathrm{S} T_2 \sqrt{3}} \tag{2.22}$$

in case of low microwave powers ($\omega_1 T_1 T_2 \ll 1$). The FWHM-linewidth of the absorption spectrum (ΔB_{FWHM}) is related to the peak-to-peak linewidth of the derivative absorption spectrum by a factor $\Delta B_{0,\mathrm{pp}}/\Delta B_{\mathrm{FWHM}} = 3^{-1/2}$.

2.3 | The Paramagnetic System

In case the electron performs a gyration around a fixed point in space it develops an additional magnetic moment $\boldsymbol{\mu}_\mathrm{L}$. The resulting orbital angular momentum $\boldsymbol{L}$ gives rise to a total electronic angular momentum of $\boldsymbol{J} = \boldsymbol{L} + \boldsymbol{S}$ and a total electron magnetic moment of $\boldsymbol{\mu}_\mathrm{J} = \boldsymbol{\mu}_\mathrm{L} + \boldsymbol{\mu}_\mathrm{S}$ due to spin orbit coupling.[11] The total magnetic moment remains constant with L and S precessing around the direction of J. In principle, this leads to a more complicated behavior of the space quantization and the Landé factor of the electron is given as:

$$g_\mathrm{J} = 1 + \frac{J(J+1) + S(S+1) - L(L+1)}{2J(J+1)} \tag{2.23}$$

and describes pure spin magnetism ($S = J = \frac{1}{2}$ and $L = 0$) with a corresponding value of $g_\mathrm{J} = 2$.[11] In case an atom or molecule is located at the center of the electrons orbit it will cause the electron to couple to its specific orbital momenta and leads to a shift of the gyromagnetic ratio γ_J of the electron due to their physical interactions. Therefore, the resulting Landé factor g_J can be considered as a first characteristic parameter of the electronic environment in any atomic or molecular system.[24,25] The various physical interactions that an electron may undergo with its immediate environment are summarized in the following sections.

2.3.1 | The Static Spin Hamilton Operator $\hat{H}_0$

In order to describe the exact energetic eigenvalues of a paramagnetic system consisting of p effective electron spins S interacting with q nuclear spins I to which the electron is associated, a reduced Hilbert space with dimension n_{pq} is spanned:[27]

$$n_{pq} = \prod_{k=1}^{p}(2S_k + 1)\prod_{k=1}^{q}(2I_k + 1) \tag{2.24}$$

For a determination of energetic eigenvalues E_i of the paramagnetic system the time-invariant Schrödinger equation $E\psi = \hat{H}_0\psi$ can be applied, where ψ is the electronic wave function. The Hamilton operator $\hat{H}_0$ is defined to comprise all magnetic interactions of the electron with the external magnetic field and internal magnetic moments in its vicinity:

$$\hat{H}_0 = \hat{H}_{EZ} + \hat{H}_{ZFS} + \hat{H}_{HF} + \hat{H}_{NZ} + \hat{H}_{NQ} + \hat{H}_{NN} \tag{2.25}$$

Individual components in equation 2.25 are listed due to the strength of their individual energetic contribution. The different energy terms describe the aforementioned electron Zeeman interaction in external magnetic fields $\hat{H}_{EZ}$, the zero field splitting $\hat{H}_{ZFS}$, the hyperfine interaction between electrons and nuclei $\hat{H}_{HF}$, and the electron Zeeman-analogous nuclear Zeeman interaction in external magnetic fields $\hat{H}_{NZ}$, the nuclear quadrupole interaction $\hat{H}_{NQ}$, and the spin-spin interactions between pairs of nuclear spins $\hat{H}_{NN}$. In the following section expressions for individual contributions $\hat{H}_i$ will be given in angular frequencies.

2.3.2 | *g*-anisotropy and Electron Zeeman Interaction

While the electron couples to an atomic nucleus, the Landé factor develops directional properties in a magnetic field. After diagonalization of the $\boldsymbol{g}_J$ tensor with the Euler angles of the magnetic field vector an anisotropic extension of the electronic g value in a molecular coordinate system is obtained:

$$\boldsymbol{g}_J = \begin{bmatrix} g_{xx} & 0 & 0 \\ 0 & g_{yy} & 0 \\ 0 & 0 & g_{zz} \end{bmatrix} . \tag{2.26}$$

According to the molecular symmetry, the g factor can adopt either isotropic ($g_{xx} = g_{yy} = g_{zz}$), axial ($g_{xx} = g_{yy} \neq g_{zz}$) or rhombic ($g_{xx} \neq g_{yy} \neq g_{zz}$) symmetry. In a simplified view for axial symmetry the $g_{zz} = g_{\parallel}$ value is defined as being parallel to the principal axis of the molecular system and $g_{xx} = g_{yy} = g_{\perp}$ perpendicular to the corresponding principal molecular axis. For entire motional freedom as for small molecules in solution ($g_{\parallel} = g_{\perp}$) the so-called isotropic g_{iso}-value is given as:

$$g_J = g_{iso} = Tr(\boldsymbol{g}_J) = \tfrac{1}{3}(g_{xx} + g_{yy} + g_{zz}) \tag{2.27}$$

As the expectation value of L for a non-degenerate state is zero, the deviation of g_{iso} towards g_S originates from the interaction of excited states and ground states of the electron, while orbital angular momentum L from the excited states is admixed to the ground state.

Due to second-order perturbation theory the g_J-tensor can therefore be expressed as:[10,25]

$$g_J = g_{ij} = g_S \delta_{ij} - 2\lambda_{SO} \sum_{n \neq 0} \frac{\langle \psi_0 | L_i | \psi_n \rangle \langle \psi_n | L_j | \psi_0 \rangle}{E_n - E_0} \tag{2.28}$$

whereas δ_{ij} is the Kronecker symbol being 1 for $i = j$ or 0 in case $i \neq j$, and λ_{SO} is the spin-orbit coupling constant. Here ψ_0 is the wave function of the electron in the ground state, and ψ_n is the wave function of the n-th excited state of an unpaired electron with E_0 and E_n being the corresponding energies. As the excited states of organic radicals are high in energy the g-values mostly deviate less than 1% from g_S. This is contrary to transition metal ions that may cover a wide range of g-values facilitating a better spectroscopic identification while simultaneously providing information about the symmetry of the paramagnetic center. Introducing the electron spin vector operator $\hat{S} = (\hat{S}_x, \hat{S}_y, \hat{S}_z)$, the electron Zeeman term can be described as:[27]

$$\hat{H}_{EZ} = \mu_B g_J \hat{S} B_z / \hbar \tag{2.29}$$

Therefore, with increasing spin-orbit coupling to the electrons environment, the deviation Δg between the g_J-value and the Landé factor g_S will increase.

2.3.3 | Nuclear Zeeman Interaction

Atomic nuclei also bear the property to couple their spin to external magnetic fields. This coupling of q nuclear spins I_k with B_z is described by the nuclear Zeeman term:[27,32]

$$\hat{H}_{NZ} = -\frac{\mu_N}{\hbar} \sum_{k=1}^{q} g_{N,k} B_z \hat{I}_k \tag{2.30}$$

The nuclear $g_{N,k}$ factor, the nuclear magneton μ_N and the nuclear spin vector operator $\hat{I}_k$ are intrinsic properties of an atomic nucleus k. For detectable nuclei the scalar spin quantum number I_k may cover the range from 1/2 (^{1}H) to 6 (^{50}V) and is connected to an intrinsic magnetic moment $\mu_I = g_{N,k} \mu_N I_k / \hbar$. The projection on the z-axis $I_z = m_{I,k} \cdot \hbar$ may adopt $(2I_k + 1)$ values ranging from $-I_k \leq m_{I,k} \leq +I_k$. The electron Zeeman interaction is $g_S \mu_B / g_N \mu_N$ is almost 658 times stronger than for protons, for all other nuclei this ratio is even larger.

2.3.4 | Hyperfine Interaction

The hyperfine interaction $\hat{H}_{HF}$ between an electron spin and nuclear spins in its immediate environment provides important information in EPR spectroscopy. It is defined as the sum of the isotropic Fermi contact interaction $\hat{H}_{FC}$ and the dipolar coupling of the electron and nearby nuclei $\hat{H}_{EN}$:

$$\hat{H}_{HF} = \hat{H}_{FC} + \hat{H}_{EN} = \sum_k^q a_{iso,k} \hat{S} \hat{I}_k + \sum_k^q \hat{S} T_k \hat{I}_k = \sum_k^q \hat{S} A_k \hat{I}_k \quad . \tag{2.31}$$

T_k is the dipolar coupling tensor and A_k is termed the hyperfine coupling tensor (*vide infra*) and the factor a_{iso} of the Fermi contact term $\hat{H}_{\text{FC}} = \sum a_{\text{iso},k} \hat{S}\hat{I}_k$ is given by:

$$a_{\text{iso}} = \frac{2}{3} \frac{\mu_0}{\hbar} g_S g_N \mu_B \mu_N |\psi_0(0)|^2$$ (2.32)

The origin of the Fermi contact term is the non-vanishing spatial probability density $|\psi_0(0)|^2 \neq 0$ of an electron in the s-orbital at the nuclear locus ($L = 0$). In case an unpaired electron resides in an orbital with $L \neq 0$, the spin density can also be generated by exchange conditioned spin polarization mechanisms or orbital configuration interaction.[33] In the simplest case the magnetic moments of electron spin and nuclear spin give rise to a dipolar coupling that can be treated in analogy to the classical description of the magnetic dipole interaction energy U_{ij} of two different magnetic dipoles μ_i and μ_j separated by a distance r_{ij} with the point-dipole approximation:[34,35]

$$U_{ij}(r)_{\text{dip}} = \frac{\mu_0}{4\pi r_{ij}^3} \left[(\mu_i \cdot \mu_j) - \frac{3(\mu_i \cdot r_{ij})(\mu_j \cdot r_{ij})}{r_{ij}^2} \right]$$ (2.33)

Hence, r_{ij} is the vector connecting the positions of the individual magnetic moments. In terms of the magnetic moments μ_S of an electron and μ_I of a nucleus the dipolar interaction term $\hat{H}_{\text{EN}}$ can be expressed as:[10]

$$\hat{H}_{\text{EN}} = \frac{\mu_0}{4\pi \hbar r_{ij}^3} g_S g_N \mu_B \mu_N \left[\hat{S} \cdot I - \frac{3(\hat{S} \cdot r_{ij}) \cdot (\hat{I} \cdot r_{ij})}{r_{ij}^2} \right]$$ (2.34)

In the hyperfine principal axis system this dipolar interaction is given by the diagonal tensor:

$$T_k = \frac{\mu_0}{4\pi \hbar r_{ij}^3} g_S g_N \mu_B \mu_N \begin{bmatrix} -1 & & \\ & -1 & \\ & & -2 \end{bmatrix} = \begin{bmatrix} -T & & \\ & -T & \\ & & -2T \end{bmatrix}$$ (2.35)

As this representation is only valid for isotropic electron Zeeman interaction, it can only be applied where g_J-anisotropy is small. In a first approximation, neglecting g_J-anisotropy, the hyperfine coupling tensor A_k can be represented with the following relation:[10]

$$A_k = a_{\text{iso}} I_3 + T_k = Tr(A_k) \cdot I_3 + T_k$$ (2.36)

where a_{iso} is given as the trace of the anisotropic hyperfine coupling tensor ($Tr(A_k) = (A_{xx}+A_{yy}+A_{zz})/3$) while I_3 is the unit matrix.

2.3.5 | Nuclear Quadrupole Interaction

As the nuclear spin angular momentum is connected to the overall shape of the associated nucleus it will depend on the symmetry of its time-averaged charge distribution.[10] For atomic nuclei with spin $I_k \geq 1$ the charge distribution of the nuclear protons will exhibit a non-spherical symmetry.[36]

Therefore an electric field gradient (EFG) is generated by the electron charge distribution and other surrounding nuclei that couple to the electric nuclear quadrupole moment Q_M. The Hamiltonian is described as:

$$\hat{H}_{NQ} = \sum_{I_k \geq 1} \hat{I}_k^T V_k \hat{I}_k \qquad (2.37)$$

with V_k being the nuclear quadrupole tensor. The superscript 'T' indicates the transposed matrix of the nuclear spin operator $\hat{I}_k$. In its principal axis system V_k is traceless leading to the alternative notation:[37,38]

$$\hat{H}_{NQ} = V_{xx}I_x^2 + V_{yy}I_y^2 + V_{zz}I_z^2 = \frac{e^2 q_{zz} Q_M}{4I(2I-1)} \left[3I_z^2 - I(I+1) + \eta_N(I_x^2 - I_y^2) \right] \qquad (2.38)$$

including the nuclear asymmetry parameter $\eta_N = (V_{xx} - V_{yy})/V_{zz}$ and the electric field gradient $eq_{zz} = V_{zz} = \partial^2 V/\partial z^2$. The nuclear quadrupole interaction is disclosed in EPR spectra as a shift of resonance lines and in the appearance of forbidden transitions. However, both contributions as second-order effects are difficult to observe experimentally.

2.3.6 | Dipolar Couplings Between Two Electron Spins S_A and S_B

The complete characterization of a system of two weakly interacting electron spins S_A and S_B requires the definition of a Hamilton operator for each electron spin S_i. Due to their mutual coupling additional terms emerge that are best represented in an extended static spin Hamilton operator:[27]

$$\hat{H}_0(S_A, S_B) = \hat{H}_0(S_A) + \hat{H}_0(S_B) + \hat{H}_{HEC} + \hat{H}_{DD} \qquad (2.39)$$

The contributions leading to the static $\hat{H}_0(S_i)$ has been explicitly discussed in previous sections. The two additional terms $\hat{H}_{HEC}$ and $\hat{H}_{DD}$ specify Heisenberg exchange coupling (HEC) and dipole-dipole coupling (DD) of both electron spins. The term $\hat{H}_{HEC}$ describing exchange interaction gets increasingly relevant when two electron spins are approaching so that their individual wavefunctions ψ_i are overlapping. In this case the electrons transform energy in terms of a spin state exchange reaction or even exchange themselves. Exchange interaction can be described by the expression:[39]

$$\hat{H}_{HEC} = -2J_{AB}\hat{S}_A\hat{S}_B \qquad (2.40)$$

whereas J_{AB} is defined as the isotropic exchange integral. In solutions, an exchange interaction may occur in biradicals or during collisions of individual paramagnetic species. In principle, the collision frequency is determined by molecular diffusion and spin concentration.[40] In solids, exchange interaction is observed when electrons encounter at distances closer than about 1.5 nm or in case the electrons are strongly delocalized. In case of equivalent spins $S_A = S_B = 1/2$, the isotropic exchange integral J_{AB} can be considered as a chemical bond.[27]

For two dipolar interacting electrons in an external magnetic field both magnetic moments $\boldsymbol{\mu}_A = \boldsymbol{\mu}_B$ are equivalent and get aligned in $\boldsymbol{B}_z$-axis direction. The corresponding interaction energy $U_{AB}(r)_{dip}$ can be written as:[41]

$$U_{AB}(\boldsymbol{r})_{dip} = -\frac{\mu_0 \boldsymbol{\mu}_A \boldsymbol{\mu}_B \hbar^2}{4\pi r_{AB}^3}\left(3\cos^2\theta_{AB} - 1\right) \tag{2.41}$$

where θ_{AB} is the angle between both magnetic moments and their connection vector r_{AB}. The dipole-dipole coupling between two electron spins can be treated in analogy to the dipolar term (equation 2.34) of the hyperfine interaction resulting in the expression:

$$\hat{\boldsymbol{H}}_{DD} = \hat{S}_A^T D \hat{S}_B = \frac{\mu_0}{4\pi\hbar r_{AB}^3} g_A g_B \mu_B^2 \left[\hat{S}_A^T \hat{S}_B - \frac{3(\hat{S}_A^T \cdot \boldsymbol{r}_{AB})(\hat{S}_B^T \cdot \boldsymbol{r}_{AB})}{r_{AB}^2} \right] \tag{2.42}$$

Here, D is the dipolar coupling tensor that is mathematically identical to the dipolar coupling tensor T from hyperfine interaction and g_A and g_B are the g_J factors of the individual electron spins S_i. Detailed information concerning the extended static spin Hamilton operator may be found in Ciecierska-Tworek *et al.*[42] As the dipole-dipole coupling is proportional to r_{AB}^{-3}, inter-electron spin distances can be extracted. The observation of inter-electron spin distances is facilitated by filtering out the dipolar and exchange interactions by cooling down a sample below 200 K,[43,44] where all molecular motions can be assumed to be frozen and the resonance lines are broadened according to dipolar interactions. This method allows for an assignment of distances in the range of 10 – 22 Å for CW EPR[45] but may be extended to 8 – 25 Å for perdeuterated electron spin-bearing macromolecular samples.[46]

2.3.7 | Dipolar Couplings between Nuclear Spins

The observation of dipolar couplings is not restricted to electrons only but the same also occurs for atomic nuclei. The Hamiltonian $\hat{\boldsymbol{H}}_{NN}$ describing dipolar couplings between q nuclear spins is given by:[28]

$$\hat{\boldsymbol{H}}_{NN} = \sum_q \sum_{j,k}^{pairs} \hat{\boldsymbol{I}}_j \boldsymbol{d}^{(j,k)} \hat{\boldsymbol{I}}_k \tag{2.43}$$

In solid state NMR the nuclear dipolar coupling tensor $\boldsymbol{d}^{(j,k)}$ provides a crucial source of structural information on macromolecules as polymers and proteins.[47] As the dipolar coupling frequency is proportional to r_{AB}^{-3} inter-spin distances can be extracted in e.g. homonuclear proton ^1H NMR experiments applying nuclear Overhauser effect spectroscopy (NOESY).[47–50] In EPR extraction of bond angles and dipolar couplings is not as straightforward as in NMR as the observed lines also depend on the internal magnetic fields generated by the electron at nuclei I_j and I_k and additionally on the electrons magnetic quantum number m_S.[27]

2.3.8 | Zero-field Splitting

In a system of electrons with group spin $S_G = \sum_k S_{G,k} > 1/2$ the degeneracy of the ground state is cancelled due to the dipole-dipole coupling of the electron spins. Therefore, line splittings can be observed even in the absence of an external magnetic field. In the principal axis system of the zero-field interaction tensor $\boldsymbol{D}_0$ the Hamiltonian is defined by the fine structure term:[27]

$$\hat{H}_{ZFS} = \hat{S}_G^T \boldsymbol{D}_0 \hat{S}_G = D_{0,x} S_{G,x}^2 + D_{0,y} S_{G,y}^2 + D_{0,z} S_{G,z}^2 \quad . \tag{2.44}$$

Zero-field splitting caused by exchange interaction in solution between two spin-bearing paramagnetic molecules (as in **Chapter 2.3.6**) may provoke a splitting of singlet ($\uparrow\downarrow$, $S_G = 0$) and triplet states ($\uparrow\uparrow$, $S_G = 1$). Usually, this effect is cancelled out due to rapid molecular motion and is therefore difficult to observe. This effect gets prominent e.g. at X-band frequencies for high spin Fe^{3+} $3d^5$ EPR resonance lines ($S_{G,3+} = 5/2$) where the effective g-value is shifted relative to the low spin Fe^{1+} $3d^7$ ($S_{G,1+} = 1/2$).[10]

2.4 | Nitroxides

A major drawback of EPR spectroscopy is that only few macromolecular systems contain intrinsic paramagnetic species as e.g. metalloproteins.[51] However, in order to circumvent this situation, diamagnetic macromolecular systems can be provided with artificial paramagnetic species. This is facilitated either by admixture or by covalent attachment of spin-bearing molecules to the substrate. In this regard, stable nitroxide free radicals[52,53] have proven to be by far the most suitable tracer molecules as they commonly exhibit high resilience against chemical and physical impacts and therefore allow for a wide variety of physicochemical and biophysical studies.[54] A representative overview of the most commonly used nitroxides is given in **Figure 2.4**. Those nitroxide species can be separated into spin probes (I–III) and spin labels (IV–VI) and may be specifically applied for screening intrinsic structural and dynamic features of a solution. As spin probes are usually applied to detect hydrophobic (I,III) and electrostatic interactions (II) or general ligand binding properties (I–III), spin labels can be used to study structural properties as inter- and intramolecular distances.[45]

Simultaneously, dynamic properties can be obtained from covalently attached spin labels (IV–VI) that arise from internal motions of a macromolecule that intricately depend on the strategic selection of significant topological and functional environments.[55] Notably, in recent years this *site-directed spin labeling* (SDSL) approach as established in the group of Harden McConnell has yielded wide acceptance and high regards in EPR spectroscopy.[56–58] SDSL with nitroxides turned out to be a decisive tool that may essentially contribute for the elucidation of structural and dynamic properties of biological and synthetic macromolecules.[55,59–66]
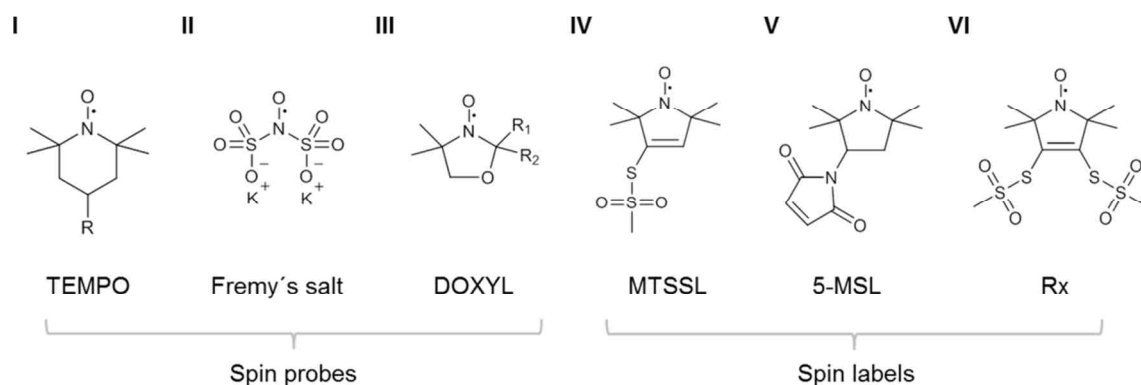
Figure 2.4 | Chemical structures of most commonly used nitroxides in EPR spectroscopy. They can be subdivided into spin probes: (**I**) 2,2,6,6-tetramethylpiperidine-1-oxyl (TEMPO), (**II**) Potassiumnitrosodisulfonat (Fremy's salt), (**III**) 4,4-dimethyl-oxazolidine-1-oxyl (DOXYL: R1, R2 are usually alkylene chains) and into covalently bound spin labels: (**IV**) (1-oxyl-2,2,5,5-tetramethylpyrroline-3-methyl)methanethiosulfonate (MTSSL)), (**V**) 3-Maleimido-2,2,5,5-tetramethyl-1-pyrrolidinyloxy (5-MSL or 3-MP), (**VI**) (1-oxyl-2,2,5,5-tetramethyl-pyrroline-3,4-bis-methyl)methanethiosulfonate (Rx).

2.4.1 | Quantum Mechanical Specification of Nitroxides in EPR spectroscopy

For homogenously distributed nitroxides in solution a spin system with $S = 1/2$ and $I = 1$ is now considered in order to account for interactions of the unpaired electron and the ^{14}N nucleus in correspondence to the Hamiltonian that was set up in **Chapter 2.3**. Although microwave irradiation induces a time-dependent character to the system with its linearly oscillating field $\boldsymbol{B}_1(t) = (2B_1\cos(\omega_{\mathrm{mw}}t), 0, 0)$, the corresponding Hamiltonian should be written as:[27]

$$\hat{\boldsymbol{H}}_1(t) = g_{\mathrm{J}}\mu_{\mathrm{B}}\boldsymbol{B}_1(t)\hat{S} / \hbar \tag{2.45}$$

that represents the static oscillatory Hamiltonian ($\hat{\boldsymbol{H}}_1$) in the rotating frame (ω_{mw}). As it was shown in **Chapter 2.1**, absorption of photons may cause changes in electronic quantum states where a differentiation of single-quantum transitions (SQT) and multi-quantum transitions (MQT) in the nitroxide system is inevitable. The SQT between the two eigenstates $|k\rangle$ and $|l\rangle$ of the static Hamiltonian $\hat{\boldsymbol{H}}_0$ with wavefunctions ψ_k and ψ_l has a transition amplitude:

$$c_{kl} = \left\langle \psi_k \middle| H_1 \middle| \psi_l \right\rangle \tag{2.46}$$

where c_{kl} is the matrix element that combines the eigenstates with the corresponding transition probabilities $P_{kl} = |c_{kl}|^2$. As photons are (gauge) bosons their angular momentum $J_z = m_{\mathrm{p}}\hbar$ can adopt values from $-\hbar < J_z < +\hbar$. The space quantization of the angular momentum allows to distinguish between left (σ^+, $J_z = +\hbar$) and right handed circular polarization (σ^-, $J_z = -\hbar$) or linear polarization of so-called π-photons ($J_z = 0$). For single-photon transitions (SPT) the angular momentum is conserved for a radiation field perpendicular to the quantization direction of the spin. Therefore π-photons bear a linear oscillating field $\boldsymbol{B}_1(t)$ parallel to the magnetic field axis $\boldsymbol{B}_z$. For systems with unequally spaced

energetic eigenstates k, l, m and n, two or more photons with the same frequency may be absorbed coincidentally. In **Figure 2.5A** it is depicted, that the transition from eigenstates k to n may be attained by three consequent SPTs, by multi-photon transitions (MPT) as two different double-photon transitions (DPT) or a triple-photon transition (TPT). For example, the DPT can be considered as a forbidden transition $\Delta m_S = \pm\,2$. Introducing virtual energy levels (l', m'), such transitions can be described as a proceeding in two consequential steps e.g. from k across l' to m with a transition
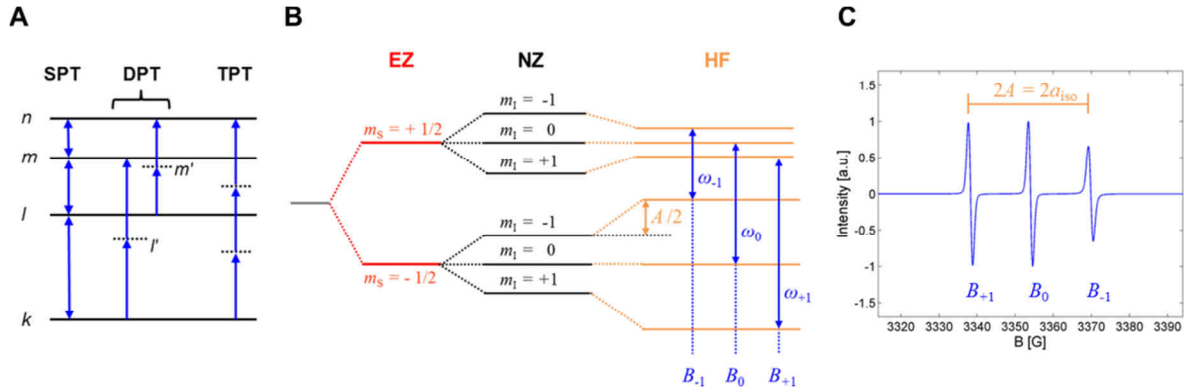

Figure 2.5 | Quantum mechanical description of the nitroxide EPR signal. (**A**) Rationale of single-photon transition and multi-photon transitions (MPT) as double- (DPT) and triple-photon transitions (TPT) from eigenstates k to n.[27] (**B**) Energetic eigenstates of a nitroxide radical comprising electron-Zeeman (EZ), nuclear-Zeeman (NZ) and hyperfine (HF) interactions and three allowed electronic transitions (ω_{-1}, ω_0, ω_{+1}). (**C**) Representation of a typical three-line quasi-isotropic CW EPR nitroxide spectrum for 16-doxyl stearic acid (16-DSA) in DPBS buffer at pH 7.4 and $T = 25°C$. The isotropic hyperfine coupling constant A is shown in (B) and (C) as the line splitting between low-field peak (B_{+1}), center-field peak (B_0) and high-field peak (B_{-1}).

amplitude c_{km} that is proportional to $B_1(t)^2$. Energetic eigenstate transitions are usually described in perturbation theory by ladder operators, whereas $\hat{S}^+$ is the raising and $\hat{S}^-$ is the lowering operator constituting a mathematical switch of the magnetic spin quantum number state from $|m_S\rangle$ to $|m_S \pm 1\rangle$.

Dilute individual nitroxides (**Figure 2.5B**) are characterized only by electron-Zeeman ($\hat{H}_{EZ}$), nuclear-Zeeman ($\hat{H}_{NZ}$) and hyperfine interactions ($\hat{H}_{HF}$) as zero-field splitting ($\hat{H}_{ZFS}$), dipole-dipole couplings between electrons ($\hat{H}_{DD}$) and nuclei ($\hat{H}_{NN}$) are too small or do not occur. Effects due to nuclear quadrupole interaction ($\hat{H}_{NQ}$) are also considered to be negligible,[67] resulting in the following spin Hamiltonian:

$$\hat{H}_{NO} = \hat{H}_{0,NO} + \hat{H}_{1,NO}(t)$$
$$\hbar\hat{H}_{NO} = g_J\mu_B\hat{S}B_z - g_N\mu_N\hat{I}B_z + \hat{S}A\hat{I} + \tfrac{1}{2}g_J\mu_B B_1\left[\hat{S}^+e^{-i\omega_{mw}t} + \hat{S}^-e^{+i\omega_{mw}t}\right]$$

(2.47)

where $\hat{H}_{1,NO}(t)$ is the additional time-dependent interaction of the electron spin with the oscillating magnetic field $B_1(t)$ by rewriting the spin operator $\hat{S}$ to the ladder operators $\hat{S}^\pm = \hat{S}_x \pm i\hat{S}_y$.[25,67] The energetic eigenvalues can be obtained by solving the Schrödinger equation for all energetic eigenstates that are related to isotropic rotation:[10]

$$U_{NO}(m_S, m_I) = g_{iso}\mu_B m_S B_z - g_N\mu_N m_I B_z + a_{iso}m_S m_I$$

(2.48)

According to the selection rules for magnetic dipole transitions corresponding to $\Delta m_S = \pm 1$ and $\Delta m_I = 0$, finally three allowed transition frequencies ω_I are obtained from the relation:

$$U_{NO}(m_I) = g_{iso}\mu_B B_z + a_{iso}m_I \tag{2.49}$$

Due to the spin multiplicity $2(I + 1)$, three equidistant resonances are obtained for nitroxides with adjacent lines separated by the isotropic hyperfine coupling a_{iso} exhibiting equivalent intensity. This is of course not always true.

2.4.2 | Nitroxide Dynamics

The theory developed so far is capable to construct the shape and position of resonance lines based on the Hamiltonian set up in equation 2.47, but only allows a description of the simplest nitroxide spectra for isotropically tumbling molecules. As the nitroxide spin probe and spin label molecules can be introduced to a vast amount of different dynamic environments, CW EPR spectra are mainly determined by polarity, viscosity and dynamic topology, as well as by their own intrinsic molecular geometry and nuclear composition. Physical information from nitroxides about the sample is often hidden in details of resonance lines or vanishes if several spectral components overlap when sensing different environments in the statistic ensemble of a sample. In fact, nitroxides are exceptionally prone for changing lineshapes, line positions and relative intensities in a highly non-trivial manner. However, those properties prove them being indispensible for investigative macromolecular applications. The physical principles of the dynamic sensitivity of nitroxides are illustrated in the following sections.

2.4.2.1 | Influence of Polarity on Nitroxide CW EPR Spectra

The local environment may decisively affect the nitroxide moiety bearing the unpaired electron. As the electron is delocalized along the $2p_z$ orbital of the N-O bond, the spin density is not exclusively localized on the ^{14}N nucleus giving rise to the hyperfine interaction $\hat{H}_{HF}$. The isotropic hyperfine coupling constant a_{iso} is rather related to the spin density fraction $\rho_{N,\pi}$ of the nitrogen nucleus due to the Karplus-Fraenkel relation:[68,69]

$$a_{iso} = Q_N\rho_{N,\pi} + Q_{NO}\rho_{O,\pi} \tag{2.50}$$

where $Q_N \gg Q_{NO}$ are constants and $\rho_{O,\pi}$ is the spin density on the oxygen atom with $\rho_{N,\pi} + \rho_{O,\pi} = 1$. In a first approximation this equation reduces to a simple McConnell relation ($a_{iso} = Q_N\rho_{N,\pi}$)[70–72] with $Q_N = 21.9$ G.[73] The exact value of Q_N is disputed as the spin density may differ for aromatic and non-aromatic nitroxides giving values from $0.6 \leq \rho_{N,\pi} \leq 0.9$ and therefore also depends on the type of paramagnetic system.[74,75] The enhanced Zeeman resolution of high-field EPR revealed that the magnetic tensor components of g_J and A are heavily affected by polarity and proticity.[76–78] Particularly, the g_{xx} and A_{zz} values may be consulted to distinguish between polar and apolar

environments.[75,76] There are three contributions leading to changes in magnetic tensor components: (*i*) the electron spin density $\rho_{N,\pi}$ on the nitrogen nucleus, (*ii*) H-bonding, leading to a change (δ) of the partial electron density c_{ny}^2 of lone-pair orbitals (c_{ny} presents the linear combination of atomic orbital (LCAO) coefficient of the $2p_y$ orbital) and (*iii*) the associated changes in difference of lone-pair orbital energy (E_n) and excitation energy $\Delta E_{n\to\pi^*}$ represented by $\delta\Delta E_{n\to\pi^*}$. The lone-pair ($n \to \pi^*$) excitation energy $\Delta E_{n\to\pi^*} = E_{\pi^*} - E_n$ is the difference of the π^* orbital energy E_{π^*} and lone-pair orbital energy (E_n), so that $\Delta E_{n\to\pi^*} = E_{\pi^*} - E_n$.[78,79] Hence, any change $\delta\Delta g_{xx}$ in $\Delta g_{xx} = g_{xx} - g_S$ can be described with the expression:

$$\frac{\delta\Delta g_{xx}}{g_{xx}} \cong -\frac{\rho_{N,\pi}}{\rho_{O,\pi}}\cdot\frac{\delta A_{zz}}{A_{zz}} - \frac{\delta\Delta E_{n\to\pi^*}}{\Delta E_{n\to\pi^*}} + \frac{\delta c_{ny}^2}{c_{ny}^2} \tag{2.51}$$

This equation correctly predicts the negative slope in g_{xx}-A_{zz}-plots[76] and furthermore helps to distinguish between protic and aprotic polar environments that modify the slope with the two last terms. As the lone-pair orbital energy E_n, that affects g_{xx} via the excitation energy $\Delta E_{n\to\pi^*}$, is also sensitive to electrostatics, the Onsager model allows to introduce an effective electric field E_x along the NO-bond, emerging from permanent electric dipole interactions, intermolecular electrostatic fields and induced dipole interactions with surrounding solvent molecules.[80,81]
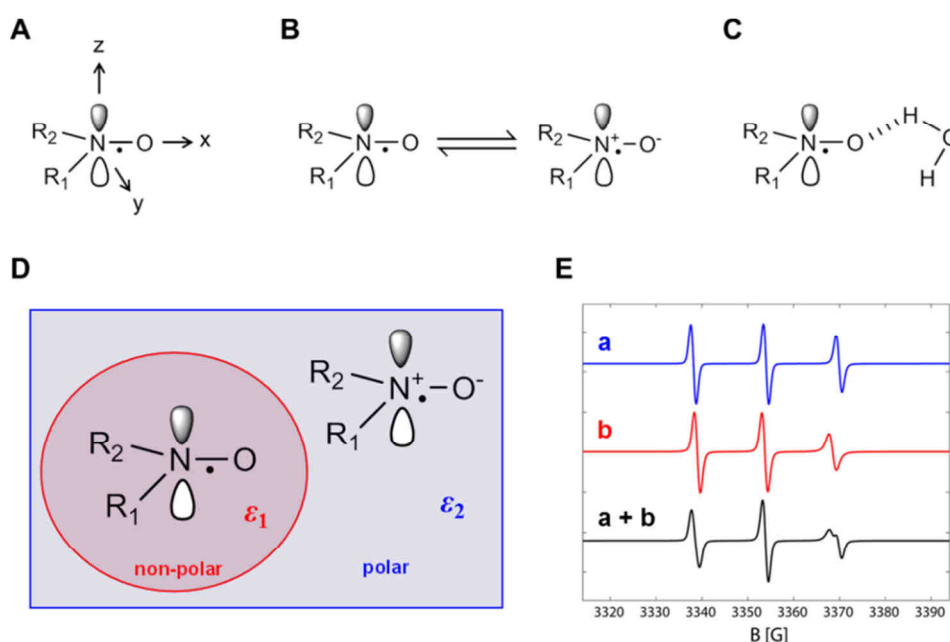
Figure 2.6 | Polarity dependence of nitroxides in EPR spectroscopy. (**A**) Definition of the molecular coordinate system of a nitroxide. (**B**) The stabilization of a zwitterionic structure of the nitroxide leads to a shift of spin density, here: towards the nitrogen atom. (**C**) Hydrogen-bonding affects the lone-pair orbital energy E_n and therefore induces changes in g_{xx}. (**D**) Sample with two environments of different polarity and intrinsic dielectric constants ε_1 and ε_2 with $\varepsilon_2 \gg \varepsilon_1$. (**E**) Corresponding simulated EPR spectra from the situation in (D). The polarity difference is sensed by the nitroxide moieties of the statistic ensemble assuming a population of polar (a) and non-polar environments (b) in a ratio of 50% each with a resulting multi-component EPR spectrum (a + b).

For X-band frequencies the changes in π-spin density on the ^{14}N nucleus may be expressed in units of a_{iso} as follows:[75]

$$\Delta a_{iso} = a_{iso} - a_{iso,\varepsilon_r = 1} = k_\rho \cdot \frac{(\varepsilon_r - 1)}{(\varepsilon_r + 1)} \ [G] \tag{2.52}$$

Hence, for electric neutral media ($\varepsilon_r \approx 1$) the change in a_{iso} is 0 G and a_{iso} will be at a constant minimum value $a_{iso,\varepsilon r = 1}$. For high ε_r-values, the hyperfine coupling will increase due to the closer proximity of the electron towards the nitrogen nucleus. The prefactor k_ρ is a nitroxide specific constant. For di-t-butyl nitroxide (DTBN) an exemplary value $k_{\rho,DTBN} = 0.8$ is reported,[75] therefore a maximum change in $\Delta a_{iso,max} = 0.8$ G is predicted ($\varepsilon_r \rightarrow \infty$) from equation 2.52. However, in high-field EPR experiments maximum changes in g_{xx} and A_{zz} of $\delta\Delta g_{xx,max} \approx 7 \cdot 10^{-4}$ and $\delta A_{zz,max} \approx 3.6 - 4.0$ G were observed.[78,82] The impact on the spectral shape for X-band CW EPR experiments is shown in **Figure 2.6** for an exemplary system consisting of two environments of varying dielectric constant $\varepsilon_1 << \varepsilon_2$. As nitroxide spectra from two environments differing in their polarity do not only depend on the dielectric constant and solvent, but also may exhibit different viscosities, the next section will be involved with their rotational dynamics.

2.4.2.2 | Influence of Rotational Diffusion on Nitroxide CW EPR Spectra

All static interactions are anisotropic. Thus, the relative orientation of a molecule towards the external magnetic field leads to a shift in resonance line positions. Hence, the appearance of an EPR spectrum does not only depend on static interactions but will also be affected by dynamic processes that are not extremely slow on the EPR timescale as e.g. the molecular tumbling in solutions or membranes.[83] The translational diffusion as a change in molecular position is not resolved in a CW EPR spectrum. Only the relative orientation modulates resonance frequencies and induces transitions by generating fluctuating local magnetic fields. This rotational diffusional motion is a random process and is characterized by the rotational correlation time τ_c that illustrates the time constant of the exponentially ceasing alignment of molecules with the same initial orientation.[25,84] Therefore, the lineshape of nitroxide EPR spectra is strongly sensitive to rotational diffusion so that its timescale can be separated in four dynamic regimes. In the *isotropic limit* ($\tau_c \leq 10$ ps), anisotropic properties of tumbling paramagnetic molecules are averaged out and only g_{iso} and a_{iso} as well as symmetric resonance lines with equal width are observable. The *fast-motion regime* ($\tau_c \leq 1$ ns) exhibits the onset of varying individual linewidths and upon further immobilization it traverses into the *slow-motion regime* ($\tau_c \geq 1$ ns) where the resonance lines are increasingly broadened and distorted considerably in a highly nontrivial manner. Maximum spectral anisotropy is observable for an additional slowdown towards the *rigid limit* ($\tau_c \geq 1$ μs) as it is seen e.g. for glasses, powder samples or frozen solutions.[83] An explicit treatment for the elaborate theory of each motional regime is cumbersome. However, the physical principles of the effects of rotational diffusion on spectral shape are given as a summary for each motional regime. Without the presence of microwave irradiation the system of spins in a sample

is in its equilibrium according to equation 2.8. For large spin systems this may be described by an equilibrium density matrix operator $\boldsymbol{\rho}_{eq}$ of the form:[25]

$$\boldsymbol{\rho}_{eq} = \frac{e^{-\hat{\boldsymbol{H}}/k_B T}}{Tr(e^{-\hat{\boldsymbol{H}}/k_B T})} \tag{2.53}$$

with the diagonal elements given by the population of a Boltzmann distribution. When a system evolves with time the wave functions $\psi_k(t)$ as well as the density matrix $\boldsymbol{\rho}(t)$ will also be functions of time. Therefore, on a very fundamental level, the time variation of a macroscopic observable $A(t)$ is determined by its expectation value:

$$\langle A(t) \rangle = Tr(\boldsymbol{\rho}(t))A \tag{2.54}$$

As we are interested in the time-dependence of the macroscopic magnetization $\boldsymbol{M}_i(t)$ that is related to the quantum mechanical spin operators $\hat{\boldsymbol{S}}_x$, $\hat{\boldsymbol{S}}_y$ and $\hat{\boldsymbol{S}}_z$, equation 2.54 can be written as:

$$\boldsymbol{M}_i(t) = -Ng\mu_B \langle \hat{\boldsymbol{S}}_i \rangle = -Ng\mu_B Tr(\boldsymbol{\rho}(t))\hat{\boldsymbol{S}}_i \tag{2.55}$$

with $i = x, y, z$. The resulting time-dependent Hamilton operator $\hat{\boldsymbol{H}}(t)$ for all members of the ensemble gives the density matrix equation of motion and is described by the quantum mechanic Liouville-von Neumann equation:[67]

$$\frac{\partial \boldsymbol{\rho}(t)}{\partial t} = i\left[\boldsymbol{\rho}(t), \hat{\boldsymbol{H}}(t)\right] = i\left[\boldsymbol{\rho}(t)\hat{\boldsymbol{H}}(t) - \hat{\boldsymbol{H}}(t)\boldsymbol{\rho}(t)\right] \tag{2.56}$$

Now a set of random variables Ω is defined representing Euler angles (α, β, γ) that in turn define molecular orientation to fully determine the time-dependent Hamilton operator $\hat{\boldsymbol{H}}(t)$. The time-dependence of Ω is described by a stationary Markov process that is given by a differential equation of the form:

$$\frac{\partial P(\Omega, t)}{\partial t} = -\boldsymbol{\Gamma}_\Omega P(\Omega, t) \tag{2.57}$$

where $P(\Omega, t)$ is the probability to find the molecule in a solid angle $d\Omega$ at a time t and $\boldsymbol{\Gamma}_\Omega$ is the rotational diffusion operator. This stochastic process has a unique equilibrium probability distribution characterized by $\boldsymbol{\Gamma}_\Omega P(\Omega) = 0$ that gives the stochastic Liouville equation (SLE) of motion in combination with equations 2.56 and 2.57:[85]

$$\frac{\partial \boldsymbol{\rho}(\Omega, t)}{\partial t} = -i\left[\hat{\boldsymbol{H}}(\Omega), \boldsymbol{\rho}(\Omega, t)\right] - \boldsymbol{\Gamma}_\Omega \boldsymbol{\rho}(\Omega, t) \tag{2.58}$$

The resulting density matrix $\boldsymbol{\rho}(\Omega, t)$ is now representing a value corresponding to an orientational state

Ω of a paramagnetic molecule suggesting a Hamiltonian operator $\hat{H}(\Omega)$ in angular units. The total spin Hamiltonian can now be separated in three components $\hat{H}(\Omega) = \hat{H}_0 + \hat{H}_1(t) + \hat{H}_2(\Omega)$ regarding the perturbation $\hat{H}_2(\Omega)$ due to the different orientation states Ω of the individual magnetic moments. The corresponding orientational Hamiltonian is given as:

$$\hat{H}_2(\Omega) = \sum_{\mu,i} \sum_{l,m,m'} (-1)^{m'} F'^{(l,-m')}_{\mu,i} D^l_{m,m'}(\Omega) A^{(l,m)}_{\mu,i} \tag{2.59}$$

where $F'^{(l,-m')}_{\mu,i}$ are spatial functions in molecule-fixed coordinates and $A^{(l,m)}_{\mu,i}$ exclusively consists of spin operators aligned to the laboratory axis system, both being irreducible tensor components of rank l and component m. The subscript μ defines the type of interaction (e.g. hyperfine interaction in equation 2.30, etc.) and i refers to different nuclei. The g-value and hyperfine coupling A are tensors of rank $l = 2$. Furthermore, the Wigner rotation matrix elements $D^l_{m,m}(\Omega)$ describe the axis transformation from molecular (x', y', z') towards laboratory coordinates (x, y, z). Those Wigner matrix elements form a complete set of orthogonal functions:

$$\int D^{j\,*}_{ml}(\Omega) D^{j'}_{m'l'}(\Omega) d\alpha \, \sin\beta \, d\beta \, d\gamma = \frac{8\pi^2}{2j+1} \delta_{jj'} \delta_{mm'} \delta_{ll'} \tag{2.60}$$

where $\delta_{ii'}$ are Kronecker deltas. In some special cases the Wigner matrices are reduced to Legendre polynomials or spherical harmonic functions $Y_{l,m}$. In the picture of the angular momentum $J = (J_x, J_y, J_z)$ of an electron spin a rotation operator R is defined as:[86]

$$R(\alpha, \beta, \gamma) = e^{-i\alpha J_z} e^{-i\beta J_y} e^{-i\gamma J_x} \tag{2.61}$$

that is related to the Wigner matrix element $D^l_{m',m}$ according to the relation:

$$D^l_{m',m}(\alpha, \beta, \gamma) = \langle lm' | R(\alpha, \beta, \gamma) | lm \rangle = e^{-im'\alpha} d^l_{m'm}(\beta) e^{-im\gamma} \tag{2.62}$$

with the reduced Wigner rotation matrices $d^l_{m',m}(\beta)$ representing real functions. The eigenfunctions of the axially symmetric rotator are the Wigner functions $D^j_{lm}(\Omega)$. With the expansion of the Dirac delta function on the complete orthogonal set of $D^j_{lm}(\Omega)$ functions and upon setting the initial probability condition to $P(\Omega, 0) = \delta(\Omega - \Omega_0)$ one obtains:[25]

$$P(\Omega, 0) = \delta(\Omega - \Omega_0) = \sum_{j,l,m} \frac{2j+1}{8\pi^2} D^{j\,*}_{lm}(\Omega_0) D^j_{lm}(\Omega) \tag{2.63}$$

with the conditional probability:

$$P(\Omega_0 / \Omega t) = \sum_{j,l,m} \frac{2j+1}{8\pi^2} D^{j\,*}_{lm}(\Omega_0) D^j_{lm}(\Omega) e^{\lambda_{jm} t} \tag{2.64}$$

that predicts the chance of still finding a molecule with given Ω_0 at time $t = 0$ in the range $(\Omega, \Omega + d\Omega)$ after time t. The exponential factor contains the eigenvalues λ_{jm} of the diffusion equation for an axially symmetric rotator that is defined as:[87]

$$\lambda_{jm} = -\left[j(j+1)D_\perp + (D_\parallel - D_\perp)m^2 \right] \tag{2.65}$$

with $D_\perp$ and $D_\parallel$ denoting the principal values of the axial rotational diffusion tensor $\boldsymbol{D}_r = (D_\perp, D_\perp, D_\parallel)$. The correlation functions for the Wigner matrices can be described with following expression:

$$\left\langle D^{j'}_{l'm'}(0)\, D^{j\,*}_{lm}(t) \right\rangle = \int D^{j'}_{l'm'}(\Omega_0)P(\Omega_0)\mathrm{d}\Omega \int D^{j}_{lm}(\Omega)P(\Omega_0|\Omega t)\mathrm{d}\Omega$$
$$= \delta_{jj'}\delta_{ll'}\delta_{mm'}\frac{1}{2j+1}e^{\lambda_{jm}t} \tag{2.66}$$

As it can be seen from equations 2.64 – 2.66 the rationale behind the rotation matrices is that their correlation functions decay with a characteristic time constant $\lambda_{jm} = -\tau_{jm}^{-1}$. For isotropic diffusion ($D_\perp = D_\parallel$), the tensor $\boldsymbol{D}_r$ therefore simplifies to the rotational diffusion constant D_r. According to equation 2.65 the characteristic time constant reduces to $\tau_j = [j(j+1)D_r]^{-1}$. Proposing different models for rotational reorientation, the following general expression is found for the rotational correlation time:

$$\tau^{j}_{\mathrm{c},n} = \frac{[1 + j(j+1)]^{\frac{n}{2}}}{j(j+1)D_r} \tag{2.67}$$

Commonly, three diffusion models are distinguished ranging from (*i*) Brownian diffusion ($n = 0$), (*ii*) free diffusion ($n = 1$) and (*iii*) jump diffusion ($n = 2$), so that the regimes are separated by a decreasing factor of $7^{-n/2}$ going from (*i*) to (*iii*) choosing $j = 2$.[88] This expression in equation 2.67 may also be expanded for anisotropic diffusion.[89] Isotropic Brownian rotation of a spherical molecule therefore leads to the well-known expression:

$$\tau^{2}_{\mathrm{c},0} = \tau_{\mathrm{c}} = \frac{1}{6D_r} = \frac{4}{3}\frac{\pi\eta a^3}{k_\mathrm{B}T} \tag{2.68}$$

with the rotational diffusion coefficient $D_r = k_\mathrm{B}T/8\pi\eta a^3$ from the Stokes-Einstein equation. In case the molecule tumbles asymmetrically, the rotational diffusion tensor $\boldsymbol{D}_r$ can be calculated from the molecular dimensions due to the theory of F. Perrin[90,91] as pointed out by J. H. Freed,[92] where the anisotropic rotational correlation time is given as an the geometrically averaged value of the kind $\tau_{\mathrm{c}} = 1/(6(D_x D_y D_z)^{1/3})$.

The method of choice for isotropic limit spectra is to calculate explicit energy levels from perturbation theory that yield the Breit-Rabi formulae from expressions similar to equations 2.48 and 2.49.[83,93] Slowing down the rotational motion leads to an increase in τ_{c} that modifies linewidths in comparison to spectra in the fast limit. As the relative line broadening $\Delta\Delta B_{0,\mathrm{pp}}$ depends on the nuclear magnetic

quantum number m_I, broadening in the fast-motion regime is different for each line and can be described with the relation:[10,83,94,95]

$$\Delta\Delta B_{0,pp}(m_I) \propto \frac{1}{T_2(m_I)} = -R_{\alpha\alpha'\alpha\alpha'} = A_0 + A + Bm_I + Cm_I^2 \qquad (2.69)$$

where $T_2(m_I)$ is related to the FWHM of a Lorentzian line and the linewidth parameters A, B and C describe the broadening from rotational motion. The first term A_0 describes all additional contributions to line broadening and $R_{\alpha\alpha'\alpha\alpha'}$ is the rotation matrix. With exact knowledge of the magnetic tensors $\boldsymbol{g}$ and $\boldsymbol{A}$, this method works quite well in the moderately fast rotational motion regime of 10 ps $< \tau_c <$ 3 ns when a rotational diffusion tensor $\boldsymbol{D}_r$ of spherical symmetry is assumed. Thus, the linewidth parameters A, B, and C can be represented by the simplified expressions:[25]

$$A = \frac{4}{45}\frac{\mu_B^2}{\hbar^2}B_0^2\Delta g^2\tau_c + \frac{1}{30}\frac{I(I+1)}{\hbar^2}\Delta A^2\tau_c \quad, \qquad (2.70a)$$

$$B = \frac{8}{45}\frac{\mu_B}{\hbar^2}B_0\Delta g\Delta A\tau_c \quad, \qquad (2.70b)$$

$$\text{and} \qquad C = \frac{\Delta A^2}{18\hbar^2}\tau_c \quad. \qquad (2.70c)$$

The tensor expressions are defined as $\Delta g = g_{zz} - 1/2(g_{xx} + g_{yy})$ and $\Delta A = A_{zz} - 1/2(A_{xx} + A_{yy}) = A_\parallel - A_\perp$, as nitroxides have an almost axial hyperfine coupling tensor $\boldsymbol{A}$ with the principal values $A_\perp$ and $A_\parallel$. The expressions shown in equation 2.70a – 2.70c facilitate calculations of τ_c from relative linewidths or line intensities.

Calculating slow motion CW EPR spectra is not as straightforward and is therefore only described schematically. The basic approach is to rewrite the SLE in the following form:[83]

$$\frac{\partial\Lambda(\Omega,t)}{\partial t} = -\left[i\hat{H}^Z(\Omega(t)) + \Gamma_\Omega^D\right]\Lambda(\Omega,t) = -\hat{Z}_L(\Omega,t)\Lambda(\Omega,t) \qquad (2.71)$$

with the out-of-equilibrium density $\Lambda = \rho - \rho_{eq}$, the Hamiltonian commutation superoperator $\hat{H}^Z$ and the stochastic Liouville superoperator $\hat{Z}_L$. Γ_Ω^D is the diffusion superoperator that models reorientational motions emphasizing additional effects like anisotropic viscosity or reorientation potentials. The stochastic Liouville theory gives a frequency-swept CW EPR spectrum $S_{EPR}(\omega - \omega_0)$ in compact matrix element notation:[89]

$$S_{EPR}(\omega - \omega_0) = \left(\frac{1}{\pi}\right)\left\langle v \left| \left[\hat{Z}_L + i(\omega - \omega_0)\hat{W}\right]^{-1} \right| v \right\rangle . \qquad (2.72)$$

Here, ω is the angular frequency position in the spectrum, $\omega_0 = g_{iso}\mu_B B_{z,0}/\hbar$ and $\hat{W}$ is the identity operator. The supervector v describes $M_x(t)$ and contains the spin operator for allowed EPR transitions and the equilibrium probability distribution for molecular orientation (equation 2.63). The numerical calculation proceeds from (*i*) construction of the matrices of $\hat{H}^Z$ and Γ_Ω and supervector v in the basis j,

l and *m* for the Wigner functions $D^j_{lm}(\Omega)$ to (*ii*) the reduction of $\hat{\boldsymbol{Z}}_L$ to a tridiagonal matrix via a Lanczos-algorithm and (*iii*) point-by-point numerical computation of the experimental spectrum from the tridiagonal matrix. For example, in rigid limit spectra of solids and glasses, all orientational dynamics are frozen and explicit calculations have to be conducted by adaptive modeling of energy levels[96] but are considered not being of great relevance for this work.

2.4.3 | Calculation of Nitroxide CW EPR Spectra

In the previous section the spin system was only considered for a homogenous spin species acting with a uniform behavior throughout the whole sample volume. In CW EPR spectra of proteins and polymers multiple overlapping spectral features, emerging from different environments, may appear, so that spectral analysis experiences a further complication as some dynamic features apparently vanish (see also **Figure 2.6E**) due to fractional occupations of motional regimes. In this work many multiple-component CW EPR spectra of up to four dynamic subspecies were simulated and analyzed with the MATLAB-based software package EasySpin[97] that incorporates optimized algorithms of the theoretical considerations in previous sections, especially to calculate spectra in the aforementioned four motional regimes. An example for the change in spectral shape due to rotational dynamics from τ_c = $1{\cdot}10^{-11}$s to τ_c = $2{\cdot}10^{-7}$s is given in **Figure 2.7**, covering most of the spectral appearances of nitroxides tumbling relative to the external magnetic field. It is often sufficient to extract the apparent hyperfine coupling constant (outer extrema separation: $2A_{//}$) as an empirical measure for the anisotropy of rotational motion, or the degree of nitroxide probe immobilization in a sample.[98]
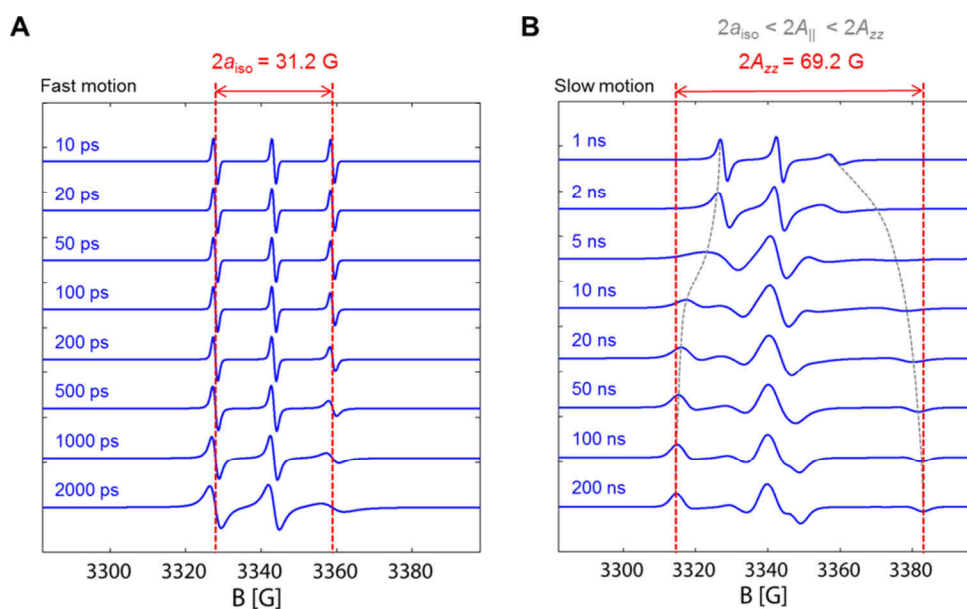
Figure 2.7 | Rotational motion in X-band nitroxide CW EPR spectra. All simulated spectra were generated with the EasySpin software package.[97] (**A**) The fast motion regime is shown with spectral shapes in the range from 10 ps $\leq \tau_c \leq$ 2 ns. (**B**) The slow motion regime is shown with spectral shapes in the range from 1 ns $\leq \tau_c \leq$ 200 ns. A typical nitroxide hyperfine coupling tensor A = [6.4 5.7 34.6] G was chosen. The gray dotted lines in (**B**) represent the anisotropic shift of the outer spectral extrema due to line broadening giving the apparent hyperfine coupling constant $2A_{//}$.

Apart from the special case of continuous microwave irradiation discussed so far, the next section is dedicated to extend our view towards the opportunity to manipulate spin systems in a more sophisticated way by well-defined durations of microwave irradiation and application of various microwave frequencies accompanied with associated effects and applications.

2.5 | Pulse EPR

Nowadays, a wide variety of pulse EPR experiments are accessible to yield information from a paramagnetic sample. After Erwin L. Hahn reported the successful observation of a spin echo in 1950 from NMR spectroscopy,[99] this finding formed the basis of many pulse experiments in magnetic resonance. It was in 1958 that due to his and A. G. Redfield's impetus also a first electron spin echo (ESE) was recorded on sodium ammonia solutions at room temperature by R. J. Blume.[100] Indeed, the theoretical concepts of pulse EPR are closely related to NMR spectroscopy but instrumental requirements are much more demanding due to reduced relaxation timescales of about three orders of magnitude.[27] In principle, this circumstance resulted in a technologically limited developmental delay of EPR compared to NMR. Thus, during the 1960s, pulse EPR was restricted to a small number of labs mainly comprising W. B. Mims at the Bell Laboratories and Yu. D. Tsvetkov in Novosibirsk. Nevertheless, those pioneering groups established methods to conduct experiments routinely, so that with upcoming commercially available fast switching digital electronics in the 1970s and 1980s the first commercial pulse X-band EPR spectrometer was available in 1987. Despite the wide variety of nowadays accessible experiments ranging from e.g. 2p-ESEEM,[101,102] pulsed ENDOR[103,104] and HYSCORE,[105] this work will exclusively focus on the potential of elucidating structural and dynamic effects of macromolecules utilizing 4-pulse double electron-electron resonance spectroscopy (4p-DEER) in EPR. The basic principles and spectroscopic strategies leading to a successful application of 4p-DEER experiments and its intrinsic advantages are represented in the following section.

2.5.1 | Propagation of Magnetization in Pulse EPR

The external perturbation of a spin system is now considered as being temporary in contrast to **Chapter 2.2**, where the interaction of a spin ensemble $M(t)$ with continuously applied MW irradiation was described. The simplest case of producing a pulse is to switch the microwave source on and off. In case of an on-resonant ($\Omega_Z = 0$, $\omega_L = \omega_1 = \omega_{mw}$) microwave pulse that sustains for a time span t_p and advances along the +x-axis of the rotating frame coordinate system (**Figure 2.2C**), the macroscopic magnetization M is flipped around the x-axis by an angle δ:[27]

$$\delta = \omega_1 t_p = \gamma_S B_1(t) t_p \tag{2.73}$$

Therefore, a pulse is best described in terms of its flip-angle characteristics. For a flip-angle of $\delta = 90°$ = $\pi/2$ the causative perturbation is denoted as a $(\pi/2)_x$-pulse and for $\delta = 180° = \pi$ it is a $(\pi)_x$-pulse

(**Figure 2.8A+B**). In a pulse EPR experiment the typical value for t_p of a $(\pi)_x$-pulse is about 32 ns and an approximate excitation profile can be estimated from FT of the pulse shape in the time-domain. Thus a rectangular pulse ranging from $-t_p/2 < t < +t_p/2$ has the excitation bandwidth $\Delta\nu_{FWHM} = 0.8/t_p$.[106] The according absolute probability density of the excitation profile is best described by a sinc-function[107] as it is shown in **Figure 2.8C**. The first zero-crossings are given at $\Delta\nu_0 = 1/t_p$ but are only for small flip angles $< 9°$.[27]
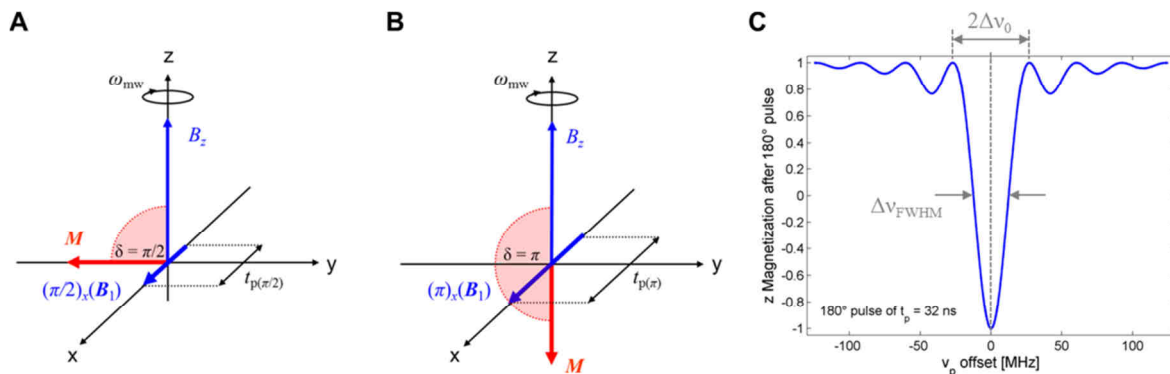

Figure 2.8 | The effect of pulse duration t_p on magnetization in the rotating frame. (**A**) A $(\pi/2)_x$–pulse along the $+x$-axis flips the magnetization to $–y$-direction. (**B**) A $(\pi)_x$-pulse along the $+x$–axis flips the magnetization to $–z$–direction. The pulse duration t_p is given in relative lengths along the x-axis. (**C**) Excitation profile of a $(\pi)_x$-pulse of duration $t_p = 32$ ns. The blue trace gives the Bloch solution for z–magnetization and has been calculated using EasySpin software.[97] The first zero-crossings of the excitation profile are $2\Delta\nu_0 = 54.3$ MHz apart and $\Delta\nu_{FWHM} = 25$ MHz.

As the pulse duration is usually much shorter than the time scale of the involved relaxation processes ($t_p << T_1, T_2$, equations 2.12 – 2.14) the artificially induced lapse of equilibrium magnetization will be restored after the pulse is terminated. The reset of an equilibrium magnetization after $t >> T_1, T_2$, is now dictated by the Bloch equations (**Chapter 2.2**) and the longitudinal (T_1) and transversal (T_2) relaxation time constants direct the spatial trajectories of individual spin packets in the ensemble towards the $+z$–direction.

2.5.2 | The Density Operator Formalism

As the initial state of a system should be known for a pulse experiment, the picture of the equilibrium spin density matrix ρ_{eq} is given by equation 2.53. It is common practice to introduce a reduced density operator $\sigma_{eq} = (\rho_{eq} - a)/b$ with the constants a and b. Usually the electron Zeeman term $\hat{H}_{EZ} = \omega_S S_z$ dominates the Hamiltonian $\hat{H}_0$ in the high-field approximation and the high-temperature approximation $\hbar\omega_S << k_B T$ can be used ($T > 4.5$ K).[27] With the series expansion of the exponential in equation 2.53 we find:

$$\sigma_{eq} \cong \mathbf{1} - \frac{\hbar\omega_S}{k_B T} S_z = -S_z \tag{2.74}$$

with the invariant identity operator *I* that can be discarded in experimental considerations and the resonance frequency ω_S. This expression defines the initial spin state to be aligned antiparallel to the quantization axis of the external magnetic field B_z as well as the macroscopic magnetization $M_{z,0}$. When the Hamiltonian $\hat{H}$ is time-dependent due to an external perturbation of e.g. a MW or RF pulse, the integration of the Liouville-von Neumann equation for the reduced density operator σ_{eq} yields:

$$\sigma(t) = e^{-i\hat{H}t}\sigma(0)e^{i\hat{H}t} = U\sigma(0)U^{\dagger} \tag{2.75}$$

in analogy to $\rho(t)$ in equation 2.56. The exponential operator $U(t) = \exp(-i\hat{H}t)$ is the propagator that executes a unitary transformation $U^{-1} = U^{\dagger}$ upon $\sigma(0)$, corresponding to a rotation in Hilbert space. Assuming that the Hamiltonian remains constant in each time interval a sequence of propagators U_1, U_2, U_3, …, U_n facilitates the calculation of the density operator at any time t_n after n time steps with:

$$\sigma(t+t_n) = U_n...U_3U_2U_1\sigma(0)U_1^{\dagger}U_2^{\dagger}U_3^{\dagger}...U_n^{\dagger} \tag{2.76}$$

The propagator corresponds either to a MW perturbation or a time of free evolution. The expectation value of any observable *A* may again be calculated due to the relation given in equation 2.54.

The concept of the density matrix operator has to be generalized if a system of multiple spins is treated. In a simplified model system comprising spin $J_1 = 1/2$ and $J_2 = 1/2$ the Hilbert space dimension is $n_{pq} = 4$ and the resulting set of eigenstates $|lk\rangle$ classify the density matrix elements. In an adequate four-level system (**Figure 2.9A**) the attention is now again directed towards the SQT and MQT if the transition frequencies $\omega_{kl}(J_i)$ are decisively different (see **Chapter 2.3.3**).
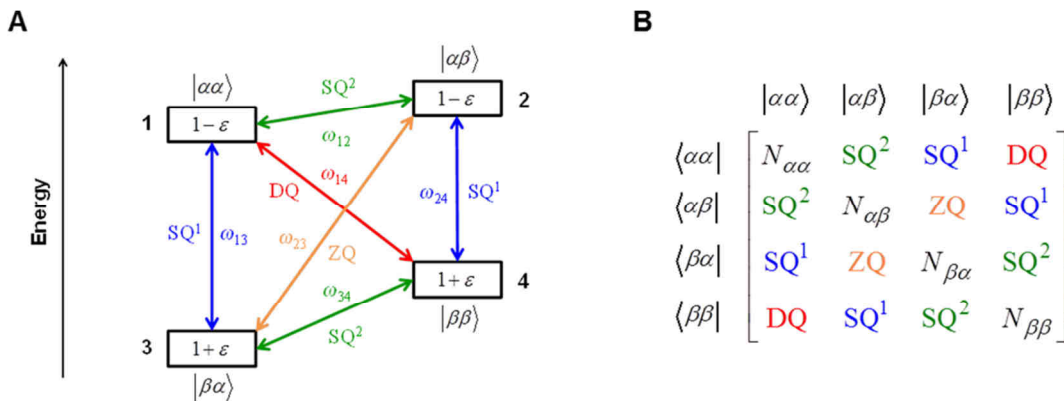
Figure 2.9 | Elements of a density matrix. Elements in a four-level (1 – 4) system of a spin system $J_1 = J_2 = 1/2$ in the weak coupling case.[27] (**A**) Energy level diagram with single quantum (SQ), double quantum (DQ) and zero quantum (ZQ) transitions of angular frequencies ω_{jk}. The factors $(1 - \varepsilon)$ and $(1 + \varepsilon)$ are the equilibrium populations in case $\omega_{kl}(J_1) >> \omega_{kl}(J_2)$. Allowed SQTs between eigenstates $|k\rangle$ and $|l\rangle$ for J_1 and J_2 are shown in blue and green, respectively. Forbidden transitions are shown in orange (ZQT) and red (DQT). (**B**) Density matrix elements with diagonal elements N_{pq} denoting the spin population and off-diagonal elements giving the coherences of order $p = 0$ (ZQ), $p = \pm 1$ (SQ) and $p = \pm 2$ (DQ).

This is the case for an electron spin ($J_1 = S$) coupled to a nuclear spin ($J_2 = I$) with corresponding equilibrium populations ($1 \pm \varepsilon$). As there is a non-zero probability for a spin $J_2 = I$ being flipped by a microwave pulse exciting J_1, the forbidden zero (ZQT) and double quantum transitions (DQT) can be at least partially induced. The complete description of this two-spin system is given by the density matrix in **Figure 2.9B**. For $k = l$ the diagonal matrix elements σ_{kk} give the population of state $|k\rangle$ and for $k \neq l$ the off-diagonal matrix elements σ_{kl} give the coherences between states $|k\rangle$ and $|l\rangle$.[27] With the observation of transversal and longitudinal magnetization all populations and coherences of the order $p = \pm 1$ can be obtained from the allowed transitions.

2.5.3 | The Product Operator Formalism

As we have seen that the density matrix consists of n_{pq}^{2} matrix elements, the calculation of the time-evolution for larger systems consisting of J_1, J_2, … J_n spins will be tedious and laborious. As the number of required basis operators coincides with the number of matrix elements the Liouville space with $n_L = n_{pq}^{2}$ dimensions is spanned. It is therefore convenient to express the density matrix $\boldsymbol{\sigma}$ as a linear combination of base operators $\boldsymbol{B}_s$ and time-dependent factors $b_s(t)$:[108]

$$\boldsymbol{\sigma}(t) = \sum_s b_s(t) \boldsymbol{B}_s \tag{2.77}$$

where the complexity of practical calculations depends strongly on the choice of the base set $\{\boldsymbol{B}_s\}$.[109] The Liouville space for an individual spin $J = 1/2$ consist of $n_L = 4$ dimensions and can be described by the Cartesian basis operators J_x, J_y, J_z and the identity operator $\boldsymbol{1}$. The already familiar system of electron spin $J_1 = S = 1/2$ coupled to a nuclear spin $J_2 = I = 1/2$, is therefore written as the direct tensor product of the base sets of the individual spins as:

$$\{\boldsymbol{B}_1, \boldsymbol{B}_2, ..., \boldsymbol{B}_{16}\} = \{S_x, S_y, S_z, 1\} \otimes \{I_x, I_y, I_z, 1\} \tag{2.78}$$

Thus, a system of n spins $J_n = 1/2$ consists of 4^n product operators $\boldsymbol{B}_s$, each exhibiting a specific physical meaning in terms of coherence or magnetization polarization.[27,109] Since any Hamiltonian can be expressed in Cartesian product operators a product operator $\boldsymbol{A}$ that evolves under a second product operator $\boldsymbol{B}$ is written as:

$$e^{-i\delta B} \boldsymbol{A} e^{i\delta B} = \boldsymbol{C} \qquad , \tag{2.79}$$

resulting in the product operator $\boldsymbol{C}$. Here, we again use the flip angle δ or $\delta = \omega_i t_i$ with ω_i being the amplitude of one of the interactions of the Hamiltonian. Equation 2.79 is conveniently expressed in the shorthand notation:

$$\boldsymbol{A} \xrightarrow{\delta B} \boldsymbol{C} \tag{2.80}$$

with the condition that the commutator $[B,A] \neq 0$. As the Hamiltonian can be subdivided as the sum of several product operators ($\hat{H} = \sum \omega_i B_i$), pulse experiments may be commonly described by the following relations:

$$A \xrightarrow{\delta_1 B_1} C_1 \xrightarrow{\delta_2 B_2} C_2 \cdots \xrightarrow{\delta_n B_n} C_n$$
$$\triangleq A \xrightarrow{\hat{H}_1 t_1} C_1 \xrightarrow{\hat{H}_2 t_2} C_2 \cdots \xrightarrow{\hat{H}_n t_n} C_n$$

(2.81)

With the initial case of a sustaining equilibrium spin density σ_{eq}, a non-selective pulse with flip-angle δ will transform an individual spin J_z according to the relation:[27]

$$\sigma_{eq} = -J_z \xrightarrow{\delta J_x} -\cos\delta J_z + \sin\delta J_y$$

(2.82)

and for the system consisting of two non-equivalent spins $J_{1z} = S = 1/2$ and $J_{2z} = I = 1/2$ with the off-resonant spin J_{2z} an analogous expression is found:

$$-J_{1z}J_{2z} \xrightarrow{\delta J_{1x}} -\cos\delta J_{1z}J_{2z} + \sin\delta J_{1y}J_{2z}$$
$$\text{or} \quad -S_z I_z \xrightarrow{\delta S_x} -\cos\delta S_z I_z + \sin\delta S_y I_z \quad ,$$

(2.83)

since non-resonant spins as a Cartesian operator can be multiplied to both sides of the equation.

2.5.4 | Basics of FT EPR Experiments

A striking example for the working principle of a pulse EPR experiment is the church bell analogy. Recording the resonance frequency is facilitated by exciting the bell with a frequency-tunable oscillator that excites the resonance frequencies sequentially (CW), while amplitude changes are recorded with a microphone. The pulse analogy is to hit the bell with a hammer while recording the time-dependent response containing all inherent resonances. After Fourier-transforming the time-domain pulse response signal, a frequency spectrum is finally obtained with all intrinsic resonances of the bell.[110] Therefore, in contrast to CW EPR experiments, each data point of a pulse EPR experiment contains information about the whole spectrum. Due to the strong microwave pulses in X-band EPR (≈ 1 kW), even the simplest pulse EPR experiment exhibits several obstacles that have to be overcome to successfully record a time-domain signal.

2.5.4.1 | Dead-time t_d

When a MW pulse enters the resonator containing the sample, its energy is dissipated or stored in this specific volume. As the resonator resembles a bandpass filter that is characterized by resistance (R), capacitance (C), and inductivity (L), its properties can be described by an intrinsic quality factor $Q = R(C/L)^{-1/2}$.[111] The main aim is to decrease the time while a pulse is reflected inside the resonator and

thus the loss factor $d = Q^{-1}$ describing the power losses due to resonator wall currents, dielectric absorption and coupling to the antenna. Consequently, Q has to be typically lowered to a value of about 100 at X-band frequencies. The resonance absorption line (*dip*) shape of the resonator with $v_{FWHM} = v/Q$ is also crucial in defining the minimum pulse length possible as $t_{p,min} = 1/v_{FWHM}$. Accordingly, this resonator property defines the excitation bandwidth of the pulse. If one wants to excite the whole EPR spectrum of the width Δv_{EPR} the excitation bandwidth of the pulse should be $0.8/t_p \geq \Delta v_{EPR}$. The characteristic time constant that gives the decay $P(t)$ of the incident pulse power P_0 in the resonator is the ringdown-time t_r:[27]

$$P(t) = P_0 e^{-t_r v_{FWHM}/2\pi Q}$$

(2.84)

and the time of the whole dissipation process is the dead-time t_d,[112] that also determines the maximum possible repetition rate of individual pulses. For X-band frequencies the dead-time is usually in the range of $t_d = 100$ ns. For this reason the response signal of the sample cannot be recorded during the dead-time.

2.5.4.2 | Free Induction Decay (FID)

The simplest experiment in pulse EPR and NMR consists of a $(\pi/2)_x$-pulse of duration t_p that induces the whole spin system with equilibrium magnetization σ_{eq} to flip from S_z into the x-y-plane. After the dead-time t_d the free induction decay (FID) can be monitored representing the time-dependent evolution of the spin system leading to the recovery of equilibrium magnetization $M_{z,0}$. In case of on-resonant irradiation ($\Omega_S = 0$) the FID has an exponential shape (**Figure 2.10A**) and in the non-resonant case ($\Omega_Z = \Omega_S \neq 0$) the FID is sinusoidal (**Figure 2.10B**) and the magnetization vector describes a right- ($\Omega_S > 0$) or left-handed ($\Omega_S < 0$) spiral in the x-y-plane. The corresponding carrier frequency can be obtained from Fourier transformation (FT, **Figure 2.10C**).[114] The respective magnetization trajectories (**Figure 2.10D–F**) follow the Bloch equations and the timescale of the spin evolution is therefore determined by T_1 and T_2. While T_1 is the reorientation time constant in z-direction, T_2 leads to a fanning out of spin packets in the x-y-plane. Both processes affect the position of the net magnetization vector tip simultaneously and for evolution times $t_E \gg T_1, T_2$ the equilibrium magnetization is rearranged. In the picture of the spin density operator formalism this experiment is best described by the expression:

$$\sigma_{eq} \xrightarrow{(\pi/2)_x S_x} \sigma(t) = \cos(\Omega_S t)S_y - \sin(\Omega_S t)S_x$$

(2.85)

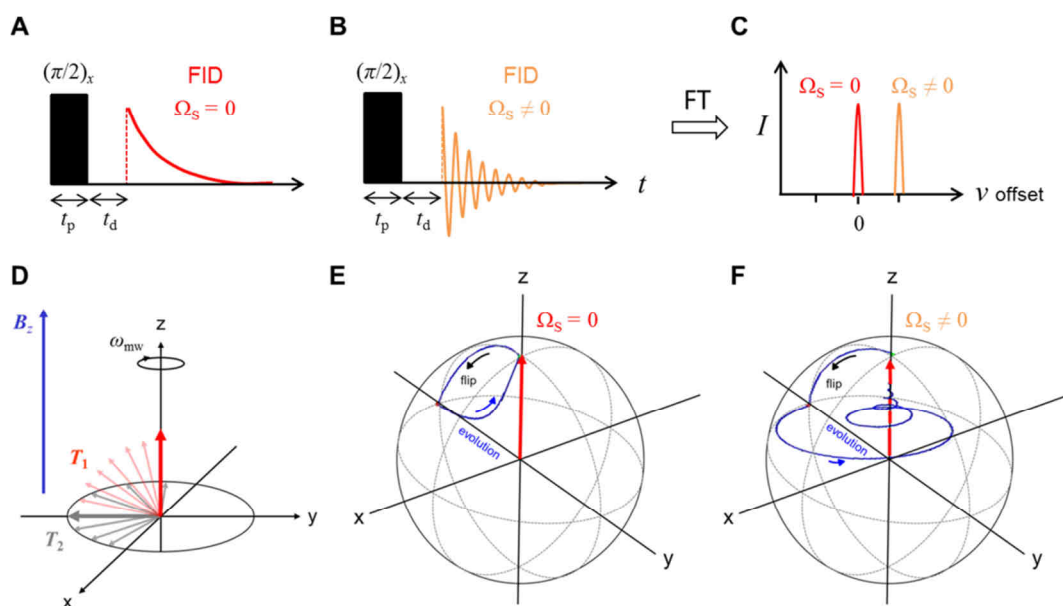facilitating the separation of polarization (cos) and coherence (sin) contribution terms of the evolving system.

Figure 2.10 | One-pulse experiment leading to a FID. (**A**) An on-resonant $(\pi/2)_x$ pulse ($\Omega_S = 0$) of duration t_p and dead-time t_d flips the equilibrium spin state σ_{eq} into the x-y-plane. The resulting FID signal vanishes with time. (**B**) Off-resonant $(\pi/2)_x$ pulse ($\Omega_S \neq 0$). (**C**) A Fourier transform (FT) of the time-domain signal gives the resonance frequency ($\Omega_S = 0$). (**D**) Vector representations of the relaxation processes after the pulse with time constants T_1 (red) and T_2 (gray). The time evolution of the magnetization vector tip is depicted in a Bloch sphere as a reaction to an (**E**) on-resonant and (**F**) off-resonant MW pulse. The magnetization trajectory (blue) was calculated with the BlochSolver[113] toolkit for a $t_p = 11$ ns pulse, $T_1 = 10$ µs, $T_2 = 2$ µs and an evolution time of $t_E = 40$ µs.

2.5.4.3 | The Primary Echo

As important information may be clipped by the dead-time in pulse EPR experiments it is convenient to circumvent this problem by the application of an appropriate combination of pulses. In 1950 Erwin Hahn gave a detailed strategic description of how the reappearance of the magnetization as a so-called *spin echo*, or *primary echo* of the equilibrium magnetization can be obtained.[99] This constructive interference of macroscopic magnetization is generated with the pulse sequence $(\pi/2)_x - \tau - (\pi)_x - \tau -$ echo, whereas $\tau > t_d$ is the intrinsic time of free evolution. The successful conduction of this experiment is based on the condition that $T_1 \gg T_2$ with T_1 usually being in the order of milliseconds.[115] In **Figure 2.11** it is shown that after flipping the equilibrium magnetization into the x-y-plane (1), individual spin packets will fan out during the first evolution time τ gaining different phase shifts according to their intrinsic resonance offsets $\Omega_{S,i}$ (2) and the net magnetization is therefore reduced (see FID). By inverting the dephased spin packets with a $(\pi)_x$ pulse (3), all resonance offsets are refocused simultaneously after a time $t = 2\tau$ in the $+y$-direction and the initial magnetization appears as an echo outside the dead-times of both pulses (4). Changing the evolution times τ leads to a likewise variation of the echo amplitude. Generally, as the evolution time τ is increased, the echo amplitude V_E decreases exponentially with a specific phase memory time T_m by the relation:[117]

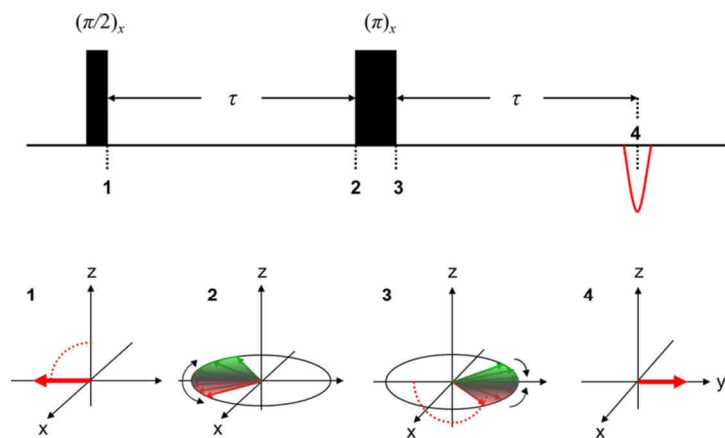$$V_E(2\tau) = e^{-(2\tau/T_m)^x} \qquad . \qquad (2.86)$$

Figure 2.11 | Schematic principle of a spin echo experiment. Characteristic positions in the pulse sequence (top) are given in a vector diagram of the rotating frame scheme (bottom) denoting the time evolution (1–3) of the ensemble magnetization.[116] The net magnetization depends on the pulse positions that cause the formation of a spin echo after $t = 2\tau$ (4). The red dotted lines indicate the MW pulse induced flip angle δ.

T_m comprises all processes leading to a loss of electron spin coherence and can be measured in a 2p-ESEEM experiment[101,102] that is not discussed in detail here. The value of the factor x in equation 2.86 indicates the type of involved processes leading to a dephasing. In case of $x = 1$ the spin-spin relaxation time constant T_2 can be replaced by T_m in the Bloch equations.

2.5.4.4 | Spectral Diffusion and Spin Diffusion

The width of individual spectra in pulse EPR often exceeds the excitation bandwidth of the applied pulses and only spins with resonance frequencies close to ω_{mw} can be excited. The excited spins are usually termed A spins, whereas those being unaffected by the MW pulse are called B spins. The excitation of A spins leads to a magnetization transfer to regions of the spectrum that are not excited by the pulse itself. In return, the remanent equilibrium magnetization of the B spins is transferred to the excited part of the spectrum simultaneously and hence influences the transverse relaxation time (T_2) of the A spins.[27] The individual transition frequencies may also be altered in experiments where the rotational reorientation is in the timescale of the experiment. In this case the polarization is relocated to spectral regions of the new orientation by *spectral diffusion*. For dipolar coupling frequencies (ω_{dd}) in the range of the difference of A and B spin resonance frequencies the process of polarization mixing of both spin types is probable. The rate of this *spin diffusion* process depends on the interspin distance r_{AB} and is proportional to r_{AB}^{-6}.

2.5.4.5 | Instantaneous Diffusion ($x = 1$)

The proximity of individual spins in a homogenous sample is primarily dependent on the concentration of paramagnetic centers and dipolar interactions come into account. Flipping of dipolar coupled A spins leads to a change of the local magnetic field at each individual spin A. In a statistical ensemble of A spins the individual orientations of adjacent spins is distributed isotropically and the changes in local fields are therefore also diverse. Thus, the application of a pulse induces a variety of resonance frequencies to a system that initially consisted of uniform resonances. This phenomenon of instantaneous diffusion has been first described by Klauder and Anderson.[118] For a narrow EPR

spectrum that can be completely excited by a single MW pulse, an extrapolation to infinitely small flip angles and statistically distributed electron spins gives the following expression:[27,117]

$$\frac{1}{T_{ID}} = C \frac{\pi}{9\sqrt{3}} \frac{\mu_0 g^2 \mu_B^2}{\hbar} \sin^2 \frac{\delta}{2}$$

(2.87)

where $C = N_A c$ is the unit spin concentration [m^{-3}]. Assuming typical values of τ = 200 ns, a spin concentration of $C = 3 \cdot 10^{23}$ m^{-3} (0.5 mM) and a flip angle of δ = 180°, the decay rate of transverse magnetization due to instantaneous diffusion is $T_m = T_{ID}$ = 4.0 µs. The primary echo intensity is therefore diminished to about 90 % according to equation 2.86 when compared to the initial equilibrium magnetization. In case the whole spectral width cannot be excited, the flip angle will be a function of resonance offset $\delta(\Omega_S)$. The final signal strength $V_E(2\tau)$ can be obtained by integration of the $\sin^2(\delta/2)$-term over the resonance offsets $d\Omega_S$ after multiplication with an appropriate EPR lineshape function $f(\Omega_S)$.[27]

2.5.4.6 | Phase Cycling

In **Chapter 2.5.2** it was shown that an ideal pulse may induce coherences in an already very simple spin system of an electron and a nucleus of spin $S = I = 1/2$. Those induced coherences can lead to a variety of primary echoes (PE), stimulated echoes (SE) and refocused echoes (RE). In a sequence of n pulses with arbitrary phases and flip angles, the maximum number ζ_{PRS} of observable echoes after the nth pulse is defined as:[27]

$$\zeta_{PRS} = \frac{1}{2}(3^{n-1} - 1)$$

(2.88)

Depending on the measurement, a desirable contribution can be filtered out by phase cycling that is targeted for a detailed investigation. The experiment $(\pi/2)_x - \tau - (\pi/2)_x$ with non-selective pulses and a $+x$ and $-x$ phase cycle for the second $(\pi/2)_x$ pulse ($S = 1/2$) may be described by the product operator formalism by:

$$\sigma_{eq} = -S_z \xrightarrow{(\pi/2)_x S_x} S_y \xrightarrow{\Omega_S \tau S_z} \cos(\Omega_S \tau)S_y - \sin(\Omega_S \tau)S_x = \sigma_2$$

$$+x: \qquad \sigma_2 \xrightarrow{+(\pi/2)_x S_x} + \cos(\Omega_S \tau)S_y - \sin(\Omega_S \tau)S_x = \sigma_3$$

$$-x: \qquad \sigma_2 \xrightarrow{-(\pi/2)_x S_x} - \cos(\Omega_S \tau)S_y - \sin(\Omega_S \tau)S_x = \sigma_3'$$

(2.89)

Thus the polarization terms (cos) in equation 2.89 have a different sign, whereas the coherence (sin) remains negative. The signal addition of both experiments selects a coherence-transfer pathway for coherence and the subtraction leads to a polarization coherence-transfer pathway. Hence, the aim of the phase cycling procedure is controlling the coherence order during the free evolution periods in between the pulses.[119] Apart from this simple example, the strategy can be expanded to any kind of pulse sequences leading to a reduction of unwanted FIDs, echoes, QD receiver imbalances and offsets.[120]

2.5.4.7 | Field-detected Electron Spin Echo (FD ESE)

A strategy to circumvent the insufficient excitation bandwidth of the MW pulses is to apply a field sweep during the pulse experiment in analogy to CW EPR. The pulse sequence and MW frequency is kept constant and accordingly a magnetic field-dependent echo amplitude is recorded as shown for a model biradical in **Figure 2.12** (compound 1 in Godt *et al.*[121]). Since the phase memory time T_m for nitroxides is much too short for ambient temperatures, the strong temperature dependence of the relaxation time constants T_1 and T_2 facilitates the observation of an optimum echo intensity in the temperature range from 50 – 80 K where $T_1/T_2 \approx 10^3$.[115] Considering the restoration of equilibrium magnetization, T_1 has to be kept short ($T_1 \sim 10^{-3}$ s, $T_2 \sim 10^{-6}$ s), so that the experiment can be conducted in appropriate time frames. Those low experimental temperatures require that samples are equipped with 20 – 30 % glycerol enabling a homogenous vitrification that also affects the echo quality. The advantage of this approach is that the field sweep visualizes orientation selection of different spin packets and therefore helps to detect the exact position of the maximum echo intensity with its according field position. Recording such a FD ESE spectrum is decisive for the frequency choice in DEER experiments as it will be shown in the next chapter.
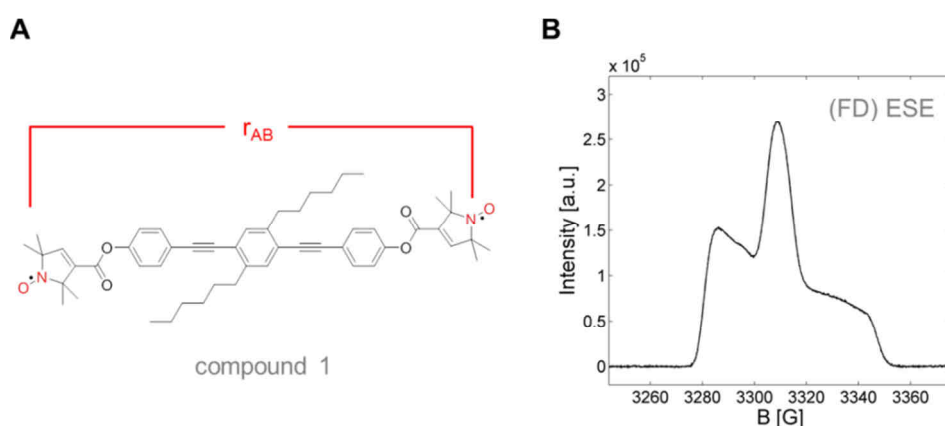
Figure 2.12 | Result from an X-band field-detected electron spin echo (FD) ESE experiment. (**A**) The model nitroxide biradical (compound 1 in Godt *et al.*[121]) was used for highlighting an exemplary (**B**) FD ESE experiment in perdeuterated ortho-terphenyl (OTP-d_{14}, see also **Appendix C7**). Pulse lengths were set to 16 ns and 32 ns for π and $\pi/2$ pulses, respectively ($\tau = 396$ ns). The field position of the maximum echo amplitude is at about $B_{z,0} = 3309$ G at a frequency of 9.306 GHz. The field sweep has to be chosen larger than the powder spectrum width to detect all observable spin packets (~ 70 G).

2.5.5 | Double Electron–Electron Resonance (DEER) Spectroscopy

As already described in **Chapter 2.3.6** dipole-dipole couplings between electrons can be employed to extract structural and dynamic distance information from macromolecules that have been made accessible to EPR by covalently attached spin labels or bound spin probes. This can be exceptionally well done with pulsed EPR spectroscopy, as it will be shown in this chapter. During the pursuit of this distinct objective several single-frequency techniques (SIFT) have evolved as the 2+1 sequence,[122,123] double quantum coherence (DQC)[124–126] and refocusing of dipolar couplings (SIFTER)[127] with the aim to filter out dipolar contributions from a spin system. As many pulse EPR experiments would

require a much larger excitation bandwidth as an individual single frequency pulse can generate, a second microwave affecting the spin system can be introduced. This pulsed electron-electron double resonance (PELDOR) principle was first experimentally realized by Bowers and Mims[128] and discloses experimental options that were hitherto concealed. In the early 1980s the group of Y. D. Tsvetkov developed the 3-pulse DEER sequence as a strategy to detect electron interspin distances in solids and model biradicals,[129,130] which was thereafter devotedly included into the repertoire of several EPR groups.[131,132] This approach is analogous to the spin echo double resonance (SEDOR) experiment[133,134] in solid state NMR where nuclear and in particular ^{1}H-^{1}H and ^{13}C-^{13}C dipolar couplings can be converted into structural information of compounds.[135] In pulsed EPR, the choice of those two required microwave frequencies ω_A and ω_B is based on the appearance of the FD ESE spectrum. For nitroxides at X-band frequencies the maximum echo intensity position and the left shoulder are usually separated by approximately 65 MHz or 23 G (**Figure 2.13A**), so that the applied pulses with a typical duration of 32 ns do not overlap in their spectral excitation bandwidth.

The general strategy for 3p-DEER is to apply a primary echo sequence $((\pi/2)_{x,A} - \tau - (\pi)_{x,A})$ with observer frequency ω_A on the spin system while a $(\pi)_B$-pump pulse with frequency ω_B is triggered after a variable time delay t with respect to the $(\pi/2)_{x,A}$ pulse. This pump pulse is triggered during the fixed evolution time τ where the magnetization is now considered to evolve with resonance offset $\Delta\omega_A$ together with the dipole-dipole interaction (**Figure 2.13B**). As both frequencies correspond to different sections of the EPR spectrum, the spin packets excited by the observer pulses are called A spins and the spin packets excited by the pump pulse are called B spins (**Figure 2.13C**). In case of an absent pump pulse the A and B spins and their couplings are refocused as in a conventional spin echo experiment. When the pump pulse is triggered during the evolution time τ, the B spins are inverted and in turn modulate the Hahn echo intensity depending on the pump pulse position t. Another possibility to measure interspin distances is the application of the 4-pulse DEER sequence[136,137] that is widely applied in this work. This method is essentially free of intrinsic dead-time artifacts compared to the 3-pulse version and thus permits a full characterization of also very broad distance distributions.

The rationale behind the 4-pulse DEER sequence is now to trigger the $(\pi)_B$ pump-pulse after the dead-time t_d of the $(\pi)_{x,A}$ pulse from the Hahn-echo sequence has elapsed, but prior to the generated primary echo that occurs after $2\tau_1$ (**Figure 2.13D**).

The resulting echo amplitude of the observer sequence is then recorded by applying a second $(\pi)_{x,A}$ pulse after a dipolar evolution time τ_2 after the Hahn echo that consolidates the A spin magnetization after a time $2\tau_2$ and captures residual coherence of the evolving spin system. Therefore, the fourth pulse in the 4p-DEER sequence is termed refocusing pulse. When the pump pulse is triggered at a variable time t, the B spins are also inverted as in the 3p-DEER experiment, but now modulating the coherence transfer echo intensity that is created by the second $(\pi)_{x,A}$ pulse. Hence, both DEER-sequences induce a sign inversion perturbation in the local magnetic fields around the A spins by inverting the B spins and reveal the mutual electron-electron coupling through space.
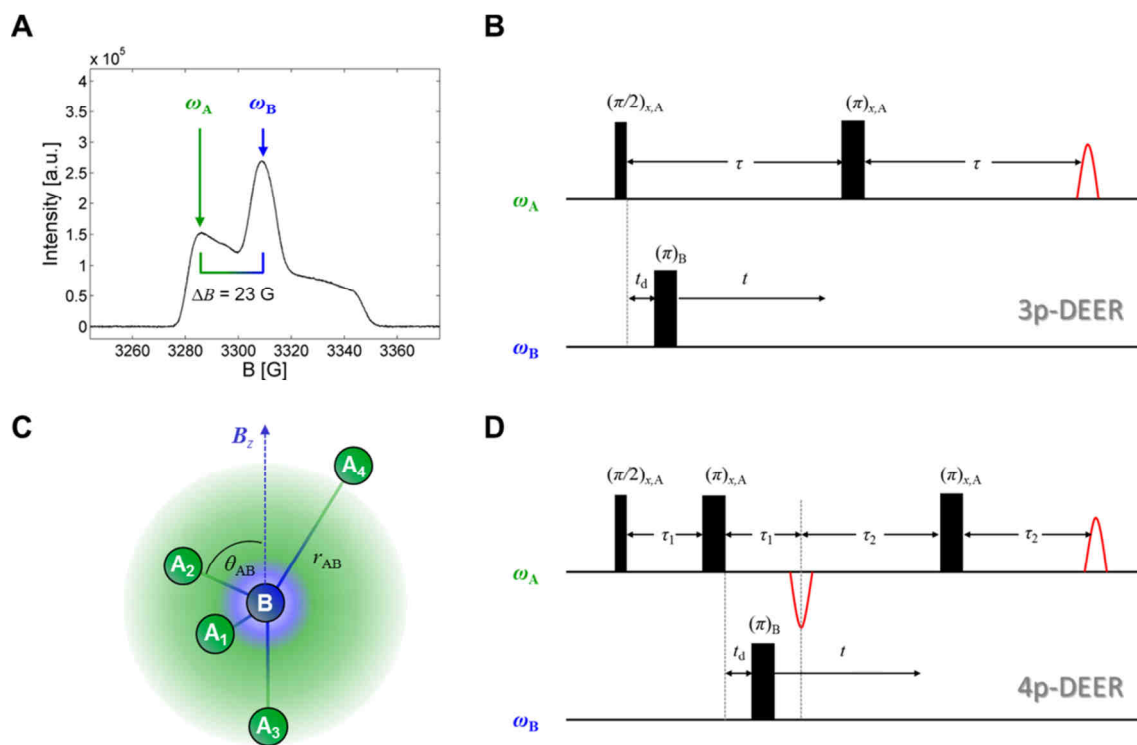
Figure 2.13 | Basic principles of DEER experiments. (**A**) (FD) ESE of a model biradical as also shown in **Figure 2.12** with the spectral positions of observer frequency ω_A and pump frequency ω_B separated by $\Delta B = 23$ G ≈ 65 MHz. (**B**) 3p-DEER sequence with the pump pulse being initiated during the first evolution time τ of the ESE sequence. (**C**) Schematic representation of the effective topology in a spin system with observer spins A and pump spins B for different situations in a sample in DEER spectroscopy: A_1 is at the lower resolution distance limit due to experimental pulse excitation and ^1H modulation restrictions, A_2 and A_3 are in experimentally accessible distance ranges and A_4 is outside the informative volume. Additionally, the schematic interspin distance r_{AB} between observer spin A and pump spin B and the angle θ_{AB} between interspin vector and applied magnetic field B_z are given. (**D**) 4p-DEER sequence with the pump pulse being initiated after the first $(\pi)_{x,A}$ pulse and a second $(\pi)_{x,A}$ pulse used as an additional echo refocusing pulse.

The phase reversal after the $(\pi)_{x,A}$ pulse in a spin echo experiment is therefore prevented by the $(\pi)_B$ pulse and so the spin echo partially vanishes.[134] Whereas observer pulses are conventionally set to lengths of $t_p = 32$ ns, the pump pulse is applied for only 12 ns as it has to excite a much larger fraction of spins. By shifting the pump pulse position by a variable time t, the resulting echo intensity in the time domain will be modulated with the dipolar coupling frequency.[137] This is because the precession frequency of A spins changes with variable time t by the electron-electron coupling ω_{ee} due to changes in the local magnetic field caused by the inverted B spins. At the time of echo formation the magnetization is therefore out of phase by an angle $\phi_{ee} = \omega_{ee}t$ that finally generates a sinusoidal time domain signal.[27] A dead-time free setup of the 4p-DEER sequence bears the predominant advantage that the decisive maximum echo intensity can be observed from the refocused coherence transfer echo in the time domain signal that is experimentally inaccessible in 3p-DEER.

For a theoretical treatment an isolated two-spin system in the rotating coordinate frame is now considered that consists of $S_{z,A} = S_{z,B} = 1/2$ as it is also shown in **Chapter 2.3.6**. In the high-field approximation the corresponding DEER-Hamiltonian $\hat{H}_{DEER}$ can be written as:[132]

$$\hat{H}_{\text{DEER}} = \omega_A S_{z,A} + \omega_B S_{z,B} + \omega_{ee} S_{z,A} S_{z,B} \qquad (2.90)$$

whereas ω_{ee} is the angular dependent electron-electron coupling frequency, that can be described by following expression:

$$\omega_{ee} = \omega_{dd}(3\cos^2\theta_{AB} - 1) + J \qquad (2.91)$$

Assuming the validity of the point-dipole approximation for localized spins with the dipole-dipole coupling frequency ω_{dd}:[137]

$$\omega_{dd} = \frac{\mu_0 \mu_B^2 g_A g_B}{4\pi\hbar r_{AB}^3} \qquad , \qquad (2.92)$$

equations 2.91 and 2.92 lead to an analogous expression as in equations 2.41 and 2.42. Besides the A–B spin pairs in the observable range, the refocused echo intensity is furthermore affected by contributions from A spins coupled to B spins that reside outside the excitation window of the pump pulse as e.g. spin A_4 in **Figure 2.13C**.[27] For a distribution of spin pairs A and B throughout the sample we have:[138]

$$V_{\text{inter}}(t) = \exp(-\lambda C k t^{D/3}) \qquad (2.93)$$

with

$$k = \frac{2\pi\mu_0\mu_B^2 g_A g_B}{9\sqrt{3}\hbar} \qquad , \qquad (2.94)$$

where λ is the modulation depth parameter giving the fraction of B spins excited by the pump pulse, and C is the volume concentration of electron spins. The fractal dimension D may be used to obtain information about the spatial constraints in a sample. For $D = 3$ an idealized spatially unconstrained homogenous distribution is present in a sample, for $D = 2$ a spin pair may experience a confinement in two dimensions as in liposomes or membrane proteins,[139] whereas in a polymer physical view $D = 1.67$ may be indicative for spin pairs in an expanded linear chains.[140] Since D is not necessarily an integer number it may thus be chosen to fulfill an appropriate model. With this expression for $V_{\text{inter}}(t)$, intermolecular spins within a sphere radius of about 20 – 40 nm of the active volume of a intramolecular spin pair are considered.[139,141] This intramolecular part of the DEER time trace is described by:[27]

$$V_{\text{intra}}(t,\theta_{AB},r_{AB}) = F(t) = 1 - \int_0^{\pi/2} \lambda(\theta_{AB})\sin\theta_{AB}[1 - \cos(\omega_{ee}(\theta_{AB},r_{AB})t)]d\theta_{AB} \qquad (2.95)$$

where the orientation-dependent modulation depth parameter $\lambda(\theta_{AB})$ takes into account the partial excitation of an EPR spectrum. In a glassy sample the angle θ_{AB} is distributed between 0 and $\pi/2$ and

weighted with $\sin\theta_{AB}$. The full 4p-DEER signal $V(t)_{4p\text{-DEER}}$ is therefore best described by multiplication of inter- and intramolecular contributions:

$$V(t)_{4p\text{-DEER}} = V_{\text{intra}}(t,\theta_{AB},r_{AB}) \cdot V_{\text{inter}}(t) = F(t) \cdot B(t) \qquad (2.96)$$

where $V_{\text{intra}}(t,\theta_{AB},r_{AB}) = F(t)$ is usually referred to as the form factor and $V_{\text{inter}}(t) = B(t)$ is called the background factor.[142]
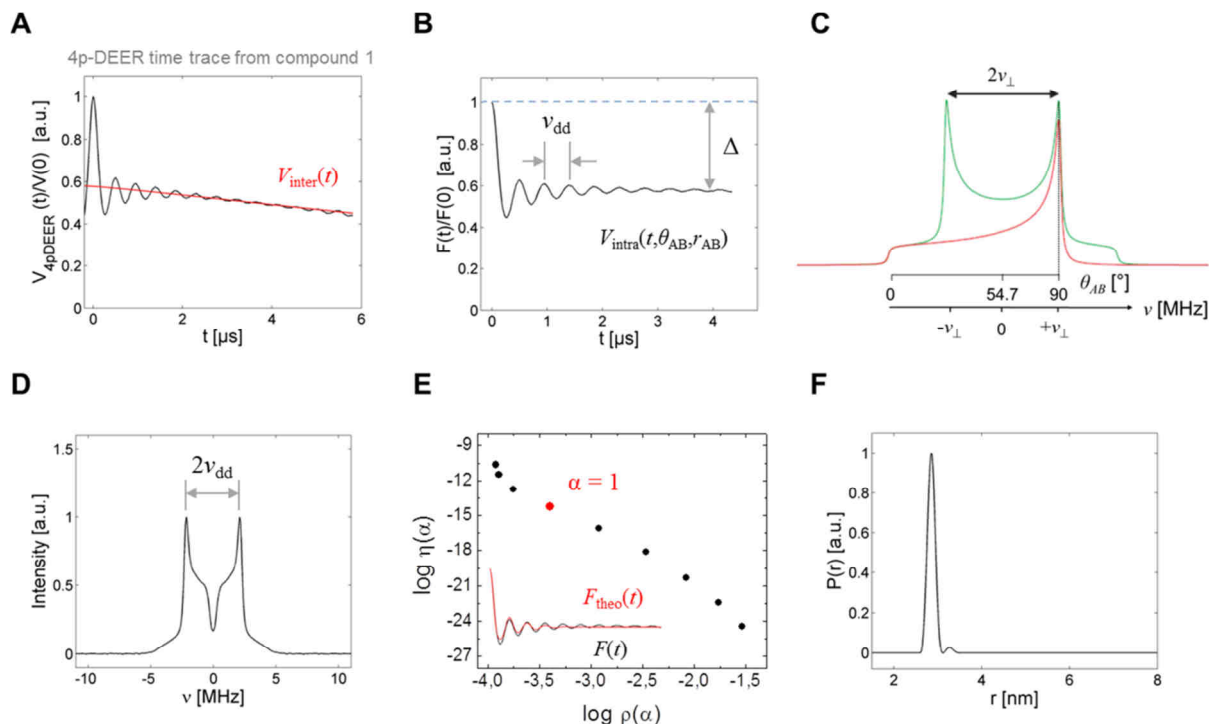

Figure 2.14 | Exemplary analysis of 4p-DEER data from the model biradical compound 1. Results from a 4p-DEER measurement at X-band on the nitroxide model biradical compound 1 in OTP-d$_{14}$ at 50 K (see also **Figure 2.12A** and **Appendix C7**). The pulse lengths were set to 32 ns for π and $\pi/2$ pulses, with a pump pulse length of 12 ns and $\tau_1 = 396$ ns. The pump frequency was set to $h\nu_B = \hbar\omega_B = 9.3061$ GHz at a field position $B_{z,0} = 3309$ G. The observer frequency $h\nu_A = \hbar\omega_A$ was set to 9.3709 GHz, so that $\Delta\nu = 64.8$ MHz. (**A**) Normalized 4p-DEER time trace $V_{4p\text{DEER}}(t)/V(0)$ of compound 1. The background function $V_{\text{inter}}(t) = B(t)$ is highlighted in red with a best fit for $D = 3.41$. (**B**) Normalized dipolar evolution function $F(t)/F(0) = V_{\text{intra}}(t,\theta_{AB}, r_{AB})$ containing information about the intramolecular dipolar coupling frequency $\nu_{dd} = \omega_{dd}/2\pi$ and modulation depth Δ. (**C**) A schematic Pake pattern is shown for $\nu_{dd} = \nu_{\perp}$.[120] (**D**) Pake pattern from the dipolar evolution function in (B) highlighting the dipolar coupling frequency $\nu_{dd} = \omega_{dd}/2\pi$. (**E**) A calculated L curve is presented after Tikhonov regularization. The inset shows the fit curve $F_{\text{theo}}(t)$ to data shown for $F(t)$ in (B) with $\alpha = 1$, giving the (**F**) resulting distance distribution $P(r)$. Data evaluation has been obtained with the MATLAB based program package DeerAnalysis2013.[139]

As the echo amplitude basically scales with $V_E(2\tau) = \exp(-2\tau/T_m)$, as shown in equation 2.86, the proper choice of temperature may lead to decisive gain in signal intensity. As it is pointed out in Fajer *et al.*,[115] the optimum temperature in 4p-DEER is at about 50 K for nitroxides, so this temperature has been used throughout this work. In **Figure 2.14** an exemplary analysis of a 4p-DEER time trace from a model compound 1 in **Figure 2.12A** is shown. In a simplified view, the evaluation strategy is to deconvolute the 4p-DEER time trace into intermolecular and intramolecular contributions as shown in

Figure 2.14A+B, with the latter contribution containing the dipolar coupling frequency v_{dd}. The Fourier transform of the 4p-DEER time domain data is a Pake pattern in the frequency domain, yielding the dipolar coupling frequency $v_{\perp} = v_{dd}$ in terms of a maximum at an angle $\theta_{AB} = 90°$ (**Figure 2.14C**). The differences in theoretical (**Figure 2.14C**) and experimental Pake patterns (**Figure 2.14D**) originate from slight deficiencies from signal processing, as background subtraction ($B(t)$) and the lack of the parallel spin orientations at $\theta_{AB} = 0°$.[143] In **Figure 2.14D** the corresponding Pake pattern is shown with a maximum at $v_{dd} = 2.16$ MHz facilitating a manual calculation of an interspin distance of $r_{AB} = 2.89$ nm following equation 2.92 and assuming that $g = g_A = g_B \approx 2$. Besides this straightforward result, additional information about the distribution of distances can be obtained with a more sophisticated approach. As the extraction of distance distributions from 4p-DEER time traces is an intrinsically ill-posed problem, it could be shown that the application of approximate Pake transformations (APT) and moment analyses[144] leads to reasonable results, however, it has turned out that the most reliable method for this purpose is the conduction of a Tikhonov regularization[145] in combination with a consequent analysis of the resulting L curve[146] of 4p-DEER data as shown in **Figure 2.14E**.[139] Generally, a Tikhonov regularization is the solution of the least squares problem:

$$\min_{\boldsymbol{x}_{\alpha}}\left\{\left\|\,\boldsymbol{Ax}-\boldsymbol{b}\,\right\|^2 + \alpha\left\|\,\hat{\boldsymbol{G}}\boldsymbol{x}\,\right\|^2\right\} \tag{2.97}$$

of finding a vector $\boldsymbol{x}$ so that matrix $\boldsymbol{A}$ and vector $\boldsymbol{b}$ fulfill the condition $\boldsymbol{Ax} = \boldsymbol{b}$, while α controls the weight of minimization of the seminorm $\|\,\hat{\boldsymbol{G}}\boldsymbol{x}\,\|$ of the solution relative to the residual norm $\|\,\boldsymbol{Ax} - \boldsymbol{b}\,\|$.[146] In case of extracting distance distributions $P(r)$ from fits of $F_{theo}(t) = K(t,r)P(r)$ to dipolar evolution functions $F(t)$ in 4p-DEER, equation 2.97 can be written as:[139]

$$\min_{P(r)_{\alpha}}\left\{\left\|\,K(t,r)P(r)-F(t)\,\right\|^2 + \alpha\left\|\,\frac{\mathrm{d}^2}{\mathrm{d}r^2}P(r)\,\right\|^2\right\} \tag{2.98}$$

with the kernel function:

$$K(t,r) = \int_0^1 \cos\left[(3x^2-1)\omega_{dd}t\right]\mathrm{d}x \qquad . \tag{2.99}$$

Here, $\hat{\boldsymbol{G}}$ is a differential operator[147] giving the smoothness of the distance distribution. In this special case α controls the weight of mean square deviation $\rho(\alpha) = \|\,K(t,r)P(r) - F(t)\,\|^2$ between calculation and measurement as well as the smoothness $\eta(\alpha) = \|\,\mathrm{d}^2P(r)/\mathrm{d}r^2\,\|^2$. The L curve now helps to decide which α value has to be chosen and is therefore plotted as log $\eta(\alpha)$ versus log $\rho(\alpha)$.[139] Usually, the α value in the kink region is the best choice (**Figure 2.14E**). As a rough estimate it can be stated that the less pronounced this kink is, the broader is the distance distribution. The resulting distance distribution $P(r)$ can be regarded as being related to a spin-spin pair correlation function $G(r)$ of a spin cluster with

the relation:[144]

$$P(r) = 4\pi r^2 G(r) \tag{2.100}$$

Mathematically, $P(r)$ is a probability density function:[148]

$$W(r) = \int_{r_{min}}^{r_{max}} P(r)\mathrm{d}r = \langle n \rangle - 1 \tag{2.101}$$

with $\langle n \rangle$ representing the average number of spins per cluster. In case of model compound 1 the number of spins per cluster is exactly $\langle n \rangle = 2$ and $r_{AB} = 2.86$ nm being very close to the manual result. Thus, the density function $W(r)$ gives the probability of finding an electron spin within a shell of radius r of thickness $\mathrm{d}r$ in the experimentally accessible distance range $r_{min} \leq r \leq r_{max}$. The shell-factorization model predicts a lower boundary for r_{min} of 1.5 nm for conventional 4p-DEER experiments and $r_{max} = 40$ nm for accessible dipolar evolution times of $t_{max} = 8$ µs.[149] For spin clusters within individual polymers or proteins r_{max} may be estimated from the hydrodynamic dimensions of the macromolecular structure that usually does not exceed 5 – 6 nm.

As the modulation depth parameter λ of the 4p-DEER time trace is a spectrometer specific constant for a defined set of pulse lengths and amplitudes, a quantitative assessment of the average number of cluster spins can be obtained. For $\lambda \ll 1$, the modulation depth is defined as $\Delta = \lambda(\langle n \rangle - 1)$ for a dipolar evolution function $F(t)$ at sufficiently long times ($t \rightarrow \infty$),[130] so that $\Delta = \lambda$ for $\langle n \rangle = 2$.[150] A more generalized approach[139,151] suggests the expression:

$$1 - \Delta = \lim_{t \to \infty} F(t) = \exp\left[-\lambda(\langle n \rangle - 1)\right] \tag{2.102}$$

that can be further simplified, yielding:

$$\langle n \rangle = 1 - \frac{\ln(1 - \Delta)}{\lambda} \quad . \tag{2.103}$$

In case of the model biradical compound 1,[121] the modulation depth in **Figure 2.14B** is $\Delta = 0.422$ with a corresponding modulation depth parameter $\lambda = 0.548$. Thus equation 2.103 enables to count the number of electron spins in a cluster with an accessible shell of an experimentally defined radius r_{max}. Originally, the spatial resolution of DEER was legitimately estimated to range from 1.5 – 8.0 nm for optimized model systems[137] that has also been proven experimentally.[121] Throughout this work, 4p-DEER data aquisition was exclusively performed at X-band frequencies on a conventional pulse EPR spectrometer (BRUKER Elexsys E580) and data analysis was conducted with the well-approved software package DeerAnalysis.[139]

3 | Serum Albumin – A Model System in EPR Spectroscopy

Albumin is the major transport protein in blood plasma and facilitates binding of an innumerable amount of individual exogenous and endogenous small molecules as e.g. vitamins, steroids, toxins, drugs, fatty acids, lipids, bile acids, and also ions.[1,2] Albumin is genetically highly conserved among mammals, it is synthesized in the liver and it usually has a molecular weight of about 66.5 kDa corresponding to about 580 – 585 amino acids throughout most of the mammal organisms that benefit from its ubiquitous presence in all body fluids. The high blood plasma concentration of about 0.631 ± 0.053 mM (= 42.0 ± 3.5 mg/ml) in humans is owed to its high solubility that emerges due to a very large total number of charged residues at physiological conditions. The strongest ligand binding is observed for hydrophobic organic anions of medium size ranging from 100 – 600 Da,[1] while the flexible structure of albumin provides a multitude of binding sites of up to seven in case of long-chain fatty acids (LCFA).[3] Generally, it provides an artificial depot for many ligands way beyond their individual solubility in blood plasma. Some of them are bound site-specific and some of them unspecifically, depending on their chemical and physical properties as charge, hydrophobicity and shape.

In this work particular attention has been directed upon the mutual dynamic interactions and structural alignments of albumin with fatty acids as it can be observed by EPR spectroscopy. Herein, the basis of studies concerning albumin is its intrinsic self-organizing behavior with fatty acids[4] utilizing spin-labeled stearic acids as 5-DSA and 16-DSA (DSA = doxyl stearic acid, **Figure 3.1A**) as well as the spin labeling approach e.g. by targeting accessible cysteine residues at polypeptide position 34 (Cys34).[1,5] This Cys34 residue is common to most mammal albumins and is not involved in structure-stabilizing disulfide bridges.[6] As albumin has now been investigated for over 50 years in EPR spectroscopy,[7] a thorough literature survey of a rich selection was conducted to certify a minimum of redundant studies besides calibration and occasional test rows. Additionally, based on precursor studies a new concept of an EPR spectroscopic albumin research platform will be worked out for a strategic localization of previous deficits in literature and the rationalized setup of new creative projects studying the intricate structural and dynamic properties of this protein. It is beyond question that setting up a list of all related scientific contributions ($>>10^3$) in this research field cannot be mentioned exhaustively, however, some representative studies are given at appropriate positions in the following sections of this and also in forthcoming chapters.

3.1 | Spin Labeling of Albumin

The first site-directed spin labeling strategies have been developed in the group of Harden McConnell with the result that the first biomacromolecule that has been made accessible to EPR spectroscopy was bovine serum albumin in 1965 using 2,2,5,5-tetramethyl-3-isocyanatopyrrolidine-1-oxyl as a spin label.[7] Back then, it served as an initial fundamental example of how dynamic and structural information can be obtained from CW EPR spectra as the lineshape theory already had been

developed.[7–11] Initially, as various albumins contain an accessible Cys34 residue, the maleimido proxyl spin-labels are utilized to obtain dynamical information from the protein via CW EPR[12–16] and also saturation transfer (ST) EPR.[17] The disadvantage of this approach is that also surface exposed lysines may be labeled unspecifically due to the pH-dependent dual affinity character of the maleimido group towards cysteines and lysines.[12] The high intrinsic mobility of these spin labels has been attempted to overcome by attaching the nitroxide moiety closer to cysteine by generating thiyl radicals $(RS^{\bullet})$ with Ce^{4+} that is finally spin trapped by a nitrone,[18] unfortunately with rather noisy spectra. Furthermore, the purely cysteine specific spin label MTSSL[19] offers the opportunity to exclusively target the Cys34 residue on albumin on albumin fragments[20] or the full HSA protein,[21] promoting it as a monoradical with a single MTSSL residue. The same principle applies for the 4-(2-Iodo-acetamido)-TEMPO (IAA) spin label.[22] From this labeling approach, several studies indicate that the accessible cysteine is in a crevice on the surface of BSA.[7,12,13] Its imidazoline derivative IMTSL as a molecular pH-sensitive probe[23] has also been attached to HSA[24] with the aim to detect the proteins surface potential as a function of the pK_a shift of the amino group in the radical bearing moiety. In case of HSA the surface potential was found to be 33 mV in 0.01 M KCl and 65 mV without salt according to the Gouy-Chapman theory. The possibility for sensing pH with appropriate nitroxides in EPR spectroscopy is still devotedly pursued[25,26] and it remains to be seen what future studies might further reveal.

3.2 | Spin Probing Albumin with Paramagnetic Fatty Acids

The discovery that fatty acids bind to albumin by Kendall[27] generally opened the way for studying the interactions of various small low-polarity molecules with this protein. The drastic advances that have been made in membrane biophysics were also strongly promoted by EPR spectroscopy accompanied with upcoming synthesis of spin-labeled lipids,[28–32] steroids[30,33,34] and fatty acids[28,35,36] that led to a broad variety of available spin probes. Again Harden McConnell and coworkers pioneered the successful application of spin-labeled fatty acids to albumin in CW EPR spectroscopy.[37] Apart from the intrinsic albumin-induced fatty acid rotational dynamics,[38] the self-assembly of substrate and ligand facilitates the extraction of additional kinetic parameters originating from non-covalent interactions as binding association (K_A) or dissociation constants ($K_D = K_A^{-1}$) as well as binding capacities (N) that can be obtained from binding isotherms as e.g. Scatchard plots[39] or Hill plots.[40,41] From EPR spectroscopic studies it is commonly reported that HSA as well as BSA bind 4 – 8 paramagnetic fatty acids with a K_D in the low micromolar range.[42–49] Particularly, the highly insoluble LCFAs ($C_{16} – C_{20}$) that are crucial intermediates in lipid metabolism are permanently attached to the albumin molecules. The physiological plasma concentration of fatty acids is usually about 1 mM and about 99.9 % are bound to albumin. Furthermore, fatty acids have an pK_a value of about 4.8 and occur predominantly as anionic salts ($RCOO^-$) at pH 7.[1]

Generally, the basis for a successful binding study is the presence of multi-component EPR spectra that in the simplest case comprise at least a distinguishable bound (*b*) and a free (*f*) fraction. The concomitant impact of decreased rotational diffusion on EPR spectra upon nitroxide immobilization was already shown in **Chapter 2.4.3**. Since small molecules have characteristic rotational correlation times τ_c of several picoseconds and exhibit three line spectra at viscosities about liquid water at room temperature ($\eta_{H20}(25°C) = 0.893$ mPa·s),[50] immobilized spin probes (and spin labels) bound to a macromolecule manifest themselves as a severe line broadening with correlation times of several nanoseconds being close to the rigid limit as it is shown in **Figure 3.1B** for 16-DSA in HSA. The electron spin relaxation can be considered to occur via phonons[51] of the surrounding crystal-like macromolecule.[52,53] In this example the rotational correlation times in 20% v/v glycerol of free 16-DSA is about $\tau_{c,f} = 150$ ps and for 16-DSA bound to albumin about $\tau_{c,b} = 20$ ns. The latter one largely reflects the rotational motion of the protein itself while the ligand becomes an integral part of the macromolecular system. Compared to other methods like electric birefringence,[54] nuclear magnetic resonance dispersion (NMRD),[55] fluorescence polarization of intrinsic tryptophane residues[56–61] and phosphorescence depolarization,[62] the results for global Brownian rotational diffusion from general EPR experiments are in very good agreement, yielding τ_c values of 21 – 57 ns for DSA spin probes.[47,63] Detectable deviations in rotational dynamics in different published studies are mostly due to variations in experimental parameters such as the choice of spin probe, temperature or sample viscosity. For an elaborate study concerning rotational dynamics of a large set of DSA and doxyl methyl stearic acid (DMS) spin probes in BSA the reader is referred to Ge *et al.*[48]
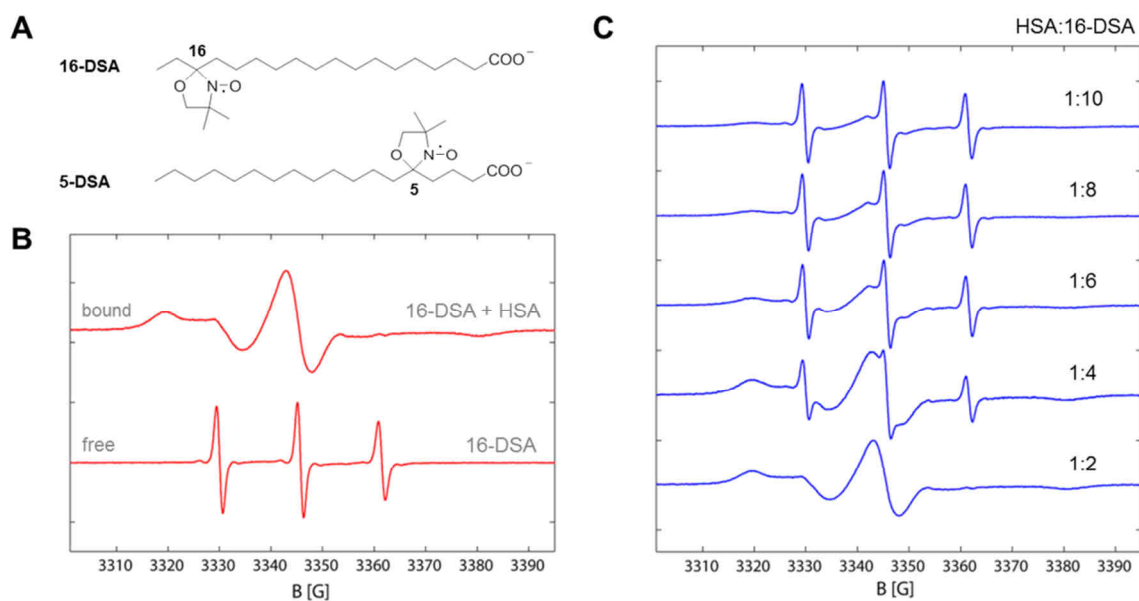

Figure 3.1 | Fatty acid-spin probed albumin in EPR spectroscopy. (**A**) Chemical structures of 5-DSA and 16-DSA. (**B**) CW EPR spectra of freely tumbling 16-DSA (lower trace) and 16-DSA bound to HSA. (**C**) CW EPR spectra of various nominal loading ratios of HSA:16-DSA from 1:2 to 1:10. Spectra were obtained at $T = 25°C$ in DPBS buffer[64] pH 7.4 and 20% v/v glycerol.

In a first approximation the perception of free and bound fractions is therefore straightforward and by rigorous decomposition and analysis of individual spectra in a loading study (**Figure 3.1C**) a binding isotherm can be constructed from the variations in fractional occupation of the corresponding dynamic regimes. This is very similar to other techniques as e.g. the equilibrium partition (EP) method.[65,66]

Beyond the detection of ligand capacities and intrinsic motional dynamics, those parameters furthermore establish the basis for experimental investigations extending the scope towards EPR-based denaturation studies[67,68] complementary to standard methods as circular dichroism (CD),[69,70] fluorescence correlation spectroscopy (FCS),[71,72] differential scanning calorimetry (DSC)[73,74] and dynamic light scattering (DLS).[75–77] To date, in several EPR studies this approach has been successfully applied to albumin.[78–82] Upon loading albumin with DSA, some more sophistications have to be considered that will be pointed out in the following chapters.

3.3 | Dynamic and Structural Aspects of Fatty Acid Binding

In case of albumin the immobilization of amphiphilic fatty acid spin probes is an entropic effect,[83] accompanied by a release of water and thus it is supposed to lock the ligands to the protein mainly due to hydrophobic interactions along the alkylene chain.[4,38] It has been observed from pulsed dielectric relaxation measurements that for HSA an opened or activated state is intrinsically triggered by the low-entropy water arrays on hydrophobic binding site surfaces of the protein with a frequency of about 3 s^{-1}.[83] Thus, after a diffusion-controlled fast initial unspecific ionic bond of the carboxylic acid group with the outer protein surface, the occurrence of an activated state permits the fatty acids to gain access to the hydrophobic interior, while the protein repeatedly closes and water is partially expelled.[84] Those intrinsic breathing motions of HSA[61] appear to be crucial for most of the ligand binding processes. Notably, a X-ray crystallographic structure of HSA co-crystallized with medium and long-chain fatty acids revealed seven binding pockets for fatty acids spread along the three homologous domains, as well as their location and corresponding spatial alignment in the protein interior (PDB ID: 1e7i).[3] Since it was already known that for several binding sites fatty acids may attach to ionic anchor points located in the hydrophobic binding channels of the protein interior,[48,84–88] the nature of the seven individual binding-sites appeared to be highly non-uniform and asymmetric[87] regarding physical and structural aspects. Furthermore, the strength of fatty acid binding was also shown to depend on chain length, where longer chains in principle experience higher affinity.[4,65,89,90] In EPR spectroscopy the bound paramagnetic fatty acids exhibit a slightly lowered a_{iso} value being indicative of a more hydrophobic character of the protein interior.[48] Five of those fatty acid binding pockets contain ionic anchors, so that hydrophobic and electrostatic interactions may contribute to the binding energy simultaneously. Those five pockets can be further subdivided into three long and narrow (2, 4 and 5) high affinity binding sites and two short and wide low-affinity binding sites (1 and 3). As binding sites 6 and 7 lack potential electrostatic interactions they are also commonly referred to as low-affinity binding sites.[3,91–93] A strategic EPR spectroscopic investigation on BSA

revealed that fatty acids experience the strongest immobilization from such a high-affinity binding site in the mid-section of the alkylene chain.[46] From numerical solutions of stepwise equilibrium binding models[94,95] it is assumed from the equilibrium partition (EP) method that each of the seven binding sites has an individual dissociation constant $K_{D,i,EP}$ between 7 and 360 nM for [1-^{14}C]-labeled stearic acids.[66] The chemical modification of stearic acids with a doxyl group for EPR experiments may deplete this high affinity for one or two orders of magnitude to the range of $K_{D,i,EPR} = 0.2 - 158$ µM as it was observed for 5-DSA.[44] A summary of those findings is given in **Table 3.1** and the missing values for 5-DSA for both binding sites 3 and 4 is assumed to be due to a mutual cooperative kinetic effect.

Table 3.1 | Individual binding site dissociation constants $K_{D,i}$ and physiological free fatty acid (FFA)-to-albumin ratios under varying conditions.

	Dissociation constants[a]		FFA:Albumin ratios for various physiological conditions	
Reaction	**[1-^{14}C] stearic acid[66]**	**5-DSA[44]**	**Healthy**	**FFA:Albumin [eq][b]**
$PL_{i-1} + L \rightarrow PL_i$	$K_{D,i,EP}$ [nM]	$K_{D,i,EPR}$ [nM]	Normal[96–98]	0.32 – 1.39
$P + L \rightarrow PL_1$	6.7	199.6	Fasting[96,99]	1.49 – 2.27
$PL_1 + L \rightarrow PL_2$	18.8	794.3	Epinephrine medication[96]	1.11 – 2.76
$PL_2 + L \rightarrow PL_3$	52.9	–	**Acute** (pathologic)	
$PL_3 + L \rightarrow PL_4$	179.9	–	Nephrotic Syndrome[97]	0.87 – 1.40
$PL_4 + L \rightarrow PL_5$	224.7	5011.8	Non-Thyroidal Illness (NTI)[98]	1.12 – 1.94[c]
$PL_5 + L \rightarrow PL_6$	269.5	15848.9	Myocardial Infarction[100]	1.90 – 3.17
$PL_6 + L \rightarrow PL_7$	314.5	6329.1	Psychological Stress[101]	1.88 – 2.89
$PL_7 + L \rightarrow PL_8$	359.7	158489.3	Uncontrolled Diabetes[102]	4.15 – 4.79
			Heparin Treatment[1]	≤ 6.00
			Chronic (pathologic)	
			Obesity[96]	0.90 – 2.28
			Endogenous Hypertriglyceridemia[103]	2.93 – 4.69
			Insulin treated diabetes mellitus[96]	0.69 – 1.57

[a]Dissociation constants of individual fatty acid binding sites were obtained from equilibrium partition binding method[66] and from EPR spectroscopy[44] with data being analyzed assuming stepwise equilibria. [b]If FFA equivalents were not directly shown, the given plasma fatty acid concentrations have been used to calculate a FFA:Albumin ratio at an average blood plasma concentration of $c_{HSA} = 0.631$ mM. Lower and upper limits were taken from individual studies. [c]The Standard deviations were here converted into lower and upper limits using the given mean value.[98]

It has first been suggested from EPR[104] and NMR[105] studies, that those two fatty acids bind to a shared binding pocket, and by now this claim has been confirmed by the aforementioned crystal structure (PDB ID: 1e7i).[3] Hence, this collaborative property of all fatty acid binding sites presumably allows albumin to adjust individual affinities for momentary physiological and metabolic requirements. Svenson determined the dissociation rate constant $k_{-1} = 0.036$ s^{-1} at 23°C leading to a half-life of 19.3 s for palmitic acid dissociation.[106] This leads to an extrapolated association half-life of 0.2 – 1.6 ms for the binding of 1 equivalent of palmitic acid in a physiological 0.631 mM albumin solution for the three high affinity binding sites using values from Ashbrook.[66] The corresponding

residence time of the ligand associated to the protein is then about $\tau_r = 1/k_{-1} = 28$ s.[107] Fatty acid binding is also a sophisticated thermodynamic process as the binding sites are statistically occupied, of course depending on the divergence of individual $K_{D,i}$ values (**Table 3.1**). Thus, there is no strict filling in the nominal order of binding affinities, so that at intermediate fatty acid loadings of 2 – 3 equivalents various binding site occupations will be present in individual albumin molecules of a sample.[85,108] Furthermore, it is widely accepted that binding site 5 (FA5) may exhibit the highest affinity towards fatty acids.[88,109] In equilibrated physiological conditions the molar steady-state blood plasma FFA:Albumin ratio is usually < 1.0 for healthy individuals and it only transiently exceeds 1.0 as e.g. for fasting or upon medication (**Table 3.1**). For several acute or chronic pathological conditions that are also listed, this ratio may be elevated to 1.0 – 3.0 and even to about 5.0 for uncontrolled diabetes[102,110] and endogenous hypertriglyceridemia.[103] Some occasions may raise the FFA level to 6.0 for heparin treatment or even more for diabetic ketoacidosis complicated by nephrosis.[110]

Additionally, HSA's property of allosteric modification upon binding of low molecular weight biomarkers as peptide fragments related to cancer, sepsis or diabetes,[111] as well as drugs,[112] lead to altered fatty acid uptake capabilities. Several interesting pilot studies aiming for clinical applications such as e.g. cancer diagnosis and prognosis have been undertaken with EPR spectroscopy in this regard utilizing the fatty acid spin probing approach.[111,113–118]

The competitive and cooperative binding of albumin ligands[119–121] is also a favored subject in EPR spectroscopic investigations utilizing spin-labeled thyroxine analogs,[122] spin-labeled drugs and small molecules,[49,123–125] or spin-labeled stearic acids as competitive ligands.[47,126] Hereby, it is possible to at least indirectly detect variations in K_D values conditioned by binding site cooperativity,[47] or a change in the total number of available binding pockets for spin-labeled compounds as induced by competitive binding of EPR-silent ligands as heparin[47] or ibuprofen.[126]

Besides fatty acid binding sites, several other specific binding sites have been identified in HSA for a vast amount of ligands. In this regard, the two main drug binding sites, also termed as the Sudlow-sites,[119] are located in subdomain IIA and IIIA and accomplish binding of at least one ligand with acidic or electronegative properties.[127] Meanwhile, a quick search in the protein data base[128] reveals a list of at least 98 HSA crystal structures and 80 ligands (accessed Jun 5, 2018) and therefore some exemplary physiological and medically relevant ligands are given in **Figure 3.2** to accentuate the significant importance albumin holds as a physiological drug transporter.

The interplay of the various ligand binding sites of albumin appears to be of a most intricate nature as it is governed by allosteric and cooperative effects that influence the protein properties decisively. A good example of this complex dynamic inner working is the binding of Thyroxine. Upon saturation with myristic acid a fifth high affinity thyroxine binding site appears due to allosteric structural adaptations by opening the cleft between domains I and III and therefore the thyroxine binding cooperativity changes from negative to positive.[121]
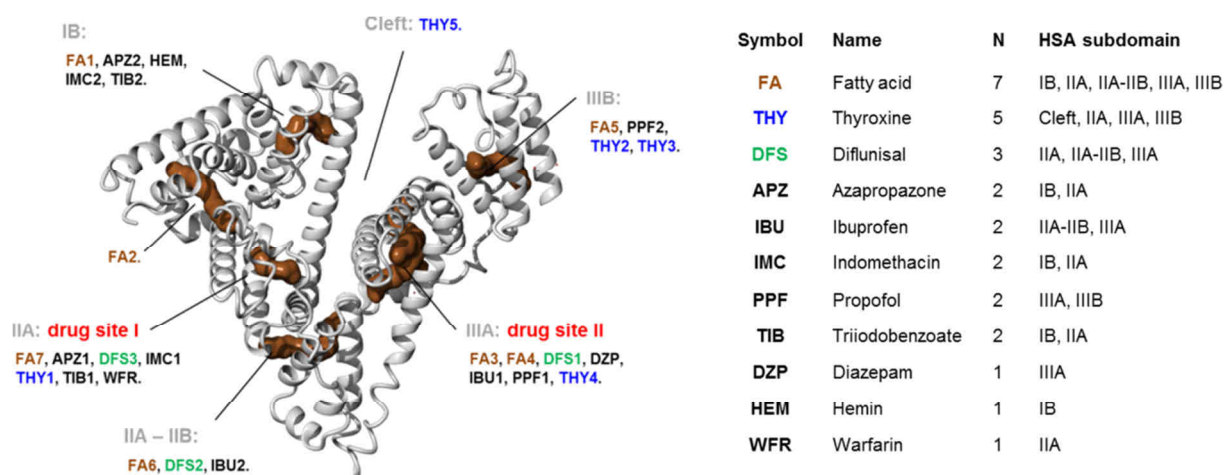
Symbol	Name	N	HSA subdomain
FA	Fatty acid	7	IB, IIA, IIA-IIB, IIIA, IIIB
THY	Thyroxine	5	Cleft, IIA, IIIA, IIIB
DFS	Diflunisal	3	IIA, IIA-IIB, IIIA
APZ	Azapropazone	2	IB, IIA
IBU	Ibuprofen	2	IIA-IIB, IIIA
IMC	Indomethacin	2	IB, IIA
PPF	Propofol	2	IIIA, IIIB
TIB	Triiodobenzoate	2	IB, IIA
DZP	Diazepam	1	IIIA
HEM	Hemin	1	IB
WFR	Warfarin	1	IIA

Figure 3.2 | Site-specific ligand binding capacity of HSA. A selection of ligand molecules is shown as adapted from Ghuman *et al.*[127] The structure of HSA co-crystallized with seven stearic acids (PDB ID: 1e7i)[3] is depicted and subdomain specific binding-sites for a set of 11 different ligands are presented. Ligands with highest binding scores are color-coded in brown (FA = fatty acids), blue (THY = Thyroxine) and green (DFS = Diflunisal). All other ligands are given in the list at the right hand side.

Another fatty acid based effect is the induction of bimodality in melting curves by ligand redistribution and the increased structural stabilization observed from the positive melting temperature shifts of 15 – 30 °C in albumin samples.[74,129,130] Fatty acid binding is also pH-dependent[48] as the albumin structure is commonly believed to e.g. expand in acidic solutions below pH 4 due to static charge repulsion.[1,61] Additionally, the fatty acid carboxyle group gets protonated and interactions with the ionic anchor in the high affinity binding sites decrease. In alkaline solutions above pH 11.5 structural disulfide bonds are broken also leading to a release of fatty acids.[1] Therefore, the effect of an acidic environment comprises a crucial step in the defatting purification process of albumin where fatty acids can be ultimately removed from albumin by passage over a hydrophobic resin.[1,131]

3.4 | Saturation Transfer (ST) EPR and Non-linear EPR Experiments on Albumin

A subtle extension of the detectable timescales of CW EPR from 10^{-12} s to 10^{-6} s is offered by saturation transfer EPR experiments.[132] The basic principle of saturation transfer is to achieve saturation of absorption by very strong microwave irradiation and modulation. The response of the spin system is then followed via the spectral diffusion that leads to a transfer of the generated population saturation to other electronic transition frequencies. This transfer particularly depends on translational molecular motion and extends the timescale for three orders of magnitude toward the millisecond regime (10^{-3} s).[133] Hence, translational diffusion rates D_T have been measured for maleimide spin-labeled HSA yielding a value of $D_T = 6.6 \cdot 10^{-11}$ m^2 s^{-1},[134] which is in excellent agreement with literature.[94] A significant gain in signal quality and resolution was observed by testing perdeuterated variants of MSL on BSA.[17] Another very interesting study was contributed by a non-linear EPR spectroscopic approach on maleimide spin-labeled BSA in comparison to 5-DSA and 16-DSA spin-probed BSA.[63] The rationale behind this study was to detect spin lattice relaxation

enhancements upon spin-spin interaction of the nitroxides with the paramagnetic ferricyanide ion ($[Fe(CN)_6]^{3-}$). The variations in the bound spin probe encounter frequency towards the aqueous ion resulted in further evidence and a kinetic model for an opened and closed state of the albumin solution structure as already found by Scheider.[83,84]

3.5 | Differences among Albumins from CW EPR and Other EPR Spectroscopic Approaches

Historically, the detection of functional differences in between albumin species can be traced back to the early days of albumin research. During the WWII plasma fractionation program it has turned out, that highly purified serum made from BSA caused soldiers to die from kidney failure, whereas serum made from HSA saved their lives upon dispensing infusions. Since then there has been a variety of distinct implications that divergent evolution came up with a variety of sophisticated functional adaptations to albumins of individual organisms,[1] while standard biochemistry textbooks may still tend to treat albumins unintentionally as static interchangeable structures for simplicity.[135] Already in the 1950s Charles Tanford pioneered many physicochemical strategies in protein biophysics with the albumin model system at hand. Yet, slight differences between HSA, BSA and ESA (equine serum albumin) solution structures were preferentially addressed to variations in sample preparation.[136] Meanwhile, the scientific view on differences between albumin species gets steadily refined in various disciplines like e.g. photometric approaches using bromocresol green (BCG).[137,138] Not least due to the exploding number of available albumin crystal structures in the protein data bank (PDB) that emerge from different organisms, computational approaches are conducted that aim for comparing albumins ranging from lamprey to humans[139] and calculations are performed yielding theoretical titration curves with isoelectric points (pI) in correlation with pH-dependent charges.[140] CW EPR spectroscopy has also been employed for a long time to perform comparative studies on different albumins, with a preference for HSA and BSA. One important structural aspect was initially promoted partly with the spin labeling approach where several studies indicate that the aforementioned Cys34 residue is in a crevice on the surface of BSA,[7,12,13] while it is found for HSA to be rather surface exposed as it can be seen from UV/Vis and optical rotatory dispersion analysis.[13,141] Rehfeld *et al.*[44] directly compared ligand binding of 5-DSA to HSA and BSA by the stepwise equilibrium method[94] and also found that stearic acids appear to be stronger immobilized in HSA. Gantchev and Shopova[47] also tested HSA and BSA with 5-DSA and 16-DSA and found from binding isotherms that the total number of binding sites is equivalent for both proteins ($N_T = 8 \pm 1$) but the macroscopic dissociation constant (K_D) appears to be slightly lower for HSA that accordingly possesses a higher affinity for stearic acids. From thermodynamic spin probe analyses it was concluded, that fatty acids appear to permanently migrate between specific binding sites and cavities of the albumin subdomains at physiological conditions.[142,143] Hence, a hydrophobic channel linking model was advanced that differs for HSA and BSA in terms of activation energy of a rather obscure interconversion mechanism that

was observed from immobilized 16-DSA spin probes. This hypothesis will be further investigated in **Chapter 10** and **Chapter 11** of this work.

3.6 | Early Pulse EPR Experiments on Albumin

The first pulse EPR experiments were performed on a pulse X-band spectrometer by W. B. Mims at Bell Laboratories on a system of BSA self-assembled with cupric acetate as a paramagnetic species (Cu^{2+}).[144] This two-pulse electron spin echo envelope modulation (2p-ESEEM)[145] study gave valueable insights into the coordination of metal ions with biomacromolecules and the coupling of a remote nitrogen nucleus associated with a histidyl imidazole ligand to the copper was observed. As pulsed EPR was not a widespread method back then, data processing and analysis turned out to be still of a highly sophisticated nature. It was not until 2007 that the group of Derek Marsh took on investigations with the albumin spin probing approach using echo-detected (ED) EPR in combination with 2p-ESEEM. These methods were applied to several stearic acids with the doxyl labels located at five different positions (C_5-, C_7-, C_{10}-, C_{12}-, and C_{16}) along the C_{18} alkylene chain while tightly bound to HSA.[109] The Fourier transformed 2p-ESEEM spectra measured in D_2O showed that water accessibility is preserved throughout the whole length of the bound fatty acid exhibiting librational motions very similar to surface bound and water exposed maleimide spin labels. This finding indicates that albumin facilitates ligand exchange while still providing strong binding. The biggest water depletion was obtained for the C_7 position pointing to strongest hydrophobic interactions in the middle of the fatty acid chain in qualitative accordance with findings of Perkins *et al.*[46]

3.7 | Spatial Alignment of Fatty Acids in Albumin – The 4-pulse DEER Approach

In fact, the spatial alignment of medium- and long-chain fatty acids in HSA is already well-known from crystallographic studies that have mainly been pioneered in the 1990s in the group of Stephen Curry.[3] However, it was not until 2010 that an approach was intensified for screening the dynamic internal arrangement of spin-labeled fatty acids in HSA by the upcoming 4-pulse DEER method,[146] although all constituents of this self-assembling system were readily commercially available for decades. Elementary details on 4-pulse DEER experiments and data processing have been already described in **Chapter 2.5.5**. This spin probing approach on albumin in DEER spectroscopy has been verified to contribute further interesting aspects about functionality on a more coarse-grained level compared to e.g. X-ray crystallography. Basically, this DEER-based approach also shares certain analogies with Förster resonance energy transfer (FRET) experiments that have been conducted on albumin.[147] Furthermore, a general direct comparison of FRET and DEER is given in Klose *et al.*[148]

Albumin sample preparation for DEER measurements inherently combines some practical as well as physiological aspects. Upon addition of 20% v/v glycerol the solution viscosity increases to about 2 mPa·s for CW EPR experiments at 25°C being a bit closer to the actual physiological value (see **Chapter 5**). Although there is not an exact reference value due to hemodynamical effects, the actual

viscosity of blood usually exceeds 3.5 mPa·s when considering it as a non-Newtonian fluid.[149] As those samples have to be cooled down rapidly below the glass-transition temperature to create a vitrified, glass-like sample for pulse EPR experiments at 50 K, glycerol also serves as a cryoprotectant[150,151] and thermodynamic stabilizer for proteins.[152] In principle, this vitrified sample then reflects the canonical, dynamic ensemble of all possible room temperature protein conformations and ligand alignments. Usually, DEER measurements are conducted on model biradicals,[153,154] doubly spin-labeled macromolecules,[155–157] or singly labeled dimers[158] that bear covalently attached and therefore localized paramagnetic centers in the broadest sense. Principally, the resulting distance distribution in case of a biradical originates from a single distance between spins S_A and S_B bearing additional information about local dynamics that may affect the shape of a DEER distance distribution. To this effect the FA-Albumin system is different in this regard as the paramagnetic fatty acids are non-covalently associated with albumin and may statistically attach to each of the $N = 7$ binding sites.[3] Therefore, the number of potential interspin distances in albumin when spin probed with paramagnetic fatty acids rises from $N_r = (N^2 - N)/2 = 1$ for $N = 2$ in a biradical to $N_{r,FA} = 21$ in albumin. Binding site saturation is also no option for DEER on albumin, as multispin effects cause artificial line broadenings,[159] ghost distances by combinations of dipolar coupling frequencies,[160] as well as an overestimation of small distances and suppression of large distances for more than two spins per protein.[161] Those multispin effects can be circumvented by spin dilution, i.e. only two paramagnetic probes are allowed to enter the protein, while fatty acid loadings exceeding a Albumin:FA ratio of 1:2 require the reduction of paramagnetic probes to EPR-silent species.[146] The reduction of the nitroxide moiety towards a hydroxylamine is usually facilitated with aqueous solutions of phenylhydrazine or ascorbic acid.[162] As the average number of coupled spins is required to be $\langle n \rangle > 1$ in order to detect dipolar coupling frequencies within a macromolecular unit, the albumin-to-fatty acid ratio is set to 1:2 in a standard experiment. The result of such a standard DEER experiment on albumin self-assembled with spin probes 5-DSA and 16-DSA is shown in **Figure 3.3**. Successful interpretation of these obtained distance distributions is only achieved in-depth by comparison with an appropriate crystal structure. Starting with the first purified HSA structures resolved by He and Carter[163,164] and complemented by a high resolution structure of Sugio *et al.*,[165] fortunately the group around Stephen Curry was able to resolve an additional structure with seven stearic acids (PDB ID: 1e7i),[3] perfectly suited for EPR spectroscopic needs. By molecular modeling of the seven bound stearic acids to either 5-DSA or 16-DSA (assuming entirely occupied binding sites, $N = 7$)) the relative positions of nitrogen atoms of the fatty acid doxyl groups can be gained that are associated with the protein matrix (see also **Appendix A1**). These theoretical crystal structure distances or data from molecular dynamics simulations are then artificially broadened with a Gaussian function in order to correlate the ligand-based protein topology with DEER-derived distance distributions as shown in **Figures 3.3C+D**.[166]

Experimentally, the two different labeling positions at the 5- and 16-position of the methylene chain allow for a selective view on the functional structure of albumin. Being close to the carboxylic acid moiety, 5-DSA retrieves the environment of the ionic anchor points and the groups donating the hydrogen bonds.[3] In contrast, 16-DSA holds its paramagnetic center at the opposite end of the methylene chain probing the entry points of the fatty acid binding pockets on the protein surface. Therefore, this approach accomplishes an approximate ligand-based inside-outside (5-DSA versus 16-DSA) viewpoint on the albumin protein.[146]
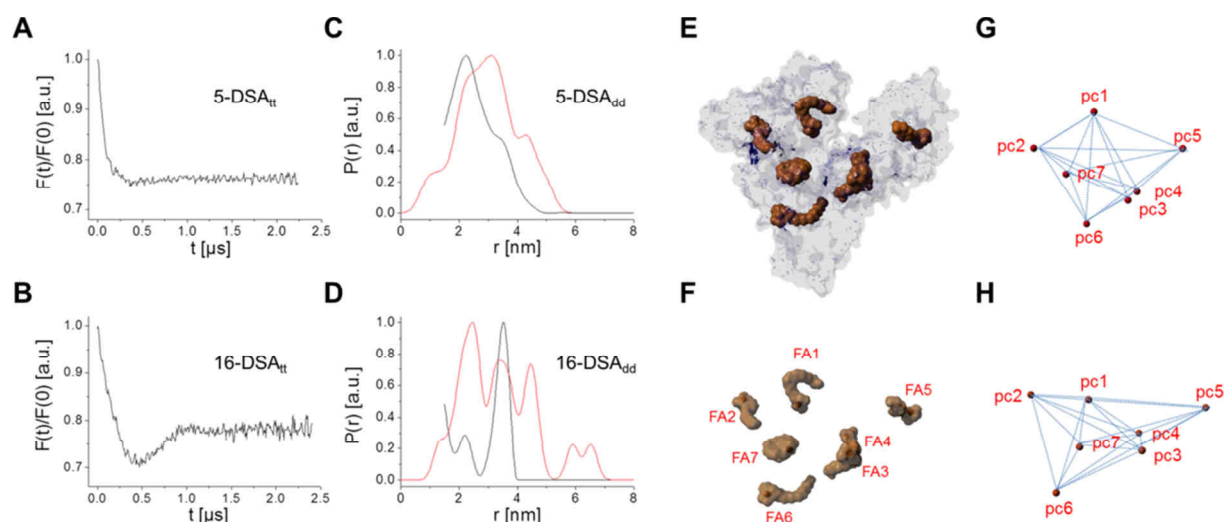

Figure 3.3 | DEER experiments and data interpretation from DSA-spin probed HSA. DEER experiments on 0.4 mM HSA at pH 7.4 spin probed with DSA in the ratio 1:2 (HSA:DSA) at 50 K. Background corrected time traces $F(t)/F(0)$ of (**A**) 5-DSA and (**B**) 16-DSA spin probes bound to HSA. The resulting distance distributions $P(r)$(black) from (**C**) 5-DSA and (**D**) 16-DSA probed HSA are supplemented with calculated distance distributions (red) from the 7×7 distance matrices given in **Table A1**. DEER distance distributions (black) were calculated with the MATLAB-based DeerAnalysis2013 software package.[167] The relative alignment of (**E**) fatty acids (brown) in albumin (transparent blue) and their (**F**) paramagnetic centers (pc, red dots) are shown in case they occupy all seven binding pockets (PDB ID: 1e7i).[3] The $N_{r,FA} = 21$ interspin distances (blue lines) are shown between paramagnetic centers (pc) of (**G**) 5-DSA and (**H**) 16-DSA. All structures in (E-H) were constructed using YASARA Structure software.[168]

Although the protein-bound doxyl-moieties of 16-DSA generally exhibit a higher mobility,[48] they constitute a much narrower experimental distance distribution ($P_{max,16}(r) = 3.6$ nm, black, **Figure 3.3D**) compared to 5-DSA, suggesting a much more symmetric alignment of binding pocket entry points, substantially deviating from the crystal structure-derived curve.[146] However, a much broader distance distribution with $P_{max,5}(r) = 2.3$ nm obtained from bound 5-DSA (nitroxide close to the ionic anchor) indicates a much more asymmetric alignment of binding pockets as it was already proposed by Curry *et al.* (**Figure 3.3C**).[87] While the 5-DSA-derived picture of the proteins interior coincides quite well with the crystal structure, the prominent peak in the DEER-derived 16-DSA distance distribution is particularly intriguing and clearly deviates from the many details of the crystal structure distribution.

One possible interpretation of this simple distance pattern from DEER is that of a highly symmetric, almost octahedral, binding pocket entry point distribution, assuming six binding sites[146] on a

spheroidal albumin surface.[136] This interpretation could be justified in terms of the tetrahedral and octahedral principle of R. Buckminster Fuller of how nature aligns structures spontaneously on various length scales.[169] This lead to the conclusion, that HSA is rigid on the inside while the surface appears to be flexible and of high structural plasticity that also constitutes a potential explanation for the surface adaptability for so many different ligands in BSA[170] and HSA.[171] Both, the higher rotational mobility of 16-DSA compared to 5-DSA[48] and results from fluorescence quenching experiments[61] further confirm the interpretation of surface adaptability and plasticity of HSA. Another DEER study on albumin, self-assembled with a copper porphyrin and 16-DSA[172] was in line with the observations that binding pocket entry points are symmetrically aligned across the HSA surface. Again, this study benefited from an already available crystal structure of HSA co-crystallized with myristic acid and hemin (PDB ID: 1O9X)[173] and complemented evidence of allosteric activation or stabilization by ligand uptake of BSA[74] that is also postulated to occur for HSA.[174,175]

3.7.1 | Using DEER for Folding Studies of Albumin as Induced by Different Solvents

Another possibility to apply DEER spectroscopy is to investigate the stability of albumin against denaturing influences combined with CW EPR spectroscopy. It is known that stability of HSA is not only dependent on disulfide bonds[6] but also on physicochemical factors in the environment. In recent years, employment of ionic liquids (ILs) as designer solvents has become a research branch of mainstream chemistry. This is mainly due to several intrinsically adjustable physical parameters such as viscosity, miscibility, density and polarity, as well as their low toxicity, high chemical and thermal stability, which all made them a welcome complement and alternative to traditional organic solvents.[176–178] The physical basis of protein interactions with ionic liquids is the change in the second osmotic virial coefficient B_{22}, establishing the solvent averaged interaction potential between individual macromolecules[179] and mutual electrostatic and hydrophobic interactions of the protein with ILs at a molecular scale.[180] The chaotropicity of ILs thus leads to a denaturing effect of protein structure by disturbing the stabilizing water cage around a protein.

Primarily, it could be shown by DEER that strong denaturing effects can be observed by an increase of FA distances that occurs upon addition of Emimdca (Emim$^+$ = 1-ethyl-3-methyl imidazolium; dca$^-$ = dicyanamide, see **Figure 3.4A–E**).[82] This is in agreement with fluorescence correlation spectroscopy (FCS) studies detecting a 50 – 60% increase of hydrodynamic radii of HSA during denaturation.[72] On the other hand, a tertiary structure stabilizing IL like choline dihydrogenphosphate (dhp) could be characterized as rigidifying the protein interior and overall stabilizing the proteins global structure[81] as also reported in Constantinescu *et al.*[179] A very surprising result was achieved by unfolding of HSA upon addition of 35% v/v ethanol and Emimdmp (dmp$^-$ = dimethylphosphate) as can be seen in **Figure 3.4A–E**. This finding revealed that the proposed rigid protein interior stretches by shifting $P_{max,5}(r)$ to distances from 2.3 to about 4.5 nm, while counterintuitively the HSA surface seems to stay largely intact for higher Emimdmp and also ethanol concentration exposures.[82] Qualitatively, one

may interpret this as HSA denaturing from the inside out during unfolding. This may well be correlated with the denaturing agents soaking the protein matrix and thereby effectively weakening the structure-stabilizing interactions in the interior while the overall surface may still be kept intact, e.g. by preferentially being solvated with water.
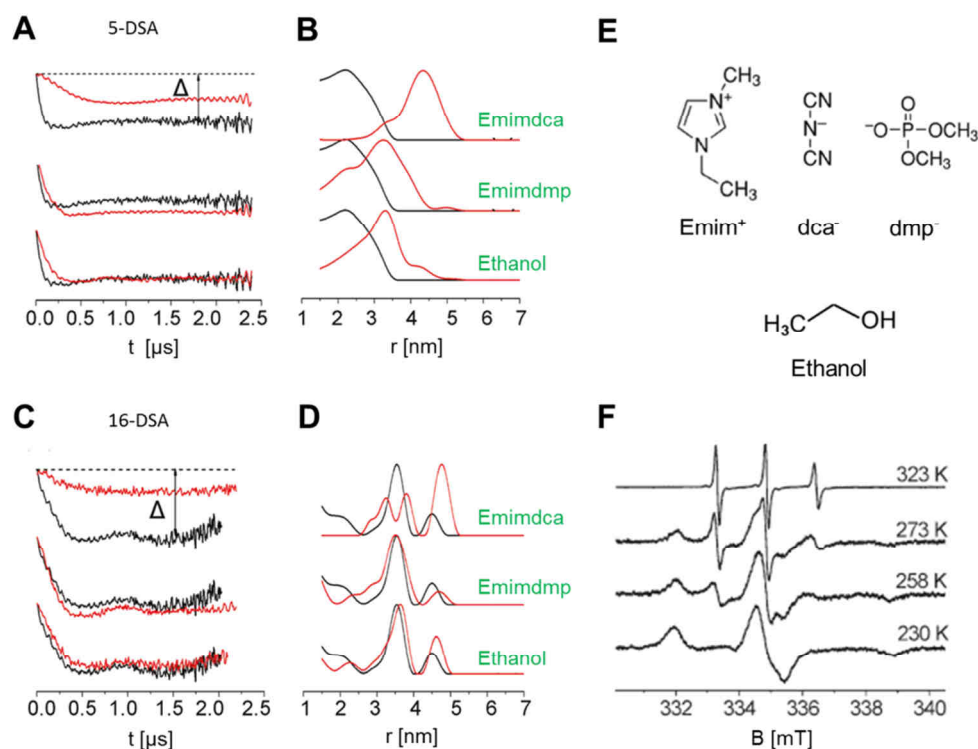

Figure 3.4 | Observing the folding state of albumin with CW EPR and DEER. (**A**) Dipolar evolution functions of 5-DSA in HSA, buffer and 15% v/v glycerol (black) and upon addition of 35% v/v of cosolvents Emimdca, Emimdmp and ethanol (red) (**B**) Distance distributions from time domain data in (A). (**C**) Dipolar evolution functions of 16-DSA in HSA, buffer and 15% v/v glycerol (black) and upon addition of 35% v/v of cosolvents Emimdca, Emimdmp and ethanol (red). (**D**) Distance distributions from time domain data in (C). (**E**) Chemical structures of Emim$^+$, dca$^-$, dmp$^-$ and ethanol. (**F**) Temperature-dependent change of CW EPR spectra in the presence of 35% v/v Emimdca in HSA, buffer and glycerol. All graphs are adapted from Akdogan *et al.*[82]

Beside the pure denaturing and stabilizing effects of ILs, there is strong evidence that Emimdca is capable of refolding HSA at low temperatures (**Figure 3.4F**) as a low-temperature kosmotropic or antichaotropic agent. The two-component CW EPR spectra at 273 K and 258 K indicate bound (*b*) and free (*f*) FAs although at higher temperatures (323 K) only free FAs are found. Besides a general decrease in viscosity, this can solely be explained by a partial refolding of the protein structure at lower temperatures. One should always bear in mind that this effect may be enhanced by a small allosteric stabilization due to fatty acid binding itself.[74,129] A recent study with IAA-spin-labeled BSA facilitated the observation of conformational rearrangements in its dimerized structure during the adsorption process on bioceramic substrates.[22] Therefore, the spin labeling approach also bears potential to reveal information about structural features of albumin with DEER spectroscopy, however, depending on the respective system to be observed.

3.7.2 | Using DEER for Studying Posttranslational Modifications of HSA

The functionality of serum albumins may also be significantly altered by the introduction of post-translational modifications.[181] For polycationic HSA-derivatives (cHSA), as well as for cHSA-conjugates with multiple polyethylene oxide (PEO) chains (see **Figure 3.5A–C**) of different lengths have been shown to form a protein-based core-shell structure.[182] When the net surface charge at pH 7.4 for physiological HSA ($Q_1 = -19e$)[1,183] is changed to be strongly cationic ($Q_2 = +Z \cdot e$) by attaching primary amino groups to almost all negatively charged aspartic acid and glutamic acid residues, it was found with this EPR-based albumin spin probing approach that a large number of at least $N = 25$ FAs can diffusely and electrostatically be bound to the surface.[182] This could be achieved by detecting the immobilization of all FAs in these cHSA-derivatives using CW EPR spectroscopy.
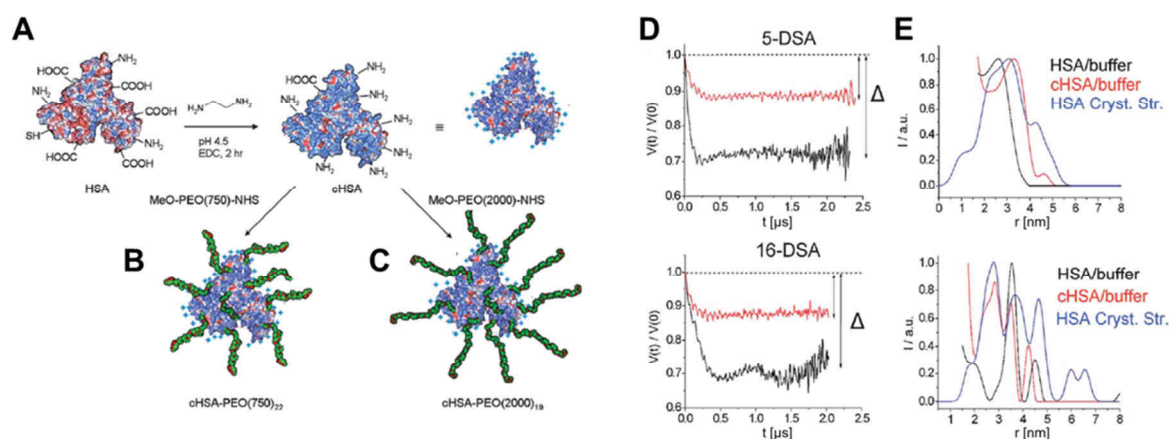

Figure 3.5 | An example for posttranslational modifications of albumin. (**A**) Primary amino groups are attached to almost all aspartic and glutamic acid residues on the surface of HSA leading to a cationized modification of the protein (cHSA). (**B**) Core-shell protein cHSA–PEO(750)$_{22}$. (**C**) Core-shell protein cHSA–PEO(2000)$_{19}$. (**D**) Intramolecular part of the DEER time domain data for 5-DSA and 16-DSA bound to cHSA (red) and native HSA (black). The symbol Δ denotes the corresponding modulation depths and the blue traces show the distance distribution obtained from the crystal structure (see also **Figure 3.3C+D**). (**E**) Distance distributions of data shown in (D) obtained by Tikhonov regularization. All graphs are adapted from Akdogan *et al.*[182]

In comparison to the native protein this increased ligand capacity of posttranslationally modified variants may thus hint towards new and potentially unforeseen pharmaceutical drug delivery applications. Again, from the DEER-derived distance distributions of 5-DSA and 16-DSA, it could be deduced, that the introduction of a large number of positive charges on the protein surface induces a pronounced rigidification of the solution structures of cHSA that resembles the crystal structure-derived fatty acid distribution of HSA better (**Figure 3.5D–E**).

3.8 | Materials and Methods

Materials. Lyophilized powder of HSA (Calbiochem), the spin probes 5-DSA (Sigma-Aldrich) and 16-DSA (Sigma-Aldrich) as well as glycerol (87% in water, ACROS) were used as obtained. DPBS buffer pH 7.4 was prepared as described in **Appendix C1**.[64]

EPR Spectroscopy. *Sample Preparation:* For CW EPR experiments the protein was prepared as a 1 mM HSA stock solution in DPBS buffer pH 7.4. The spin probe stock solutions were adjusted to 26 mM 16-DSA with 0.1

M KOH. The nominal concentration of 16-DSA was kept constant at 0.4 mM, whereas HSA concentrations were varied from 0.04 – 0.20 mM, so that the loading ratio could be adjusted in the range from 1:2 to 1:10 in steps of 2 equivalents. For DEER experiments, the protein stock was prepared as a 2 mM HSA solution in DPBS buffer pH 7.4 and the spin probe stock solutions were adjusted to 26 mM 5-DSA and 26 mM 16-DSA with 0.1 M KOH. Each sample with a final volume of 100 – 200 µl was equipped with 20% v/v glycerol and again titrated to pH 7.4. For CW EPR experiments about 15 µl of the final solutions were filled into micropipettes (BLAUBRAND® IntraMARK) and for DEER measurements about 80 µl were filled into 3 mm (outer diameter) quartz tubes (Heraeus Quarzglas GmbH & Co. KG) and were subsequently shock-frozen in liquid nitrogen-cooled 2-methylbutane.

CW EPR Experiments: A Miniscope MS200 (Magnettech GmbH) benchtop spectrometer was used in order to record X-band CW EPR spectra for all EPR-active samples (**Figure 3.1B–C**) at microwave frequencies of 9.39 GHz that were recorded with a frequency counter (RACAL DANA, model 2101). All measurements were performed at $T = 25°C$ using modulation amplitudes of 0.1 mT and a sweep width of 12 mT at microwave powers of $P_{MW} = 10$ mW.

DEER Experiments: EPR-active HSA samples were investigated with the 4-pulse DEER sequence:[184,185]

$$\pm(\pi/2)_{obs}-\tau_1-(\pi)_{obs,1}-(t_d+t_0+N_t\Delta t)-(\pi)_{pump}-(t'-N_t\Delta t+t_d)-(\pi)_{obs,2}-\tau_2-echo$$

in order to obtain dipolar time evolution data at X-band frequencies of 9.1– 9.4 GHz with a BRUKER Elexsys E580 spectrometer equipped with a BRUKER Flexline split-ring resonator ER4118X–MS3. The temperature was set to 50 K for all experiments by cooling with a closed cycle cryostat (ARS AF204, customized for pulse EPR, ARS, Macungie, PA) and the resonator was overcoupled to $Q \approx 100$. The pump frequency ν_{pump} was set to the maximum of the field swept electron spin echo (ESE)-detected spectrum. The observer frequency ν_{obs} was set to $\nu_{pump} + \Delta\nu$ with $\Delta\nu$ being in the range of 65 MHz and therefore coinciding with the low field local maximum of the nitroxide ESE spectrum. The observer pulse lengths for each DEER experiment were set to 32 ns for both $\pi/2$– and π–pulses and the pump pulse length was 12 ns. Additionally, a 2-step phase cycle (±) was applied to the first $\pi/2$ pulse of the observer frequency for cancelling out receiver offsets and unwanted echoes. For albumin samples containing paramagnetic 5-DSA and 16-DSA spin probes the pump pulse position $t_d + t_0$ after the first observer π-pulse deadtime t_d was typically incremented for N_t timesteps of $\Delta t = 8$ ns in the range $t_0 + t' = \tau_1 + \tau_2 - 2t_d$, whereas τ_1 and τ_2 were kept constant. Proton modulation was averaged by addition of eight time traces of variable τ_1 starting with $\tau_{1,1} = 200$ ns, incrementing by $\Delta\tau_1 = 8$ ns and ending up at $\tau_{1,8} = 256$ ns.

Data Analysis: All DEER time traces obtained from spin probed HSA samples were exclusively analyzed with the MATLAB-based program package DeerAnalysis2013 (**Figure 3.3A–D**).[167] The resulting data sets were obtained assuming a background dimensionality of $D = 3.74$ with regularization parameters $\alpha_5 = 1000$ and $\alpha_{16} = 100$ for 5-DSA and 16-DSA, respectively.[146,166] The crystal structure-derived theoretical distance distributions for 5-DSA and 16-DSA aligned in HSA were constructed according to the 7×7 matrix scheme in **Table A1** and the general procedure is presented in **Appendix A1**.[166]

Structural Aspects. All graphical depictions and molecular models of HSA co-crystallized with seven stearic acids (PDB ID: 1e7i)[3] were constructed using YASARA Structure software[168] and the Jmol molecular visualization applet (**Figure 3.2** and **Figure 3.3E–H**). The pictures shown in **Figure 3.4** and **Figure 3.5** were adapted and modified from Akdogan *et al.*[82,182] and can be also found in Reichenwallner and Hinderberger.[186]

4 | Evidence for Water-tuned Structural Differences in Albumins

As most biochemical processes occur in aqueous environments,[1] the question about how water interacts with biomacromolecules at a molecular level has been a long standing issue in biological sciences. Investigations about this topic were in particular fueled by the work of Kirkwood[2] and Kauzmann.[3] While thermodynamic functions in principal only unravel global views on a problem, they usually do not at all describe local properties such as density, flexibilities, composition and solvation effects at the level of solvent-solute interfaces.[4] Several quite promising efforts have been undertaken to elucidate such physicochemical interactions between solvent and macromolecules on the nanoscale.[5–10]

This initial study employs serum albumin as a model protein for investigating protein-solvent interactions[11,12] with the purpose to elucidate the molecular mechanisms and physical origins that may lead to deviations in crystal structures vs. solution structures by comparing HSA with BSA. This type of deviation in protein appearance has already been reported by Heidorn and Trewhella[13] for Calmodulin and Troponin C in a X-ray solution scattering study.

Structural flexibility appears to constitute a key role in the ligand binding of albumin as it was found by e.g. Trivedi *et al.*[14] In previous EPR spectroscopic studies the functional structure of HSA was probed with respect to fatty acid ligands[15–18] and a copper porphyrin ligand[19] employing the 4-pulse DEER approach (see also **Chapter 3.7**). Therefore, the DEER-derived solution structure of BSA from this study is compared with those previously published EPR- and crystal structure-derived data from HSA, where applicable. The differences that are found in the functional solution structures of HSA and BSA are traced back to differences in local conformational adaptability and flexibility that ensue from differences of individual amino acid hydropathies in their primary structures. Small changes in the amino acid sequences that induce tremendous effects on protein functionality have been reported by inserting artificial mutations,[20] or by analyzing epigenetic amino acid exchanges.[21] In many cases it is the difference in hydrophilicity or rather hydrophobicity in amino acids that drives such functional changes.[10,22,23] Hence, the potential interactions of specific albumin regions with water are particularly scrutinized with its H-bonding network to unravel the origins of different conformational arrangements as observed from internally aligned paramagnetic fatty acids.

4.1 | Experimental Results

All CW EPR results of 5- and 16-DSA bound to BSA and HSA are displayed in **Figure B1** and essentially do not exhibit compelling differences and are here only discussed phenomenologically (see **Appendix B1**). These CW EPR measurements primarily give prove that BSA rigidly binds a similar amount of fatty acids as HSA. As it has been pointed out in **Chapter 3.7**, studying the occupation of the seven binding sites requires the depletion of multispin effects in DEER time traces. To this end, paramagnetic and diamagnetic FAs (r-DSA) are added simultaneously in order to facilitate higher ligand loadings of the protein, while keeping the average number of paramagnetic FAs at about two.

For HSA, these spin-diluted systems have been shown to provide almost identical DEER distance distributions regardless of the overall number of FAs added.[15] However, after addition of two spin-labeled 5-DSA and additional r5-DSA to BSA, a new set of pronounced distances is obtained at about 3.2 nm and 3.9 nm (**Figure 4.1A+B**) that were not observed in HSA. While those new distance peaks emerge in BSA upon addition of an increasing amount of FAs, the immobilized fractions of CW EPR spectra (**Figure B2**) remain of a rather identical shape regardless of the number of loaded paramagnetic and diamagnetic FAs.
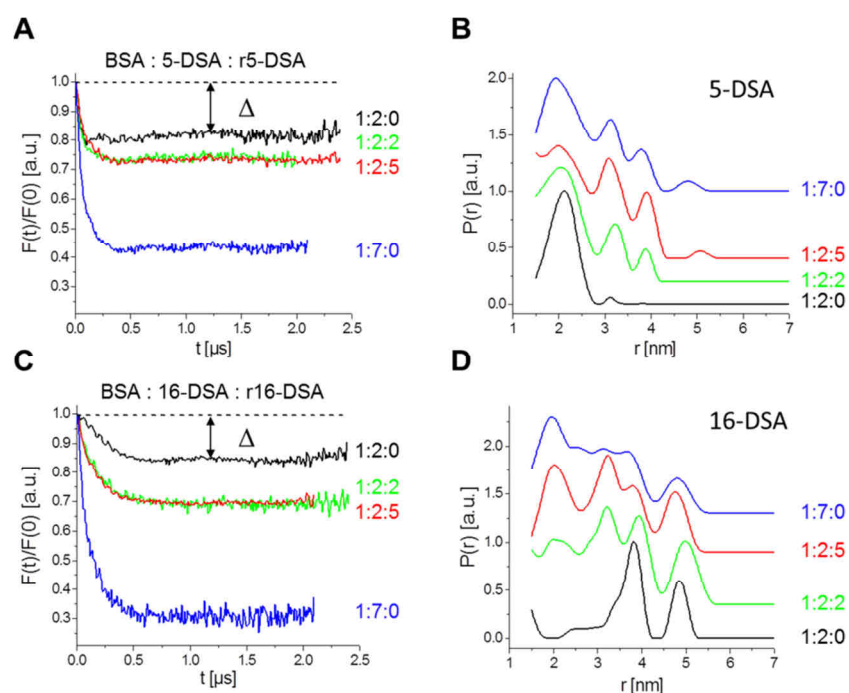

Figure 4.1 | DEER results from 5-DSA and 16-DSA spin probed BSA. BSA solutions were equipped with various ratios of paramagnetic (DSA) and diamagnetic (r-DSA) fatty acids. (**A**) Background corrected time traces $F(t)/F(0)$ of BSA loaded with 5-DSA and r5-DSA in various ratios with (**B**) their respective distance distributions $P(r)$. (**C**) Background corrected time traces $F(t)/F(0)$ of BSA loaded with 16-DSA and r16-DSA in various ratios with (**D**) their respective distance distributions $P(r)$. The symbol Δ denotes the modulation depth for 16BSA 120.

Finally, a rather broad, asymmetric DEER-derived distribution of 5-DSA can be observed in BSA, covering a range similar to that of 5-DSA in HSA with the exception that in BSA more prominent peaks are observed (**Figure 4.2A**). DEER measurements on the system of BSA that is self-assembled with 16-DSA show dominant peaks in the distance distributions in **Figure 4.1D**. Those peaks are located at 3.82 nm and 4.85 nm, and in the corresponding HSA crystal structure (PDB ID: 1e7i)[24] the distances are 3.83 nm (distance between sites 2–6), 3.70 nm (sites 4–6) and 4.64 nm (sites 2–3)).[15] For 5-DSA and BSA, the dominant peak is centered at 2.13 nm and the corresponding sites in HSA are 2.14 nm (sites 4–5), 2.18 nm (sites 4–6) and 2.18 nm (sites 6–7) apart from each other (**Table A1**). These analyses show that FAs are predominantly located at binding sites of 6 and 4, but also other binding sites 2, 3, 5, 7 are filled. For a short description of how these calculated distance distributions are obtained the reader is referred to **Appendix A1**. This suggests that at the used protein concen-

trations (~ 0.2 – 0.8 mM) the FA binding to BSA is not strictly consecutive but already at low albumin:FA ratios (1:2) rather all sites appear to be occupied to a certain degree, just as it can be observed for HSA. Remarkably, when r16-DSA is added to BSA in solution, distances
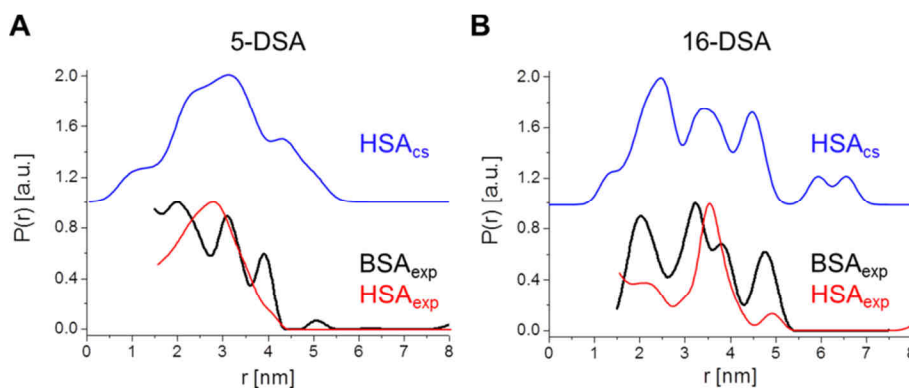

Figure 4.2 | Comparison of fatty acid-derived DEER distance distributions in HSA and BSA. Distance distributions $P(r)$ from (**A**) 5-DSA and (**B**) 16-DSA obtained from DEER measurements on shock frozen solutions of HSA (HSA$_{exp}$, red, loading ratio: 1:2:4) and BSA (BSA$_{exp}$, black, loading ratio: 1:2:5 from red traces in **Figure 4.1B+D**) together with calculated distributions (**Appendix A2**) from the crystal structure of HSA (HSA$_{cs}$, blue, ratio 1:7:0)[15,24] co-crystallized with seven stearic acids assuming that all binding sites are fully occupied by fatty acids (Albumin:DSA:r-DSA).

at about 2.0 nm and 3.3 nm are found for 16-DSA (ratio 1:2:5) that are not present or pronounced in the HSA solution structure (**Figure 4.1D** (red curve) and **Figure 4.2B** (black curve)). **Figure 4.1** also shows time domain DEER data and distance distributions when BSA is exclusively loaded with seven paramagnetic 5-DSA or 16-DSA ligands (ratio 1:7:0). This shows that there is no large qualitative difference between the spin-diluted and the fully paramagnetic systems. However, the distance peaks are narrower and of slightly varying relative intensity in the spin-diluted systems as they are intended to be devoid of multi-spin effects.[17,25]

For 5-DSA, a broad distance distribution again reveals a highly asymmetric distribution of the C5-positions of FAs aligned in HSA[15] as well as in BSA. These DEER-derived distributions of 5-DSA in BSA (**Figure 4.1B** and **Figure 4.2A**) are largely in agreement with the distance distribution expected from the HSA crystal structure, however, individual peaks are more pronounced in the experimentally derived data. As the C5-position of most fatty acids probes the region in the binding channels close to the deeply buried ionic anchor groups,[24] a justified conclusion can be drawn that the interior of HSA and BSA is rather rigid and inflexible while they qualitatively correspond to the HSA crystal structure. In striking contrast, the DEER-derived nitroxide distance distributions of 16-DSA in BSA are clearly different as compared to those in HSA. Primarily, the distribution of 16-DSA in BSA is in better agreement with the HSA crystal structure-derived distribution than the respective DEER data of HSA. The three characteristic peaks at 2.5, 3.5, and 4.5 nm in the HSA crystal structure are intriguingly matched experimentally in the BSA solution structure (at 2.0, 3.3, and 4.7 nm).

Judging from a comparison of individual datasets, 5-DSA distance distributions generally yield lower RMSD values, substantiating that in case of 5-DSA being close to the FA anchor groups the

experimental albumin and the crystal structure-derived distributions are in rather good agreement (see **Appendix B2**). The two experimental curves of 5-DSA probed albumins in **Figure 4.2A** (HSA$_{exp}$ and BSA$_{exp}$) in fact give the lowest RMSD of 0.171 as summarized in **Table B1**. The 16-DSA distance distributions (**Figure 4.2B**) illustrate that the best agreement was found between HSA$_{cs}$ (blue) and BSA$_{exp}$ (black) with an RMSD of 0.201. Surprisingly, the lowest similarity was found just between HSA$_{exp}$ (red) and the HSA crystal structure (HSA$_{cs}$ (blue)) yielding a value of 0.317. In principle, this finding reinforces a quantitative picture of assuming that the number and topology of binding sites is identical for HSA and BSA (see **Figure B1**).[26] However, this suggests a much more asymmetric FA entry point distribution in BSA as observed from 16-DSA. In this "coarse-grained" fatty acid-based structural picture as given by the 16-DSA distance distributions in **Figure 4.2**, the BSA solution structure may be interpreted as obviously resembling HSA in its crystalline, desiccated and water-free state (**Figure 4.2B**, black and blue), while HSA's solution structure strongly deviates from the HSA crystal structure (**Figure 4.2B**, red and blue).

Unfortunately, to this date no topology file of stearic acids co-crystallized with BSA has been reported, although a first BSA dimer structure was uploaded on the RCSB protein data base in early 2012.[27] Thus, the HSA crystal structure co-crystallized with stearic acids (PDB ID: 1e7i)[24] has still to be considered as the reference standard for comparative studies, also comprising BSA solution data. Nevertheless, both proteins may be compared in terms of their ligand-free state (PDB ID: 3v03[27] and PDB ID: 1BM0[28]). Therefore, both crystal structures were aligned with the MUSTANG algorithm[29] (see **Appendix B3**) yielding a RMSD of 1.361 Å and a sequence identity of 75.52 % along 572 aligned residues, indicating a very good mutual structural compliance of HSA and BSA in their crystalline state. This is visualized in **Figure 4.3** together with the sites of accumulated amino acid differences (green).
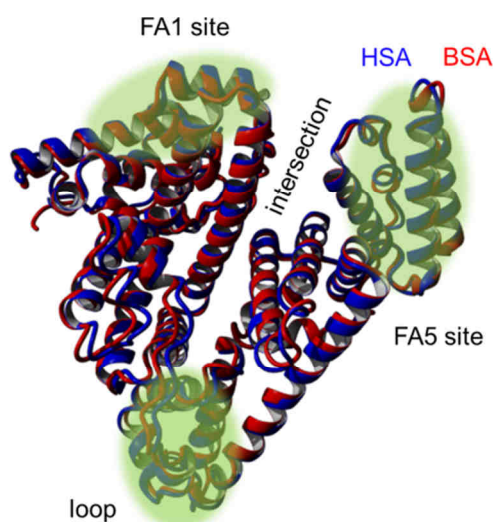

Figure 4.3 | MUSTANG alignment of HSA and BSA. Alignment of fatty acid-free crystal structures of HSA (blue, PDB-ID: 1BM0)[28] and BSA (red, PDB ID: 3v03)[27] utilizing the MUSTANG algorithm.[29] The functional regions of highest interest are highlighted in transparent green (FA1 site, FA5 site, intersection region and loop region).

4.2 | Differences in Primary Structures of HSA and BSA

The main interest in this section is to identify the origin of the DEER-derived functional differences in the solution structures of HSA and BSA on a molecular scale. As their sequence identity is only about 75.52 %, it is self-evident to screen both proteins' primary amino acid sequence for physical properties and their mutual topological correlation. Since hydrophilicity and hydrophobicity have turned out to represent highly important parameters, describing interactions between solvent (water) and solute,[30] local thermodynamics are considered as a key quantity of any study considering biochemical processes in solution. The biochemical origins for amino acid differences in between albumin types may be manifold. Besides evolutionary reasons, the availability of certain nutrients can also play a rather short-termed decisive role that was proposed to lead e.g. to an epigenetic formation of albumin polymorphisms (= alloalbumins) in geographically restricted regions in between a single species of *macacca mulatta* (rhesus monkey), leading to a proposed difference in bioavailability of certain nutrients or toxins.[21]

Currently, many different methods are in use to assess hydrophobic regions in proteins, as e.g. the molecular hydrophobicity potential (MHP).[22,23] Here, four rather simple hydropathy scales of independent origin are consulted in order to obtain a quantitative analysis of differences in hydrophobicity or hydrophilicity of BSA and HSA, namely the scales of Engelman *et al.* (GES),[31] Eisenberg *et al.* (ES),[32] Naderi-Manesh *et al.* (NM)[33] and the scale of Kyte and Doolittle (KD).[34]

Those four scales are cross-correlated in detail and a positive (+) or negative (−) linear dependence between the scales can be found that is quantified with a Pearson's R value. In all cases, this mutual correlation value is given as $R_{ij} > \pm 0.85$ (**Table 4.1**), indicating that all hydropathy scales are strongly correlated, although originating from different theoretical and experimental foundations.

Table 4.1 | Mutual correlation coefficients R_{ij} of several hydropathy scales[a]

	KD	GES	ES	NM
KD	1			
GES	−0.850	1		
ES	+0.878	−0.936	1	
NM	+0.920	−0.870	+0.887	1
R_{ij}	KD	GES	ES	NM

[a]Correlation coefficients R_{ij} are obtained from specific entries in the AAindex database:[35–37] KYTJ820101 (KD), ENGD860101 (GES), EISD840101 (ES) and NADH010102 (NM).

It has been positively proven whether those four hydropathy scales quantitatively lead to the same results (**Figure B4** and **Appendix B4**), so that a detailed discussion of differences from HSA and BSA may be reduced to the hydropathy scale of Kyte and Doolittle,[34] being the most commonly used scale for thermodynamic characterization of amino acids. Specifically, hydropathy indices (HI) from the Kyte and Doolittle scale describe the change in Gibbs free energy when exposing an amino acid residue from a purely hydrophobic environment to bulk water. Hence, negative hydropathy values

denote polar and strongly hydrogen-bonding amino acids, while positive values stand for hydrophobic amino acids. Each congruent amino acid pair of HSA and BSA was compared to obtain a resulting net hydropathy index difference $\Delta HI = HI_{HSA,i} - HI_{BSA,i}$,i.e. the Kyte & Doolittle (KD) window range here equals one. This allows focusing on the smallest primary structural differences and additionally reduces noisy scales. Thus, positive ΔHI values can be interpreted as a hydrophobic ($\Delta HI > 0$) and negative values ($\Delta HI < 0$) as a hydrophilic shift in solvation character of HSA in direct comparison to BSA, respectively. Where appropriate, the amino acid hydropathies are compared one by one (**Table B2**). Principally, the KD hydropathy scale is often used for membrane-bound proteins[34,38] with window ranges of 7 – 20 amino acids. A detailed explanation of this approach, correlating crystal structure-derived protein topology with primary structure differences leading to discrepancies in solution structures can be found in **Appendix B3** and **Appendix B4**.

Generally, the overall hydropathy of HSA is $\Omega_{HSA} = \Sigma_i \, HI_{x,i} = -230.8$ (see equation B.3) and has an excess of $\Delta\Omega_{KD} = \Omega_{HSA,KD} - \Omega_{BSA,KD} = +48.4$ hydropathy points compared to BSA ($\Omega_{BSA} = -279.2$) and therefore, HSA should altogether exhibit a more hydrophobic character in its solvation behavior. This tendency can be confirmed by all three other hydropathy scales ($\Delta\Omega_{KD} = +48.4$, $\Delta\Omega_{NM} = +34.8$, $\Delta\Omega_{ES} = 16.8$, $\Delta\Omega_{GES} = 9.4$) when the scales are normalized to KD (**Table B3**). Remarkably, the topological residue positions that exhibit composition deviations in between HSA and BSA are not homogeneously spread throughout the full sequence but rather occur clustered (see also **Figure B3**). A similar observation was also made by Billeter *et al.*[39] when comparing prion protein structures of different mammalian species.

Many primary structural differences in albumins are even located at residues that are surface-exposed, being of utmost importance when keeping in mind that HSA can be globally considered as less hydrophilic than BSA as evidenced by their individual Ω_x values. Four regions were identified that came forward as being of high structural and functional interest, exhibiting an accumulation of amino acid differences and ΔHI maxima in between HSA and BSA: (*i*) the intersection region between subdomains IB and IIIA, prominently located in the geometric center of the proteins, (*ii*) a surface-exposed loop region in subdomain IIB, and two FA binding sites, (*iii*) one site in subdomain IB (FA1) and (*iv*) another site in subdomain IIIB (FA5).[40] These topological regions are explicitly indicated in **Figure 4.3**. Interestingly, Majorek *et al.*[27] found very similar regions in bovine (BSA), equine (ESA) and rabbit serum albumin (RSA) during the identification of antibody epitopes serving immunological studies. Beyond this immunological aspect, those regions are therefore also supposed to be of special ligand binding functionality, especially in the context of exposure to an aqueous environment.

An in-depth discussion of those regions is given in the following and differences between HSA and BSA are explicitly reported in terms of the KD hydropathy scale. Hydropathy histrograms in **Figure 4.4** and **Figure 4.5** are presented as an illustration that the findings are independently confirmed by each of the four applied hydropathy scales (KD, GES, ES and NM). **Figure 4.4A** highlights the solvent accessible intersection region between subdomains IB and IIIA in both proteins. Except for

one arginine (R186), HSA and BSA differ throughout all residues from 182 to 191 in a helical region of subdomain IB, albeit the formation of an equivalent helix array in a cooperative context of a polypeptide chain may still be provided as Kabsch and Sander have proposed.[41] While amino acid residues 182, 185, 188, 189, 195 and 199 are solvent inaccessible, residues 184, 190 and 191 appear to be solvent-exposed and are therefore accessible by bulk water. The obtained ΔHI values between HSA and BSA in this region are strongly pronounced, i.e. HSA exhibits exceptionally strong hydrophilic properties, while BSA has strong hydrophobic properties at residues 189 and 190.
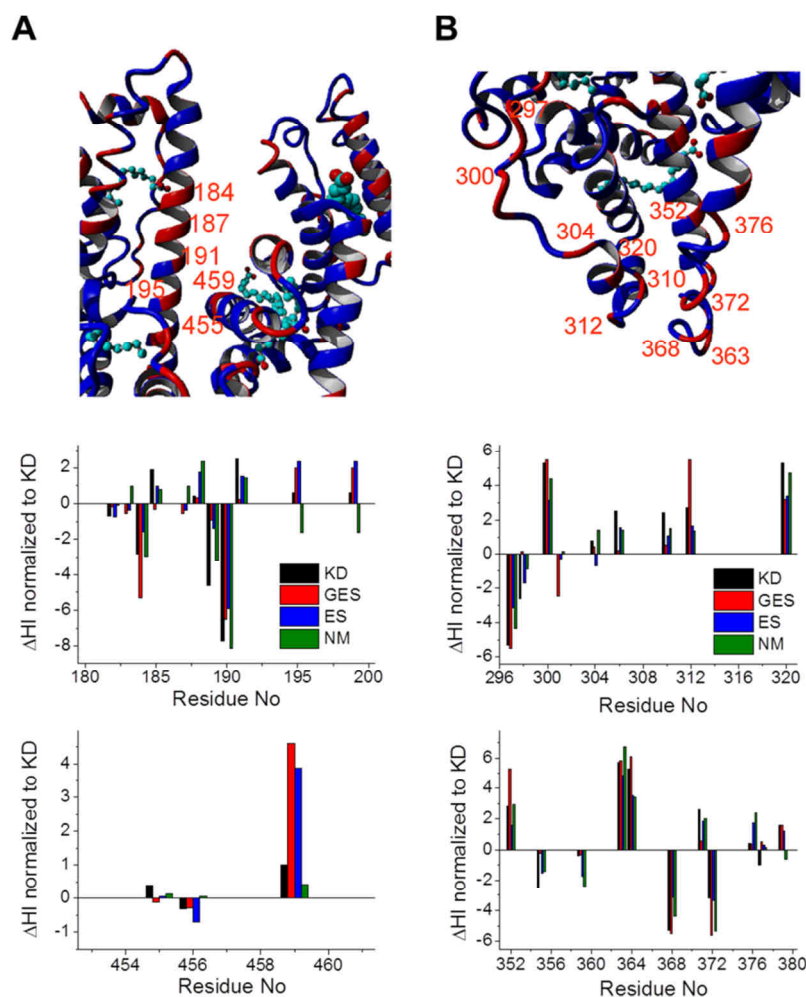

Figure 4.4 | Hydropathy analysis of the intersection and loop regions. Depiction of the loop and intersection regions of HSA (blue) and BSA (red) together with hydropathy plots (ΔHI). Here, the structure alignment was conducted with HSA self-assembled with stearic acids (PDB ID: 1e7i)[24] in order to depict the topological arrangement of HSA, BSA (PDB ID: 3v03)[27] and according ligands. (**A**) Subdomains IB and IIIA define the intersection region of HSA and BSA and the decisive, topologically opposed, amino acid residues (180–200 and 452–460) are shown in a hydropathy plot (ΔHI). (**B**) Subdomain IIB forms the loop region in HSA and BSA and decisive amino acid residues (297–320 and 351–380) are highlighted in the hydropathy plot (ΔHI). The hydropathy values of GES (red), ES (blue) and NM (green) are normalized to the scale of Kyte and Doolittle (KD, black), see also **Table B3**.

Upon closer inspection, residue 190 (K = –3.9) in HSA coincides with L = +3.8 in BSA. This fact indicates that domains IB and IIIA might render a different set of mutual conformational arrangements in HSA and BSA according to the Lum-Chandler-Weeks (LCW) theory.[6] Thereby, both proteins'

individual hydration state is supposed to decisively differ, because of a potential hydropathy lock immobilization between the two domains in BSA regarding hydrophobic residues 455 (L) and 456 (I) and the opposing hydrophobic region at residues 189 (V) and 190 (L). In HSA, this region may still be water-accessible due to the strongly hydrophilic residues. Additionally, residue 189 in HSA is varied from $G = -0.4$ to a much more hydrophobic $V = +4.2$ in BSA. Therefore, according to the LCW theory, BSA could produce a drying out phase transition zone, which depletes the water density between both domains. The sequence of the helix in domain IIIB ranging from residue 455 to 456 also differs in composition, but in both proteins it can be considered as extremely hydrophobic. From those distinctive interdomain-located differences, structural flexibility and the kind of water interaction may be anticipated to be triggered by individual hydrophilic and hydrophobic amino acid patches leading to large structural differences, even on a larger topological scale. In the following sections, such differences on the molecular scale are considered as inducing a dynamic "tuning" of the local solution structure topology in the presence of water.

Another site of interest is identified as a loop region in subdomain IIB, where significant hydropathy differences are found in between BSA and HSA (**Figure 4.4B**). This loop region, being located between residues 295 and 312, appears to be solvent-exposed and residues 297 and 300 show pronounced ΔHI values. All six varying residues in between position 300 and 320 are more hydrophobic in HSA when compared to corresponding residues in BSA. The other significant albumin differences are in close proximity to this loop and are situated on the opposing solvent-exposed loop ranging from residue 360 to 376. In this second loop, there is again a strong hydrophobic hydropathy shift in HSA at residues 363 and 364. Those more hydrophobic amino acids are right at the bottom tip of HSA's crystal structure. By hypothetically exposing this region to water, this region should flip into the protein interior leading to a slightly altered, more globular topological shape of HSA.

As these solvent-exposed loops with an instrinsically high degree of motional freedom,[42,43] are connected to several helices in HSA, this supposed topological rearrangement upon solvation should have a significant impact on the proteins tertiary structure in solution. Very similar observations were made for Calmodulin and Troponin C[13] and such an argument is also reinforced by an EPR study of Kim *et al.*,[44] confirming that (stabilizing) solutes may lead to a more compact and globular shape of outer membrane transporters by the conformational sampling of loops. In contrast, BSA very likely exposes this loop region to the water bulk with a set of amino acids that are strongly hydrophilic, ranging from chain position 363–367 (K, D, D, P, H) and 311–323 on the opposing loop. An interesting view on opposing hydrophilic residues has been given by Arieh Ben-Naim,[7] who claims, that double hydrogen-bonded bridges can be formed by water molecules, that also might stitch together two opposing domains. Such a domain linkage and participation of these loops in the water H-bonding network for BSA could additionally lead to a reduced conformational flexibility at this decisive topological region.
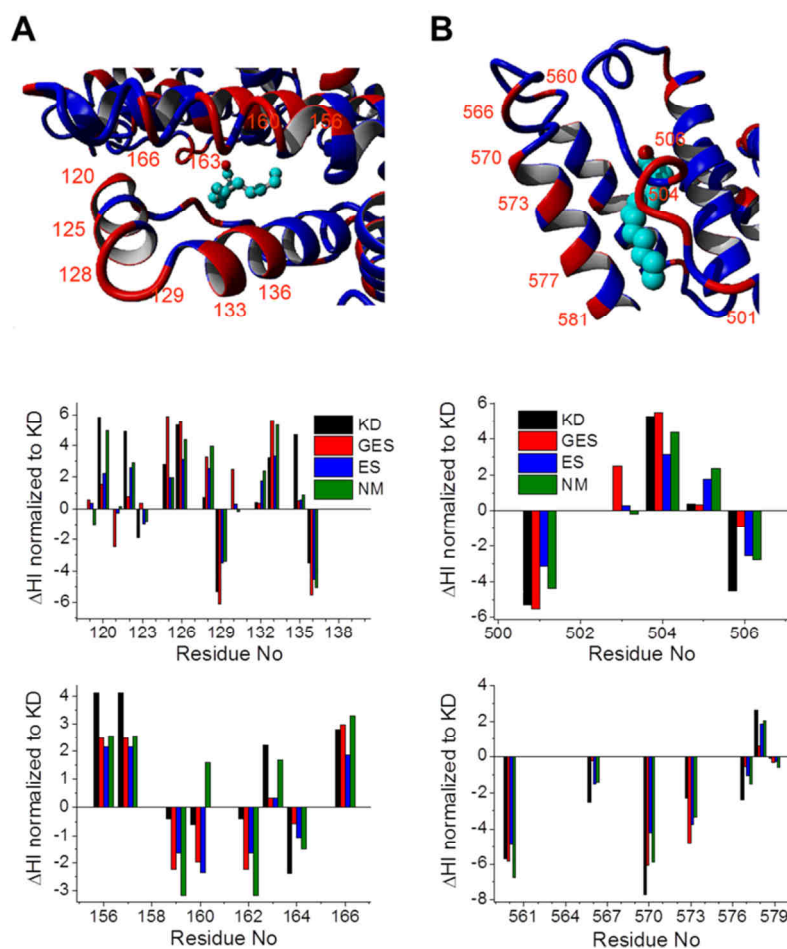
Figure 4.5 | Hydropathy analysis of FA binding site 1 and site 5. Depiction of both highlighted FA binding sites 1 and 5 in HSA (blue) and BSA (red) together with hydropathy plots (ΔHI). Here, the structure alignment was again conducted by HSA self-assembled with stearic acids (PDB ID: 1e7i)[24] in order to depict the topological arrangement of HSA, BSA (PDB ID: 3v03)[27] and according ligands. (**A**) Fatty acid binding site 1 in subdomain IB with residues 119–136 and 154–168 shown in a hydropathy plot (ΔHI). (**B**) Fatty acid binding site 5 in subdomain IIIB and its decisive amino acid residues (498–509 and 560–580) depicted in a hydropathy plot (ΔHI). The hydropathy values of GES (red), ES (blue) and NM (green) are normalized to the scale of Kyte and Doolittle (KD, black), see also **Table B3**.

Figure 4.5A shows fatty acid binding site 1 that is solvent accessible and centered in the four helix arrangement of subdomain IB. Therein, congruent amino acid positions in HSA are once more equipped with a more hydrophobic character as compared to BSA, alike the loop region (**Figure 4.4B**). More precisely, the much more hydrophobic residues in HSA (120, 122, 126) are all located on a small surface-exposed helical patch. In HSA, residues 156 and 157 are also predominantly more hydrophobic, while residues 159–162 are extremely hydrophilic in both albumins. Remarkably, only two amino acids are identical in the range from 156–164 (A at position 158 and Y at position 161, see also **Table B2**), indicating a potential difference in how fatty acids may be associated with each of the two proteins. The solution topology of this binding pocket may well be different and additionally, water exposition could tune its dynamic properties as e.g. binding affinity (K_A). This proposed effect is supposed to constitute a rough accordance with the mechanism that can be inferred for the loops in subdomain IIB (**Figure 4.4B**).

Fatty acid binding site 5 (**Figure 4.5B**) is located at a hydrophobic channel of subdomain IIIB in HSA and exhibits an inverted pattern that has been observed so far, with HSA being more hydrophilic at solvent-exposed residues 560 and 577. Apart from residue 579, all of the deviating amino acids in this region are solvent exposed and residue 570 shows an exceptionally large ΔHI value of –7.7 between HSA (E = –3.5) and BSA (V = +4.2). Residue 570 is far away from the FA entry point but lies in a transition region from a helical to a loop region which may control the motion of the helices forming the mouth for fatty acid admission. Therefore, both albumins may adopt clearly different solution conformations in this area, as residue 560 may contribute in performing a hinge task in HSA, being located at the other end of this aforementioned loop (loop residues: 560–570). When comparing fatty acid-free (PDB ID: 1BM0)[28] and fatty acid-loaded HSA crystal structures (PDB ID: 1e7i),[24] the outer helix of site 5 is displaced outwards about half a nanometer upon fatty acid loading. Accordingly, the RMSD is then only 1.796 Å over 378 aligned residues of HSA, being in much worse correspondence than an alignment of fatty acid-free HSA and BSA (PDB ID: 3v03,[27] *vide supra*).

The opposing side of the binding channel mouth is complemented by a loop ranging from residues 501 to 506, that are surface-exposed throughout. The ΔHI values exhibit a drastic change from residue 501 onwards, where a charged and therefore strongly hydrophilic glutamic acid (E) in HSA coincides with a electrostatically neutral, slightly hydrophobic alanine in BSA ($E_{HSA} - A_{BSA} = -5.3$) to residue 504 where this occurrence is inverted ($A_{HSA} - E_{BSA} = +5.3$). Furthermore, at residue 506 a threonine in HSA with rather neutral HI is opposed by a strongly hydrophobic leucine in BSA ($T_{HSA} - L_{BSA} = -4.5$). Therefore, the dynamic interplay with water at the surface region of FA binding site 5 in HSA clearly deviates from that in BSA. The helix region from residues 570–580 is also clearly more hydrophilic in HSA than for BSA. Thus, site 5 in HSA should also be a more "anchored" to the H-bonding network of solvent molecules.

In the picture of hydropathy alignment, a further speculation about the molecular mechanism of FA binding should comprise that the opposing loop region (residues 500–507) may play a crucial role by being flipped inside (closed) or outside (solvent exposed = open). BSA is clearly more hydrophobic in this loop region, while HSA includes an interesting, alternating pattern of strongly hydrophilic and hydrophobic amino acid residues. Principally, this alternating hydropathy pattern that neither seems to have a strong energetic propensity to be exposed to water, nor to be buried, may again translate into more conformational entropy, flexibility, or adaptability, that is supposed to strongly govern protein-ligand interactions.[45]

4.3 | Correlation of Differences in Albumins Primary, Crystal and Solution Structures (DEER)

Despite the quite similar primary structures of BSA and HSA, experimental DEER results present BSA to be rather rigid in solution and therefore deviates in its functional structure from HSA as observed from more asymmetrically bound paramagnetic fatty acids on the nanoscale. Four regions were identified in both proteins that feature intriguingly different hydropathy properties as observed

from their respective amino acid composition. While DEER-derived differences in between the solution structures of HSA and BSA cannot be directly traced back to the difference in hydropathies, some preferably plausible arguments comprising the clustering amino acid differences have been given. Those arguments may elucidate several profound variations in solution structures of different albumins when exposed to water, as it had been observed for other proteins before.[9,13]

The compelling crystal structure similarities between HSA and BSA are mirrored in the solution structure of BSA. In the "coarse-grained" view of bound paramagnetic fatty acids, a distinct three peak pattern that strongly resembles the FA distribution in HSA's crystal structure is found. Facing the current lack of a BSA crystal structure being self-assembled with stearic acids, the crystal structure of HSA very likely describes a conformation close to the minimum of the potential energy surface, rendering a very good description of the energetic minimum in fatty acid-loaded BSA in solution. Based on the results from DEER on BSA, it can be plausibly speculated that HSA in solution, in contrast to BSA, gains a much larger conformational entropy and the overall conformational ensemble of HSA exposes a much more symmetric surface to potential ligands that are to be transported. BSA does not seem to have this prominent flexibility at the surface affecting protein function.

This study shows, that although proteins with similar functions across different species may have similar crystal structures,[46] their functional properties in solution may vary decisively. This claim is very much founded on recent investigations giving strong evidence that water immersion may heavily affect functional properties of solutes.[10] Close proximity of water molecules to extended hydrophobic patches is energetically unfavorable as hydrogen bonding networks can no longer be maintained. Hence, the nearby water density is depleted close to the hydrophobic surface, leading to a drying transition not least depending on length scale.[6,10,30] In their seminal work, Kabsch and Sander[41] already explained very clearly that amino acid sequence homologies in proteins do not necessarily reveal functional relationships in between them. In converse argument, it can be stated confidently that sequence homologues do not necessarily have to feature identical conformations in their crystal structures. On the other hand, a comparison of crystal structures from HSA (PDB ID: 1BM0)[28] and BSA (PDB ID: 3v03)[27] reveals that a 75.52 % sequence homology generates almost identical 3D crystal structures (see **Figure 4.3**). This is in accordance with the proposed 3D structural homology threshold of 25% sequence compliance for proteins longer than 80 residues.[47]

Hence, those topologically well-defined amino acid differences, as observed for HSA and BSA, do not necessarily alter the energetically minimized, desiccated state of a protein very strongly in its crystal structure. Many of the amino acid sequence differences that are clustered at certain regions in the protein may strongly influence dynamic solution properties as the fatty acid binding (binding sites 1 and 5, **Figure 4.5**) or the global 3D structure (central interface between subdomains IB and IIIA and loop regions in subdomain IIB, **Figure 4.4**). Thus, the apparent rigidity observed in BSA may be partly accredited to the proposed hydropathy "lock" in the prominent intersection region between subdomains IB and IIIA (see **Figure 4.4A**), while in the intersection region of HSA water may deeply

penetrate this structural feature leading to a preferred spatial separation of both domains. The loop region at the bottom tip of albumin (subdomain IIB) is strongly water-exposed and simultaneously bridges large helix-containing regions of albumin. Thus, even slight alterations in hydrophobicity as for HSA may increase structural agility and lead to structural changes at seemingly remote regions. From DEER measurements on the functional solution structures of both albumins, these differences are supposed to be rather correlated with specific modifications that tune the shape, flexibility, adaptability and binding capacities of an albumin molecule. This is supposedly facilitated by non-specific interactions with the surrounding solvent molecules and by generating fluctuations in water density.[5,6,10]

Meanwhile, an interesting nuclear magnetic resonance (NMR) approach has been established by Nucci *et al.*[9] combining NOE/ROE-ratios and reverse micelle encapsulation for monitoring the surface hydration of a protein. The authors found that there are regions of hydration clusters with strongly varying dynamics all over a protein surface that can be principally regarded as strong evidence for water taking a protagonist role in modifying protein functions such as shaping, folding, stability and dynamics. Concluding from ^{13}C-NMR experiments, Marlow *et al.*[45] linked the hydrophobic effect to conformational entropy that is suspected to decisively affect ligand binding thermodynamics. The site-specific findings in albumin from local hydropathy values and the coarse-grained, DEER-derived structural information delivers similar, however, indirect confirmation of such effects. A comparative study of bromocresol green (BCG) binding constants of different mammalian serum albumins[14] also supports the claim, that exchange of only few individual amino acids in a binding pocket region could give a creature an evolutionary advantage.[21] Therefore, those single amino acid exchanges may not only enhance or deplete distinctive properties, but may also transfer physiologically active proteins to their pathological amyloid fibril storage in tissue.[48–50]

In terms of crystal structure and solution structure correlations in albumins, a phosphorescence depolarization study was used to understand this intricate functional interrelation, and it was found that the overall protein conformation in neutral solution of BSA is very similar to the heart shaped structure observed in the HSA crystal.[12] This also supports the findings made here from fatty acid alignments in respective DEER distance distributions (**Figure 4.2**). The 16-DSA-probed surface of BSA mirrors the crystal structure surface of HSA, while the solution structure of HSA probed by 16-DSA exhibits relatively strong deviations.

As drying transition zones occur next to hydrophobic patches of amino acid residues,[6] the conformational flexibility on HSA's surface may be correlated with a lack of energetically hospitable water interactions. However, this rather hypothetical assumption could be quantified and mirrored by an excess net hydropathy sum value of $\Delta\Omega_{KD} = +48.4$ of HSA compared to BSA, representing the less hydrophilic nature of HSA. Locally, many of these more hydrophobic sites in HSA are explicitly water-exposed, giving rise to the assumption that HSA may facilitate an enhanced attraction towards hydrophobic or amphiphilic ligands, as reflected in the proposed pre-binding character during fatty

acid association as found from pulsed dielectric relaxation spectroscopy.[51] Featuring less favorable interactions with water at some decisive functional regions (e.g. loop region in **Figure 4.4A** and site 1 in **Figure 4.5B**) drives HSA in gaining a relative lack of bulk water integration that may be interpreted as a decrease in overall protein tertiary structural stability. This in turn would force HSA to locally sample a larger conformational space leading to an increased flexibility compared to BSA. According to the LCW-Theory,[6] the term protein flexibility, as it is used here, can be as well understood as water density. Thus, a viscosity decrease at hydrophobic surfaces leads to an increased mean square displacement of hydrophobic residues that are described best by the Stokes-Einstein equation[52] in a first approximation.

All these local changes may then globally add up to a solution structure that severely deviates from according crystal structures. Finally, individual topological patches from defined amino acids may tune local and global functional features as shape, conformational entropy (flexibility) and ligand binding site affinity for small hydrophobic or amphiphilic ligands as fatty acids.

4.4 | Discussion

Experimental evidence has been presented for the significant effect that water can have on the functional structure of proteins in solution. Human and bovine serum albumin served as model proteins with an amino acid sequence identity of 75.52%. The DEER-derived distance distributions of HSA (reported previously) and BSA (reported here) loaded with paramagnetic fatty acids globally characterize the tertiary protein structure in solution from the bound ligands' points of view. The solution structures reported here complement findings from the primary structures and crystal structures of HSA and as of recently also BSA. Intriguingly, it can be shown that the characteristic asymmetric FA distribution from the crystal structure of HSA can be observed by DEER from BSA in solution. This indicates that the conformational ensemble of BSA in solution seems to be closely related to the crystal structure and is hence less flexible in comparison to HSA, where a much more symmetric FA distribution was found. Conformational adaptability and flexibility of proteins can be verified on the surface of the HSA solution structure as probed with 16-DSA. This is in line with the proposition by Heidorn and Trewhella[13] that a conformational rearrangement occurs when a protein is exposed to water. Here, evidence is presented that BSA largely lacks the conformational flexibility observed in HSA and that water does not behave linearly on the protein surface. It can be rationalized from crystal structures that water may build up clusters of varying dynamical properties as already shown by Nucci *et al.*[9] in NMR experiments. Therefore, it is presented that differences in amino acid hydropathies are not homogeneously distributed but are clustered in specific structural regions. Four regions were identified that may be strongly influenced by interactions with water, comprising the fatty acid binding at binding sites 1 and 5, the central interface between subdomains IB and IIIA and the loop regions in subdomain IIB. Evidence is provided with a straightforward measure like the hydropathy index (HI) and it is possible to approximate potential effects on tertiary structure that can

arise from protein-water interactions in general. For a more detailed view concerning the specific effects of hydrophobic surface patches one may have to use solution-NMR based methods as NOE/ROE ratios. Advanced MD simulation approaches employing the 3-dimensional molecular hydrophobicity potential (MHP)[22] may also reveal further insights to water-amino acid interactions between BSA and HSA.

In **Chapter 6** a further set of mammal albumins is screened in terms of their DEER-derived, fatty acid-based distance distribution fingerprints and in **Chapter 9** a novel strategy is presented utilizing spin-labeled derivatives of HSA and BSA in combination with 5-DSA and 16-DSA in order to better localize bound paramagnetic fatty acids within the protein structure.

Given the often encountered view that BSA and HSA may well be interchanged and treated as if they are identical, some of the apparent functional and structural differences should be taken into account thoroughly. Hence, the main claim of this study is that there is no trivial correlation in between crystal structures and solution structures of proteins in general. Particularly, a re-evaluation of the hydrophobic effect as proposed by Alan Cooper[53] could lead to a better understanding of these complex structure-function relationships of proteins in solution, especially at physiological conditions.

4.5 | Materials and Methods

Materials. Lyophilized protein powders of HSA (>95%, Calbiochem) and BSA (Sigma-Aldrich), 5-DSA, 16-DSA (Sigma-Aldrich) and 87 wt % glycerol (ACROS/Fluka) were used without further purification. The paramagnetic fatty acids (DSA) were reduced to EPR-silent hydroxylamines (r-DSA) upon addition of phenylhydrazine (97%, Sigma-Aldrich). A modified protocol of the DSA reduction scheme was set up similar to a strategy shown by Matthias Junk[54] and is given in **Appendix B5**.

EPR Spectroscopy. *Sample Preparation:* Aqueous solutions of 2 mM HSA were prepared with 0.11 M phosphate buffer (pH 7.2) and 26 mM DSA and r-DSA were prepared in 0.1 M KOH. The combined concentration of DSA and r-DSA in final buffered solutions of pH 7.4 was kept constant at 1.5 mM, while the protein concentration was varied from 0.21 – 0.75 mM. The molar ratios of DSA and r-DSA per albumin molecule were therefore varied as 2:0, 2:2, 2:5 and 7:0. The final aqueous solutions of DSA-spin probed albumins were supplied with 20% v/v glycerol to prevent crystallization upon freezing. For CW EPR measurements, about 15 µl of sample were filled into a glass capillary (BLAUBRAND® IntraMARK) with ca. 1 mm outer diameter. For DEER measurements about 100 µl of the final solutions were filled into 3 mm (outer diameter) quartz tubes and shock-frozen in liquid-nitrogen-cooled 2-methylbutane for subsequent DEER measurements.

CW EPR Experiments: A Miniscope MS200 (Magnettech GmbH) benchtop spectrometer was used for X-band CW EPR measurements at a microwave frequency of 9.4 GHz (**Appendix B1**). All measurements were performed at $T = 25°C$ using a modulation amplitude of 0.05 mT. The microwave frequency was recorded with a frequency counter model 2101 (RACAL-DANA).

DEER Experiments: All EPR-active HSA samples were measured with the 4-pulse DEER sequence:[55,56]

$$\pm(\pi/2)_{obs}-\tau_1-(\pi)_{obs,1}-(t_d+t_0+N_t\Delta t)-(\pi)_{pump}-(t'-N_t\Delta t+t_d)-(\pi)_{obs,2}-\tau_2-echo$$

in order to obtain dipolar time evolution data at X-band frequencies of 9.1– 9.4 GHz with a BRUKER Elexsys E580 spectrometer equipped with a BRUKER Flexline split-ring resonator ER4118X–MS3. The temperature was set to 50 K for all experiments by cooling with a closed cycle cryostat (ARS AF204, customized for pulse

EPR, ARS, Macungie, PA) and the resonator was overcoupled to $Q \approx 100$. The pump frequency ν_{pump} was set to the maximum of the field swept electron spin echo (ESE)-detected spectrum. The observer frequency ν_{obs} was set to $\nu_{pump} + \Delta\nu$ with $\Delta\nu$ being in the range of 65 MHz and therefore coinciding with the low field local maximum of the nitroxide ESE spectrum. The observer pulse lengths for each DEER experiment were set to 32 ns for both $\pi/2$– and π–pulses and the pump pulse length was 12 ns. Additionally, a 2-step phase cycle ($\pm$) was applied to the first $\pi/2$ pulse of the observer frequency for cancelling out receiver offsets and unwanted echoes. For albumin samples containing paramagnetic 5-DSA and 16-DSA spin probes the pump pulse position $t_d + t_0$ after the first observer π-pulse deadtime t_d was typically incremented for N_t timesteps of $\Delta t = 8$ ns in the range $t_0 + t' = \tau_1 + \tau_2 - 2t_d$, whereas τ_1 and τ_2 were kept constant. Proton modulation was averaged by addition of eight time traces of variable τ_1 starting with $\tau_{1,1} = 200$ ns, incrementing by $\Delta\tau_1 = 8$ ns and ending up at $\tau_{1,8} = 256$ ns.

Data Analysis: Raw time domain DEER data were processed with the MATLAB-based program package DeerAnalysis2008.[57] Intermolecular contributions were removed by division by an exponential decay with a fractal dimension of $D = 3.8$. The deviation from a homogenous background dimensionality $D = 3.0$ originates from excluded volume effects due to the size of the protein.[15] Calculated distance distributions (HSA$_{cs}$) were constructed from symmetric 7×7 distance correlation matrices[15,54] according to a scheme given in **Appendix A1**. The RMSD analysis of the crystal structure-derived distance distribution of fatty acids in comparison with experimental DEER time traces was conducted as described in **Appendix B2**.

Structural Analysis of Albumins. Molecular Modeling, visualization and structural alignments (**Appendix B3**) of HSA and BSA were carried out using YASARA Structure software.[58] Further details about the applied hydropathy scales and their analysis can be found in **Appendix B4**.

5 | Optimum Control of the Albumin System for EPR Spectroscopy

In this chapter an optimization strategy is presented for albumin samples that are investigated by CW EPR and pulsed EPR (DEER) spectroscopy at X-band frequencies. Generally, proteins may react sensitively on external stimuli and varying experimental conditions. Therefore, the main requirement of each sample is to exhibit as comparable and constant physical properties as possible, comprising pH, ionic strength, protein concentration and viscosity. Each of those physical properties may lead to precipitation or denaturation of a protein when not properly adjusted, resulting in difficulties in data analysis and reproduction. Therefore, several adjustments have been made that facilitate optimum control of those properties although albumin is generally considered as a very stable protein.[1] First, anticipating the study in **Chapter 6**, not all albumin types are routinely commercially available and as abundant and relatively low-priced as HSA and BSA, so a general strategy has been followed to principally optimize protein consumption and data quality for subsequent EPR spectroscopic studies.

5.1 | Ionic Strength and pH – The Choice of an Appropriate Buffer for Albumin Solutions

The choice of an optimum buffer for albumin samples is of utmost importance in any study. Although a broad variety of buffers is available in the purpose of biochemical studies, in case of albumin, its regular physiological environment in blood should be best reproduced by a type of Ringer's solution.[2,3] In fact, this Ringer solution is isotonic, but it should not contain any form of metabolites that may already occupy ligand binding sites that are targeted in conceivable loading studies with small molecules. As the blood pH is tightly regulated in the range from pH 7.35 – 7.45,[4] the desirable buffer should also preserve this adjusted pH for longer terms, e.g. when a sample is frozen or stored in the fridge. In case of Dulbecco's phosphate buffered saline (DPBS)[5] that has originally been developed for observing poliomyelitis virus plaques on monolayer tissue cultures of monkey kidney and monkey testis, all those requirements are fulfilled for these experimental needs. In a preparation procedure following the original description, the buffer is isotonic (310.6 mosmol/l) and is initially titrated to pH 7.4. Upon preparing a sample with glycerol, protein and ligand stock solution, potentially comprising any organic solvent, the final sample pH is usually deviating from pH 7.4 not least due to the charge compensation processes of the protein itself with buffer ions.[6] Although albumins can be considered as being functional and stable from pH 4.3 – 10.5,[7] ionic strength was also shown to have an impact on functionality as the net charge and therefore, both the chemical potential[8] of individual charges and the surface potential of the protein as a multivalent ion is modified by charge screening effects (see also **Chapter 7**).[9–11] Therefore, a strategy has been developed for optimum titration of the sample to readjust pH 7.4, keeping the solutions osmolality above ca. 220 mosmol/l. This is facilitated with a broad set of DPBS buffers equipped with a defined amount of hydrochloric acid or sodium hydroxide ranging from about pH 0.2 – 13.5 (**Table C2**). A precise instruction of how this buffer, its according series of titration derivatives and an albumin or EPR-active albumin sample can be assembled according to this scheme can be found throughout

Appendix C1 – C4. This strategy of retaining control over sample properties forms the basis for strategic adjustments of any physicochemical parameter in EPR-active albumin samples throughout this work.

5.2 | Protein Concentration and Excluded Volume in Buffered Albumin Solutions

In several studies an exact knowledge about protein concentration is inevitable for drawing precise conclusions from the collected data sets. Usually, the commercially available lyophilized albumin powders are dissolved in appropriate amounts of buffer. However, depending on the amount of added protein powder, an apparent excluded volume may be formed originating from the proteins themselves that is impenetrable and inaccessible for solvent molecules. During this work, several strategies have been pursued to quantify this excluded volume. A first straightforward approach is to prepare a Lowry,[12] bicinchoninic acid (BCA),[13] or Bradford assay[14] in order to quantify the protein content of a solution, whereas all three assays strictly rely on colorimetric methods. The effectivity of BCA assays is based on a color change from lime green to deep purple when Cu^{2+} is reduced to Cu^+ by peptide bonds at high temperatures. The BCA reagent replaces the Folin-Ciocalteu reagent (FCR) in the Lowry assay and coordinates Cu^+ ions in a chelate complex with a strong absorbance at $\lambda = 562$ nm. The advantage of BCA is that it does not interact with buffer components or other contaminants[15] and absorbance changes linearly with protein concentrations. A minor drawback is that the coloration reaction takes some time (10 min at 65°C) and is also present at low temperatures with the BCA reagent interacting with cysteine, N-acetyltryptophane, tyrosine and indoles in general.[16] The Bradford assay is based on another principle that involves binding of the Coomassie Brilliant blue G-250 (CBBG) dye to arginine, tryptophane, tyrosine, histidine and phenylalanine residues of a protein.[15] While the free dye has an absorption maximum at $\lambda = 470$ nm, the bound dye shifts this maximum to $\lambda = 595$ nm leading to a bluish coloration of a sample containing protein. The advantage is that Bradford assays can be conducted much faster as the dye binding reaction is virtually completed after 2 min at room temperature,[14] but absorbance increases in a non-linear fashion with protein concentration.[15] Thus, the BCA assay was chosen for imposing quantitative protein concentration data and the Bradford assay was used for qualitative quick tests unifying the major advantages of both methods. Detailed descriptions of those procedures are given in **Appendix C5.** It has been tested whether the BCA assay exhibits differences in sensitivity between various albumin types. In principle it has been found that throughout all concentration tests slightly lower concentration values have been found than it was expected. On average, the obtained value was $c_{Albumin} = (0.836 \pm 0.058)$ mM for samples that were prepared from 1 mM 0.137 M DPBS pH 7.4 stock solutions (see **Table C5**). While BSA is used in this test as an internal standard no such result is expected but the reason lies close at hand.

Albumin has a very high solubility in water and due to its high average specific volume of solvent incorporation (1.07 grams/gram protein) a provisional volumetric approach was chosen in order to

determine the excluded volume of BSA solutions in DPBS at pH 7.4, although it is commonly assumed to be experimentally inaccessible.[17] The concentrations were chosen to range from 10 – 200 mg/ml and individual samples have been prepared with utmost care. It turns out that solutions with lower concentrations of BSA (< 5% volume increase for up to c_{nom} = 50 mg/ml) are quite insensitive to volume increases on a macroscopic scale, but as 1 mM or 2 mM stock solutions of BSA are prepared, no exuberant, but clearly detectable changes of solution volume emerge as shown in **Figure 5.1A**. The concentration-dependent excess volume fraction $\phi(c)$ of the solution caused by the presence of BSA is shown in **Figure 5.1B**. The linear relation between the volume fraction $\phi(c)$ and the nominal concentration c_{nom} can be written as:

$$\phi(c) = b \cdot c_{nom} \tag{5.1}$$

with $b = 8.126 \cdot 10^{-4}$ ml/mg or m³/kg describing the slope of the red line in **Figure 5.1B.** This leads to an expression that directly yields the volume-corrected BSA concentration c_{corr}:

$$c_{corr} = c_{nom}\left(1 - \phi(c)\right) = c_{nom} - bc_{nom}^2 \tag{5.2}$$

of an arbitrary prepared albumin stock solution in 0.137 M DPBS buffer at pH 7.4.
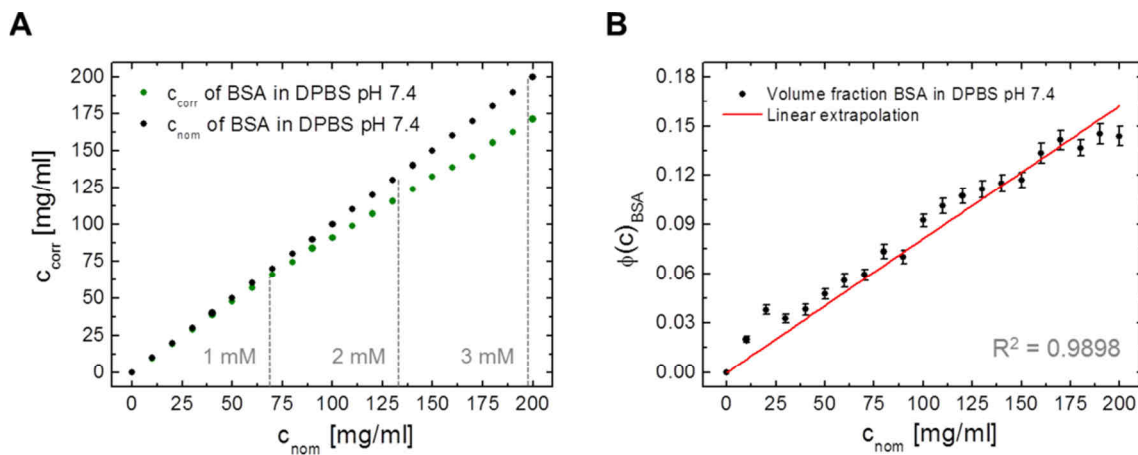
Figure 5.1 | Concentration-dependent excluded volume of BSA in DPBS solutions. Volume increase of BSA solutions in 0.137 M DPBS pH 7.4 in the range from 10 – 200 mg/ml of dissolved protein. (**A**) The nominal BSA concentration (c_{nom}, black) is plotted versus the volume-corrected BSA concentration (c_{corr}, green). Markers have been set for c_{nom} = 1 mM = 66.463 mg/ml, c_{nom} = 2 mM = 132.926 mg/ml and for c_{nom} = 3 mM = 199.389 mg/ml. (**B**) Change in BSA volume fraction $\phi(c)_{BSA}$ compared to c_{nom} due to increase in protein concentration. A linear extrapolation of data points with a high correlation is shown in red.

Based on the excluded volume fraction $\phi(c)$ the hydrodynamic radius $R_{H,V}$ of a single BSA particle can be estimated from following definition:[17]

$$\phi(c) = \frac{N_A c_{nom} V_H}{MW_{BSA}} \tag{5.3}$$

where $MW_{BSA} = 66{,}463$ kg/mol is the molecular weight of BSA,[18] N_A is Avogadro's number and V_H is the hydrodynamic volume. Assuming that BSA is a spherical particle with $V_H = (4/3)\pi R^3_{H,V}$ and constant shape in the investigated concentration ranges, following equation is obtained:

$$R_{H,V} = \left[\frac{3\phi(c) MW_{BSA}}{4\pi N_A c_{nom}}\right]^{1/3} = \left[\frac{3 MW_{BSA}}{4\pi N_A c_{corr}} \cdot (\phi(c) - \phi^2(c))\right]^{1/3} \tag{5.4}$$

giving $R_{H,V} = 2.78$ nm. As a good approximation it has been found that the product of albumin lot purity (P_{ALP} is usually $\geq 95\%$) and c_{corr} gives reasonable estimates of the real protein concentration c_r:

$$c_r = P_{ALP} \cdot c_{corr} = P_{ALP} \cdot \left(1 - \phi(c)\right) \cdot c_{nom} \tag{5.5}$$

leading to a value of about $c_{r,1mM} \approx 0.9$ mM and $c_{r,2mM} \approx 1.7$ mM for albumin stock solutions with a nominal concentration of $c_{nom} = 1$ mM and 2 mM, respectively. These real concentrations are exceptionally important for, e.g. the construction of Scatchard plots that are shown in **Chapter 7** and **Chapter 11** and correspond much better with results from BCA assays ($c_{r,1mM} = 0.84$ mM, see above).

5.3 | Viscosity and Density of Albumin Solutions Containing 20% v/v Glycerol

As it was already derived by Albert Einstein in 1906, the total number of suspended particles also has an influence on the inner friction of a solution.[19] Extensive viscometric studies have been already performed on albumin in the 1930s to 1950s.[7,20–22] Nevertheless, the dynamic viscosity $\eta_{dyn} = \eta$ and the solution density ρ of albumin samples equipped with 23% v/v of 87 wt% glycerol was tested on the BSA system in the conventional protein concentration ranges (0 – 60 mg/ml albumin) that were used throughout this work. With a given solution density of 87 wt% glycerol of $\rho_{gly} = 1.227$ g/ml the glycerol weight percentage of the final solution can be estimated to be about 27%. However, the properties of such binary mixtures cannot be extrapolated in such a straightforward manner as it will be shown in the following. Principally, it turned out that rheological measurements on such solutions with relatively low viscosities reveal much more reasonable results on a viscometer (Ubbelohde) than on a rheometer (cone-plate), although several obstacles like bubble formation are omnipresent in both. Hence, only viscometric results are used for subsequent analyses, however, both methods generally revealed that sample viscosity does not change considerably in this concentration range. The change in viscosity with the concentration of any macromolecule is best described by the expression:[17]

$$\eta = \eta_0(1 + v_S\phi(c)) \tag{5.6}$$

where η_0 is the pure solvent viscosity and v_S is the Simha parameter.[23] For suspended spherical particles ($v_S = 2.5$) the original equation from Einstein is obtained and the Simha parameter can be used to estimate an ellipsoidal solution shape of a particle for $v_S > 2.5$.
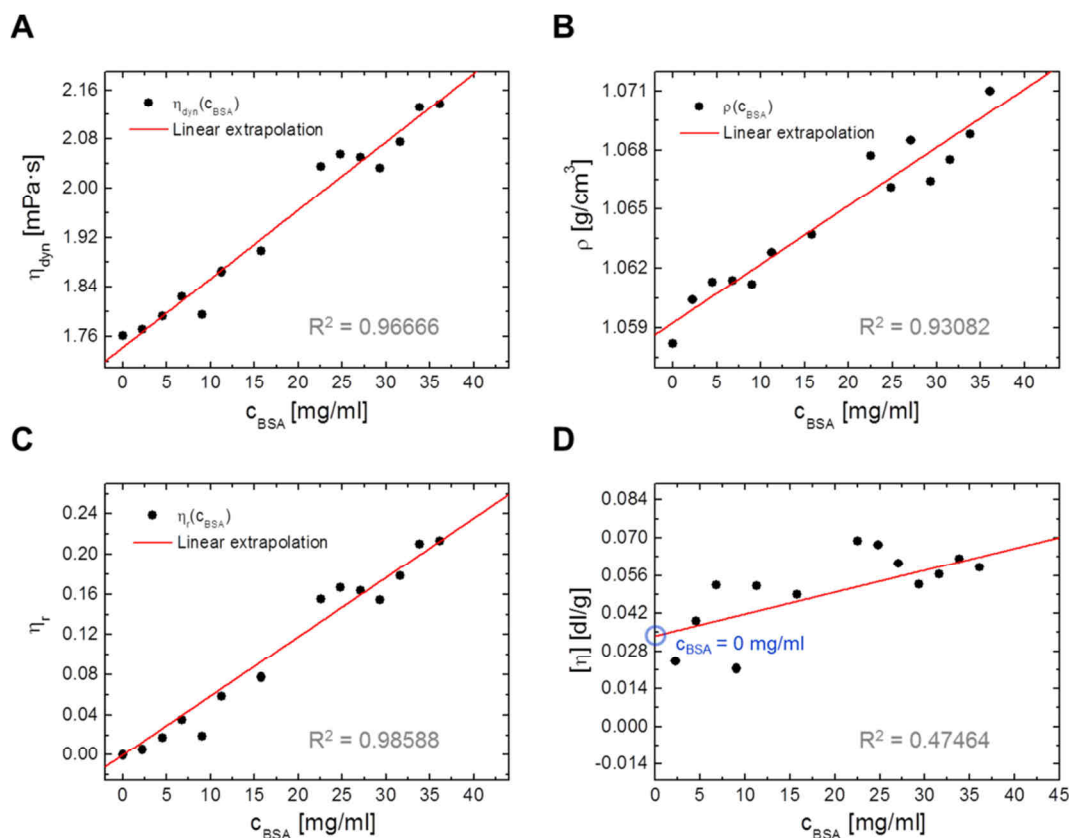

Figure 5.2 | Viscosities and densities of BSA solutions prepared in DPBS pH 7.4 and 23% v/v of 87 wt% glycerol. Viscosities and densities of the BSA solutions in DPBS pH 7.4 and glycerol are plotted versus the corrected protein concentrations $c_{corr} = c_{BSA}$ for $T = 25°C$. (**A**) Concentration-dependent dynamic viscosities $\eta_{dyn}(c_{BSA})$ of BSA/glycerol solutions. (**B**) Concentration-dependent solution densities ρ of BSA/glycerol solutions. (**C**) Concentration-dependent relative viscosities η_r of BSA/glycerol solutions. (**D**) Determination of the intrinsic viscosity $[\eta]$ at $c_{BSA} = 0$ mg/ml (blue circle). The linear dependence of datasets is confirmed by a high correlation coefficient values (R^2) of the linear extrapolations for $\eta = \eta_{dyn}$, η_r and ρ (red).

The experimentally observed relative increase in viscosity is usually given as the relative (η_r) or specific viscosity (η_{sp}):[17,24]

$$\eta_r = \eta_{sp} = \frac{\eta - \eta_0}{\eta} \tag{5.7}$$

that should be ideally concentration independent. In **Figure 5.2** a collection of viscometric results at $T = 25$ °C are shown from samples with varying BSA concentrations. Although being of a rather

phenomenological nature, some linear relations can be derived:

$$\eta = \eta_0 + k_1 c_{\text{BSA}} = (1.74234 \pm 0.01111 \text{ ml} \cdot \text{mg}^{-1} \cdot c_{\text{BSA}}) \text{ mPa} \cdot \text{s} \tag{5.8}$$

$$\rho = \rho_0 + k_2 c_{\text{BSA}} = (1.05924 + 2.96511 \cdot 10^{-4} \text{ ml} \cdot \text{mg}^{-1} \cdot c_{\text{BSA}}) \text{ g} \cdot \text{cm}^{-3} \tag{5.9}$$

$$\eta_r = k_3 c_{\text{BSA}} = 0.00589 \text{ ml} \cdot \text{mg}^{-1} \cdot c_{\text{BSA}} \tag{5.10}$$

from linear regressions that facilitate some predictive calculations of any value of η, η_{r} or ρ in an albumin (BSA) sample equipped with 23% v/v of 87 wt% glycerol at $T = 25°\text{C}$ that is buffered in 0.1 M DPBS at pH 7.4 and lies in the valid concentration range from 0 – 36 mg/ml. Note that equations 5.8 – 5.10 only apply when the corrected concentration $c_{\text{corr}} = c_{\text{BSA}}$ is given in mg/ml. In order to describe the extrapolated concentration independence of η_{r} a limiting parameter is introduced for zero concentration:[21–26]

$$[\eta] = \lim_{c \to 0} \frac{\eta - \eta_0}{\eta_0 c} = \lim_{c \to 0} \frac{\eta_r}{c} \tag{5.11}$$

being called the *intrinsic viscosity* $[\eta]$. Although the linear fit is not perfect this value can be read out from the zero intercept in **Figure 5.2D** giving $[\eta]_{\text{BSA}} = 0.03352 \pm 0.00593$ dl·g in 0.1 M DPBS pH 7.4, being in line with earlier results obtained by Tanford ($[\eta]_{\text{BSA}} = 0.0365 \pm 0.0009$ dl·g at ionic strength $I = 0.1$).[7] Additionally, this intrinsic viscosity is again related to the hydrodynamic radius by the relation:[17]

$$R_{\text{H},[\eta]} = \left[\frac{3 M_{\text{BSA}} [\eta]}{10 \pi N_{\text{A}}} \right] \tag{5.12}$$

yielding $R_{\text{H},[\eta]} = 3.346$ nm for BSA, that nicely corresponds with prevalent literature ($R_{\text{H},[\eta]} = 3.370$ nm).[17] Finally, the Simha parameter $v_{\text{S}} = 7.85$ was obtained from $c_{\text{BSA}} = 33.232$ mg/ml = 0.5 mM and by combining equation 5.6 and 5.8. Usually, bulky formulae have to be used to predict the axial ratio $J = a/b$ of an ellipsoidal particle of revolution. However, Alfred Polson found a linear empiric relation connecting the Simha parameter with the squared axial ratio:[20]

$$J = \frac{a}{b} = \sqrt{\frac{(v_{\text{S}} - 4)}{k_4}} \tag{5.13}$$

giving $J = 6.27$ with the constant $k_4 = 0.098$. This obtained value is also largely in agreement with literature values for albumin ranging from $J = 4.9$ for serum albumin at its isoelectric point (pH 4.8)[20] and $J = 6.5$ at more physiological conditions[17] applying the numerical solutions from Simha for prolate rod-shaped ellipsoids.[21] Finally, those data from intrinsic viscosities also shed light on the

hydration state of a protein.[27] With some correction terms for hydration regarding the partial specific volume of solvent ($\delta_1 \approx 0.2$) the axial ratio can be corrected to $J = 3.3$.[17] However, the crystal structure of the BSA molecule (PDB ID: 3v03)[28] suggests arbitrary average diametral dimensions of about ($83 \times 73 \times 35$) Å and a radius of gyration of $R_G = 26.2$ Å originating from the center of mass. **Table 5.1** summarizes some benchmark data that compare viscometry and some supplementary results from rheology.

Table 5.1 | Viscosities and densities of solutions with increasing complexity

$T = 25°C$	Sample	Viscometer	Densimeter	Rheometer	Literature
c_{BSA} [mg/ml]	(composition)	η [mPa·s]	ρ [g/ml]	η [mPa·s]	η [mPa·s]
0	H_2O	–	$(0.997)^a$	0.862	0.893^b
0	0.137 M DPBS pH 7.4	–	–	0.899	–
0	24 wt% glycerol in H_2O	–	$(1.059)^b$	–	1.754^b
0	23% v/v of 87 wt% glycerol in 0.1 M DPBS pH 7.4	1.742^c	1.0592^c	1.66	–
32	23% v/v of 87 wt% glycerol in 0.1 M DPBS pH 7.4	2.098^d	1.0687^d	2.11^e	–

^{a}taken from CRC handbook of chemistry and physics[29]; ^{b}taken from Sheely[30] with the assumption that therein 24 wt% glycerol fits experimental values of η and ρ best (the calculated value is: $100 \cdot V_{gly}\rho_{gly}/(V_{gly}\rho_{gly} + V_{H2O}\rho_{H2O}) = 26.9$ wt%, when ρ_{gly} (87 wt%) = 1.227 g/ml, see **Table C3**). ^{c}Extrapolated from equation 5.8 and 5.9 for $c_{BSA} = 0$ mg/ml. ^{d}Extrapolated from equation 5.8 and 5.9 for $c_{BSA} = 32$ mg/ml. ^{e}The nominal concentration is $c = 32$ mg/ml, the corrected value according to equation 5.2 is $c_{BSA} = 29.7$ mg/ml assuming an excluded volume fraction of $\phi(c) = 0.0721$ for an experimental BSA stock solution concentration of 88.7 mg/ml. For all original data obtained by rheology, see **Appendix C6**.

Viscometric and densimetric data suggest that upon addition of 23% v/v of 87 wt% glycerol to the buffered protein solution the obtained values correspond best with a solution of water containing 24 wt% glycerol.[30] For simplicity, all such prepared samples are defined to contain 20% v/v glycerol ($0.23 \cdot 0.87 \approx 0.20$). Furthermore, it can be stated that no significant changes occur in the solution structure and shape of BSA when comparing the data with established values found in literature.

5.4 | The Choice of Albumin Concentration in CW EPR Experiments

Recording CW EPR spectra of DSA-spin probed albumin samples is virtually always successful. However, very subtle changes in these spectra may occur with a change in any physicochemical parameter that mainly comprises changes in protein-ligand interactions.[31–33] Therefore, one of the major limitations in the preparation of EPR-active albumin samples is the proper adjustment of relative concentrations of ligand and protein. Furthermore, albumin stability has been shown to depend on protein concentration[34] and the number of molar equivalents of fatty acids as well.[35] Fatty acids themselves offer a wide variety of phase states depending on ionization[36] and concentration.[37] When all albumin binding sites ($N_T = 7$)[38] are saturated or when albumin is absent, CW EPR spectra usually reveal spin exchange phenomena as an additive spectral feature that emerges as a consequence of ligand-based micelle formation.[39] Data analysis therefore becomes more complex in terms of spectral simulation. In order to circumvent this complication the loading ratio should usually not exceed 1:7 paramagnetic fatty acid equivalents. As an example HSA was loaded with 5-DSA and 16-DSA in the

constant protein-to-fatty acid ratio of 1:2 (**Figure 5.3**). Here, the only varying parameter is the equivalent concentration that was adjusted in the range from 0.1 – 0.7 mM corresponding to 0.2 – 1.4 mM of fatty acids, respectively. It can be observed that all spectra of either 5-DSA or 16-DSA look rather identical for $c_{HSA} \geq 0.2$ mM. For $c_{HSA} = 0.1$ mM the noise level for 5-DSA is typically high and artifacts that may be intrinsic to individual EPR spectrometers (*) may dominate the spectral shape.
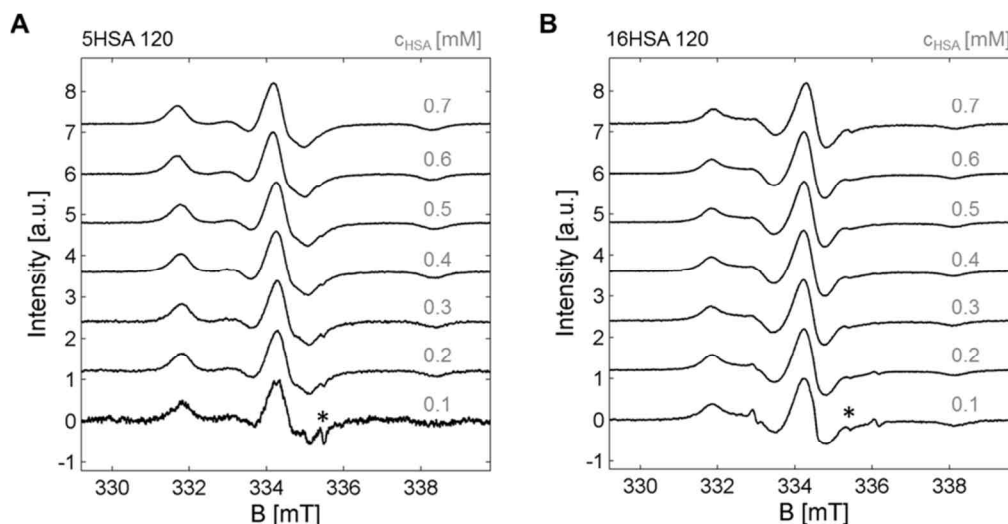

Figure 5.3 | CW EPR spectra of spin probed HSA at varying protein concentrations. All CW EPR experiments were conducted with spin probed HSA samples in DPBS pH 7.4 and 20% v/v glycerol at $T = 25°C$. Paramagnetic fatty acids (Y-DSA) as (**A**) 5-DSA and (**B**) 16-DSA were loaded on HSA in the nominal ratio of 1:2 (YHSA 120). All parameters were kept constant apart from the equivalent concentration c_{HSA} that was varied in the range from 0.1 – 0.7 mM. For example, the asterisk (*) at about $B = 335.5$ mT marks an artifact that is intrinsic to the Miniscope MS200 benchtop spectrometer.

This is a frequently encountered drawback for 5-DSA probed albumin samples and in case this spin probe is applied all relative concentrations should thus be adjusted to $c_{5\text{-DSA}} > 0.2$ mM. In contrast, 16-DSA exhibits high signal quality even at the lowest equivalent concentration, however, the freely tumbling (*f*), unbound component (signal at 0.333 T and 0.336 T) is slightly larger than for all other concentrations. For now, this may be simply ascribed to a kinetic concentration-based effect due to the extraordinary ligand binding properties of albumin[40] and the decrease in HSA stability with increasing protein concentration.[34] Here, 5-DSA-probed HSA samples do not show a similar behavior. Hence, the comparability of CW EPR spectra of 5-DSA and 16-DSA probed albumin samples is only given for $c_{5\text{-DSA}} > 0.2$ mM or $c_{HSA} = c_{DSA}/N > 30$ µM and is based on the individual spin probe signal strength and spectrometer sensitivity.

5.5 | Excluded Volume Effects and Constraints in DEER Experiments on Albumins

The assessment of large and comparable DEER datasets from fatty acids bound to albumins requires good knowledge about experimental settings and sample conditions. Primarily, it has to be certified that a high data quality is obtained that sufficiently resolves all characteristic details in a distance distribution while simultaneous optimization of the experimental time schedule has to be also taken

into account. As it was already shown in **Chapter 3** and **Chapter 4**, that interpretation of fatty acid-based interspin distances from DEER experiments is often difficult, especially due to the self-assembling properties of paramagnetic fatty acid ligands and protein. The separation of background signals from true distance information (see also **Chapter 2.5.5**) is therefore additionally hampered in albumins compared to spin-labeled proteins,[41–44] oligomers,[45,46] polymers,[47] or polypeptides.[48] To this effect, it is inevitable to obtain experimental data with adequate concentrations, signal-to-noise ratios (SNR) and dipolar evolution times (τ_2) that allow for sufficient distance resolution[49] and background filtering[50–52] that minimize artifacts in the resulting distance distributions $P(r)$.

First, the effect of protein concentration on DEER time traces of 5-DSA and 16-DSA-probed HSA is tested with the CW EPR samples that were already shown in **Figure 5.3** with constant nominal molar equivalents in the range from 0.1 – 0.7 mM and a loading ratio of 1:2. As it was shown for BSA in **Chapter 5.2** the excluded volume is primarily a concentration-based effect that induces an excess volume to a sample that is occupied by protein accompanied by a net concentration depletion. Here, the excluded volume effect on DEER-derived distance distributions, background dimensionalities D, modulation depths Δ and time trace quality in general is investigated with experimental data shown in **Figure 5.4**. All experimental results were analyzed with DeerAnalysis2013[53] for maximum artifact depletion in distance distributions $P(r)$, while regularization parameters were kept constant ($\alpha_5 = 1000$ for 5-DSA and $\alpha_{16} = 100$ for 16-DSA). Whereas modulation depths are rather stable and insusceptible to background corrections when the signal phase is properly adjusted, an appropriate choice of background dimensionalities D is inevitable for getting rid of unwanted artifacts in individual distance distributions.

The adjusted concentration-dependent parameters Δ and D are shown in **Figure 5.5A**. It can be shown that both parameters change with concentration in a non-linear fashion. The modulation depths from DEER time traces of 5-DSA remain largely constant at $\Delta_{5\text{-DSA}} = 0.19 \pm 0.04$ for all concentrations, whereas 16-DSA exhibits very large values ($\Delta \approx 0.42$) for $c_{\text{HSA}} < 0.3$ mM and constant values at $\Delta_{16\text{-DSA}} = 0.26 \pm 0.02$ for $c_{\text{HSA}} \geq 0.3$ mM. All adjusted fractal background dimensionalities are in the range from $3.06 < D < 3.77$ and exhibit a general increase with concentration up to a plateau-like region at about $c_{\text{HSA}} \geq 0.5$ mM. However, the dimensionality of 5-DSA seems to be a bit lower than for 16-DSA. In terms of time trace quality an artificial quality parameter Γ is introduced that is solely accessible from experimental and analytic values from DeerAnalysis:

$$\Gamma = \frac{\Delta}{B_{\text{r.m.s.}}\sqrt{X}} \tag{5.14}$$

comprising Δ, the background fit root mean square (r.m.s.) $B_{\text{r.m.s.}}$ and the square root of the scan number $X^{1/2}$. All calculated values for Γ are shown in **Figure 5.5B**.
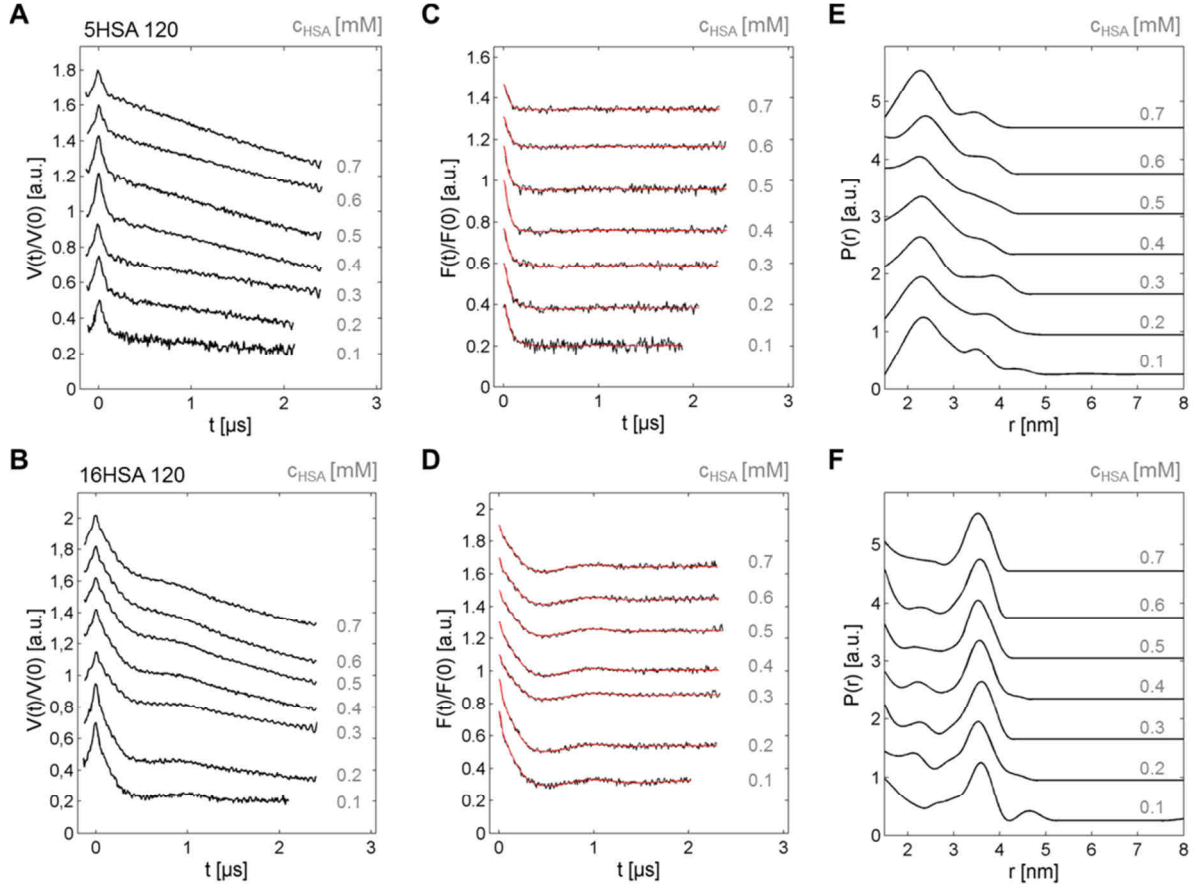
Figure 5.4 | Effect of protein concentration on $P(r)$ in DEER experiments on spin probed HSA. Samples containing 5-DSA and 16-DSA probed HSA in the loading ratio 1:2 were tested for varying HSA concentrations between 0.1 – 0.7 mM nominal equivalents (gray inset numbers). Experimental DEER time traces $V(t)/V(0)$ are given for (**A**) 5HSA 120 and (**B**) 16HSA 120 at varying HSA concentrations c_{HSA}. The corresponding background-corrected DEER time traces $F(t)/F(0)$ are given together with their regularized fits (red) for (**C**) 5HSA 120 and (**D**) 16HSA 120. The regularization parameters were chosen as $\alpha_5 = 1000$ for 5-DSA and $\alpha_{16} = 100$ for 16-DSA probed HSA throughout. The resulting distance distributions $P(r,c)$ are also shown for (**E**) 5HSA 120 and (**F**) 16HSA 120.

While the curve shape of Γ for 16-DSA is dominated by Δ, 5-DSA exhibits a clear maximum at $c_{HSA} = 0.4$ mM. It is therefore concluded that the optimum concentration for comparing 5-DSA and 16-DSA probed HSA samples should be chosen at about this empirical value c_{HSA}, where the application of both spin probes leads to similar signal qualities. The echo formation in pulse EPR experiments is also not linearly increasing with concentration due to instantaneous diffusion and effects from temperature that are associated with strong changes in T_1 and T_2 relaxation.[51] Yet, with knowledge about the inversion efficiency ($\lambda = 0.534$, see **Appendix C7**) of the 12 ns pump pulse in DEER experiments applied here (see also Junk *et al.*[54]), following relation can be used to estimate an optimum experimental spin concentration:[51]

$$c_{opt} = \frac{9\sqrt{3}}{2\pi} \cdot \frac{\hbar}{\lambda g_A g_B \mu_0 \mu_B^2 N_A t_{max}} = \frac{9\sqrt{3}}{8\pi^2} \cdot \frac{1}{\lambda N_A t_{max} A} \tag{5.15}$$

with $A = \mu_0 \mu_B^2 g_A g_B / (4\pi\hbar)$.

From accessible dipolar evolution times in the range 1.88 µs < t_{max} < 2.36 µs (**Figure 5.4C+D**) it follows that the optimum spin concentration c_{opt} should range from 0.792 mM < c_{opt} < 0.995 mM.
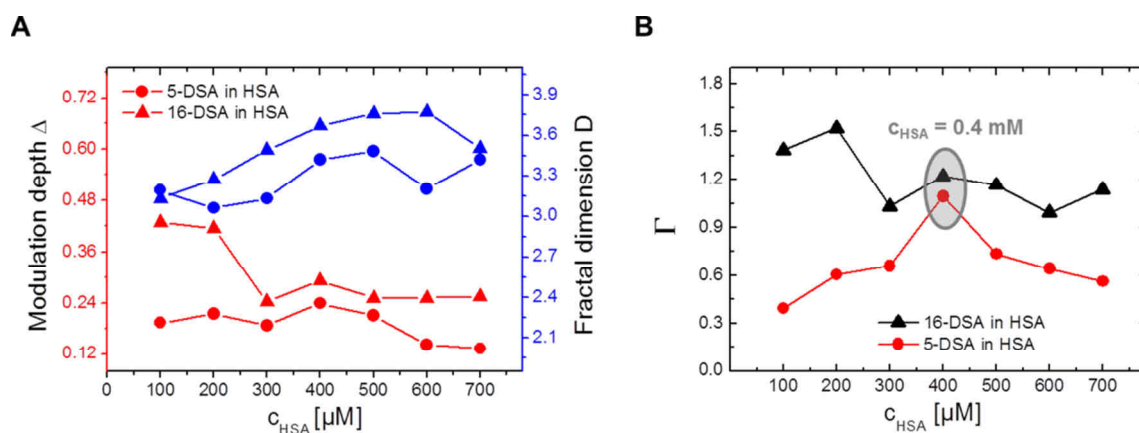

Figure 5.5 | Concentration-dependent DEER parameters from spin probed HSA. Significant parameters from regularization procedures conducted in **Figure 5.4C–F** and the corresponding signal qualities of 5-DSA (•) and 16-DSA (▲) spin probed HSA samples are summarized here. The HSA:DSA loading ratio was kept constant at 1:2 with varying equivalent concentrations in the range from 0.1 – 0.7 mM. (**A**) Modulation depths Δ (red) and fractal background dimensionalities D (blue) are plotted against HSA concentration (c_{HSA}). (**B**) The corresponding time trace quality Γ identifies an optimum concentration c_{HSA} = 0.4 mM that is also used for some of the subsequent studies that compare 5-DSA (red) and 16-DSA (black) probed HSA samples.

This is in astonishing compliance with the findings for 5-DSA in **Figure 5.5B** where 0.4 mM of HSA correspond to a nominal fatty acid concentration of 0.8 mM. Furthermore, data shown in **Figure 5.4** were also subject to a simultaneous Tikhonov regularization approach as in Brandon *et al.*[55] with the assumption that all sets of concentration-dependent DEER time traces of 5-DSA or 16-DSA spin probed HSA contain identical distance distributions.[56]
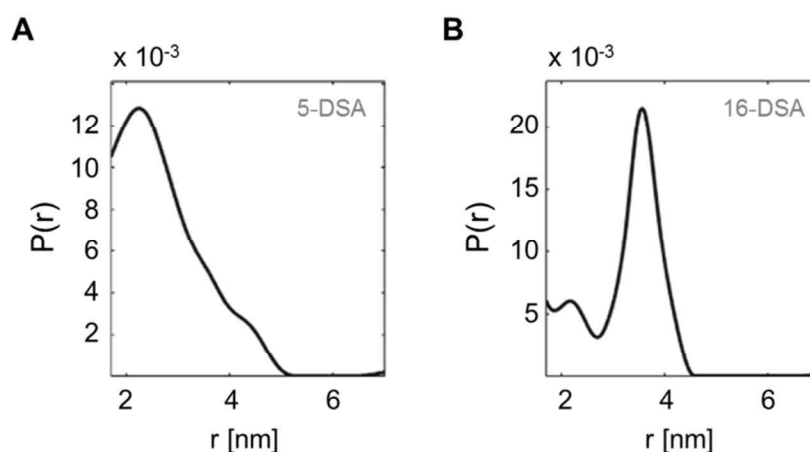
Figure 5.6 | Distance distributions from spin probed HSA after global DEER time trace regularization. The results from a global analysis of data in **Figure 5.4** is presented here. The investigated concentration ranges were set to 0.1 – 0.7 mM for (**A**) 5-DSA and 0.2 – 0.7 mM for (**B**) 16-DSA probed HSA for simultaneous Tikhonov regularization with $α_5$ = 3000 and $α_{16}$ = 300 and D = 3.74. The two individual graphs are adapted from Kattnig *et al.*[56]

Therein, background parameters were iteratively refined and artifacts due to excluded volume effects could be eliminated. This rather sophisticated strategy was devised by D. R. Kattnig and the most relevant results can be found in **Figure 5.6**. Note, that these background-filtered spin probe distributions shown in **Figure 5.6** also resemble the results in **Figure 5.4E+F** at about $c_{HSA} = 0.4 \pm 0.1$ mM quite well. This complex analytic approach gives further proof that the distance feature at $r \approx 4.5$ nm in distance distributions of spin probed HSA is an artifact depending on concentration and the choice of the onset of background correction (t_{BG}).

In the following, a short summary is given of how an excluded volume of HSA solutions and therefore the radius R of the corresponding pervaded volume of HSA can be obtained from DEER data. Primarily, the excluded volume in DEER time traces is hidden in the background decay function that is given for fractal dimensions D in the form:[47,57]

$$B(t) = \exp(-\lambda Ckt^{D/3}) = \exp(-\lambda CQ(t)) \tag{5.16}$$

with

$$k = \frac{8\pi^2 A}{9\sqrt{3}} \tag{5.17}$$

and the integral representation:[58]

$$Q(t) = 4\pi \int_r K\left(\frac{At}{r^3}\right) G(r) r^2 dr \,. \tag{5.18}$$

Upon substitution of $At/r^3 = u$ and $\omega t = u(1 - 3\cos^2\theta)$ the kernel $K(u)$ can be written as:[56]

$$K(u) = \int_0^{\pi/2} (1 - \cos\omega t)\sin\theta \, d\theta = \frac{2}{\sqrt{3u}} \int_0^{\sqrt{3u}} \sin^2\left(\frac{1}{2}(u - z^2)\right) dz \tag{5.19}$$

with $z = x \cdot (\pi/2)^{1/2}$. In the homogenous limit when the pair correlation function is $G(r) = 1$ and the background dimensionality is $D = 3$ it can be derived from equation 5.16 and 5.18 that $Q(t) = kt$. For a hypothetical dilute solution of spherical colloids that all contain an electron spin in their geometrical center the pair correlation function can be approximated with the expression:[59]

$$G(r) = \Theta(r - d) \,, \tag{5.20}$$

where Θ is the Heavyside step function that contains information about the distance d of closest contact that is equivalent to the diameter of the excluded or pervaded volume. For systems with a significant volume fraction $\phi(c) = (4/3)\pi\rho R^3 = (1/6)\pi cd^3$ (see also equation 5.3) the pair correlation

function $G(r)$ assumes a sinusoidal shape that strongly deviates from the step function shape ($\rho = N/V$ = number density, d = particle diameter).[56] This crowding effect can be considered in the framework of the Percus-Yevick approximation[60] with the contact value $d^+ = 2R^+$ derived from the background function that is given as:[61]

$$G(d^+) = \frac{1 + \frac{\phi(c)}{2}}{(1 - \phi(c))^2} \tag{5.21}$$

Thus, the samples used in the respective DEER experiments exhibit $\phi(c) < 0.05$ throughout and $G(d^+)$ < 1.13 so that the step function approximation (equation 5.20) can be used for all data sets. From equation 5.18 and $At \cdot (d^+)^{-3} = u_d$ it can be derived that the decay of $B(t)$ is governed by:[56]

$$Q_d(t) = \frac{8\pi^2 At}{9\sqrt{3}} \alpha(u_d) \tag{5.22}$$

with

$$\alpha(u_d) = \frac{3}{2\pi} \left(h(u_d) - \frac{\sqrt{3}}{u_d} K(u_d) \right) \tag{5.23}$$

and

$$h(u_d) = \int_{x=0}^{\sqrt{3}} \frac{(1 - x^2) \sin((1 - x^2)u_d)}{u_d} \, dx \quad . \tag{5.24}$$

Here, the kernel $K(u_d)$ is equivalent to equation 5.19 with u replaced by u_d. All derivations and calculations are explicitly given in Kattnig et al.[56] The global data fitting procedure in this study was conducted in a similar fashion as in Brandon et al.[55] and finally a likelihood function was used to obtain the most probable value of R^+. Both, 5-DSA and 16-DSA spin probes, yielded values of about $R^+ = 2.64 \pm 0.03$ nm.[56] This finding corresponds well with previously reported radii of gyration (R_G = 2.74 nm) obtained by small-angle neutron scattering (SANS) experiments on HSA[62] and also with the results shown from the volumetric approach using BSA ($R_{H,V} = 2.78$ nm) in **Chapter 5.2**.

In a second viewpoint, the effect of varying dipolar evolution times on the distance distributions of 16-DSA probed HSA is tested in the range from 0.8 µs < τ_2 < 2.6 µs as the pulse timing in DEER is generally considered to be of utmost importance.[63] The nominal loading ratio was chosen as 1:2 at 0.4 mM equivalents and is shown in **Figure 5.7**. All data were analyzed identically for filtering out the sole impact of the maximum available dipolar evolution time ($t_{max} \approx \tau_2 - t_d$) on data quality, i.e. the stability of the distribution shape (typically $t_d = 80$ ns). An astonishing finding is that the main distance peak at $P_{max}(r) = 3.5$ nm is clearly visible in all distance distributions, however, the distribution shape changes decisively with increasing τ_2. Ultimately, all three reported features at $r_S = 2.2$ nm, $r_M = 3.5$

nm and $r_L > 4.0$ nm in DEER-derived distance distributions of 16-DSA probed HSA[64] are only detectable together for $\tau_2 \geq 1.6$ µs (**Figure 5.7C**).
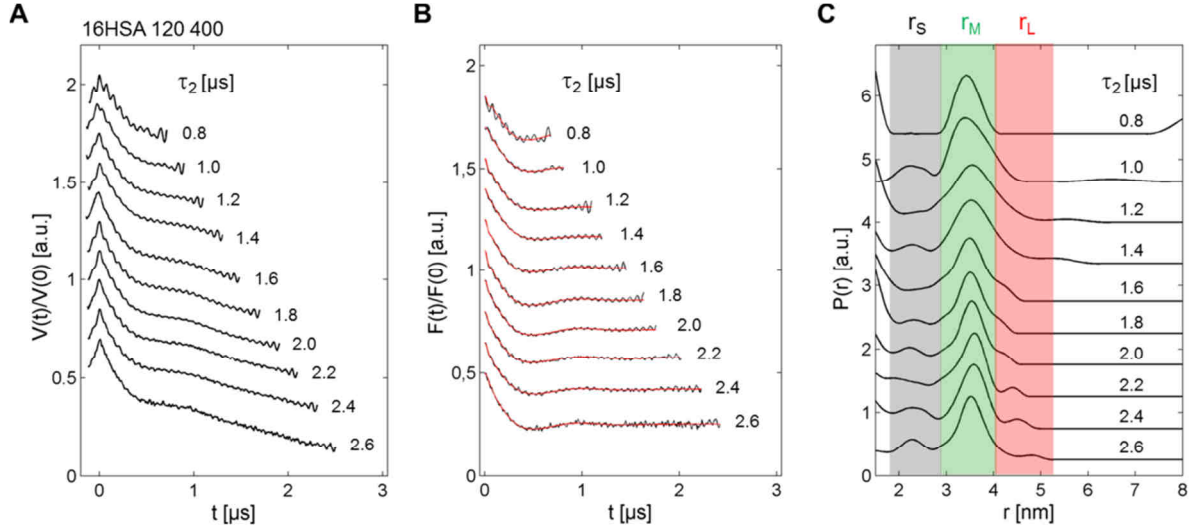

Figure 5.7 | Effect of dipolar evolution time τ_2 on $P(r)$ in DEER experiments on 16-DSA probed HSA. A sample containing 16-DSA probed HSA in the loading ratio 1:2 at 0.4 mM equivalents was subject to a set of varying dipolar evolution times τ_2. The corresponding (**A**) experimental DEER time traces $V(t)/V(0)$, (**B**) background corrected DEER time traces $F(t)/F(0)$ with regularized fits (red) and (**C**) distance distributions $P(r, \tau_2)$ are given in increasing steps of $\Delta \tau_2 = 0.2$ µs with the most prominent features highlighted in gray (r_S), green (r_M) and red (r_L). All time traces were consistently analyzed with a background dimensionality $D = 3.74$ and a regularization parameter $\alpha_{16} = 100$.

When all important interspin distance features (r_S, r_M, r_L) emerge in the distance range from $1.5 - 5.0$ nm, it can be estimated that the minimum required available dipolar evolution time t_{max} that has to be adjusted for sufficient resolution is given as:[50]

$$t_{max} = \frac{5\pi^2 \hbar r_L^3}{g_A g_B \mu_0 \mu_B^2} \simeq \frac{5\pi^2 \hbar r_L^3}{4\mu_0 \mu_B^2} \tag{5.25}$$

giving a value of $t_{max} = 1.496$ µs with the assumption that $t_{max} = 5\pi/(4\omega_{min})$. Furthermore, it is conventional to approximate the intrinsic g-value product of nitroxide observer and pump spins with $g_A g_B \approx 4$. This coincides well with experimental observations made in **Figure 5.7C** and actually means that recording 5/8 of a full dipolar oscillation period is sufficient to extract the corresponding maximum distance (r_L). Additionally, based on a given t_{max}, the maximum resolvable distance in case of a given $t_{max} = 0.72$ µs can be calculated from equation 5.25 to $r_{max} = 3.92$ nm and for $t_{max} = 2.52$ µs it would be $r_{max} = 5.95$ nm, respectively. In this concern, there are two established rules of thumb that help to discern in between valid mean distances ($r_{max,\langle r \rangle}$) and valid distribution widths ($r_{max,\sigma}$) with the relations:[52]

$$r_{max,\langle r \rangle} = 5 \cdot \sqrt[3]{\frac{t_{max}}{2\mu s}} \tag{5.26}$$

$$r_{\max,\sigma} = 4 \cdot \sqrt[3]{\frac{t_{\max}}{2\mu s}} \tag{5.27}$$

that yield similar values at $r_{\max,\langle r \rangle}$ = 3.56 nm and 5.40 nm, respectively. Thus, the corresponding distribution shapes may be reliably interpreted below $r_{\max,\sigma}$ = 2.85 nm and 4.32 nm. Furthermore, from experimental data with a time increment of the ELDOR pump pulse of Δt = 8 ns and a given number of data points $N_t \gg 4$ the minimum resolvable distance can be defined as:[50]

$$r_{\min} = \left(\frac{4(N_t - 1)\mu_0 \mu_B^2 \Delta t}{(2N_t - 7)\pi^2 \hbar} \right)^{1/3} \approx \left(\frac{2\mu_0 \mu_B^2 \Delta t}{\pi^2 \hbar} \right)^{1/3} \tag{5.28}$$

and yields $r_{\min} \approx 1.18$ nm for $t_{\max}$ = 0.72 µs as well as for $t_{\max}$ = 2.52 µs. Therefore, this parameter mainly depends on Δt, i.e. the x-axis resolution and $r_{\min}$ is anyway considered as experimentally inaccessible due to ^{1}H nuclear modulation artifacts in DEER time traces ($v(^1$H) = 14.1 MHz at B_0 = 0.33 T). This corresponds to a phantom distance of about $r(^1$H) $\approx$ 1.6 nm as it can be seen in the upper traces of **Figure 5.7A+B** where proton modulation dominates the time domain data. Usually, $t_{\max}$ is defined by the cutoff of noisy data during data processing in DeerAnalysis[53] and t_d should be replaced by $t_{\text{cut}} \geq t_d$ being in the range of about 120 – 200 ns. From these available datasets it is concluded that all dipolar evolution times should be recorded at least for $\tau_2 = t_{\max} + t_{\text{cut}} \geq 1.6$ µs for experimental DEER time traces on 16-DSA probed HSA that deliver reproducible distance distributions.

In order to obtain the impact of the SNR on the distribution quality several time traces were recorded for 5-DSA and 16-DSA probed HSA, again in the nominal loading ratio of 1:2 at 0.4 mM equivalents (**Figure 5.8**). Here, the increase in number of scans $X = 2^n$ was rationalized with $n \in \mathbb{N}_0$, while constant experimental dipolar evolution times (τ_2 = 2.5 µs) were adjusted. In principle, the general duration of an individual DEER experiment (t_{DEER}) can be approximated by the relation:

$$t_{\text{DEER}} = X \cdot t_X \tag{5.29}$$

with

$$t_X = \frac{n_{\text{pp}} n_{\text{pc}} k_{\text{NMA}} t_{\text{SRT}} \left(\tau_1 + \tau_2 - 2t_d \right)}{\Delta t} \quad . \tag{5.30}$$

Typically, n_{pp} = 10 are the shots per point, n_{pc} = 2 is the number of phase cycling steps, k_{NMA} = 8 is the number of time increments for nuclear modulation averaging, t_{SRT} = 1.5 ms is the shot repetition time (SRT) and τ_1 = 200 ns is the dephasing time of the Hahn echo sequence. The number of data points in time domain data can be obtained from $N_t = (\tau_1 + \tau_2 - 2t_d)/\Delta t$. Thus, one scan in a usual spin probed albumin DEER experiment takes about t_X = 76.3 s. Particularly, in the view of data quality for 5-DSA

probed HSA (**Figure 5.8A**) it is of considerable interest to minimize t_{DEER} as in this case $P(r)$ appears to be only stable above $X_5 \geq 1024$ (**Figure 5.8E**).
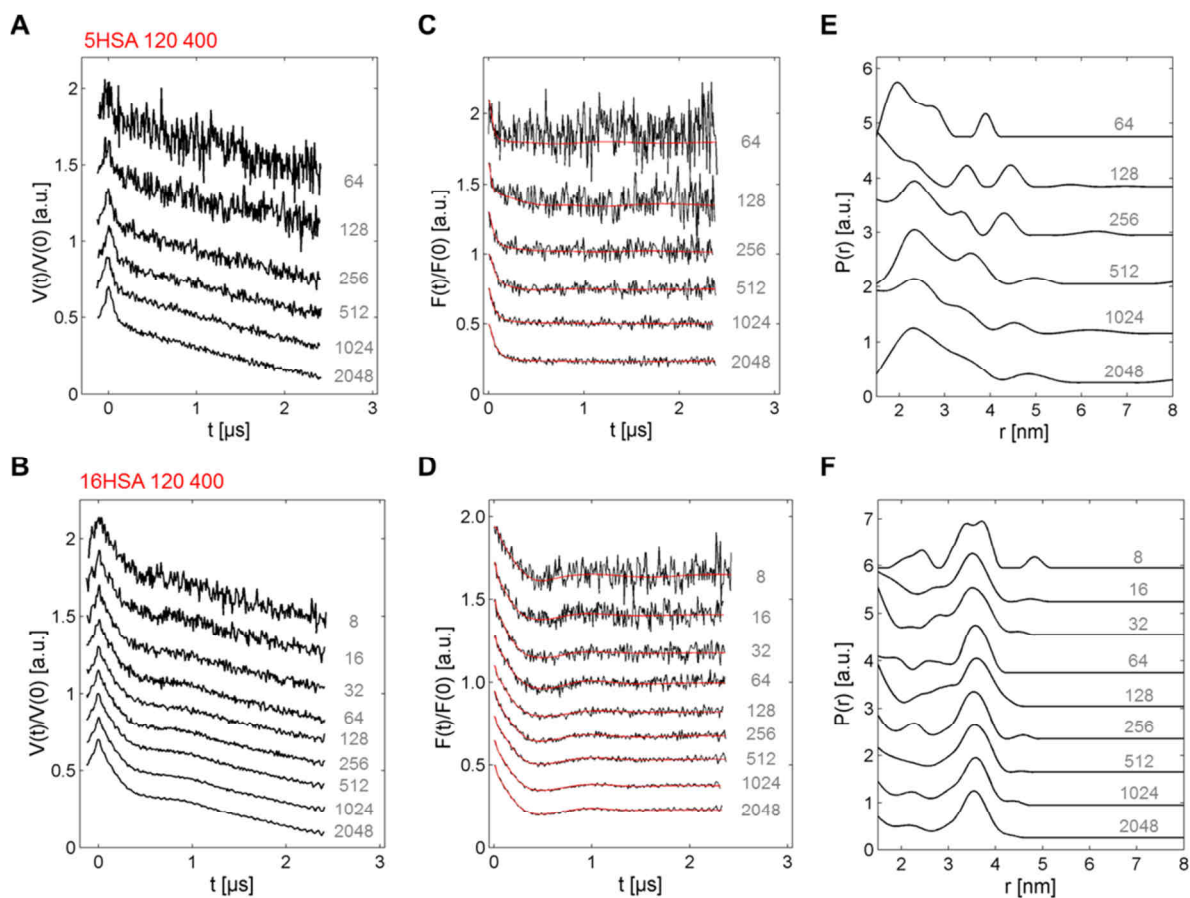
Figure 5.8 | Effect of experiment duration (t_{DEER}) on $P(r)$ in DEER experiments on spin probed HSA. Samples containing 5-DSA and 16-DSA probed HSA in the loading ratio 1:2 and 0.4 mM equivalents were subject to varying numbers of scans X (gray inset numbers) with equal maximum dipolar evolution times $t_{max} = 2.5$ µs. Experimental DEER time traces $V(t)/V(0)$ are given for (**A**) 5HSA 120 and (**B**) 16HSA 120. Corresponding background corrected DEER time traces $F(t)/F(0)$ are given together with their regularized fits (red) for (**C**) 5HSA 120 and (**D**) 16HSA 120. The resulting distance distributions $P(r,X)$ are also shown for (**E**) 5HSA 120 and (**F**) 16HSA 120.

This corresponds to a minimum experimental duration of $t_{DEER,5} = 22$ hours. Unlike in 5-DSA, the 16-DSA spin probe already reveals consistent time traces above $X_{16} \geq 256$ that consistently require only about 25% of the measurement time ($t_{DEER,16} = 5.5$ hours, **Figure 5.8F**).

The results for $P(r)$ concerning the experimentally adjusted dipolar evolution times in a time trace (τ_2) are graphically summarized in **Figure 5.9A** by investigating individual peak positions in $P(r,\tau_2)$. The most sensitive features are r_S and r_L as they have low relative intensities and are not clearly detectable in $P(r)$ throughout the whole τ_2-range. Whereas $r_S = 2.27 \pm 0.02$ nm and $r_M = 3.53 \pm 0.04$ nm reveal rather constant values, $r_L = 4.36 \pm 0.26$ nm shifts to larger distances with increasing τ_2. This is a strong indication that r_L values (red dots) are noise artifacts that emerge due to slight differences in background correction procedures[53,65] and are only observed for $\tau_2 \geq 1.6$ µs. Additionally, all peaks

are compared to $r_{\mathrm{max},\langle r\rangle}$ and $r_{\mathrm{max},\sigma}$ values according to equations 5.26 and 5.27 suggesting that reliable distribution shapes are only obtained for $\tau_2 > 1.4\ \mu\mathrm{s}$ (gray dotted line).
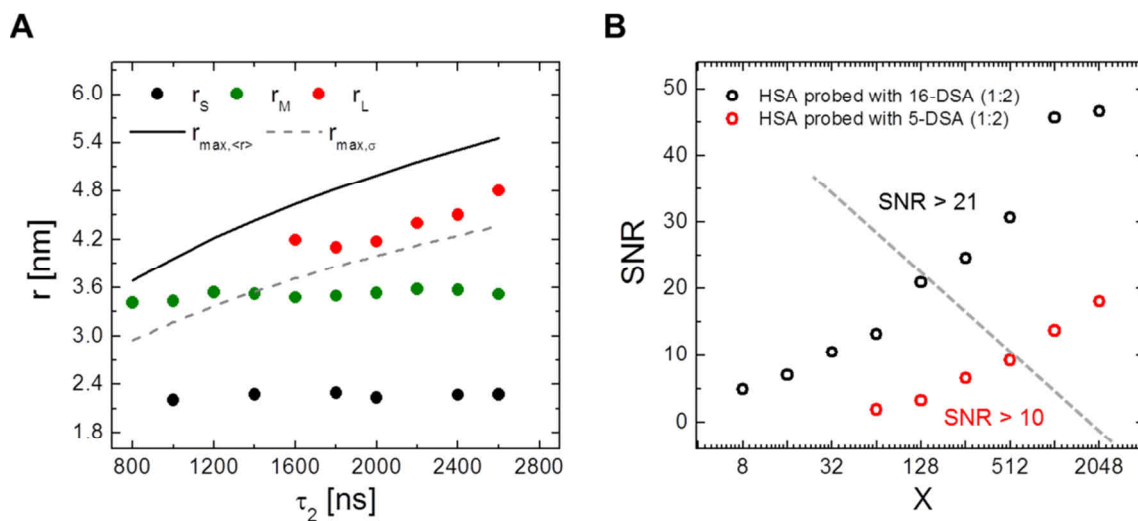

Figure 5.9 | Effect of experimental limitations on data quality of spin probed HSA. Rationalization of experimental limitations in typical DEER experiments on spin probed HSA. (**A**) Graphical representation of interspin distance features (r_{S}, r_{M}, r_{L}) emerging due to the differently adjusted dipolar evolution times τ_2. The curves for $r_{\mathrm{max},\langle r\rangle}$ (black solid curve) and $r_{\mathrm{max},\sigma}$ (gray dotted curve) are calculated according to equations 5.26 and 5.27.[52] (**B**) Logarithmic representation of the increase in SNR of spin probed HSA with 16-DSA (black) and 5-DSA (red) at an increasing number of scans X. The gray dotted line gives an acceptable threshold for sufficient data quality when using these spin probes.

This can be seen as an experimental proof of what has been found by the simultaneous Tikhonov regularization approach.[56] The feature r_{L} can be seen as an artifact that emerges due to uncertainties in the background correction of DEER time traces obtained from 16-DSA probed HSA. The SNR values shown in **Figure 5.9B** were obtained according to the relation:

$$\mathrm{SNR} = \frac{\dfrac{1}{N_t}\displaystyle\sum_i^{N_t}\Delta_i}{\dfrac{1}{(N_t-1)}\displaystyle\sum_i^{N_t}\left(V_i(t)-F_i(t)\right)^2} \tag{5.31}$$

whereas Δ_i are individual modulation depths and the difference between experimental data ($V_i(t)$) and the calculated dipolar evolution functions ($F_i(t)$, **Figure 5.8C+D**) is used for extracting noise contributions. Therefore, all time traces have to be recorded with a SNR > 21 for 16-DSA and a SNR > 10 for 5-DSA in order to obtain reliable distance distributions from spin probed HSA. It is assumed that due to the higher complexity of 16-DSA-based distance distributions the SNR-threshold has to be set a bit higher than for 5-DSA. Therefore, 16-DSA is evidently the preferable spin probe for high resolution DEER-based structural investigations. From now on 16-DSA will be employed when there is no specific need for screening the albumin interior with 5-DSA.[64]

5.6 | Discussion

In this chapter the importance of control over physical properties of albumin solutions was emphasized. A strategy has been developed in order to reliably adjust sample pH and ionic strength in these complex composite colloid suspensions made from glycerol, DPBS buffer and albumin particles. Some simple rulers about solution viscosity and solution density could be set up with help from rheological studies when albumin concentration is varied in 20% v/v glycerol and DPBS buffer at physiological pH 7.4. This rationalization allows for subjecting each individual sample to various experimental conditions, especially in terms of varying ligand loading ratios that are essential in e.g. CW EPR studies at room temperature and pulse EPR experiments at cryogenic temperatures (typically 50 K for DEER). Furthermore, the tremendous effect that protein concentration exerts on solution properties could be exploited for extracting an approximate intrinsic viscosity $[\eta]$ and excluded volumes ($\phi(c)$). The latter one can be obtained from volumetric approaches as well as from DEER time traces provided that data sets are available that contain strategic variations in albumin concentrations.[56] After all, the recurrence of quite similar values for molecular dimensions of about $R = 3.0 \pm 0.4$ nm for HSA and BSA that were assessed from various experiments ($R_{\mathrm{H,V}}$, R^+ and $R_{\mathrm{H},[\eta]}$) may serve as an intrinsic standard quality control for further optimization strategies in this regard. In essence, the most important outcome is that albumin shape and functionality is rather unaffected when 20% v/v glycerol is added to a sample.

Once established, control about albumin sample quality can be further refined in terms of protein consumption and signal quality in EPR experiments. It was found that in CW EPR experiments with 5-DSA probed HSA sufficient signal quality is only observed for $c_{\text{5-DSA}} > 0.2$ mM whereas application of 16-DSA leads to better resolved spectral features. For example, this finding is of significant importance in case when only a small amount of sample is available as it was the case in the studies shown in **Chapter 7** (PTM). The comparability of CW EPR spectra from 5-DSA and 16-DSA probed albumin samples is therefore only guaranteed for $c_{\text{Albumin}} > 30$ µM provided that most of the binding sites are saturated with paramagnetic spin probes. In principle, the upper limit of protein concentration is given by albumin solubility in DPBS pH 7.4 (ca. $c_{\max} < 7.5$ mM ≈ 500 mg/ml albumin stock solution).[17] However, a good estimate would be that protein concentration in an EPR-active sample should not exceed $c_{\text{Albumin}} = 1.0 - 1.5$ mM and six molar equivalents of DSA spin probes per albumin in order to prevent protein aggregation, albumin gel formation as well as micelle formation of ligand. For sufficient resolution in CW EPR experiments with any purpose it is not necessary to exceed $c_{\text{Albumin}} = 0.1 - 0.2$ mM with 16-DSA as a spin probe in loading ratios from about 1:1 to 1:7.

In principle, DEER experiments reveal much more sophisticated concentration effects. It is well-known that the increase in signal quality depends on a variety of parameters that are either based on experimental settings as τ_1 and τ_2, TWT attenuation,[54] temperature[66] with its associated changes in spin dynamics of T_1 and T_2,[51,63] the duration of an experiment (t_{DEER}) with all of its adjustable parameters (equation 5.30), modulation depth Δ, the ligand loading ratio,[64] protein concentration

($c_{Albumin}$) as well as spin concentration (c_{DSA}) that in turn affect background dimensionality D.[51] In this mostly rather straightforward approach it was only tested to which extent protein concentration, X and τ_2 or t_{max} affect the quality of the resulting distance distribution $P(r)$. The complex distance distribution of 16-DSA-probed HSA can be fully resolved for $t_{max} \geq 1.4$ μs as it can be also predicted from customary equations.[50,52] However, it can be shown that reliable DEER-derived distance distributions from 16-DSA require a higher SNR (SNR > 21) compared to 5-DSA (SNR > 10). On the other hand, time traces of 5-DSA-probed HSA accomplish this requirement only for $X \geq 1024$ scans. Additionally, it was found empirically that a nominal equivalent concentration of $c_{HSA} = 0.4$ mM yields best results in comparative studies of 5-DSA- and 16-DSA-probed HSA. This corresponds to $c_{DSA} = 0.8$ mM and can be also predicted with $c_{opt} = 0.8 - 0.9$ mM[51] in case the inversion efficiency of a 12 ns ELDOR pump pulse in a given resonator is accessible. The inversion efficiency $\lambda = 0.534 \pm 0.009$ of the pump pulse was determined from well-studied model biradicals.[46,67] This parameter also corresponds with a value that was reported earlier from the same spectrometer ($\lambda = 0.52$).[54] From now on it is considered as the intrinsic modulation depth parameter of the applied split-ring resonator of the used pulse EPR spectrometer throughout this work. Both, from simultaneous Tikhonov regularization and experimental optimization of concentration-dependent 16-DSA-probed HSA solutions the enigmatic feature in $P(r)$ at about 4.36 ± 0.26 nm can be ruled out to be an excluded volume artifact that emerges due to the application of incorrect background models in data analysis. Despite its glaring intrinsic complexity that is here faithfully witnessed in a straightforward and coherent outline, the simultaneous Tikhonov regularization approach[55,56] seems to be a promising method for handling some of the previously enigmatic effects in DEER-derived distance distributions of spin probed albumin. Presumably, with its general theoretical basis this method bears the intrinsic potential to obliterate background artifacts in a wide variety of paramagnetic systems. Recently, a modulation depth scaling approach has been introduced that seems to be another promising strategy for separation of intra- and intermolecular contributions in DEER time traces.[68]

5.7 | Materials and Methods

Materials. Lyophilized powders of HSA (> 95%, Calbiochem), BSA (Sigma-Aldrich), GSA (Sigma-Aldrich), SSA (Sigma-Aldrich), 5-DSA (Sigma-Aldrich), 16-DSA (Sigma-Aldrich), glycerol (87% in water, ACROS), pH 1–12 reference buffers (ROTI® CALIPURE, Carl Roth), pH 4.01 – 10.00 reference buffers (Technical buffers, WTW), Pierce™ BCA protein assay kit (Thermo Scientific), Coomassie brilliant blue G-250 (CBBG, AppliChem), ethanol absolute (>99.8% CHROMASOLV, Riedel-de Haen), OTP-d$_{14}$ (98 atom % D, C/D/N Isotopes), toluene (>99.9% ROTISOLV HPLC, Carl Roth), phosphoric acid (85%, J.T. Baker) and all salts were used as received from commercially available sources. The model biradical compounds PPE$_1$, PPE/B$_1$, PPE$_3$, PPE/B$_2$, PPE/B$_3$ and PPE/B$_4$ that were used for pulse EPR spectrometer calibration (λ) were kindly provided by Prof. Dr. Adelheid Godt and Miriam Hülsmann from Bielefeld University, Germany.[46,67]

Controlling Sample pH and Ionic Strength. The general preparation of an appropriate DPBS buffer,[5] its pH adjustment and an exemplary sample is described in **Appendix C1 – C4** and **Table C1 – C3**. In principle all pH measurements have been performed on a pH meter (Mettler Toledo EL20) equipped with a microelectrode (Mettler Toledo InLab® Micro pH 0 – 14) and calibration buffers in the range from pH 1 – 12 (Technical buffers,

WTW, as well as ROTI® CALIPURE buffer solutions, Carl Roth). For DPBS buffer preparation a pocket pH meter was occasionally used at the MPIP (WTW pH320).

Determination of Qualitative and Quantitative Albumin Content. The components used for quantitative BCA assays were purchased as precast commercially available kits (Pierce™ BCA Protein Assay Kit, Thermo Scientific) and were used as received according to a modified protocol as described in **Appendix C5** and **Table C4**. Absorption at $\lambda_{BCA} = 562$ nm was either recorded at $T = 20°$ on an UV/Vis spectrophotometer (Hewlett-Packard HP 8453) in combination with a Peltier temperature controller for the sample cell (Hewlett-Packard HP 89090A) at MLU Halle or on a 96-well microplate reader at the MPIP Mainz (Tecan Infinite® M1000). Results for two independent concentration measurements of 1 mM stock solutions of HSA, BSA, GSA and SSA are shown in **Table C5**. The Bradford reagent was prepared very similar to the original procedure[14] and was only used for qualitative quick tests (**Appendix C5**).

Assessing Excluded Volume. The samples for determination of the excluded volume were prepared with greatest caution. First an appropriate amount of lyophilized BSA powder was weighed in tared Eppendorf reaction tubes on special accuracy weighing machines (Mettler Toledo AX205 (MPIP) and AT261 Deltarange (MLU): $\Delta m_{BSA} \approx 0.03$ mg). Thereafter, the powder was carefully dissolved in precisely adjusted and calculated volumes V_1 (ca. $400 – 1100$ µl) of 0.137 M DPBS pH 7.4 (Eppendorf Reference $100 – 1000$; $\Delta V_1 = 2$ µl) with occasional centrifugation (1 min at about 10.000 g) in order to deplete bubble formation. When a bubble-free solution was obtained and the protein was completely dissolved, the initially added volume V_1 that was used to adjust the nominal BSA concentration c_{nom} was in turn removed as a supernatant and the residual volume $V_{ex} = V_{total} − V_1$ was virtually taken as the excluded volume. Intuitively, the measurement of the residual volume V_{ex} was conducted with a $10 – 100$ µl Eppendorf Reference pipette ($\Delta V_{ex} \approx 2\%$) with utmost care and occasional centrifugation of the solutions. The concentration range was set in the range from $c_{nom} = 10 – 200$ mg/ml. The excluded volume reached peak values of up to $V_{ex} = 80$ µl for the highly concentrated solutions with $c = 200$ mg/ml exhibiting a total volume of about $V_{total} = V_1 + V_{ex} \approx 0.5$ ml. Results from these experiments are shown in **Figure 5.1**.

Viscometry and Densimetry. All samples for viscometry and densimetry have been prepared from 120 mg/ml BSA stock solutions ($\phi(c) = 0.0975$) in DPBS buffer that were equipped with 20% v/v glycerol (87% glycerol, ACROS) and titrated to pH 7.4 with appropriate pH buffers. The results are shown in **Figure 5.2**. The solution densities ρ were measured on a densimeter (DM 40, Mettler-Toledo). The dynamic viscosities η of BSA-containing solutions were determined with a water bath-immersed Ubbelohde viscometer (capillary: 53713/Ic) and an automatic flow time measuring system in an AVS 370 setup at $T = 25°C$ (ViscoSystem®, SCHOTT) using the relation $\eta = C\rho t_f$ as described in Cannon *et al.*[69] Here, $C = 0.02998$ mm² s⁻¹ is a device constant of the viscometer and t_f is the flow-time of the liquid. Both devices were operated in the polymer analytics service division of the MPIP in Mainz and all experiments were patiently conducted by Sandra Seywald. For matching the requirements of the instrument the final sample volume has been adjusted to 6 ml each. It was found that bubble formation constitutes a major drawback for all experiments.

Rheology. All supplementary experimental rheological data given in **Table 5.1** were obtained from a Physica MCR 301 Rheometer (Anton Paar) provided with a CP50–2/TG gauge head forming a cone-plate measuring system. Samples were prepared from ultrapure water, 87 wt% glycerol, DPBS buffer pH 7.4 and a 88.7 mg/ml BSA stock solution in DPBS ($\phi(c) = 0.0721$) with a required sample volume of 1.25 ml titrated to pH 7.4. The shear rate-associated dynamic viscosities η were recorded with increasing complexity of the solution in the range from $0 – 2000$ s⁻¹ and were back-extrapolated to zero-shear rate from the linear regime of shear-thickening[70] from about $500 – 1800$ s⁻¹ similar to standard procedures reported elsewhere.[71,72] The experimental shear curves are shown in **Figure C3** of **Appendix C6**.

Arbitrary Shape of BSA. An estimate about the radius of gyration (R_G) of BSA and its average rhombic heart shape was made with help of the YASARA Structure software[73] using the pure crystal structure of BSA (PDB ID: 3v03).[28]

EPR Spectroscopy. *Sample Preparation:* In principle, all EPR-active HSA samples have been prepared according to the scheme presented in **Appendix C4** and **Table C3**. The sole specification to be made is that the protein stock solutions were prepared as 2 mM HSA in DPBS buffer pH 7.4 and the spin probe stock solutions were adjusted to 26 mM 5-DSA and 16-DSA with 0.1 M KOH. The nominal concentrations of HSA and DSA were adjusted in the range from 0.1 – 0.7 mM and 0.2 – 1.4 mM, respectively. Thus, the molar ratio of HSA:DSA was kept constant at 1:2 molar equivalents for all experiments. Each sample was equipped with 20% v/v glycerol and titrated to pH 7.4.

The biradicals were prepared in the concentration range from 0.27 – 0.85 mM in perdeuterated ortho-terphenyl (OTP-d$_{14}$, see **Table C6**) very similar to a procedure described in Godt *et al.*[46] This is typically done in order to expand the accessible time domain range in DEER experiments (t_{max}), as electron-nuclear spin-spin interactions in deuterated solvents (e-^{2}D) contribute much less to relaxation processes as in hydrogen-containing samples (e-^{1}H).[47] A thorough description of the sample preparation scheme and experimental results is given in **Appendix C7**. For CW EPR experiments about 15 μl of the final solutions were filled into micropipettes (BLAUBRAND® IntraMARK) and for DEER measurements about 40 – 80 μl were filled into 3 mm (outer diameter) quartz tubes (Heraeus Quarzglas) and were subsequently shock-frozen in liquid nitrogen-cooled 2-methylbutane.

CW EPR Experiments: A Miniscope MS200 (Magnettech GmbH) benchtop spectrometer was used in order to record X-band CW EPR spectra for all EPR-active samples (**Figure 5.3**) at microwave frequencies of 9.39 GHz that were recorded with a frequency counter (model 2101, RACAL-DANA). All measurements were performed at $T = 25°C$ using modulation amplitudes of 0.1 mT and a sweep width of 12 mT. The microwave power was set to $P_{MW} = 10$ mW.

DEER Experiments: A wide variety of DEER experiments was performed on EPR-active HSA samples and model biradicals.[46,67] The preparation of these biradical samples in perdeuterated ortho-terphenyl (OTP-d$_{14}$) is explicitly described in **Appendix C7** and all associated structures and parameters are given in **Figure C4** and **Table C6**. The general 4-pulse DEER sequence:[74,75]

$$\pm(\pi/2)_{obs}-\tau_1-(\pi)_{obs,1}-(t_d+t_0+N_t\Delta t)-(\pi)_{pump}-(t'-N_t\Delta t+t_d)-(\pi)_{obs,2}-\tau_2-echo$$

was used to obtain dipolar time evolution data at X-band frequencies of 9.1– 9.4 GHz with a BRUKER Elexsys E580 spectrometer equipped with a BRUKER Flexline split-ring resonator ER4118X–MS3. The temperature was set to 50 K for all experiments by cooling with a closed cycle cryostat (ARS AF204, customized for pulse EPR, ARS, Macungie, PA) and the resonator was overcoupled to $Q \approx 100$. The pump frequency ν_{pump} was set to the maximum of the field swept electron spin echo (ESE)-detected spectrum. The observer frequency ν_{obs} was set to $\nu_{pump} + \Delta\nu$ with $\Delta\nu$ being in the range of 65 MHz and therefore coinciding with the low field local maximum of the nitroxide ESE spectrum. The observer pulse lengths for each DEER experiment were set to 32 ns for both $\pi/2$– and π–pulses and the pump pulse length was 12 ns. Additionally, a 2-step phase cycle (±) was applied to the first $\pi/2$ pulse of the observer frequency for cancelling out receiver offsets and unwanted echoes.

For albumin samples containing paramagnetic 5-DSA and 16-DSA spin probes the pump pulse position $t_d + t_0$ after the first observer π-pulse deadtime t_d was typically incremented for N_t timesteps of $\Delta t = 8$ ns in the range $t_0 + t' = \tau_1 + \tau_2 - 2t_d$, whereas τ_1 and τ_2 were kept constant. Here, the impact on data quality was investigated by strategic variation of albumin concentrations (**Figure 5.4**), dipolar evolution times τ_2 (**Figure 5.7**) and the number of scans X (**Figure 5.8**). The impact of concentration was investigated with the same samples as used for CW EPR ($c_{HSA} = 0.1 – 0.7$ mM) whereas optimization of X and τ_2 was exclusively conducted with samples that contained $c_{HSA} = 0.4$ mM and 0.8 mM Y-DSA. The increments of the number of scans was rationalized by $X = 2^n$ with $n \in N_0$ and dipolar evolution times were individually adjusted for each experiment in the range from $\tau_2 = 0.8 – 2.6$ μs in steps of $\Delta\tau_2 = 0.2$ μs with a shot repetition time of $t_{SRT} = 1.5$ ms. Proton modulation was averaged by addition of eight time traces of variable τ_1 starting with $\tau_{1,1} = 200$ ns, incrementing by $\Delta\tau_1 = 8$ ns and ending up at $\tau_{1,8} = 256$ ns.

As the model biradicals were embedded in a deuterated matrix (OTP-d$_{14}$) the maximum echo amplitude was found for $\tau_1 = 396$ ns and $t_{SRT} = 3.0$ ms. Dipolar evolution times and time increments were adjusted in the range from $\tau_2 = 4 – 22$ μs and $\Delta t = 8 – 32$ ns, respectively. This was done in order to keep the number of data points in

the range $400 < N_t < 700$. A conventional ^{1}H modulation averaging procedure was applied as for DSA-probed HSA as ^{2}D modulation from OTP-d_{14} was found to have no or at least a minor effect on the distance distributions. In a conventional experimental setup the maximum TWT gate time limits the range of recordable dipolar evolution times to about 10 µs. This problem could be overcome by simply increasing the t_d value (d$_3$) in the pulse programmer to about 300 ns. The runtime for the DEER experiments was in between $t_{DEER} = 1.5 - 17.0$ h. However, after $2 - 3$ h most of the time traces had a sufficient SNR facilitating straightforward data analyses. The experimental results are given in **Figure C5A** and **Table C7**.

Data Analysis: All DEER time traces were exclusively analyzed with the MATLAB-based program package DeerAnalysis2013.[53] DEER time traces obtained from spin probed HSA were analyzed with different strategies. The concentration-dependent experiments (**Figure 5.4**) were regularized with $\alpha_5 = 1000$ and $\alpha_{16} = 100$ throughout. In this study the background dimensionality D was regarded as an adjustable parameter and the results are shown in **Figure 5.5**. The same data set was subject to a home-written simultaneous Tikhonov regularization procedure that was explicitly described and conducted by Dr. Daniel R. Kattnig. The filtered distance distributions free of background and excluded volume artifacts are shown in **Figure 5.6**.[56]

The effect emerging from different τ_2 values that was tested for 16-DSA probed HSA was filtered out assuming a constant background dimensionality of $D = 3.74$ and $\alpha_{16} = 100$ (**Figure 5.7**). It was found that only $\tau_2 \geq 1.6$ µs leads to stable distance distributions $P(r)$ where all features can be resolved. The effect emerging from different scan numbers was filtered by analyzing the SNR (equation 5.31) for 5-DSA and 16-DSA probed HSA in the range from $1 < X < 2048$ scans, or $0 < n < 11$ for $X = 2^n$. Therefore, the parameters $\tau_2 = 2.5$ µs, $D = 3.74$, $\alpha_5 = 1000$ and $\alpha_{16} = 100$ were kept constant throughout.

DEER time traces of biradicals were analyzed with fitted background dimensionality values in the range from $3.17 - 3.55$. The regularization parameters α, interspin distances in the range from 2.85 nm $< r <$ 7.52 nm and modulation depths Δ can be found in **Table C7**. All corresponding data analyses are graphically represented in **Figure C5B–D**. The distance-independent value of the modulation depth parameter of the BRUKER Elexsys E580 pulse EPR machine equipped with the Flexline split-ring resonator ER4118X–MS3 was determined as $\lambda = 0.5342 \pm 0.0092$ (**Figure C6**) according to an approach that was already outlined by Hilger *et al.*[42]

6 | The Genetic Fingerprint of Spin Probed Albumins

Here, the effect of genetic variety on the mode that fatty acids align in albumins has been investigated in a similar way to **Chapter 4** mainly utilizing DEER spectroscopy. Commonly, most of the mammal albumins have an amino acid sequence identity of 72.0 – 82.0 % compared to HSA[1,2] with a few exceptions such as 93.5 % for rhesus macaque monkeys[3] and other primates in general. As it was already shown in **Chapter 4** in a comparison of HSA and BSA, only few amino acid replacements at decisive regions of the primary structure may lead to a different appearance of the DEER-derived distance distribution of albumin self-assembled with paramagnetic fatty acids. To this effect, Fanali *et al.*[4] claimed that most amino acid residues in albumins that are involved in ligand binding are largely conserved among mammal albumins. In order to detect some tangible albumin-bound fatty acid fingerprints from DEER, three additional commercially available albumins, goat serum albumin (GSA), sheep serum albumin (SSA) and feline serum albumin (FSA) are directly compared to the reference standard HSA[5] in a more qualitative way. Furthermore, these additional mammal albumins were strategically chosen as their HSA-based sequence similarity spans the aforementioned similarity range from 74.5 – 81.8 % to a sufficient extent. The most important bioinformatic benchmark data are summarized in **Table 6.1** also including data for BSA as obtained from the Universal Protein Resource (UniProt),[6] and from the Basic Local Alignment Search Tool for proteins (BLASTP).[7–9]

Table 6.1 | Several properties of the investigated mammal albumins

Organism	Species	Acronym	Taxid[a]	FASTA[b]	AMW[c] [kDa]	HSA similarity[d] [%]	Cys34[e]	N_{aa}[f]
Human	*Homo sapiens*	HSA	9606	F6KPG5	66.54	100.0	+	585
Cow	*Bos taurus*	BSA	9913	P02769	66.44	75.5	+	583
Goat	*Capra hircus*	GSA	9925	B3VHM9	66.32	74.5	+	583
Sheep	*Ovis aries*	SSA	9940	P14639	66.34	74.7	+	583
Cat	*Felis catus*	FSA	9685	P49064	65.85	81.8	+	584

[a]Taxid = Taxonomic identifier according to the NCBI nomenclature. [b]FASTA = UniProtKB accession code for FASTA sequence.[6] [c]Albumin molecular weights (AMW) were calculated from the corresponding FASTA sequence with a protein molecular weight calculator tool.[10] [d]HSA similarity of each type of albumin was calculated from FASTA sequences utilizing the BLASTP 2.6.1 software.[7–9] [e]Cys34 = in case the cysteine at chain position 34 is present that is not involved in a disulfide bridge[11–14] a (+)-sign is accredited. [f]N_{aa} = number of amino acids in the albumin primary structure from individual FASTA sequences.

Beyond the aim of comparing mammal albumins by their DEER-derived fingerprint of paramagnetic fatty acid alignments, first of all their mutual evolutionary relationship can be represented in a phylogenetic tree as shown in **Figure 6.1**. Allover, there are three evolutionary branches represented by the choice of albumin types that may principally exhibit slight differences in functionality and solution shape. Cattle, goats and sheep are genetically closely related with a mutual albumin sequence identity of > 92.1 % (**Figure 6.1**) and < 78.2 % compared to FSA and HSA. They all belong to the realm of the ruminant even-toed ungulates with horns and exhibit a sequence gap at residue position 116 being valid for all hoofed animals,[1] as it was already noticed in **Appendix B4** for BSA. Cats are derived from the carnivore branch comprising an HSA sequence identity of 81.8 % and 76.4 – 77.7 %

compared to the three ruminant even-toed ungulates. The human organism originates from the branch of rodents (= *glires*) traversing the evolution of primates.
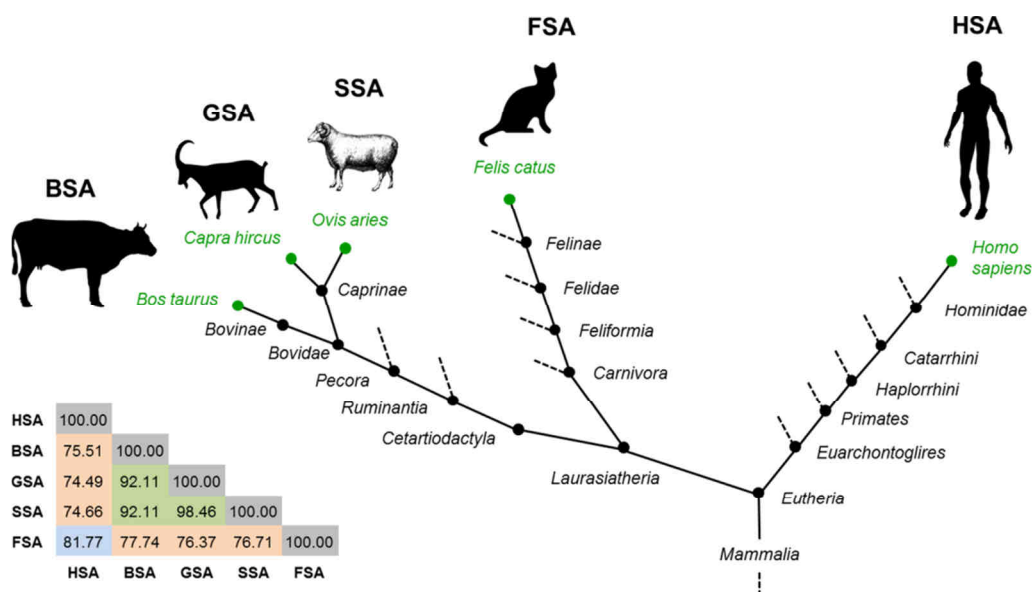
Figure 6.1 | Phylogenetic tree of mammals and albumin homology. This phylogenetic tree highlights organisms whose albumins are investigated here and throughout this work. Albumin-derived sequence similarities in percent were calculated with the BLASTP 2.6.1 program[7–9] and are given in a schematic correlation matrix at the bottom left. All mammal silhouette depictions were obtained from a public domain image provider.[15] The phylogenetic tree was constructed from the taxonomic lineage as found in the UniProt database.[6]

6.1 | Experimental Results

The primary strategy is now to expose these albumins to varying fatty acid loadings with the spin dilution approach[5] as it was also shown in **Chapter 4** for BSA. [16] It is now assumed to be crucial that all compared albumin samples are prepared at completely identical protein concentrations ($c_{XSA} = 0.4$ mM) and identical equivalent ratios of albumin:DSA:r-DSA. The positive side effect of this approach is that all experimental parameters (especially SNR and t_{max}) of the DEER time traces can be adjusted similarly for optimum and comparable data analyses. An exemplary demonstration of the significant improvement in the distance distribution resolution by an appropriate choice of equivalent concentrations can be found in **Figure D1**. Until now, CW EPR studies were not pursued in great detail, however, an exemplary loading ratio of 1:2:0 to all four albumins suggests that not only ligand binding affinities may vary from albumin to albumin, but also the diffusion tensors have slightly different properties when comparing binding of 5-DSA as well as 16-DSA to diverse albumin species (**Figure D2**). Interestingly, already on the stage of albumin stock solution preparation, complications arose in case of FSA, as its solubility appears to be somewhat lower compared to all other albumins. While a 2 mM stock of FSA in 0.137 M DPBS at pH 7.4 contained sediments of presumably undissolved protein, a dilution towards 1 mM showed a clear solution and did not exhibit this kind of behavior anymore. Therefore, a SDS PAGE was conducted as a precaution, confirming that no considerable aggregates or impurities are present in the FSA stock solutions (**Figure D3**).

Due to the vast amount of combinatoric possibilities of different paramagnetic and diamagnetic fatty acid loadings, a strategy was chosen that confines the ratios to 1:1:0, 1:2:0, 1:2:2 and 1:2:4 (N_N = 4), assuming that all albumins (XSA) possess at least six fatty acid binding sites so that a major ligand fraction is constantly absorbed by all albumin samples. Applying the 5-DSA and 16-DSA (N_{DSA} = 2) spin probes in order to survey the interior (C5) and surface (C16) ligand-associated nitroxide alignments in the four albumins (N_{XSA} = 4), a minimum set of $N_{DEER} = N_{DSA} \times N_{XSA} \times N_N = 32$ successful DEER experiments has to be collected. Nevertheless, several measurements had to be conducted in duplicate, triplicate or in differing loading ratios for obtaining reasonable time traces. The 1:1:0 loadings are primarily intended to provide a basis for an estimation of the background dimensionality (D) of the intermolecular part from a DEER time trace. This strategy is usually pursued and realized with singly spin-labeled proteins (monoradicals) in EPR spectroscopy lacking dipolar evolution functions.[17,18] Therefore, the 1:1:0 albumin:DSA ratios should constitute a mimetic monoradical approach as shown in Junk *et al.*[5] However, it turned out that due to excluded volume effects from the 2 mM albumin stock solutions ($\phi(c) \approx 0.108$, see **Chapter 5.2**), the calculated albumin:DSA ratios from sample preparation actually may cause a slight effective overpopulation (ca. $\langle n \rangle = 1.1 - 1.4$ equivalents of DSA per albumin, see equation 2.103) resulting in the emergence of time traces with dipolar oscillations of low modulation depths ($\Delta_{110} = 0.06 - 0.20$) as the self-assembled system statistically generates 1:2:0 occupation ratios by chance. This dynamic effect can be observed in DEER time traces as soon as a small fraction of albumins in a sample forms such 1:2:0 complexes to a certain percentage and was already mentioned as a minor drawback for DEER data analysis.[19] The reason for this effect may be concealed in the statistical, non-uniform loading order of individual binding sites in albumins[20,21] as it was already outlined in **Chapter 3**. Consistently, not all DEER experiments with a nominal 1:1:0 equivalent loading ratio may deliver reliable distance distributions, however, the results in this regard are attached in **Figure D4**.

A complete set of DEER time traces $V(t)/V(0)$, dipolar evolution functions $F(t)/F(0)$ and distance distributions $P(r)$ of each of the four albumins is shown in **Figure 6.2** (5-DSA) and **Figure 6.3** (16-DSA) in the loading ratio ranging from 1:2:0 – 1:2:4. All datasets have been cross-correlated to certify an appropriate choice of background dimensionalities D_i and modulation depths Δ_i. A summary of the obtained parameters together with their standard deviations in this regard is given in **Table 6.2**.

It has been shown earlier, that the background dimensionality of DSA-probed HSA is about 3.74,[19,22] although this parameter may also be explicitly concentration-dependent in a non-trivial fashion (**Chapter 5**). However, it turned out here that each albumin may hold an intrinsic individual background dimensionality that can be isolated by empiric cross-correlation of data sets. The resulting fractal dimensionalities D_i are found to be independent of the use of spin probe for all albumins apart from HSA, showing a slight discrepancy in between 5-DSA and 16-DSA. Surprisingly, background dimensionalities of FSA were below 3.0 throughout all experiments ranging from 2.65 – 2.91, deviating from all other albumins (D = 3.3 – 3.7).

Table 6.2 | Background dimensionalities and modulation depths in spin probed albumins (XSA)

	$D_{5\text{-DSA}}$[a]	$D_{16\text{-DSA}}$[a]	$\Delta_{5\text{-DSA}}$[b]	$\Delta_{16\text{-DSA}}$[b]
HSA	3.52 ± 0.07	3.74 ± 0.03	0.212 ± 0.023	0.290 ± 0.054
GSA	3.29 ± 0.03	3.29 ± 0.09	0.292 ± 0.020	0.408 ± 0.076
SSA	3.41 ± 0.14	3.49 ± 0.09	0.166 ± 0.049	0.258 ± 0.044
FSA	2.78 ± 0.11	2.81 ± 0.06	0.155 ± 0.016	0.204 ± 0.015

[a]Fractal background dimensionalities D_i are given as the mean values of fatty acid loadings 1:1:0, 1:2:0, 1:2:2 and 1:2:4 from **Figure 6.2**, **Figure 6.3** and **Figure D4**. [b]Modulation depths Δ_i are given as the mean values of the fatty acid loadings 1:2:0, 1:2:2 and 1:2:4 from **Figure 6.2** and **Figure 6.3**. All errors are given as the standard devations from the mean value.

Figure 6.2 | XSA loaded with 5-DSA and r5-DSA in the ratio 1:2:0 to 1:2:4. DEER experiments were conducted with HSA (X = H, black), GSA (X = G, orange), SSA (X = S, gray) and FSA (X = F, blue) loaded with 5-DSA and r5-DSA in the albumin-to-ligand ratios (**A**) 1:2:0, (**B**) 1:2:2 and (**C**) 1:2:4 (1 eq = 0.4 mM). All original raw DEER time traces are shown on the left, dipolar evolution functions (black) with fit curves (red) are shown in the middle and the distance distributions can be seen on the right. All samples have been equipped with 0.4 mM equivalents of albumin, DSA and r-DSA at pH 7.4 and 20% v/v glycerol.
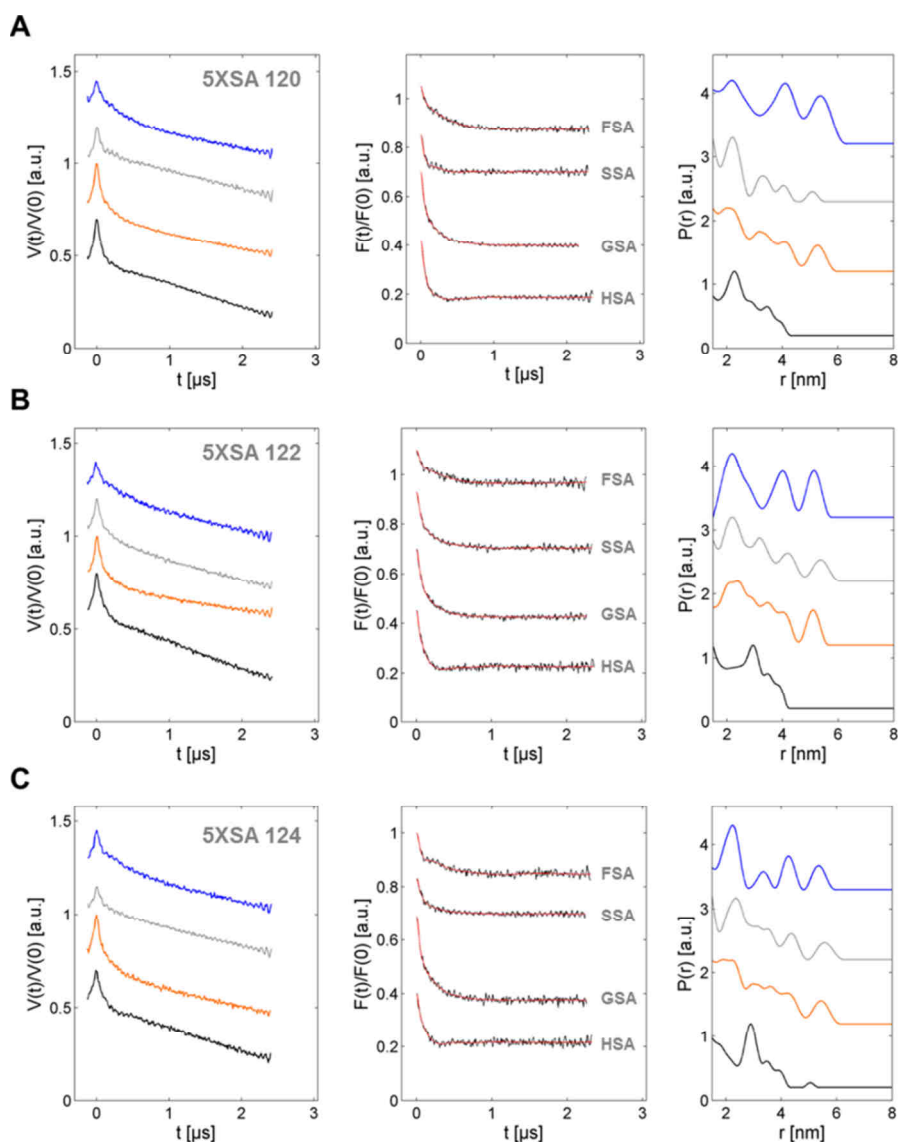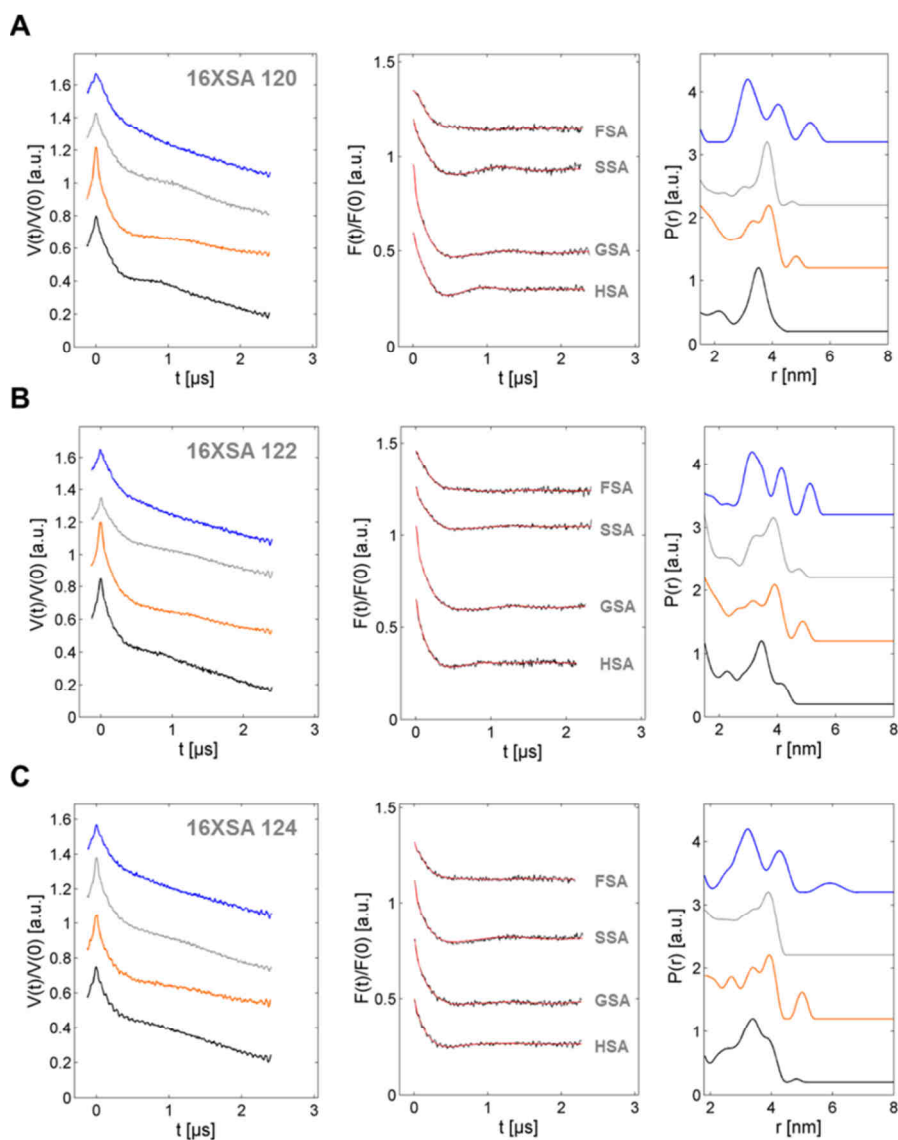
Figure 6.3 | XSA loaded with 16-DSA and r16-DSA in the ratio 1:2:0 to 1:2:4. DEER experiments were conducted with HSA (X = H, black), GSA (X = G, orange), SSA (X = S, gray) and FSA (X = F, blue) loaded with 16-DSA and r16-DSA in the albumin-to-ligand ratios (**A**) 1:2:0, (**B**) 1:2:2 and (**C**) 1:2:4 (1 eq = 0.4 mM). All original raw DEER time traces are shown on the left, dipolar evolution functions (black) with fit curves (red) are shown in the middle and distance distributions can be seen on the right. All samples have been equipped with 0.4 mM equivalents of albumin, DSA and r-DSA at pH 7.4 and 20% v/v glycerol.

On the other hand, the observed modulation depths from GSA are much higher than for other albumins, although samples and experiments have all been prepared exactly in the same way. Though distance distributions from 5-DSA aligned in all albumins commonly appear complicated (**Figure 6.2**), it can be clearly seen that the distributions for GSA and SSA are practically identical for 1:2:0 loading ratios. For this 1:2:0 loading ratio all albumins possess their maximum distance probability $P_{max}(r)$ at 2.1 – 2.3 nm (**Figure 6.2A** (right hand side)). GSA, SSA, and FSA have pronounced distance peaks at 2.1 – 2.4 nm and 4.0 – 4.4 nm throughout all loadings for 5-DSA and with increasing fatty acid content additional peaks are emerging or splitting in between these two pronounced features. Only HSA shifts its maximum peak from 2.3 to 2.9 nm at higher loadings as it was reported earlier.[5] Primarily, distance features exceeding 5.2 nm should be regarded as artifacts because $t_{max} \approx 2.3$ µs (see

equation 5.26).[23] The distance distributions from 16-DSA loadings appear slightly less complicated, but again GSA and SSA exhibit quite similar distribution shapes with the most prominent peaks of varying intensity at 3.0 – 3.4 nm, 3.8 – 3.9 nm and 4.7 – 4.9 nm emerging almost throughout all fatty acid loading equivalents. Exclusively, the 4.7 nm peak of SSA vanishes at 1:2:4 equivalents of 16-DSA. Therefore, this feature is most probably a regularization artifact for all $P(r)$ in this study (see also **Chapter 5**). Again, with increasing fatty acid loading, the distribution of GSA evolves to a bit more anisotropic shape than observed for SSA with a clearly resolved additional peak at 2.7 nm. The distribution from HSA exhibits the well-known peaks at about 2.3 and 3.5 nm with an additional peak at 3.9 nm arising only at higher loadings. Thus the peak singularities of HSA resemble quite well with GSA and SSA for higher loadings albeit being of obviously different intensities. FSA again has a conserved distribution shape at all loadings exhibiting maxima at 3.2 and 4.2 nm with the latter one seemingly not coinciding with all other albumins.
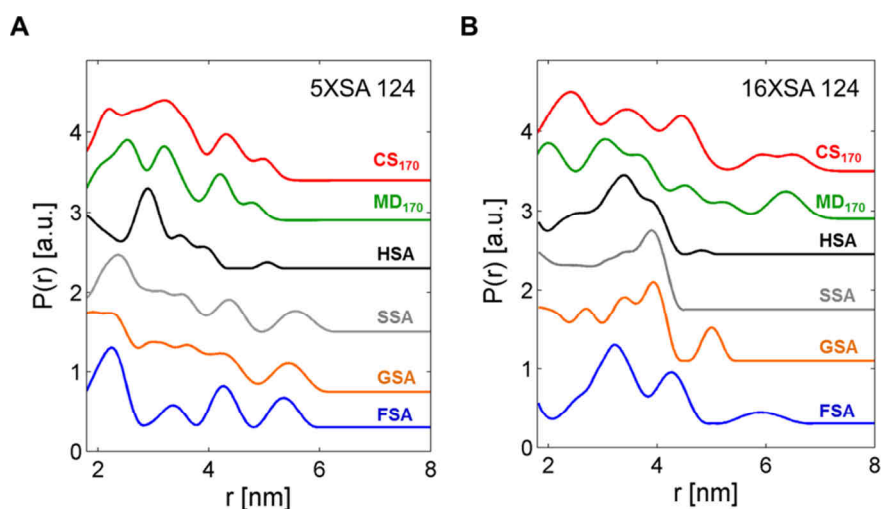
Figure 6.4 | Comparison of theoretical and experimental $P(r)$ for maximum binding site occupation of all albumins. The theoretical distance distributions from HSA's crystal structure (PDB ID: 1e7i)[24] are presented together with experimental DEER results. The extrapolated distances CS_{170} (red) from this crystal structure (**Table A1**)[5] and the theoretical solution structure MD_{170} (green) from a 3.8 ns MD simulation snapshot were taken from the matrices in **Table G3**. The line widths have been adjusted with a Gaussian broadening of $\sigma_5 = 0.13$ for 5-DSA and $\sigma_{16} = 0.18$ for 16-DSA (see equation A.1). Experimental DEER results from (**A**) 5-DSA and (**B**) 16-DSA alignments are taken from fatty acid loadings 1:2:4 in **Figure 6.2C** and **Figure 6.3C**. Here, all regularization parameters were chosen equally at $\alpha_5 = \alpha_{16} = 100$.

In **Figure 6.4** a comparison of all 1:2:4 loadings of HSA, GSA, SSA and FSA from **Figure 6.2C** and **Figure 6.3C** is given for 5-DSA and 16-DSA. Additionally, the crystal structure-derived fatty acid alignment data (CS_{170})[5] and MD-derived data (MD_{170}) of the solution structure from a snapshot at 3.8 ns runtime are given (taken from **Table G3** in **Chapter 9**), assuming that the fully occupied HSA molecule has equivalent binding site association constants. Here, paradoxically, the albumin interior as monitored by 5-DSA gives the largest deviation for HSA compared to HSA's crystal structure (CS_{170}) and solution structure (MD_{170}). An analysis of RMSD values in between all $P(r)$ shapes as shown in **Chapter 4** was not conducted (**Table B1**).

All other albumins, GSA, SSA and FSA, resemble several features that also emerge from the theoretical predictions for 5-DSA, especially the peaks at 2 and 4 nm in MD_{170}. The MD simulation for HSA self-assembled with 16-DSA gives quite promising results, especially the bimodality from the maximum at 3.0 nm and 3.7 nm can be qualitatively observed for HSA, GSA and SSA, while FSA lacks the peak at 3.7 nm.

Finally, a direct experimental comparison of $P(r)$'s from BSA (see also **Figure 4.1B**) with SSA and GSA at a low concentration 1:2:0 loadings with 5-DSA (1 eq = 0.17 mM) is given in **Figure 6.5A**. Apart from the lack of peak resolution in SSA compared to **Figure 6.2A**, all three distance distributions are very similar (corresponding time traces and regularized fits are given in **Figure D5**) reflecting the high mutual sequence identity of > 92.1 %. Therefore, the fatty acid ligands align in an almost identical fashion in ruminant albumins. Meanwhile a crystal structure of SSA has been released (PDB ID: 4LUF).[25] A comparison of the structural alignments of SSA with HSA (RMSD = 1.539 Å for PDB ID: 1BM0)[26] and BSA (RMSD = 1.207 Å for PDB ID: 3v03)[27] using the MUSTANG algorithm[28] again reveals that SSA is closer related to BSA's structure than to HSA (**Figure 6.5B**).
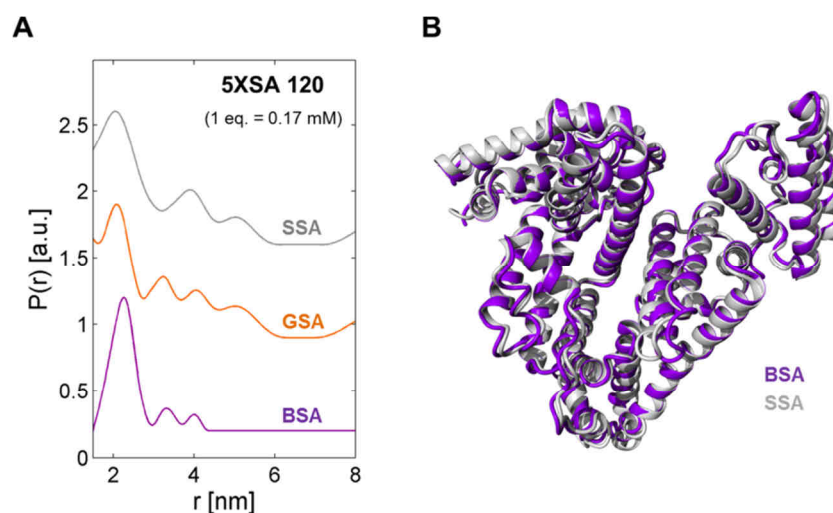
Figure 6.5 | Comparison of the ruminant albumins BSA, SSA and GSA at low concentration. (A) Distance distributions from DEER experiments on BSA, SSA and GSA are compared for a 5-DSA loading ratio 1:2:0 (BSA = deep purple, GSA = orange, SSA = gray) and at 0.17 mM protein concentration (= 0.34 mM 5-DSA). **(B)** MUSTANG alignment[28] of BSA (PDB ID: 3v03, deep purple),[27] and SSA (PDB ID: 4LUF, gray).[25]

6.2 | Discussion

Here, the choice of all investigated albumin species has been conducted by sequence identity and commercial availability. The degree of similarity of fatty acid alignments in the DEER-derived distance distributions $P(r)$ appear to be closely related to the mutual sequence identity of all investigated albumins. Although greatest care has been exercised upon sample preparation and experimental setups according to the findings in **Chapter 5**, several experimental parameters that supposedly are under control still comprise a certain bandwidth of values (e.g. Δ_i). Nevertheless, a maximum accuracy and quality of the DEER time traces could be achieved for all levels of fatty acid

loadings of the albumins (XSA, apart from 1:1:0), so that data analysis leads to comparable results. The solution shape of individual albumins is only detected indirectly by DEER, but may in fact be hidden in the fractal background dimensionality (D) as shown in **Table 6.2**. The determination of the actual solution shapes of all albumins should be effectively determined by SAXS,[29] or by established light scattering methods like DLS.[30,31]

A more unintentional side aspect of the choice of albumins is that the respective organisms are indeed exposed to varying diets *in vivo*. While BSA, GSA and SSA are derived from herbivore organisms, FSA is from a carnivore and HSA from an omnivore. Interestingly, each albumin of a specific evolutionary branch seems to obey a certain intrinsic ligand alignment principle. This finding was already proposed from thorough bioinformatic analyses.[4] Whereas herbivore albumins exhibit very similar fatty acid alignments with complex and corrugated appearances of $P(r)$, generally resembling the rigid crystal structure (PDB ID: 1e7i)[24] much better than HSA and FSA, carnivore and omnivore albumins disclose a much smoother and stable appearance of the distribution shape, regardless of the level of binding site occupation. It has been proposed earlier, that this is due to a flexible and isotropic surface of HSA.[5] In **Chapter 4** it was found from a descriptive bioinformatic analysis that the differences in the DEER distance distributions from fatty acids between HSA and BSA can be partially traced back to differences in hydropathy. This strategy has not yet been applied here.

Being the major transport protein in the mammal body, it is appealing to conclude that the adaptability, flexibility or isotropy of albumin as proposed by Karush[32,33] has to rise with an increasing complexity and variety from customary food supply of each organism. In a recent review of Litus *et al.*[34] it was highlighted that albumins have a highly conserved propensity for intrinsically disordered structural regions, being valid for HSA as well as for BSA. In case this structural disorder was supposedly present in all mammal albumins, consistently, the different DEER-derived fingerprints from 5-DSA and 16-DSA may also be caused by different ligand binding affinities of individual binding sites, resulting in a variation of relative distance peak intensities in $P(r)$ as observed in **Figure 6.2** and **Figure 6.3**. However, a thorough discussion of this subject is beyond the scope of the collected data sets. It is therefore inevitable to survey some more albumins from carnivores (e.g. dog) and omnivores (e.g. rat and monkey) with an additional quantification of the number of binding sites and binding affinities (see e.g. **Chapter 7**). This is usually done by constructing Scatchard plots from CW EPR spectra from exclusively paramagnetic fatty acids interacting with albumin.[35]

Therefore, the ligand-based anisotropy in $P(r)$ as observed in ruminant albumins, unlike HSA and FSA, can only be explained with the consecutive filling of more topologically fixed binding pockets according to their individual association constants ($K_{A,i}$).[36] Many of the features in $P(r)$ can be reproduced qualitatively with theoretical approaches as it is shown in **Figure 6.4**. Unfortunately, as each distance peak of an experimentally observed fatty acid distribution is composed of at least 2, 3 or more of the altogether $N_{r,FA} = 21$ potential interspin distances (assuming $N_T = 7$ binding sites as for HSA),[24] there is no clear strategy at hand to find out which binding site is occupied first based on the

data sets collected here. A more dedicated approach in this regard is presented in **Chapter 9** where data from the MD simulations originate from (**Figure 6.4**, green trace). The observed inconsistencies in modulation depths Δ_i in **Table 6.2** should be investigated in terms of inversion efficiencies from inversion recovery experiments, as it was already tested for HSA by Junk *et al*.[37] When inspecting the findings for HSA in **Chapter 5**, it is evident that also the optimum concentration for comparative DEER measurements may be intrinsic for each albumin. This optimum concentration depends on spin dynamics and the dynamic and structural nature of the internal fatty acid arrangement. Some of these aspects should be at least partially accessible by T_1 and T_2 measurements, as well as from Scatchard plots and further dynamic analyses of continuative CW EPR studies.

6.3 | Materials and Methods

Materials. Lyophilized powders of HSA (>95%, Calbiochem), BSA, GSA, SSA (Sigma-Aldrich), and FSA (Equitech-Bio), 5-DSA and 16-DSA (Sigma-Aldrich), and 87 wt% glycerol (ACROS) and phenylhydrazine (97%, Sigma-Aldrich) were used without further purification. DPBS buffer[38] at pH 7.4 was prepared according to the original protocol as shown in **Appendix C1**.

Sample Preparation. Albumin stock solutions were prepared by dissolving the lyophilized powders in 0.137 M DPBS buffer (pH = 7.4) giving aqueous solutions of 1 or 2 mM XSA. The paramagnetic spin probe solutions were prepared with appropriate amounts of 0.1 M KOH giving a concentration of 26 mM DSA. The reduced EPR-silent spin probes (r-DSA) were prepared according to the procedure described in **Appendix B5**. The final albumin concentrations in the samples were kept constant at 0.4 mM, while appropriate equivalents of paramagnetic and diamagnetic spin probes were added as multiples of 0.4 mM to yield the desired 1:1:0, 1:2:0, 1:2:2 and 1:2:4 loading ratios. The final aqueous solutions of albumin together with fatty acids were supplied with 20% v/v of glycerol to prevent crystallization upon freezing and were finally titrated to pH 7.41 ± 0.03 with appropriate DPBS titration buffers (see **Appendix C2**). Some of the samples have also been prepared according to a scheme similar to **Chapter 4**, where the combined concentration of DSA and r-DSA is here kept constant at 0.34 mM and the protein concentration is decreased accordingly (**Figure 6.5** and **Figure D5**). All samples were prepared individually and as an example the impact of concentration on the quality of distance distributions is shown in **Figure D1**. For CW EPR measurements, about 15 µl of sample were filled into a quarz capillary with ca. 1 mm outer diameter. For DEER measurements about 80 µl of the final solutions were filled into 3 mm (outer diameter) quartz tubes and shock-frozen in liquid-nitrogen-cooled 2-methylbutane for subsequent DEER measurements.

Stuctural Alignments. The crystal structures of HSA (PDB ID: 1BM0),[26] BSA (PDB ID: 3v03)[27] and SSA (PDB ID: 4LUF)[25] were aligned with YASARA Structure[39] utilizing the MUSTANG algorithm.[28] According to the procedure described in **Appendix B3** a RMSD value of 1.207 Å and a sequence identity of 91.85% over 577 aligned residues was found for a comparison of BSA and SSA. Furthermore, the comparison of HSA with SSA yielded a RMSD of 1.539 Å and a sequence identity of 74.34 % over 569 aligned residues.

EPR Spectroscopy. *CW EPR Experiments:* Miniscope MS200 and MS400 (Magnettech GmbH) benchtop spectrometers were used for X-band CW EPR measurements at microwave frequencies of 9.39 – 9.43 GHz that were recorded with model 2101 frequency counters (RACAL-DANA). All measurements were performed at $T = 25°C$ using a modulation amplitude of 0.1 mT and a sweep width of 12 mT. Some representative results of comparable CW EPR spectra are given in **Figure D2**.

DEER Experiments: In total a broad set of DEER experiments was performed on spin probed, EPR-active XSA samples. The general 4-pulse DEER sequence:[40,41]

$$\pm(\pi/2)_{obs} - \tau_1 - (\pi)_{obs,1} - (t_d + t_0 + N_t\Delta t) - (\pi)_{pump} - (t' - N_t\Delta t + t_d) - (\pi)_{obs,2} - \tau_2 - echo$$

was used in order to obtain dipolar time evolution data at X-band frequencies of 9.1– 9.4 GHz with a BRUKER Elexsys E580 spectrometer equipped with a BRUKER Flexline split-ring resonator ER4118X–MS3. The temperature was set to 50 K for all experiments by cooling with a closed cycle cryostat (ARS AF204, customized for pulse EPR, ARS, Macungie, PA) and the resonator was overcoupled to $Q \approx 100$. The pump frequency ν_{pump} was set to the maximum of the field swept electron spin echo (ESE)-detected spectrum. The observer frequency ν_{obs} was set to $\nu_{pump} + \Delta\nu$ with $\Delta\nu$ being in the range of 65 MHz and therefore coinciding with the low field local maximum of the nitroxide ESE spectrum. The observer pulse lengths for each DEER experiment were set to 32 ns for both $\pi/2$– and π–pulses and the pump pulse length was 12 ns. Additionally, a 2-step phase cycle ($\pm$) was applied to the first $\pi/2$ pulse of the observer frequency for cancelling out receiver offsets and unwanted echoes. Proton modulation was averaged by addition of eight time traces of variable τ_1 starting with $\tau_{1,1} = 200$ ns, incrementing by $\Delta\tau_1 = 8$ ns and ending up at $\tau_{1,8} = 256$ ns. The pump pulse position $t_d + t_0$ after the first observer π-pulse deadtime t_d was typically incremented for N_t timesteps of $\Delta t = 8$ ns in the range $t_0 + t´ = \tau_1 + \tau_2 - 2t_d$, whereas τ_1 and τ_2 were kept constant. Dipolar evolution times could be kept constant at $\tau_2 = 2.5$ µs for all samples with 0.4 mM equivalent concentrations.

Data Analysis: The collected time traces have been analyzed in a consistent global manual fit procedure with DeerAnalysis2013.[42] Wherever possible, the regularization parameter has been set to $\alpha = 100$ for all datasets in order to obtain comparable distance peak resolutions. All background dimensionalities D_i have been thoroughly analyzed with the integrated validation tool of DeerAnalysis2013. The theoretical distance distributions $P_{MD}(r)$ from the crystal structure (CS$_{170}$) and 3.8 ns simulation snapshots (MD$_{170}$) for 5- and 16-DSA probed HSA were constructed from **Table A1** and **Table G3**, respectively, according to the procedure described in **Appendix A1**.

SDS PAGE. The SDS PAGE was prepared as a discontinuous electrophoretic system (6% loading gel and 10% separating gel), according to a modified procedure as described by Laemmli.[43] Albumin stock solutions were diluted to a concentration of 1 mg/ml with ultrapure water (MilliQ) and about 10 µg of protein was loaded in each pocket of the gel. As a reference standard the PageRuler[TM] Prestained Protein Ladder (10 – 170 kDa, Fermentas) was used. The gel was allowed to run for about 1 – 1.5 h at 150 V and is shown in **Figure D3**.

7 | Posttranslational Modifications in Albumin Molecules

The EPR spectroscopic characterization of structural and dynamic effects that go along with post-translational modifications of albumin as a model system is presented here. Beyond the typical drug delivery and biocompatibility aspect of such systems, emphasis is here placed on the causes that alter internal dynamics and therefore functionality of the albumin protein. In order to detect these effects, exclusively the paramagnetic fatty acid derivative 16-DSA was loaded on several modified albumin samples that were prepared according to strategies for surface dendronization, glycation and polymer-protein conjugation. Several case-specific CW EPR spectroscopic strategies are refined for investigations concerning ligand binding and extraction of associated parameters as binding affinity (K_A), the total number of binding sites (N_T) and binding cooperativity (C) of modified albumins. It can be rationalized how these parameters may change with the extent of surface modification. Besides CW EPR spectroscopy, other methods as dynamic light scattering (DLS), Zeta potential (ζ) and 4-pulse DEER experiments can be conducted to supplement these findings.

7.1 | Introduction

The occurrence of posttranslational modifications (PTMs) in proteins is a natural physiological and an important biochemical event that includes a vast variety of chemical and physical processes.[1] After successful translation of a specific protein, these processes mainly comprise covalent attachment of small organic (glycation, methylation) or inorganic (phosphorylation) compounds as well as non-covalent uptake of cofactors, ligands and ions.[2,3] Furthermore, PTMs may define the onset of the duty cycle of a protein, e.g. by formation of quarternary complexes,[4] or its imminent termination by ubiquitination.[5] Thus, each externally induced change in the proteins structural integrity and purity may have fundamental influence on its inherent functionality that in turn affects cellular functions as it is best exemplified by the *histone code hypothesis* in epigenetics where combined or sequential modification processes bring about distinct downstream events.[6] On a more general level, it is often disordered proteins or disordered protein regions that are affected by posttranslational modifications as it is also found for albumins.[3]

Albumins are commonly subjected to a broad variety of subtle PTMs as e.g. with glycosylation,[7,8] acetylation,[9,10] ligand binding,[2] modification of the redox-active Cys34 residue[11–14] and the highly reactive lysine residues.[15,16] While the primary structures of BSA[17] and HSA[18] contain as much as 59 lysines, altogether 25 – 35 of them can be targeted for PTM-related reactions in vitro.[19–21] It is therefore intuitive that albumin has become a model protein for many applications ranging from initial spin labeling studies in EPR spectroscopy[22–24] to the construction of polymer-protein conjugates in materials science, nanomedicine and polymer chemistry.[25]

A critical issue is the maintenance of the native, functional structure of the protein during modification procedures that is assumed to be cooperatively manipulated in its bio-activity.[26] However, applicable methods vary strongly in between different proteins in case these functional changes are to be

detected. As it was pointed out in **Chapter 3.2** it is well-known since the early 1940s that albumin binds fatty acids in its crystalline,[27] as well as in its native form in solution.[28] With the availability of appropriately spin-labeled fatty acids,[29–31] a vast amount of EPR spectroscopic studies emerged from the self-assembled, paramagnetic fatty acid-probed albumin system,[32,33] revealing several strategies over time that can be applied (**Chapter 3**).[34] Recently, posttranslationally modified albumins have been investigated with this EPR spectroscopic approach, with cationized albumin surfaces that appear to electrostatically enhance fatty acid uptake.[35] Here, three different systems of posttranslationally modified albumins are presented comprising the effects of surface modifications towards HSA core-shell biohybdrids by poly(amido amine)(PAMAM) dendrimers,[36] glycosylation of HSA and the efficient "grafting from"-construction of BSA polymer-protein conjugates by squaric acid (SA) mediated atom transfer radical polymerization (ATRP) of oligo(ethylene glycol) methyl ether methacrylate (OEGMA). The still rather abstract picture of structural flexibility and adaptability of the albumin surfaces[37,38] will be considered as of major interest in this chapter. As an appropriate spin probe, 16-DSA[39] was chosen for all studies due its superior signal quality (see **Chapter 5**) and of course due to the intrinsic propensity of stearic acids for binding to the hydrophobic pockets in albumin.[33,40,41] While 16-DSA bears its doxyl-spin label at the 16-position close to its hydrophobic tail end, it should therefore monitor changes related to albumins surface structure and dynamics,[42,43] where most of the applied chemical alterations of albumins can be expected to take place. Beyond that, for each system a different empiric strategy of data extraction from CW EPR spectra is presented in a stepwise optimized fashion that consistently evolves from method A towards method C.

7.2 | Dendronized HSA Core-shell Biohybrids

Introducing a branched surface topology to albumin is an innovative strategy in the application of targeted posttranslational modifications. Therefore, the unique architecture and structural perfection of PAMAM dendrimers[44] is tested for its impact on drug binding properties in combination with an albumin core. First successful attempts that portrayed protein-dendron conjugates aiming towards biomimetic nanoscale materials in disease control were made with J591 anti-PSMA antibodies,[45] green fluorescent protein (GFP)[46] and streptokinase.[47] It could be shown that DNA-binding of genetically engineered hydrophobin[48] and BSA[49] is enhanced by formation of protein-dendron conjugates and that hydroxyapatite in bone tissue can be also targeted by dendronized BSA.[50]

Depending on their structural generation, PAMAM dendrimers alone are notorious for providing an adjustable number of functional endgroups as well as branched hydrophobic cavities that facilitate a high binding capacity, bioavailability and transport efficiency,[51] as well as an increased non-covalent accommodation[52] and solubility[53] of drugs due to their intrinsic amphiphilic nature. PAMAM dendrimers are positively charged at physiological pH and therefore their toxicity was shown to increase with generation and concentration[54–57] affecting cell membrane integrity that may lead to disruption and cytoplasm leakage.[58] It was also shown that their tissue storage specificity changes

with increasing generation.[59] Especially, G4-PAMAM dendrimers have been also shown to bind HSA via non-covalent hydrophilic and hydrophobic interactions that may also trigger conformational changes in the protein.[60]

Unlike the general Starburst[TM] shape of unimolecular micelle PAMAM dendrimers,[44] here G2- and G3-PAMAM dendrimers with an ethynyl focal point were used for Huisgen 1,3-dipolar cycloaddition reactions similar to a scheme presented in Lee *et al.* (see **Figure 7.1**).[61] Therefore the diazo-transfer agent imidazole-1-sulfonyl azide hydrochloride (IS-N$_3$·HCl)[62] had to be used for transforming surface lysines into azido groups.[63] Altogether, 36 ± 4 azide group could be introduced to a single HSA molecule that is here denoted as N$_3$-HSA.[36] This azido-albumin was conjugated with ethynyl-G2.0- and ethynyl-G3.0-PAMAM via a copper-catalyzed cycloaddition in order to obtain the dendronized albumin proteins (Gy-DHSA), namely G2-DHSA and G3-DHSA.
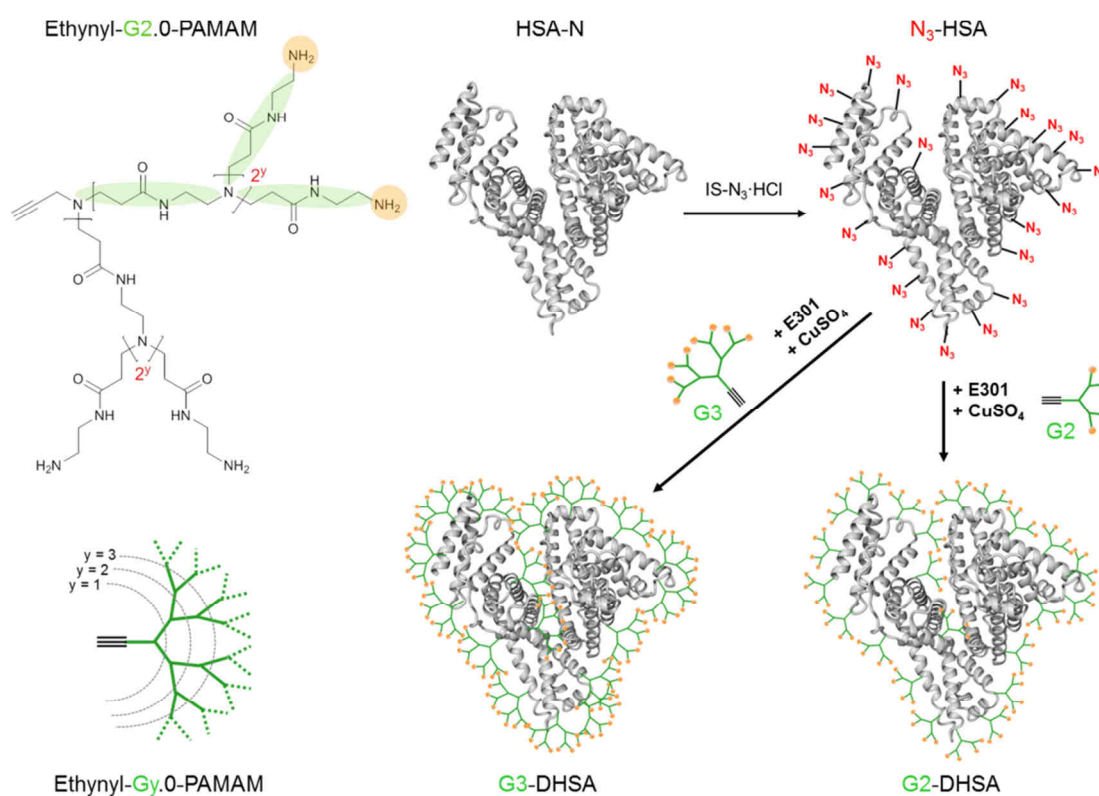
Figure 7.1 | Preparation scheme for Gy-DHSA construction. An exemplary chemical structure of ethynyl-G2.0-PAMAM is presented on the top left and a schematic representation of the degree of generation (Gy) in the dendrimers is shown on the bottom left (green = branches, yellow = end groups). Native HSA (= HSA-N) is converted to azido-HSA (= N$_3$-HSA) upon addition of imidazole-1-sulfonyl azide hydro-chloride (IS-N$_3$·HCl). Bioconjugation towards Gy-DHSA is then facilitated by addition of the respective dendrimer (Gy) with copper sulfate (CuSO$_4$) and sodium ascorbate (E301). This graph was adapted and modified according to the scheme given in Kuan *et al.*[36]

These constructs were thoroughly analyzed and characterized via MALDI-TOF, fluorescence correlation spectroscopy (FCS), UV CD, SDS PAGE, UV/Vis, IR, Zeta potential, FITC-labeling in combination with confocal microscopy, a A549 cell viability assay, their doxorubicin uptake capabilities, as well as their involvement in apoptotic signaling cascades via a caspase 3/7 assay.[36]

The most important physical parameters are summarized in **Table 7.1**. It could be shown that the α-helix content is slightly increased in DHSA compared to native HSA (HSA-N) and that the Zeta potential changes sign from $\zeta_{HSA} \cong -20$ mV to $\zeta_{G3-DHSA} \cong +30$ mV being indicative for a large increase of the net positive charge ($Q = +Z \cdot e$). This positive charge increase could be correlated with an increased cytotoxicity for G3-DHSA above 2.0 µM, whereas G2-DHSA showed first signs of cytotoxicity only well above 100 µM. The G2-DHSA construct exhibited an increased cellular uptake compared to unmodified HSA, while there seems to be a tendency to form minor quantities of larger aggregates due to the interaction with HSA.[36]

Increased caspase activity is well-known to play a key role in apoptosis.[64,65] Hence, the doxorubicin (DOX = adriamycin)[66,67] capacity was determined to be at least 11 mole equivalents per G2-DHSA and its cytotoxicity after 24 h is at least 40 times higher than for pure DOX as it could be estimated from the half maximum inhibitory concentration (IC$_{50}$). This suggests that G2-DHSA may act as a cytotoxic enhancer.

7.2.1 | Results from CW EPR Spectroscopy on Modified HSA – Method A

Here, the dendronized albumin samples were prepared and characterized in the group of Prof. Dr. Tanja Weil, Ulm University, Institute of Organic Chemistry III.[36] G*y*-DHSA samples were kindly provided by Dr. Yuzhou Wu. The sample preparation was conducted according to the scheme given in **Appendix C4** with 16-DSA as an EPR-active spin probe in order to detect potential differences in protein-ligand interactions in between a native HSA reference (HSA-N) and the dendronized albumins (G*y*-DHSA).

The results from the DOX-based studies did not clearly reveal any functional aspects of the HSA-core structure. As a start, ligand uptake capabilities are here coarsely estimated from the relative fractions ϕ_i of free (*f*) to a single bound (*b*) ligand component *i* from subspectra $F_i(B)$ (see **Figure 7.2A**) as it was presented in Ge *et al.*[68] When the albumin system is saturated with 16-DSA ligand, an excess fraction may also accumulate in micelles (*a*) that can be used for a total unbound ligand fraction assessment ($\phi_{af} = \phi_a + \phi_f$) in this kind of analysis. As HSA possesses $N = 7$ long-chain fatty acid binding sites,[41] the G*y*-DHSA constructs can be directly compared to its native precursor analog HSA-N in a ligand loading study. Here, all samples were supplied with three equivalent HSA:16-DSA ligand loading ratios (1:2, 1:4 and 1:8) and it is observed how strong the system interacts with them.

First, from the maximum number of binding sites in native HSA, micellar fractions can be expected to occur in the highest loading ratio of 1:8. However, the extraction of spectral fractions (ϕ_f, ϕ_b, ϕ_a) is only facilitated by explicit spectral simulations that were conducted for all measured samples. The results from these analyses are shown in **Figure 7.2B–D** and can be found as individual fractions in **Table 7.1** (ϕ_i). Simulation parameters were only chosen empirically in order to reproduce spectral shapes best (see **Table E1**).
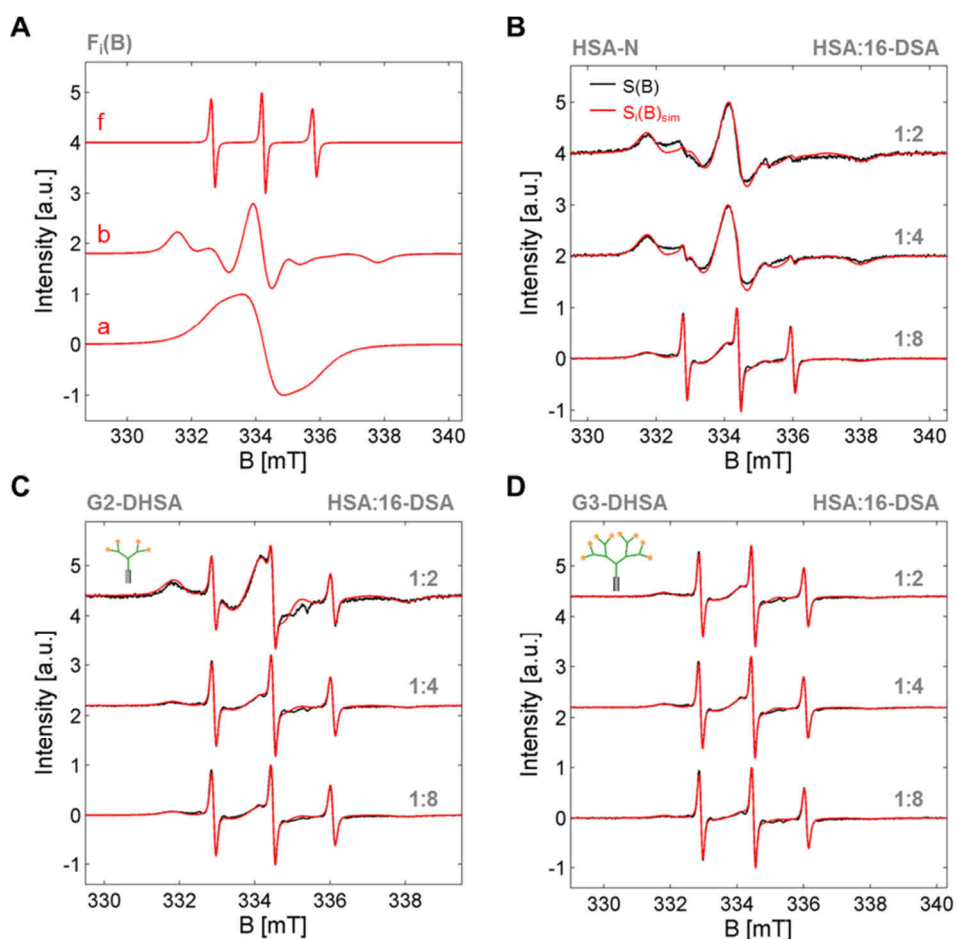
Figure 7.2 | CW EPR experiments and spectral simulations of HSA-N and Gy-DHSA samples. Experimental results of 16-DSA bound to HSA-N are given in black ($S(B)$) and simulations ($S_i(B)_{sim}$) are shown in red for nominal molar ratios of 1:2, 1:4 and 1:8. (**A**) Simulated spectral components that were used here comprise free (*f*), bound (*b*) and micellar (*a*) fractions ϕ_i that were applied to reconstruct (**B**) reference experiments of 16-DSA interacting with unmodified HSA-N, (**C**) G2-DHSA and (**D**) G3-DHSA.

In native HSA more than 99.4 % of 16-DSA ligands are strongly bound throughout loading ratios of up to 1:4. For the 1:8 loading ratio still about 82 % of the ligands are bound, while the free fraction is decisively increased to 8.6 % and a micellar fraction of 9.5 % has to be taken into account in order to obtain reasonable fit curves during spectral simulation (ϕ_{af} = 18.1%, N_L = 8·ϕ_b = 6.6). A different picture is observed for Gy-DHSA, where the free fraction is strongly increased to 3.8 % in G2-DHSA and 14.9 % in G3-DHSA even at the lowest ligand loading ratio (1:2).

As the bound fractions in Gy-DHSA are ϕ_b > 59% for both dendronized albumins throughout all loading ratios, the strong relative increase in the free fractions of the 1:2 loading can be traced back to a reduced intrinsic binding affinity (K_A = [PL]/([P]$_f$[L]$_f$), whereas [PL] = conc. of protein ligand complex, [P]$_f$ = conc. of free receptors on protein and [L]$_f$ = conc. of free ligand, see below).[69] This effect is even more pronounced for G3-DHSA giving rise to the assumption that the PAMAM dendrimers sterically shield the protein core from ligand penetration. For the 1:8 loading ratio of Gy-DHSA more than 30% of the ligand fraction is free (ϕ_{fa} > 0.3) for both constructs.

Table 7.1 | EPR spectroscopic and several physical parameters of Gy-DHSA samples

EPR Spectroscopy	HSA-N			G2-DHSA			G3-DHSA		
Dynamic fractions ϕ_i	ϕ_b	ϕ_f	ϕ_a	ϕ_b	ϕ_f	ϕ_a	ϕ_b	ϕ_f	ϕ_a
(16-DSA : HSA) **2:1**	0.9967	0.0033	–	0.9624	0.0377	–	0.8507	0.1493	–
4:1	0.9949	0.0051	–	0.8548	0.1452	–	0.8385	0.1616	–
8:1	0.8190	0.0860	0.0950	0.6641	0.1142	0.2217	0.5989	0.1797	0.2214

Miscellaneous[a]			
MW[b] [kDa]	66.5	91.4	115.0
N_{Gy}[c]	0	32 ± 2	32 ± 4
R_H[d] [nm]	3.3 ± 0.2	5.5 ± 0.3	8.3 ± 0.5
Z[e] $= Q \cdot e^{-1}$	–14	+77	+205

[a]All values are taken from Kuan *et al.*[36] and simulation parameters are given in **Table E1**. [b]MW = Molecular weights were obtained from MALDI-TOF. [c]N_{Gy} = degree of conjugation by comparison of several preparations from MALDI-TOF results for Gy-DHSA with pure HSA, assuming MW_{G2} = 740.6 Da and MW_{G3} = 1656.1 Da. [d]R_H = Hydrodynamic radii as obtained from FCS experiments. [e]Z = Net charges were calculated from amino acid sequences.

Besides this qualitative reduction in binding affinity it is remarkable that the ligand capacity per dendronized HSA is still well above $N_L = 8 \cdot \phi_b = 4.79$ and that a large fraction of binding sites compared to native HSA remains accessible to 16-DSA. However, this does not comply with former results from 16-DSA loaded on cationized HSA and its poly(ethylene oxide)(PEO)-modified core-shell systems[35] where the ligands were assumed to be electrostatically captured on the surface to large extents. From these findings it can be claimed, that both Gy-DHSA samples largely retain the ligand capacity of HSA, while sterically altering the ligands accessibility towards the protein core and therefore also their binding affinity K_A. Following this precursory and qualitative study, the next section deals with PTMs that are found in a more physiological context of albumins, accompanied with a more solid strategy to unravel the complex CW EPR spectra from EPR-active fatty acids interacting with albumin-containing solutions.

7.3 | The Effect of Maillard Reactions on Albumin under Physiological Conditions

In thermally processed foods as well as under physiological conditions, the Maillard reaction, or non-enzymatic browning, describes the reaction of reducing sugars with amino acids[70] in analogy to a general caramelization procedure.[71] Physiologically, the high reactivity of glyoxal and methylglyoxal with arginine, and lysine gives rise to glycation adducts[72] that potentially lead to a vast amount of PTMs as mono- and bivalent lysine, monovalent arginine and bivalent lysine-arginine modifications. Especially, the bivalent modifications may lead to intramolecular crosslinks[73] that restrict the degree of freedom of internal protein dynamics. In principle, the associated Amadori rearrangement during this chemical reaction is considered as being stable[74] and therefore primarily irreversible, although pathways have been described that reverse or decompose Amadori compounds.[75] Thus, once a protein is glycated *in vivo* it will primarily remain in the organism in this state as long as it will be degraded,[76] as the Amadori adduct has an estimated half-life of at least 3 weeks[74] to about several

months.[75] Albumin is a protein that has a relatively long reported half-life of 12–19 days[2,76] and therefore it may be exposed to a considerable degree of post-translational modification by reactive carbohydrate compounds *in vivo*, depending on sugar abundance,[77] previous impacts and other processes that lead to reactive Maillard intermediates.

The accumulation of stable products of the Maillard reaction, the so-called advanced glycation endproducts (AGEs) in blood[78] are found to be associated with aging[79,80] and several diseases, as diabetes mellitus[7] and its chronic complications that come along as nephropathy, neuropathy and retinopathy.[72,81] Furthermore, the emergence of AGEs can be correlated to Alzheimers disease,[82,83] cataract formation[84,85] and macrovascular diseases.[86,87] The pathological impact of AGEs is mediated by ubiquitous, transmembrane receptors for advanced glycation endproducts (RAGE)[88,89] that induce signal cascades and pathways that lead to cytokine and growth factor secretion[90] and therefore RAGE also raised suspicion to play a role in cancer.[91] Currently, RAGE activation is suggested to be an appropriate target for therapeutic strategies for handling the aforementioned disease patterns.[89]

In particular, glycated BSA was found to display an increased endothelial and vascular permeability and additionally downregulates the anticoagulant cofactor thrombomodulin.[92] Furthermore, it could be shown that macrophages release proinflammatory cytokines IL-1 and TNF upon binding of glycated HSA.[93,94]

7.3.1 | Results from CW EPR Spectroscopy on Glycated HSA – Method B

Here, the α-dicarbonyl compound glyoxal (GLX) was used to generate a set of glycated HSA-derivatives with a varying degree of modification *c*. The preparation and characterization of all native and glycated HSA samples and corresponding CW EPR spectroscopic experiments were conducted by DLC Stephanie Schaarschmidt and DLC Christian Henning in the group of Prof. Dr. Marcus Glomb, Institute of Chemistry, Food Chemistry, Martin-Luther-University Halle-Wittenberg.[95] The sample preparation was conducted S. Schaarschmidt according to the scheme given in **Appendix C4** with 16-DSA as an EPR-active spin probe in order to detect potential differences in protein-ligand interactions between a native HSA reference (HSA-N) and different glycated albumins (HSA-GLX*c*). Due to the fact, that this is an initial trial study, only some few aspects and strategies are presented for two examples which are considered suitable for the presentation of an appropriate data assessment strategy.

Unlike in **Chapter 7.2.1** (G*y*-DHSA), all spectra in this study were analyzed starting off from a more advanced strategy as presented e.g. in Kazmierczak *et al*.[96] This kind of simulation model is nowadays routinely conducted[97–99] and pursues the case-specific extraction of four different dynamic regimes from CW EPR spectra that can be adopted by 16-DSA interacting with albumin, comprising free (*f*), strongly immobilized (b_1), weakly immobilized (b_2) and micellar (*a*) subspectra $F_i(B)$ emerging in the relative fractions ϕ_i. As this strategy is not rationalized to an end in prevalent literature, an in-depth description of the choice of simulation parameters and parameter extraction is

given in **Appendix E2** and will be used in variations throughout this thesis where it is considered as appropriate. Here, the physical nature of the dynamic "bifurcation" in the bound species towards a strongly and weakly bound subspecies (b_i) is not considered as important, however, it was initially suggested to emerge due to intra-albumin migration of fatty acids.[97] This controversial topic is further discussed in **Chapter 10** and **Chapter 11**, considering temperature-dependent experiments from 16-DSA interacting with amphiphilic polymer model-systems and HSA.

The extracted spectral fractions ϕ_i are then used to calculate individual ligand concentrations in the occupied dynamic regimes $[L]_i = \phi_i [L]_t$ of a sample. The total ligand concentration $[L]_t$ can be either obtained from sample preparation protocols as a nominal concentration, or by double integration (DI, **Appendix E3**) of experimental EPR spectra $S(B)$, providing a quantitative measure of the amount of ligand residing in the sample (see **Figure 7.3A**). This analytic step was already described by Jost and Griffith[100] and is here considered as exceptionally important for continuative data processing in terms of a physicochemical analysis. In principle, the total HSA-bound fraction of 16-DSA is simply the sum of both bound fractions $\phi_b = \phi_{b1} + \phi_{b2}$ ($[L]_b = c_{16\text{-DSA}} \cdot \Sigma \phi_{bi} = [L]_{b1} + [L]_{b2}$) and the total free fraction ϕ_{af} is the sum of micelles (a) and freely tumbling 16-DSA (f), i.e. $[L]_{af} = [L]_a + [L]_f$ (see **Chapter 7.2.1** and **Figure 7.3B**). Thus, this strategy allows for characterizing the fatty acid binding properties of the samples in Scatchard plots[101] that can be directly obtained from spectral simulations.

Although being considered as a gross oversimplification in case of complex ligand binding processes as observed in albumins,[102] Scatchard plots, i.e. a plot of $v = [L]_b/([L]_f \cdot c_H)$ versus the number of bound ligand equivalents N_L (**Figure 7.3C**) are quite helpful in detecting the response of the system depending on the number of added ligand molecules. Therefore, the native HSA samples were successively loaded in the range from about 1.4 to a maximum of about 12.4 equivalents of 16-DSA for complete binding site saturation and beyond. The results from this EPR spectroscopic simulation-derived Scatchard plot analysis is given for HSA-N in **Figure 7.3C** assuming an albumin concentration of $c_H = 0.179$ mM according to equation 5.5 in **Chapter 5.2** (purity: $P_{\text{ALP,HSA}} = 0.95$).

The observable linear phase in the Scatchard plot ranges from about $1 < N_L < 7$ and can be evaluated with following expression:[69]

$$v = \frac{[L]_b}{[L]_f \cdot c_H} = \frac{[L]_t - [L]_f}{[L]_f \cdot c_H} = -K_A \cdot \left(N_L - N_E\right) + v_{N_{L} \to 0} \tag{7.1}$$

where K_A is the association constant, N_E the number of equivalent binding sites and $v_{N_L \to 0}$ is the y-axis intercept. The obtained values for 16-DSA interacting with HSA-N are $N_E = 6.45 \pm 0.45$ binding sites and $K_A = (1.94 \pm 0.09) \cdot 10^6$ M^{-1} and correspond reasonably well with findings from former studies ($N_E = 7 \pm 1$).[41,103] However, a biphasic Scatchard plot for 16-DSA- probed HSA-N as presented in Gantchev and Shopova[103] is not found here.
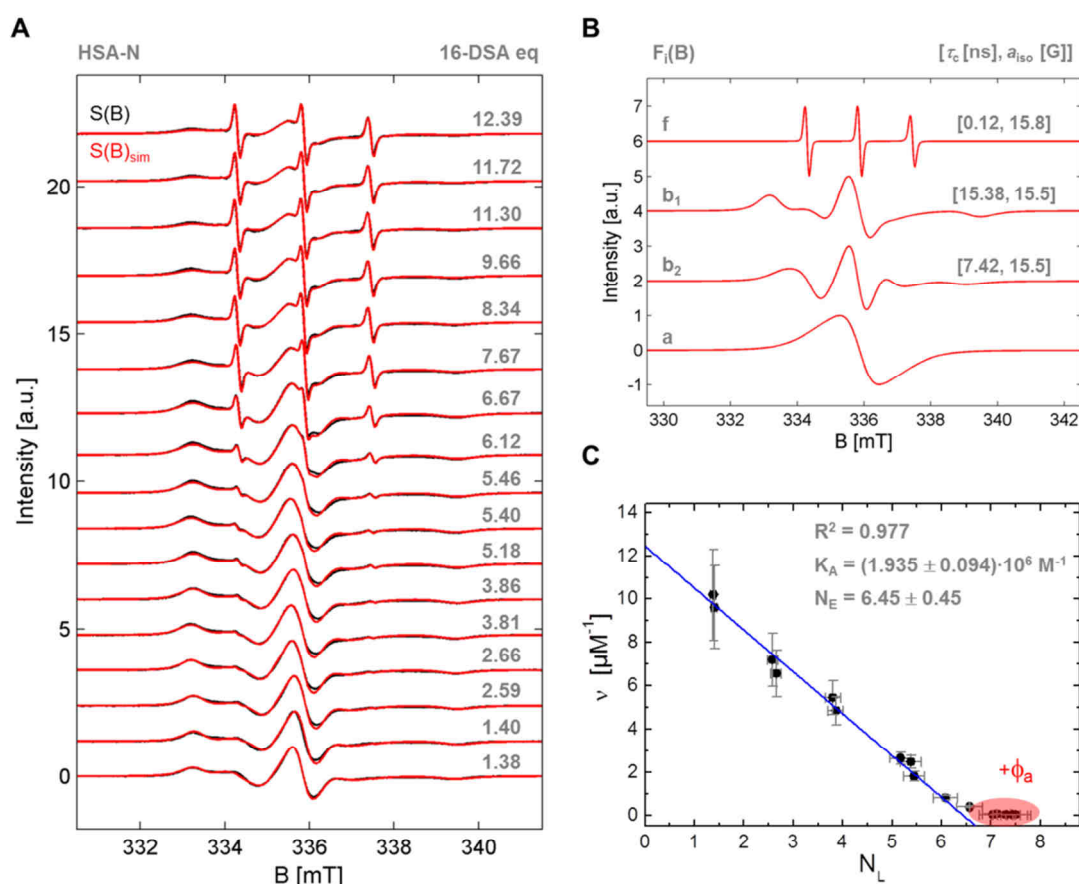
Figure 7.3 | Scatchard plot construction for 16-DSA-probed native HSA samples (HSA-N). (**A**) Experimental CW EPR spectra $S(B)$ (black) and their spectral simulations $S(B)_{\text{sim}}$ (red) are shown in the loading ratio from about 1.4 to 12.4. (**B**) Exemplary simulations (red) of subspectra $F_i(B)$ emphasizing free (*f*), strongly bound (*b₁*), weakly bound (*b₂*) and micellar components (*a*) of 16-DSA interacting with HSA-N that were used to reconstruct experimental spectra $S(B)$. Additionally, the rotational correlation time τ_{c} and a_{iso} values are given in brackets for bound (*b_i*) and free (*f*) components. (**C**) The corresponding Scatchard plot that can be constructed from simulation data shown in (A). Decisive parameters as association constant (K_{A}), number of equivalent binding sites (N_{E}) and correlation coefficient (R^2) from data analysis in the linear region ($0 < N_{\text{L}} < 7$) are given as gray insets and are calculated from a linear extrapolation that uses equation 7.1 or E.29 (blue). For $N_{\text{L}} > 7$ the micellar fraction ϕ_{a} (red area) increasingly dominates CW EPR spectra but does not contribute to further information about the protein-ligand system.

It can be concluded that *v*-values for $N_{\text{L}} > 7$ do not reveal further information about the ligand-saturated albumin protein as these values accumulate in a certain dense area (red, ϕ_a). This finding can be traced back to a concealed equilibrium that is based on the solubility of 16-DSA. An explicit simulation-based Scatchard plot construction approach is therefore believed to be advantageous compared to more classical strategies[40,103–105] that e.g. do not appropriately resolve micellar fractions (ϕ_a), polarities (a_{iso}) and also do not differentiate in between various rotational dynamic regimes (τ_{c}). Furthermore, this strategy was also applied to other EPR-active ligands in a similar fashion,[106,107] where it could be shown that EPR might also constitute a promising alternative to e.g. ITC studies.

In a next step the same procedure is applied to HSA which was incubated for 24 h at 37°C with a glyoxal concentration of $c_{\text{GLX}} = 10$ mM (glycated HSA-GLX10). The resulting CW EPR spectra are shown in **Figure 7.4A** and the corresponding Scatchard plot is given in **Figure 7.4B**. Obviously, the

linearity as observed in HSA-N is eliminated and an almost exponential-shaped Scatchard plot is obtained. This near exponential-shaped Scatchard plot can be interpreted as biphasic, i.e. the system contains two types of non-interacting binding sites with $N_1 \neq N_2$ and $K_{A,1} \neq K_{A,2}$.

An elegant analytic method has been devised by H. E. Rosenthal[108] that is based on a mixture of graphical and mathematical considerations. In principle, it is assumed that at each point P on the L-shaped data curve (**Figure 7.4B**, blue), the free ligand concentration $[L]_f$ is in equilibrium with the bound ligands concentration $[L]_b$ at each of the two groups of binding sites ($i = 1,2$). Mathematically, these two independent classes of binding sites are described with the expression:

$$v = \sum_i^2 \frac{N_i K_{A,i}}{1+[L]_f K_{A,i}} = \frac{N_1 K_{A,1}}{1+[L]_f K_{A,1}} + \frac{N_2 K_{A,2}}{1+[L]_f K_{A,2}} \tag{7.2}$$

As an analytical solution of equation 7.2 has been proven to be accessible but cumbersome,[109] two lines (L_1 and L_2) are introduced with each representing an individual binding system.
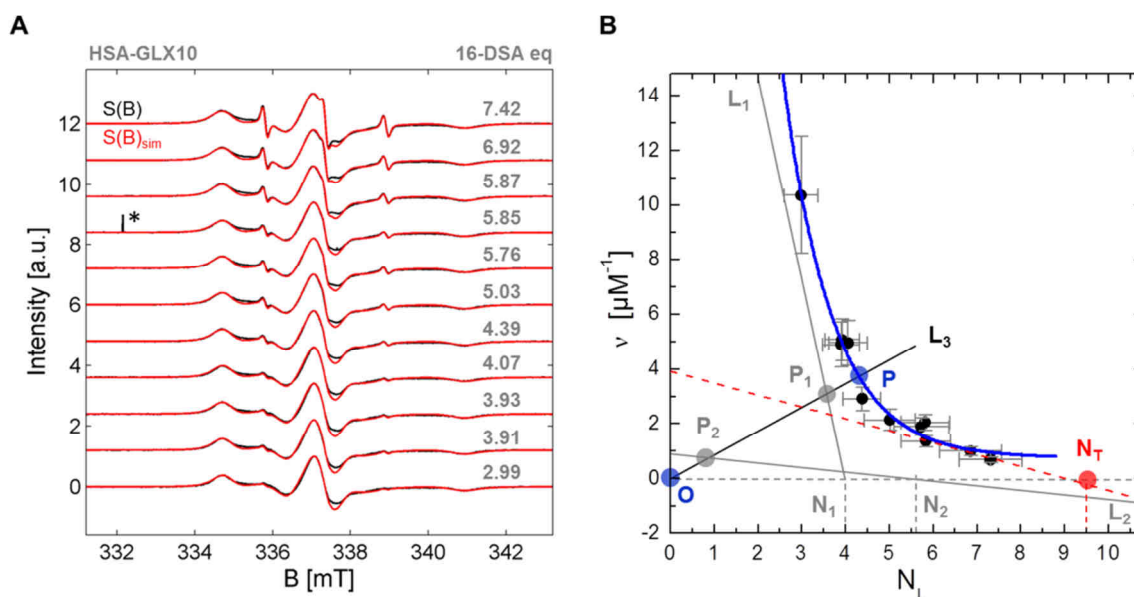
Figure 7.4 | Scatchard plot of 16-DSA-probed glycated HSA-GLX10. (A) Experimental CW EPR spectra $S(B)$ (black) and their spectral simulations $S(B)_{sim}$ (red) are shown in the loading ratio from about 3.0 to 7.4 (* = noise artifact/spike from MS100 spectrometer). (B) Scatchard plot (black dots) of data extracted from (A). Individual data points were fitted with an exponential curve (blue). An analysis was conducted according to a scheme given by Rosenthal.[108] Here, $N_T = N_1 + N_2$ denotes the total number of binding sites and is determined with a linear fit (red dotted line) to data points at the right hand side of the Scatchard plot ($N_L > 5.8$). The points P_i on line 3 (L_3) that elevates from the coordinate origin (O) are needed for construction of the gray lines (L_1 and L_2) that yield association constants $K_{A,i}$ in a proposed biphasic Scatchard plot.

Their intersections P_1 and P_2 with a third line (L_3) that comes from the coordinate origin O and cuts the Scatchard curve in P has to be constructed so that following condition:[108]

$$\overline{OP} = \overline{OP}_1 + \overline{OP}_2 \tag{7.3}$$

is fulfilled. Data extraction is now facilitated by two additional conditions:[103,110,111]

$$N_{L,v\to 0} = N_1 + N_2 = N_T \tag{7.4}$$

$$v_{N_{L,2}\to 0} = N_2 K_{A,2} \qquad . \tag{7.5}$$

In HSA-GLX10 the total number of binding sites $N_{L,v\to 0} = N_T = 9.5 \pm 2.6$ is the abscissa intercept that is obtained from **Figure 7.4B** by linear regression of data points for $N_L > 5.8$. When the number of strong interacting binding sites (large K_A) is chosen as $N_1 = 4.0$ it follows that $N_2 = N_T - N_1 = 5.5$. The ordinate intercept $v_{NL,2\to 0} = 0.9\ \mu M^{-1}$ of L_2 yields the slope and therefore $K_{A,2} = 1.64 \cdot 10^5\ M^{-1}$. Furthermore, parameters for binding system L_1 can be obtained identically ($i = 1$). The results from this analysis are summarized in **Table 7.2**.

Table 7.2 | Results from Scatchard analyses of HSA-N and HSA-GLX10

sample	i	N_T	N_i	$K_{A,i}\ [M^{-1}]$	$K_{D,i}\ [\mu M]$
HSA-N	-	6.5 ± 0.5	-	$(1.94 \pm 0.09) \cdot 10^6$	0.515 ± 0.023
HSA-GLX10	1	9.5 ± 2.6	4.0 ± 1.1	$(6.90 \pm 1.68) \cdot 10^6$	0.144 ± 0.035
	2		5.5 ± 1.5	$(1.64 \pm 0.52) \cdot 10^5$	6.088 ± 1.909

Compared to HSA-N there is an increase in $N_T = \Sigma N_i > N_E$ of about $\Delta N = 3.0$, although the error is about 30%. Primarily, the glycation process obviously changes intrinsic HSA dynamics and the nature of its binding site cooperativity. However, explicit spectral simulation and cross-correlation of several dozens, or even hundreds of CW EPR spectra in a single study is exceptionally time-expensive and tedious. Therefore, a further refinement of this strategy has been developed for analyzing the binding capacities ($N_T = N_E$), binding affinities (K_A), and cooperativity of (any kind of) albumin. Thus, the Scatchard plot construction in the next section solely focuses on some decisive spectral characteristics that allow for extraction of ligand fractions ϕ_i by simply correlating simulation reference data with peak heights from test samples.

7.4 | BSA-based Macroinitiators and Polymer-protein Bioconjugates

PTMs such as the covalent attachment of inert synthetic polymers in bioconjugation are efficient methods to protect proteins from metabolic degradation, epitope accessibility, plasma protein binding and may furthermore lead to an improvement of pharmacokinetic properties compared to unmodified proteins.[25,112] To this effect, it is also expected that e.g. polyethylene glycol (PEG)-based[19,113] and polyglycerol (PG)-based[114,115] polymer-protein conjugates exhibit high biocompatibility. Due to the recent progress in controlled radical polymerization techniques as atom transfer radical polymerization (ATRP),[116] an increased interest is dedicated to the development of protein macroinitiators that

provide access to polymer-protein conjugates in a "grafting-from" approach.[117–127] Here, BSA-macroinitiators with ten lysine-bound ATRP sites were applied for grafting oligo(ethylene glycol) methacrylate (OEGMA) from the functionalized protein surface. These macroinitiators and graft copolymers were prepared as described previously[128] by selective squaric acid coupling to accessible surface lysins[21] in order to form a core-shell-like structure.

In this study, DLS experiments are combined with LASER Doppler velocimetry (LDV) in an electrophoretic light scattering (ELS) setup. Additionally, CW EPR is used in combination with 4-pulse DEER revealing binding properties that facilitate a simultaneous view on dynamic as well as on some structural properties of EPR-active PTM-albumin samples.

7.4.1 | Characterization of Modified BSA Samples

Three different squaric acid-based BSA-Ix macroinitiators (x = number of modifications per BSA) were prepared according to a procedure described in Wurm *et al.*[21] and serve as reference standards to monitor influences on protein functionality depending on the degree of surface modification. Synthesis of two BSA-*g*-P(OEGMA)$_n$ graft copolymers (BSA-Pn) of different sizes was facilitated by utilizing BSA-I10 macroinitiators equipped with lysine-bound squaric acid ATRP initiating sites. The modified albumin samples were prepared and partly characterized by Dr. Tobias Steinbach and Dr. Anja Thomas in the group of Prof. Dr. Holger Frey, Institute of Organic Chemistry, Johannes Gutenberg-Universität Mainz, Germany. All macroinitiators BSA-Ix and polymer-protein conjugates BSA-Pn were kindly provided by Dr. Anja Thomas.

The chemical composition and schematic representations of all investigated structures are presented in **Figure 7.5**. Principally, the number x of ATRP sites in BSA-Ix macroinitiators is determined by the respective weight increase in MALDI-TOF spectra compared to the native precursor BSA-N (MW$_N$ = 66.431 Da, see **Table 7.3** and **Figure E2**). Each additional squaric acid (SA, $x + 1$) residue increases the macroinitiator weight for MW$_{SA}$ = 288.11 Da. However, due to their inaccessibility in MALDI-TOF experiments, molecular weights of the BSA conjugates (BSA-Pn) were determined by sodium dodecyl sulfate polyacrylamide gel electrophoresis (SDS PAGE)[129] in combination with a silver staining procedure.[130] A significant increase in molecular weight to 125.000 – 160.000 Da is observed for both polymer-protein conjugates as compared to pure BSA, confirming the successful grafting reaction with high initiation efficiency (**Figure E3**).

This allows for an estimation of the degrees of polymerization (DP = n) obtained with OEGMA$_{475}$ monomers (MW$_{OEG}$ = 475 Da) yielding n = 11 (BSA-P11) and n = 18 (BSA-P18). The exact topological location of the PTMs was not investigated and is assumed to occur in a quantitative, statistical manner. The results from DLS suggest a rational increase in hydrodynamic radii a_k with increased surface modification x of the albumin molecules.
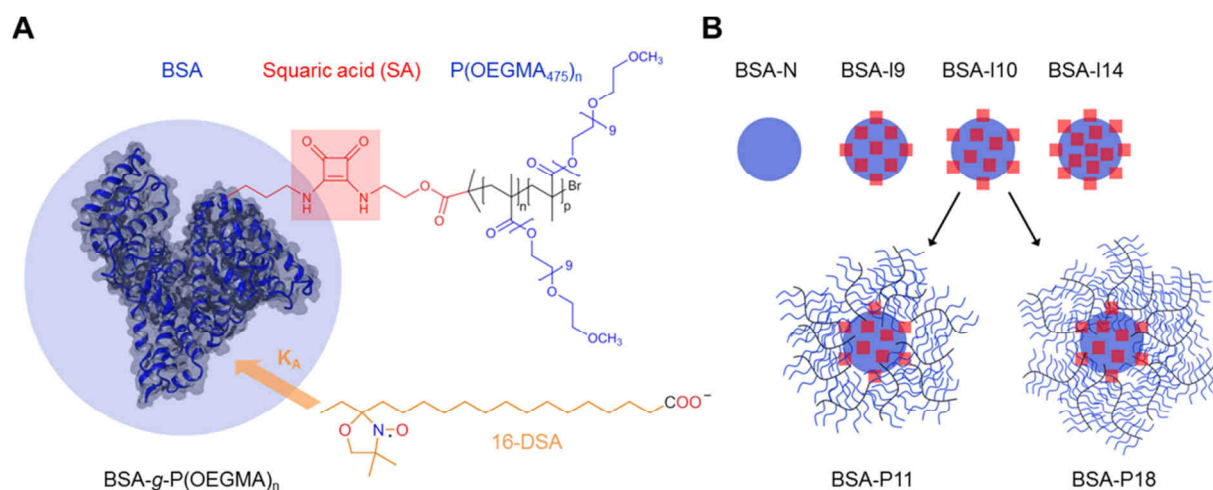
Figure 7.5 | Chemical structure of macroinitiators BSA-I*x* and polymer-protein conjugates BSA-P*n*. (**A**) The native protein BSA-N (blue sphere, PDB ID: 3v03)[131] is here depicted with the chemical structures of a squaric acid (SA) ATRP initiator (red square) from where OEGMA$_{475}$ monomers (blue) are grafted from. Together they form the polymer-protein conjugate BSA-*g*-P(OEGMA)$_n$ = BSA-P*n*. The EPR-active 16-DSA spin probe is here depicted in orange with a schematic affinity (K_A) towards the protein core. (**B**) The native precursor apoprotein BSA-N (x = 0) and different available macro-initiators BSA-I*x* (with x = 9, 10 and 14) are schematically presented with the colored symbols shown in (A). BSA-I10 was exclusively employed for construction of the polymer-protein conjugates BSA-P*n* (with n = 11 and 18).

Whereas the precursor native apoprotein (BSA-N) exhibits familiar values compared to previously published studies,[132,133] the slight increase in molecular weights for all BSA-I*x* macroinitiators already leads to significant changes in hydrodynamic radii. Note, that the analog rate of diffusion D_k is strongly reduced in the polymer-protein conjugates. Therefore, it can be generally assumed that surface modifications on BSA lead to strong alterations of solvent entanglement, especially in polymer-protein conjugates.[19]

Table 7.3 | Characterization of modified BSA samples

PTM type k	MW$_k$ [Da]	x	n	yield [wt%]	a_k^a [nm]	D_k^a [×10^7 cm^2 s^{-1}]	ρ_k^b [kg m^{-3}]
N	66.431^{c,d}	0	–	–	3.24 ± 0.24	7.56 ± 0.56	774 ± 172
I9	68.976^d	8.8	–	–	3.85 ± 0.30	6.34 ± 0.49	479 ± 112
I10	69.415^d	10.4	–	–	3.95 ± 0.28	6.21 ± 0.44	447 ± 95
I14	70.357^d	13.6	–	–	4.38 ± 0.33	5.60 ± 0.42	332 ± 75
P11	125.000^e	10.4	11.3	55	7.78 ± 0.37	3.15 ± 0.15	105 ± 15
P18	160.000^e	10.4	18.4	95	7.75 ± 0.44	3.17 ± 0.18	136 ± 23

^{a}All hydrodynamic radii a_k and diffusion coefficients D_k were obtained from DLS experiments from the well-known relation $D_k = k_B T \cdot (6\pi\eta a_k)^{-1}$ that interconverts both parameters.[134] $^b\rho_k$ = molecular density calculated from the relation $\rho_k = 3 \cdot MW_k \cdot (4\pi a_k^3)^{-1}$. ^{c}A reference value MW$_{BSA}$ = 66.463 Da can be found in Chafer-Pericas *et al.*[135] ^{d}MW$_{Ix}$ of BSA-I*x* from MALDI-TOF spectra in **Figure E2**. ^{e}MW$_{Pn}$ of BSA-P*n* from SDS PAGE in **Figure E3**.[130]

This is further substantiated by the strong decrease in molecular densities ρ_k upon surface modification, exhibiting a significant fraction of water-pervaded volume, especially in case of the BSA-P*n* nanostructures (**Table 7.3**).

The Zeta potential of BSA-N is negative at $\zeta_N = -18.6$ mV (**Table 7.4**) as it is commonly observed at physiological pH and ionic strengths about $I \approx 0.1$ M.[136–138] The associated electrophoretic mobility $\mu_{e,k}$ is defined as:[138]

$$\mu_{e,k} = \frac{2\varepsilon_0 \varepsilon_r \zeta_k F(\kappa a_k)}{3\eta} \quad , \tag{7.6}$$

whereas ε_0 represents the vacuum permittivity, $F(\kappa a_k) = 1.09$ is Henry's function, $\varepsilon_r = 78.4$ is the dielectric constant for water[139] and $\eta = 0.89$ mPa·s is the corresponding dynamic viscosity[140] at $T = 25°C$. The (monomer) mobility value for BSA-N is $\mu_{e,N} = -1.05 \cdot 10^{-8}$ m^2 V^{-1} s^{-1} (see **Table E3**) and corresponds well with previous reports on albumins.[133,141] The ζ_k values for BSA-Ix decrease with the degree x of modification, while BSA-Pn again has similar values compared to BSA-N (**Table 7.4**). Generally spoken, BSA-Ix particle suspensions gain stability (ca. $\pm$ 30 mV), while increasing their mutual electrostatic repulsion upon further modification.[142–144] The primary reason for this behavior should be the covalent attachment of squaric acid initiators to the positively charged lysines that shifts the net charge Z_k of the BSA surface to more negative values.

First, the number of uncompensated charges $N_{c,k}$ can be determined from individual Zeta potentials ζ_k with help of a strategy that was suggested by Adamczyk *et al.*[145] giving the relation:

$$N_{c,k} = \frac{6\pi\eta a_k}{e} \cdot \mu_{e,k} \quad . \tag{7.7}$$

The number of uncompensated charges $N_{c,N} = -3.6 \pm 0.6$ (**Table E3**) for BSA-N was also observed in HSA solutions.[133] Unlike the results from titration experiments on BSA,[146] the observed number of uncompensated charges here is quite low due to counterion condensation[147–149] in between buffer ions and BSA protein.[138,145] The unique property of a stepwise lysine-blocking across the BSA-Ix samples reveals (**Figure E4**) that there are linear relationships in between the degree of surface modification x and both the Zeta potential ζ_k and $N_{c,k}$:

$$\zeta_k(x) = k_\zeta x + \zeta_N \tag{7.8}$$

$$N_{c,k}(x) = k_Q x + N_{c,N} \quad , \tag{7.9}$$

where $k_\zeta = -(0.938 \pm 0.052)$ mV SA^{-1}, $\zeta_N = -(18.76 \pm 0.46)$ mV, $k_Q = -(0.342 \pm 0.021)$ SA^{-1} and $N_{c,N} = -(3.46 \pm 0.21)$. Therefore, each squaric acid-blocked lysine residue of BSA lowers ζ for about 1 mV and the uncompensated charge $N_{c,k}$ decreases for $\Delta Q = -1 \cdot e$ for about each three blocked lysines in the observed range from $0 < x < 14$. It can be estimated from this k_Q value that about two-thirds ($\sigma = 1 - k_Q = 0.658$) of the BSA surface charges are screened by buffer ions with the assumption that

each blocked lysine directly depletes one positive charge. Thus, the reduced net charge $Z_k = Q_k \cdot e^{-1}$ can be directly obtained with the expression:

$$Z_k = \frac{N_{c,k}}{k_Q} = -\frac{4\pi a_k \varepsilon_0 \varepsilon_r \zeta_k F(\kappa a_k)}{e k_Q} \qquad , \qquad (7.10)$$

yielding $Z_N = -10.5 \pm 2.3$ that is virtually identical with values at about physiological pH that are observed in BSA from other experimental methods ($-18 < Z_{N,exp} < -8$).[132,146,150] However, the values calculated from amino acid sequences alone seem to be slightly higher ($Z_{N,calc} = -17$)[2] but serve as a good estimate. An explicit treatment of the charge calculations is given in **Appendix E6**. The calculated values from equation 7.10 are shown in **Table 7.4**. Moreover, Z_{Pn} corresponds quite well with the value for BSA-I10, so the "grafting from" approach obviously does not change the charge state of the protein core as observed from the macroinitiators. However, in comparison to BSA-I10 the Zeta potential of the polymer-protein conjugates ζ_{Pn} amounts to only about 45% of this value. This effect is interpreted as emerging due to the presence of the P(OEGMA)$_n$-shell that significantly increases the separation for about $d_{Pn} = 3.8$ nm from the charge-bearing macroinitiator surface ($a_{I10} = 4.0$ nm) from the hydrodynamic slipping plane ($a_{Pn} = 7.8$ nm) where the Zeta potential is actually detected (**Figure 7.6**). The slipping plane alone separates the mobile bulk solvent from the colloid,[151] or in this case the polymer-protein conjugate structure.

Table 7.4 | Results from Zeta potential measurements

PTM type k	$\zeta_k{}^a$ [mV]	$Z_k{}^b$	$\rho_{Q,k}{}^c$ [×10^{-7} C m^{-3}]	$\varepsilon_{eff,Pn}{}^d$
N	-18.6 ± 1.5	-10.5 ± 2.2	-1.18 ± 0.51	–
I9	-27.4 ± 1.5	-18.6 ± 3.9	-1.25 ± 0.55	–
I10	-28.7 ± 1.1	-20.1 ± 3.7	-1.25 ± 0.50	–
I14	-30.9 ± 0.9	-24.2 ± 4.6	-1.10 ± 0.46	–
P11	-12.4 ± 1.6	-18.3 ± 5.8	-0.149 ± 0.069	69.7 ± 26.8
P18	-13.2 ± 1.3	-19.4 ± 5.9	-0.159 ± 0.075	73.0 ± 28.2

$^a\zeta_k$ = Zeta potential. $^bZ_k = Q_k \cdot e^{-1} = N_{c,k} \cdot k_Q^{-1}$ number of net charges calculated from equation 7.10 (see also **Table E3**). $^c\rho_{Q,k}$ is the charge density as calculated from the relation $\rho_{Q,k} = Q_k \cdot V_k^{-1} = 3Z_k e \cdot (4\pi a_k^3)^{-1}$. $^d\varepsilon_{eff,Pn}$ = effective dielectric constant of the polymer layer as estimated from equation 7.11 (see also **Appendix E6**).

An intriguing fact is that the charge density $\rho_{Q,k}$ is almost constant at $-(1.19 \pm 0.07) \cdot 10^7$ C m^{-3} for BSA-N and BSA-Ix, but experiences a significant drop about almost one order of magnitude for BSA-Pn giving $\rho_{Q,Pn} = -(1.54 \pm 0.08) \cdot 10^6$ C m^{-3} (see **Table 7.4**). In a general electrostatic view, the potential V that is generated from the BSA charge density decreases with this separation by d^{-1}.[152] With this assumption a consistency check (see **Appendix E6**) proves that the separation $d = a_{Pn} - a_{I10}$ between BSA-I10 macroinitiator surface and slipping plane of BSA-Pn leads to a decrease in Zeta potential that can be approximated via the relation $a_{I10}\zeta_{I10} \approx a_{Pn}\zeta_{Pn}$ for $a_k > a_N$ (see equation E.23).

Furthermore, the distance dependent decrease in $\zeta_{\mathrm{P}n}$ allows for an estimation of the dielectric constant $\varepsilon_{\mathrm{eff},\mathrm{P}n}$ of the water-pervaded polymer layer assuming an average equivalent number of uncompensated charges $Z \cdot k_Q = N_c = -6.58$ for BSA-I10, BSA-P11 and BSA-P18 with the relation:

$$\varepsilon_{\mathrm{eff},\mathrm{P}n} = \frac{N_c \cdot e}{4\pi\varepsilon_0 \Delta\zeta_n} \cdot \left(\frac{1}{a_{\mathrm{P}n} F(\kappa a_{\mathrm{P}n})} - \frac{1}{a_{\mathrm{I}10} F(\kappa a_{\mathrm{I}10})} \right) \quad , \qquad (7.11)$$

giving values of $\varepsilon_{\mathrm{eff},\mathrm{P}18} = 73.0$ and $\varepsilon_{\mathrm{eff},\mathrm{P}11} = 69.7$ (**Table 7.4**) being a bit lower, however, quite close to that of pure water ($\varepsilon_r = 78.4$). Here, the parameter $\Delta\zeta_n = \zeta_{\mathrm{P}n} - \zeta_{\mathrm{I}10}$ is the Zeta potential difference at individual slipping planes of samples k. However, the intrinsic errors $\Delta\varepsilon_{\mathrm{eff},\mathrm{P}n}$ appear to be quite large at about 38 %. A comprehensible derivation of equation 7.11 is given in **Appendix E6** from an approach emphasizing mainly electrostatic considerations[152] from an uncompensated point charge that is located at the coordinate system origin of a spherical BSA-I10 macroinitiator being surrounded by a dielectric shell of thickness $d = a_{\mathrm{P}n} - a_{\mathrm{I}10}$ (**Figure 7.6**). Analyses of the involved corresponding electrostatic free energies[153] are considered as beyond the scope of this work. This result shows that the polymer shell does not have a large effect on the dielectric properties of the medium that surrounds the BSA protein core and again shows that the polymer shell is strongly pervaded by water, while it serves as an attenuator for the electrostatic potential at the core. The next section extends this viewpoint by an investigation to which extent ligand binding dynamics is affected by these PTMs.
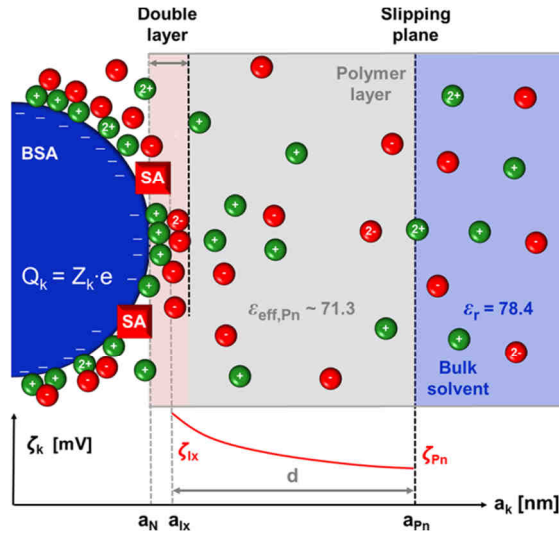
Figure 7.6 | Schematic representation of the Zeta potential from modified BSA samples in DPBS buffer. The BSA core (dark blue) with radius a_{N} bears the charge Q_k and is surrounded by an electrical double layer (DL, pale red) composed of different DPBS buffer ions of varying valency (– charge red, + charge green spheres). For simplicity only the negative uncompensated charges ($N_{\mathrm{c},k}$) are shown here on the protein surface. The squaric acid initiators (SA, red squares) of BSA-Ix interrupt the electrical DL and the Zeta potential $\zeta_{\mathrm{I}x}$ is measured at $a_{\mathrm{I}x}$. The water-pervaded polymer layer (gray) of BSA-Pn is assumed to bear no charge at all but is permeable for solvent and ions with an average effective dielectric constant $\varepsilon_{\mathrm{eff},\mathrm{P}n} = 71.3$. The value of $\zeta_{\mathrm{P}n}$ at the slipping plane (SP) between polymer and bulk solvent (pale blue) is therefore much lower, as indicated by the red dotted graph.

7.4.2 | Results from CW EPR Spectroscopy on Modified BSA – Method C

A further specific characterization of intrinsic dynamics changes upon BSA modification was obtained by adding 16-DSA to the solutions of the posttranslationally modified BSA samples in order to study their fatty acid binding properties. The sample preparation of the native BSA reference (BSA-N), BSA-Ix and BSA-Pn was conducted according to the scheme given in **Appendix C4** with 16-DSA as an EPR-active spin probe. First, all 16-DSA-loaded samples shown in **Figure 7.7** have been equipped with a 1:1 equivalent ratio of 16-DSA at a nominal concentration of 0.13 mM. The emergence of clearly detectable bound (b) and freely tumbling (f) 16-DSA spin probes already facilitates a qualitative estimate of the ligand binding affinity.

Primarily, the free component f increases with further protein modification, being strongly indicative of a decrease in ligand binding affinity $K_{A,k}$. The decrease in $K_{A,k}$ is most pronounced for the polymer-protein conjugates BSA-Pn. Furthermore, it is known that the rate of ligand association k_a is proportional to the diffusion constant D_k (see **Table 7.3**) in the respective ligand association reaction R + L → RL.[154,155] This circumstance would lead to a decrease in $K_{A,k}$ of a factor of about D_N/D_{P18} = $K_{A,N}/K_{A,P18}$ = 2.38.
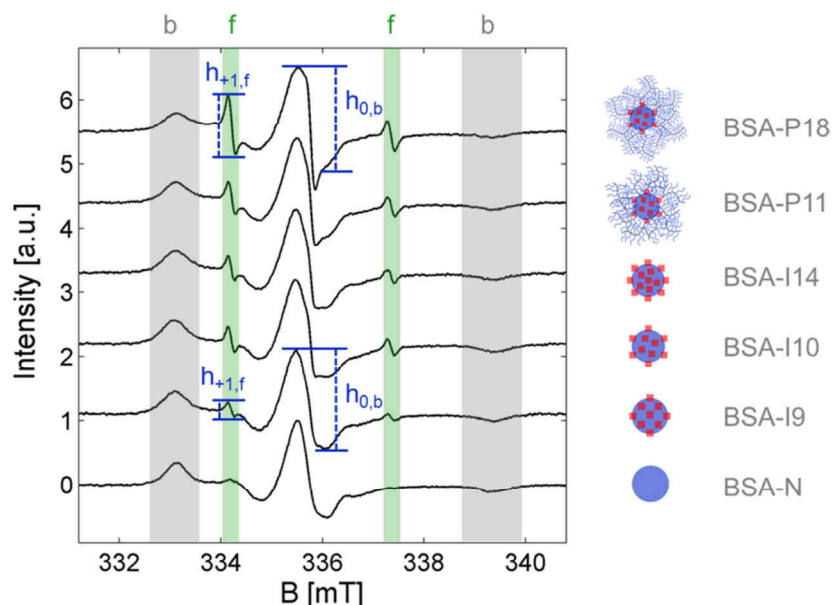
Figure 7.7 | CW EPR spectra of modified BSA samples loaded with 16-DSA. Recorded CW EPR spectra are shown for a nominal 1:1 loading ratio of 16-DSA comprising all posttranslationally modified BSA samples BSA-Ix and BSA-Pn at an equivalent concentration of about 0.13 mM together with the unmodified precursor BSA-N. Significant spectral features as the bound (b, gray) and freely tumbling species (f, green) are highlighted. The inset graphics on the right hand side represent the corresponding modified BSA samples as shown in **Figure 7.5**. The low-field peak height of the free spectral fraction ($h_{+1,f}$) and the center-field peak height of the bound spectral fraction ($h_{0,b}$) can be used to circumvent explicit spectral simulations for assessing free and bound ligand concentrations (see equations 7.12 and 7.13).

As these individual EPR spectra do not provide a complete view on the ligand binding properties of a substrate, again some Scatchard plots[101] were constructed. Individual samples were then successively loaded in the range from about one to a maximum of seven equivalents of 16-DSA to prevent micelle formation of 16-DSA. As it is sufficient to only extract the free (f) and bound (b) spectral fractions for

Scatchard plot construction in EPR spectroscopy,[103–105,107] explicit spectral simulations were only conducted on the reference sample BSA-N (**Table E2** and **Figure E5A**). However, due to the large data sets that were recorded, a simple strategy was devised from these reference simulations that allows for quick extraction of the required spectral fractions by directly correlating peak height ratios to spectral fractions. It is found, that the ligand concentrations $[L]_i$ of free ($i = f$) and bound ($i = b$) 16-DSA can be directly obtained from the relations:

$$[L]_f = k_L \cdot [L]_{t,k} \cdot \frac{h_{+1,f}}{h_{0,b}} = \phi_f \cdot [L]_{t,k} \tag{7.12}$$

$$[L]_b = [L]_{t,k} \left(1 - k_L \cdot \frac{h_{+1,f}}{h_{0,b}} \right) = \phi_b \cdot [L]_{t,k} \qquad , \tag{7.13}$$

where $[L]_{t,k}$ is the total ligand concentration in a sample, $h_{+1,f}$ is the peak height of the low-field line of the free fraction (ϕ_f) and $h_{0,b}$ is the peak height of the center-field line of the bound spectral fraction (ϕ_b) as depicted in **Figure 7.7**. The constant $k_L = 0.02486$ is a correlation constant that joins readout values of $h_{+1,f}$ and $h_{0,b}$ with corresponding peak heights from EPR spectral simulations. This simple method may avoid cumbersome and time-expensive simulations as presented in previous chapters and an explicit description of this approach is given in **Appendix E7** as a substantiation of this strategy.

The relative deviations from simulation values have been found to range in between 2 – 9 %. However, this strategy is for now only tested and therefore applicable to BSA in DPBS buffer at pH 7.4 equipped with 20% v/v glycerol. After extraction of the relative concentrations of the spectral fractions ($[L]_i = [L]_{t,k} \cdot \phi_i$), a Scatchard analysis is then conducted in a plot of $v = [L]_b/([L]_f \cdot c_B)$ versus the number of bound ligand equivalents N_L where c_B is the protein (BSA) concentration in the sample. The resulting Scatchard plots from all six samples are shown in **Figure 7.8** and all corresponding CW EPR spectra are given in **Figure E5A** and **Figure E6**. Primarily, the linear phases p in the Scatchard plots of samples k can be evaluated with following generalized expression of equation 7.1:[69]

$$v = \frac{[L]_{b,k}}{[L]_{f,k} \cdot c_{B,k}} = \frac{[L]_{t,k} - [L]_{f,k}}{[L]_{f,k} \cdot c_{B,k}} = -K_{A,k,p} \cdot \left(N_L - N_{E,k,p} \right) + v_{k,p,N_L \to 0} \qquad , \tag{7.14}$$

where $K_{A,k,p}$ is the association constant, $N_{E,k,p}$ the number of equivalent binding sites and $v_{k,p,N_L \to 0}$ are the y-axis intercepts in samples k and Scatchard phases p. The individual phases p shown in **Figure 7.8** are either denoted as a single phase spanning the whole data range (I), individual linear phases that span at least three data points (Ia, Ib, or Ic), or a linear phase that is usually identified as the weak binding part in an apparent biphasic Scatchard plot (II)[110] as presented in **Chapter 7.3.1**.
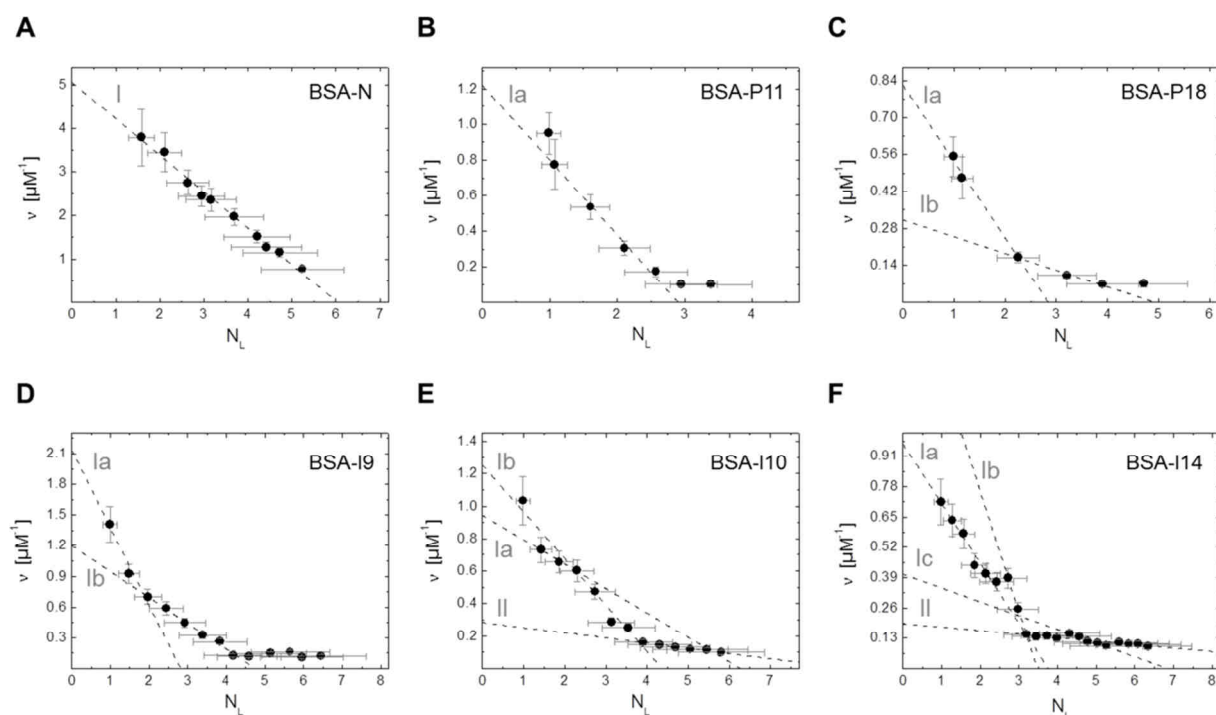
Figure 7.8 | Scatchard plots of native BSA, BSA-I*x* and BSA-P*n* interacting with 16-DSA ligands. All of the Scatchard plots were constructed from CW EPR spectra shown in **Figure E5A** and **Figure E6**. Individual samples were loaded with 16-DSA in different molar ratios for testing the ligand concentration-dependent response of the substrates (**A**) native BSA-N ($c_{B,N} = 0.15$ mM), polymer-protein conjugates (**B**) BSA-P11, (**C**) BSA-P18 ($c_{B,Pn} = 0.06 - 0.32$ mM) and the macroinitiators (**D**) BSA-I9, (**E**) BSA-I10 and (**F**) BSA-I14 at $c_{B,Ix} = 0.1$ mM each. Each CW EPR spectrum is here reduced to a single data point (black) with appropriate error bars (gray). Scatchard plots may exhibit linear phases I, Ia, Ib, Ic or II that were subject to a linear regression procedure for data point ranges $q \geq 3$ (dashed lines, black, see **Table 7.5** and **Table E4**).

A typical biphasic Scatchard plot is generally expected to have an exponentially decreasing curve shape due to the overlap of two classes of a specific number of independent strong (N_S, K_S) and weak (N_W, K_W) binding sites.[103,110,111,156] Several strategies have been devised to extract N_i and K_i (see also **Figure 7.4**),[108,110] but in terms of comparability their use is precluded in these BSA-based systems as the number of non-interacting binding systems has to be assumed as unknown, especially in BSA-I*x*. Therefore, emphasis is placed on the qualitative change in the number of equivalent binding sites $N_{E,k,p}$. From the pure phases I or II a total number of binding sites ($N_{T,k,p}$) can be extracted, as the *x*-axis intercepts of these phases in principle correspond to $N_T = N_{E,k,I} = N_{E,k,II} = N_S + N_W$ as it can be also seen in equation 7.4.[111]

Furthermore, a cooperativity test was conducted according to the classical strategy presented by Tanford.[157] Cooperativity, as observed in proteins with multiple ligand binding sites is believed to originate from binding site heterogeneity and conformational adaptability,[37] but may also be induced by modifications in local environments already due the mere presence of ligands,[158] that mutually affect their binding properties. In principle, this effect is encountered when the number of occupied binding sites of a macromolecule is a non-linear function of the relative concentration of applied ligand to protein.[159] Cooperativity is therefore understood as an interaction in between ligands in binding sites that mutually affect their individual binding affinities by allosteric modulation of the

binding substrate. A scheme given by De Meyts and Roth[156] allows for differentiating in between negative cooperative (–), positive cooperative (+), as well as locked, non-cooperative (N.C.) phases p. The physical basis of cooperativity is defined by an intrinsic association constant $K_{A,int}$ that is the limiting value of K_A for $N_L \rightarrow 0$. The intrinsic standard free energy change $\Delta G^{\circ}_{A,int}$ is then used to introduce the effect of binding site interaction with an arbitrary function $\Phi(N_L)$ for $N_L > 0$:[157]

$$\Delta G_A^{\circ} = \Delta G_{A,int}^{\circ} + RT \cdot \Phi(N_L) \qquad , \qquad (7.15)$$

where the variable association constant is then given as:

$$K_A = K_{A,int} \cdot e^{-\Phi(N_L)} \qquad (7.16)$$

and $\Phi(N_L) = 0$ for $N_L = 0$. Here, ΔG°_A and $\Phi(N_L)$ are average properties across all binding sites and protein configurations. Upon combining equation 7.16 with the equilibrium condition that defines the degree of association:

$$K_A[L]_f = \frac{[L]_b}{N_T c_B - [L]_b} \qquad , \qquad (7.17)$$

following expression is obtained:

$$\ln K_{A,int}^* = \ln K_{A,int} - \Phi(N_L) = \ln\left(\frac{[L]_b}{N_T c_B - [L]_b}\right) - \ln[L]_f \qquad . \qquad (7.18)$$

When the right-hand side of equation 7.18 is plotted versus N_L, a so-called cooperativity plot is obtained. The results from a cooperativity test for all samples is shown in **Figure 7.9**, assuming a constant number of binding sites for all BSA, or BSA-derivatives ($N_T = 6$) for simplicity. In case the observed slope is negative, cooperativity is also negative (–) and $\Phi(N_L)$ is an increasing function that lowers $\ln K_{A,int}^*$. Positive cooperativity (+) coincides with $\Phi(N_L)$, being a decreasing function and reveals itself in a positive slope. Non-cooperative binding (N.C.) is observed, when $\Phi(N_L) = 0$ for all N_L. Therefore, $\ln K_A = \ln K_{A,int}$ and the slope in the cooperativity plot is locked at a constant value of $\ln K_{A,int}^*$.[156] For convenience, an auxiliary parameter $C_{k,p}$ is here introduced that gives the type of cooperativity in a straightforward manner:

$$C_{k,p} = \text{sgn}\left(\frac{\partial \ln K_{A,int}^*}{\partial N_L}\right) \qquad . \qquad (7.19)$$

Unfortunately, not all phases of the samples can be appropriately resolved, but an exhaustive set of results from these analyses are summarized in **Table 7.5**. The fit parameters for calculations of $K_{A,k,p}$ and $N_{E,k,p}$ are given in **Table E4** and free energies of association $\Delta G^{\circ}_{A,k,p}$ are also given as energetic equivalents to the association constants $K_{A,k,p}$. Note, that the association reaction, although individual values may decisively decrease (e.g. in macroinitiators BSA-I10 and BSA-I14), remains strongly exergonic $(\Delta G^{\circ}_{A} < 0)$ throughout all phases.
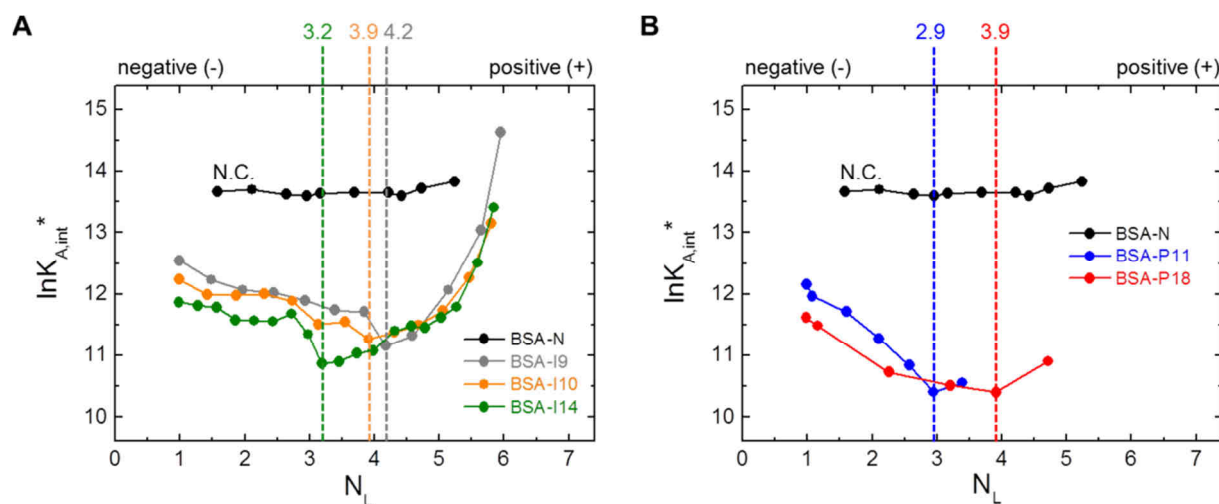

Figure 7.9 | Cooperativity test of 16-DSA-binding to posttranslationally modified BSA. (**A**) Cooperativity of 16-DSA binding to BSA-N is compared to macroinitiators BSA-I9 (gray), BSA-I10 (orange) and BSA-I14 (green). (**B**) Cooperativity of 16-DSA binding to BSA-N is compared to polymer-protein conjugates BSA-P11 (blue) and BSA-P18 (red). Individual regions of negative (–) and positive (+) cooperativities are separated by a dotted line indicating the number N_L of bound ligands that lead to an inversion in cooperativity from (–) to (+). Specifically, BSA-N exhibits non-cooperative binding with a locked value of $\ln K_{A,int}^{*}$ (N.C.). The colored dotted lines denote a cooperativity transition at specific ligand loadings N_L from negative to positive.

Whereas native BSA-N (**Figure 7.8A**) is the only sample that clearly exhibits a linear alignment of all v-values with an increasing number of bound ligands N_L (I), all posttranslationally modified BSA derivatives show multimodal curve shapes. The evaluation of the linear Scatchard plot for BSA-N interacting with 16-DSA is straightforward and yields $N_{E,N} = 6.0$ equivalent, non-cooperative binding sites with a locked (N.C.) macroscopic association constant of $K_{A,N} = 8.4 \cdot 10^{5}$ M^{-1}. A comparison with obtained data from spectral simulation yields almost identical values (see also **Table 7.5**) and is in reasonable correspondence with values for stearic acids that were obtained or reported in earlier studies.[103,105,160–162] However, here a biphasic Scatchard plot was not obtained for BSA interacting with 16-DSA as it was described elsewhere.[105] Potential reasons may be found in experimental differences like temperature, buffer composition, sample viscosity., as well as in the applied method for data extraction.

The polymer-protein conjugates BSA-Pn exhibit non-linear Scatchard plots (**Figure 7.8B+C**), each with a steep initial decrease (Ia) indicating about $N_{E,Pn,Ia} = 2.9$ equivalent strong binding sites. It can be anticipated that due to the higher degree n of OEGMA side-chain polymerization, effectively shielding the protein core from ligand penetration, the 16-DSA affinity is a bit lower for BSA-P18.

Table 7.5 | Parameters from phase-specific linear regressions in Scatchard plots of samples k

k	l	$N_{T,k,p}$	$N_{E,k,p}$	$K_{A,k,p}$ [M^{-1}]	$\Delta G°_{A,k,p}$ [a] [kJ mol^{-1}]	[L]$_{t,k}$ [b] [eq]	q [c]	$C_{k,p}$ [d]
BSA-N	I[e]	6.37 ± 0.33	–	$(7.50 \pm 0.23)\cdot10^5$	-33.54 ± 0.08	$1.59 - 5.29$	10	N.C.
	I	6.05 ± 0.33	–	$(8.38 \pm 0.28)\cdot10^5$	-33.81 ± 0.08	$1.59 - 5.29$	10	N.C.
BSA-I9	Ia	–	2.97 ± 0.82	$(7.58 \pm 1.43)\cdot10^5$	-33.56 ± 0.47	$1.00 - 2.00$	3	–
	Ib	–	4.77 ± 0.31	$(2.52 \pm 0.10)\cdot10^5$	-30.83 ± 0.10	$2.00 - 4.50$	6	–
BSA-I10	Ia	–	6.34 ± 0.72	$(1.51 \pm 0.13)\cdot10^5$	-29.56 ± 0.21	$1.45 - 2.34$	3	N.C.
	Ib	–	4.45 ± 0.82	$(2.87 \pm 0.32)\cdot10^5$	-31.15 ± 0.28	$2.34 - 4.15$	5	(+)
	II	9.02 ± 1.31	–	$(3.20 \pm 0.30)\cdot10^4$	-25.71 ± 0.23	$4.15 - 6.38$	6	+
BSA-I14	Ia	–	3.80 ± 0.47	$(2.56 \pm 0.22)\cdot10^5$	-30.87 ± 0.21	$1.00 - 2.50$	6	(–)
	Ib	–	3.48 ± 0.01	$(5.15 \pm 0.01)\cdot10^5$	-32.60 ± 0.01	$2.80 - 3.41$	3	(+)
	Ic	–	7.00 ± 1.29	$(5.89 \pm 0.65)\cdot10^4$	-27.23 ± 0.27	$4.61 - 5.80$	5	(N.C.)
	II	12.87 ± 0.94	–	$(1.51 \pm 0.08)\cdot10^4$	-23.85 ± 0.13	$3.41 - 7.00$	8	+
BSA-P11	Ia	–	2.92 ± 0.25	$(4.20 \pm 0.23)\cdot10^5$	-32.10 ± 0.14	$1.08 - 2.69$	4	–
BSA-P18	Ia	–	2.86 ± 0.25	$(2.90 \pm 0.14)\cdot10^5$	-31.18 ± 0.12	$1.00 - 2.35$	3	–
	Ib	–	4.99 ± 0.73	$(6.34 \pm 0.58)\cdot10^4$	-27.41 ± 0.23	$2.35 - 4.70$	3	(+)

[a] Free energies of ligand association are calculated from association constants $K_{A,k,p}$ with $\Delta G°_{A,k,p} = -RT\cdot\ln K_{A,k,p}$ (see also **Table E4** for all obtained fit parameters). [b][L]$_{t,k}$ [eq] = the range of total ligand concentration is here given in added molar equivalents to BSA. [c]q = number of fit-employed data points ($\forall_q \geq 3$). [d]$C_{k,p}$ = type of cooperativity for observed ligand binding phases p from **Figure 7.9** and equation 7.19. Cooperativities in parentheses only give tendencies, whereas N.C., – and + are clearly observed. [e]Result from explicitly simulated CW EPR spectra (**Figure E5A+B**).

Note, that the differences in strong K_A values in phase Ia of BSA-Pn compared to phase I in BSA-N correspond astonishingly well with the observed differences in diffusion constants in **Chapter 7.4.1** ($K_{A,N,I}/K_{A,Pn,Ia} \approx 2.4 \pm 0.5$, see **Table 7.3**). Nevertheless, a second linear region can be found for BSA-P18 (Ib) indicating the formation of almost exactly $N_{E,P18,Ib} = 5.0$ equivalent binding sites by slight positive cooperativity, however, with a much lower affinity. The slightly higher molecular density (**Table 7.3**) of BSA-P18 compared to BSA-P11 may be a significant feature that prevents 16-DSA to enter the binding sites in the bulk protein.

A more complicated behavior is found for the polymer-free macroinitiators BSA-Ix. Overall, each investigated macroinitiator shows a different Scatchard plot appearance with varying but recurrent multiphasic characteristics. Phase Ia in BSA-I9 reveals $N_{E,I9,Ia} = 3.0$ equivalent binding sites with a dissociation constant that is comparable to native BSA (**Figure 7.8D**, $K_{A,I9,Ia} = 7.6\cdot10^5$ M^{-1}). In phase Ib, the number of equivalent binding sites is increased to $N_{E,I9,Ib} = 4.8$, but with a threefold lower 16-DSA affinity ($K_{A,I9,Ib} = 2.5\cdot10^5$ M^{-1}). The cooperativity test in **Figure 7.9A** shows that the decrease in binding affinity seems to be counterbalanced by the gain in additional equivalent binding sites, however, leading to an overall negative cooperativity. Here, the region above $N_L > 4.2$ is coined by positive cooperativity, yet, linearity is not observed and a total number of binding sites cannot be determined for BSA-I9.

Phase Ib in BSA-I9 recurs as a slightly positive cooperative upward bend in the Scatchard plots of BSA-I10 and BSA-I14 (**Figure 7.8E+F**). In principle, all macroinitiators BSA-Ix exhibit a transition from negative cooperativity at low N_L to positive cooperativity at higher N_L. However, upon increasing the degree of modification x, this (±)-transition region is shifted to lower N_L (**Figure 7.9**).

While BSA-I9 changes to positive cooperativity at $N_L = 4.2$, BSA-I14 passes this threshold already at $N_L = 3.2$. This largely coincides with the decreasing number of equivalent binding sites N_E in phase Ib with increasing x. Simultaneously, the affinity of this decreasing number of binding sites increases considerably, so the loss in $N_{E,Ix,Ib}$ is also compensated by $K_{A,Ix,Ib}$ to some extent.

Phase II in BSA-I10 and BSA-I14 gives the maximum number of 16-DSA binding sites of a macroinitiator, i.e. $N_{T,I10,II} = 9.0 \pm 1.3$ and $N_{T,I14,II} = 12.9 \pm 0.9$. This can be clearly stated without any knowledge about the individual numbers of weak and strong binding sites.[111] A closer look at phase II in BSA-I14 additionally reveals an intriguing feature that is for now termed as phase Ic, interrupting the linearity in phase II in the range from $4.3 < N_L < 5.3$ bound molar equivalents of 16-DSA (or 4.6 – 5.8 total ligand equivalents added). Phase Ic is also slightly non-cooperative, while this positive cooperative phase II is suspended and discloses only $N_{E,I14,Ic} = 7.0$ equivalent binding sites. These findings imply that positive cooperativity in BSA-Ix emphasizes the staggered formation of new binding sites and that their total number of binding sites $N_{T,x}$ may be a function of the loading status of BSA. However, these additional binding sites are only formed at the expense of their equivalent binding affinity at high N_L. From the characterization results in **Chapter 7.4.1** it can be concluded that the 16-DSA affinity decreases as the values of the Zeta potentials ζ_{Ix} are getting more negative with increasing x. As 16-DSA is negatively charged at physiological pH, the ligands are therefore suspected to experience a stronger electrostatic repulsion. Thus, the Zeta potential at the slipping plane, or rather the surface charge Z_k, has decisive influence on ligand binding properties. This would also explain why BSA-Pn exhibits differently shaped Scatchard plots compared to BSA-Ix, as it was shown that the water-pervaded polymer shell decisively weakens the electric field emerging from the charged BSA sphere in the applied physical model (**Appendix E6**). Overall, ligand binding remains strong with at least 80 % of ligands bound for all investigated BSA samples in the observed loading range from one to seven equivalents of 16-DSA. It can be concluded that posttranslational modifications applied here allow for subtle functional adjustments of the fatty acid binding affinities and capacities of BSA as regulated by sterical (d in BSA-Pn) and electrostatic (ζ_{Ix} in BSA-Ix) hindrance.

7.4.3 | DEER Experiments on Modified BSA

In a next step the modified BSA samples are screened for potential differences in ligand distributions and alignments in the bulk protein matrix. This can be realized with DEER experiments as it was shown earlier for native HSA[42,163] and BSA[43] (see also **Chapter 4** and **Chapter 6**), as well as for cationized HSA constituting another example of a posttranslational functional modification of the protein surface.[35] In **Figure 7.10** DEER results are shown for BSA-N, BSA-Ix macroinitiators and

BSA-Pn protein-polymer conjugates. Despite the similarities in time traces and dipolar evolution functions (**Figure 7.10A+B**), the distance distributions in **Figure 7.10C** reveal some interesting features and differences.

Compared to BSA-N, all macroinitiators exhibit similar broad distributions showing a slight relative increase of a distance peak at 2.34 ± 0.11 nm with the degree of modification x. For BSA-N this peak is only similarly pronounced for fatty acid loadings above four equivalents (see also **Figure 4.2**).[43] This observation may already indicate a change in the order of binding site occupation in the modified BSA-Ix molecules, although the surface has just a few modifications that increase its molecular weight for only about 2.5 – 3.9 kDa (see **Table 7.3**). Extending the comparison to the BSA-Pn conjugates, again a mutual similarity in $P(r)$ is displayed, however, with an even more prominent short distance peak that emerges at about 2.0 nm. Two general remarks have to be made in terms of comparing distance distributions of all compounds.

Firstly, all distance distributions for 1:2:0 equivalents (k-120) exhibit the features at 2.22 ± 0.18 nm (a), 3.24 ± 0.06 nm (b), 3.74 ± 0.06 nm (c) and 4.76 ± 0.02 nm (d). It was already shown in **Chapter 4.1**, that the 16-DSA distance distribution in BSA represents the distance distribution from HSA's crystal structure quite nicely as obtained with co-crystallized stearic acids.[41,42]
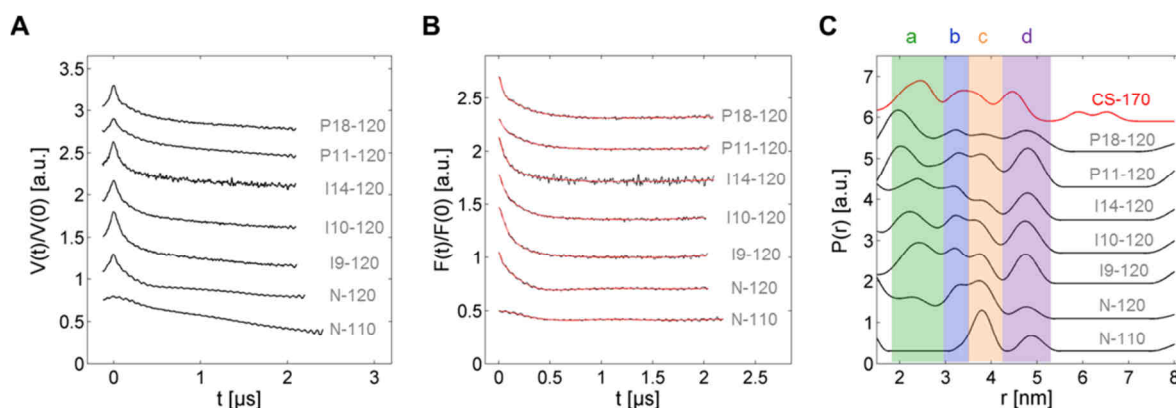

Figure 7.10 | DEER experiments on modified BSA samples. DEER experiments were conducted on samples that contained 0.15 – 0.17 mM BSA and two nominal equivalents of 16-DSA (1:2:0, for BSA-N also 1:1:0) apart from the reference sample of 0.4 mM BSA-N that was loaded with one equivalent. The 16-DSA concentration was therefore kept in the range from 0.3 – 0.4 mM for all DEER experiments. Experimental results as (**A**) raw time domain data $V(t)/V(0)$, (**B**) dipolar evolution functions $F(t)/F(0)$ (black) with regularized fits (red) and (**C**) distance distributions $P(r)$ are shown for all samples. Additionally, the red trace in (C) is the theoretical distribution (CS-170, $\sigma = 0.15$) that was obtained from the crystal structure of HSA co-crystallized with seven stearic acids (PDB ID: 1e7i)[41] as given in Junk et $al.$ (see **Appendix A1**).[42] As an aid to the eye, regions with corresponding peaks are color shaded with green (a), blue (b), orange (c) and purple (d). All samples were equipped with DPBS buffer and 20% v/v glycerol at pH 7.4.

Note, that $P(r)$ from HSA's crystal structure (CS-170, red, **Figure 7.10C**) is constructed and discussed under the assumption that all individual binding sites possess equal ligand binding affinities (K_A) and that the fatty acid binding sites in HSA or BSA are fully occupied (1:7:0, see **Appendix A1**).[42,43] Unfortunately, a crystal structure of BSA co-crystallized with stearic acids is not available to date in the protein data base (accessed Mar 1, 2018).[164]

Secondly, the obvious comparability of all $P(r)$ shapes strongly suggests, that the macroinitiators BSA-Ix and the BSA-Pn polymer-protein conjugates force the ligand configuration, and therefore also BSA, into a more crystal-like structure (compare to CS-170). The same effect was observed in DEER experiments on the cationized human serum albumin (HSA) self-assembled with 16-DSA.[35]

It is also probable that differences in fatty acid distance distributions emerge due to modified binding site selectivities in terms of local electrostatic repulsion (BSA-Ix) and sterical hindrance (BSA-Pn), or a combination of both effects. Finally, each of the fatty acid distance distributions can be seen as fingerprints for pure BSA, BSA-Ix and BSA-Pn and all three groups reveal specific and characteristic shapes. Nevertheless, all fatty acid binding sites and interspin distances of 16-DSA seem to stay largely conserved throughout the different stages of modification with all of them indicating a compact, native-like structure of the BSA-core as indicated by the regions (a–d). A crystal-like or dynamically frozen behavior of BSA is further substantiated by the multiple staggered changes in ligand binding affinities as e.g. observed in the Scatchard plots of BSA-Ix. From these available data it is therefore generally concluded that the applied PTMs freeze BSA's structural plasticity in solution.

7.5 | Discussion

This chapter presents the development from rather coarse to more elaborate EPR spectroscopic and analytic strategies that accomplish to unveil ligand binding dynamics depending on both the extent and the physicochemical nature of the applied posttranslational modification. It is found that changes in the binding behavior of 16-DSA to modified HSA and BSA can be mainly traced back to electrostatic (Gy-DHSA, BSA-Ix) and sterical effects (Gy-DHSA, BSA-Pn) that decrease ligand binding affinities (K_A), while the total number of binding sites (N_T) may be increased simultaneously (HSA-GLX10, BSA-Ix). The total number of binding sites of HSA and BSA is found to be almost identical at $N_T = 6.4 \pm 0.4$ (**Table 7.2** and **Table 7.5**) in case data are derived from explicit spectral simulations, while protein concentrations are slightly corrected for excluded volume effects ($\Delta c < 10\%$, see **Chapter 5.2**). This is in nice agreement with earlier findings on HSA[28,41] and BSA,[103,105,160,161] although 16-DSA-derived Scatchard plots obtained here for native albumins were linear throughout. Additionally, a fast peak-picking method for Scatchard plot construction is developed from BSA-based samples having a comparable precision (2 – 9% deviation) to data obtained from spectral simulations (**Appendix E7**).

All investigated PTM albumins were proven to contain at least 3 – 5 remaining binding sites, independent of the applied analytic method. For glycated HSA-GLX10, BSA-I10 and BSA-I14 an increase in the total number of binding sites was found to exceed $\Delta N_T > +2.6$ giving values of $N_T > 9$ throughout. For BSA-I14 even a total of $N_{T,I14} = 12.9 \pm 1.0$ was found and it can be assumed that N_T is a tunable property, so that squaric acid initiators alone may significantly alter the ligand binding capacity of albumin. Unfortunately, data sets for dendronized albumins are sparse, but for all other samples it is found that independent of the kind of modification the linearity of the HSA-N and

BSA-N reference Scatchard plots is perturbed. Instead, a biphasic or multiphasic ligand binding curve is obtained upon posttranslational modification, revealing negative cooperativity at lower levels of bound ligand equivalents to positive cooperativity at higher loadings above 3 – 4 bound 16-DSA equivalents. This was explicitly analyzed for BSA-derived samples.

The widely approved Rosenthal method[108] was successfully applied to the biphasic Scatchard plot of HSA-GLX10 assuming two non-interacting types of binding systems with ($N_1 = 4.0 \pm 1.1$) very strong and ($N_2 = 5.5 \pm 1.5$) rather weak binding sites. Primarily, the effect of glycation on albumin dynamics should originate in either net charge alterations by lysine- and arginine-blocking, or the introduction of restricted internal motions and adaptability due to lysine-lysine or arginine-lysine cross-linking reactions.[73]

The multiphasic Scatchard plots of BSA-Ix encouraged further characterizations via DLS and Zeta potential experiments in order to retrieve some of the physical origins that lead to this sophisticated behavior. Thus, the clearest functional picture is obtained from the BSA-derived modified albumins. It can be shown that charge (BSA-Ix) and rate of diffusion (BSA-Pn) play significant roles in protein-ligand interactions. The binding characteristics of native BSA change from non-cooperative to a delicate staggered alteration of K_A and the number of equivalent binding sites ($N_{E,Ix}$) in all BSA-Ix samples are governed by cooperativity effects (**Table 7.5** and **Figure 7.9**). The Rosenthal method was not applicable here, however, a qualitative description of the multiphasic Scatchard plots is provided.

Beyond that, these dynamic effects emerging from surface modifications provide access to explicit calculations of the net surface charge Q_k of BSA or the effective dielectric constant $\varepsilon_{\mathrm{eff},Pn}$ in the grafted polymer layer (**Appendix E6**). This is possible as the Zeta potential (ζ_k) was found to decrease linearly with the degree of surface modification in BSA-Ix macroinitiators. In a very simple picture from the BSA-Pn core-shell structures, the polymer shell constitutes a type of diffusion boundary that camouflages fatty acid binding pockets and BSA surface charge Q_k from the solvent and the dissolved fatty acids therein. This is due to the increase in hydrodynamic radii (a_k) as obtained from DLS experiments that also shed light on the statistical reasons for the decrease in ligand affinity.[154,155] As particle size and solvent entanglement cannot be the sole reason for a decrease in $K_{A,k}$, it is concluded, that the polymer shell (Pn) as well as the squaric acid ATRP initiators (Ix) exert an influence on the binding site accessibility and solvent entanglement of BSA. This is mainly provided by retarded diffusion and charge-induced repulsion, as it could be shown in a comparison of BSA-N, BSA-Ix and BSA-Pn.

In the course of processing BSA towards its proposed role as a polymer-coated drug delivery device, the protein-core itself is forced, or remains in a native-like and compact crystalline state. This can be observed when spatial ligand alignments in DEER experiments are directly compared (**Figure 7.10**). Furthermore, these spatial alignments of fatty acids are only observed when corresponding sets of binding sites are still intact. The apparent rigidification is observed as a change in binding site occupation and occurs throughout all modified BSA samples and can be justified as the positions of

emerging distance peaks largely persist (a–d, **Figure 7.10C**). This effect was also observed in DEER experiments from cationized HSA[35] samples and was also thoroughly investigated with strategies beyond EPR spectroscopy for Gy-DHSA.[36] From a ligands' point of view (16-DSA) the binding site selection and preference appears shuffled or redistributed according to the degree of post-translational modification. Together with the results from CW EPR a picture is promoted that features a loss of BSA's functional plasticity due to global electrostatic and sterical alterations.

All this suggests that the ligand affinity (K_A), capacity (N_T) and binding site cooperativity (C) in albumins can be fine-tuned by posttranslational modifications that basically cause net charge variations and sterical obstacles. Furthermore, being the main target for PTMs, functionalization of only a few surface lysines only leads to marginal increases in molecular weight (e.g. BSA-Ix) that after all cause disproportionally strong functional effects.

7.6 | Materials and Methods

Materials. Lyophilized powders of native HSA (HSA-N, >95%, Calbiochem), BSA (BSA-N, Sigma-Aldrich), Gy-DHSA (y = 2, 3), BSA-macroinitiators (BSA-Ix, with x = 8, 11 and 12), BSA-g-P(OEGMA)$_n$ conjugates (BSA-Pn), 16-DSA (Sigma-Aldrich) and glycerol (87 wt% in water, ACROS) were used without further purification. DPBS buffer pH 7.4 was thoroughly prepared according to the original protocol[165] given in **Appendix C1**. Preparations of posttranslationally modified albumins as Gy-DHSA,[36] HSA-GLX10,[95] BSA-Ix and BSA-Pn were described elsewhere.[21,128,130]

EPR Sample Preparation. Aqueous stock solutions of 1 mM HSA-N, 0.389 mM G2-DHSA, 0.174 mM G3-DHSA dendronized albumins, 1 mM BSA-N, 0.5 mM BSA-Ix macroinitiators, 0.929 mM BSA-P11 and 0.426 mM BSA-P18 polymer-protein conjugates were prepared in 0.137 M DPBS buffer pH 7.4, depending on the accessible amount of lyophilized powders (all powders: $m_k \geq 2.0$ mg).

For the study with dendronized HSA in **Chapter 7.2**, appropriate 16-DSA stock solutions were prepared in 0.1 M KOH with 4 mM for G2-DHSA and 8 mM for HSA-N and G3-DHSA that were loaded in the nominal HSA to 16-DSA ratios of 1:2, 1:4 and 1:8. The final solutions with $V = 0.05 – 0.20$ ml contained a constant albumin concentration of 0.07 mM and were titrated to pH 7.40 ± 0.05 as described in **Appendix C4**.

In the study in **Chapter 7.3** that was concerned with glycated HSA, all HSA-GLXc protein concentrations were set to about 0.1 mM. As the HSA-N reference samples were prepared from a 1 mM HSA-N stock solution, the excluded volume approach from **Chapter 5.2** leads to a corrected real concentration of $c_H = P_{ALP} \cdot c_{nom} \cdot (1 - b \cdot c_{stock}) = 0.179$ mM, where $c_{nom} = 0.2$ mM and $b = 8.126 \cdot 10^{-4}$ ml mg^{-1} as obtained from BSA (equation 5.1). In all sample preparations as conducted by DLC Stephanie Schaarschmidt, 26 mM 16-DSA in 0.1 M KOH were used to load the $V = 0.1$ ml samples in the range from 1:1 to 1:10 nominal equivalents of HSA:16-DSA.[95] Here, the actual 16-DSA concentrations were extracted by double integration (see **Appendix E3**) of individual CW EPR spectra.

In the polymer-protein conjugate study in **Chapter 7.4** all final BSA-N, modified BSA-Ix and BSA-Pn protein concentrations were set in the range from 0.06 – 0.32 mM for CW EPR and 0.15 – 0.40 mM for DEER experiments with sample volumes of $V = 0.06 – 0.20$ ml. Upon addition of appropriate amounts of 8 – 26 mM stock solutions of 16-DSA spin probe dissolved in 0.1 M KOH nominal equivalent concentrations of 1:1 to 1:7 of BSA:16-DSA were adjusted for CW EPR samples ($c_{16\text{-DSA,CW}} = 0.10 – 0.74$ mM) and 1:2 for DEER samples ($c_{16\text{-DSA,DEER}} = 0.30 – 0.40$ mM). The 1:1 DEER reference sample of 0.4 mM BSA was an exception as it has been prepared for gaining sufficient SNR. The nominal equivalent concentrations of 16-DSA were used for Scatchard plot construction and were optimized according to the added volumes from the sample preparation protocols. At these low 16-DSA concentrations micelle formation that hampers spectral evaluation can be excluded and overall more than 80% of the ligands are bound to the BSA moieties of all samples ($\phi_b > 0.8$).

Each sample was prepared individually with a 10 – 20 % titration volume for adjusting pH values with a predefined set of acidic and basic 0.12 M DPBS buffers in the pH range from 0.5 – 13.5 (see **Appendix C2**). All

pH values were adjusted in the range from 7.39 ± 0.03 with a well-calibrated pH microelectrode (Mettler Toledo InLab®Micro pH 0 – 14 in combination with the EL20 Mettler Toledo pH meter). The final 0.1 M DPBS protein solutions were equipped with 16-DSA and 20% v/v glycerol to prevent crystallization upon freezing for potential DEER experiments. For CW EPR measurements, about 15 µl of sample were filled into a quarz capillary (BLAUBRAND® IntraMARK) with ca. 1 mm outer diameter. About 80 µl of the final solutions were filled into 3 mm (outer diameter) quartz tubes (Heraeus Quarzglas) and shock-frozen in liquid-nitrogen-cooled 2-methylbutane for subsequent DEER measurements.

EPR Spectroscopy. *CW EPR Experiments:* The Miniscope benchtop spectrometers MS100, MS200 and MS400 (Magnettech GmbH) were used for X-band CW EPR measurements at microwave frequencies of 9.39 – 9.43 GHz that were recorded with frequency counters (RACAL DANA, model 2101, or Magnettech FC400). All measurements were performed at $T = 25°C$ using microwave powers of $P_{MW} = 3.16 – 10.00$ mW and modulation amplitudes of 0.1 mT using sweep widths of 12 – 15 mT. A complete set of recorded CW EPR spectra is given in **Figure 7.2B–D**, **Figure 7.3A**, **Figure 7.4A**, **Figure 7.7**, **Figure E5A** and **Figure E6**.

DEER Experiments: In order to obtain nanoscale distance information from EPR-active modified BSA molecules the 4-pulse DEER sequence:[166,167]

$$\pm(\pi/2)_{obs}-\tau_1-(\pi)_{obs,1}-(t_d+t_0+N_t\cdot\Delta t)-(\pi)_{pump}-(t´-N_t\cdot\Delta t+t_d)-(\pi)_{obs,2}-\tau_2-echo$$

was used to obtain dipolar time evolution data from the bound 16-DSA spin probes. The experiments were performed at X-band frequencies of 9.1– 9.4 GHz using a BRUKER Elexsys E580 spectrometer equipped with a BRUKER Flexline split-ring resonator ER4118X–MS3. The temperature was set to 50 K for all experiments by cooling with a closed cycle cryostat (ARS AF204, customized for pulse EPR, ARS, Macungie, PA) and the resonator was overcoupled to $Q \approx 100$. The pump frequency ν_{pump} was set to the maximum of the field swept electron spin echo (ESE)-detected spectrum. The observer frequency ν_{obs} was set to $\nu_{pump} + \Delta\nu$ with $\Delta\nu$ being in the range of 65 MHz and therefore coinciding with the low field local maximum of the nitroxide ESE spectrum. Observer pulse lengths for each DEER experiment were set to 32 ns for both $\pi/2–$ and π–pulses and the pump pulse length was 12 ns. Additionally, a 2-step phase cycle (±) was applied to the first $\pi/2$ pulse of the observer frequency for cancelling out receiver offsets and unwanted echoes. Proton modulation was averaged by addition of eight time traces of variable τ_1 starting with $\tau_{1,1} = 200$ ns, incrementing by $\Delta\tau_1 = 8$ ns and ending up at $\tau_{1,8} = 256$ ns. For all samples the pump pulse position $t_d + t_0$ after the first observer π-pulse deadtime t_d was typically incremented for N_t timesteps of $\Delta t = 8$ ns in the range $t_0 + t´ = \tau_1 + \tau_2 - 2t_d$, whereas τ_1 and τ_2 were kept constant. DEER time traces were recorded for 12 – 48 hours giving rise to reliable distance information in between about 1.6 and 5.0 nm as the maximum accessible dipolar evolution time was $t_{max} > 2$ µs throughout.[168]

Data Analysis: Spectral simulations of CW EPR data from 16-DSA probed albumin samples (**Figure 7.2**, **Figure 7.3A+B**, **Figure 7.4A** and **Figure E5A**) have been exclusively evaluated in MATLAB 2008b (v.7.7) utilizing the MATLAB-based EasySpin software package.[169] This program comprises a toolkit that implements the application slow tumbling nitroxide theory[170,171] for specific sample requirements in feasible and straight-forward procedures. All MATLAB codes were optimized for 3- to 4-component nitroxide spectra comprising one (*b*) or two immobilized components (*b*$_1$ and *b*$_2$), a free component (*f*) and occasionally also micellar components (*a*) as it is rationalized in **Appendix E2**. This strategy is nowadays routinely conducted for EPR-based simulations on albumins.[68,97–99] Best fits were obtained with a_{iso} values of about 15.3 – 15.5 G for components b_i and 15.8 G for component *f*, as it was suggested earlier for 16-DSA spin probes interacting with albumin.[68] The errors for individual spectral fractions b_i are estimated as $\Delta\phi_i = 3\%$ and the accuracy for the other parameters is $\Delta a_{iso} = 0.03 – 0.30$ G and $\Delta\tau_c = 8\%$. For a complete set of simulation parameters and the simulation approach the reader is referred to **Table E1–E2** and **Appendix E1–E3**. This rather laborious simulation approach can be circumvented by a corresponding readout scheme that is realized by introducing a correlation constant $k_L = 0.02486$ as it is presented in **Chapter 7.4.2** and **Appendix E7**. However, for now this shortcut method is thought to be only applicable for BSA in 0.1 M DPBS pH 7.4 and 20% v/v glycerol. The Scatchard plots were constructed as described in the main text according to equation 7.1, equation 7.14 and equation E.29. A complete set of fit parameters from linear regressions in Origin as shown in **Figure 7.8** is listed

in **Table E4**. Raw time domain DEER data were processed with the MATLAB-based program package DeerAnalysis2013[172] utilizing the Tikhonov regularization procedure applying background dimensionalities of $D = 3.71 \pm 0.01$ that are due to excluded volume effects of the BSA molecules (see **Chapter 5.2**).[42,173] The theoretical distance distribution (CS-170) was derived from the structure of seven stearic acids co-crystallized with HSA (PDB ID: 1e7i)[41] that was modified for 16-DSA according to the procedure in Junk *et al.* that is also described in **Appendix A1** (width: $\sigma = 0.15$).[42] No significant differences in background dimensionalities in between native (BSA-N) and posttranslationally modified BSA samples (BSA-I*x* and BSA-P*n*) have been noticed.

DLS and Zeta Potential Measurements. All DLS data from BSA, BSA-I*x* and BSA-P*n* samples were obtained with an ALV-NIBS high performance particle sizer (HPPS) equipped with an ALV-5000/EPP Multiple Tau Digital Correlator (ALV-Laser Vertriebsgesellschaft m. b. H.). This device facilitates HeNe-LASER irradiation with a typical wavelength of $\lambda = 632.8$ nm and 3 mW output power with an automatic attenuator for optimum count rates recorded in a backscattering detection angle of 173° relative to the incident monochromatic light. The sample cell temperatures were kept constant at $T = 25$°C with a Peltier temperature control unit. All samples have been prepared from the 0.5 mM stock solutions giving final BSA concentrations of 4.2 – 11.4 µM at pH 7.39 ± 0.03. The final sample volumes of 300 – 430 µl were measured in 1.5 mL PMMA semi-micro cuvettes (BRAND). Data were extracted from the intensity correlation functions by a $g_2(t)$-DLS exponential and a mass weighted regularized fit in the ALV-NIBS software v.3.0 utilizing the CONTIN algorithm.[174] Each sample was measured at least 4 times at constant temperature for 60 s and was averaged at least over four individual values. The mean values $a_k = R_{\text{H},k}$ of the most prominent particle size peaks and their statistical fluctuations are given as the standard deviation in **Table 7.3**. The corresponding diffusion coefficients were calculated according to the Stokes-Einstein relation: $D_k = k_B T \cdot (6\pi\eta \cdot R_{\text{H},k})^{-1}$ from individual values of a_k.[134]

Zeta potentials (ζ_k) were obtained from electrophoretic mobility measurements at $T = 25$°C utilizing the LASER Doppler velocimetry (LDV) technique in an electrophoretic light scattering (ELS) setup (see **Table E3** and **Table 7.4**). Therefore, a constant voltage $U = 87$ V was applied between the electrodes of an Omega cuvette in a Litesizer™ 500 (Anton Paar GmbH) device. This Omega cuvette prevents electric field gradients at the measurement position and allows for precise and reproducible experiments. All data were analyzed with the novel continuously monitored phase-analysis light scattering technology (cmPALS)[175] as implemented in the provided software package Kalliope™ 1.8.0. All samples were prepared at identical concentrations ($c = 1.5$ µM, i.e. ranging from 0.10 – 0.25 g/l) in 0.05 M DPBS buffer at pH 7.51 ± 0.04 with an ionic strength of $I = 0.062$ M. Consistently, the thickness of the electrical double layer (DL) is $\lambda_D = \kappa^{-1} = 1.222$ nm and $\kappa a_k > 1$ for all samples (see **Table E3**). All Zeta potential values were averaged over 5–7 individual experimental values. The measured conductivities of all solutions were in the range of $\kappa_{\text{el}} = 6.7 \pm 0.3$ mS cm^{-1}. Furthermore, the dielectric constant ε_r = 78.4,[139] refractive index $n_{\text{H2O}} = 1.332$ (for $\lambda = 632.8$ nm)[176] and viscosity $\eta = 0.89$ mPa·s[140] were assumed to be constant for all solutions (also in DLS experiments). Calculations of corresponding Henry functions $F_{\text{SF}}(\kappa a)$ were conducted according to Swan and Furst,[177] however, in all experiments reproducible Zeta potentials were only obtained for $F(\kappa a) = 1.09$ as calculated for BSA-N. All important experimental parameters, as $\mu_{\text{e},k}$, $\kappa_{\text{el},k}$ and calculated values of κa_k, $F_{\text{SF}}(\kappa a_k)$, $N_{\text{c},k}$, Z_k and $\varepsilon_{\text{eff},\text{P}n}$ are explained, derived, summarized and presented in **Appendix E6**.

Molecular Weights of BSA-I*x* and BSA-P*n*. The molecular weights of native BSA and of the corresponding macroinitiators (BSA-I*x*) were determined with MALDI-TOF mass spectrometry by Dr. Christian Schmelzer and can be found in **Figure E2**. The calculation of the number of squaric acid residues was conceived by the relation:

$$x = \frac{\text{MW}_{\text{I}x} - \text{MW}_N}{\text{MW}_{\text{SA}}} \tag{7.20}$$

assuming that $\text{MW}_{\text{SA}} = 288.11$ Da. Molecular weights of polymer-protein conjugates (BSA-P*n*) were determined by SDS PAGE[129] using gels containing 8% bisacrylamide as a crosslinker and silver staining for visualizing the bands (see **Figure E3**) as it was already presented by Dr. A. Thomas.[130] As graphical references, BSA-N and BSA-I10 have been added to highlight the weight increase after conjugation. The degree of polymerization of polymer-protein conjugates BSA-P*n* (DP = *n*) was calculated according to the relation:

$$n = \frac{MW_{Pn} - MW_{Ix}}{x \cdot MW_{OEG}} \qquad , \qquad (7.21)$$

assuming that MW_{OEG} = 475 Da. For convenience, x =10.4 in equation 7.21, as all polymer-protein conjugates were grafted from BSA-I10 macroinitiators. All such derived molecular weights are summarized in **Table 7.3**.

8 | Exploring the pH-induced Functional Phase Space of HSA

A systematic pH screening is conducted covering a broad range from pH 0.7 – 12.9 mainly using EPR spectroscopic methods on the self-assembled solution system of HSA and paramagnetic fatty acid derivatives (5-DSA and 16-DSA). The maintenance of all physicochemical parameters except pH is only provided by the established optimized control of sample properties that was introduced in **Chapter 5**. It is tested to which extent the well-known pH-induced dynamic states and features of HSA reveal themselves in CW EPR spectra from this spin probing approach in combination with an established spin labeling strategy utilizing 3-maleimido proxyl (5-MSL). Most analyses are conducted on simplistic empirical levels with some established as well as situational strategies that allow for the detection of dynamic changes of ligand as well as protein. Moreover, it is investigated how the solution shape of HSA as obtained from dynamic light scattering (DLS) and DEER-derived nanoscale distance distributions from bound fatty acids is affected by pH.
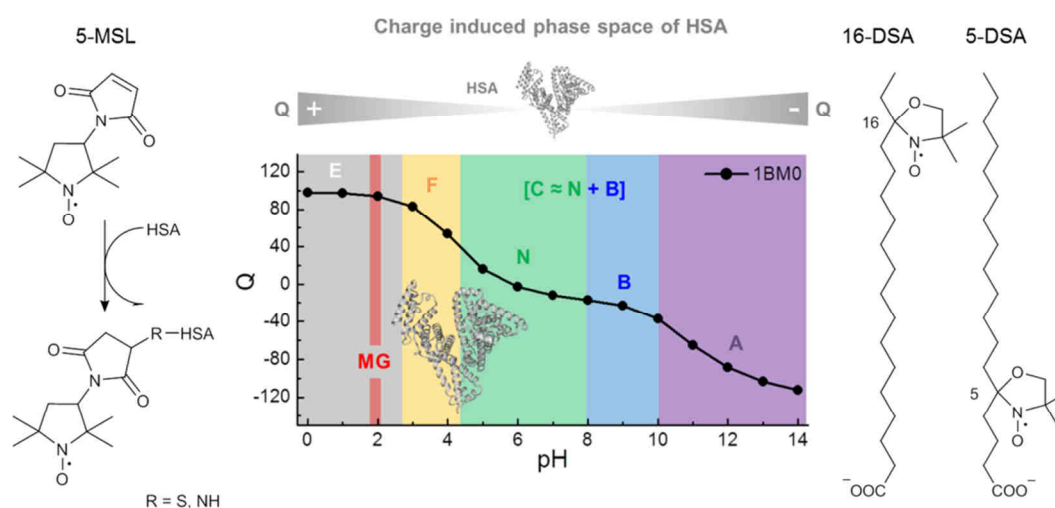
8.1 | Introduction

The pH denaturation phenomenon has been a long standing issue in protein science.[1–6] Primarily, the principles of this process are well-known and are linked to electrostatic repulsive and attractive forces due to changes in the protonation state of charge bearing amino-groups ($R-NH_3^+$) in mainly lysine and arginine residues at alkaline pH (pK_a 10.8 – 12.5)[7] and carboxyl groups ($R-COO^-$) in glutamate and aspartate residues in acidic environments ($pK_a = 3.8 – 4.5$).[8] Thus, it is generally assumed that charge repulsion leads to an elongation of the polypeptide chain as a result of collective protonation or deprotonation of individual amino acids.[3,9,10] General protein folding from an unfolded (U) to a native state (N) is classically expected to either proceed according to the *framework model*,[11–13] where hydrogen bonds form secondary structures early in the folding process, or the *hydrophobic collapse model* where nonpolar residues reconfigure into the protein interior after chain collapse.[14] It is proposed that this protein folding may generally advance in three stages comprising an additional intermediate compact state, the *molten globule* (MG).[15,16] This intermediate compact state is defined

by slowly fluctuating tertiary structure as first observed from the acid form of α-lactalbumin by Dolgikh *et al.*[17] This molten globule state is generally detected by circular dichroism (CD),[17,18] intrinsic viscosities [η], tryptophane fluorescence,[17] or ANS (8-Anilino-1-naphthalenesulfonic acid)[19] as a hydrophobic fluorescent probe that binds to exposed hydrophobic regions of partially folded proteins.[20,21] A general overview of applicable methods for molten globule state detection of proteins is given e.g. by Kuwajima.[22] An intriguing analogy of how protein thermodynamic states can be related to bulk systems was demonstrated by Pande and Rokhsar[23] in a phase diagram where the native protein (N) corresponds to the solid (s), the molten globule (MG) represents the liquid (l) and the unfolded chain (U) represents the vapor state (v) of a protein.

EPR spectroscopy has been also proven suitable to qualitatively detect such molten globule states[24,25] by using the SDSL approach[26,27] in combination with simple but appropriate lineshape analyses.[28,29] Molten globules were also found in acidic HSA solutions at pH 2.0[30,31] and alkaline BSA solutions at pH 11.2.[32] Historically, an acidic molten globule-like state was experimentally already described for BSA as early as 1954 by Yang and Foster[33] as they detected a salt-dependent increase in intrinsic viscosity between pH 2.2 – 2.7 that was later also found in EPR spectroscopic studies in the same pH region.[34] However, these experiments were conducted with the lack of the molten globule definition given almost 30 years later.[15]

Here, the protein phase space[35] of HSA is explored in a very broad pH range from at least pH 1 to 12 mainly using spin-labeled fatty acids for monitoring the proteins solution structure.[36–41] As it was pointed out in **Chapter 3**, this spin probing approach emphasizes effects as ligand binding capabilities, rotational dynamics, local polarity (CW EPR) and distance measurements between the paramagnetic centers of the protein-aligned FAs.

Basically, the carefully adjusted pH values of individual solutions are here used to trigger changes in the charge state of HSA and therefore the structural and dynamic phase space[23,35] is systematically screened in terms of pH-induced conformational isomers in the extended (E, pH < 2.7), fast migrating (F, pH < 4.3), native or norm (N, 4.3 < pH < 8.0), basic (B, 8.0 < pH < 10.0) and aged form (A, pH > 10), that have been thoroughly described earlier.[31,42–44] Specifically, the potential of an EPR-spectroscopic detection of the HSA molten globule (MG) state at pH 2.0[30] by paramagnetic fatty acids is investigated and compared to the generally applied lysine-directed maleimido spin labeling strategy for albumin[45–51] in order to resolve this somewhat enigmatic (thermo)dynamic state.

Additionally, dynamic light scattering (DLS) experiments are presented that are utilized to follow proposed changes in solution size of the albumin particles and therefore also serve as a spatial correlation for corresponding DEER results.

Taken together these findings are finally combined towards a coarse-grained EPR-spectroscopic picture of the functional charge-induced albumin phase space.

8.2 | Experimental Results

Before studying the pH-dependent changes in HSA with EPR spectroscopy, some simple bioinformatic calculations were conducted that are later correlated to the findings from the spin-labeled and spin probed HSA samples. Generally, a wide variety of approaches is available for extracting information from CW EPR spectra. Due to the large amount and the inherent complexity of the obtained EPR datasets herein, explicit spectral simulations are here considered as dispensable and all analyses are reduced to the extraction of some established empiric parameters that are sufficiently sensitive to monitor dynamic changes of protein and ligand. Therefore, additional useful strategies are employed and developed that principally rely on relative changes in lineshapes and line positions (see also **Figure 8.4A** and **Figure F1**).

8.2.1 | Calculation of the pH-dependent Stability and Charge of HSA

In order to obtain an approximate notion of the charge state of HSA at a certain pH value, the stability and charge of the protein molecules in solution were calculated with help of PROPKA 3.0[8,52,53] for two structures, stearic acid free HSA (PDB ID: 1BM0)[54] and HSA loaded with seven stearic acids (PDB ID: 1e7i).[55] In **Figure 8.1A** the free energies of folding (ΔG_f) are shown as functions of pH for both structures. Overall, the curve shapes are quite similar exhibiting a predicted optimum HSA stability at about $pH_{opt} = 9.8 \pm 0.1$ for $T = 25°C$. On a qualitative level, the structure of HSA with bound stearic acids (PDB ID: 1e7i) exhibits a further stability increase of $\Delta\Delta G_f = -7.5$ kcal mol^{-1} $= -31.4$ kJ mol^{-1} (**Table 8.1**) compared to HSA alone as it can be commonly expected for fatty acid-loaded albumin structures (see also **Chapter 11**).[56,57]

Table 8.1 | Results from PROPKA 3.0 calculations

PDB ID	pH_{opt}	ΔG_f [kcal mol^{-1}]	pI
1BM0	9.7	74.2	5.79
1e7i	9.9	66.7	5.79

Beyond that, the stability curves in **Figure 8.1A** are provided with color-coded pH regimes of reversible conformational HSA isomers according to the scheme given by Peters[43] and Qiu *et al*.[44] In the acidic regime, the norm form (N) of HSA changes to a fast migrating form (F) below pH 4.3 and for pH < 2.7 a further transition occurs to an extended form (E). In the basic regime of pH > 8, the norm form changes to the basic form (B) and for pH > 10, HSA is expected to convert into an aged form (A). The general shape appearance of HSA is expected to follow an acidic expansion (pH < 3.5) and a basic contraction (pH > 8).[44] The prediction from PROPKA 3.0 gives HSA net charges $Q = Z \cdot e$ in the range from $-113 < Z < +99$ for both investigated structures with a calculated isoelectric point at pI = 5.79 (see **Figure 8.1B**) that coincides well with experimental values from the fatty acid free form of HSA ($5.1 < pI < 5.8$)[31,58–61] and may as well be domain specific.[59] The onsets of the F and A

forms are clearly associated with a strong change in net charge *Q*. Wherever applicable, the color-coded pH regimes are given in due form as phase space bars at the top of a graph in the following sections.
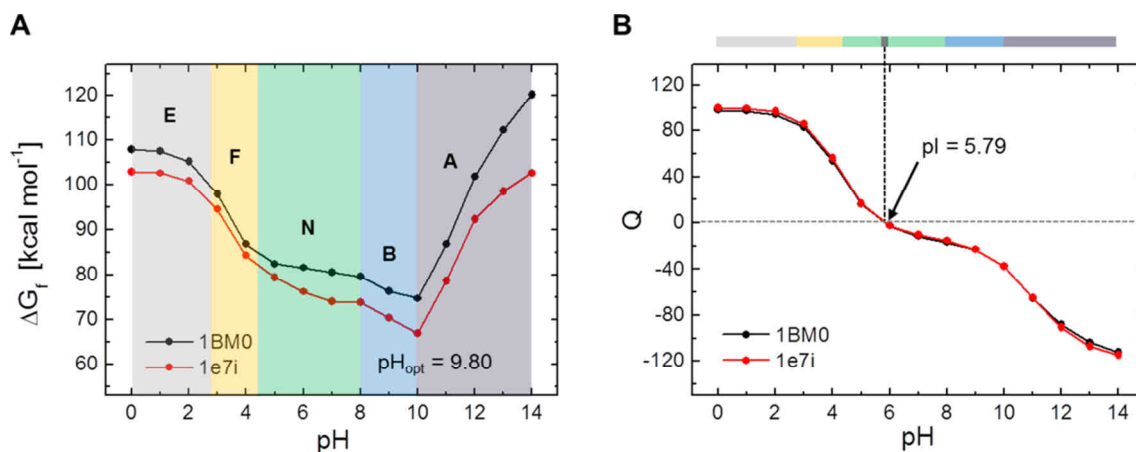

Figure 8.1 | Calculation of HSA folding stability ΔG_f and corresponding net charges *Q*. (A) Calculated free energy of folding ΔG_f as a function of pH for HSA alone (black, PDB ID: 1BM0)[54] and for HSA loaded with seven stearic acids (red, PDB ID: 1e7i).[55] The black bold letters denote pH-induced dynamic regimes of HSA according to Qiu *et al.*[44] with conformational isomers in the extended form (E, gray), fast migrating form (F, yellow), norm form (N, green), basic form (B, blue) and an aged form (A, purple). Additionally, the calculated pH of optimum stability (pH$_{opt}$ = 9.80) is shown where ΔG_f is at its minimum. (B) Calculated titration curves show the net charge $Q = Z \cdot e$ as a function of pH for HSA alone (black, PDB ID: 1BM0) and for HSA loaded with seven stearic acids (red, PDB ID: 1e7i). The isoelectric points (pI) at $Q = 0$ can be found at pH 5.79 for both curves. All data were generated at $T = 25°C$ with PROPKA 3.0[8,52,53] and the conformational isomers (E – A) are given as a phase space bar at the top of the graph with the color code given in (A).

8.2.2 | CW EPR Experiments on 5-MSL HSA Solutions at pH 0.72 – 11.96

The 3-maleimido-proxyl spin-label (5-MSL) was among the first reported EPR-active reporter groups that were applied to albumin and proteins in general.[45,62] It was ruled out early by N-ethyl maleimide blocking[45] that the apparent immobilization as seen in the outer spectral extrema ($A_{//}$, see **Chapter 2.4.5**)[63] originate from 5-MSL-labeled cysteines, whereas the fast rotating three-line components of spectra are due to unspecifically labeled lysines on the albumin surface exhibiting an almost isotropic rotation.[45] With 59 lysines in its primary sequence[54,64] and one accessible redox-active cysteine[65–67] at chain position Cys34 being intrinsic for each mammalian and avian albumin,[43] each HSA molecule contains a maximum of 60 potential labeling sites. At least 30 – 35 lysines are reported to be accessible to such non-specific lysine-targeted posttranslational modification procedures for BSA (see also **Chapter 7**).[68] The resulting 5-MSL labeling sites are therefore assumed to be statistically distributed across each individual albumin surface. It was shown early that lysine-targeted spin-labels remain covalently attached to (poly)lysines and BSA in the range from at least about pH 1.5 – 11.8[34] and therefore a rich set of *N* = 44 individual EPR spectra was recorded in the range from pH 0.72 – 11.96 that is presented in **Figure 8.2A,** very similar to earlier studies by Cornell and Kaplan,[69,70] or a recent one by Pavicevic *et al.*[51] Therefore, this study can be regarded as a reference data set.

In **Figure 8.2A** it can be seen for pH > 9.6 (green) that the isotropic three-line component increasingly dominates the spectral shape. This is due to an increased pH-induced flexibility of 5-MSL bound to the ε-amino groups of the lysines. The observation of the outer extrema separation $A_{//}$ is also provided in the whole tested pH range as presented in **Figure 8.2B**. While $A_{//}$ does not largely change from pH 3.7 – 10.9 (C = compact), a significant drop is observed for pH > 10.9 that indicates the emergence of the A form coinciding with a structural weakening of HSA. A further slight drop is observed from pH 3.7 to 2.8 indicating the fast migrating (F) form of HSA. For the acidic region at pH < 2.8 no further changes of this parameter are seen and HSA is assumed to remain in the extended form (E).

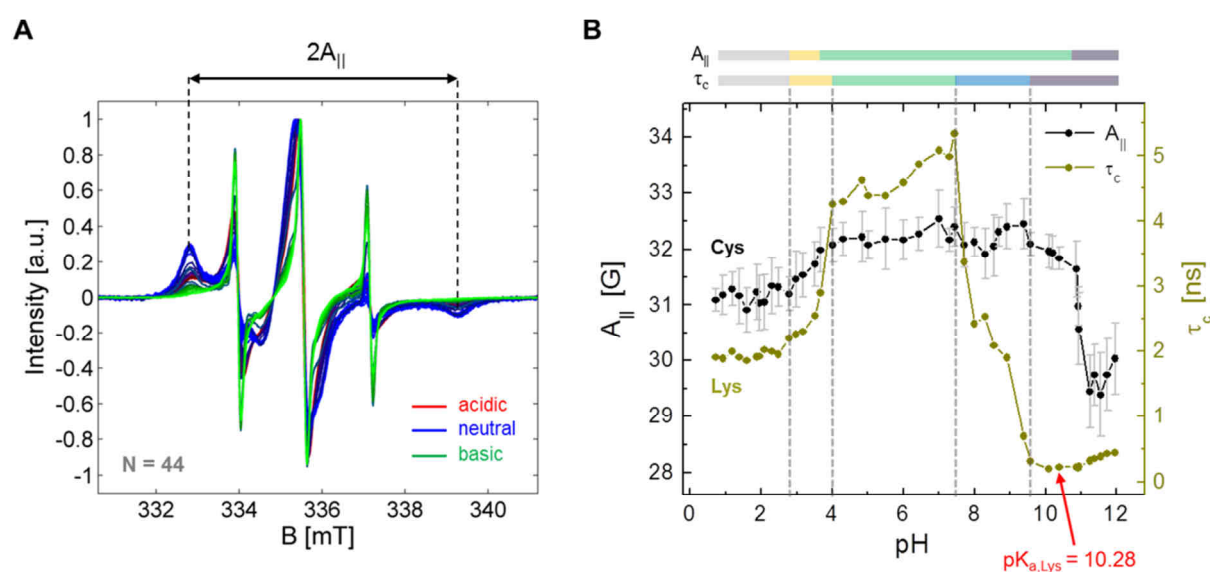**Figure 8.2 | CW EPR experiments on 5-MSL HSA depending on pH.** (**A**) CW EPR spectra of N = 44 different 5-MSL HSA solutions between 0.72 < pH < 11.96 are shown. The black dotted lines indicate the apparent hyperfine coupling constant as obtained from the outer extrema ($2A_{//}$) of recorded spectra. All spectra are color-coded in red (acidic), blue (neutral, or compact) and green (basic). (**B**) Corrected apparent hyperfine coupling constants $A_{//}$ (black) and the collective rotational correlation times τ_c (dark yellow, for calculations see **Appendix F1**) are shown together as functions of pH from CW EPR experiments in (A). The different regions in the τ_c curve can be subdivided into five dynamic regimes according to Qiu *et al.*[44] displaying the extended (E, gray), fast migrating (F, yellow), norm (N, green), basic (B, blue) and aged (A, purple) form of HSA. Phase space bars are given for τ_c and $A_{//}$ where a compact region (C, green) was identified that ranges from pH 3.7 – 10.9. The collective lysine pK$_a$ value (pK$_{a,Lys}$ = 10.28 (red)) was calculated with PROPKA 3.0[8,52,53] as shown in **Appendix F2**. All measurements on 5-MSL HSA were performed at a protein concentration of 0.09 mM and T = 25°C. Error bars of $\Delta A_{//}$ (gray) are the relative maximum accuracies from values obtained from individual spectra (equation F.3).

A further dynamic parameter in CW EPR spectroscopy is provided by the rotational correlation time τ_c that was calculated as a collective value from emerging spectral features of 5-MSL attached to HSA (see **Appendix F1**). In a direct comparison to $A_{//}$ in the range from pH 0.72 – 7.44 (**Figure 8.2B**) it turns out that the curve features of τ_c are much more pronounced and exhibit sharper, clear-cut boundaries of the different dynamic regimes. However, compared to the $A_{//}$ curve, the onset of the F form in the acidic region is slightly shifted to pH 4.0 when the N form is clearly terminated by a quick drop in τ_c. These lysine-based dynamics in the N form as observed from 5-MSL appear strongly immobilized (τ_c = 4.68 ± 0.37 ns). Again, the E form emerges at pH < 2.8 exhibiting constant values of about τ_c = 1.93 ± 0.05 ns throughout. A completely different picture is observed from τ_c in the basic

regime. Upon exceeding the physiological value of about pH 7.4, there is a significant increase in pH-induced lysine side-chain flexibility. This state persists until about pH 9.6. Interestingly, this transition region almost perfectly coincides with the proposed basic form (B) of HSA from pH 8 – 10.[43,44] The picture of a loss in rigidity in the B form[43] coincides well with a highly flexible lysine behavior, i.e. in return the lysines might indeed play a significant role in establishing this stable basic conformational isomer at pH_{opt} = 9.8 (see also **Figure 8.1A** and **Table 8.1**). Finally, for pH > 9.6 all CW EPR spectra are dominated by least immobilized 5-MSL spin labels with rotational correlation times in the range from 0.20 – 0.44 ns. The origins of this almost two-fold increase in τ_c for pH > 11 remain elusive, but it was stated early from experiments on poly-L-lysine[71] and spin-labeled poly-L-lysine variants[34,62] that a coil-helix transition occurs at pH > 9 for these polyaminoacids. Although this effect might not be as pronounced for HSA as in a polypeptide homopolymer, the significance of this feature is therefore presented as pH-induced changes of relative heights of high-field and low field peaks in **Figure F2**. Together with the PROPKA calculations a mean collective $pK_{a,Lys}$ = 10.28 can be derived for unmodified HSA-based lysines, almost perfectly coinciding with a maximum in these relative line heights and a collective lysine pK_a value reported earlier.[72] It is therefore assumed that 5-MSL may also serve as a probe for the determination of this $pK_{a,Lys}$ value (see **Appendix F2**). From 5-MSL spin-label dynamics the F and B forms of HSA are detected as pronounced dynamic transition regions (τ_c). Unfortunately, these unspecifically attached spin-labels (Lys, Cys)[45,62] do not exhibit any salient characteristics from $A_{//}$ and τ_c in pH regions where the emergence of a molten globule intermediate is expected (pH 2.0).[30,31] Due to the inherent statistical, unspecific and almost quantitative attachment of 5-MSL to cysteine and lysine residues (5 molar equivalents, see **Chapter 8.4**), DEER experiments are discouraged due to multispin-effects and uncorrelated spatial arrangements of 5-MSL in individual albumin molecules. Some initial DEER test measurements on 5-MSL BSA were highly discouraging. Therefore, this study proceeds with a further EPR spectroscopic approach elucidating the pH-dependent protein-ligand interactions of spin probed HSA.

8.2.3 | CW EPR Experiments on 5- and 16-DSA-probed HSA Solutions from pH 0.8 – 12.9

Here, the pH-dependent self-assembly properties of HSA with the spin probes 5-DSA and 16-DSA[73] are tested thoroughly. The spectral features of pH-denatured albumin samples are investigated on an empirical level as it will be shown in the following. All CW EPR spectra in the studied pH range are depicted in **Figure 8.3A–C** and for convenience the equivalent concentration, loading status and type of probe is again given as an appropriate abbreviation in the following (e.g. 16HSA 120 0400 mM = 16-DSA-probed HSA with 0.4 mM equivalents of 1 × protein, 2 × EPR-active 16-DSA probes and 0 × r16-DSA). The spin probes can be regarded as sufficiently stable at all pH values in the time frame of a typical CW EPR experiment, as no significant loss of signal intensity or SNR is detected.
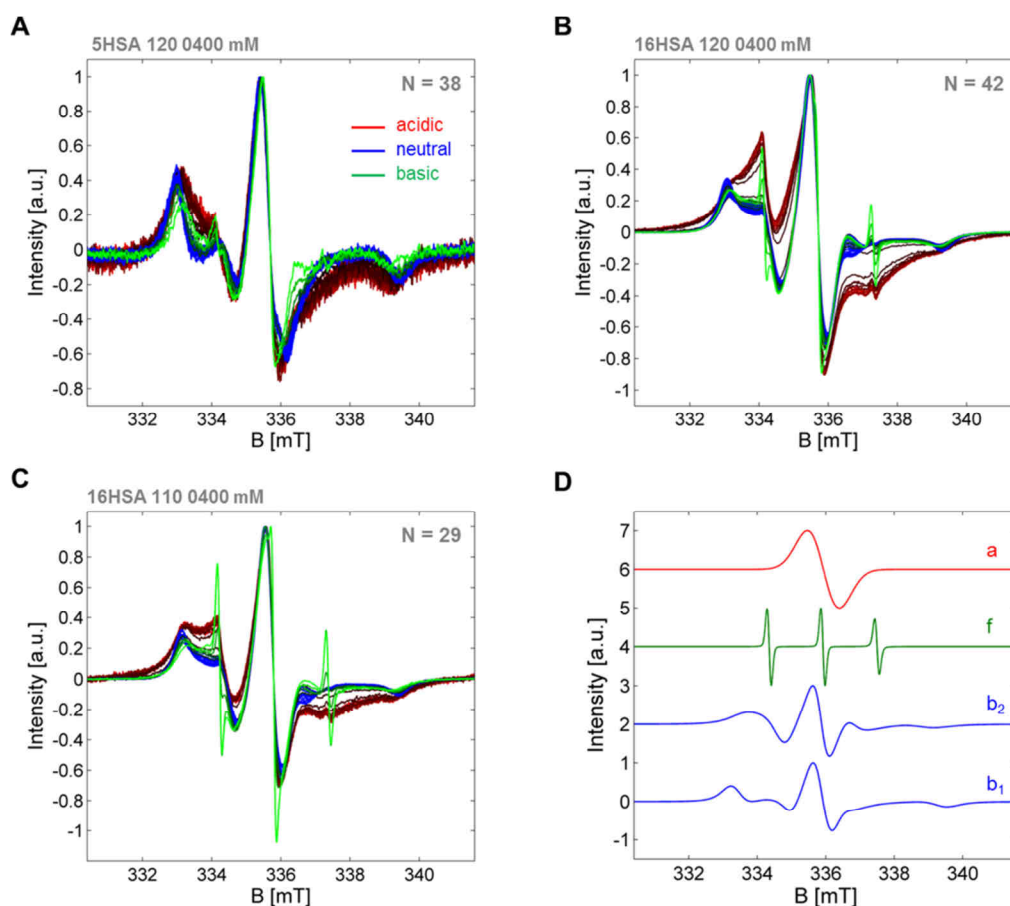
Figure 8.3 | CW EPR experiments on spin probed HSA depending on pH. Here, CW EPR spectra of 5- and 16-DSA spin probed HSA solutions between 0.81 < pH < 12.87 are shown. All pH-dependent spectra are color-coded in red (acidic), blue (neutral, or compact) and green (basic) in overlapping graphs of N spectra. (**A**) All experimental CW EPR spectra of 5-DSA-probed HSA solutions are shown in the range from 0.81 < pH < 12.20 ($N = 38$) loaded with two equivalents spin probe (120). (**B**) All CW EPR spectra of 16-DSA-probed HSA solutions are shown in the range from 0.89 < pH < 12.24 ($N = 42$) loaded with two equivalents spin probe (120). (**C**) All CW EPR spectra of 16-DSA-probed HSA solutions are shown in the range from 0.98 < pH < 12.87 ($N = 29$) loaded with one equivalent spin probe (110). All samples were recorded at $T = 25°C$ and 0.4 mM molar equivalents of protein to spin probe. (**D**) Some exemplary simulations of 16-DSA interacting with HSA (see **Appendix F3**) are shown from the most prominent spectral features of micelles (a, red), free ligand (f, green) and bound ligand (b_1, b_2, blue) that dominate the spectral shape at specific pH ranges.

The reported pK_a value for the carboxyl group of stearic acids is usually in the range of 4.5 – 4.7.[74–77] Thus, due to the intrinsic pH-dependent solubility of the probe itself, it is expected that it mainly exists in the protonated state at about pH 1.0. Therefore, the more insoluble, protonated spin probes at acidic pH accumulate in micelles, while at the same time HSA's affinity towards fatty acids decreases when the protein is in the fast (F) and extended form (E). This circumstance is also exploited in purification strategies during which fatty acids are removed from albumin-containing solutions.[43,78] In this context, the acidic spectra reveal a spin exchange-induced (J_{AB}) baseline shift that is typical for micellar components in EPR spectra (see **Figure 8.3D**, a, red).[79] Some initial investigations of the pH-dependent properties of the self-assembled system of a spin-labeled fatty acid (12-DSA) to BSA are given in Ge *et al.*,[72] also claiming the strong insolubility of the spin probe as well as from BSA itself at low pH.

A similar but inverse effect is observed at pH > 11, when HSA is in the aged form (A). Obviously, HSA again loses affinity towards the spin probes as detected by the increasing fraction of typical three-line spectra that emerge for freely tumbling paramagnetic ligands in EPR (*f*, green). At such high pH values 5-DSA and 16-DSA are in their deprotonated and in a much better soluble state compared to pH 1.0. The spectral shapes of spin probed HSA samples remain largely constant in the range from about pH 4.0 – 11.0 and can be understood to depict a native-like, compact form (C) as it was reported to be in a similar range for BSA.[80] In this compact form the albumin protein binds almost all spin probes (*b*, blue).[72] Due to the complex spectral composition consisting of the fractions *a*, b_1, b_2 and *f* throughout most pH regimes, an alternative strategy is now rationalized that allows for extracting useful information from these datasets. For example, a comparison of **Figure 8.3B** and **Figure 8.3C** reveals that micelle formation (red) is significantly hampered by adding only one instead of two equivalents of 16-DSA.

8.2.3.1 | Monitoring Global Spectral Changes from CW EPR Spectra of Spin Probed HSA

The strong pH-dependent spectral changes as seen in **Figure 8.3** can be reduced to distinct parameters that monitor the strongest shape and position alterations with pH and are summarized in **Figure 8.4A**. Especially, for 16-DSA the observed micelles cause severe positive (3330 G < *B* < 3350 G) and negative (3370 G < *B* < 3390 G) intensity shifts. Therefore, the parameter $h_\perp$ is introduced that monitors these special characteristics. Strategically, it is set to the *B*-field positions of the readout values of the $A_\perp$ component of immobilized spectra that are typically used in the determination of order parameters in membrane biophysics (see below).[63,81] Additionally, the high-field peak height (h_{-1}) is used to obtain information about the relative amount of free spin probes, while the center-field height (h_0) is used to normalize both parameters ($h_\perp$ and h_{-1}) to each other. Thus, an empirical expression:

$$I_{abf} = \frac{h_\perp + h_{-1}}{h_0}$$

(8.1)

is defined serving as a straightforward measure mainly containing information about micelle formation and fatty acid release. **Figure 8.4B** shows the results from a corresponding analysis of 16-DSA-probed HSA (120). It turns out that there are two individual Boltzmann-shaped curve sections in the range from pH 1–9.

In the acidic range from pH 0.8 – 4.5 an increasing amount of micelles is formed when pH is lowered that induces a height shift I_a and has an inflection point $pH_{a,0}$. The region from pH 4.5 – 9.0, where HSA remains in its compact form and most of the probes are bound, reveals that I_{abf} is again subjected to a sigmoidal increase with the height I_b and an inflection point $pH_{b,0}$. It can be seen in **Figure 8.3B+C** that this feature clearly emerges due to slight changes in $h_\perp$, although no micelles are present.
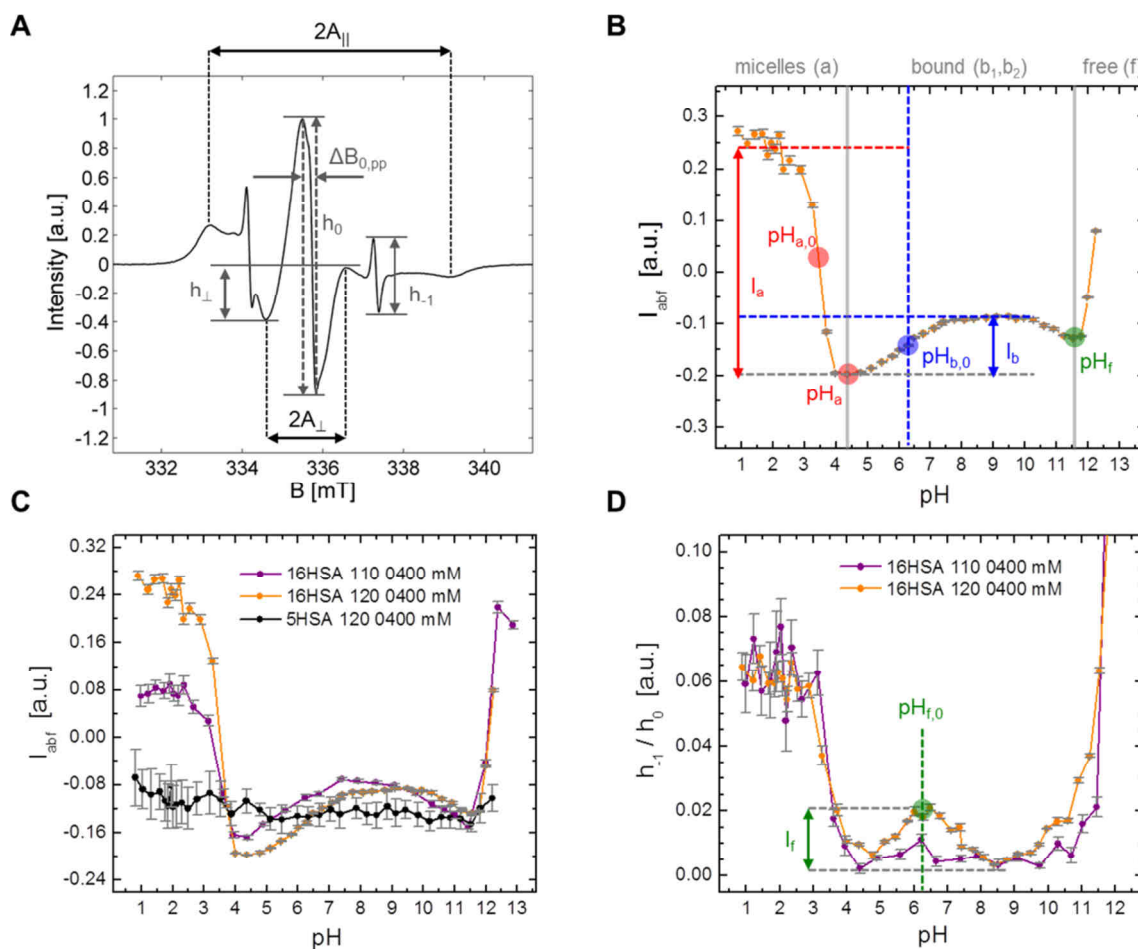
Figure 8.4 | Lineshape readout scheme for spin probed HSA samples and the pH-dependent I_{abf} parameter. Here, a scheme is presented that traces characteristic changes in CW EPR spectra from spin probed HSA solutions with pH. (**A**) A representative spectrum of 16-DSA-probed HSA loaded with two equivalents spin probe (120) at 0.4 mM equivalents is shown for pH 12.24. Vertical parameters are the center-field peak height (h_0), high-field peak height (h_{-1}) and the intensity shift $h_\perp$. The horizontal parameters are $A_\parallel$, $A_\perp$ and the center-field peak width ($\Delta B_{0,pp}$), that are also used in this study (see below). (**B**) An I_{abf} parameter analysis and readout scheme for 16-DSA-probed HSA solutions (120) is shown at all pH (orange). There are three regions that can be clearly assigned to be caused by spin probes in micelles (*a*), bound to HSA (b_1, b_2) and free in solution (*f*). The onset of fatty acid release, or micelle formation (pH_a) increases I_{abf} for a maximum value I_a. The onset of fatty acid release in the basic region is termed pH_f. While the bound spin probes also change I_{abf} for a value I_b, $pH_{a,0}$ and $pH_{b,0}$ denote the midpoint of an individual transition range. (**C**) Analyses for all spectra emerging from 5-DSA (black, 120 loading) and 16-DSA probed HSA (110 (purple) and 120 loading (orange)) are presented in **Figure 8.3A–C**. (**D**) Exclusive spectral contribution from the free fraction h_{-1}/h_0 of 16-DSA-probed HSA samples. An intermediate increase of the free ligand fraction is observed for $pH_{f,0}$.

Therefore, this feature emerges due to dynamic population changes in the bound fractions ϕ_{b1} and ϕ_{b2} as it was already described by Muravsky *et al.*,[73] where a straightforward kinetic model was applied (with $\phi_{b1} = N_{S0}$ and $\phi_{b2} = N_{W0}$). The results from curve regressions on I_{abf} curves are explicitly discussed in **Appendix F4** and are summarized in **Table 8.2**. Counterintuitively, it was found that the asymmetric minimum features between about $3 < pH < 6$ as well as from about $9 < pH < 12$ can be determined by an appropriate Nelder model function:[82]

$$I_{abf} = \frac{pH + \alpha}{\beta_0 + \beta_1(pH + \alpha) + \beta_2(pH + \alpha)^2} \qquad . \qquad (8.2)$$

This kind of rational function is usually applied in modeling crop yield responses to nitrogen fertilizer[83] and milk yield lactation curves from dairy cattle.[84] It can be shown (see **Appendix F4**) that the fit parameters directly yield the acidic minimum with $pH_a = -\alpha + (\beta_0/\beta_2)^{-1/2}$ and the basic minimum at $pH_f = -\alpha - (\beta_0/\beta_2)^{-1/2}$. In **Figure 8.4C** all datasets are compared by I_{abf}, revealing that 5-DSA-probed HSA is rather insensitive to pH in this aspect, however, with slight positive changes for extreme pH. Both 16-DSA loading ratios (110 and 120) reveal several recurrent and invariant features that can be detected by I_{abf}. The obtained values around $pH_a = 4.3$ and $pH_f = 11.4$ can be interpreted as the onsets of acidic and basic fatty acid release, respectively. This is also indicative of a compact protein shape for the range $pH_a < pH < pH_f$ that contains functional fatty acid binding pockets. Furthermore, these data sets suggest that micelle formation is most pronounced at the acidic inflection point $pH_{a,0} = 3.45$ and according to the values listed in **Table 8.2**, $pH_{a,0}$, pH_a and pH_f are apparently largely independent of the loading status and the amount of micelles formed (I_a).

A closer inspection of the relative free fraction (h_{-1}/h_0) of 16-DSA-probed HSA as presented in **Figure 8.4D** reveals an interesting bump at about $pH_{f,0} = 6.2 - 6.3$ where an increase (I_f) in the relative amount free ligand is observed. This increase of free ligand is also about twice as high when the loading ratio is doubled and seems to be correlated to the inflection point $pH_{b,0}$ when the bound spectral features exhibit the strongest dynamic changes. Both, the strong dynamic changes in bound fatty acids and the simultaneous release of fatty acids have to be mainly charge-induced. Therefore, in combination with **Figure 8.1B** it is concluded that $pH_{f,0}$ and $pH_{b,0}$ arbitrarily correspond to an experimentally observable isoelectric point (pI = 5.79, **Table 8.1**) in CW EPR spectroscopy. Here, the $pH_{b,0}$ values slightly differ for both investigated 16-DSA loadings.

Table 8.2 | Characteristics observed from 16-DSA-probed HSA in I_{abf} and h_{-1}/h_0 curves[a]

Model	Parameter	110	120
Boltzmann	I_a	0.247 ± 0.009	0.443 ± 0.011
	I_b	0.103 ± 0.017	0.110 ± 0.002
	$pH_{a,0}$	3.44 ± 0.03	3.45 ± 0.03
	$pH_{b,0}$	5.60 ± 0.21	6.19 ± 0.03
Gauss	I_f	0.00891	0.0178 ± 0.0011
	$pH_{f,0}$	6.20 ± 0.21	6.33 ± 0.04
Nelder	pH_a	4.26 ± 0.15	4.39 ± 0.14
	pH_f	11.36 ± 0.04	11.46 ± 0.10

[a]Explicit analyses and fit parameters from I_{abf} curves are shown in **Appendix F4**.

8.2.3.2 | Monitoring Changes in Spin Probe Immobilization ($A_{\parallel}$) and Polarity (A_{zz}) in HSA

As for the 5-MSL spin label, apparent hyperfine coupling constants $A_{\parallel}$ are here again used as a measure for the compactness of HSA. This directly accessible spectral parameter is widely used due to its little ambiguity[85] and is here observable throughout all pH values for all spin probes. Additionally, the well-known polarity probing properties of doxyl stearic acids[72,86] are tested here with the A_{zz} value

in order to detect variations in solvent accessibility or hydrophobicity.[87] ANS is well-known to sense hydrophobic patches on proteins[20,88] that either have an increased accessibility, or are more surface-exposed in the molten globule state.[21] Therefore, a hypothesis is tested whether the spin probes may act as *EPR spectroscopic ANS-analogues* that enable the detection of an acidic molten globule state of HSA[30,31] by A_{zz}.

Figure 8.5A shows all pH-dependent $A_{||}$ values that were observed for 5-DSA and 16-DSA, however, the determination of outer extrema separations may be afflicted by strong read-out errors of up to $\Delta A_{//} = 0.95$ G, especially at strongly acidic pH. The three curves exhibit similar trends with slightly differing peculiarities. For clarity, a color-coded phase space bar has been inserted to each curve that designates observable changes in $A_{||}$. In principle, the more immobilized the spin probes are, the larger the $A_{||}$ values get. For 5-DSA-probed HSA the observed overall changes in $A_{||}$ are most pronounced ($\delta A_{//,5} \approx 3.4$ G and $\delta A_{//,16} \approx 2.0$ G, corresponding to maximum variations in $A_{||}$ of about $\delta A_{||,k}/A_{||,k,\max} = 6 - 10$ %) with a maximum feature between $7.86 < \mathrm{pH} < 9.84$ (I., see **Figure 8.5B**) that can be rationalized as the most compact or stable state of HSA (B form) in correspondence with the stability curve in **Figure 8.1A**. Therefore, this feature is correlated to $\mathrm{pH}_{\mathrm{opt}} = 9.84$. However, this B form is not observed in 16-DSA-probed HSA. At $\mathrm{pH} > 9.8$ a steady decrease is observed for 5-DSA and this region is therefore termed as the aged (A) form similar to the results from 5-MSL HSA. For $\mathrm{pH} < 3.87$ a decrease is observed that can be correlated with the onset of the F form and the E form is identified below $\mathrm{pH} < 2.78$. At about pH 2, where the molten globule state is supposed to appear, an indentation in the $A_{||}$ curves of 5-DSA (120, II.) and 16-DSA-probed HSA (110, IV.) can be observed that are missing for 16-DSA probed HSA at a higher loading ratio (120, III.).

In order to further substantiate this finding a Gaussian fit curve was applied for 5-DSA (120), whereas a Gumbel[89] fit curve was used for 16-DSA (110) yielding $\mathrm{pH}_{\mathrm{MG,5}} = 2.13 \pm 0.13$ and $\mathrm{pH}_{\mathrm{MG,16}} = 1.90 \pm 0.14$, respectively (**Appendix F5**). The emergence of these two features is now intrinsically ambiguous as it can be either induced by a drop in polarity, i.e. a decrease in A_{zz}, or by a structural softening of the protein. For clarification, an additional set of pH-dependent A_{zz} values was recorded in the whole investigated pH range with emphasis on the region around the MG state (**Appendix F6**). It turns out, that all recorded A_{zz} values for 5-DSA and 16-DSA vary in a quite narrow range from $33.5 - 34.6$ G throughout all pH values and applied spin probes. However, from the difference $\delta A_{zz} = A_{zz,5} - A_{zz,16}$ it is revealed that there is indeed a distinctive feature at pH 2.05 with $\delta A_{zz,\mathrm{MG}} = +1.07$ G that in fact exceeds the uncertainty from data extraction (**Figure 8.5C**).

This EPR-based finding constitutes that the MG state is a structurally weakened folding state of HSA that is observed as a spontaneous and slight decrease in spin probe immobilization. The relative increase in $A_{zz,5}$ further substantiates this claim as it is indicative for 5-DSA-monitored solvent exposure of the protein interior[36] that would go along with a structural opening of HSA. At all other pH this effect is considered as too weak for being detected, apart from pH 6 where a very low $A_{zz,5}$ value is found while $A_{zz,16}$ monitoring the protein surface is the overall highest.
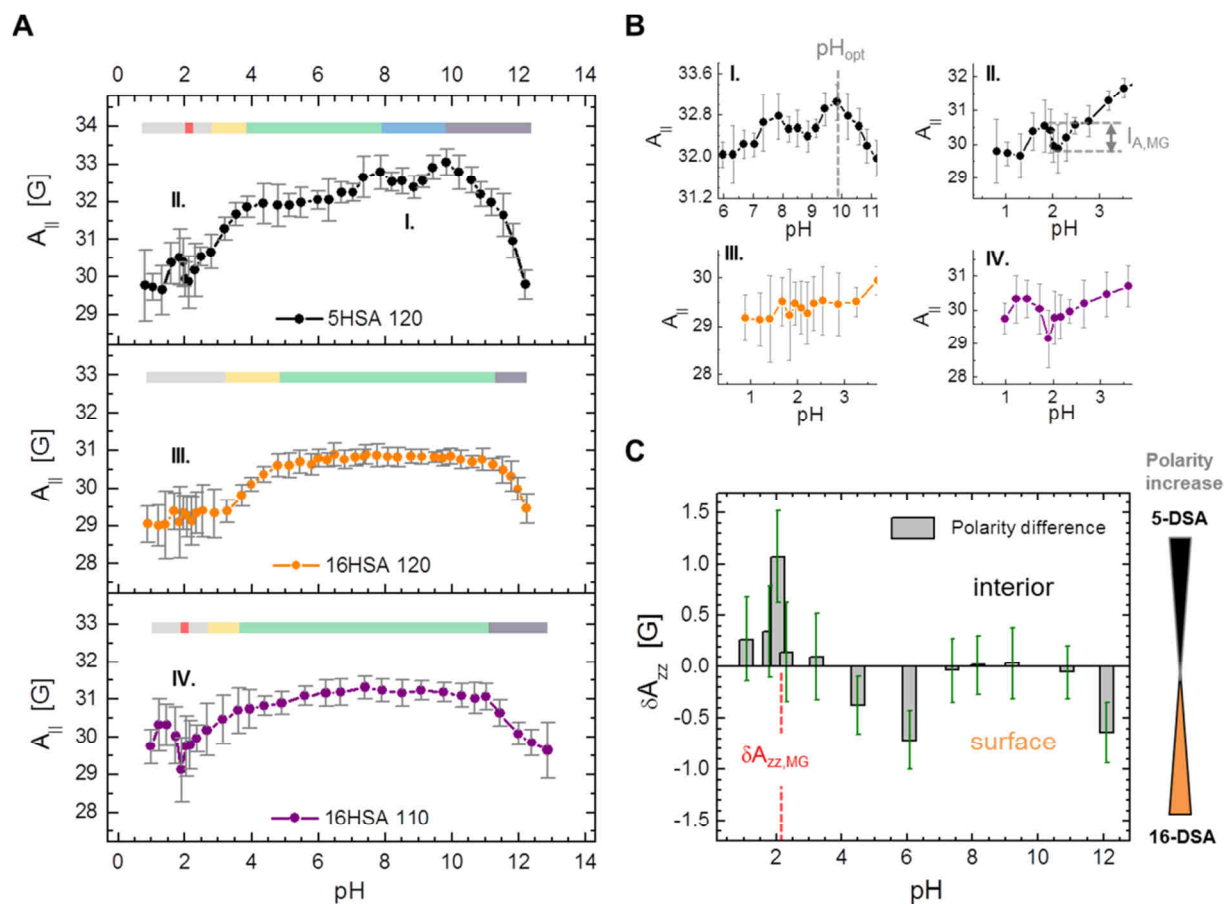
Figure 8.5 | pH-dependence of $A_\parallel$ as observed from spin probed HSA. The outer extrema separations $2A_\parallel$ from CW EPR spectra in **Figure 8.3A–C** are plotted in the observed pH range for (**A**) 5HSA 120 (black), 16DSA 120 (orange) and 16HSA 110 (purple) at 0.4 mM equivalents. Individual phase spaces containing conformational isomers E, F, C and A are given as a color-coded bar at the top of each curve according to the scheme given in **Figure 8.1**. Additionally, molten globule (MG) states are here also given in red bars when a corresponding feature emerges. Significant features are marked with roman numerals (I. – VI.). (**B**) Significant curve features that belong to the pH range of maximum stability (pH_{opt}, I.), or the molten globule state (MG, II. – IV.) with corresponding intensity changes ($I_{A,MG}$) are highlighted as shown in (A) for better visibility. (**C**) A polarity difference plot $\delta A_{zz} = A_{zz,5} - A_{zz,16}$ is constructed from CW EPR spectra that were recorded at $T = 150$ K (see **Appendix F6**). Differences in polarity are given as gray columns with green error bars. Positive values indicate a polarity increase for 5-DSA (protein interior)[36] and consistently, negative values indicate a polarity increase for 16-DSA (protein surface)[36] bound to HSA. The maximum change in polarity at about pH 2.0 is denoted with $\delta A_{zz,MG}$. Error bars of $\Delta A_{\parallel}$ (gray) are the calculated relative maximum accuracies from values of individual spectra.

Generally, there is an inside-out-polarity inversion from pH 6 towards pH 2 as observed from the two different spin probes. The slight decrease in $A_{zz,16}$ at pH 2 proves that (more) hydrophobic patches form at the 16-DSA-probed surface[88] of HSA. This gives a first estimate about the potential of the paramagnetic fatty acid derivatives to rival ANS in order to detect molten globule states as long as $I_{A,MG}$ (0.8 – 1.1 G) is larger than changes in $A_{zz,k}$ (0.4 – 0.5 G) around pH_{MG}.

From 16-DSA probed HSA a quite clear cut plateau-like region is observed in the $A_\parallel$ curve that ranges from pH 3.60 – 11.02 for singly loaded (110) and pH 4.79 – 11.23 for doubly loaded HSA (120). This feature is indicative of a compact form (C) of HSA that is transformed to the aged form (A, pH > 11.0) and to the fast rotating form (F, pH < 3.6). This is largely in agreement with the ranges observed from corresponding $A_\parallel$ values of 5-MSL HSA. The shift in the onset of the F form in 16-DSA-loaded HSA (120, orange) may be due an acidic structural weakening that originates from the sheer presence of

fatty acids. The onset of the E form is also shifted from pH 2.66 to pH 3.26 upon addition of a second spin probe. This may be due to the bimodality of spin probe immobilization (b_1, b_2). Furthermore, there is no evidence for the presence of a MG at pH 2 for HSA containing two 16-DSA spin probes. It is concluded that fatty acid loading affects the dynamic behavior of HSA essentially in the acidic pH range (pH < 5), where the occurrence of the F and E forms are expected. As $A_\parallel$ can be observed throughout the whole investigated pH range, it is self-evident that a considerable fraction of the spin probes always remains bound to the protein.

8.2.3.3 | Monitoring Changes in Center-field Linewidths ($\Delta B_{0,\mathrm{pp}}$) from Spin Probed HSA

The center-field linewidth $\Delta B_{0,\mathrm{pp}}$ is intrinsically related to the transversal relaxation times T_2 (see equation 2.22). The dominant contributions to T_2 are motional modulations of the hyperfine coupling tensor (A) that provide information about molecular reorientation.[81] As this rotational reorientation of spin probes bound to HSA is anisotropic, bimodal (b_1, b_2) and very slow ($\tau_{c,b1}$ = 14.2 ns and $\tau_{c,b2}$ = 5.8 ns at pH 7.4, see **Table F1**), linewidths themself are here regarded as a sufficient qualitative measure for dynamic changes of spin probed HSA. **Figure 8.6A** shows all pH-dependent linewidths $\Delta B_{0,\mathrm{pp}}$ that were extracted from 5-DSA and 16-DSA-probed HSA according to the readout-scheme presented in **Figure 8.4A**.

It is obvious, that the advantage compared to $A_\parallel$ lies in the small readout errors throughout all investigated pH values and the tremendous relative spectral changes that are about 4 – 8 times stronger than for $A_\parallel$ ($\delta\Delta B_{0,\mathrm{pp},5} \approx 4.0$ G and $\delta\Delta B_{0,\mathrm{pp},16} \approx 2.3$ G, corresponding to maximum variations in $\Delta B_{0,\mathrm{pp}}$ of about $\delta\Delta B_{0,\mathrm{pp},k}/\Delta B_{0,\mathrm{pp},k,\max}$ = 39 – 50%). The curves obtained from 5-DSA and 16-DSA differ decisively, however, it can be shown that the information content is very similar. Again, a color-coded phase space bar has been inserted to each curve that designates observable changes in $\Delta B_{0,\mathrm{pp}}$. In principle, the more rotational freedom the spin probes experience, the lower the $\Delta B_{0,\mathrm{pp}}$ values get. Overall seven different features can be assigned from 5-DSA-probed HSA alone.

Specifically, the symmetric N_1 section can be analyzed by a Gauss curve due to the continuous and symmetric change in linewidth (**Figure 8.6B**, I.) for about I_B = –0.76 G that exhibits a minimum at $\mathrm{pH}_{B,0}$ = 6.25 ± 0.08. Note, that very similar curve shapes were recorded from tyrosyl fluorescences of HSA (domain III) by Dockal *et al.*[31] Here, the F form is also clearly identified by a step-like feature ranging from pH 2.78 – 3.87. The lower linewidth values in the acidic range below pH 2.78 are assigned to the E form and values beyond pH 11.19 to the A form of HSA.

The linewidths around pH 2 are clearly diminished for about $I_{B,\mathrm{MG}} \geq 0.2$ G in all obtained curves (**Figure 8.6B**, II.–IV.), indicating a slight release in motional restriction that is again ascribed to emerge due to the formation of a molten globule-like state (MG). The exact positions and widths of these diminished acidic linewidth features were fitted with Gaussian functions that revealed midpoint values of $\mathrm{pH}_{\mathrm{MG},5}$ = 2.16 ± 0.37, $\mathrm{pH}_{\mathrm{MG},16}$ = 2.01 ± 0.13 (110) and $\mathrm{pH}_{\mathrm{MG},16}$ = 1.87 ± 0.95 (120) (see also **Appendix F7**).
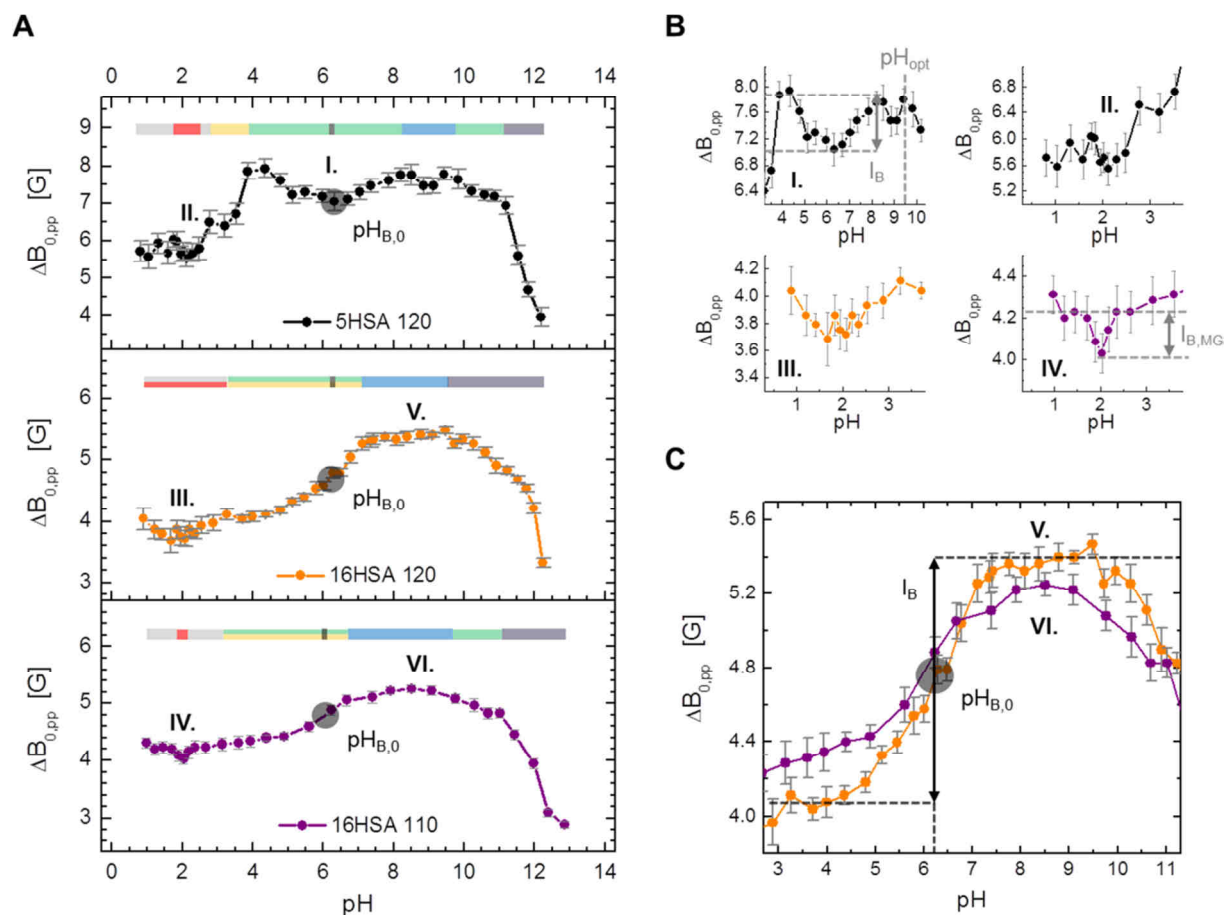
Figure 8.6 | pH-dependence of $\Delta B_{0,pp}$ as observed from spin probed HSA. The center-field linewidths $\Delta B_{0,pp}$ from CW EPR spectra in **Figure 8.3A–C** are plotted in the observed pH range for (**A**) 5HSA 120 (black), 16DSA 120 (orange) and 16HSA 110 (purple) at 0.4 mM equivalents. Individual phase spaces containing conformational isomers E, F, N (C), B and A are given as a color-coded bar at the top of each curve according to the scheme given in **Figure 8.1A**. Additionally, the molten globule (MG) state is here given in red and $pH_{B,0}$ is given in black. Significant features are marked with roman numerals (I. – VI.). In case of ambiguous curve shapes the phase space bars have been set in parallel (e.g. E and F for 16-DSA at pH < 7). (**B**) Collection and close up representation of significant curve features (I.–IV.) from $\Delta B_{0,pp}$ of 5-DSA as well as 16-DSA-probed HSA that can be fitted with a Gaussian model function. Intensity changes in the range from pH 4 – 9 are given as I_B for 5-DSA and $I_{B,MG}$ for the pH range from pH 1–3 for both spin probes. A local maximum feature is observed for 5-DSA at pH 9.43 that is again correlated to pH_{opt}. (**C**) Collection and close up representation of curve features (V. and VI.) that are exclusively visible in 16-DSA probed HSA. The range from pH 3 – 9 can be fitted with a Boltzmann model function. The maximum changes in linewidth $\Delta B_{0,pp}$ is termed I_B and for simplicity the inflection point of the curves is again represented by $pH_{B,0}$.

The higher 16-DSA ligand loading ratio (120) obviously blurs the sharp position of the MG state. As for $A_\parallel$, this circumstance again proves that the molten globule is characterized with a structural widening that is accompanied with increased motional freedom of the spin probes. The pH-dependent linewidth curves from 16-DSA probed HSA are a bit more ambiguous.

Apart from the acidic region from about pH 0.8 – 3.2 where the E forms and molten globules can be observed for both loading ratios, there is no sharp transition to an F form. The linewidths rather increase sigmoidally from pH 3 to about pH 7 until a plateau is reached that is again maintained until about pH 10. Therefore, this plateau is coined as the B form with the strongest motional restriction. The transition region from pH 3 – 7 is interpreted as bimodal, i.e. the F and N forms of HSA are inseparable. In fact, the two different modes of ligand immobilization (b_1 and b_2) are suspected to

decisively contribute to this feature.[73] Due to the transition-like behavior, both curves were analyzed with Boltzmann fit curves and it turns out that the pH value of the inflection point is almost identical to the $pH_{B,0}$ value observed in 5-DSA-probed HSA. More precisely, the obtained values are $pH_{B,0}$ = 6.01 ± 0.07 (110) and $pH_{B,0}$ = 6.21 ± 0.06 (120) that provide sufficient evidence for substantiating this striking coincidence (**Appendix F7**).

The detection of the onset of the A form is also blurry for 16-DSA-probed HSA as the plateau ranging from pH 7–10 does not end abruptly, but rather continuously decreases its linewidth for extremely basic pH. Generally, all spin probes monitor a significant gain in motional freedom for pH > 11 due to the structural weakening of HSA in the A form.

8.2.3.4 | Monitoring Changes from Order Parameters (S) in Spin Probed HSA

The order parameter (S) can be used as a measure for mean angular fluctuations of a system.[81] Originally it was thought for investigating liquid crystalline systems by their degree of molecular order.[90,91] The extraction and use of order parameters is well realized in EPR spectroscopy. Most applications in this concern are mainly restricted to physical properties of biological or artificial membrane systems,[63,92–102] but have been also tested, or discussed for albumin.[103–105] Here, analyses are restricted to 16-DSA-probed HSA as the 5-DSA spin probe appears to lack decisive spectral features for order parameters due to the intrinsic strong immobilization as well as strong, irreducible spectral noise. A similar issue was already mentioned by Morrisett et al.[104]

In principle, pH-dependent values for $A_{\parallel}$ and $A_{\perp}$ are read out from individual spectra according to the scheme given in **Figure 8.4A**, whereas the corresponding order parameter-based isotropic hyperfine coupling constant is $a_{iso,S} = (1/3) \cdot (A_{\parallel} + 2A_{\perp})$.[85] The magnetic parameters of the bound spin probe species are provided by an explicit spectral simulation performed on 16-DSA-probed HSA (120 loading with $a_{iso,b} = (1/3) \cdot (A_{xx} + A_{yy} + A_{zz})$, see **Appendix F3**). Thus, potential polarity differences between $a_{iso,S}$ and $a_{iso,b}$ that may emerge can be considered in the construction of the order parameter that is given by:[63,81]

$$S = \frac{(A_{//} - A_{\perp})}{(A_{zz} - A_{xx})} \cdot \frac{a_{iso,b}}{a_{iso,S}} \qquad . \qquad (8.3)$$

For simplicity, the denominator term $(A_{zz} - A_{xx})$ = 28.43 G is considered as a constant throughout all investigated pH values as it was shown in **Appendix F6** that changes in A_{zz} are hardly detectable at X-band frequencies. A complete pH-dependent set of 16-DSA-derived order parameters is given in **Figure 8.7A** for both loading ratios (S_{110} and S_{120}). Interestingly, there is no distinct phase detectable in both curves, however, maximum order ($S_{max,16}$) is found for pH 7.6 ± 0.2. Thus, all order parameters are found to continuously change with pH in a quite narrow range from 0.52 < S < 0.73 that would indicate a nematic behavior[91] of the HSA-bound spin probes in a figurative sense. Generally, S_{120} values are a bit lower than S_{110}, speaking in favor that the more fatty acids are bound to HSA, the

weaker the binding affinity (K_A),[106–108] or in other words, the higher is the occupation of the spectral fraction ϕ_{b2} (see also **Chapter 11**).[109] Whereas S_{120} has an approximate two-state process-like curve shape, S_{110} exhibits an additional, rather broad feature at about pH 2 that indicates a state of maximum spin probe disorder. This finding is correlated to the molten globule state and a Gaussian curve fit reveals that the extrapolated value is at $pH_{MG} = 2.31 \pm 0.57$ (**Figure F9**).

The detectable change of the order parameter due to this feature is about $I_{S,MG} = 0.033$ (see also **Appendix F8**). Furthermore, the order parameter can be related to a spin probe wobbling angle γ by the relation:[85]

$$2S = \cos\gamma + \cos^2\gamma \tag{8.4a}$$

that can be translated into the expression:

$$\gamma = \arccos\left(\frac{\sqrt{8S+1} - 1}{2} \right) . \tag{8.4b}$$

This wobbling angle can be understood as a restricted random walk of the main diffusion axis on the surface of a sphere (here: albumin) or a fluctuation between the diffusion axis and the sample axis.[85] Nominally, the wobbling angle is the rotation on a cone with a semi-cone angle γ indicating the spin probe fluctuation amplitude.[110–112]
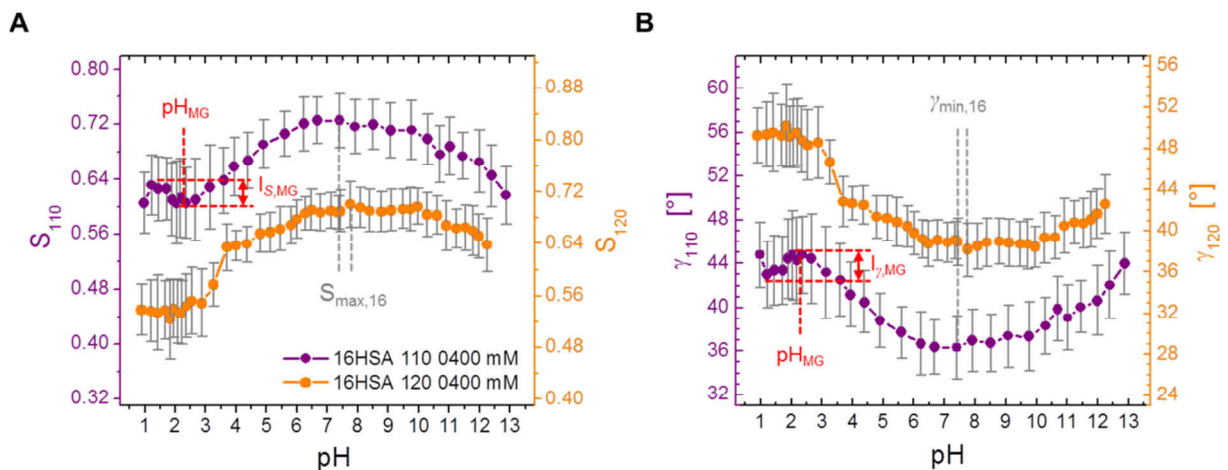
Figure 8.7 | pH-dependence of order parameters *S* and wobbling angles *γ* from 16-DSA-probed HSA. The order parameters and wobbling angles of 16-DSA-probed HSA extracted from CW EPR spectra in **Figure 8.3B–C** are plotted in the observed pH range for both loading ratios (110 (purple) and 120 (orange)). Molten globule-related features are highlighted with red dotted lines. All calculated error bars are given in gray. (**A**) The order parameters S_{110} and S_{120} of 16-DSA interacting with HSA are given as a function of pH. The global maximum value for both curves is given with gray dotted lines ($S_{max,16}$). The order parameter depletion $I_{S,MG}$ around pH 2 is correlated with the molten globule state. (**B**) The wobbling angles γ_{110} and γ_{120} of 16-DSA interacting with HSA are shown as a function of pH. The global minimum value for both curves is given with gray dotted lines ($\gamma_{min,16}$). The increase of the wobbling amplitude $I_{\gamma,MG}$ around pH 2 is correlated with the molten globule state.

Corresponding results are found in **Figure 8.7B** and show an inversed curve shape of the order parameter with decisive features ($S_{\max,16} = \gamma_{\min,16}$) at identical pH values. For both curves the wobbling angles range from $36.5° < \gamma < 50.3°$. The changes observed in the wobbling angle that appear due to the emergence of the molten globule-like state of HSA are here considered as more illustrative with $I_{\gamma,MG} = (2.2 \pm 0.4)°$, corresponding to a relative maximum change of about 26%. The absence of the depletion region around pH 2 for two equivalents of 16-DSA interacting with HSA (orange) gives rise to the assumption that a higher fatty acid loading prevents the formation of a molten globule state as it was already observed in the $A_\parallel$ curves (**Figure 8.5A**). However, from this viewpoint, the molten globule state can be understood as an intermediate state of maximum ligand disorder and wobbling amplitude.

8.2.4 | DEER Experiments on 16-DSA-probed HSA Solutions at pH 1.03 – 12.15

The pH denaturation of 16-DSA-probed HSA solutions was also conducted in a complementary view to CW EPR (see **Chapter 8.2.3**) by DEER spectroscopy[113,114] in order to screen the system for the occurrence of structural changes that can be monitored by bound ligand displacements in the associated HSA scaffolding. For successful DEER experiments with sufficient modulation depth (Δ) and signal-to-noise ratio (SNR), the nominal loading ratio of fatty acid to albumin was conveniently chosen as 2:1.[36] Thus, an average of two spin probes should be located inside one HSA molecule. The reduction in protein concentration from 0.40 mM to 0.17 mM was considered as necessary for attenuating the effect of micelle formation propensity of 16-DSA when it is partially released below pH 4.0.[43,78] Additionally, information about HSA is lost when bound fatty acids with their messenger duty would be completely released from the protein.

All DEER results from the pH denaturation process of HSA are shown in **Figure 8.8**. Due to the large data set of 19 individual measurements the presentation is subdivided in an acidic regime from pH 1.03 to pH 7.40 and a basic regime from pH 7.40 to pH 12.15. The time traces in **Figure 8.8A+B** and the dipolar evolution functions in **Figure 8.8C+D** reveal that clear dipolar modulation is only obtained in the range from pH 3.83 – 11.35, covering the entire compact norm form (C) regime of HSA as almost identically detected in $A_\parallel$ curves (**Figure 8.5A**) from corresponding CW EPR experiments. The resulting micelles constitute a direct recording of meaningful time traces of intramolecular distances of HSA-bound fatty acids as impossible. The presented distance distributions $P(r)$ are restricted to this pH range where background dimensionalities of $D = 3.73 \pm 0.01$ are typically used in HSA, reflecting an effective excluded volume due to the rather sizeable HSA molecules.[36,115]

For a detailed discussion on the background dimensionality of 16-DSA probed HSA in the native state at pH 7.4 the reader is referred to **Chapter 5.5** and a thorough analysis given by Kattnig *et al.*[115] The background dimensionality slightly decreases for pH > 11.35 and in the acidic regime of the fast migrating HSA form (F) it is about $D = 3.1$. It furthermore reaches relatively stable values of 2.0 – 2.5 in the extended HSA form (E) below pH 2 when 16-DSA micelles dominate all CW EPR spectra

(**Figure 8.3B+C**). Such dimensionality features largely correspond to findings in previous studies on different planar systems of, e.g., spin-diluted micelles giving values of $D = 2 - 3$.[116–119] An overview of pH-dependent background dimensionalities is given in **Figure F10**.
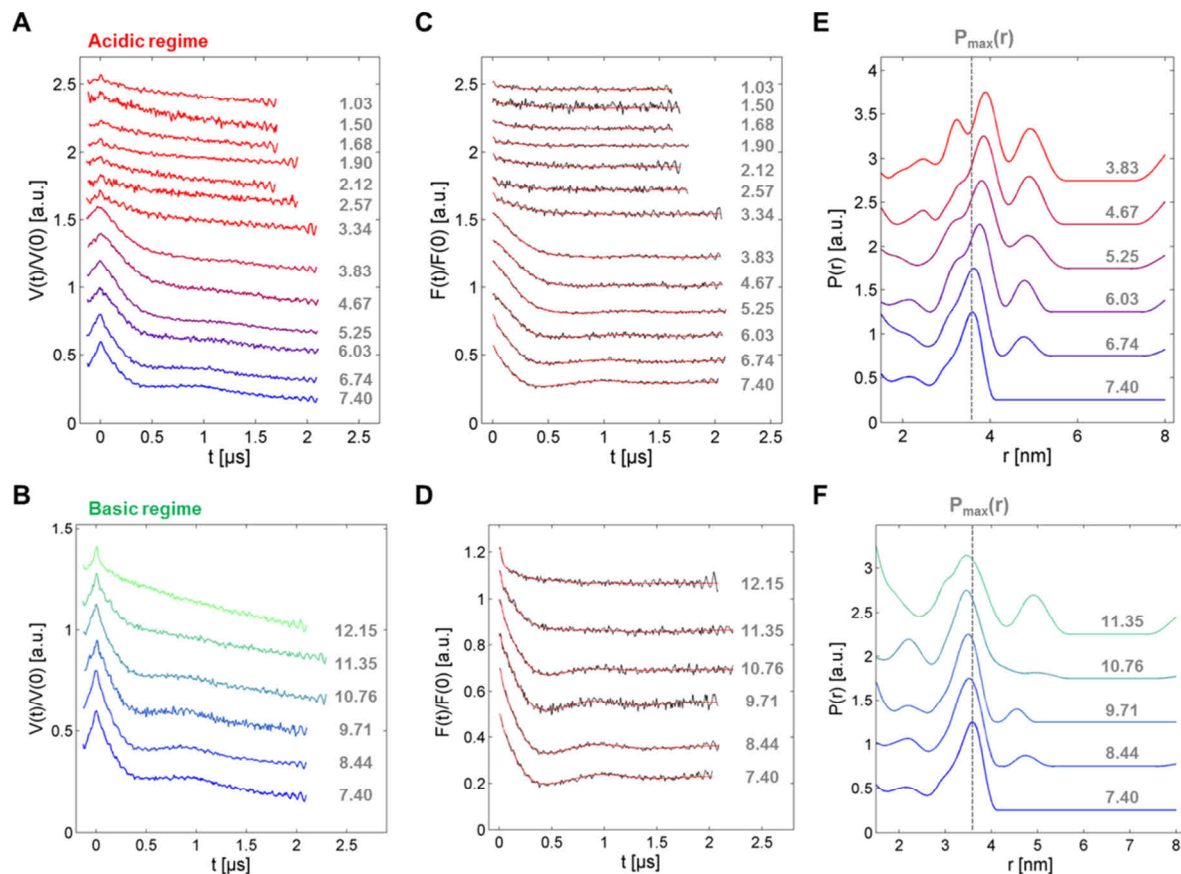
Figure 8.8 | DEER experiments on 16-DSA-probed HSA at various pH values. All DEER data were recorded from 16-DSA-probed HSA solutions in the range from pH 1.03 – 12.15 and are subdivided in acidic (pH ≤ 7.4) and basic (pH ≥ 7.4) experimental data. The fatty acid loading ratio was set to 16HSA 120 at 0.17 mM equivalents. Raw DEER time traces $V(t)/V(0)$ are shown in (**A**) the pH range from 1.03 – 7.40 and (**B**) pH 7.40 – 12.15. Dipolar evolution functions $F(t)/F(0)$ (black) with regularized fits (red) are shown in the range (**C**) from pH 1.03 – 7.40 and (**D**) pH 7.40 – 12.15. Distance distributions $P(r)$ from data shown in (**C**) and (**D**) are shown in (**E**) from pH 3.83 – 7.40 and (**F**) pH 7.40 – 11.35. The gray dotted lines in (**E**) and (**F**) are an aid to the eye for indicating relative changes in $P_{max}(r)$ compared to physiological conditions at $r = 3.58$ nm (pH 7.40). All samples were prepared in DPBS buffer equipped with 20% v/v glycerol.

Unfortunately, the pH region where the molten globule state of HSA is supposed to form (pH 2.0) does neither exhibit features of a regain or loss in ordered ligand alignment, nor detectable changes modulation depth Δ. However, this is in agreement with CW EPR data at 120 loadings (**Figure 8.5A** and **Figure 8.7A**). With the domination of micellar contributions in DEER time traces and the absence of any dipolar modulation it has to be assumed that an interpretable shape of $P(r)$ is not detectable from 16-DSA ligands for the molten globule state in HSA. Although a substantial amount of the stearic acid derivatives still interact with HSA at this low pH, the spin probes from micellar fractions in DEER samples obviously suppress the extraction of protein-associated information. Besides a general fanning out of individual distance peaks in $P(r)$ that corresponds well with an increase in

ligand disorder in the acidic pH regime (**Figure 8.7A**), close inspection of the distance distributions in **Figure 8.8E+F** reveals a general shift in the maximum probability density of $P(r) = P_{max}(r)$ that is depicted as a function of pH in **Figure 8.9A**.
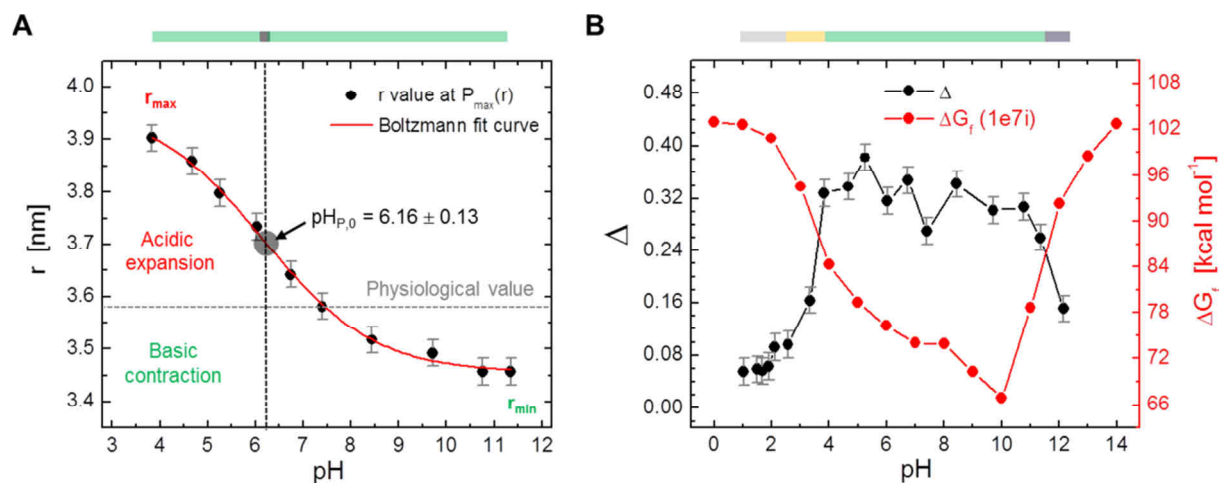
Figure 8.9 | Parameter shifts during pH denaturation of 16-DSA-probed HSA from DEER data. (**A**) The pH-induced variation of the main distance peaks from $P_{max}(r)$ in **Figure 8.8E+F** (black) are shown together with a sigmoidal fit curve (red) in the compact form (C) of HSA. Error bars are related to the resolution ($\Delta r = 0.025$ nm) in corresponding distance distributions. The gray dotted line gives the physiological distance value for pH 7.40 and the black dotted line indicates the midpoint ($pH_{P,0}$) from the sigmoidal fit from equation 8.5. Additionally, the trend in acidic expansion (red) and basic contraction (green) is indicated as proposed in Qiu *et al.*[44] with r_{max} and r_{min} highlighted. (**B**) The variation in corresponding modulation depths Δ is given as a function of pH (black) together with the stability curve of HSA loaded with seven stearic acids (red, PDB ID: 1e7i)[55] as given in **Figure 8.1A**. Significant and comparable modulation depths from DEER data are only observed in the compact form (C) of HSA. Error bars for modulation depths Δ are given as suggested in Bode *et al.*[120] with $\Delta\Delta = 0.02$.

This charge-induced peak shift in $P_{max}(r)$ with pH exhibits a sigmoidal curve shape that can be reproduced by a Boltzmann-type of function:

$$r(\text{pH}) = r_{min} + \frac{(r_{max} - r_{min})}{(1 + e^{(\text{pH}-\text{pH}_{P,0})/d\text{pH}_{P,0}})} \tag{8.5}$$

with extrapolated values for $r_{max} = 3.96$ nm and $r_{min} = 3.46$ nm ($\Delta r_{pH} = 0.50$ nm) with a correlation coefficient of $R^2 = 0.9972$ (see **Table F10**). The midpoint $\text{pH} = \text{pH}_{P,0} = 6.16 \pm 0.13$ gives the inflection point of the fit curve and $d\text{pH}_{P,0}$ is related to the width of this hypothetical transition from r_{min} to r_{max}. Note, that $\text{pH}_{P,0}$ is again close to the calculated isoelectric point pI = 5.79 where HSA's net charge should be $Q = 0$. Furthermore, the shift in $P_{max}(r)$ corroborates the picture of a proposed acidic expansion and basic contraction of HSA[44] as detected from bound messenger ligands. The pH-dependent modulation depths Δ in **Figure 8.9B** are schematically combined with the calculated stability curve of HSA loaded with seven stearic acids (see also **Figure 8.1A**, PDB ID: 1e7i).[55] This graphical comparison elucidates that the general emergence of modulation depths (here: $\Delta > 0.26$) can be effectively correlated to a rather stable and compact state (C) of HSA that strongly binds 16-DSA

ligands. The F form is here identified by the region of strong changes in Δ in between pH 2.57 and 3.83. However, no characteristic modulation depths are detected that would help to identify the presence of a molten globule, but similar to the pH-dependent $A_{//}$ values in **Figure 8.5A**, a stable, compact (C) and largely functional pH region can be identified between about pH 3.83 and 11.35. Note, that the increasing ligand disorder S below pH 6 is mirrored by the emergence of additional peaks in $P(r)$. The main characteristics from parameter analyses of bound spin probes ($A_{\|}$, A_{zz}, $\Delta B_{0,pp}$, S and $P(r)$) are summarized in **Table 8.3**.

Table 8.3 | Characteristics observed from 5- and 16-DSA probed HSA

Observable	Parameter	5HSA 120	16HSA 120	16HSA 110
$A_{\|}$	pH_{MG}	2.13 ± 0.13	–	1.90 ± 0.14
	$I_{A,MG}$ [G]	-0.80 ± 0.02	–	-1.05 ± 0.18
A_{zz}	$A_{zz,MG}$ [G]	34.6 ± 0.5	33.6 ± 0.4	33.5 ± 0.4
	$A_{zz,pH}$ [G]	34.1 ± 0.3	34.0 ± 0.3	34.0 ± 0.3
$\Delta B_{0,pp}$	pH_{MG}	2.16 ± 0.37	1.87 ± 0.95	2.01 ± 0.13
	$I_{B,MG}$ [G]	(≤ -0.50)	(≤ -0.20)	-0.20 ± 0.01
	$pH_{B,0}$	6.25 ± 0.08	6.21 ± 0.06	6.01 ± 0.07
	I_B [G]	-0.76 ± 0.05	1.37 ± 0.03	0.92 ± 0.02
S	pH_{MG}	–	–	2.31 ± 0.57
	$I_{S,MG}$	–	–	0.033 ± 0.006
	$I_{\gamma,MG}$ [°]	–	–	2.21 ± 0.43
$P(r)$	$pH_{P,0}$	–	6.16 ± 0.13	–

8.2.5 | DLS experiments on HSA between pH 1.01 – 12.31

In order to complement the findings from DEER experiments the obtained averaged hydrodynamic radii (R_H) from DLS experiments on HSA are shown in **Figure 8.10**. Although it only serves as a reference experiment for elucidating the pH-dependent solution size of HSA, the obtained results are in very good agreement with prevalent literature[121–123] ranging from 3.33 ± 0.24 nm in the compact C form to 4.25 ± 0.27 nm in the E form.
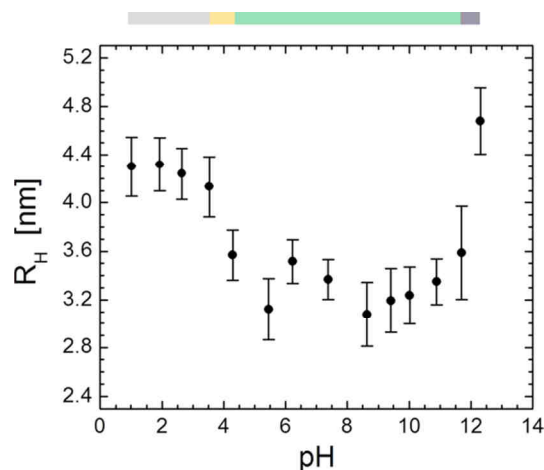

Figure 8.10 | pH-dependent DLS experiments on HSA.
Hydrodynamic radii R_H of HSA are given as a function of pH. The phase space bar gives the extended form (E, gray), compact form (C, green) and the aged form (A, purple) that are clearly separated. A fast migrating form (F, yellow) is assumed to appear in a narrow range between pH 3.5 and 4.3.

Another pH-induced increase in the hydrodynamic radius of HSA can be seen in its aged form (A) for pH > 11.7, when R_H reaches values about 4.68 ± 0.27 nm. Very similar results have been described by Tanford *et al.*[124] for BSA at a comparable ionic strength of $I = 0.15$ M. The F form is here indirectly detected to occur in a quite sharp range between 3.5 < pH < 4.3 and no specific hydrodynamic size is here determined. Strong deviations in the obtained values from the real R_H values of albumin due to the electroviscous effect[125] are not expected as it was already ruled out by Tanford and Buzzell.[80] Although several measurements were averaged to obtain an individual data point, DLS experiments are most probably not sensitive enough for detecting slight structural rearrangements of $\Delta R_H < 0.3$ nm assuming an intrinsic sensitivity of about 5 – 10 % in this method.[126] However, note that the pH-dependent modulation depths Δ from DEER experiments (**Figure 8.9B**) are qualitatively reproducing this curve shape in DLS quite well.

8.3 | Discussion

All previously reported pH-induced conformational isomers of HSA could be discovered by CW EPR spectroscopy (E, F, N, B and A),[43,44] including the somewhat enigmatic molten globule (MG) state at about pH 2.[30,31] This was facilitated by screening the samples in the pH range from pH 0.7 – 12.9. Spin probing HSA with 5-DSA and 16-DSA, as well as spin labeling HSA with 5-MSL turns out to yield information of exceptionally intricate but valuable information that will be correlated in the following. Therefore, stability and charge curves (**Figure 8.1**) served as a reference for better understanding the EPR spectroscopic features emerging at the isoelectric point (pI = 5.79) and in the region of HSA's optimum stability (pH$_{opt}$ = 9.80). Throughout all observed parameters there were several invariant features that can be indirectly, but clearly assigned to certain functional features that are not always self-evident, as e.g the molten globule state (MG), the isoelectric point and the optimum stability of albumin. A complete list of significant pH values of structural isomerization and fatty acid based features is given in **Table F11**. Consequently, all recurrent and pH-invariant features were combined and averaged across all applied experiments and analyses yielding significant values of functional and structural singularities. Thus, a pH-induced functional phase space can be constructed as presented in **Figure 8.11**.

Basically, the results can be subdivided in items that can be extrapolated from protein-based findings of covalent (5-MSL: $A_\parallel$ and τ_c), non-covalent interactions (5-DSA and 16-DSA spin probes are either bound (b_1 and b_2): $A_\parallel$, A_{zz}, $\Delta B_{0,pp}$, S, γ, $P(r)$ or free (f and a): I_{abf}, h_{-1}/h_0)) from EPR-active nitroxide reporter groups that exhibited sufficient stability throughout all applied pH values. Additional aspects from the solution shape of HSA were obtained in DLS experiments.

The compact C form of HSA ranges from the onset of the F form (pH$_F$ = 4.0 ± 0.4) towards the onset of the A form (pH$_A$ = 11.2 ± 0.3) and can be similarly observed from free (interval: [pH$_a$, pH$_f$]) and bound ligands (interval: [pH$_F$, pH$_A$]). Furthermore, the C form can be subdivided in two norm forms that are separated by the intermediate basic form, so that C comprises the phases N$_1$, B and N$_2$

(interval: $[N_1, N_2]$). DEER-derived parameters (Δ, D and $P(r)$) are also found to be exceptionally sensitive for compactness and sample homogeneity and provide valuable and consistent insights about the structural integrity of the protein.

The B form is characterized by a strong increase in lysine rotational dynamics (τ_c) as observed from 5-MSL (**Figure 8.2B**), from a maximum motional restriction of 5- and 16-DSA spin probes ($\Delta B_{0,pp}$), or maximum compactness of the protein interior as monitored by 5-DSA ($A_\parallel$). Intriguingly, the onset of the B form coincides with a maximum ligand ordering (S_{max}) where least dynamic ligand fluctuations occur (γ_{min}) at about the physiological pH value (pH$_S$ = 7.6 $\pm$ 0.2). Moreover, the appearance of the B form ends when maximum compactness of HSA is achieved at pH$_{opt}$ = 9.6 $\pm$ 0.2.

The A form is generally well-detected by a loss in protein compactness as monitored by $A_\parallel$ in CW EPR (5-MSL HSA or 16-DSA probed HSA) or further parameters from DEER. This happens as a consequence to the basic loss in structural features that are also accompanied with ligand release (pH$_f$ = 11.4 $\pm$ 0.1). However, the linewidths ($\Delta B_{0,pp}$) were found to yield ambiguous curve shapes in this pH range for 5-DSA, as well as for 16-DSA. Evaluation of the order parameter (S) exhibited similar issues due to the continuous and smooth curve progress.

The onset of an E form of HSA could be easily detected for all spin probed and spin-labeled HSA samples by mainly tracing an increase in $A_\parallel$, $\Delta B_{0,pp}$, Δ or τ_c with the onset of the F form (pH$_E$ $\leq$ 2.9). Beyond that, the E form is not necessarily a linear dynamic region but may exhibit features that allow for the identification of an acidic molten globule (MG) state at pH$_{MG}$ 2.0 $\pm$ 0.1.

The molten globule state is here exclusively observed from spin probing experiments and it is generally best characterized by an increase in rotational motion of all applied paramagnetic ligands ($\Delta B_{0,pp}$ of 5-DSA and 16-DSA). All relevant curve features in this concern could be extrapolated with Gaussian-shaped fit curves in order to determine precise minima positions and their widths (average width: σ_{MG} = 0.29 G). From the obtained order parameters and wobbling angles of 16-DSA-probed HSA (110 loading) it can be concluded that the ligands exhibit an intermediate state of highest disorder during the emergence of the molten globule state and therefore a maximum in mean angular fluctuations of the ligand is observed. The compactness of the protein as monitored by $A_\parallel$ appears to be also slightly depleted in the molten globule state. Although A_{zz}-values remain largely constant across all pH (34.0 $\pm$ 0.3 G for all loadings and probes, **Table F6**), the difference in probed polarity of 5-DSA and 16-DSA has a significant global maximum at pH 2.0 ($\delta A_{zz,MG}$ = 1.1 $\pm$ 0.5 G). This means that a slight polarity inversion takes place in the MG state, while the protein interior (5-DSA) becomes more solvent-accessible and the probed surface (16-DSA) becomes more hydrophobic. Thus, the $A_\parallel$ values are slightly biased by this polarity effect, but the simultaneous increase in ligand mobility seems to outweigh this ambiguity in a direct comparison to the associated linewidths ($I_{A,MG}$ > $A_{zz,k,MG}$). Additionally, the large uncertainties in data readouts from $A_\parallel$ reinforce the notion that the center-field linewidths $\Delta B_{0,pp}$ with changes of about 0.2 – 0.5 G serve as the most reliable parameter for the detection of MG states in spin probing experiments as polarity effects are absent.

Generally, the ANS-based detection of molten globule states[20] is therefore rivaled by the applied spin probes. These paramagnetic probes can be considered as EPR-spectroscopic ANS analogues as the MG states can be identified. However, the emerging spectral features are not always clearly pronounced. For higher loadings of 16-DSA (120) these features appear to be additionally blurred or even cancelled out. Currently, further studies are conducted in order to quantitatively characterize the relative sensitivity of ANS and spin probes in this concern.

Setting up an auxiliary parameter (I_{abf}) for monitoring relative changes in free and micellized spin probe fractions is straightforward and gives a clear notion about pH-induced affinity changes of HSA towards fatty acids. However, 5-DSA-probed HSA did not show large sensitivities in this kind of analysis. Nonetheless, the associated curve features from 16-DSA-probed HSA exhibited compelling transition regions for both loading ratios (110 and 120) that were analyzed with Boltzmann shaped fit curves. A maximum rate of micelle formation was extracted with high precision at $pH_{a,0} = 3.45 \pm 0.01$ and was found to be independent of the loading status of HSA. The pH range where practically all spin probes are bound also has an inflection point at $pH_{b,0} \approx 6$. This feature is ascribed to relative changes in internal fatty acid dynamics that mainly show two differently immobilized types of bound fatty acids (b_1 and b_2) as presented in Muravsky et al.[73] with an obvious effect on the signal height $h_\perp$. An exemplary spectral simulation has been employed to certify this conclusion (**Figure 8.3D** and **Figure F3**). In order to precisely extract the main pH-induced onsets of fatty acid release, Nelder[82] model fit curves have been applied that facilitated the extrapolation of precise acidic ($pH_a = 4.3 \pm 0.1$) and basic ($pH_f = 11.4 \pm 0.1$) minimum features. This defines the compact state (C) of HSA in the viewpoint from free fatty acid ligands. Here, it should be mentioned that the pK_a value of the fatty acids (16-DSA) also falls in the range of pH_a. The corresponding ligand protonation has an additional effect on HSA's ligand affinity, as the partial electrostatic nature of ligand,[127] or more specifically fatty acid association to albumins is well-known.[55,75,106,128–130]

The emergence of an increase in h_{-1}/h_0 at $pH_{f,0} \approx 6.2$ indicates the charge-induced release of 16-DSA molecules. It is proposed that this is due to the emergence of the isoelectric point where the net charge of HSA is $Q = 0$ and fatty acids experience the absence of electrostatic forces. An inverse peculiarity was observed for BSA at pH 6 where fatty acid binding exhibits an overall maximum affinity to the protein as observed from 12-DSA.[72] Although it was proven that HSA experiences a shift in pI from 5.6 to 4.8 upon fatty acid binding,[58] EPR-based spectral characteristics that would indicate a distinct detectability of such an isoelectric point from the protein alone remain vague.

While the probed compactness (Δ, R_H, $A_\parallel$) of HSA remains largely unaffected at pH 6, internal fatty acid dynamics ($\Delta B_{0,pp}$) experience strongest changes ($pH_{B,0}$). Whereas 5-DSA exhibits an intermediate state of minimum motional restriction at $pH_{B,0} = 6.2$, the 16-DSA-derived curves (**Figure 8.6C**) reveal that it is a transition from an acidic unrestricted motion towards a basic restricted motion in the range from about pH 3 – 9. A complementary picture was obtained from distance distributions $P(r)$ from DEER experiments on the pH-dependent 16-DSA ligand alignment in HSA.

Meaningful distance distributions are only observed in the C form of HSA ranging from pH 3.8 – 11.4, when a sufficiently large fraction of the HSA molecules has two ligands bound. Additionally, in the aged form (A) as observed in DEER (pH > 11.4) no considerable distance distribution was obtained, although no micelles are present in solution. Since the fatty acid binding sites are mostly situated at internal hydrophobic interfaces of secondary structure elements in HSA, in particular α-helices,[55,129] the loss in the DEER signal also reflects the loss of some well-defined ligand binding sites by partial denaturation. The DEER-derived peak shift of $P_{max}(r)$ in the distance distributions from the compact C form (**Figure 8.9A**) could be fitted with a sigmoidal function that confirmed the picture of an acidic expansion and basic contraction of HSA.[44] Again, an inflection point at $pH_{P,0} = 6.16$ of this curve was found for this self-assembled system. However, in DEER the system is here only observed from the paramagnetic, EPR-active ligands' point of view and might as well indicate, at least a partial, charge-induced electrophoretic inside/outside migration of respective fatty acids, while the HSA protein remains compact as seen in DLS experiments (**Figure 8.10**). The experimentally observed maximum shift of $P_{max}(r)$ is considerable ($\Delta r_{PH,exp} = 0.45$ nm) compared to the observed systematic error in DEER ($\Delta r_{DEER} < 0.03$ nm for $r > 2.5$ nm)[131] and may therefore be regarded as reliable and significant. DEER distance data (**Figure 8.9A**)) also indicate a very slight reduction (~ 0.13 nm) in the average aligned fatty acid interspin distance at pH > 7.4. The ionic anchor points in hydrophobic pockets are not well conserved but mainly consist of arginines and lysines[55,129] with pK_a values between about 10.8 – 12.5.[7] Since the oppositely charged fraction of deprotonated 16-DSA molecules becomes ever larger above pH 7.4, a pure electrophoretic effect "dragging" the ligands a bit further into the protein interior appears not unlikely.

Considering the 5-MSL HSA pH denaturation experiment a drastic increase in lysine side chain mobility on the protein surface is observed in the basic regime (B). In the aged form (A) a maximum lysine mobility is observed at about pH 10.4 in EPR that can be predicted from the averaged lysine pK_a values ($pK_{a,Lys} = 10.28$, see **Figure F2**). In principle, this contradicts the hypothesis of a basic contraction, but may also explain the increased motional restriction in 16-DSA between pH 7 and pH 10 when lysines and the protruding spin probe tails (bearing the nitroxide moieties) are competing for motional freedom on the protein surface (**Figure 8.6A**).

It can be easily seen that all spin probe-based experiments obviously exhibit intriguing features at about pH 6 that can be detected either from free (*f*) or bound ligands (*b*). Since these features are close to the isoelectric point (pI), the justified assumption is made that an electrostatic activation (EA) of the spin probes takes place at $pH_{EA} = 6.1 \pm 0.2$ with $pI \approx pH_{B,0} = pH_{b,0} = pH_{f,0} = pH_{P,0} = pH_{EA}$.

During the structural weakening of HSA in the F form, the acidic onset of fatty acid release (pH $\leq$ 4.3) can also be partially explained by an electrostatic drag ($Q > +50$) that is exerted on the still deprotonated fraction of ligands. In fact, DEER data most probably show an overlap of both, HSA expansion (DLS) and electrophoretic migration of bound fatty acids that makes them leave the protein interior.

From **Figure 8.1B** it can be concluded that a compact form of HSA exists as long as the absolute value of the protein charge $|Q| < 50$. Therefore, on a very fundamental level of argumentation, HSA expands its structure (F and A) with extreme pH to compensate for the ever growing charge density ($\pm\rho_Q$) in the limiting regions of the compact state (C). As the relative magnitude of electrostatic free energy ΔG_{el} is generally much lower for elongated structures,[3] these conformational isomerizations may counteract the relative increase of ΔG_{el} in comparison to the free energy of folding (ΔG_f). Explicit calculations considering protein shape, charge screening and counterion condensation[132] are for now considered as being far beyond the scope of this study, but may deliver further interesting insights into this issue. Apart from the onset difference of the compact form in 16-DSA-probed HSA with different loading ratios (pH 3.6 (110) and pH 4.8 (120)), there is no striking evidence for fatty acid induced changes in pH stability. However, it was shown for fatty acid-free BSA that slight decreases in melting temperatures or bimodal melting curves can be induced by pH alone in the range from pH 3 – 4.[133]
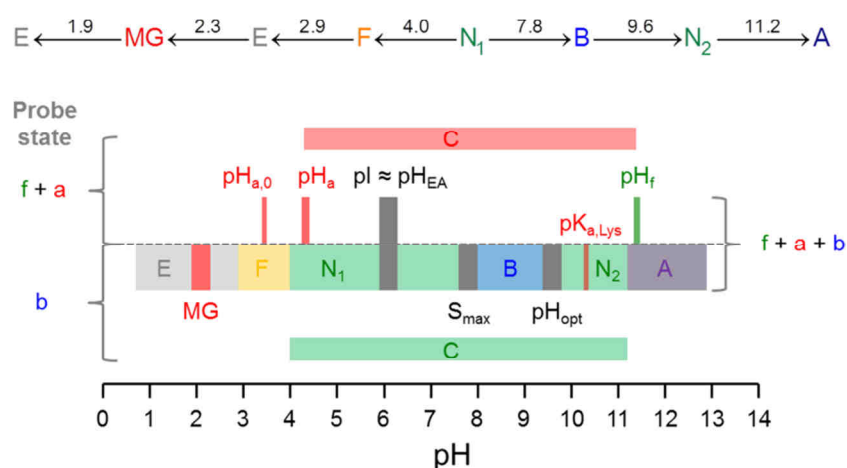
Figure 8.11 | Functional phase space obtained from pH-dependent EPR and DLS experiments on HSA. A condensed graphical overview is given about all observables from EPR spectroscopy and DLS that can be found in **Table F11**. The pH-induced conformational isomers in the elongated (E, gray), fast migrating (F, yellow), norm (N_1 and N_2, green), basic (B, blue) and aged form (A, purple) are identified in an averaged phase space bar in the range from pH 0.7 – 12.9. The compact form (C) comprises the N_1, B and N_2 isomers and can be obtained from free ligand ($f + a$, red bar), bound ligand (b), 5-MSL spin labels or from DLS (green bar). The molten globule state (MG, red) and the pH of maximum ligand order (S_{max}, black) are exclusively obtained from spin probing experiments. An isoelectric point (pI, black) can be extrapolated from both, the bound and free ligands ($f + a + b$) and is detected as an electrostatic activation of ligands (pH_{EA}). The I_{abf} parameter monitors the behavior of the free ligands and elucidates the acidic (pH_a) and basic onset of fatty acid release (pH_f) with a clearly extractable maximum rate of micelle formation ($pH_{a,0}$). The point of maximum stability of HSA (pH_{opt}) as well as the collective lysine pK_a ($pK_{a,Lys}$) can be either calculated, or are also detected in several EPR-based data sets (see **Chapter 8.2.1**). The color-coded isomerization scheme (top) is given with corresponding averaged pH values with N_1 as the main functional, physiological cardinal point.

This claim should be also valid for slight discrepancies in the onsets of individual dynamic regimes when comparing DLS and 5-MSL spin labeling to the 16-DSA spin probing approach. From the averaged values, all phase onset standard deviations are smaller than $\Delta pH = 0.4$ (**Table F11**).

The pH-induced manipulation of HSA's structural integrity was here successfully observed, again revealing the high structural plasticity of HSA.[36,44] A slight drawback concerning the results from DEER experiments is the immense amount of required time-expensive experiments for obtaining

sufficient pH resolution as well as the onset of micelle formation below pH 3.8. Nevertheless, recording an additional set of pH-dependent DEER data from 5-DSA probed HSA should reveal further interesting structural data for proving the validity of an acidic expansion and basic contraction of the protein (**Figure 8.9A**).

Recently, a study was published that also employed EPR spectroscopy in combination with rheology concerning the temperature- and pH-induced gel formation in albumins, however at much higher protein concentrations. It could be shown, that different macroscopic gel properties can be tuned with appropriate pH adjustments that are also based on the occurrence of these conformational isomers. Optimum control of these properties may therefore yield interesting biocompatible materials and drug delivery vehicles in medical applications.[134]

From this study it remains yet unsettled to which extent pH-sensitive EPR-active imidazolidine spin labels (IMTSL),[135] or lipid spin probes (IMTSL-PTE)[136] may contribute to a better understanding of HSA's phase space due to their intrinsic capability to act as internal pH and polarity sensors.[137–139] This direct detection of pH-dependent surface potentials of HSA might reveal further or more precise information about the complex interplay of albumins charge and shape. Additionally, further progress is expected by rigorous simulation of CW EPR spectra that facilitates extraction of dynamical parameters as ligand binding affinities (K_A) and rotational correlation times (τ_c), however, an explicit treatment of this issue is far beyond the scope of this analysis. It may be anticipated that this EPR-spectroscopic spin probing approach with paramagnetic fatty acid derivatives may rival alternatives as fluorescence-based (quantum dot = QD) studies that are usually insensitive to extreme pH values, limited to certain pH ranges and associated sensitivities,[140] or are subject to photodecomposition[141] and aggregation,[142] however, with the latter property being intrinsic to fatty acids, too. This approach may be as well expanded to pH-dependent, self-assembled systems of ligand and protein of other albumins and beyond.

8.4 | Materials and Methods

Materials. Lyophilized HSA powder (>95%, Calbiochem), 5-DSA, 16-DSA (Sigma-Aldrich), 5-MSL (Santa Cruz Biotechnology) and glycerol (87 wt% in water, ACROS) were used without further purification. The 0.137 M DPBS buffer[143] pH 7.4 was prepared according to the procedure described in **Appendix C1**. The preparation of 0.12 M DPBS titration buffers in the range from pH 0.2 – 13.5 containing up to 0.6 M HCl and 0.4 M NaOH is given in **Appendix C2**.

Protein Stability and Charge Calculation. For stability (ΔG_f) and charge (Q) calculations as presented in **Figure 8.1** and **Table 8.1** the web-accessible program PROPKA 3.0 was used employing the AMBER forcefield.[8,52,53] The original HSA topology files (PDB ID: 1BM0 and PDB ID: 1e7i)[54,55] were cleaned from dispensable components such as additional albumin molecules (PDB ID: 1BM0, contains two HSA molecules as a dimer), residual ions and water molecules in order to obtain comparable results. An average $pK_{a,Lys} = 10.28 \pm 0.89$ was calculated from 58 out of a total of 59 Lysine residues in the primary structure from a cleaned structure (PDB ID: 1BM0) for obtaining an estimate for the highest 5-MSL mobility from EPR data (see **Appendix F2**) that can be correlated with $pK_{a,Lys}$.

5-MSL Spin Labeling of HSA. The spin-labeled HSA samples were obtained by incubating 4 – 8 ml of 0.2 mM albumin in 0.136 M DPBS buffer pH 7.4 for 16 – 24 h at room temperature with a 5-fold molar excess of 5-MSL and 1% ethanol. The resulting 5-MSL HSA molecules were separated from unreacted label with PD-10 columns (GE Healthcare) containing Sephadex G-25 resins. Individual fractions were collected and tested for protein content with Bradford reagent[144] and an additional CW EPR spectroscopic quality control. The purified 5-MSL HSA solutions were concentrated with spin columns (Vivaspin® 2 and Vivaspin® 4, 10.000 MWCO, Sartorius AG) and a benchtop centrifuge (Centrifuge 5810 R, Eppendorf AG) to about 0.3 – 0.5 ml stock solutions. A commercially available BCA[145] assay (Pierce™ BCA Protein Assay Kit, Thermo Scientific) was used for quantification of stock solution protein content ($c_{5\text{-MSL HSA}}$ = 1.12 – 1.35 mM) as described in **Appendix C5**. The BCA absorption values were recorded with a UV/Vis spectrometer (Hewlett Packard HP 8453 and HP 89090A) at a characteristic wavelength of λ = 562 nm. The total 5-MSL HSA yield of the spin labeling procedure is about 65–70% of the initially applied amount of pure HSA. An explicit preparation and purification procedure for 5-MSL HSA was already shown in the Bachelor thesis of B. Sc. Chem. Marie-Therese Oehmichen[146] and is performed in analogy to the scheme given in **Appendix G1** by simply replacing MTSSL with 5-MSL.

Sample Preparation. All spin probed EPR samples were prepared from 1 mM HSA stock solutions in 0.137 M DPBS buffer pH 7.4 to final protein concentrations of 0.40 mM for CW EPR and 0.17 mM for DEER experiments with a sample volume of 100 – 300 µl. Upon addition of appropriate amounts of 26 mM stock solutions of 5-DSA and 16-DSA spin probes in 0.1 M KOH nominal equivalent concentrations of 1:1 ($c_{16\text{-DSA}}$ = 0.40 mM) or 1:2 (c_{DSA} = 0.80 mM) were adjusted for CW EPR samples and 1:2 for DEER samples ($c_{16\text{-DSA}}$ = 0.34 mM). Additionally, a 16-DSA reference sample containing 0.4 mM spin probe without HSA was also prepared. The 5-MSL HSA samples were prepared at concentrations of 0.09 mM in 0.137 M DPBS pH 7.4. All EPR samples that are shown in **Figure 8.2** and **Figure 8.3A–C** were individually prepared with a 20 – 25 % titration volume for adjusting pH values with the predefined set of acidic and basic 0.12 M DPBS buffers in the pH range from 0.2 – 13.5 as described above. All pH values were carefully controlled with a thoroughly calibrated pH microelectrode (Mettler Toledo InLab®Micro pH 0 – 14 in combination with the EL20 pH meter). It is estimated from several consequent calibrations with reference buffers pH 1 – 12 (ROTI® CALIPURE, Carl Roth) that the maximum error in this pH range is about ΔpH_{exp} < 0.15 (**Appendix C2**). Depending on the pH range of the dynamic regimes, pH spacings were adjusted in the range from 0.14 to 0.73 for all CW EPR experiments. The final 0.1 M DPBS solutions of HSA equipped with 16-DSA and 5-MSL are supplied with 20% v/v glycerol for internal comparability and to prevent crystallization upon freezing for potential DEER experiments. Compared to EPR samples, the preparation of 0.1 mM HSA samples for DLS was conducted without addition of 16-DSA and glycerol. The final protein concentrations were adjusted with DPBS titration buffers to a final sample volume of 500 µl and in the range from pH 1.01 – 12.31.

For CW EPR measurements, about 15 µl of sample were filled into a quarz capillary (BLAUBRAND® intraMARK) with ca. 1 mm outer diameter. For DEER measurements about 80 µl of the final solutions were filled into 3 mm (outer diameter) quartz tubes (Heraeus Quarzglas) and shock-frozen in liquid nitrogen-cooled 2-methylbutane.

Dynamic Light Scattering (DLS). All DLS data were obtained with an ALV-NIBS high performance particle sizer (HPPS) equipped with an ALV-5000/EPP Multiple Tau Digital Correlator (ALV-Laser Vertriebsgesell-schaft m. b. H.). This device uses HeNe-LASER irradiation with a typical wavelength of λ = 632.8 nm and 3 mW output power with an automatic attenuator for optimum count rates recorded in a backscattering detection angle of 173°, relative to the incident monochromatic light. The sample cell temperatures were adjusted to T = 25°C by a Peltier temperature control unit. All samples were measured in 1.5 mL PMMA semi-micro cuvettes (BRAND). Data were extracted from the intensity correlation functions by a $g_2(t)$-DLS exponential and a mass weighted regularized fit in the ALV-NIBS software v.3.0 utilizing the CONTIN algorithm.[147] The refractive index and solvent viscosity were assumed to be constant at n_{H2O} = 1.332[148] and η = 0.89 mPa·s,[149] respectively. A significant viscosity increase of the solutions due to the electroviscous effect[125] and intrinsic viscosity [η] can be ruled out for the applied albumin concentration.[80] Each sample was measured five times at constant pH and temperature for 120 s and a mean value R_H was calculated. The pH-dependent mean values R_H of the most prominent particle size peaks and their statistical fluctuations are given as the standard deviation as depicted in the error bars in **Figure 8.10**. Besides some additional calibration experiments, these data sets were collected by B. Sc. Chem. Marie-Therese Oehmichen during her Bachelor thesis.[146]

EPR Spectroscopy. *CW EPR Experiments:* A Miniscope MS400 (Magnettech GmbH) benchtop spectrometer was used for X-band CW EPR measurements (**Figure 8.2**, **Figure 8.3**, **Figure F1** and **Figure F3**) at microwave frequencies of 9.43 GHz that were recorded with a frequency counter (RACAL-DANA, model 2101, or with Magnettech FC400). Low-temperature measurements for pure A_{zz} extraction[150] at $T = 150$ K were conducted with modulation amplitudes of 0.2 mT, a sweep width of 15 mT and microwave powers of $P_{MW} = 3.16$ mW (**Figure F1A** and **Figure F7A–C**). All other measurements were performed at $T = 25°C \approx 298$ K, using modulation amplitudes of 0.1 mT and a sweep width of 12 – 15 mT at microwave powers ranging from $P_{MW} = 1.00 – 3.16$ mW.

DEER Experiments: The 4-pulse DEER sequence:[113,114]

$$\pm(\pi/2)_{obs}-\tau_1-(\pi)_{obs,1}-(t_d+t_0+N_t \cdot \Delta t)-(\pi)_{pump}-(t'-N_t \cdot \Delta t + t_d)-(\pi)_{obs,2}-\tau_2-echo$$

was used to obtain dipolar time evolution data from paramagnetic 16-DSA spin probes at X-band frequencies of 9.1– 9.4 GHz with a BRUKER Elexsys E580 spectrometer equipped with a BRUKER Flexline split-ring resonator ER4118X–MS3 (**Figure 8.8**). The temperature was set to $T = 50$ K by cooling with a closed cycle cryostat (ARS AF204, customized for pulse EPR, ARS, Macungie, PA) and the resonator was overcoupled to $Q \approx 100$. The pump pulse position $t_d + t_0$ after the first observer π-pulse deadtime t_d was typically incremented for N_t timesteps of $\Delta t = 8$ ns in the range $t_0 + t' = \tau_1 + \tau_2 - 2t_d$, whereas τ_1 and τ_2 were kept constant. Proton modulation was averaged by addition of eight time traces of variable τ_1 starting with $\tau_{1,1} = 200$ ns, incrementing by $\Delta\tau_1 = 8$ ns and ending up at $\tau_{1,8} = 256$ ns. Additionally, a 2-step phase cycle ($\pm$) was applied to the first $\pi/2$ pulse of the observer frequency for cancelling out receiver offsets and unwanted echoes. The pump frequency ν_{pump} was set to the maximum of the field swept electron spin echo (ESE)-detected spectrum. The observer frequency ν_{obs} was set to $\nu_{pump} + \Delta\nu$ with $\Delta\nu$ being in the range of 65 MHz and therefore coinciding with the low field local maximum of the nitroxide ESE spectrum. The observer pulse lengths for each DEER experiment were set to 32 ns for both $\pi/2$– and π–pulses and the pump pulse length was 12 ns.

Data Analysis: For CW EPR experiments a sweep width correction factor $k_{SW} = 0.9944 \pm 0.0021$ was obtained from a Manganese standard Mn^{2+} in ZnS (Magnettech GmbH) to correct the magnetic field readout values $B(x_i)$ from corresponding spectra. The corrected apparent hyperfine coupling constants ($k_{SW} \cdot A_{//}$) from 5-MSL HSA (**Figure 8.2B**), 5-DSA and 16-DSA spin probed HSA (**Figure 8.3A–C**) were calculated from outer extrema separations $2A_{//}$ of corresponding CW EPR spectra as described in **Appendix F1**.

In order to estimate collective rotational correlation times τ_c from multi-component CW EPR spectra of 5-MSL HSA a classical approach from lineshape theory (**Figure F1** and equations F.8 and F.9)[34,151] was chosen as it is also presented in **Chapter 10**. The required magnetic parameters (*g*- and *A*-tensor) of the 5-MSL spin label were either taken from Marzola *et al.* ($g_{xx} = 2.0084$, $g_{yy} = 2.0061$, $g_{zz} = 2.0025$),[152] or were determined from an approach described in Meirovitch and Freed,[153] yielding $A_{xx} = A_{yy} = 5.91 \pm 0.13$ G and $A_{zz} = 35.78 \pm 0.20$ G corresponding to an isotropic hyperfine coupling of $a_{iso} = 15.86 \pm 0.04$ G for an axial symmetric nitroxide geometry. These values largely correspond with prevalent literature.[152,154] An explicit description of this approach can be found in **Appendix F1**.

Exemplary simulations on 16HSA 010 0400 mM and 16HSA 120 0400 mM have been conducted with the MATLAB-based EasySpin program package[155] for extracting all emerging subspectra ($F_i(B) \in a, f, b_1, b_2$) and the magnetic *g*- and *A*-tensors (**Appendix F3**). This was considered as necessary for the construction of order parameters S and wobbling angles γ. Mathematical details about analyses of I_{abf}, $A_{\parallel}$, A_{zz}, $\Delta B_{0,pp}$, order parameter (S) and wobbling angle (γ) curves are given in **Appendix F4–8**. All fit curves and corresponding parameters were generated with Microcal Origin.

All raw time domain DEER data in **Figure 8.8** were analyzed and processed in a consistent global manual fit procedure with DeerAnalysis2013[156] utilizing Tikhonov regularization. The regularization parameter has been set to $\alpha = 100$ for all dipolar evolution functions obtained from 16-DSA in order to produce comparable distance peak resolutions in the investigated pH range. Special emphasis has been placed on the region from $3.83 < pH < 11.35$. In this pH region, the background dimensionality has been set to $D = 3.73 \pm 0.01$, with a deviation from a homogenous 3-dimensional background emerging from the specific size and shape of the albumin molecule as it was pointed out in **Chapter 5**.[36,115] The sigmoidal curve fit to the pH-dependent shift in

$P_{max}(r)$ was also conducted with Microcal Origin. Measurements at pH < 3.83 were only evaluated to yield modulation depths Δ and rough estimates of background dimensionalities D. The dimensionality values at low pH could only be fitted with $2.0 < D < 3.1$ mainly indicating the dominating micellar content of the samples. For a whole set of background dimensionalities the reader is referred to **Figure F10**.

9 | Fatty Acid Triangulation in Albumins Using a Surveillance Benchmark Spin (SBS)

In this study an attempt is made to find out whether EPR spectroscopy serves as a tool to spatially correlate and resolve fatty acid-based distance distributions from DEER to individual locations of binding sites in albumins. Therefore, a strategy is presented that combines the spin labeling and spin probing approach introducing a surveillance benchmark spin (SBS). This SBS is covalently attached to albumins' surface at a defined position and should thus provide a fixed spatial reference point for monitoring consequent or simultaneous fatty acid entry. The question is raised to which extent individual albumin-bound fatty acids can be identified from the resulting DEER-derived distance distributions. In this regard, experimental results have to be substantiated with theoretical predictions from MD simulations.

9.1 | Introduction

In previous chapters, a major drawback of the established self-assembled system consisting of fatty acids and albumin[1–3] is the entanglement of multiple and partially coincident nitroxide distances in the corresponding 7×7 distance matrices,[1] that are usually obtained from a structure of albumin co-crystallized with seven stearic acids.[4] Due to the inherent lack of any spatial reference point as a consequence to statistical binding processes of fatty acids in spin probing experiments, a hybrid strategy is tested here that combines spin probing and spin labeling with the purpose to address distance peaks from DEER-derived fatty acid distance distributions to distinct locations in the protein.

This study is inspired by the earliest spin labeling experiments on albumin that were conducted with the 3-amino-proxyl,[5] or 3-maleimido-proxyl spin label.[6,7] However, this maleimido spin labeling approach typically leads to a mixture of lysine and cysteine labeled albumins,[6] as it was already discussed in **Chapter 8.** A successful attempt in exclusively targeting the highly conserved Cys34 residue[8] in HSA with the cysteine-specific MTSSL spin label was already made during the diploma thesis of Dipl. Chem. Till Hauenschild.[9] This labeling strategy on albumin was first reported by Park *et al.*[10] as a tool for investigations on albumin fragment dynamics. Recently, this approach was also adopted for proving interactions of HSA with the copper transporter Ctr1 utilizing DEER spectroscopy[11] and for investigating surface adhesion effects of BSA that was however equipped with the iodacetamine (IAA) spin label at Cys34.[12] The main interest here is focused on the fact that the albumin protein is equipped with a located, singular and covalently attached paramagnetic MTSSL moiety, generating a C34R1 single mutant that is here employed to monitor fatty acid entry.

A major effort has been undertaken from the 1950s throughout the 1970s to mathematically unravel the complex and dynamic binding behavior of long chain fatty acids to albumins.[13–18] Later on, some significant breakthroughs have been achieved with NMR and X-ray crystallography, revealing information about the chemical environment of individual binding sites[19–21] as well as the binding site locations that could be assigned by X-ray crystallography to occur as an asymmetric spatial fatty acid

arrangement.[4,22,23] Furtheron, these binding sites have been spatially correlated and assigned to high and low affinity binding sites (see also **Chapter 3.3**).[24,25]

Here, it is investigated to which extent this covalently attached paramagnetic residue may help to contribute for unraveling the complexity of the arbitrary and isotropic fatty acid alignment that was initially observed in DEER data by Junk *et al.*[1] In this regard, the intrinsic potential of this so-called *surveillance benchmark spin* (SBS) should be the tracking of the order of binding site occupation by increasing the relative ligand concentration. Additionally, this strategy is presented in a comparative view from HSA and BSA to further unravel this fundamental spectroscopic and analytical problem. DEER-derived distance distributions are then correlated with MD simulation data that are derived from appropriate molecular models that are conventionally obtained from the crystal structure of HSA containing the seven paramagnetic stearic acids (PDB ID: 1e7i, see **Figure 9.1A**).[4]

9.2 | Results

9.2.1 | Site-directed Spin Labeling of Albumins by Targeting the Cys34 Residue

Although this hybrid spin probing and spin labeling strategy appears straightforward, the preparation of appropriate samples turns out to be the most crucial step. First, both albumins were spin-labeled with MTSSL using a strategy that is described in **Appendix G1**. The application of dithiothreitol (DTT) as a sulfhydryl-reducing agent during the labeling procedure was discouraged, as even the lowest amounts of added DTT (about 1 – 10 eq) indicated a slightly deteriorating effect on protein functionality in the view of ligand affinity (**Figure G2A**). Therefore, the free sulfhydryl content of the pure albumin solutions and the spin-labeled albumin solutions was investigated with a standard Ellman's test (**Appendix G2**).[26]

These values were used together with the quantitative BCA protein assay[27] to determine the labeling efficiency similar to Berliner *et al.*[28] A further confirmation of successful MTSSL labeling to albumin was performed with CW EPR (**Figure 9.1B** and **Figure G2B**) and MALDI-TOF mass spectrometry (**Appendix G3**) with the latter one revealing weight increases of about 187 ± 9 Da for HSA and BSA as it is theoretically expected ($\Delta MW = +184.28$ Da). It could be shown by explicit spectral simulations that purified MTSSL HSA contains less than about 0.3% of residual free label. Furthermore, bound MTSSL exhibits dynamic regimes of strong (68.0%) and weak immobilization (31.7%),[9] intriguingly similar to the observations made from the dynamics of bound fatty acids (b_1 and b_2, see **Chapter 7** and **Chapter 11**). Furthermore, a very nice correspondence is found in the experimental molecular weights of pure HSA and BSA when compared to the formerly calculated values that are given in **Table 6.1** with a deviation of less than 0.009 kDa throughout. CW EPR spectra of MTSSL albumins resemble the reported lineshapes in Park *et al.*[10] quite well and are indicative for strongly immobilized MTSSL by covalent attachment to the protein with few residual unreacted labels present (**Figure 9.1B**).
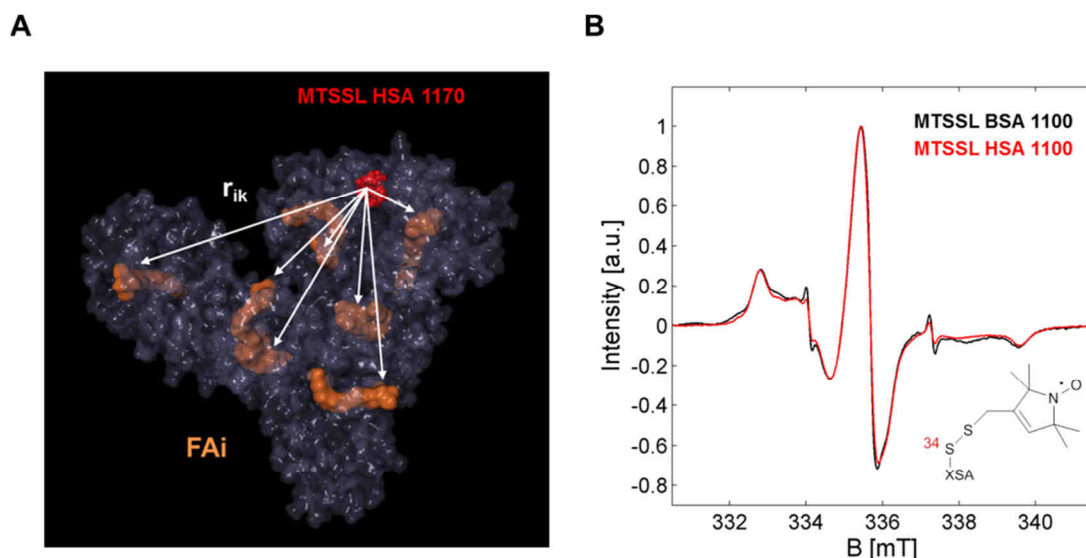
Figure 9.1 | Introducing a surveillance benchmark spin (SBS) to albumin for fatty acid triangulation. (**A**) Molecular model of MTSSL HSA (C34R1 is here shown in red and the complete model is constructed from PDB ID: 1e7i)[4] that facilitates tracking of individual distances ($r_{i,k}$) to a maximum of seven (1170) aligned fatty acid spin probes (FAi, orange). (**B**) CW EPR spectra of MTSSL spin-labeled HSA (red) and BSA (black) at a concentration of $c_X = 0.62$ mM in DPBS buffer and 20% v/v glycerol at pH 7.4 (without fatty acids samples it will be generally termed as MTSSL XSA 1100). The inset graph represents the labeling position at the Cys34 residue in arbitrary albumins (XSA).

All results from the MTSSL albumin characterization are summarized in **Table 9.1**. The deviations in 1 mM albumin stock solution concentrations from the nominal value are discussed in **Chapter 5.2** and are assumed to occur mainly due to excluded volume effects.

Table 9.1 | Characterization of MTSSL albumins

Sample	$c_{BCA}{}^a$ [mM]	$c_{SH}{}^b$ [mM]	$\phi_{SH}{}^c$ [%]	MW^d [Da]
1 mM BSA	0.936 ± 0.098^e	0.511	54.6	66446
1 mM HSA	0.818 ± 0.044^e	0.243	29.7	66531
MTSSL BSA	0.422 ± 0.025	–	–	66642
MTSSL HSA	1.000 ± 0.090	–	–	66709

^{a}All protein concentration values (c_{BCA}) were determined from BCA assays.[27] ^{b}Free sulfhydryl content (c_{SH}) was determined from Ellman's tests (see **Appendix G2**).[26] $^c\phi_{SH} = c_{SH}/c_{BCA}$ is the fraction of accessible thiols per albumin. ^{d}Molecular weights (MW) were determined with MALDI-TOF (see **Appendix G3**). ^{e}Concentrations deviate from the nominal value of 1 mM due to excluded volume effects (see **Chapter 5.2**).

It is commonly accepted that the thiol content in albumin samples exhibits a certain heterogeneity[29] that mainly depends on physiological conditions.[30] Generally, an antioxidant role is ascribed to the conserved Cys34 residue in albumins.[31–33] Unexpectedly, the obtained values for HSA are quite low compared to prevalent literature suggesting that 70 – 80% of the thiols exist in the reduced form in healthy individuals ($\phi_{SH,H} = 0.7 - 0.8$).[31,34] For BSA various values are reported (ranging from $0.36 < \phi_{SH,B} < 0.69$)[35] and in contrast to HSA, these reference values coincide quite well with the

findings made here. There was no evidence of a yellow color reaction from Ellman's tests on spin-labeled albumin solutions, constituting another positive proof for a successful labeling procedure.

First of all, a practical sample short-hand notation is applied for including the MTSSL residue in the nomenclature. The abbreviation Y-MTSSL XSA $Z_1Z_2Z_3Z_4$ will be used in the following that denotes nominal equivalents of MTSSL (Z_1), XSA (Z_2), Y-DSA (Z_3) and rY-DSA (Z_4) that identifies each individual albumin (XSA) sample. Herein, the investigated systems will be restricted to $X \in B, H$ and $Y \in 5, 16$. According to the different MTSSL labeling efficiencies of HSA and BSA (**Table 9.1**) the MTSSL concentration was adjusted to be constant at 0.1 mM in each sample to certify sufficient signal strength for all EPR measurements. Therefore, a 0.1 mM equivalent of MTSSL corresponds to c_H = 0.336 mM HSA and c_B = 0.183 mM BSA. Double integration of corresponding CW EPR spectra of spin probe-free MTSSL XSA 1100 also gave similar values, confirming the validity of this labeling approach that primarily circumvents the application of DTT (**Figure G2A** and **Chapter 9.5**).

9.2.2 | DEER Experiments on Spin Probed MTSSL Albumins

In this section, the impact on the DEER-derived distance distributions is tested that emerges from introducing a surveillance benchmark spin. In **Figure 9.2** all experimental DEER time traces are shown that were obtained from MTSSL XSA equipped with spin-diluted fatty acids (rY-DSA, see **Appendix B5**)[1] to keep the nominal number of coupled spins below $\langle n \rangle = 2$.

Keeping in mind that the SBS is already attached to albumin, only one equivalent of paramagnetic fatty acid and an increasing number of reduced fatty acids (2, 4 and 6 equivalents) have to be added to both MTSSL-labeled albumins. The upper trace in **Figure 9.2** shows MTSSL albumins alone (1100) as a reference, resembling a monoradical protein that exhibits largely modulation free time traces ($\Delta < 0.08$) with background dimensionalities of about $D = 3$ and $\langle n \rangle = 1.05 - 1.16$ (**Appendix G5**). A clear increase in SNR and modulation depth Δ is observable upon loading fatty acids 5-DSA, 16-DSA and their respective reduced forms (rY-DSA) on albumin. Although CW EPR-based spin counting routines of spin-diluted samples are intrinsically hampered and hence all CW EPR spectra look quite similar (**Appendix G4**), the obtained modulation depths Δ from corresponding dipolar evolution functions indicate that the reduction procedure was successful (**Figure G11A**), as all albumin (X) and fatty acid (Y)-specific dipolar evolution functions exhibited similar modulation depths. Furthermore, the application of a device specific modulation depth parameter $\lambda = 0.534$ (determined with model biradicals, see **Appendix C7**) can thus be used to approximate an average number of coupled spins $\langle n \rangle = 1.39 \pm 0.10$ for spin probed MTSSL HSA and $\langle n \rangle = 1.69 \pm 0.09$ for spin probed MTSSL BSA samples as shown in **Figure G11B**. This corresponds well with data obtained from Ellman's tests (**Table 9.1**) and suggests that the accessible thiols are occupied by MTSSL to large extents. In **Figure 9.3** all distance distributions are shown that are derived from raw time domain data in **Figure 9.2**. At first sight the general shape of individual probability densities $P(r)$ is intricate.
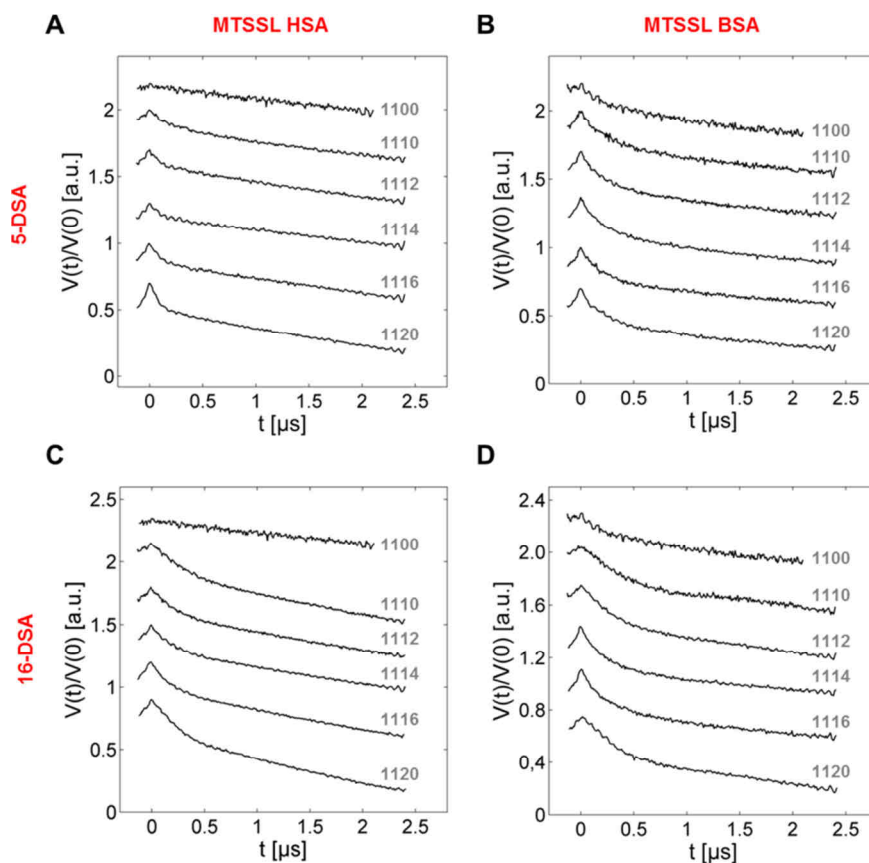
Figure 9.2 | DEER time traces of spin probed MTSSL XSA. This collection of raw DEER time traces $V(t)/V(0)$ shows (**A**) MTSSL HSA loaded with 5-DSA, (**B**) MTSSL BSA loaded with 5-DSA, (**C**) MTSSL HSA loaded with 16-DSA and (**D**) MTSSL BSA loaded with 16-DSA. The $11Z_3Z_4$ samples were equipped with paramagnetic (Z_3) to reduced (Z_4) fatty acid ratios of 1:0, 1:2, 1:4, 1:6 and 2:0. Additionally, the corresponding fatty acid free sample (1100) is presented for both albumins in order to highlight the dipolar modulation effect in DEER time traces. The MTSSL concentration was set to 0.1 mM corresponding to $c_H = 0.336$ mM HSA and $c_B = 0.183$ mM BSA. All samples were prepared in DPBS buffer equipped with 20% v/v glycerol at pH 7.4.

Therefore, analyses of corresponding DEER time traces were conducted in a consistent scheme, assuming a background dimensionality of $D = 3.74 \pm 0.03$ throughout.[1,36] Additionally, the setting of regularization parameters was kept constant for all samples containing 5-DSA ($\alpha_5 = 1000$) and 16-DSA ($\alpha_{16} = 100$), so that all distance distributions $P(r)$ should be of a comparable resolution. The validity of most distance distributions is primarily provided by recurrent characteristic peaks as well as by the general absence of any distance probability density in the region of the hydrodynamic diameter of albumin ($R_H \sim 6.2 – 7.0$ nm).[37] This is particularly obvious for 5-MTSSL BSA in **Figure 9.3B** when $P(r) \approx 0$ at about 6.7 nm.

However, this ascribed significance in $P(r)$ is only of a qualitative nature, due to the short dipolar evolution functions that range from about $t_{max} = 1.8 – 2.3$ µs (**Figure G10**), i.e. that only distances in the range from about $1.8 – 5.2$ nm[38] can be attributed with valid assignments to the origin of individual fatty acids FA*i*. All peak characteristics beyond 6 nm are considered to emerge due to background artifacts during the regularization procedure.[39]
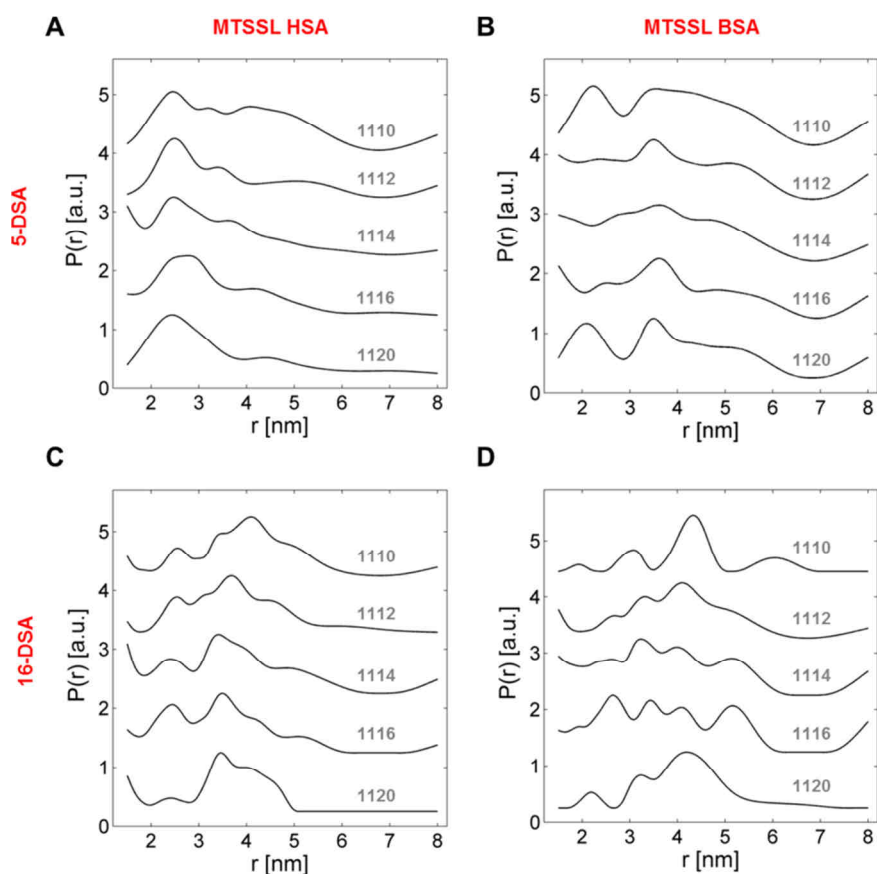
Figure 9.3 | DEER-derived distance distributions *P*(*r*) of spin probed MTSSL XSA. This collection of DEER-derived distance distributions $P(r)$ shows fatty acid alignments from (**A**) MTSSL HSA loaded with 5-DSA, (**B**) MTSSL BSA loaded with 5-DSA, (**C**) MTSSL HSA loaded with 16-DSA and (**D**) MTSSL BSA loaded with 16-DSA after Tikhonov regularization in DeerAnalysis.[39] The $11Z_3Z_4$ samples were equipped with paramagnetic (Z_3) to reduced (Z_4) fatty acid ratios of 1:0, 1:2, 1:4, 1:6 and 2:0. The MTSSL concentration was set to 0.1 mM corresponding to 0.336 mM HSA and 0.183 mM BSA. All samples were prepared in DPBS buffer equipped with 20% v/v glycerol at pH 7.4.

9.2.3 | Rationalizing Distance Distributions from Spin Probed MTSSL Albumins

For realizing a credible distance peak assignment, two molecular models were constructed from the crystal structure of HSA co-crystallized with stearic acids (PDB ID: 1e7i)[4] that contain a MTSSL residue at backbone position Cys34 and are filled with seven 5-DSA or 16-DSA ligands each. In order to rationalize the emerging complex characteristics in the resulting distance distributions, an expanded strategy had to be devised utilizing MD simulations of these molecular models (see **Appendix G7**). Additionally, reference measurements with albumins that are loaded with fatty acids alone should partly resemble the investigated system, however lacking covalently attached MTSSL (see also **Appendix G8**). This approach is based on the scheme applied in Junk *et al.*[1] and bears the expanded potential of simultaneously tracking theoretical distances in between MTSSL and individual fatty acids, as well as to arbitrarily combine all potential interspin distances. This means that a *reduced interspin system* can be observed with seven distinct individual distances ranging from the surveillance benchmark spin (SBS) towards each individual fatty acid binding pocket ($P_{SBS}(r)$), instead of considering a complete set of $N_{r,FA} = (N_{FA}^2 - N_{FA})/2 = 21$ fatty acid interspin distances that are aligned in space in the 7×7 matrix of the *standard interspin system* ($P_{FA}(r)$).[1] However, by introducing the

SBS an overall correlation of interspin connections leads to an *expanded interspin system $P(r)$* resembling an 8×8 matrix with $N_{r,\text{SBS}} = 28$ interspin distances (see **Tables G2–G4**). The first step is now to analyze the reduced interspin system (see **Figure 9.1A**) from MD simulations yielding a list of probe-specific MTSSL-FA distances ($r_{Y,i,k}$) that is presented in **Table 9.2**. For clarity, the distances are given together with a correlation to respective individual fatty acid (FAi) locations in corresponding subdomains.[4,40] Individual distance values are taken as an average from $10 - 15$ simulation snapshots of according trajectories in **Figure G12** for $t_{\text{MD}} > 5$ ns. This strategy is here considered as largely sufficient as the standard deviations of individual values are quite small ($\Delta r_{Y,i,k} \leq 0.27$ nm).

Table 9.2 | MTSSL-FA distances $r_{Y,i,k}$ obtained from MD Simulations

MTSSL = k	5-DSA	16-DSA	FAi location
FAi	$r_{5,i,k}{}^{\text{a}}$ [nm]	$r_{16,i,k}{}^{\text{b}}$ [nm]	Subdomain$^{\text{c}}$
1	2.48 ± 0.10	2.65 ± 0.11	IB
2	3.25 ± 0.08	1.49 ± 0.19	IB
3	5.26 ± 0.15	5.11 ± 0.13	IIIA
4	5.03 ± 0.14	3.69 ± 0.16	IIIA
5	5.43 ± 0.27	6.06 ± 0.17	IIIB
6	5.22 ± 0.14	4.86 ± 0.09	IIA-IIB
7	3.77 ± 0.10	3.62 ± 0.13	IIA

$^{\text{a}}$Averaged distance values $r_{5,i,k}$ in the range from 6.5 ns $< t_{\text{MD}} <$ 21.3 ns simulation runtime in **Figure G12A**. $^{\text{b}}$Averaged distance values $r_{16,i,k}$ in the range from 5.8 ns $< t_{\text{MD}} <$ 27.1 ns simulation runtime in **Figure G12B**. $^{\text{c}}$Domain assignment according to Bhattacharya *et al.*[4] and Ghuman *et al.*[40]

In principle, all paramagnetic centers of the modeled fatty acids can be considered to range within remote distances relative to MTSSL that are smaller, or equal to the gyration diameter $2R_{\text{G}} = 5.74$ nm that can be also obtained from MD simulations (**Figure G12**). This nicely corresponds with results from SANS experiments ($2R_{\text{G}} = 5.48$ nm)[41] and from excluded volume studies herein ($R_{\text{H,V}} = 2.78$ nm in **Chapter 5.2** and $R^{+} = 2.64$ nm in **Chapter 5.5**).

For 16-DSA-probed MTSSL XSA, FA2 ($r_{16,2,k} \sim 1.5$ nm) and FA5 ($r_{16,5,k} \sim 6.1$ nm) are here considered as being experimentally inaccessible in DEER due to the limited time trace resolution ($t_{\text{max}} \leq 2.5$ µs) and proton modulation. For 5-DSA, several fatty acids (FA3 – 6) exhibit coinciding distances, that should be indistinguishable in DEER experiments. The same accounts for fatty acid pairs (FA3, FA6) around 5 nm and (FA4, FA7) at about 3.6 nm in 16-DSA-probed MTSSL XSA. However, characteristics in $r_{Y,i,k}$ being unique in this reduced interspin system distance list should be identifiable. In principle all values in **Table 9.2** are distance vectors that are defined by length and direction. Unfortunately, the latter information is usually inaccessible due to inherent systematic complexities but can be investigated with specialized experimental setups.[42] Furthermore, strategies were developed for rigid systems, as e.g. spin-labeled DNA,[43] or other spatially confined biradicals,[44–46] that facilitate the extraction of interspin orientations even at X-band frequencies that were however not

tested here. A further obstacle for data analysis is that individual distance peaks may vary in relative intensity and position upon fatty acid loading due to the general configurational adaptability of albumins.[47]

As fatty acids themselves are capable to generate a characteristic distance distribution in albumins (see also **Chapter 4** and **Chapter 6**), the key distance distributions (1110, 1120 and 1116) from **Figure 9.3** are compared to identical XSA samples (0110 and 0120) in **Figure 9.4**, lacking the SBS ($Z_1 = 0$) for highlighting its direct effect on $P(r)$. Additionally, data from MTSSL XSA samples with fully occupied fatty acid binding sites (1116) are compared to theoretical distributions (1170) from simulation snapshots at 9.4 ns runtime (**Table G4**). The results from experiments on the exclusively fatty acid loaded HSA and BSA samples at identical concentrations are deposited in **Appendix G8**.

In **Figure 9.4A**, the 5-MTSSL HSA system shows clear deviations from the pure fatty acid-based distributions at lowest 5-DSA loadings (0110, gray, upper trace). There are three distinct peaks that can be solely assigned to MTSSL-FAi distances at 2.48 nm (FA1), 3.18 nm (FA2), 4.08 nm (FA7) and a broad, continuous part between about 4.5 and 6.0 nm that would correspond to all four spare distance vectors (FA3 – FA6). In **Figure 9.4B**, the 5-MTSSL BSA system shows a very similar distribution apart from the lack of the 3.2 nm feature (FA2). It is therefore assumed that FA2 and FA7 distances coincide here (2,7) and FA3 – FA6 also form the broad continuous part in the range from 4.5 – 6.0 nm. Unlike HSA, the combined distance peak of FA2 and FA7 (2,7) in 5-MTSSL BSA persists throughout all loading ratios. This is indicative of how the labeling efficiency influences $P(r)$.

The distribution shape in 5-MTSSL HSA approaches the standard interspin system ($P_{FA}(r)$) distribution with higher loadings (FA, gray arrow), while 5-MTSSL BSA is still dominated by the reduced interspin system characteristics, mainly exhibiting MTSSL-FA distances (SBS, green arrow). This characteristic difference is also reflected in the theoretical distance distribution (1170, red) where each individual distance value $r_{Y,i,j,k}$ of the 8×8 matrix is represented with identical weight. Even at lowest 5-DSA loadings (5-MTSSL XSA 1110) a largely complete set of fatty acid assign-ments can be obtained. This means that binding sites are not filled consecutively, but appear to be more or less equivalent ($N_T = N_E = 7$) as they are randomly occupied in the observed ensembles. As described above, FA2 and FA5 distances from bound 16-DSA in the reduced system are assumed to be experimentally inaccessible with DEER. This is well confirmed for FA5 by comparing theoretical distributions with experiments (**Figure 9.4C+D**, red asterisk, lower traces) as the feature around 6.2 nm in the red dotted line does not occur in experimental distance distributions at all.

Data from the 16-MTSSL HSA system in **Figure 9.4C** again shows clear deviations from the fatty acid-based distributions at lowest 16-DSA loading (1110, gray, upper trace). Here, four peaks emerge that can be assigned to FA1 (2.55 nm), a combination of FA4, FA7 at 4.09 nm (green dotted line), as well as a broad feature that is here ascribed to FA3 and FA6.
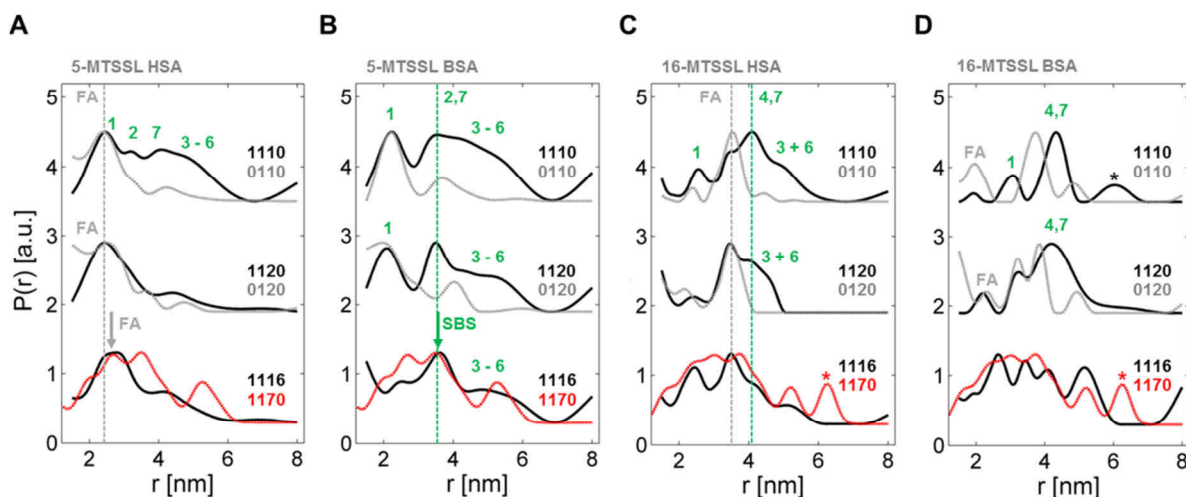
Figure 9.4 | Rationalization of distance peaks in key distance distributions of spin probed MTSSL XSA. A comparison is shown in between MTSSL XSA samples (black) and unmodified albumin samples that lack the SBS (gray) for (**A**) 5-MTSSL HSA, (**B**) 5-MTSSL BSA, (**C**) 16-MTSSL HSA and (**D**) 16-MTSSL BSA (* = black, regularization artifact). Both types of albumins were either loaded with one ($Z_1$110, upper traces) or two ($Z_1$120, middle traces) equivalents of 5-DSA or 16-DSA. Theoretical distributions (1170, σ = 0.17, red) were aligned with the fully occupied MTSSL XSA 1116 samples (lower traces) from snapshots at t_{MD} = 9.4 ns (**Table G4**, * = red, inaccessible in DEER experiments conducted here). Resemblances with fatty acid-induced distribution shapes are denoted as "FA" (gray) and conformity with values in **Table 9.2** are denoted with corresponding fatty acid identifiers (i = 1–7, green) from the reduced interspin system (SBS). When applicable, recurrent characteristics are aligned with dotted lines or arrows in according colors.

Obviously, when compared to higher ligand loadings, the feature at 3.5 nm is identified to be mainly generated by $P_{FA}(r)$ (gray dotted line) and unfortunately represents at least six interspin distances of individual fatty acids bound to HSA (see **Table G4**). In contrast, the 16-MTSSL BSA system in **Figure 9.4D** shows a different distribution, however, resembling the combined and unique (4,7) feature at about 4.33 nm that can be also observed in 16-MTSSL HSA. The peak at 3.09 nm is only explicable when assigned to FA1 and the small bump at about 2.1 nm that is visible in 1110 and 1120 loadings, is also most probably induced by $P_{FA}(r)$. Supposed regularization artifacts have been marked with black asterisks (*). The distribution for 16-MTSSL BSA 1120 again discloses the fatty acid system-based origin of the typical 3.23 nm peak in purely fatty acid probed BSA (see also **Chapter 4**), when compared to the corresponding DEER measurement without the SBS (0120). Unfortunately, the distance peaks for FA1 in $P_{SBS}(r)$ of 5-MTSSL HSA and BSA coincides with $P_{FA}(r)$ in the standard interspin system and is also found to be not clearly distinguishable.

The general nature of the DEER-derived distance distributions from MTSSL albumins is therefore assumed to represent an expanded mixture distribution $P(r)$ of the reduced interspin system ($P_{SBS}(r)$) and the standard interspin system ($P_{FA}(r)$) that is exclusively generated from fatty acids (**Figure 9.5A+B**). Mathematically, this mixture distribution can be described by the relation:[48,49]

$$P(r) = \sum_{m}^{N} f_m \cdot P_m(r)$$

(9.1)

with $\sum f_m = 1$.

The parameter m defines the origin (SBS or FA) of the considered distance probability density that is here either termed as $P_{SBS}(r)$ or $P_{FA}(r)$. The relative weight f_m is assumed to strongly depend on labeling efficiency as derived from **Table 9.1** ($\phi_{SH} \approx \langle n \rangle_X - 1$), the relative affinity ($K_{A,i}$) of individual fatty acid binding sites, the number N_L of loaded fatty acid equivalents and the absolute distance values $r_{Y,i,j,k}$ themselves. The latter one bears an additional complication that is based on the blurred distribution shape and an increased distribution width for long distances above $4 - 5$ nm as a consequence of regularization, as it was already mentioned in Godt *et al.*[50] (compare to **Figure C5D**).
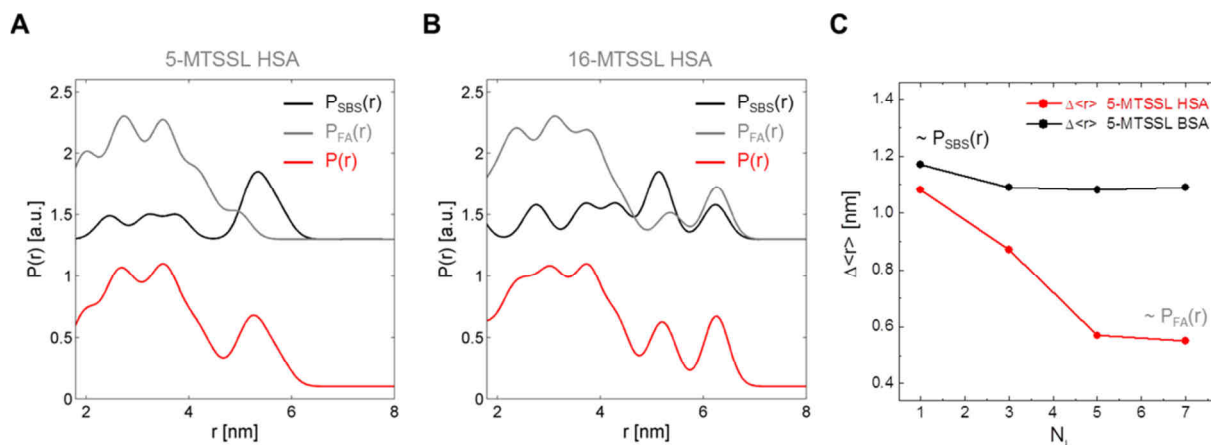
Figure 9.5 | Theoretical mixture distributions $P(r)$ derived from the molecular model of MTSSL HSA. A mixture distribution $P(r)$ can be rationalized from the superposition of a reduced interspin system fraction f_{SBS} and a standard fatty acid based fraction f_{FA}. Therefore, $P_{SBS}(r)$ (black) and $P_{FA}(r)$ are combined to yield $P(r)$ (red) for (**A**) 5-DSA and (**B**) 16-DSA aligned in MTSSL HSA 1170 from simulation snapshots at 9.4 ns (**Table G4** with $\sigma = 0.17$). The relative weights were set to $f_{SBS} = 0.355$ and $f_{FA} = 0.645$ for visualizing the individual contributions to $P(r)$. (**C**) The experimental difference in first moments,[39] or mean distances $\Delta\langle r \rangle = \langle r \rangle - \langle r \rangle_{FA}$ between $P(r)$ of 5-MTSSL XSA loading experiments in **Figure 9.3** and pure FA-based distributions (0110 loading, **Figure 9.4** and **Figure G16**) is taken as a qualitative measure for the change in spectral appearances in **Figure 9.4A+B**. This is due to the increased fatty acid influence on $P(r)$ when the labeling efficiency ($\sim \phi_{SH}$) varies in between different albumin species X.

Naturally, this circumstance leads to an underestimated relative intensity of (long) distance peaks, particularly owing to an increase of applied regularization parameters and the short achievable dipolar evolution times t_{max} in this system. The relative fraction of involved interspin distances from each system (here: $N_{SBS}/N_{r,SBS} = 7/28 = ¼$) is assumed to have an additional influence on the distribution shape. Therefore, the detailed theoretical prediction of the experimental distance distribution shape is currently considered as mainly inaccessible, while individual peak positions are still quite informative. The DEER-distance distributions of MTSSL XSA allow for an identification of features that can be assigned to most of individual fatty acids entering the binding pockets of XSA.

However, one distinctive parameter can be used to accentuate how $P_{FA}(r)$ overtakes the general distribution shape $P(r)$ for higher fatty acid loadings. The first moments or mean distances $\langle r \rangle_{FA}$ of corresponding reference distributions (0110) for 5-DSA aligned with HSA and BSA (**Figure 9.4A+B**) can be compared with the mean distances $\langle r \rangle$ of individual 5-MTSSL XSA 111Z4 distributions in **Figure 9.3**. The difference in both mean distances $\Delta\langle r \rangle = \langle r \rangle - \langle r \rangle_{FA}$ reveal how $P_{FA}(r)$ dominates the

general distribution shape for HSA being the protein with the lower labeling efficiency (**Figure 9.5C**). Particularly, the viability of this $\Delta\langle r\rangle$ parameter is mainly based on the pertinent large difference $\Delta\langle r\rangle_{max} > 1$ nm for 5-MTSSL HSA and BSA.

9.3 | Continuative Studies on (MTSSL) Albumins with Novel Types of Ligands – an Outlook

In order to simplify this fatty acid spin probed MTSSL albumin system, the first rational step would be to use spin-labeled ligands that have a decisively lower total number of binding sites in albumin molecules ($N_T < 7$). However, there is no other suitable albumin ligand that is known to be commercially available in the form of a paramagnetic spin probe.

This approach presented here was inspired by a publication of Cheng *et al.*[51] that introduced a successful strategy for generating thyroxine-based spin probes in order to characterize their binding properties and internal dynamics in its albumin-bound state via CW EPR spectroscopy. Hence, in total 23 important pharmacologically active ingredients that are well-known to bind albumin were spin-labeled by Steglich esterification[52] and thoroughly characterized afterwards. The resulting TEMPO-modified pharmaceuticals (SLP = spin-labeled pharmaceuticals) were tested on the optimized albumin system (**Chapter 5**) for their individual binding affinities K_A and total number of binding sites N_T under physiological conditions in an unexpectedly laborious effort by Dipl. Chem. Till Hauenschild at the MPIP Mainz.[9,53] This was facilitated by extensive CW EPR spectral simulations and application of Scatchard analyses[54] according to procedures described e.g. in **Chapter 7.3.1**. A complete set of accessible K_A and N_T values from EPR spectroscopy is given in **Table 9.3** for 17 individual compounds.[53]

These compounds comprise drug classes for the treatment of various physiological implications, like analgesics (painkillers), anticoagulants (blood thinners), anesthetics (narcotics), antiauxins (teratogenic substances), cytostatics (mitosis inhibitors), steroids (metabolism controllers), uricosurics (ingredients for uric acid expulsion) and vitamins (nutrients).

All tested pharmacological ingredients exhibit a decisively lower number of binding sites ($N_T = 1 - 3$) and binding affinity values ($K_{A,i} = 2 \cdot 10^2 - 2 \cdot 10^5$ M^{-1}) compared to the doxyl stearic acids (for 16-DSA: $N_T \approx 7$, $K_A \approx 2 \cdot 10^6$ M^{-1}, see **Chapter 7.3.1**). For most SLPs the number of binding sites can be confirmed by literature apart from CCS-SL. Depending on solubility, a low K_A value is usually accompanied with a high amount of free, or micellar spectral components being deteriorating for recording meaningful DEER time traces (see e.g. **Chapter 8**). However, first achievements have been obtained in the successful application of DEER experiments on some of these pharmacologically relevant ingredients.

Note, that by applying these SLPs the maximum number of expanded interspin system correlation distances is $N_{r,SBS} = 6$ (TIB-SL, CCS-SL) instead of $N_{r,SBS} = 28$ for the fatty acid-based system. A graphical example for this systematic simplification is given in **Figure 9.6**.

Table 9.3 | Overview of SLP binding properties

Drug class	SLP[a]	K_A[a] [M^{-1}]	N_T[a]	$N_{T,int}$[b]	N_{Lit}[c]	Subdomain[d]	FAi[e]	Lit.[f]
analgesics	ASS-SL	$(6.33 \pm 0.31)\cdot10^3$	1.98	2	2	IIIA, IIA	3,4,7	55,56
	SAL-SL	$(1.48 \pm 0.07)\cdot10^4$	2.01	2	2	IB, IIA	1,7	56
	IBU-SL	$(2.90 \pm 0.03)\cdot10^4$	2.01	2	2	IIA-IIB, IIIA	3,4,6	40,55
	NPX-SL	$(2.17 \pm 0.17)\cdot10^4$	1.97	2	2	IIA, IIIA	3,4,7	57
	PCM-SL	$(5.36 \pm 0.29)\cdot10^2$	2.01	2	2	IIIA	3,4	58
	DCF-SL	$(6.24 \pm 0.24)\cdot10^4$	1.99	2	2	IIA, IIIA	3,4,7	59
	IMC-SL	$(4.85 \pm 0.28)\cdot10^4$	2.03	2	2	IB, IIA	1,7	40
anticoagulants	PPC-SL	$(8.04 \pm 0.57)\cdot10^3$	0.94	1	1	IIA	7	60
	WFR-SL	$(3.11 \pm 0.29)\cdot10^4$	0.99	1	1	IIA	7	55,61
	CCS-SL	$(8.42 \pm 0.38)\cdot10^2$	2.97	3	1	IIA	7	62
anesthetics	PPF-SL	$(9.46 \pm 0.69)\cdot10^3$	1.98	2	2	IIIA, IIIB	3,4,5	63
antiauxins	TIB-SL	$(1.82 \pm 0.02)\cdot10^5$	2.95	3	3	IB, IIA, IIIA	1,3,4,7	22,55
cytostatics	CBL-SL	$(5.05 \pm 0.24)\cdot10^4$	2.02	2	–	–		–
steroids	TSO-SL	$(4.39 \pm 0.37)\cdot10^4$	1.15	1	1	II	2,6,7	64
uricosurics	BBR-SL	$(1.96 \pm 0.29)\cdot10^2$	1.02	1	–	–		–
vitamins	VB3-SL	$(4.75 \pm 0.28)\cdot10^2$	2.02	2	–	–		–
	VB7-SL	$(4.69 \pm 0.42)\cdot10^2$	1.03	1	–	–		–

[a]Given three letter code acronyms are related to the brandnames or names of chemical compounds: ASS = acetylsalicylic acid, aspirin; SAL = salicylic acid; IBU = ibuprofen; NPX = naproxen; PCM = paracetamol; DCF = diclofenac; IMC = indomethacin; PPC = phenprocoumon; WFR = warfarin; CCS = coumarin-3-carboxylic acid; PPF = propofol; TIB = 2,3,5-triiodobenzoic acid; CBL = chlorambucil; TSO = testosterone; BBR = benzbromarone; VB3 = niacin, vitamin B3; VB7 = D-(+)-biotin, vitamin B7. All K_A and N_T values are also taken from Hauenschild $et\ al.$[53] [b]$N_{T,int}$ = integer values for total binding site numbers. [c]Reference number of binding sites with [d]associated binding subdomains (I – III) and corresponding [e]FAi binding site assignments from according [f]literature. The fatty acid binding site identifiers i are therefore correlated to the subdomains where SLPs bind to.

As it is well-known that fatty acid binding sites can be largely correlated to all emerging drug binding sites,[40] the distances in between both SAL-SL should emerge in between 2.1 – 2.9 nm (FA1 and FA7, see also **Figure 3.2** for assignment), for ASS-SL and NPX-SL in between 1.8 – 3.0 nm (FA3, FA4 and FA7) and for IBU-SL in between 1.7 – 3.8 nm (FA3, FA4 and FA6) as obtained from 5-DSA and 16-DSA nitroxide positions (see **Figure 9.6** and **Tables G2–G4**). This seemingly daring deduction of SLP distances or distance ranges were actually confirmed for ASS-SL alone ($P_{ASS}(r)$) and will be shown elsewhere.[65] Furthermore, relative orientation, shape and spin positions in these protein-bound compounds are not yet considered in this extrapolation and are here exclusively fatty acid-based. Experiments on SLPs with MTSSL albumins were not yet tested, however, it is desireable to filter out clear distance identifiers for each combination of binding sites that would help to assign distinct ligand binding sites. The structural correlation of albumin with all obtained SLPs in **Table 9.3** and a corresponding in-depth analysis was considered as way beyond the scope of this thesis.
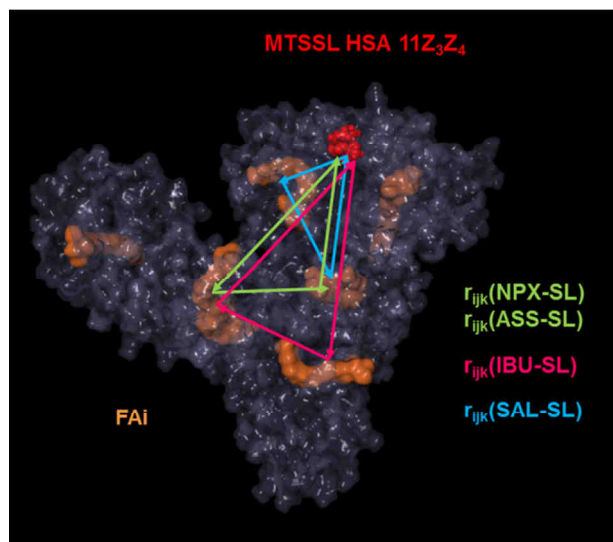
Figure 9.6 | Total interspin correlations of selected SLPs in the MTSSL albumin system. The molecular model of MTSSL-labeled HSA (red) is shown with a maximum of seven (1170) aligned fatty acid spin probes (FAi, orange). The potential interspin correlations ($r_{i,j,k}$) are given for SLPs bound to MTSSL HSA 11Z$_3$Z$_4$, occupying both Sudlow sites (ASS-SL and NPX-SL, green) in subdomains IIA and IIIA (FA3, FA4 and FA7), IBU-SL (magenta) that occupies IIA-IIB (FA6) and IIIA (FA3 and FA4) as well as SAL-SL (blue) that binds to subdomain IB (FA1) and IIA (FA7).

Furthermore, the main interest concerning these SLPs has meanwhile evolved towards another very promising approach that comprises strategic chemical modification of chemical precursor compounds with functional groups (FG). This allows for screening and regulating the strength and physical nature of ligand/albumin interactions according to distinct design principles that may also be expanded to other macromolecular systems.[65]

9.4 | Discussion

The introduction of a surveillance benchmark spin (SBS) bears intrinsic potential for a fundamental advance in understanding the nature of how ligands align in albumin. Distance peaks from spatially uncorrelated spin probe ligands in DEER distance distributions can be clearly, but not completely assigned when an SBS is introduced. Here, the feasibility is ascertained that the combination of DEER experiments and MD simulations facilitates individual fatty acid surveillance and spatial assignment to some extent by correlative spatial triangulation.

The reduced interspin system consisting of only seven MTSSL-FAi distances (N_{SBS}) simplifies the standard interspin system ($N_{r,FA} = 21$) that was applied so far[1] and allows for tracking bound fatty acids by DEER when residing in their individual binding pockets.

The results from 5-MTSSL XSA strongly exemplify that even at low levels of fatty acid loading (1110) all binding sites are occupied to a certain extent and therefore become traceable with this hybrid spin probing and spin labeling approach. This means that fatty acid binding sites are not filled consecutively, but appear to be rather randomly occupied in the observed ensembles. The (FAi) distance contributions from the reduced system $P_{SBS}(r)$ can be partially identified as singularities (1, 2 and 7), or are assigned to fatty acid groups as (2,7) and (3–6) in 5-MTSSL XSA and (4,7) and (3,6) in 16-MTSSL XSA. To this effect, experimentally inaccessible (surveillance) distances as for FA2 and FA5 in 16-MTSSL XSA samples (6.0 nm < $r_{Y,i,k}$ < 1.5 nm) hamper the complete assignment of aligned fatty acids. Appropriate molecular models and MD simulations have to be used for tracking individual fatty acids or groups of them that give clear characteristics in $P(r)$.

The labeling efficiency (ϕ_{SH}) was proven to exert significant influence on the distance distributions $P(r)$ from MTSSL albumin, as the desired characteristics may be suppressed by a dominating fatty acid standard interspin distribution ($P_{FA}(r)$) for higher loadings (see MTSSL HSA in **Figure 9.3A+C** and **Figure 9.4A+C**). In turn, spin counting in DEER qualitatively confirms the labeling efficiencies (e.g., $\phi_{SH,H,DEER} = \langle n \rangle - 1 = 0.392$ and $\phi_{SH,H,Ellman} = 0.297$) that are initially extrapolated from Ellman's tests. However, this circumstance results in the formation of mixture distributions ($P(r)$) composed of a superposition from the MTSSL-based ($P_{SBS}(r)$) and fatty acid-based interspin system ($P_{FA}(r)$). This mixture distribution is expected to also occur for albumins with a hypothetical maximum labeling efficiency ($\phi_{SH} = 1$).

By now, MD simulations do not fully reproduce $P(r)$ and a more sophisticated approach has to be devised to take effects into account like labeling efficiency, individual binding affinities ($K_{A,i}$), just as distance-dependent, analytic (α) and time resolution-related (t_{max})[66] effects or restrictions in DEER spectroscopy. Nevertheless, the Tikhonov regularization routine that was applied here proved itself as a powerful tool for analyzing these complex DEER time domain data from spin probed MTSSL albumins, as recurrent characteristics could be identified in $P(r)$ shapes from independently prepared samples.

One should not exclude the possibility that global allosteric rearrangements occur during fatty acid loading in albumin that slightly shift the expected distance peak positions from theoretical predictions that are obtained from MD simulations on molecular models with fully occupied fatty acid binding sites. Allosteric regulation of albumin by long-chain fatty acids (LCFA) is mainly based on shifts in relative orientations of domain I and domain III relative to domain II.[67] This would also explain why $P(r)$ of 5-MTSSL XSA 1110 is so broad in the range from 4.5 – 6.0 nm, assuming it represents a multitude of structurally slightly altered fatty acid-loaded states.[17] Therefore, it has to be concluded that a slightly inhomogenous ensemble of albumins is captured with DEER, depending on the individual loading status and binding site occupation of a single protein.

Apart from the fundamental impetus to resolve the riddle of dynamic fatty acid alignments in albumins, several intuitive strategies can be followed to potentially improve this hybrid approach. According to prior studies that aimed for spectrally separating ^{14}N and ^{15}N contributions in 2D-DEER on biradicals,[68] or spin probed polymer samples by mixed isotope labeling in MISS-DEER (= mixed isotopologues for spectral separation),[69] a combination of ^{15}N-MTSSL label and ^{14}N-DSA ligand could be used in albumin, or vice versa.

Contemporarily, the number of combinatoric possibilities of potential fatty acid ligand loading experiments prevents a straightforward approach to the albumin issue. Therefore, as introduced in **Chapter 9.3**, some of the established SLPs could provide a quick view on global structural effects in albumin, as e.g. in denaturation studies shown in **Chapter 8** and **Chapter 11** (pH and temperature), or in comparative studies as shown in **Chapter 4** and **Chapter 6**.

9.5 | Materials and Methods

Materials. Lyophilized powders of HSA (>95%, Calbiochem), BSA (>96%, Sigma-Aldrich), 16-DSA (Sigma-Aldrich), 5-DSA (Sigma-Aldrich), DTT (>99.5%, AppliChem), DTNB (>99%, AppliChem), MTSSL (>98%, Enzo Life Sciences), L-Cysteinechloride monohydrate (>98.5%, Carl Roth), 87 wt% glycerol (ACROS) and phenylhydrazine (97%, Sigma-Aldrich) were used without further purification. Synthesis and analysis of all SLPs compounds has been described elsewhere.[9,53] The 0.137 M DPBS buffer pH 7.4 was prepared according to the procedure described in **Appendix C1**.

Sample Preparation. *Spin Labeling of HSA and BSA:* The spin-labeled albumin samples were obtained by incubating 0.2 mM albumin in 0.136 M DPBS buffer with a 5-fold molar excess of MTSSL and 1% ethanol. 8 ml of this solution was incubated for 16 – 24 hours at room temperature and pH 7.3 ± 0.1. The resulting MTSSL albumins were purified from the incubation solution with PD-10 columns (GE Healthcare) containing Sephadex G-25 resins. Individual fractions were tested for protein content with Bradford reagent[70] and an additional investigation utilizing CW EPR spectroscopy (**Figure G2B**). The purified MTSSL albumin solutions were concentrated with spin columns (Sartorius) and a benchtop centrifuge (Eppendorf Centrifuge 5810 R) to about 0.3 – 0.5 ml stock solutions. A commercially available BCA assay[27] was used (**Appendix C5**) to determine the resulting protein content (c_X = 0.42 – 1.53 mM) and a yield of up to ϕ_{prep} = 58% of the initially applied protein ($\phi_{MTSSL\ XSA} = \phi_{prep} \cdot \phi_{SH}$ = 15 – 33 % MTSSL XSA 1100). An explicit protocol of the spin labeling routine can be found in **Appendix G1**. Additionally, the effect of 1, 10 and 100 equivalents of DTT on albumin was tested by an 24 h incubation with 0.16 mM pure HSA samples that were spin probed with about two equivalents of 16-DSA. In general, the results strongly discourage the application of DTT on albumin in this spin labeling protocol (**Figure G2A**). An alternative approach using TCEP[71] as a reducing agent instead of DTT[72] was not tested.

Ellman's Test: Quantification of accessible thiol groups was conducted with Ellman's reagent (DTNB),[26] according to a slightly modified standard protocol[73] that can be found in **Appendix G2**. A reference comprising L-Cysteine was used to calibrate the strength of the TNB^{2-} color reaction by measuring the characteristic absorption at λ_{Ellman} = 412 nm[35] on an UV/Vis spectrometer (Hewlett Packard 8453 + 89090A). Absorption values and BCA assayed protein concentrations were taken from 1 mM HSA and 1 mM BSA samples of the same lot in order to determine the amount of accessible cysteines per albumin. These values ($\phi_{SH,B}$ = 0.546 eq R-SH for BSA and $\phi_{SH,H}$ 0.297 eq R-SH for HSA, see **Table 9.1**) were here defined as the labeling efficiency.

EPR Samples: All MTSSL albumin equivalent concentrations were adjusted to 0.1 mM of MTSSL spin label, i.e. 1 eq HSA was chosen as 0.336 mM and 1 eq BSA is therefore set to 0.183 mM. This certified that the SNR in all EPR experiments is large enough for generating time traces of comparable quality and potentially meaningful distance distributions. Double integration of CW EPR spectra of MTSSL XSA 1100 (**Figure 9.1**) confirmed the validity of this approach with values of $4.99 \cdot 10^5$ for HSA and $6.27 \cdot 10^5$ for BSA corresponding to an error of about 11% compared to the average ($5.63 \cdot 10^5$).
The paramagnetic spin probe stock solutions of 5-DSA and 16-DSA were prepared with appropriate amounts of 0.1 M KOH to a final stock concentration of 26 mM DSA. The reduced EPR-silent fatty acid spin probes (26 mM rY-DSA) for spin dilution[1] were prepared according to the procedure described in **Appendix B5**. Appropriate equivalents of these paramagnetic and diamagnetic spin probes were added as 0.336 mM equivalents for MTSSL HSA and 0.183 mM for MTSSL BSA to yield the desired 1100, 1110, 1120, 1112, 1114 and 1116 loading equivalent ratios ($Z_1Z_2Z_3Z_4$). As a reference, MTSSL-free HSA and BSA samples were prepared at XSA 0110 and 0120 loading ratios ($0Z_2Z_3Z_4$), at identical equivalent concentrations. The final aqueous solutions of albumin together with fatty acids were supplied with 20% v/v of glycerol to prevent crystallization upon freezing and were finally titrated to pH 7.40 ± 0.03 with a final volume of 80 µl utilizing appropriate DPBS titration buffers (see **Appendix C2**). For CW EPR measurements, about 15 µl of sample were filled into a quarz capillary (BRAUN) with ca. 1 mm outer diameter. For DEER measurements about 65 µl of the final solutions were filled into 3 mm (outer diameter) quartz tubes (Heraeus) and shock-frozen in liquid-nitrogen-cooled 2-methylbutane for subsequent DEER measurements.

MALDI-TOF Mass Spectrometry. Dilutions of HSA, BSA, MTSSL-HSA and MTSSL-BSA stock solutions were prepared in ultrapure water (MilliQ) yielding sample concentrations of 1 mg/ml with salt concentrations less than 2 mM. MALDI-TOF experiments and data evaluation were performed on a Voyager-DE PRO (Sciex, Darmstadt, Germany) and are shown in **Appendix G3**. MALDI-MS experiments were carried out using a delayed extraction TOF mass spectrometer Voyager-DE PRO (Sciex, Darmstadt, Germany) equipped with a pulsed nitrogen laser ($\lambda = 337$ nm). Sinapinic acid was used as matrix solution that was mixed with the sample solution 10:1 (v/v) and then dried in a stream of air. Measurements were performed operating in the positive ion linear mode at a total acceleration voltage of 25 kV, with a grid voltage set to 92%, 0.15% guide wire voltage and an extraction delay of 700 ns. A low mass gate was set to $m/z = 10$ kDa to prevent detector saturation from low mass compounds. The instrument was externally calibrated using BSA and calibration mixture 3 of the Sequazyme Peptide Standards Kit (Sciex).

EPR Spectroscopy. *CW EPR Experiments:* A Miniscope MS400 (Magnettech GmbH) benchtop spectrometer was used for X-band CW EPR measurements (see **Figure 9.1B**, **Figure G2** and **Appendix G4**) at microwave frequencies of 9.41 – 9.43 GHz that were recorded with frequency counters (RACAL DANA, model 2101). All CW EPR measurements were performed at $T = 298$ K using modulation amplitudes of 0.1 mT and a sweep width of 15 mT.

DEER Experiments: In order to retrieve nanoscale distance information from spin probed MTSSL-XSA molecules the 4-pulse DEER sequence:[74,75]

$$\pm(\pi/2)_{\text{obs}} - \tau_1 - (\pi)_{\text{obs,1}} - (t_{\text{d}} + t_0 + N_t \cdot \Delta t) - (\pi)_{\text{pump}} - (t' - N_t \cdot \Delta t + t_{\text{d}}) - (\pi)_{\text{obs,2}} - \tau_2 - echo$$

was used to obtain dipolar time evolution data from bound Y-DSA spin probes. The experiments were performed at X-band frequencies of 9.1– 9.4 GHz using a BRUKER Elexsys E580 spectrometer equipped with a BRUKER Flexline split-ring resonator ER4118X–MS3. The temperature was set to 50 K for all experiments by cooling with a closed cycle cryostat (ARS AF204, customized for pulse EPR, ARS, Macungie, PA) and the resonator was overcoupled to $Q \approx 100$. The pump frequency ν_{pump} was set to the maximum of the field swept electron spin echo (ESE)-detected spectrum. The observer frequency ν_{obs} was set to $\nu_{\text{pump}} + \Delta\nu$ with $\Delta\nu$ being in the range of 65 MHz and therefore coinciding with the low field local maximum of the nitroxide ESE spectrum. The observer pulse lengths for each DEER experiment were set to 32 ns for both $\pi/2$– and π–pulses and the pump pulse length was 12 ns. Additionally, a 2-step phase cycle ($\pm$) was applied to the first $\pi/2$ pulse of the observer frequency for cancelling out receiver offsets and unwanted echoes. Proton modulation was averaged by addition of eight time traces of variable τ_1 starting with $\tau_{1,1} = 200$ ns, incrementing by $\Delta\tau_1 = 8$ ns and ending up at $\tau_{1,8} = 256$ ns. For all samples the pump pulse position $t_{\text{d}} + t_0$ after the first observer π-pulse deadtime t_{d} was typically incremented for N_t timesteps of $\Delta t = 8$ ns in the range $t_0 + t' = \tau_1 + \tau_2 - 2t_{\text{d}}$, whereas τ_1 and τ_2 were kept constant. DEER time traces were recorded for 12 – 48 hours giving rise to reliable distance information in between about 1.8 and 5.2 nm as the maximum accessible dipolar evolution times for spin probed Y-MTSSL XSA were about $t_{\text{max}} \approx 2.3$ µs throughout.[38] All recorded raw time domain DEER data are presented in **Figure 9.2** and **Figure G16**.

Data Analysis: All collected time traces have been analyzed in a consistent global manual fit procedure with DeerAnalysis2013[39] utilizing Tikhonov regularization. The regularization parameter has been set to $\alpha_{16} = 100$ for 16-DSA- and to $\alpha_5 = 1000$ for 5-DSA-probed MTSSL XSA and XSA samples for all datasets in order to obtain comparable distance peak resolutions. All time trace background dimensionalities have been set to $D = 3.74 \pm 0.03$, apart from the MTSSL XSA 1100 samples where $D = 2.94 – 2.96$ suited best to reproduce the DEER time traces of these monoradical albumins. Spin counting has been conducted by utilizing the modulation depth parameter $\lambda = 0.53421 \pm 0.00916$ as obtained from model biradicals (**Appendix C7**).[50,76]

All corresponding results of the spin counting procedure are given in **Appendix G5**. A complete set of dipolar evolution functions $F(t)/F(0)$ with regularized fit curves and DEER distance distributions $P(r)$ of all experiments can be found in **Figure 9.3**, **Figure 9.4**, **Figure G10** and **Figure G16**. The differences in first moments ($\Delta\langle r \rangle$) from distance distributions of 5-MTSSL XSA and corresponding reference data (5-DSA probed XSA) were determined from corresponding DeerAnalysis2013 output files as a qualitative measure for peak shifts in $P(r)$ (**Figure 9.5C**).

Molecular Models and MD Simulations. All molecular models of 5- and 16-MTSSL HSA were constructed from the structure of HSA co-crystallized with seven stearic acids (PDB ID: 1e7i)[4] using the YASARA Structure software.[77] Radical bearing nitroxide groups (NO•) were modeled as keto residues (C=O) and MD simulations were performed in simulation boxes with periodic cell boundaries containing the protein and an explicit water solvent with 88.300 – 89.000 atoms in total. The simulation runtime was 21.3 – 27.1 ns at pH 7.4 in 154 mM NaCl and T = 298 K applying the AMBER03 forcefield. An explicit routine of how to perform such a simulation appropriately can be found in **Appendix G6**. The extracted 8×8 distance matrices for 0.0 ns, 3.8 ns and 9.4 ns simulation runtimes t_{MD} of the expanded interspin system $P(r)$ consisting of all MTSSL and FA correlations are given in **Tables G2–G4** and were used to assign FAi distances as well as for creating theoretical distance distributions (1170, equations G.2–G.4, **Figure G13–G15**) according to a strategy presented in **Appendix G7**. The theoretical distance values of the reduced system $P_{SBS}(r)$ in **Table 9.1** were averaged across 10 – 15 individual values after ca. $t_{MD} > 5$–6 ns runtime when all values exhibited relatively constant values. All distance trajectories of $r_{Y,i,k}$ are given in **Figure G12** ($P_{SBS}(r)$). Theoretical distance distributions $P(r)$, $P_{FA}(r)$ and $P_{SBS}(r)$ of 5- and 16-MTSSL XSA 1170 (**Figure 9.5**) were each constructed from the 9.4 ns simulation snapshot (see also **Table G4**).

10 | Tunable Attachment of Ligands in Amphiphilic Core-shell Polymers

Core-shell polymers are synthetic nanoscopic objects that gain their shape and function by cooperative effects of their well-defined chemically linked modules. While individual chemical components may behave inert, their combined spatial organization in core and shell regions gives rise to superior properties that bear potential for pioneering most different applications as chemical catalysis, surface coatings and drug delivery. Depending on the chemical and physical properties of the building blocks the functionality of the core-shell structure can be significantly modified.
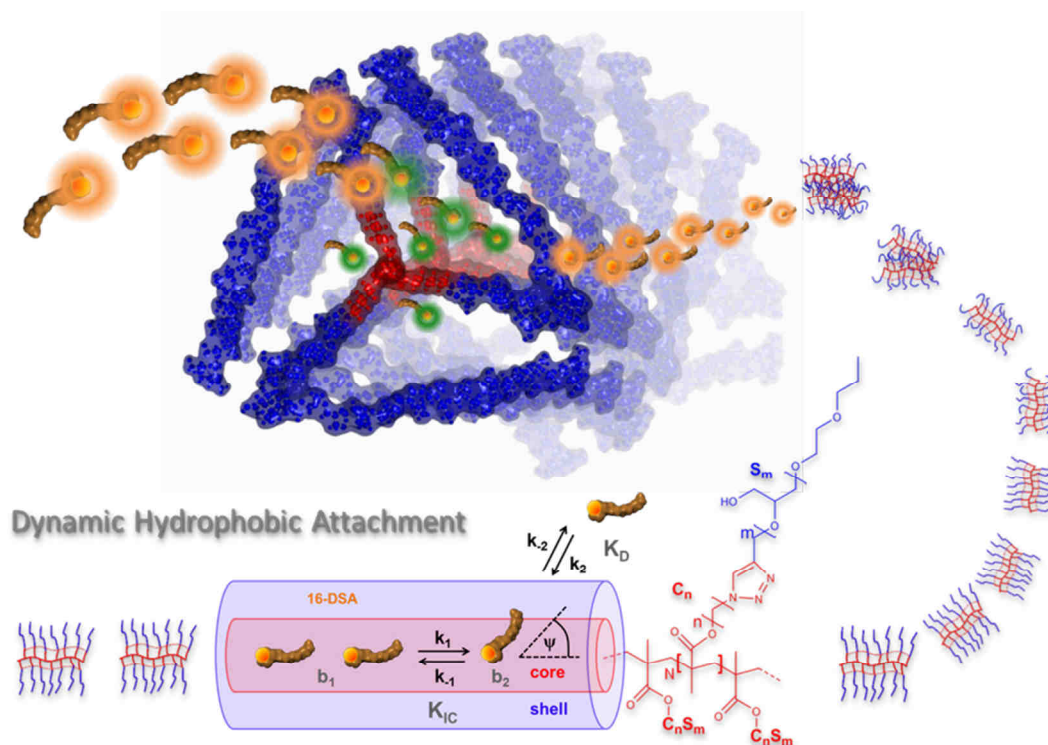
Here, graft copolymers made from amphiphilic macromonomers were used that are composed of hydrophobic alkylene tails (C_n) and hydrophilic polyglycerol chains (S_m) with each of them varying in length. All polymers were synthesized by Dr. Anja Thomas, Dr. Lutz Nuhn and Dipl. Chem. Tobias Johann in the group of Prof. Dr. Holger Frey at the Institute of Organic Chemistry, Johannes Gutenberg University (JGU) Mainz, Germany. Due to this amphiphilic, brush-like appearance of the polymers, their self-assembly properties with amphiphilic paramagnetic ligands can be investigated by EPR spectroscopy. Particularly, the temperature dependence of those polymer-ligand interactions will be of major interest in this section. Further insights on properties like shape and aggregation behavior are accessible by DLS and transmission electron microscopy (TEM), revealing additional information that substantiates observed dynamic effects from EPR. Generally, these artificial structures can be understood as simplified model systems that imitate some functional aspects of albumin on a very fundamental level.

10.1 | Introduction

In recent years synthetic pathways have been established for constructing core-shell graft copolymers from amphiphilic macromonomers[1–6] with high molecular weights of up to 470 kDa and narrow and monomodal weight distributions (PDI < 1.20).[7] Therefore, these polymers are especially well-suited for designing reproducible and specialized functional properties in the realm of smart materials.[8–11] Particularly, their capabilities to host small ligand molecules in their hydrophobic core may be employed for targeted drug delivery.[12–15]

Monitoring ligand uptake capabilities and the formation of binding sites by EPR spectroscopy can be facilitated via by spin-labeled ligands as 5-DSA and 16-DSA[16–19] and others,[20,21] as it is presented and discussed in previous chapters for the albumin model system. Likewise, albumin's ligand binding capacities can also be modulated artificially by surface-targeted alterations (see **Chapter 7**). Charged dendronized polymers have already been reported to constitute a certain type of synthetic fatty acid transporters, whose uptake capabilities appear to scale exponentially with the dendrimer generation.[22] Thus, it could already be shown that there is an intrinsic potential to specific polymers for adjustment of ligand uptake capabilities by chemical modification of polymeric building blocks. The application of external stimuli such as pH,[23] ionic liquids, salt,[22] light,[14] or temperature, as it was shown for Poloxamers (= Pluronics),[24] or elastin-like polypeptides (ELPs),[23] forms an additional experimental opportunity to selectively release bound fatty acid ligands.

Here, paramagnetic fatty acids are studied by CW EPR to determine their distribution in the different environments of a sample due to the intrinsic polarities, their individual binding affinities and their resulting partition coefficients. The two major reference points are the free (f) and immobilized (b) spectral fractions that can easily be separated by their spectral shape and therefore facilitate extraction of valuable information about the sample. The primary basis for this spectral separation is the lineshape broadening upon decelerated diffusion[25–29] as shown in **Figure 2.7**. Free ligands (f) exhibit the typical three-line spectra with a well-defined a_{iso} value. Upon binding to the macromolecular substrate such as a polymer or a protein, the rotational motion is slowed down about three orders of magnitude to the ns-timescale, as it then reflects the slower rotational motion of the corresponding macromolecular structure ($\tau_c > 0.5$ ns).[29,30] Therefore, broad anisotropic EPR lineshapes emerge that are dominated by shape, size and also polarity of the macromolecular environment, with the latter one linearly reducing the a_{iso} values with decreasing polarity (see also **Chapter 2.4.2.1**).[31,32] The spectral parameters, i.e., the individual dynamic fractions f and b, as well as τ_c and a_{iso}, are thus the key for dissecting multi-component EPR spectra. This forms the foundation of the approach of detecting structural and dynamic changes of the polymer itself, extending the established phenomenon of merely observing ligand binding towards polymers[12,14,15] towards an EPR spectroscopic thermodynamic characterization of these rather intricate interactions.

The functional molecular, EPR-spectroscopic picture of ligand binding to polymeric core-shell systems is coupled with a more macroscopic picture, where structural aspects are complemented by

dynamic light scattering (DLS), differential scanning calorimetry (DSC), electron microscopy (EM) that are aided by some coarse but significant conclusions from molecular dynamics (MD) simulations.

10.2 | Results

10.2.1 | Screening for Polymer Functionality with CW EPR Spectroscopy

In this study, three different amphiphilic core-shell polymers are characterized in-depth, where some parameters like the degree of polymerization (N) of the polymethacrylate backbone, but particularly the length of hydrophilic linear polyglycerol shells (linPPG$_m$ = S$_m$) and alkylene core spacer lengths (C_n) are varied. As a simplification all macromonomers and polymers will be denominated with an appropriate abbreviation C_nS_m according to their chemical and structural composition (**Figure 10.1A**) with respect to its most important tunable entities (m, n), also highlighting the chemical structure of the polymethacrylate backbone with N subunits. The chemical structure of 16-DSA is again shown in **Figure 10.1B** and is exclusively applied for all subsequent analyses in this thesis, as it exhibits excellent capabilities to monitor the microenvironment of polymer solutions in EPR spectroscopy.[23,33] In **Figure 10.1C–E** a schematic representation of all investigated core-shell polymers is given in a cylindrical and a brush-like scheme and the given color code is used throughout the whole study.
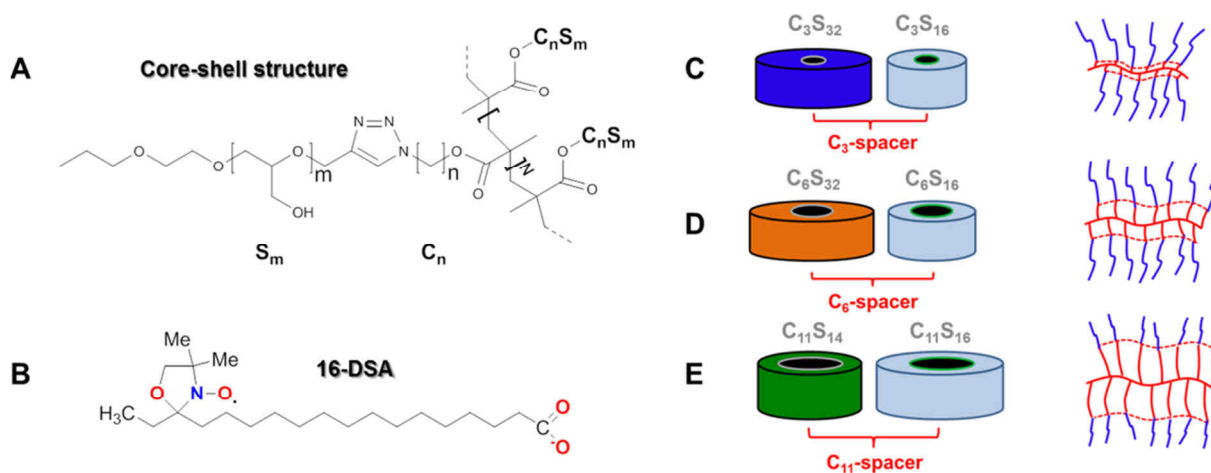
Figure 10.1 | Composition of all six available core-shell polymers C_nS_m. (**A**) Generalized chemical structure of a core-shell polymer with N macromonomer repeating units consisting of (m) glycerol and (n) methylene components. (**B**) Chemical structure of the 16-DSA spin probe. (**C**) Propylene spacer polymers C_3S_{32} (blue) and C_3S_{16} (pale blue). (**D**) Hexylene spacer polymers C_6S_{32} (orange) and C_6S_{16} (pale blue). (**E**) Undecanoylene spacer polymers $C_{11}S_{14}$ (green) and $C_{11}S_{16}$ (pale blue). On the left hand scheme in (C–E), individual polymers are schematically color-coded as they will appear in subsequent analyses. A brush-like representation of the polymers is also given on the right hand side of (C–E) highlighting the hydrophobic core (red) and according shell region (blue). The pale blue polymers are all equipped with a S$_{16}$ shell.

The advantage of using the 16-DSA spin probe is the rigid attachment of the nitroxide moiety to the alkyl chain, so that the change in motional freedom of this long chain (C_{18}) is directly and accurately reflected in an EPR spectrum.[34] A complete set of corresponding CW EPR spectra of 16-DSA co-dissolved in solutions with available core-shell polymers is given in **Figure 10.2A**. Surprisingly, the overall spectral shape only changes significantly with alkylene spacer length C_n (C_3 = propylene,

C_6 = hexylene, C_{11} = undecanoylene). The datasets for one representative polymer from each group of similar alkylene spacer lengths (C_3S_{32}, C_6S_{32}, and $C_{11}S_{14}$) are presented in the following. This selection allows for studying the effect of short alkylene spacers shielded by a thick hydrophilic shell (C_3S_{32} and C_6S_{32}) and long alkylene spacers shielded by a much thinner hydrophilic layer ($C_{11}S_{14}$), so that the maximum number of individual effects from structural properties can be observed (spacer length, shell thickness, degree of polymerization). Additionally, this choice keeps the number of datasets at a manageable level.

All important polymer data such as molecular weight (MW), macromonomer weight (MW_{MM}), polydispersity index of the macromonomer (PDI_{MM}), and degree of polymerization (N) can be found in **Table 10.1**. From an EPR spectroscopic point of view experimental spectra are encountered that are composed of a set of five distinguishable subspectra $F_{i,k}(B)$, resembling different spin probe dynamic regimes and environments as seen in **Figure 10.2B**. These different rotational and environmental regimes correspond to different locations and mobilities in the three different core-shell polymer solutions as it will be shown later.
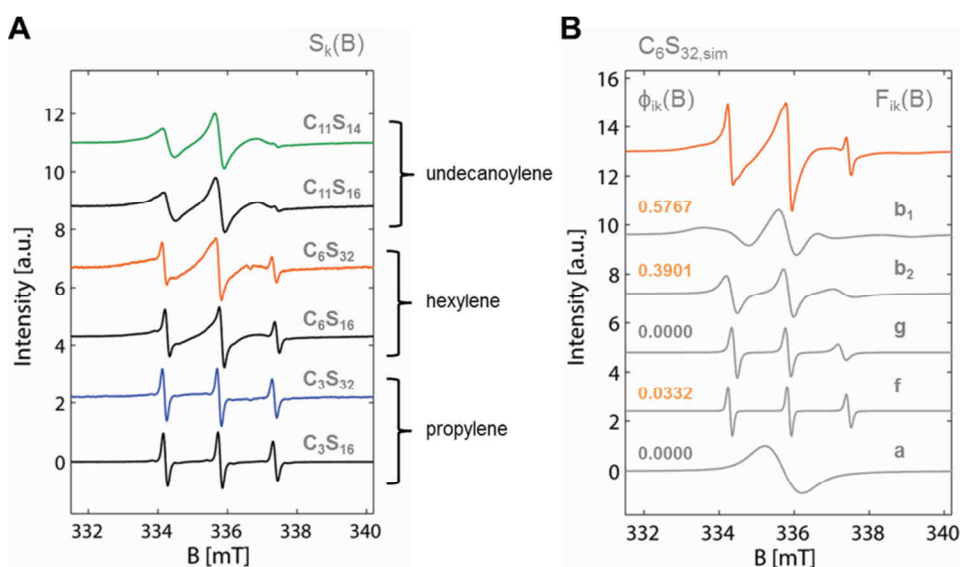
Figure 10.2 | CW EPR spectra of different amphiphilic core-shell polymers probed with 16-DSA. (**A**) EPR spectra $S_k(B)$ from polymers with propylene (C_3), hexylene (C_6) and undecanoylene (C_{11}) spacers. (**B**) Representative simulation of polymer $C_6S_{32,sim}$ (orange) composed of an overlay of three exactly balanced (see orange numbers) fractions $\phi_{i,k}(B)$ of dynamic components $F_{i,k}(B)$ in this case b_1, b_2 and f (compare to **Figure 10.2A**, orange). The components a and g are also shown for completeness. All exemplary simulation traces are shown in gray. Measurements were conducted at $T = 25°C$ in H_2O at polymer concentrations of 1 wt% (C_3) and 4 wt% (C_6 and C_{11}) and a 16-DSA concentration of about 0.2 mM.

Index i denotes the type of subspectrum and k denominates the individual polymer sample. Finally, the spectral components can be extracted from rigorous simulations of experimental EPR spectra as it will be shown in the following.

Upon addition of the 16-DSA spin probe to the polymer solutions, 16-DSA may appear as a freely tumbling species (f), a species aggregated in micelles (a), a slowly tumbling species (b_1), an intermediately slow tumbling species (b_2) and it also appears in a gel phase (g), very similar as in the

hydrogels that are described in Junk *et al.*[35] It can be explicitly shown with CW EPR that 16-DSA has a critical micellar concentration of about 0.3 mM (CMC = (0.285 ± 0.029) mM) in DPBS pH 7.4 (see also **Appendix H1**).

The respective spectral fractions of all species are explicitly given by $\phi_{i,k}$. Consequently, any experimental spectrum $S_k(B)$ can be formally reconstructed by the relation $S_k(B) = \Sigma\phi_{i,k} \cdot \iint F_{i,k}(B)$, where $\Sigma\phi_{i,k} = 1$ (see **Figure 10.2B** and **Appendix E2**). All spectra from C_6- and C_{11}-polymer-solutions show distinct, broad spectral lines stemming from strong spin probe immobilization upon binding and additionally, different dynamical regimes may overlap delicately. While C_6- and C_{11}-type polymers show 16-DSA spectra exclusively composed of b_1, b_2, and f, C_3S_{32} and C_3S_{16} exhibit three-line spectra resembling freely tumbling 16-DSA and C_3S_{32} may comprise small fractions of f, g and a. The shape and relative fractions of these spectral components will be used for subsequent analysis.

Table 10.1 | Properties of the C_nS_m polymers.

Polymer	n	m	MW [kDa]	MW$_{MM}$ [kDa]	N	PDI$_{MM}$
[a]C_3S_{32}	3	32	100	2.68	37.3	1.07
[a]C_6S_{32}	6	32	470	2.72	172.8	1.11
[b]$C_{11}S_{14}$	11	14	64.3	1.46	44.0	1.25

[a]Values are taken from Thomas *et al.*[7] and [b]from Reichenwallner *et al.*[36]

10.2.2 | Temperature Dependence of Dynamic Regime Occupations $\phi_{i,j,k}$ in C_nS_m Polymers

CW EPR measurements on the solutions were subject to a temperature ramp in order to obtain a dynamic response from the polymers via their modulated interaction with 16-DSA. First, the spin probe was tested for intrinsic rotational dynamics that occur during the heating process from 5–95°C. It can be ruled out by performing either explicit spectral simulations, or lineshape analysis that no such transition emerges from the spin probe alone (**Appendix H2** and **Appendix H3**). It turns out that the spin probe rotational dynamics change according to the expected viscosity decrease of water. Additionally, an accelerated aging test[37] of 16-DSA reveals that its signal strength has a half-life of about $t_{1/2} = 100$ days at room temperature ($T = 25°C$) and the activation energy of the reduction is at $E_a = (104.9 ± 7.8)$ kJ/mol (**Appendix H4**) that is typical for this kind of reactions.[38] As the evaluation of a multi-component EPR spectrum at a single temperature may suffer from inseparability of the individual spectral components, measuring a temperature series unravels all dynamic regimes, as the individual fractions have different temperature dependences and can thus be individually discerned and investigated in detail. In case of the polymers available this strategy proved successful. However, subspectra separation had to be conducted iteratively in a manual global fit. Where appropriate, temperatures are from now on abbreviated by index j in [°C], dynamic regimes by index i and polymers by index k ($k = 6$ for C_6S_{32} and $k = 11$ for $C_{11}S_{14}$). The results from spectral simulations of temperature-dependent measurements are displayed in **Figure 10.3A–D**, where only the spectral fractions $\phi_{i,j,k}$ of the respective components are plotted as a function of temperature. Simulation

parameters and all simulated spectra as well as the expanded deconvolution routine can be found in **Appendix H5**. The individual 16-DSA concentrations were determined by (relative) spin counting and are shown as insets throughout **Figure 10.3**.
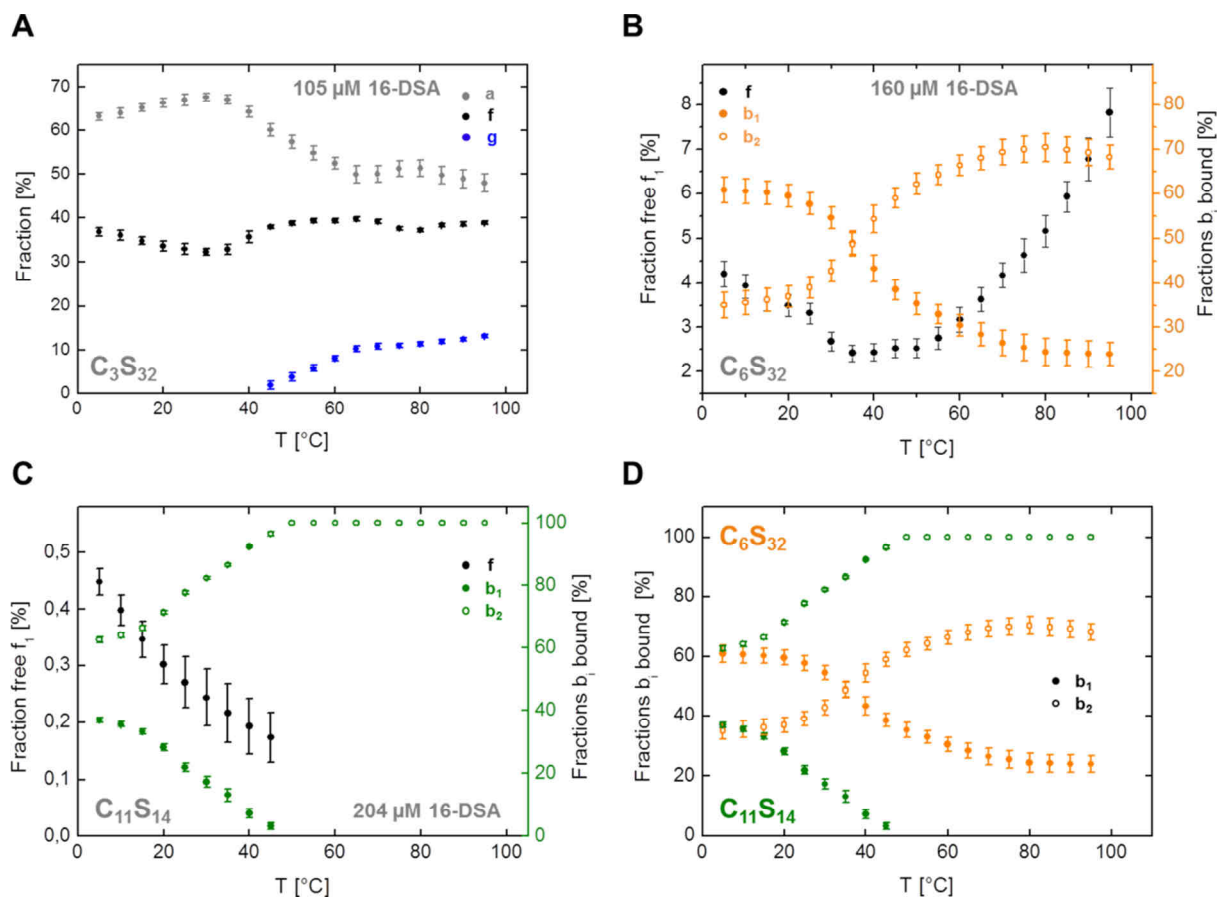
Figure 10.3 | Temperature response from 16-DSA interacting with C_nS_m core-shell polymers. Response curves from C_nS_m polymers in the temperature range from 5 – 95°C interacting with 16-DSA depicted as fractions $\phi_{i,j,k}$. (**A**) 1 wt% C_3S_{32} spin probed with 105 µM 16-DSA. (**B**) 4 wt% C_6S_{32} spin probed with 160 µM 16-DSA. (**C**) 4 wt% $C_{11}S_{14}$ spin probed with 204 µM 16-DSA and (**D**) a comparison of the slow (b_1) and intermediately slow (b_2) rotating components of C_6S_{32}- and $C_{11}S_{14}$-polymers. Micellar fractions a are shown in gray, gel fractions g in blue and free fractions f in black throughout. The responses of polymers C_6S_{32} (orange) and $C_{11}S_{14}$ (green) can be subdivided in slow rotating ($\bullet = b_1$) and intermediately slow rotating ($\circ = b_2$) regimes. Error margins have been determined from spectral simulations.

C_3S_{32} – **Figure 10.3A** reveals that the bulk of the 16-DSA molecules in the C_3S_{32} polymer solution either resides in micelles or tumbles freely in the temperature range from 5 – 40°C, i.e. corresponding CW EPR spectra only show free (*f*) and micellar (*a*) 16-DSA, with the sum of those individual fractions $\phi_{i,j,k}$ adding up to 100%. The micelle fraction decreases above 40°C giving rise to a simultaneous increase of free 16-DSA in solution, most probably by a temperature-based partial shift in equilibrium between micelles and free 16-DSA. Above 45°C a third component emerges with an a_{iso} value of 40.24 MHz (14.36 G) indicating a strongly non-polar environment with a probe rotational correlation time of $\tau_c = 0.4 – 0.7$ ns. This is indicative for the formation of a hydrogel-like environment in the C_3S_{32} polymer solution as it has been shown for thermoresponsive polymers.[39–41] Therefore, it is denoted as subspectrum *g*. A direct comparison with 16-DSA alone in DPBS buffer shows a clear

deviation in the high-field region of the EPR spectra (**Figure H8**). The steep increase of the gel fraction is non-linear over the observed temperature range and is expected to be time dependent as well. Therefore, the C_3S_{32}-core-shell polymer most probably forms small hydrogel-like units above 40°C by forming water depleted regions that are explored by the amphiphilic spin probes, while there is no such ligand uptake at temperatures close to room temperature. The reasons for this uptake behavior are discussed in subsequent sections. Generally, a complicated mechanism of competition for fatty acids between micelles and C_3S_{32} polymer can be anticipated.[42–44] The emergence of large micelle fractions at such low fatty acid concentrations of about 100 µM may indicate a polymer-induced decrease of the fatty acid solubility in aqueous solution, as the CMC of 16-DSA in the largely electrolyte-free solution is generally expected to be higher (CMC > 0.3 mM).[45] Finally, at least for ambient conditions, EPR data from the C_3S_{32} polymer indicate that effective binding and transport of amphiphilic ligands like stearic acid-derivatives can be excluded.

C_6S_{32} – Spin probes interacting with C_6S_{32}-polymers (**Figure 10.3B**) display a completely different development of the dynamic regime occupations. There are three identifiable overlapping spectral components $F_{i,j,k}(B)$ in the whole temperature range (f, b_1, b_2). The b_1 and b_2 fractions of 16-DSA strongly interact with the polymer and hence are significantly restricted their rotational motion (shown in orange). The sum of bound fractions of b_1 and b_2 ($\Sigma\phi_{b,j,k}$) constantly exceeds 92% in the whole temperature range without showing any micellar aggregates (a) or gels (g). The respective a_{iso} values (42.80 MHz = 15.27 G) for both bound fractions b_i of C_6S_{32} are more hydrophobic than for freely tumbling 16-DSA (44.26 MHz = 15.79 G). Ge *et al.*[19] found very similar a_{iso} values for 16-DSA in between free and bound species when interacting with BSA (see also **Chapter 7**). This gives rise to the assumption that the spin probe is in fact in contact with the hydrophobic and water-depleted core of the polymer.

The fundamental difference in fractions b_1 and b_2 is given by the rotational correlation time τ_c. At room temperature b_1 has a rotational correlation time of τ_c = 6.6 ns and b_2 has an about three times lower value of τ_c = 2.0 ns. There is a minimum free 16-DSA fraction of 2.4% around 35°C, exactly coinciding with the crossing of the b_1 and b_2 curves. Additionally, from 5°C onwards the free fraction decreases from 4.2% to 2.4% at 35°C, so the fatty acid uptake can be regarded to be initially enhanced by temperature. The temperature-dependent ligand uptake attains a plateau-like behavior between 35°C and 50°C. For temperatures exceeding 50°C the free fraction again increases towards 7.8% at 95°C, allowing for an optimum fatty acid uptake capability in the range from 35°C to about 50°C, which includes the range of *mammalian body temperature*. Fatty acid ligand uptake of the C_6S_{32}-polymer clearly occurs throughout the whole temperature range.

$C_{11}S_{14}$ – A slightly simpler dynamic temperature response from 16-DSA can be found for the $C_{11}S_{14}$-polymer (**Figure 10.3C**). Allover, three spectral components $F_{i,j,k}(B)$ can be identified for the C_6S_{32}-polymer (f, b_1, b_2). The $C_{11}S_{14}$-polymer features the longest alkylene spacers in the core and an almost gradual decrease of free and slow bound subspectra f and b_1 can be observed. Above 45°C those two

dynamic components vanish and leave a single spectral component b_2 behind that can be tracked to temperatures as high as 95°C. The a_{iso} values (42.44 MHz = 15.14 G) for both bound fractions of the $C_{11}S_{14}$-polymer are even more hydrophobic than for the C_6S_{32}-polymer, again suggesting strong contact to the hydrophobic core region. Unlike the C_6S_{32}-polymer, the free fraction of 16-DSA observed in $C_{11}S_{14}$ polymers is about one order of magnitude lower, decreasing from 0.45 % at 5°C to 0.17 % at 45°C. This is a clear indication of a much higher affinity of the spin probe towards the hydrophobic undecanoylene-containing core as compared to the hexylene core. For temperatures exceeding 45°C this free fraction (f) vanishes. The rotational correlation times of the two bound fractions b_1 and b_2 at room temperature are 6.6 ns and 2.6 ns, respectively, being almost identical with the values obtained for the C_6S_{32}-polymers. Thus, the fatty acid rotational dynamics seem not to be greatly affected by the molecular weight of the polymers C_6S_{32} (470 kDa) and $C_{11}S_{14}$ (64.3 kDa). In **Figure 10.3D** the dynamic regime occupation changes of b_1 and b_2 are compared that are found from C_6S_{32}- and $C_{11}S_{14}$ polymers. This graph shows that the C_n-spacer length might operate as shifting the sigmoidally shaped curves (○ and ●) along the y-axis. This implies the existence of a *first tunable dynamic property* of the core-shell polymers. However, a polymer structural correlation cannot be made from EPR data alone, but optimum functional states of the polymers are indirectly monitored by the free ligand curves in **Figure 10.3** (black, $\phi_{f,min}$).

The temperature-dependent motional dynamics of spin probes and polymers are given as a summary in **Figure 10.4**. Rotational correlation times τ_c of all immobilized fractions b_1, b_2 and g stemming from close contact with the polymers are depicted in **Figure 10.4A**, representing the whole observed temperature range. In contrast to $C_{11}S_{14}$-polymers that show an almost linear growth of $-\log \tau_c$ from 16-DSA in the semilogarithmic diagram of bound fractions b_1 and b_2, the C_6S_{32}-polymer appears to induce a more kinked and sigmoidal temperature response towards spin probe rotational dynamics. This is indicative for a two-state phase transition of the C_6S_{32} polymer leading to a slightly more restricted rotational motion of 16-DSA. For both polymers (C_6S_{32} and $C_{11}S_{14}$), τ_c of the slow component b_1 decreases from 11 ns to about 2 ns from 5 – 95°C, and τ_c of the intermediately slow component b_2 changes from about 3.6 – 5.2 ns at 5°C to 0.40 – 0.47 ns at 95°C. These values are therefore roughly similar and of course in the same rotational dynamic regime. As physically expected, simulated a_{iso} values for f, b_1 and b_2 have also been found to be slightly temperature-dependent and are shown in **Figure H6**.

With the aim to complement the findings from EPR-spectroscopic temperature series, a set of temperature-dependent DLS measurements was recorded for all three samples that were equipped with 16-DSA. These measurements reveal the hydrodynamic polymer size as a function of temperature. The actual size distributions from the regularization process[46] in DLS data evaluations appeared to partially exhibit temperature-dependent polydispersity and are given in **Figure H11**.
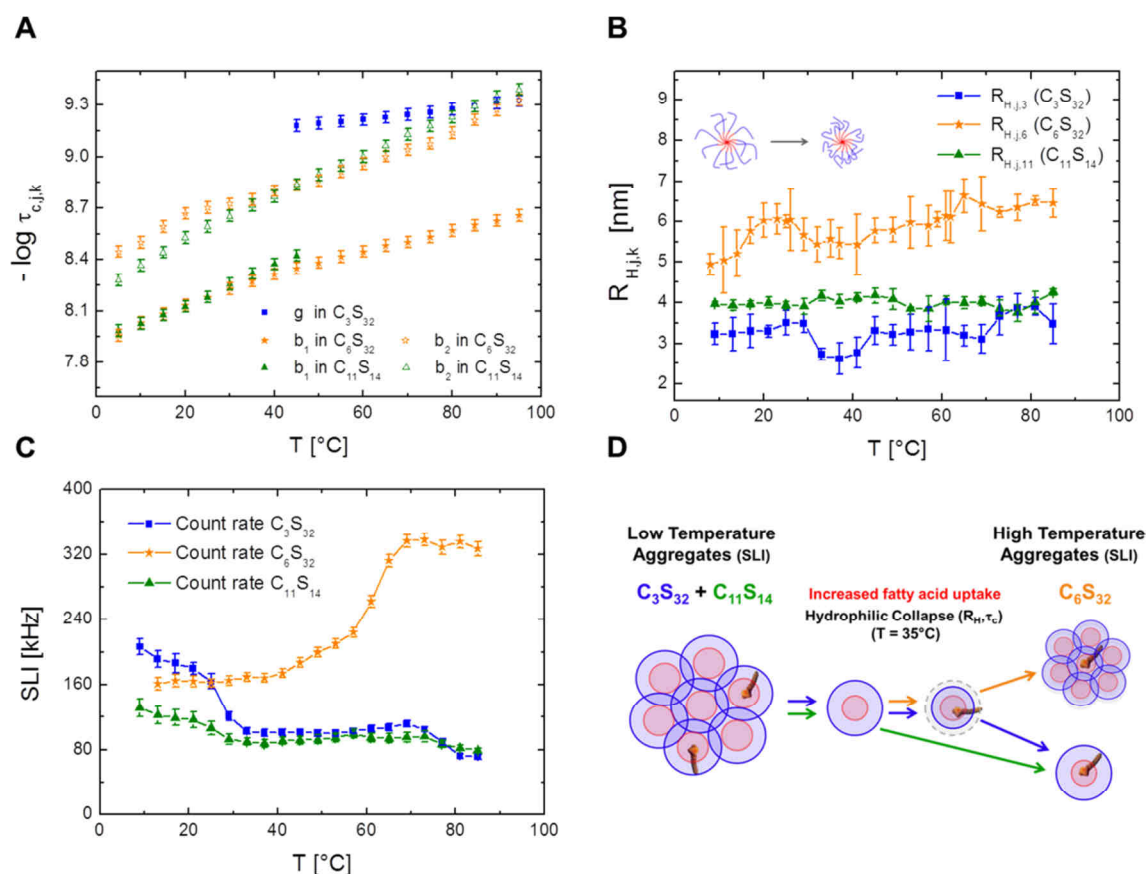
Figure 10.4 | Temperature-induced dynamics of spin probes and polymers. (**A**) Semi-logarithmic plot of all emerging temperature-dependent immobilized fractions (g, b_1, b_2) of 16-DSA in solutions of polymers C_3S_{32}, C_6S_{32} and $C_{11}S_{14}$ as monitored by τ_c. The gel phase g of the C_3S_{32}-polymer is shown in blue, the immobilized fractions b_i of the C_6S_{32}-polymer are shown in orange and $C_{11}S_{14}$-polymer fractions b_i in green. Error margins for τ_c were estimated from simulations to range about 8%. (**B**) Temperature dependence of the main hydrodynamic radii $R_{H,j,k}$ as detected by DLS. Error bars were calculated according to the fluctuation of individual measurements at constant temperature. (**C**) The scattered light intensities (SLI) are given as count rates (in kHz) from temperature-dependent DLS measurements of all three polymers. (**D**) A combined dynamic model for the temperature-dependent formation of aggregates due to SLI of (C) in the scheme of dynamic hydrophobic aggregation in all three polymers based on (A) + (C) and **Figure 10.3**. The polymer concentrations for DLS measurements were 0.13 wt% for C_3S_{32} (blue), 0.2 wt% for C_6S_{32} (orange) and 0.13 wt% for $C_{11}S_{14}$ (green) in water.

While $C_{11}S_{14}$ retains its main hydrodynamic size throughout the whole temperature range at about $R_{H,j,11} = 4.0$ nm, the shorter alkylene chain polymers C_3S_{32} and C_6S_{32} exhibit a detectable non-linear size alteration. The most prominent feature of this non-linearity is a size decrease above 25°C from 3.5 nm to 2.6 nm for C_3S_{32} and 6.1 nm to 5.4 nm for C_6S_{32} with the minimum appearing between 33°C and 42°C for both polymers. This decrease in size ($\Delta R_H \sim 0.7 - 0.9$ nm) is assumed to be related to an intramolecular structural collapse, most probably caused by the hydrophilic shell, as the short shell length polymer $C_{11}S_{14}$ does not show such a transition behavior. In turn, this complements the findings from the EPR-derived motional restriction of the spin probe of the C_6S_{32} polymer with the sigmoidal $-\log \tau_{c,j,6}$ curve above 25°C in **Figure 10.4A**.

In **Figure 10.3A+B**, the occurrence of this minimum in solution size (**Figure 10.4B**) is correlated with an initiated (C_3), or increased (C_6) accessibility of the hydrophobic core for both S_{32} polymers. The solvent quality of water can be regarded as modified for the hydrophilic shell from being a good to being a poor solvent in this temperature range. This is similar to what is generally found for ethylene-

oxide based oligomers and polymers. This in fact generates a structural breathing that will be further on termed as a *hydrophilic collapse*. This hydrophilic collapse is accompanied by a modification in ligand uptake and can be triggered by temperature. Consequently, the spin probes interacting with the polymers experience a motional slowdown when the formerly more water-swollen polyglycerol shell collapses onto the hydrophobic core. This stealth effect towards the hydrophobic core is based on the shell properties that can be varied by synthesis and is therefore designated as the *second dynamic tunable property*.

Another clearly observable effect in the DLS measurements is the change in scattered light intensity (SLI) over temperature for each polymer solution (**Figure 10.4C**). An increase in SLI is generally correlated to the formation of larger particles in solution.[47] Thus, vanishing aggregates and oligomers can be observed with increasing temperature for C_3S_{32} and $C_{11}S_{14}$, while aggregates form in C_6S_{32} (see also **Figure H11**). The polymer characteristics in **Table 10.1** reveal that the temperature-induced formation and depletion of aggregates is very likely connected with the degree of polymerization N and this aggregation probably obeys complicated thermodynamic phase transitions (C_6S_{32} by far has the highest N). This behavior is considered to be the *third tunable dynamic property* of the core-shell polymers and will be termed as *dynamic hydrophobic aggregation* (**Figure 10.4D**).

Another observation that can be made upon temperature increase is the relative change in absolute numbers of spins in between subsequently recorded EPR data shown in **Figure 10.3**. Besides the extraordinary temperature response of different subspectra, these polymers seem to exhibit a mild radical scavenger property, as the double integral of the first-derivative EPR spectra decreases with temperature. The scavenging mechanism apparently gets stronger as the alkylene chain length C_n increases. This may be correlated with an increased residence time τ_r for higher ligand binding affinity of the longer alkylene chains (decreasing equilibrium dissociation constant $K_D \sim 1/\tau_r$).[48] In principle, the reduction of the nitroxide moiety is assumed to follow a disproportionation reaction[49] for 16-DSA, most probably similar to the thermal or acidic disproportionation reaction of the TEMPO spin probe.[33,39,50,51] This circumstance proves the realization of studies comprising polymer heating as irreversible and reliable heating-cooling cycles are therefore inaccessible by EPR as, e.g., the $C_{11}S_{14}$ polymer depletes the spin concentration for 80% during a single heating procedure (2 hours, see **Figure H12**). Since only data within the first heating step were investigated, this signal loss is considered as an insignificant side effect.

10.2.3 | Duality Principle of Fatty Acid Immobilization – Proposal of the Physical Origins

The bimodal hydrophobic ligand immobilization that is observed for C_6S_{32} and $C_{11}S_{14}$ has already been detected for albumin[52] and throughout literature it is considered as a ligand activation process in the substrate transporter molecule based on mutual interference and cooperation. The exact mechanism of fatty acid binding to a hydrophobic transport protein still remains elusive,[53–55] but is thought to proceed in a stepwise scheme,[56,57] as e.g. for cell entry.[58–60] A vast amount of EPR spectroscopic

studies have provided fundamental insights to lipid, steroid and fatty acid dynamics in model membranes exhibiting lateral diffusion,[61–64] appearing among the principal physical phenomenon of the jump diffusion process that was first detected in pure water and lead.[65–67] Several statistical mechanic considerations regarding rotational reorientation in using the solution of the angular diffusion equation[68–70] lead to practical mathematical relationships that discern between Brownian diffusion, free diffusion, and jump diffusion (see **Chapter 2.4.2.2**).[29,69,71] Two different bound spectral fractions $F_{i,j,k}(B)$ were observed for polymers C_6S_{32} and $C_{11}S_{14}$ (**Figure 10.3**), namely b_1 and b_2. The intrinsic rotational correlation times τ_c of b_1 and b_2 differ by a factor of 2.41 ± 0.21 (C_{11}) and 3.42 ± 0.50 (C_6) throughout the observed temperature range. The appearance of jump diffusion in the polymer system can be excluded, as the fatty acid molecules are spatially much more separated, appearing neither in crowded systems as a micelles, nor in a membrane bilayer. The two remaining diffusion types, Brownian diffusion and free diffusion, are considered to represent the most suitable models that fit into the behavior of the polymer bound fatty acid species, as the isotropic hyperfine coupling constant a_{iso} was determined to be the same for b_1 and b_2. If 16-DSA underwent jump diffusion, while being attached to the polymer with the alkylene tail, displacements from the polymer core inside bulk water would give rise to a detectable polar spin probe environment that is monitored by an increase of a_{iso}. It is therefore assumed that rather a spontaneous displacement of the arbitrary molecular rotation angle ψ occurs as it is defined for free diffusion. This assumption anticipates that 16-DSA primarily remains attached to the polymer backbone when this angular displacement takes place. Especially, the reorientational model parameter B_2 for slow motional EPR spectra that was introduced by Freed and coworkers (see also equation 2.67)[69] separates Brownian diffusion from free diffusion by a factor of $7^{1/2} \approx 2.65$.[29,72] This is surprisingly close to the observed differences in τ_c from subspectra b_1 and b_2. Moreover, the reorientational model parameter B_2 is only explicitly determined for spherically symmetric rotation. On a very fundamental level of argumentation the intrinsic axial anisotropy in 16-DSA rotation might be responsible for small deviations from the theoretical value of 2.65 in polymers C_6S_{32} and $C_{11}S_{14}$. A further hint indicating free diffusion is given in **Figure 10.4A+B**, as the hydrophilic collapse of the polymer shell induces a sigmoidal decrease in subspectrum b_2 of polymer C_6S_{32} in the $-\log \tau_c$ curve. This contraction or collapse from the linear polyglycerol chains leads to a decreased local fluidity and therefore an increased local viscosity of the 16-DSA environment. This is only possible if 16-DSA residing in the rotational regime b_2 intercalates at the interface of hydrophobic core and hydrophilic shell, which allows the spin probe dynamics to be influenced by the shell due to its close proximity. The most reasonable physical basis of this *dynamic hydrophobic interconversion process* is a temperature-induced switching from Brownian rotational diffusion towards free diffusion of bound 16-DSA. The spin probe indirectly reflects the structural integrity and the self-assembling features of the individual fatty acid-bearing polymers by the varying spectral fractions $\phi_{b,j,k}$, while the qualitative temperature course of this process is almost identical in

C_6S_{32} and $C_{11}S_{14}$ polymers (**Figure 10.3D**, with a shift along the *y*-axis). An elementary model for this dynamic hydrophobic interconversion of fatty acids is given later in **Chapter 10.2.8**.

10.2.4 | Ligand Uptake Capabilities of C_nS_m Polymers – Scatchard Binding Isotherms

Going beyond the temperature dependence of ligand uptake of the core-shell polymers, a loading study was conducted to determine their ligand binding capacities and corresponding binding affinities at room temperature. As only C_6S_{32} and $C_{11}S_{14}$ polymers bind 16-DSA strongly at ambient conditions, the C_3S_{32} polymer is excluded from this study. The amount of ligand was added in about equidistant concentration steps while the polymer concentration is kept constant. The essential parameters (*f* and *b* fractions) can be directly assessed from spectral simulations of CW EPR data (see also **Appendix H9**). When the ratio of bound to free ligand varies, Scatchard plots[73–76] can be as well constructed for polymers[77] in analogy to the studies on albumin in **Chapter 7**. When an appropriate Scatchard formula expression:

$$\frac{[L]_{b,k}}{[L]_{f,k}} = \frac{[L]_{t,k} - [L]_{f,k}}{[L]_{f,k}} = -\frac{1}{K_{D,k}} \cdot \left([L]_{b,k} - [L]_{b,k,y=0} \right) \tag{10.1}$$

is applied that characterizes the spin probe-binding polymers k, $[L]_{b,k}$ is the concentration of bound ligand, $[L]_{f,k}$ is the concentration of free ligand, $[L]_{t,k}$ the overall concentration of added ligand, $K_{D,k}$ is the macroscopic equilibrium dissociation constant of 16-DSA towards polymer k and $[L]_{b,k,y=0}$ is the intercept with the *x*-axis, equation 10.1 can be simplified to:

$$\nu = -\frac{1}{K_{D,k}} \left(N_L - N_{E,k} \right) = -K_{A,k} \left(N_L - N_{E,k} \right) \tag{10.2}$$

with $\nu = [L]_{b,k} / ([L]_{f,k} \cdot c_{P,k} \cdot N)$. For the thermodynamic analyses in **Chapter 10.2.8** it turns out to be more practical to stay in the picture of ligand association ($K_{A,k}$) when ligand affinity will be temperature-dependent. For now, dissociation constants ($K_{D,k}$) are sufficient to compare the affinities of both polymers towards 16-DSA. The results from the Scatchard plot evaluations can be found in **Figure 10.5** and **Table 10.2**. The linearity observed in both polymer-based Scatchard plots is generally correlated with unspecific binding to equivalent binding sites (N_E).[75] Therefore, equation 10.2 allows to simultaneously extract the maximum number of equivalent binding sites $N_{E,k}$ of the polymers, or the binding sites $N_{E,MM,k}$ of a single macromonomer. Furthermore, the relation $N_{E,MM,k} = [L]_{b,k,y=0} / (c_{P,k} \cdot N)$ holds where $c_{P,k}$ is the total core-shell polymer concentration of polymer k and N is the degree of polymerization of the polymeric structures (**Table 10.1**). The change in $K_{D,k}$ values upon increasing the hydrophobic alkylene chain length from C_6 to C_{11} is therefore accompanied by a decrease of more than one order of magnitude from $K_{D,6} = 28.82\ \mu M$ to $K_{D,11} = 2.42\ \mu M$.
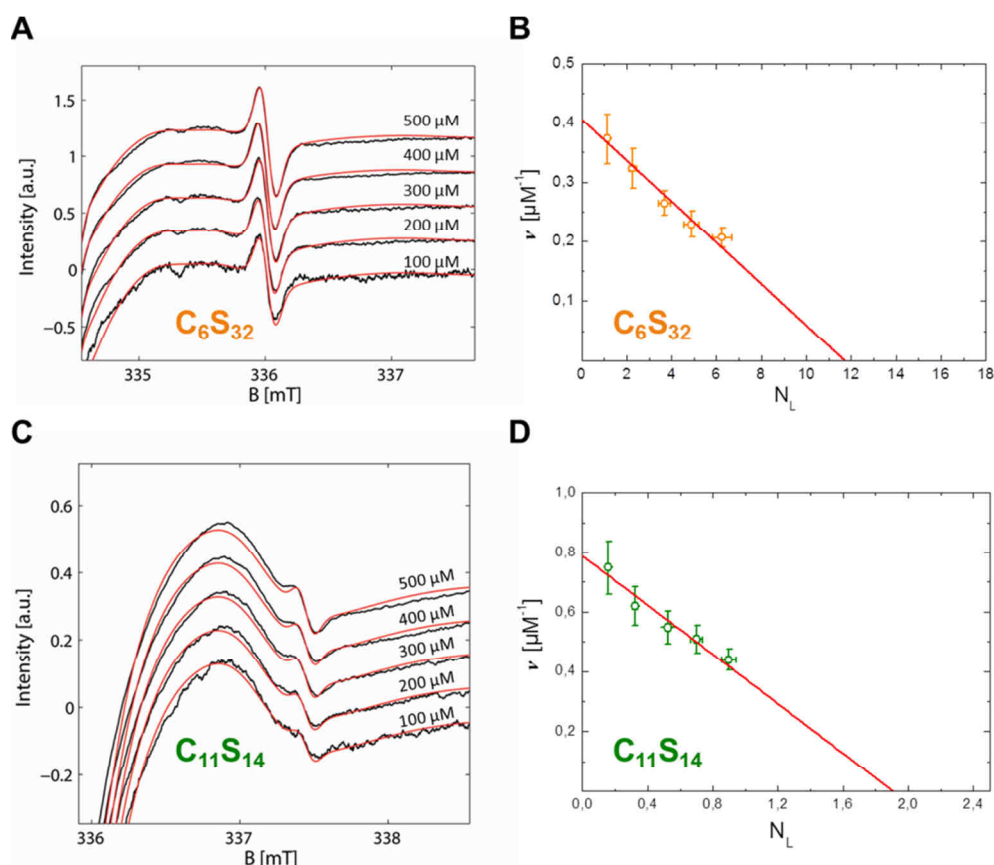
Figure 10.5 | Scatchard plots from C_6S_{32} and $C_{11}S_{14}$ polymers loaded with 16-DSA. The polymers were equipped with 16-DSA ligand in the nominal concentration range of 100 – 500 µM. The polymer concentration was 4 wt% each, i.e. 85 µM (C_6S_{32}) and 622 µM ($C_{11}S_{14}$). The most sensitive spectral parts of CW EPR spectra during ligand loading are highlighted in the high-field ranges (335 mT $< B <$ 338 mT). (**A**) All experimental CW EPR spectra (black) from the 16-DSA loading of C_6S_{32} are given together with spectral simulations (red). (**B**) Scatchard plot of C_6S_{32} from (A) with linear fit according to equation 10.2 (red). (**C**) All experimental CW EPR spectra (black) from the 16-DSA loading of $C_{11}S_{14}$ are given together with spectral simulations (red). (**D**) The Scatchard plot of $C_{11}S_{14}$ from (C) is also given with a linear fit (red).

Thus, ligand binding is obviously much stronger for $C_{11}S_{14}$ due to the better accessibility of the hydrophobic core. The strong decrease in $K_{D,k}$ upon increased alkylene spacer length is considered as the *fourth tunable dynamical parameter*. An unexpected finding is that the C_6 polymer surpasses the C_{11} polymer in terms of the maximum number of binding sites $N_{E,MM,k}$ per macromonomer. A maximum number of ligand binding sites of $N_{E,MM,6} = 0.0684$ is found for C_6S_{32} compared to $N_{E,MM,11} = 0.0445$ for $C_{11}S_{14}$. The associated reason for this may be the partial aggregation of the $C_{11}S_{14}$ polymer at room temperature. Subsequently, some spatial restrictions to the $C_{11}S_{14}$ binding sites may occur in the hydrophobic core, whereas C_6S_{32} is mainly monomeric (see DLS data in **Figure 10.4C**).

Table 10.2 | Results from Scatchard plot analyses of C_6 and C_{11} polymers

k	C_6S_{32}	$C_{11}S_{14}$
$K_{D,k}$ **[µM]**	28.82 ± 2.57	2.42 ± 0.35
$N_{E,MM,k}$	0.0684 ± 0.0079	0.0445 ± 0.0080
$N_{E,k}$	11.82 ± 1.37	1.96 ± 0.35

The actual fatty acid capacity per full polymer chain is clearly much higher for C_6S_{32} with $N_{E,6} = 11.82$ than for $C_{11}S_{14}$ with $N_{E,11} = 1.96$. The straightforward reason is the about 4-fold higher degree of polymerization of C_6S_{32} ($N = 172.8$) compared to $C_{11}S_{14}$ ($N = 44.0$). The creation of a single unspecific binding site in a core-shell polymer structure is therefore assumed to afford a minimum degree of polymerization of about $1/N_{E,MM,k} = 14 - 22$ macromonomers containing C_6 or C_{11}-spacers. The *fifth tunable functional parameter* of the core-shell structures is therefore the number of equivalent unspecific longitudinal ligand binding sites $N_{E,k}$ per polymer, as controlled by the degree of polymerization N.

10.2.5 | Molecular Dynamics (MD) Simulations of C_nS_m Polymers

Molecular dynamics simulations bear the potential to add further insight to the solution behavior of macromolecules. Although being of a purely phenomenological nature here, a global analysis of the modeled core-shell structures after MD simulation gave a strong decrease of polymer compactness with increasing alkylene chain length. On a rather empirical level, the model radius of gyration $R_{G,M,k}$ was normalized to the model molecular weight $MW_{M,k}$, giving values from 0.0362 nm kDa^{-1} for C_3S_{32}, 0.0440 nm kDa^{-1} for C_6S_{32} to 0.0580 nm kDa^{-1} for $C_{11}S_{14}$, coinciding with a slightly decreasing macromolecular density with increasing alkylene spacer length. As the C_3S_{32} polymer shape appears to be almost globular, the $C_{11}S_{14}$ structure is more sheet-like accompanied with a qualitatively decreasing diameter. The peripheric polyglycerol chains of the polymers appear curled and irregular (**Figure H13**). In the viewpoint of only short accessible length scales these polymer brushes can be seen as strictly globular (C_3) or cylindrical in shape (C_6 and C_{11}). Of course, the real polymer shape in a sample depends on the degree of polymerization N and alkylene spacer length C_n. Further details from MD simulations are given in **Table H3**.

10.2.6 | Transmission Electron Microscopy (TEM)

For obtaining a direct nanoscopic view on the polymer shape, transmission electron microscopy (TEM) was applied. Although being of a size close to the resolution limit, all types of hereby investigated alkylene spacer-based core-shell polymers (C_3S_{16}, C_6S_{32} and $C_{11}S_{14}$) could be visualized after uranyl acetate staining. In **Figure 10.6** several soft, worm-like fiber (aggregates) can be observed with diameters between 1.5 and 2.5 nm for C_3S_{16}, C_6S_{32}, and $C_{11}S_{14}$, corresponding to the approximate hydrophobic core diameter. Due to the high polymer concentration and the flexibility of the fiber (aggregates), individual fibers are difficult to be resolved in full-length, since they partly lie on top of each other. Despite the low resolution of the TEM images it is concluded from the molecular shapes that arbitrary, chain-like and stretched structures emerge unlike the proposed unimolecular micelle picture for such polymers that are given in similar studies.[14,78] Of course, each core-shell polymer solution generally assumes an ensemble of lower order aggregates, unimolecular micelles and chain structures at all temperatures with varying fractional occupations.
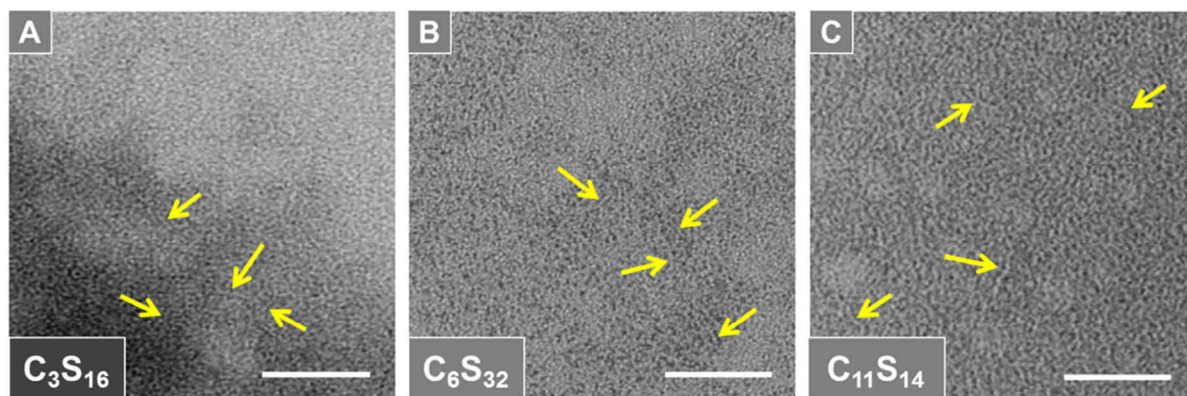
Figure 10.6 | TEM images of some negatively stained core-shell polymers. TEM images from (**A**) C_3S_{16}, (**B**) C_6S_{32} and (**C**) $C_{11}S_{14}$ polymers. Yellow arrows point to worm-like fiber (aggregates) with approximate diameters of a single polymer chain. The concentration for all polymers was set to 2 mg/ml and the scale bar length is 50 nm.

DLS data confirm that picture by showing partial polydisperse features especially for C_3S_{32} and $C_{11}S_{14}$ at low temperatures and C_6S_{32} at higher temperatures (**Figure H11**).

10.2.7 | Rationale for the Structural Origins of Tunable Dynamics in C_nS_m Polymers

A wide variety of dynamic features was revealed from the temperature dependence of the structure-based polymer-ligand and polymer-polymer interactions. In the combined picture from EPR and DLS it is found that an increased ligand uptake takes place for the collapsed shell of S_{32} polymers (**Figure 10.7A**, C_3S_{32} and C_6S_{32}), most probably due to a truncated $<r^2>$ diffusion distance from bulk water to the hydrophobic core. This can be seen as a decreasing stealth property of the hydrophilic shell with temperature. In case of high temperature aggregation (C_6S_{32}), the hydrophobic cores are shielded by polymer packing and ligand binding is therefore less probable. The inherent dynamics of polymer-bound ligands, characterized by the complex temperature response of dynamic rotational regimes b_1 and b_2 is now termed as *dynamic hydrophobic interconversion* ($K_{IC,j,k}$) and the process of ligand binding is termed as *dynamic hydrophobic binding* ($K_{D,k} = K_{A,k}^{-1}$)(**Figure 10.7B**). Together with the *dynamic hydrophobic aggregation* process as an intermolecular feature of all polymers (**Figure 10.4C**), all these processes are now summarized in terms of *dynamic hydrophobic attachment*.

The bigger a hydrophobic core is designed relative to the hydrophilic shell, the smaller is the dissociation constant ($K_{D,k}$) and the ligand binding propensity will be stronger. In **Figure 10.7C** the a_{iso} values from EPR spectral simulations are depicted for $T = 25°C$ (see also **Figure H6**). Compared to the water-exposed and unbound 16-DSA spin probe (added as C_0), a clear decrease in a_{iso} is obtained upon binding to C_6 and C_{11} polymers. The lower the a_{iso} value, the more non-polar and water-depleted appears the hydrophobic core (a_{iso} from 16-DSA that is freely tumbling in the C_3 polymer solution is also depicted). For C_3 polymers the spin probe tends to evade its exposition to the solvent by encapsulating into the small collapsed hydrophobic cores within a gel-like polymeric state. However, this phenomenon only occurs beyond the hydrophilic collapse temperature, when the hydrophobic core forms a polymer-rich, water-separated microenvironment together with the collapsed shell.

Furthermore, it can be claimed that a minimum hydrophobic spacer length is necessary to facilitate uptake of fatty acid molecules in the core-shell structure at room temperature, otherwise the core is invisible for the ligand (cloaked by the hydrophilic polyglycerol shell). This critical uptake spacer length lies somewhere in between C_3 and C_6 alkylene subunits in the macromonomer chains.
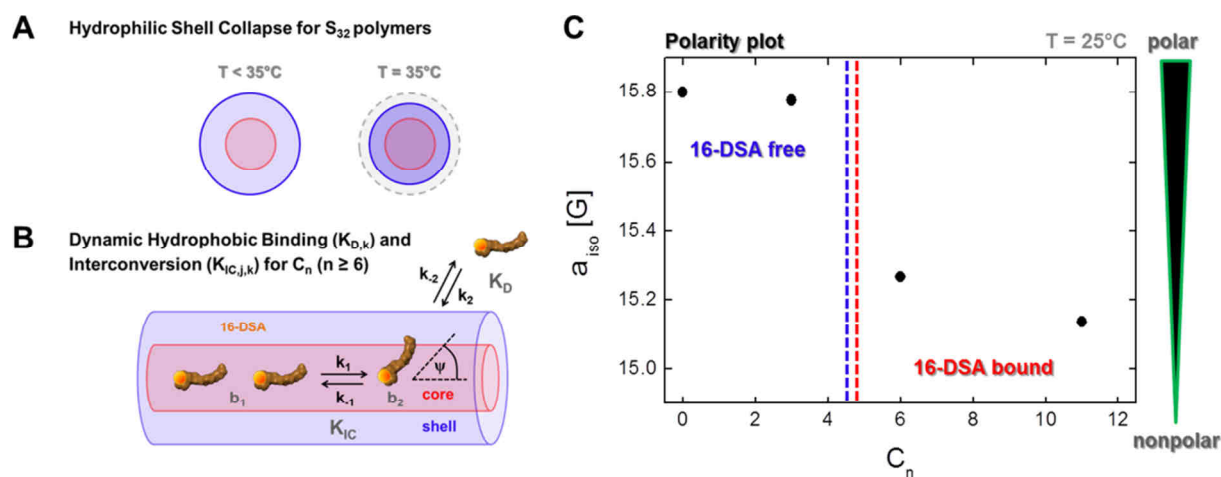

Figure 10.7 | Physical basis of the dynamic hydrophobic attachment principle. (**A**) A sketch of the hydrophilic shell collapse is given as monitored for S_{32} polymers. (**B**) A schematic depiction of dynamic hydrophobic binding ($K_{D,k}$) and interconversion ($K_{IC,j,k}$) is given with hypothetical rate constants k_i. (**C**) Polarity plot of the alkylene spacer length C_n versus hydrophobicity is constructed by means of a_{iso} values at $T = 25°C$ as probed by 16-DSA.

Especially, the C_6S_{32} polymer displays interesting functional aspects that can be described in the framework of a temperature-induced functional polymer activation as a ligand uptake optimum emerges between $35 < j < 50$, encompassing *mammalian body temperature*. It was not tested how functionality might also depend on polymer concentration. Instead, for all EPR studies the polymer and fatty acid ligand concentration ranges were set to several hundred μM that are in the approximate range of the native concentration of albumin.[53] This is a justified approach when considering such core–shell polymeric systems as protein-analogous transporters for drug delivery purposes.

The hydrophilic polyglycerol shell appears similar to water from a spectroscopic point of view. However, an intricate passive effect was found in chain and structural dynamics that implies a stealth property of the shell towards the hydrophobic polymer cores. This proposed *stealth effect* of the hydrophilic shell could be too strong for the smaller hydrophobic cores from the C_3S_{32} polymer, so that no ligand uptake may occur regularly. This is also an important aspect for their potential use as drug transporting vehicles, as the stealth effect may be promising to enhance circulation times of the polymers as polysaccharide analogues.[7] On the other hand, the water-depleted core regions need to be intact so that shell-crossing ligand migration may happen. All this is fulfilled in the modular core-shell type polymers presented in this study.

One of the hallmarks of the hydrophobic effect is the linear dependence of the increased surface area with transfer free energies when dissolving linear n-alkane chains in solvents.[79,80] In contrast, from data collected here it is apparent that the amphiphilic polymerized macromonomers display a much

more complicated cooperative intramolecular interplay than single alkylene chains of varying length would have. From a physical methods point of view, an outstanding feature of using the nitroxide in EPR that probes the dynamic molecular environment is the possibility to obtain an in-depth nanoscopic functional view of a macromolecule interacting with a ligand. A few other aspects could be clarified by complementary investigations regarding dynamic self-association and shape by TEM, DLS and molecular modeling. Especially, TEM showed that rather elongated structures than spherical collapsed micellar structures are present in solution (unimolecular micelles). A clear disadvantage of this EPR approach is the incapability of reversibility studies for increasing alkylene spacer length and the complexity of the spectral simulations. Although many functional principles of the polymers may be intuitive, a CW EPR-based view reveals a quantitative dynamic analysis of the core–shell polymers and their ligands. Some remarkable implications and several design principles are found, suggesting the potential for targeted modification of structural and dynamic core-shell parameters:

(*i*) There are three structural tuning parameters, namely alkylene spacer length (C_n), chain length of the hydrophilic shell (S_m) and the degree of polymerization (*N*) of macromonomers. These can largely be controlled by thorough and careful synthesis and subsequent polymer characterization.[5,7,36] This constitutes an elegant way to strategically tailor novel polymers for quantitatively defined delivery and uptake purposes by design. Moreover, several dynamic properties can be adjusted by chemical alteration of the core-shell structure.

(*ii*) The *dynamic hydrophobic interconversion* process $K_{IC,j,k}$ of dynamic ligand regimes b_1 and b_2 can be designed by adjustment of C_n spacer length. This interconversion process (**Figure 10.3D**) may introduce an optimum working temperature by a dynamic regime population crossing of b_1 and b_2 defining a temperature with optimum ligand uptake in the polymer. Intermolecular interactions like polymeric self-association, as well as by intramolecular interactions affect the accessibility of the hydrophobic core. Apparently, this core-accessibility is mainly determined by the internal dynamics and the size of the hydrophilic shell. This functional principle is the *first dynamic tuning parameter*. A conclusive thermodynamic interpretation that can be devised from this interconversion process is developed in **Chapter 10.2.8**.

(*iii*) A long polyglycerol chain may lead to a temperature-induced *hydrophilic collapse* of the outer shell of the full polymer chain. This is the only dynamic effect that can be conditionally associated with the S_m chain. However, it is not directly its length alone, but rather the ratio of shell size (S_m) to core size (C_n). A slight stealth effect of the hydrophilic shell is proposed that shields the hydrophobic core. This is the *second dynamic tuning parameter* of the core-shell structures and may also comprise a volume phase transition (VPT)[81–83] from a loose to a more compact structure of the polymer as it is seen from DLS data (**Figure 10.4B**). This hydrophilic collapse and stealth effect may further impose the onset of an aggregation process (C_6S_{32}), or the onset of ligand binding in a gel-like state (C_3S_{32}) to the system.

(*iv*) The intermolecular temperature-induced *dynamic hydrophobic aggregation* behavior of the polymers is found to be strongly connected to the degree of polymerization (*N*). Although implications are weak from EPR spectroscopy itself this is considered to be the *third dynamic tuning parameter* as confirmed by DLS data.

(*v*) The affinity of a ligand molecule to its binding substrate is determined by its macroscopic $K_{D,k}$ value as it can be extracted from e.g. Scatchard plots.[73] By increasing the alkylene spacer length (C_n), $K_{D,k} = K_{A,k}^{-1}$ can be adjusted within orders of magnitude. The adjustment of the *dynamic hydrophobic binding* affinity towards a ligand molecule is the *fourth dynamic tuning parameter* of the core-shell polymers.

(*vi*) The degree of polymerization (*N*) is the most decisive parameter for the definition of how many ligands can be bound to unspecific and equivalent ligand binding sites on an individual polymer ($N_{E,k}$). An increase of alkylene spacer length (C_n) does not necessarily improve the number of bound ligands per macromonomer ($N_{E,MM,k}$). This is also indicative for a longitudinal alignment of the bound ligands and is regarded as the *fifth dynamic tuning parameter* and is affected by the structure of the core-shell polymer. Partial aggregation behavior may furthermore alter the individual ligand binding capacity of a polymer. A single unspecific binding site is found to be constructed by polymerization of 14–22 amphiphilic macromonomers.

10.2.8 | Thermodynamic Analysis of Ligand Binding to C_nS_m Polymers

After all the structural and solution dynamic correlations were summarized in **Chapter 10.2.7**, a thorough analysis of some of these aspects will be conducted in this section. The aim is to elucidate the underlying energetic processes that lead to this complicated mutual self-assembly behavior of C_nS_m polymers with the 16-DSA ligand. However, the C_3S_{32} polymers are excluded from this thermodynamic analysis as they lack ligand binding processes that can be correlated with an equilibrium constant as for C_6S_{32} and $C_{11}S_{14}$. In this regard, emphasis is now placed on the strong temperature dependencies of ligand affinity (K_A) and dynamic rotational regime interconversion constants (K_{IC}). Furthermore, it is now tested to which extent those dynamic interconversion data can be interpreted in the context of functional interplay of ligand and macromolecule and how expansive the applied thermodynamic strategy is in general.

Nowadays, thermodynamic profiles of macromolecules are routinely obtained with calorimetric methods. While differential scanning calorimetry (DSC) directly monitors the phase transition temperatures (T_m)[84] and molar heat capacity changes (ΔC_P),[85] isothermal titration calorimetry (ITC) additionally delivers quantitative information about interactions in solution, such as small molecule binding to macromolecules with their corresponding binding stoichiometry (*N*), association constants (K_A) and molar enthalpy changes (ΔH).[86] The binding affinity and stoichiometry may as well be obtained by EPR spectroscopy, as it was shown in **Chapter 10.2.4** for the C_nS_m core-shell structures.

Depending on the macromolecular system, the resulting thermodynamic quantities (ΔH, ΔS = molar entropy changes, ΔG = molar free energy changes, ΔC_P) can also be explicitly temperature-dependent. When a phase transition like a denaturation or dimerization occurs in a macromolecule that either originates from a physical or chemical impact, the corresponding van't Hoff plot ($\ln K$ versus reciprocal temperature T^{-1}) exhibits an inflection point representing the midpoint transition temperature T_m of the involved process, otherwise the van't Hoff plot will be linear.[87]

The observation of non-linear van't Hoff plots was first reported by J. F. Brandts[88] and several other groups.[89,90] In the course of time, several strategies have been developed to extract thermodynamic parameters from such processes that generate curves deviating from linearity. Although being considered as an exotic method, this so-called thermodynamic calorimetry[91] may be employed to obtain thermodynamic data from any physicochemical approach in which heats of reaction cannot be measured directly as e.g. in EPR spectroscopy. The only need is the ability to simultaneously record and distinguish in between two different dynamic, temperature-dependent states of a macromolecular system that are linked by an equilibrium constant K. In case of the core-shell polymers two equilibrium constants can be extracted from ligand dynamics in CW EPR spectra, the association constant $K_A = K_D^{-1}$ and interconversion constant K_{IC}. The most common approach for quantitative evaluations of non-linear van't Hoff plots comprises the application of second,[88,92,93] or higher order polynomials[87,94] for modeling the temperature dependence of $\ln K$ as a function of T^{-1}. Subsequently, changes in molar enthalpy (ΔH), molar entropy (ΔS) and molar heat capacity (ΔC_P) can be calculated accordingly.

In the last decades, this method has been successfully applied in investigations of proteins and was adopted for methods such as hydrophobic interaction chromatography (HIC),[92] reversed-phase high performance liquid chromatography (RP-HPLC),[87,95] CW EPR,[96] pulsed EPR (DEER)[97] and also calorimetric methods as DSC[94,98,99] and ITC.[100–102] The physical reason for non-linear temperature dependences in ΔH is ascribed to large molar heat capacity changes ΔC_P, mainly originating from a change in buried nonpolar surface area as a hallmark of the hydrophobic effect[80] and a change in internal vibrational modes.[85] At neutral pH, electrostatic interactions, as e.g. in proteins, are usually weak compared to the hydrophobic effect.[103] In this study, electrostatic interactions can be considered negligible, as the hydrophilic polyglycerol shell (S_m) and the hydrophobic alkylene core (C_n) should be neutral in the investigated physiological pH range of 7.5 ± 0.5.

In water, this system may be conceptually reduced to mainly consist of dipolar H-bonding and hydrophobic interactions between ligand, water and substrate. Finally, this system turns out to constitute an appropriate model system with the potential to emulate hydrophobic binding to more complex polypeptide chains (see **Chapter 11**). The molecular basis of such dynamic intra- and intermolecular amphiphilic assemblies is not well understood for large and complex systems. Therefore, an example is provided that may aid in overcoming the lack of appropriate models that facilitate a simplified and distinct functional view,[104] especially regarding the general interplay of

substrates with fatty acids.[54] In principle, the association constant K_A is defined by relative fractions $\phi_{i,j,k}$ of purely free (*f*) and purely bound (*b*) ligands (see **Figure 10.8**). Particularly, the observed interconversion equilibrium constant K_{IC} appears to contain nanoscopic information on slight changes in polymer dynamics (see also **Figure 10.3** and **Figure 10.4**). Both rotational regimes, b_1 and b_2, could be distinguished from rigorous simulations of EPR spectra as it was shown in **Chapter 10.2.2**. These different immobilized modes of diffusion are usually defined by the microscopic order-macroscopic disorder (MOMD) model.[105] The choice of a Brownian diffusion model for b_1 and free diffusion for b_2 was justified in **Chapter 10.2.3** where it is assumed that spontaneous reorientations of molecular axes occur with arbitrary angles ψ.[29,69,72] Here, this phenomenon was observed as a temperature-induced decrease in $\tau_{c,b}$ by a scaling factor of about $\tau_{c,b1}/\tau_{c,b2} = 2.4 - 3.4$ that is quite close to the theoretical value of $7^{1/2} = 2.65$.
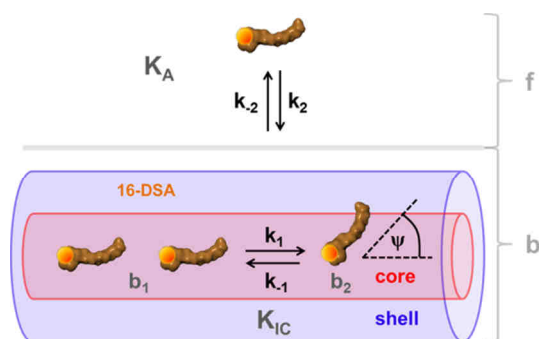

Figure 10.8 | Thermodynamic model and essential dynamic regimes of 16-DSA. Schematic model for thermodynamic analyses comprising dynamic hydrophobic binding (K_A) and dynamic hydrophobic interconversion (K_{IC}). 16-DSA appears in free (*f*) and bound rotational regimes when interacting with core-shell polymers C_nS_m (*b* summarizes bound fractions b_1 and b_2). The symbols k_i denote two independent processes with rate constants k_1 and k_2, whereas ψ is the spontaneous flip angle of the 16-DSA molecular axis in the so-called free diffusion process[29,69] that emerges in the bound state (see also **Chapter 10.2.3** and **Figure 10.7**).

In EPR spectroscopy, several van't Hoff approaches were applied in order to describe dynamic interconversion-like processes of paramagnetic moieties in proteins (linear),[52,106] as well as in order parameters (*S*) from membrane-bound lipid spin probes (non-linear),[96,107,108] but to date there is no reported study analyzing non-linear van't Hoff plots in order to investigate interconversion processes of bound ligand states to individual macromolecules. Beyond the specific characterization of dynamic hydrophobic attachment of amphiphilic molecules to core-shell polymers, a guideline is established for employing spin probing and EPR spectroscopy to macromolecules for some ample nanoscopic thermodynamic analyses. Furthermore, this study offers a theoretical treatise concentrating exclusively on ligand binding thermodynamics, while proving an unconventional strategy to advance towards an EPR-based quantification of the physical driving forces of ligand binding to macromolecules.

10.2.8.1 | Thermodynamic Considerations for 16-DSA Binding to C_nS_m Core-shell Polymers

The basis for this analytic approach is the presence of the association constant K_A and the interconversion constant K_{IC}. These values can be assessed from the different fractions $\phi_{i,j,k}$ of free (*f*) and bound (b_1, b_2) dynamic regimes of 16-DSA interacting in a temperature-dependent manner with the polymers as shown in **Figure 10.9**. Deconvolution of EPR spectra was already thoroughly analyzed in **Chapter 10.2.2**. For example, insets I and II in **Figure 10.9** show how the free spectral component *f* vanishes with rising temperature in favor of an ever growing b_2 component, while the b_1

component simultaneously vanishes noticeably with increasing temperature (see also **Figure 10.3**). Thus the two different dynamic processes are either observed from free or bound ligand ($K_{A,j,k}$ from $\phi_{f,j,k}$ and $\phi_{b,j,k}$), while there is an additional differentiation for Brownian (b_1) and free diffusion regime (b_2). $K_{IC,j,k}$ is therefore obtained from $\phi_{b1,j,k}$ and $\phi_{b2,j,k}$ from each temperature-dependent EPR spectrum $S_{j,k}(B)$. A thermodynamic analysis requires simple kinetic models for the quantitative description of the strong temperature dependences of 16-DSA dynamics when it interacts with C_6S_{32} and $C_{11}S_{14}$ polymers. First, a general kinetic model is proposed for the interconversion (IC) process with the rate equation:

$$b_1 \; \underset{k_{-1,j,k}}{\overset{k_{1,j,k}}{\rightleftharpoons}} \; b_2 \qquad , \qquad (10.3)$$

while assuming a temperature-dependent equilibrium of forward ($k_{1,j,k}$) and backward reaction ($k_{-1,j,k}$) at each temperature j corresponding to an equilibrium constant $K_{IC,j,k}$ that is defined as:

$$K_{IC,j,k} = \frac{k_{1,j,k}}{k_{-1,j,k}} = \frac{\phi_{b2,j,k}}{\phi_{b1,j,k}} = \frac{\phi_{b2,j,k}}{(1-\phi_{b2,j,k})} = \frac{[L]_{b2,j,k}}{[L]_{b1,j,k}} \qquad (10.4)$$

with $\phi_{b,j,k}$ being the temperature-dependent spectral fraction i of each bound component b_1 or b_2 and $[L]_{bi,j,k}$ is the corresponding concentration of ligand in the two bound regimes. Secondly, binding of a ligand L itself to a hypothetical arbitrary binding site or receptor R gives the receptor-ligand-complex RL by the relation:[75]

$$R + L \; \underset{k_{-2,j,k}}{\overset{k_{2,j,k}}{\rightleftharpoons}} \; RL \qquad (10.5)$$

where $k_{2,j,k}$ is the association rate constant and $k_{-2,j,k}$ is the dissociation rate constant. Due to the mass action law the equilibrium association constant $K_{A,j,k} = K_{D,j,k}^{-1}$ is given by:

$$K_{A,j,k} = \frac{[RL]_{j,k}}{[R]_{f,j,k}[L]_{f,j,k}} \qquad (10.6)$$

with $[R]_{f,j,k}$ being the free receptor concentration, $[L]_{f,j,k}$ the free ligand concentration and $[RL]_{j,k}$ the concentration of the receptor-ligand-complex, that can also be substituted by the fractions $\phi_{i,j,k}$ of each spectral component. $[RL]_{j,k}$ may be replaced by the bound fraction of ligand $[L]_{b,j,k} = [L]_{b1,j,k} + [L]_{b2,j,k}$. With a total ligand concentration $[L]_{t,k}$ that by far exceeds the free ligand concentration $[L]_{f,j,k}$ in these self-organized systems ($[L]_{f,j,k} \ll [L]_{t,k}$), tight binding characteristics apply and equation 10.6 has to be

rewritten as:[75]

$$K_{A,j,k} = \frac{[RL]_{j,k}}{([R]_{t,k} - [RL]_{j,k}) \cdot ([L]_{t,k} - [RL]_{j,k})} \tag{10.7}$$

where $[R]_{t,k}$ is the total receptor, or binding site concentration. After several rearrangements expressing the polymer concentration $c_{P,k}$ (**Table 10.3**) and the receptor number $N_{E,k}$ (**Table 10.2**) in terms of the total receptor concentration $[R]_{t,k} = c_{P,k} \cdot N_{E,k}$, it can be shown that a simple and practical formula emerges that contains only terms that are experimentally and analytically accessible:

$$K_{A,j,k} = \left[[R]_{t,k} \left(\frac{[L]_{t,k}}{[L]_{b,j,k}} - 1 \right) - [L]_{f,j,k} \right]^{-1} \tag{10.8}$$

An explicit derivation of equation 10.8 is given in **Appendix H10**. The individual values that have been used for this analysis are given in **Table 10.3** as summarized from previous chapters.
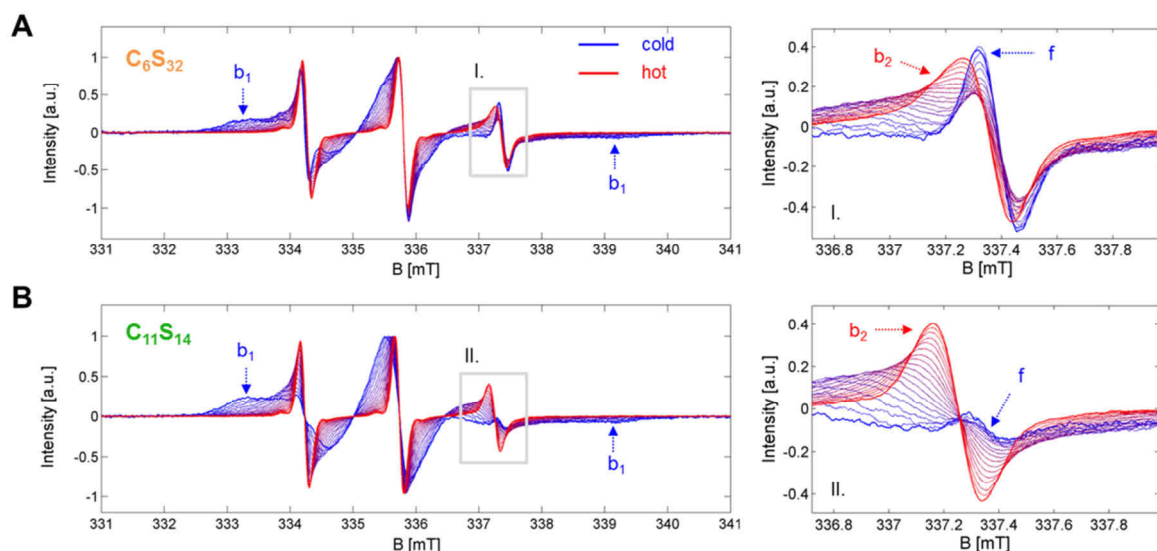
Figure 10.9 | Temperature-dependent EPR spectroscopic datasets $S_{j,k}(B)$. (A) Core-shell polymer C_6S_{32} and **(B)** Core-shell polymer $C_{11}S_{14}$ with the most prominent spectral features highlighted from dynamic fractions f, b_1 and b_2. The gray insets (I. in (A) and II. in (B)) on the left hand side are magnified on the right. EPR spectra are shown in the temperature range of 5 to 95°C in steps of 5 K. The lowest (dark blue) and highest (dark red) temperature curve is depicted in bold to create an envelope effect. Simulations of these spectra (**Figure H9** and **Figure H10**) yielded fractions shown in **Figure 10.3**.

The values for $c_{P,k}$ and $N_{E,k}$ are for now assumed to remain largely constant over the whole observed temperature range, predominantly depending on the degree of polymerization N (see **Table 10.1**). The temperature dependence of $K_{A,j,k}$ is shown in a van't Hoff plot in **Figure 10.10A**. The non-linear van't Hoff plot of C_6S_{32} can be significantly simplified by subdividing the process into separate temperature regimes. Between $5 < j < 25$ and $55 < j < 95$, the curve practically resembles straight lines (orange). Between $30 < j < 50$, the association constant remains largely unaltered at a value of $K_{A,30-50,6} =$

$(4.6 \pm 0.2) \cdot 10^4$ M^{-1} corresponding to a dissociation constant of $K_{D,30-50,6} = (21.9 \pm 0.1)$ µM. However, in direct comparison, the $C_{11}S_{14}$ polymer remarkably shows a straight decrease of $\ln K_{A,j,k}$ between $5 < j < 45$ (**Figure 10.10A**).

Table 10.3 | Dynamic parameters of C_nS_m core-shell polymers.

Method	parameter	C_6S_{32}	$C_{11}S_{14}$
DLS[a]	HCT[b] [°C]	$30 < j < 40$	–
	DHAT[c] [°C]	$j > 35$	$j < 35$
EPR[a]	DRO[d]	f, b_1, b_2	f, b_1, b_2
	$K_{A,25,k}$[e] [M^{-1}]	$(3.47 \pm 0.31) \cdot 10^4$	$(4.13 \pm 0.60) \cdot 10^5$
	$c_{P,k}$[f] [µM]	85	622
	$N_{E,k} \cdot c_{P,k}$ [mM]	1.005	1.219
	$a_{iso,b}$[g] [G]	15.27	15.14
	$a_{iso,f}$[h] [G]	15.79	15.78

[a]As observed in **Chapter 10.2.2**, [b]HCT = Hydrophilic collapse temperature (**Figure 10.4B**), [c]DHAT = Dynamic hydrophobic aggregation temperature (**Figure 10.4C**), [d]DRO = Dynamic regime occupation from $5 < j < 95$ (C_6S_{32}) and $5 < j < 45$ ($C_{11}S_{14}$) with free (f), and the two bound (b_1, b_2) regimes (**Figure 10.3**). [e]$K_{A,25,k}$ = association constant of 16-DSA towards polymers k at $j = 25$ from corresponding dissociation constants $K_{D,25,k}$ in **Table 10.2**. [f]$c_{P,k}$ = total polymer concentration and $N_{E,k}$ = number of receptors per polymer determined from Scatchard plots at $j = 25$ (**Table 10.2**). [g]$a_{iso,b}$ = isotropic hyperfine coupling constant at $j = 25$ as a hydrophobic core polarity index of bound (b_i) 16-DSA spin probes. The lower this $a_{iso,b}$ value, the less polar the probed environment. [h]$a_{iso,f}$ = isotropic hyperfine coupling constant at $j = 25$ for free (f) 16-DSA spin probes in aqueous environment. For further $a_{iso,i,j,k}$ values the reader is referred to **Table H2** and **Figure H6**.

In this context, a quantitative analysis of van't Hoff plots is conducted with a linear extrapolation procedure of data points, as the principles of ligand binding energetics are described by:[109]

$$\Delta G^\circ_{A,j,k} = -RT \ln K_{A,j,k} = RT \ln K_{D,j,k} \tag{10.9}$$

where $K_{A,j,k}$ and $K_{D,j,k}$ are again the binding association and dissociation constants ($K_{A,j,k} = K_{D,j,k}^{-1}$), R is the universal gas constant and T is the absolute temperature in Kelvin. Now equation 10.8 and equation 10.9 are combined to get an expression for $\ln K_{A,j,k}$ as obtained from EPR data:

$$\ln K_{A,j,k} = -\ln\left[[R]_{t,k} \left(\frac{[L]_{t,k}}{[L]_{b,j,k}} - 1 \right) - [L]_{f,j,k} \right]$$
$$= -\frac{\Delta G^\circ_{A,j,k}}{RT} = \frac{\Delta S^\circ_{A,j,k}}{R} - \frac{\Delta H^\circ_{A,j,k}}{R} \cdot \frac{1}{T} \tag{10.10}$$

here $-\Delta H^\circ_{A,j,k}/R$ is the slope and $\Delta S^\circ_{A,j,k}/R$ is the y-axis intercept of the straight line comprising the standard molar enthalpy ($\Delta H^\circ_{A,j,k}$) and entropy changes ($\Delta S^\circ_{A,j,k}$) of the ligand association process (see also equation H.19 and H.20). The results from this analysis are shown in **Table 10.4** and **Table H4**.
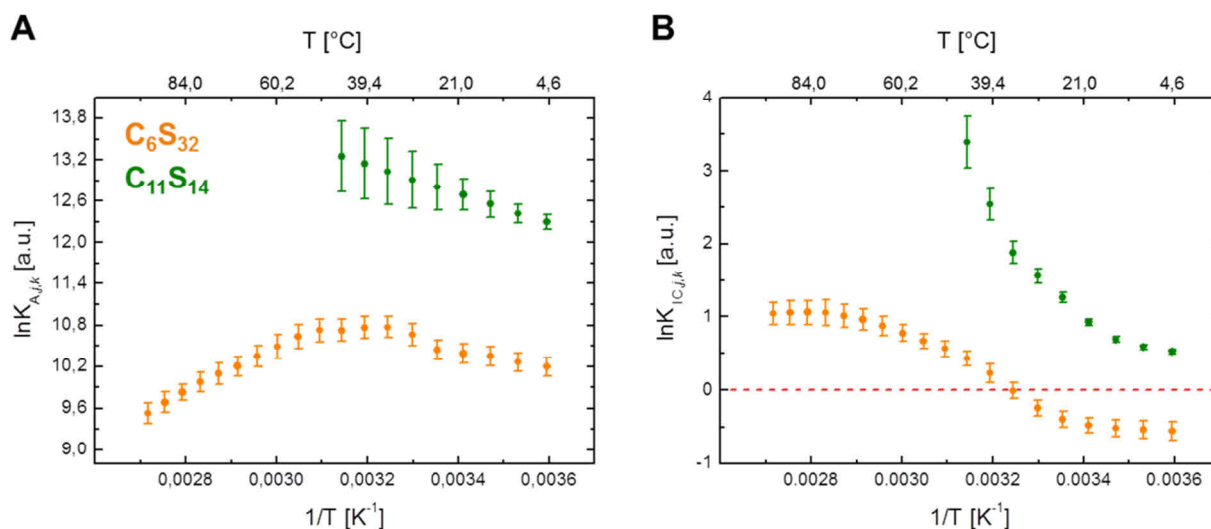
Figure 10.10 | Van't Hoff plots of 16-DSA interacting with C_nS_m polymers from EPR spectroscopy. Individual data points are calculated from EPR spectral deconvolutions shown in **Figure 10.3** for (**A**) the ligand association constant ($\ln K_{A,j,k}$) and (**B**) the interconversion process ($\ln K_{IC,j,k}$). The C_6S_{32} polymer curves are represented in orange and $C_{11}S_{14}$ polymer curves are shown in green.

Additionally, linear fits to experimental $\ln K_{A,j,k}$ curves with an R^2 between 0.9841 and 0.9989 are shown in **Figure H15A–C**. 16-DSA association at low temperatures ($j < 30$) is reproduced by a line with negative slope for both polymers, indicating a weakly endothermic binding process ($\Delta H°_{A,25,k} > 0$: 8.6 kJ mol^{-1} for C_6S_{32} and 17.5 kJ mol^{-1} for $C_{11}S_{14}$) with high positive entropy changes ($\Delta S°_{A,25,k} > 0$) of 115.7 J mol^{-1} K^{-1} for the C_6S_{32} polymer and 165.2 J mol^{-1} K^{-1} for the $C_{11}S_{14}$ polymer.

Table 10.4 | Thermodynamic parameters of $\ln K_{A,j,k}$ from C_nS_m polymers

	$\ln K_{A,j,k}{}^a$		
	C_6S_{32}		$C_{11}S_{14}$
j [°C]	($j < 30$)	($j > 50$)	($j < 45$)
$\Delta G^{\bullet}_{A,25,k}$ [kJ mol^{-1}]	–25.9 ± 1.1	–28.9 ± 1.2	–31.7 ± 0.4
$\Delta H^{\bullet}_{A,25,k}$ [kJ mol^{-1}]	8.6 ± 0.5	–27.1 ± 0.7	17.5 ± 0.2
$\Delta S^{\bullet}_{A,25,k}$ [J mol^{-1} K^{-1}]	115.7 ± 1.9	5.8 ± 1.9	165.2 ± 0.7

^{a}Errors have been determined from propagations of uncertainty according to equations H.21 – H.24.

Hence, this association reaction of 16-DSA to the polymers is exergonic ($\Delta G°_{A,25,k} < 0$) and entropy driven ($\Delta H°_{A,25,k} > 0$, $\Delta S°_{A,25,k} > 0$)[95] in the investigated low-temperature ranges (see **Table 10.4**, $j < 45$). This can be interpreted as the longer the alkylene spacer C_n and the more nonpolar the hydrophobic core is ($a_{iso,b}$, **Table 10.3**), the more positive are the entropy changes and the more endothermic is the ligand association process. In principle, this means that thermal energy from the environment is converted into binding energy.

While linearity is found throughout the whole observable temperature range for $C_{11}S_{14}$, there is a slope inversion between $30 < j < 50$ for C_6S_{32}. For $j > 50$, the ligand binding process is converted into a comparatively strong exothermic process ($\Delta H°_{A,>50,6} = -27.1$ kJ mol^{-1}) with a much smaller entropy increase upon ligand association of $\Delta S°_{A,>50,6} = 5.8$ J mol^{-1} K^{-1} in comparison to low temperatures ($\Delta S°_{A,25,6} = 115.7$ J mol^{-1} K^{-1}). So, this high temperature decrease in ligand affinity can still be regarded as exergonic in terms of ligand binding ($\Delta G°_{A,>50,6} < 0$) and was shown to be correlated with partial aggregation of C_6S_{32} polymers for $j > 35$ (see **Figure 10.4C**).

From DLS measurements and corresponding $-\log \tau_{c,j,k}$ curves in EPR data (**Figure 10.4A+B**), a partial hydrophobic polymer aggregation can be identified that is induced by a dynamic change in the C_6S_{32} polymer-water interaction between $30 < j < 40$ (HCT, **Table 10.3**). This change was initially assigned to the collapse of the hydrophilic shell. This partial aggregation subsequent to the hydrophilic shell collapse leads to a reduced fatty acid binding affinity with increasing temperature due to sterical hindrance, accompanied by a consequent strong negative enthalpy change ($\Delta H°_{A,>50,6} < 0$). Hence, the $C_{11}S_{14}$ polymer provides a higher binding affinity K_A and entropy gain for $j < 35$ ($\Delta S°_{A,25,11} > \Delta S°_{A,25,6}$, see **Table 10.4**). Ligand binding towards the hydrophobic core is apparently enhanced by absence of aggregation in direct comparison to the C_6S_{32} polymer (**Figure 10.4C**).

This strategy of extracting K_A values is nowadays routinely applied in EPR spectroscopy,[16,18,76,110,111] corresponding to findings that can be made from ITC studies. Although no ITC measurements were conducted here, it can be assumed that the solution properties may change decisively in chemical potential, pH, and ionic strength upon 16-DSA ligand titration. The results in the next section are considered to reveal an analytic method that is assumed to be exclusively accessible by EPR spectroscopy. Regarding the temperature-dependent rotational diffusion regime interconversion constant $K_{IC,j,k}$ (see **Figure 10.10B**), a more intricate approach is required compared with the ligand association process. The aim is to introduce fit functions for $\ln K_{IC,j,k}$ in order to reproduce the obtained van't Hoff curve shapes,[87] as it was recently shown by EPR spectroscopy for gel and fluid-like phases in pulmonary surfactants.[96]

These fit curves are crucial for the derivation of the required thermodynamic functions (ΔH, ΔS, etc.). In the $\ln K_{IC,j,k}$ graphs (**Figure 10.10B**) non-linearity is observed throughout for both polymers. Generally, the temperature dependence of equilibrium constants K_i is well described by the van't Hoff equation:[112,113]

$$\frac{d \ln K_i}{d\left(\frac{1}{T}\right)} = -\frac{\Delta H_{v.H.}}{R} \qquad , \qquad (10.11)$$

when $\Delta H_{v.H.}$ constitutes the van't Hoff enthalpy and the inverse temperature (T^{-1}) represents an x-axis. Consequently, the observed interconversion equilibrium ($K_{IC,j,k}$) as it was defined in equation 10.4 and **Figure 10.8** can be thermodynamically evaluated with a continuative set of equations:[92,100]

$$\Delta G^{\circ}_{\mathrm{IC},j,k} = -RT \ln K_{\mathrm{IC},j,k} = \Delta H^{\circ}_{\mathrm{IC},j,k} - T\Delta S^{\circ}_{\mathrm{IC},j,k} \tag{10.12}$$

$$\Delta C^{\circ}_{\mathrm{P,IC},j,k} = \left(\frac{\partial \Delta H^{\circ}_{\mathrm{IC},j,k}}{\partial T} \right)_{\mathrm{P}} \ . \tag{10.13}$$

The fit functions for the $\ln K_{\mathrm{IC},j,k}$ van't Hoff plots for C_6S_{32} and $C_{11}S_{14}$ polymers that have been ruled out to describe the curve progressions best are shown in equations 10.14 – 10.21. While the C_6S_{32}-polymer requires a fourth order polynomial (equation 10.14) to reproduce the curve, it suffices to use a simple exponential function (equation 10.18) in case of $C_{11}S_{14}$. Note, that exponential functions are not conventionally applied to such kind of analysis. Equations 10.15 – 10.17 and equations 10.19 – 10.21 can be directly derived from equations 10.14 and 10.18 by applying the mathematical expressions in equations 10.11 – 10.13. Both original non-linear fit curves of data shown in **Figure 10.10B** are given in **Figure H15D–E**.

In **Figure 10.11** all fit-derived functions shown in equations 10.14 – 10.21 are plotted for both polymers in the whole investigated temperature range ($5 < j < 95$). For a polynomial analysis of the 16-DSA-probed C_6S_{32} polymers the fit parameters are chosen as α_z (with $z = 1 - 5$), while the fit parameters from exponential analyses of the $C_{11}S_{14}$ polymers are given as κ_y (with $y = 1 - 3$).

$$\ln K_{\mathrm{IC},j,6} = \alpha_1 + \frac{\alpha_2}{T} + \frac{\alpha_3}{T^2} + \frac{\alpha_4}{T^3} + \frac{\alpha_5}{T^4} \tag{10.14}$$

$$\ln K_{\mathrm{IC},j,11} = \kappa_1 \cdot e^{\frac{1}{\kappa_2 T}} + \kappa_3 \tag{10.18}$$

$$\Delta H^{\circ}_{\mathrm{IC},j,6} = -R\left(\alpha_2 + \frac{2\alpha_3}{T} + \frac{3\alpha_4}{T^2} + \frac{4\alpha_5}{T^3} \right) \tag{10.15}$$

$$\Delta H^{\circ}_{\mathrm{IC},j,11} = -\frac{\kappa_1 R}{\kappa_2} \cdot e^{\frac{1}{\kappa_2 T}} \tag{10.19}$$

$$\Delta S^{\circ}_{\mathrm{IC},j,6} = R\cdot\left(\alpha_1 - \frac{\alpha_3}{T^2} - \frac{2\alpha_4}{T^3} - \frac{3\alpha_5}{T^4} \right) \tag{10.16}$$

$$\Delta S^{\circ}_{\mathrm{IC},j,11} = R\cdot\left(\left(1 - \frac{\kappa_2}{T}\right)\cdot \kappa_1 \cdot e^{\frac{1}{\kappa_2 T}} + \kappa_3 \right) \tag{10.20}$$

$$\Delta C^{\circ}_{\mathrm{P,IC},j,6} = R\cdot\left(\frac{2\alpha_3}{T^2} + \frac{6\alpha_4}{T^3} + \frac{12\alpha_5}{T^4} \right) \tag{10.17}$$

$$\Delta C^{\circ}_{\mathrm{P,IC},j,11} = \frac{\kappa_1 R}{\kappa_2^2} \cdot \frac{e^{\frac{1}{\kappa_2 T}}}{T^2} \tag{10.21}$$

A complete set of fit parameters is given in **Table H5**. The free energy changes $\Delta G^{\circ}_{\mathrm{IC},j,k}$ from the interconversion process (**Figure 10.11B**) are obtained in a straightforward procedure from the well-known relation $\Delta G^{\circ}_{\mathrm{IC},j,k} = -RT\ln K_{\mathrm{IC},j,k}$ in compliance with equation 10.9.

It is reasonable to assume that the interconversion process may reflect a structural and/or dynamic transition in the combined ligand-polymer systems as ligands should be able to sense the structural rearrangements of polymeric substrates when present. The system is assumed to be in a state in which small structural perturbations may lead to changes in stability and therefore to small changes in the melting temperatures $T_{\mathrm{m}} = \Delta H^{\circ}\cdot\Delta S^{\circ -1}$ where free energy is zero ($\Delta G^{\circ} = 0$),[87,114] as it is usually discussed for proteins.[115] These dynamic instabilities of the rotational regime interconversion K_{IC} are now tracked with strategies from protein biophysics.

This step facilitates access to thermodynamic properties of polymer-bound ligands from a nanoscopic view on the system without the need for measuring macroscopic properties like heat.

As $C_{11}S_{14}$ exhibits exponentially shaped curves throughout $\ln K_{IC,j,11}$, $\Delta G^\circ_{IC,j,11}$, $\Delta H^\circ_{IC,j,11}$, $\Delta S^\circ_{IC,j,11}$ and $\Delta C^\circ_{P,IC,j,11}$ (**Figure 10.11A–E**, green) without any zero-crossings, it is assumed that the interconversion process from Brownian to free diffusion of bound 16-DSA is purely entropy driven for this polymer ($\Delta H^\circ_{IC,j,11} > 0$, $\Delta S^\circ_{IC,j,11} > 0$) at all temperatures. The rise in positive $\Delta C^\circ_{P,IC,j,11}$ with temperature denotes increased apolar hydration ($\Delta C_P > 0$)[91] of bound ligands, illustrating the mere opening of the buried core segments from lower to higher temperatures without any macroscopically detectable transitions (see below). As ligand association to this polymer can be regarded as entropy driven and exergonic at all temperatures ($\Delta H^\circ_{A,j,11} > 0$, $\Delta S^\circ_{A,j,11} > 0$, $\Delta G^\circ_{A,j,11} < 0$; **Table 10.4**), this finding is also in agreement with DLS data (**Figure 10.4C**), as partial $C_{11}S_{14}$-aggregates were shown to vanish for $j > 35$, therefore increasing the ligands' accessibility to the hydrophobic core (**Table 10.3**). However, the reduction in the spectral fraction b_1 coincides with a simultaneous depletion of the free fraction f of 16-DSA in underlying EPR spectra (**Figure 10.9**). Thus, the corresponding ligand binding affinity (K_A) does not seem to be energetically coupled to the interconversion process (K_{IC}).
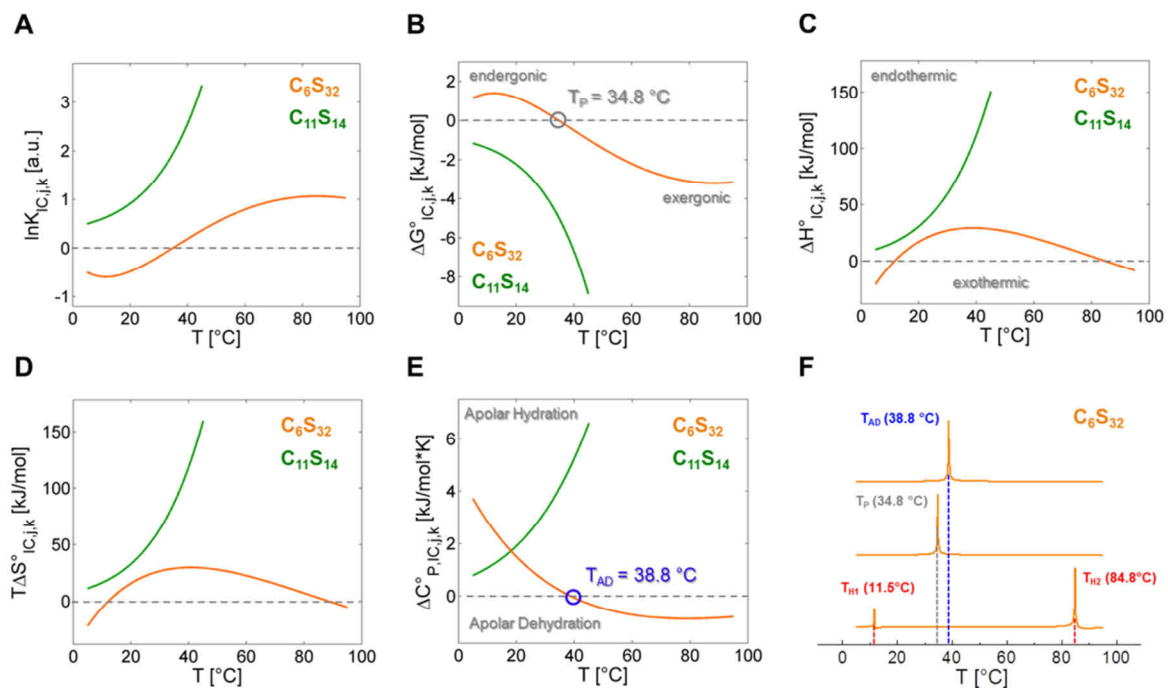
Figure 10.11 | Graphical representation of the thermodynamic functions calculated from $\ln K_{IC,j,k}$. Continuous depiction of (**A**) $\ln K_{IC,j,k}$ vs. T from equations 10.14 and 10.18, resulting in the (**B**) molar Gibbs free energy change $\Delta G^\circ_{IC,j,k}$ with the performance temperature T_P at 34.8°C (gray), as well as endergonic ($\Delta G^\circ_{IC} > 0$) and exergonic ($\Delta G^\circ_{IC} < 0$) regions. (**C**) Temperature-dependent change of molar enthalpy $\Delta H^\circ_{IC,j,k}$ calculated from equations 10.15 and 10.19 with endothermic ($\Delta H^\circ_{IC} > 0$) and exothermic ($\Delta H^\circ_{IC} < 0$) regions. (**D**) Temperature-dependent change of molar entropy $T\Delta S^\circ_{IC,j,k}$ calculated from equations 10.16 and 10.20. (**E**) The changes in molar heat capacity $\Delta C^\circ_{P,IC,j,k}$ are highlighted with the apolar dehydration temperature $T_{AD} = 38.8$°C (blue). Those curves are calculated from equations 10.17 and 10.21 and regions of apolar hydration ($\Delta C^\circ_{P,IC} > 0$) and apolar dehydration ($\Delta C^\circ_{P,IC} < 0$) can be separated. (**F**) Determination of T_P, T_{AD} and compensation temperatures T_{H1} and T_{H2} (red)[87] for polymer C_6S_{32} using the normalized absolute values of the functional ratios shown in equations 10.22 – 10.24. In all figures the C_6S_{32} polymer curves are represented in orange and $C_{11}S_{14}$ polymer curves are in green.

C_6S_{32} exhibits a zero-crossing for $\ln K_{IC,j,6}$ and $\Delta G^{\circ}_{IC,j,6}$ at $T = 34.8°C$ (**Figure 10.11A+B**) when both bound dynamic fractions b_1 and b_2 are occupied to exactly 50% each. Interestingly, this is in the temperature range where the amount of free ligand f is at a minimum and therefore $K_{A,j,k}$ is at its maximum (**Figure 10.10A**). At this temperature, polymer aggregation is initiated and the hydrophilic shell collapse is most pronounced as seen in DLS (**Figure 10.4B+C**). Therefore, the hydrophilic shell of the C_6S_{32}-polymer is in its most densely packed ($R_{H,j,6,min}$), and best ligand binding ($K_{A,j,6,max}$) state. This characteristic temperature is now termed as *performance temperature* $T_P = 34.8°C$. Exactly at this temperature, bound ligands monitor a thermodynamic instability ($\Delta G^{\circ}_{IC,TP,6} = 0$) of the energetic landscape, i.e. a majority of spin probes exhibit free diffusion (b_2) at temperatures above T_P. While this interconversion process is endergonic at low temperatures ($\Delta G^{\circ}_{IC,<TP,6} > 0$) it spontaneously proceeds ($\Delta G^{\circ}_{IC,>TP,6} < 0$, exergonic) at all temperatures above T_P. The interconversion equilibrium is then shifted towards free diffusion (b_2 regime). In **Figure 10.11C+D** it is revealed that the interconversion equilibrium ($K_{IC,j,6}$) is entropy driven between about $12 < j < 85$ ($\Delta H^{\circ}_{IC,12-85,6} > 0$, $T\Delta S^{\circ}_{IC,12-85,6} > 0$), and enthalpy driven below and above these temperatures ($\Delta H^{\circ}_{IC,12>j>85,6} < 0$, $T\Delta S^{\circ}_{IC,12>j>85,6} < 0$). Another marked difference among the two polymers is the change in molar heat capacity $\Delta C^{\circ}_{P,IC,j,k}$ of the interconversion process (**Figure 10.11E**).

While $C_{11}S_{14}$ has a positive and constantly increasing interconversion heat capacity change that is indicative of apolar hydration by increased hydrophobic surface exposure of the polymer core, $\Delta C^{\circ}_{P,IC,j,6}$ of C_6S_{32} constantly decreases in the whole temperature range with a zero-crossing at $T_{AD} = 38.8°C$. This characteristic temperature is now termed as the *apolar dehydration temperature*. This second characteristic temperature marks the transition from a system with slight *apolar hydration* below T_{AD} to distinct *apolar dehydration*[91] of the ligands above T_{AD}. This finding can be directly correlated to the solvent accessibility of the hydrophobic polymer core, where bound paramagnetic ligand probes are located. Thus, the paramagnetic ligands screen the macromolecular substrate for nanoscopic environmental properties. The zero-crossing of $\Delta C^{\circ}_{P,IC,j,6}$ is also exactly where $\Delta H^{\circ}_{IC,j,6}$ and $T\Delta S^{\circ}_{IC,j,6}$ have their individual overall maximum value ($T_{AD} = 38.8°C$). This is in agreement with equation 10.13, as the $\Delta C^{\circ}_{P,IC,j,6}$ curve should exhibit a zero-crossing when $\Delta H^{\circ}_{IC,j,6}$ experiences curve slope inversion. This is also completely in line with the onset of C_6S_{32} aggregation observed from DLS data (**Table 10.3**) and gives a positive consistency proof of the validity of the applied equations. Given that the C_6S_{32} polymer is not aggregated below 35°C, the hydrophobic fatty acid-bearing core is much more accessible to solvent in this state and therefore accessible to apolar hydration. Therefore, the inverting behavior in the sign of $\Delta C^{\circ}_{P,IC,j,6}$ can be directly linked to the hydrophilic shell collapse and subsequent polymer aggregation.

The endothermic, temperature-induced increase in ligand affinity of polymer $C_{11}S_{14}$, that initially also occurs for C_6S_{32} is therefore supposed to counteract the increased solvent hydration of the hydrophobic core and indirectly reflects its increased accessibility. Due to the thinner hydrophilic shell, the hydrophobic surface exposure of $C_{11}S_{14}$ to water is presumably too high and cannot be counter-

balanced by a (S_{32}-based) hydrophilic shell collapse that induces hydrophobic self-assembly and aggregation[104] as observed in the C_6S_{32} polymer.

Thermodynamic EPR data for polymer C_6S_{32} support the picture of a soft dynamical transition at $T_P = 34.8°C$ to a more compact structure with a hydrophilic shell collapse as its trigger. Further evidence for this conclusion was also found in the depleted rotational correlation times $\tau_{c,j,6}$ of ligands in the b_2 rotational regime and the reduced hydrodynamic radii $R_{H,j,6}$ of the polymer for this temperature range (**Figure 10.4A+B**). Energetically, it is also probable that this process in C_6S_{32} is a compensatory hydrophilic collapse as an apolar dehydration process was calculated to occur above $T_{AD} = 38.8°C$. From a polymer functional viewpoint, this could be the hallmark of a *stealth effect* of the hydrophilic shell for the C_6S_{32} polymer, that is supposed to camouflage the hydrophobic core from apolar hydration beyond the hydrophilic collapse, or the performance temperature ($j > T_P$). In this picture the increase of free ligand for $j > 50$ may indeed be ascribed to an increased expulsion of ligand because of the aforementioned sterical restriction upon hydrophilic collapse together with polymer aggregation.

Using the fit-based functions (equations 10.14 – 10.21) has turned out to be exceptionally well-suited for calculations of thermodynamic parameters at *any* temperature in the investigated range. A direct thermodynamic comparison of ligands in both polymers is summarized in **Table 10.5** referring to their calculated $\Delta G°_{IC,25,k}$, $\Delta H°_{IC,25,k}$, $\Delta S°_{IC,25,k}$ and $\Delta C°_{P,IC,25,k}$ values at ambient conditions ($j = 25$). For further information about the origins of this energetic behavior the reader may be referred to the work of e.g. Privalov and Makhatadze.[98,99] From **Table 10.5** it can also be seen that the use of C_{11}-spacers instead of C_6-spacers leads to a doubling of the respective values for $\Delta H°_{IC,25,k}$ and $\Delta S°_{IC,25,k}$. This finding illustrates that the interconversion process ($K_{IC,j,k}$) of 16-DSA gets increasingly favorable with rising alkylene chain length and temperature. This effect is also seen in the enthalpy values $\Delta H°_{A,25,k}$ of ligand association (**Table 10.4**). The zero-crossing ($\Delta G°_{IC,TP,6} = 0$) that coincides with optimum ligand binding properties for C_6S_{32} at $T_P = 34.8°C$ essentially requires the fraction of dynamic b_1 species to exceed 50% at low temperatures ($\phi_{b1,<30,6} > 0.5$). The induction of a performance temperature T_P in solution in terms of optimum ligand binding is therefore related to the structurally tunable functional units of the core-shell polymers that energetically regulate the degree of structural hydration.

Table 10.5 | Thermodynamic parameters of $\ln K_{IC,j,k}$ of C_nS_m polymers at ambient conditions

	$\ln K_{IC,j,k}$	
$j = 25$	C_6S_{32}	$C_{11}S_{14}$
$\Delta G^\bullet_{IC,25,k}$ **[kJ/mol]**	0.86	–2.87
$\Delta H^\bullet_{IC,25,k}$ **[kJ/mol]**	23.12	42.79
$\Delta S^\bullet_{IC,25,k}$ **[J/(mol·K)]**	74.71	153.24
$\Delta C^\bullet_{P,IC,25,k}$ **[kJ/(mol·K)]**	1.01	2.86

In **Figure 10.11F** a strategy is presented for identifying characteristic temperatures from polymer C_6S_{32} according to following expressions:

$$T_P = \max\left\{\left/ \Delta S^\circ_{IC,j,6} \cdot \Delta G^{\circ -1}_{IC,j,6} \right/\right\} \tag{10.22}$$

$$T_{AD} = \max\left\{\left/ \Delta H^\circ_{IC,j,6} \cdot \Delta C^{\circ -1}_{P,IC,j,6} \right/\right\} \tag{10.23}$$

$$T_{H,i} = \max\left\{\left/ \Delta S^\circ_{IC,j,6} \cdot \Delta H^{\circ -1}_{IC,j,6} \right/\right\} \tag{10.24}$$

revealing maxima (in Kelvin) of absolute values in between key energy function ratios. Those maxima arise from the zero values of the denominator energy term. This easy scheme directly provides the performance temperature $T_P = 34.8°C$ from the zero intercept of free energy $(\Delta G°_{IC})$,[91,114] the apolar hydration temperature $T_{AD} = 38.8°C$ from the zero intercept of $\Delta C°_{P,IC}$, as well as the enthalpy compensation temperatures $T_{H1} = 11.5°C$ and $T_{H2} = 84.8°C$ from zero intercepts of $(\Delta H°_{IC})$.[95]

10.2.8.2 | Differential Scanning Calorimetry (DSC) – A Consistency Check

Results from several DSC experiments show that this standard method fails to detect those nanoscopic polymer details that are found from dynamic changes in ligand diffusion from CW EPR spectroscopy. Temperature-dependent transitions of those assemblies could NOT be detected upon heating both individual 16-DSA-probed polymer complexes, i.e. neither peaks that would be indicative for a first order phase transitions, nor steps that are indicative for second order phase transitions were observed in the heat capacity traces (**Figure H16**). As the ligand content in the samples was very low (1.7 mol% and 1.0 mol% for C_6S_{32} and $C_{11}S_{14}$, respectively), any heat effects resulting from 16-DSA transitions are supposed to be below the detection limit of DSC. In turn, the polymer concentration was chosen such that thermotropic phase transitions would be detectable just in case that different polymer phases occur that vary in enthalpy or heat capacity. The absence of such transitions shows that the variations in polymer self-aggregation triggering the observed transitions in the ligand dynamics are not identical to thermodynamic phase transitions. A soft kind of volume phase transition (VPT) as observed in DLS experiments (**Figure 10.4B**) can therefore be assumed to be of a most intricate nature.[82,83]

10.2.8.3 | The Thermodynamic Fingerprint of 16-DSA Bound to C_nS_m Polymers

EPR spectroscopy on amphiphilic paramagnetic ligands is demonstrated to shed light on the ligand binding behavior and some intricate thermodynamic properties of macromolecules on the nanoscale. In case of the C_6S_{32} polymer a functional stabilization and a maximum of ligand uptake $(K_{A,max})$ at performance temperature T_P is monitored by an observed crossing of the fractions in both dynamically interconverting components b_1 and b_2 of bound 16-DSA $(\Delta G°_{IC,TP,6} = 0)$. Therefore, fatty acid ligands can be employed as indirect sensors for the nanoscopic structural and dynamical agility of the polymers. They may exhibit a complicated relation between interconversion entropy $(\Delta S°_{IC,k,6})$ and

enthalpy changes ($\Delta H^\circ_{\text{IC},k,6}$) for C_6S_{32}, or almost perfect entropy-enthalpy compensation (EEC), as obtained for $C_{11}S_{14}$. This is achieved by observing and correlating their polymer-bound dynamic interconversion process ($K_{\text{IC},j,k}$) with the dynamic polymer structure affecting the mode and specificity of their rotational diffusion regime (**Figure 10.12**).

Linear EEC behavior is commonly observed during the unfolding process of proteins,[116] or supra-molecular guest encapsulation in solvents.[117] The vanishing aggregates of $C_{11}S_{14}$ that are observed in DLS experiments with rising temperature (**Figure 10.4C**) are accompanied by increased ligand uptake, or rather an increase in ligand binding affinity due to endothermic reaction conditions. This is most probably due to a polymer core-shielding by the ligand that partially prevents apolar hydration. As an overview of the thermodynamic findings, the *nanoscopic thermodynamic fingerprints* from the polymer-bound ligands performing dynamic hydrophobic interconversion ($K_{\text{IC},j,k}$) of their rotational regimes are summarized in **Figure 10.12**, utilizing a well-established representation scheme that is adopted from protein biophysics,[95,114] by plotting $T\Delta S^\circ_{\text{IC},j,k}$ versus $\Delta H^\circ_{\text{IC},j,k}$.
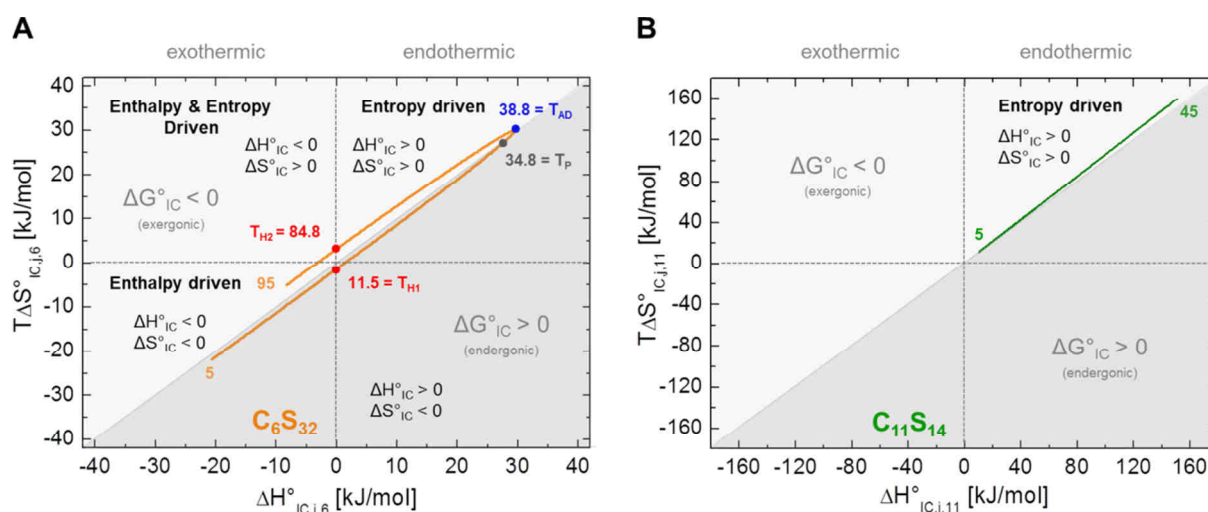

Figure 10.12 | Thermodynamic fingerprint of 16-DSA bound to C_nS_m polymers. The interconversion process $K_{\text{IC},j,k}$ as observed for 16-DSA bound to C_6S_{32} and $C_{11}S_{14}$ is depicted as an energetic fingerprint in the style presented by Boysen *et al.*[95] (**A**) An energy plot of entropy ($T\Delta S^\circ_{\text{IC},j,6}$) versus enthalpy ($\Delta H^\circ_{\text{IC},j,6}$) of the dynamic hydrophobic interconversion equilibrium $K_{\text{IC},j,6}$ of 16-DSA is shown when it is bound to polymer C_6S_{32}. The apolar dehydration temperature (T_{AD} = 38.8°C) is highlighted in blue, the performance temperature (T_{P} = 34.8°C) is shown in gray and the enthalpy compensation temperatures (T_{H1} = 11.5°C and T_{H2} = 84.8°C) are given in red. (**B**) Energy plot of entropy ($T\Delta S^\circ_{\text{IC},j,11}$) versus enthalpy ($\Delta H^\circ_{\text{IC},j,11}$) of the dynamic hydrophobic interconversion equilibrium $K_{\text{IC},j,11}$ of 16-DSA bound to polymer $C_{11}S_{14}$, exhibiting almost perfect EEC behavior. Exergonic and endergonic regions of the plot have been separated by a diagonal line and are color-coded in different shades of gray. The orange and green inset numbers denote the respective temperatures of interest.

DSC measurements that have been conducted here turned out to be largely insensitive to effects observed in EPR spectroscopy. Neither phase- nor glass transitions could be detected in aqueous suspensions of the polymers. However, DLS data suggest a soft *volume phase transition* (VPT)[81,82] of polymer C_6S_{32} between $30 < j < 40$ that was termed as a hydrophilic collapse (see HCT, **Table 10.3**, **Figure 10.4B**). However, it has to be emphasized, that both energetic processes that were obtained from EPR ($\ln K_{\text{A},j,k}$ and $\ln K_{\text{IC},j,k}$) are monitored by 16-DSA and do not depict direct heat capacity

changes (ΔC_P) of the macromolecules themselves. The heat capacity signature $\Delta C^{\circ}_{P,IC,j,k}$ from the interconversion process ($K_{IC,j,k}$) can be structurally devised as to switch a bound ligand state from an unfavorable apolar hydration towards an apolar dehydration (C_6S_{32}). This conclusion is derived from the polymeric self-assembly as seen in DLS experiments and is thermodynamically reflected in the apolar dehydration temperature $T_{AD} = 38.8°C$ where $\Delta C^{\circ}_{P,IC} = 0$ (**Figure 10.11E**).

While polymers with long alkylene and short polyglycerol chains are subject to apolar hydration throughout the whole temperature range ($C_{11}S_{14}$), a slight *stealth effect* of the hydrophilic shell is obtained for long polyglycerol and shorter alkylene chains being mirrored in terms of a kink in the thermodynamic fingerprint (T_{AD}, **Figure 10.12A**). Those kind of polymers may intrinsically shield their hydrophobic core from apolar hydration. This inversion in direction of heat capacity change $\Delta C^{\circ}_{P,IC,j,k}$ from the interconversion process (**Figure 10.11E**) can be seen as facilitating the detection of a transition from a loose to a more compact structure of the polymer shell along the backbone. This is accompanied by partial aggregation and an optimum performance temperature $T_P = 34.8°C$ for ligand uptake ($K_{A,max}$) at about physiological temperatures. Therefore, the hydrophilic shell thickness S_m dominates the water accessibility of the hydrophobic core with vast effects on ligand binding and the intricate dynamic behavior of the polymer.

10.3 | Discussion

The overall characteristics of the mutual interactions of amphiphilic ligands and amphiphilic polymer-based transporter molecules can be summarized in the concept of *dynamic hydrophobic attachment*. This term shall comprise an intermolecular polymeric *dynamic hydrophobic aggregation*, a ligand based *dynamic hydrophobic binding*, as well as *dynamic hydrophobic interconversion* that was proven to react sensitively on soft structural rearrangements of the core-shell substrate. Those dynamic properties can be structurally tuned in terms of ligand uptake ($N_{E,k}$ and $K_{A,k} = K_{D,k}^{-1}$), intramolecular properties as hydrophilic collapse (S_m) and aggregation (N), as well as bound ligand dynamics ($K_{IC,k}$) as it is discussed in **Chapter 10.2.7**. The global rotational dynamics of the spin probes as monitored by τ_c do not depend strongly on the polymer molecular weight and therefore on the degree of polymerization (N). It can be argued that comparative studies as it was shown here are decisively simplified by this property. Elsewise, due to the complexity of the EPR analysis, this strategy might not have been evolved.

The use of nitroxide-bearing ligands in this EPR spectroscopic study turns out to deliver several new perspectives on the inner working of macromolecules and their dynamic interactions with ligands. As compared to established calorimetric methods as ITC or DSC, this approach reveals the possibility to obtain an indirect but in-depth functional view of the polymer-ligand interaction without any other influences as e.g. mixing enthalpies that might alter the results or prove thermodynamical data, e.g. from the interconversion process, as inaccessible.

This approach also has some limitations as in the thermodynamic evaluation of the $C_{11}S_{14}$ polymer, because ligand association ($K_{A,j,k}$) and interconversion processes ($K_{IC,j,k}$) are only detectable up to 45°C for $C_{11}S_{14}$, when the free (f) and the immobilized (b_1) component indicating Brownian rotational diffusion vanish. Potential consequences of such data accessibility limitations have been widely covered in calorimetric literature[112,118–121] and have been incorporated in this study as far as possible.

As it was shown from van't Hoff plots of $\ln K_{A,j,k}$, especially for $C_{11}S_{14}$ (**Figure 10.10A**), the fatty acid ligand 16-DSA may indeed contribute to the stability of the self-assembled system consisting of polymer and ligand in water, as it reveals strong entropy increases upon binding (**Table 10.4**), while polymer aggregates dissolve and unimeric polymer structures are released (DLS). For C_6S_{32}, an energetic inversion of the ligand binding process from endothermic ($j < 30$) to exothermic ($j > 50$) was observed, resulting from a virtual structural breathing of the hydrophilic shell.

It is commonly accepted that the solubility of nonpolar compounds in water, as the 16-DSA ligand, may exhibit exactly this energetic inversion behavior.[122] Additionally, the hydrophobic effect intricately depends on the length scale of the solutes,[123,124] leading to contact of extended apolar surfaces of objects being less than 5 nm apart due to spontaneous water depletion. This gives a further explanation for the different aggregation behavior of both investigated polymers. Compared to $C_{11}S_{14}$, the C_6S_{32} polymer is much larger, not only due to its thicker hydrophilic shell, but also due the about 4-fold higher degree of polymerization (N). Therefore, the combination of an intermediate length hydrophobic alkylene core together with a larger hydrophilic shell and large degrees of polymerization seem to make C_6S_{32} more versatile than $C_{11}S_{14}$ in employment of the hydrophobic effect for ligand binding. Moreover, it was proposed that hydrophilic interactions play a crucial role in the amphiphilic self-assembly behavior in protein-protein association and molecular recognition.[125]

It is generally assumed that the hydrophobic effect and hydrogen bonding make a comparable contribution to globular protein stability.[126] On a very fundamental level of argumentation, hydrogen bonding is seen as an electrostatic dipole-dipole interaction between two molecular moieties differing in electronegativity.[127,128] This leads to a broad variety[129] of tunable dynamic, structural and functional characteristics for macromolecules, as it was also observed here from temperature-induced changes in the interaction between solvent molecules and polymer structural elements (cores and shells) that in turn affect ligand uptake performance.

The application of an exponential function for the $C_{11}S_{14}$-polymer for evaluating the temperature-dependent interconversion process ($K_{IC,j,k}$) proved to be very practical for the mathematical derivation procedures and can be analyzed in a simple manner. Analytical solutions for the calculation of transition temperatures from fit-derived functions at $\Delta G° = 0$ have not been found as it is presented in Boysen *et al.*[87] The values for performance temperature (T_P), apolar dehydration temperature (T_{AD}) and enthalpic compensation temperatures (T_{H1} and T_{H2}) were determined by applying the absolute values of the quotients shown in equations 10.22 – 10.24 (see **Figure 10.11F** and **Figure 10.12A**).

The combination of alkylene cores C_n and hydrophilic shells S_m of variable length, facilitates the construction of cooperative entities that exhibit highly non-trivial thermal responses from interaction with ligand and water. Explicitly, this means that an increase in C_n spacer length strengthens the hydrophobic character of the polymer core ($a_{\text{iso},j,k}$ decreases, **Table 10.3**). Likewise, the positive enthalpy changes $\Delta H^\circ_{\text{A},25,k}$ and also the positive entropy changes $\Delta S^\circ_{\text{A},25,k}$ of the system increase as observed from the ligand association process ($K_{\text{A},j,k}$). The ligand binding process observed here remains exergonic ($\Delta G^\circ_{\text{A},j,k} < 0$) for all investigated temperatures (**Table 10.4**). Here, it could be shown that energetics of ligand binding are subject to the structural and dynamic features of the macromolecule in solution in a most sophisticated way.

This study revealed that especially the heat capacity changes of the dynamic hydrophobic interconversion process ($\Delta C_{\text{P,IC}}$) of an amphiphilic paramagnetic ligand bear potential to detect (soft) phase transitions in complex macromolecules. In this regard, it can be also expected that amphiphilic spin probes other than 16-DSA may exhibit the same or at least similar effects.[76]

In summary, when a slight dynamic rearrangement of the macromolecule occurs, the ligands exhibit complex entropy-enthalpy plots of K_{IC}, whereas the absence of such a hydrophilic shell transition results in almost perfect EEC (**Figure 10.12**). Besides potential drug delivery applications,[130–132] such core-shell systems appear to be well-suited to provide new experimental evidence of how the hydrophobic effect guides small molecules towards or inside transport molecules, how the mutual interaction of transport molecules with ligands occurs, and how the transport molecules may vary their functional appearance on a coarse-grained molecular level. In this study the K_{IC} process has been characterized in-depth and it was identified to be useful for monitoring changes of hydration states of ligand and macromolecular substrate. This might also shed new light on various aspects in the vast research field of ligand binding to proteins or macromolecules in general. Therefore, this method is transferred to the 16-DSA-probed HSA model system as shown in **Chapter 11**.

10.4 | Materials and Methods

Materials. Synthesis and characterization of all C_3-, C_6-and C_{11}-based core-shell polymers (**Figure 10.1**) has been reported elsewhere.[7,36] A complete set of white lyophilized powders of C_3S_{16}, C_3S_{32}, C_6S_{16}, C_6S_{32}, $C_{11}S_{14}$ and $C_{11}S_{16}$ polymers, as well as 16-DSA (Sigma-Aldrich) were used without further purification. The 0.137 M DPBS buffer[133] was prepared according to the procedure described in **Appendix C1**. The preparation of 0.12 M DPBS titration buffers in the range from pH 0.2 – 13.5 is given in **Appendix C2**.

Sample Preparation. All core-shell polymers were dissolved in ultrapure water (MilliQ) to polymer stock concentrations of 2.5 – 9.4 wt% corresponding to about 0.2 to 1.2 mM. For adding the spin probe molecules to the polymer samples a solution of 8 mM 16-DSA in 0.1 M KOH was prepared. The final concentrations were adjusted by adding pure water for a final sample volume of 40 µl. Due to addition of 0.1 M KOH the pH values were precautiously checked with a microelectrode (Mettler Toledo InLab®Micro pH 0 – 14 in combination with an EL20 pH meter) exhibiting almost neutral values in the range of pH 7.5 ± 0.5. The 16-DSA reference samples were prepared in the concentration range from 0.02 – 3.30 mM in 0.137 M DPBS buffer and were thoroughly titrated to pH 7.4. About 10 – 15 µl of the final solutions were filled into micropipettes (BLAUBRAND® intraMARK) that were subsequently capped with capillary tube sealant (Leica Critoseal®) that facilitates an immediate supply to the EPR spectrometer.

All DLS samples have been prepared with a polymer concentration of 0.13 – 0.20 wt% (equivalent concentrations of about 4.3 µM < $c_{P,k}$ < 20.7 µM) and were measured in 1.5 mL PMMA semi-micro cuvettes (BRAND). For sustaining comparability, a 1 mM 16-DSA stock solution in 12.5 mM KOH was used to equip the polymers with the same fatty acid loading as for the EPR measurements, in this case well below the critical micelle concentration (CMC). The polymer concentrations were adjusted with ultrapure water (MilliQ) to a final sample volume of 400 – 600 µl giving slightly alkaline solutions at about pH 8.1. All samples were filtered through cellulose acetate (CA) syringe filters with a pore size of 0.2 µm (Rotilabo, Carl Roth) to minimize adhesion.

DSC experiments were performed with 16-DSA-probed C_6S_{32} and $C_{11}S_{14}$ polymer suspensions that were prepared as for the EPR experiments and loaded to the sample cell. The concentration of macromonomers was $N \cdot c_{P,k}$ = 1.66 mM and 1.78 mM and the 16-DSA concentration was 29.1 µM and 18.4 µM for C_6S_{32} and $C_{11}S_{14}$, respectively. In addition, 16-DSA was measured without polymers below its critical micellization concentration (CMC) at pH 8.8 – 9.5 (KOH). For a successful recording of electron microscopy (EM) images the core-shell polymer samples were prepared in pure water at concentrations of 0.2 wt%.

CW EPR Measurements. All measurements were conducted on Miniscope MS200 and Miniscope MS400 (Magnettech GmbH) benchtop spectrometers at X-band microwave frequencies at about 9.4 GHz. Measurements were performed with microwave powers between P_{MW} = 3.2 – 10.0 mW with a sweep width of 12 – 15 mT and modulation amplitudes of 0.1 mT. For precise temperature adjustments (intrinsic error 0.3 K) a temperature controller (Magnettech Temperature Controller H03) was used and the microwave frequency was recorded with a frequency counter (RACAL DANA, model 2101). EPR spectra that were used for 16-DSA-based temperature response curves of the polymers were recorded in steps of ΔT = 5 K from 5 < j < 95 with a precautionary incubation time for each temperature step of about 2 – 3 min. The time dependence in accelerated aging studies (**Appendix H4**) was monitored with a stopwatch (Hama GmbH & Co KG, model SW-104) at the time when the last scan of an experiment ended.

EPR Spectral Analysis. All strategies for extracting the CMC, temperature stability and rotational dynamics from 16-DSA-derived CW EPR spectra are explicitly described in **Appendix H1–H4** and **Appendix H7**. All spectral simulations were performed exclusively in MATLAB R2008b utilizing the EasySpin software package.[134] All home-written MATLAB routines have been optimized for 1 – 3 component nitroxide CW EPR spectra (individual combinations of subspectra f, b_1, b_2, a, g) as it is observed from 16-DSA. These routines comprise applications that facilitate spectral simulations of slowly tumbling nitroxides.[29,135] In principle, individual subspectra were extracted in an iterative global manual procedure by comparison of the temperature-dependent changes in fit parameters. CW EPR spectra were double-integrated for extracting the spectral fractions $\phi_{i,j,k}$ of the corresponding dynamic populations for reconstruction of experimental spectra $S_{j,k}(B)$. A reasonable set of simulation parameters was obtained from the simulation approach described in **Appendix H5** and is given in **Table H2**. Scatchard plots[73] as shown in **Figure 10.5** were constructed from simulations that were obtained in the same way and are shown in **Appendix H9**. The evaluation was performed according to the strategy described in **Chapter 10.2.4**.

Thermodynamic Analysis of EPR Data. All calculations of thermodynamic quantities emerging from calculated equilibrium constants $K_{A,j,k}$ (**Figure 10.10A**) and $K_{IC,j,k}$ (**Figure 10.10B**) have been facilitated with fit parameters from linear, polynomial and exponential curve regression methods in Microcal Origin (**Appendix H11** and **Appendix H12**). Thermodynamic functions for $\ln K_{IC,j,k}$, $\Delta G°_{IC,j,k}$, $\Delta H°_{IC,j,k}$, $\Delta S°_{IC,j,k}$ and $\Delta C°_{P,IC,j,k}$ as shown in **Figure 10.11** were computed in a quasi-continuous 500 point grid corresponding to a 0.08 – 0.18 K temperature resolution. This was done with home-written codes in MATLAB R2008b. Therein, fit parameters from the aforementioned curve regressions in Origin were incorporated.

DLS Measurements. All DLS data were obtained with an ALV-NIBS high performance particle sizer (HPPS) equipped with an ALV-5000/EPP Multiple Tau Digital Correlator (ALV-Laser Vertriebsgesellschaft m. b. H.). This device facilitates HeNe-LASER irradiation with a typical wavelength of λ = 632.8 nm and 3 mW output power with an automatic attenuator for optimum count rates recorded in a backscattering detection angle of 173° relative to the incident monochromatic light. The sample cell temperatures were adjusted in the range from 8 < j < 85 in steps of ΔT = 3 – 4 K by a Peltier temperature control unit. Data were extracted from the intensity

correlation functions by a $g_2(t)$-DLS exponential and a mass weighted regularized fit in the ALV-NIBS software v.3.0 utilizing the CONTIN algorithm.[46] While the refractive index was assumed to be constant at $n_{H2O} = 1.332$ for all temperatures (and $\lambda = 632.8$ nm),[136] the water viscosity was corrected for each applied temperature j [°C] according to the relation:[137]

$$\log \frac{\eta(j)}{\eta_0} = \frac{20 - j}{j + 96} \cdot \left(1.2378 \ - \ 1.303 \cdot 10^{-3} \cdot (20 - j) + 3.06 \cdot 10^{-6} \cdot (20 - j)^2 + \ 2.55 \cdot 10^{-8} \cdot (20 - j)^3 \right) \ , \quad (10.25)$$

assuming that $\eta_0 = 1.002$ mPa·s at $j = 20$.[137–139] Each sample was measured at least four times at constant temperature for 60 s and was averaged at least over three individual values. The mean values $R_{H,j,k}$ of the most prominent particle size peaks and their statistical fluctuations are given as the standard deviation as depicted in the error bars in **Figure 10.4B**. The experimental duration of a single heating procedure was about 8 – 12 h. The temperature-dependent particle size distributions are given in **Figure H11** as indicated in the main text.

Molecular Dynamics (MD) Simulations. All molecular models of the core-shell polymers were constructed using the YASARA Structure software.[140] MD simulations were performed in simulation boxes with periodic cell boundaries containing the polymer and an explicit water solvent with 370.000 – 403.000 atoms in total similar to the scheme given in **Appendix G6**. The simulation runtime was $t_{MD} = 12 – 13$ ns at pH 7.0 in 0.0 M NaCl and $T = 298$ K applying the AMBER03 force field. Due to calculational effort, the model sizes were limited to a molecular weight of about $MW_{M,k} = 100$ kDa ($N = 32 – 37$) and are therefore only consulted for generalized phenomenological conclusions. Further information can be found in **Appendix H8**.

Negative Stain Electron Microscopy (EM). All electron microscopy experiments were performed by PD Dr. Annette Meister. Negatively stained samples (0.2 wt%) were prepared by spreading 5 µL of the dispersion onto a Cu grid coated with a Formvar-film (Plano GmbH). After 1 min excess liquid was blotted off with filter paper. 5 µL of 1% aqueous uranyl acetate solution were placed onto the grid and drained off after 1 min. Specimens were air-dried and examined in an EM 900 transmission electron microscope (Carl Zeiss Microscopy GmbH). Micrographs were taken with a SSCCD SM-1k-120 camera (TRS).

Differential Scanning Calorimetry (DSC). All DSC measurements were performed by Dr. Christian Schwieger with a Microcal VP-DSC instrument (MicroCal Inc.). In all experiments heating rates of 0.5 K/min and cooling rates of 1 K/min were used. Data were recorded with a time resolution of 4 s in the temperature range from $5 < j < 95$, the same temperature range as for EPR experiments. Three consecutive up- and down scans were performed for each sample to allow equilibration and for proving reproducibility. The presented curves originate from the second heating scan. The third heating scan was identical to the second one. The reference cell was filled with degassed ultrapure water. From all presented polymer/16-DSA thermograms, a water/water reference, as well as a thermogram of pure 16-DSA was subtracted, before normalizing ΔC_P to the macrounimer concentrations. Data processing was performed with the DSC module for Origin software (MicroCal Inc.)

11 | Temperature-induced Solution Dynamics of the Spin Probed HSA System

In this chapter the validity of the analytic strategy that has been developed with the core-shell polymers in **Chapter 10** will be applied to 16-DSA-probed HSA solutions. Again, solution dynamics and ligand binding thermodynamics are analyzed thoroughly. The aim is now to unravel internal dynamics of HSA solutions with fatty acids by applying continuous wave electron paramagnetic resonance (CW EPR) with a clear, well-defined experimental system without containing micelles in order to reduce complexity in data analysis. It is shown that a consistent thermodynamic interpretation is obtained about how fatty acids interact with HSA in the investigated temperature range from 5 – 97°C. This is facilitated with careful spectral observation and simulation. Additionally, data from CW EPR are corroborated by DLS, DSC and DEER experiments for promoting a fairly holistic functional and dynamic picture of HSA.

11.1 | Introduction

Due to their enormous complexity, CW EPR spectra from spin-labeled fatty acids bound to albumin were predominantly treated phenomenologically in the 1970s and 1980s,[1–8] with most of these approaches aiming for uptake capabilities and ligand interaction of albumin towards paramagnetic fatty acids. Beyond the fruitful outcome of these studies, the first reasonable and rigorous simulation-based dynamic analysis of albumin associated to a variety of spin-labeled fatty acids was claimed for BSA by Ge *et al.*[9] apart from a very early successful attempt by Gaffney and McConnell.[10] In recent years, spectral simulations of spin probed or spin-labeled albumin samples has been taken up again by the EPR spectroscopic community not least due to the broad accessibility of powerful spectral simulation tools in CW EPR.[11–26]

This study is an attempt to collect and surmount the remarkably inconsistent diversity of EPR spectroscopic data interpretations and strategies of fatty acid probed albumin ranging from overall 2 – 5 spectral components[9,14,22] that can be found throughout aforementioned literature. This pheno-menon emerges due to specific analytic requirements, different sample compositions and the supposed inseparability of all individual spectral components.[27] The findings from spectral simulations in **Chapter 7** and **Chapter 10** are here recapitulated and were tested for consistency in order to build a strong and meaningful physical basis of fatty acid assembly in albumin on the HSA system.

It was already shown, that albumin also exhibits two different types of immobilized spectral components from 16-DSA that are commonly assigned to weak and strong binding sites.[16,17,20,22] As these components change their relative spectral fractions with temperature and fatty acid loading it was proposed that the occupation of weak and strong binding sites changes due to an intra-albumin migration mechanism with an apparent activation energy of 35.2 kJ/mol for BSA and 26.8 kJ/mol for HSA.[16] EPR spectroscopic thermal denaturation studies based on spectral simulation of both, spin probed HSA and BSA, have already been conducted in the range from 20 – 50°C,[16,17] however, well below their individual denaturation temperature T_D.

Beyond the impressive thermostability of HSA that is mainly based on the 17 disulfide bridges,[28,29] these previous findings are tested here and will be expanded to a mainly EPR spectroscopic picture of HSA temperature denaturation. Therefore, CW EPR data are complemented with other techniques as DSC, DLS and DEER that reveal a robust solution dynamic model of albumin interacting with fatty acid ligands in the temperature range of liquid water. In this regard several well-known phenomena are recapitulated, discussed and integrated in this model. For convenience, temperature may be replaced with $j = T$ [°C], or replaced with $x = T^{-1}$ where appropriate as it was introduced in **Chapter 10**.

11.2 | Results

11.2.1 | Temperature-dependent Dynamic Regime Occupation of 16-DSA in HSA Solutions

As classical, more empirical approaches in EPR spectroscopy, like measuring the ratios of different line amplitudes,[2,30] might fail to depict the variety of processes involved in temperature denaturation, all 16-DSA-probed HSA samples were strictly prepared and measured at pH 7.4. The spectral simulations were again conducted in an iterative manual global simulation procedure as for the core-shell polymers (see **Chapter 10**).
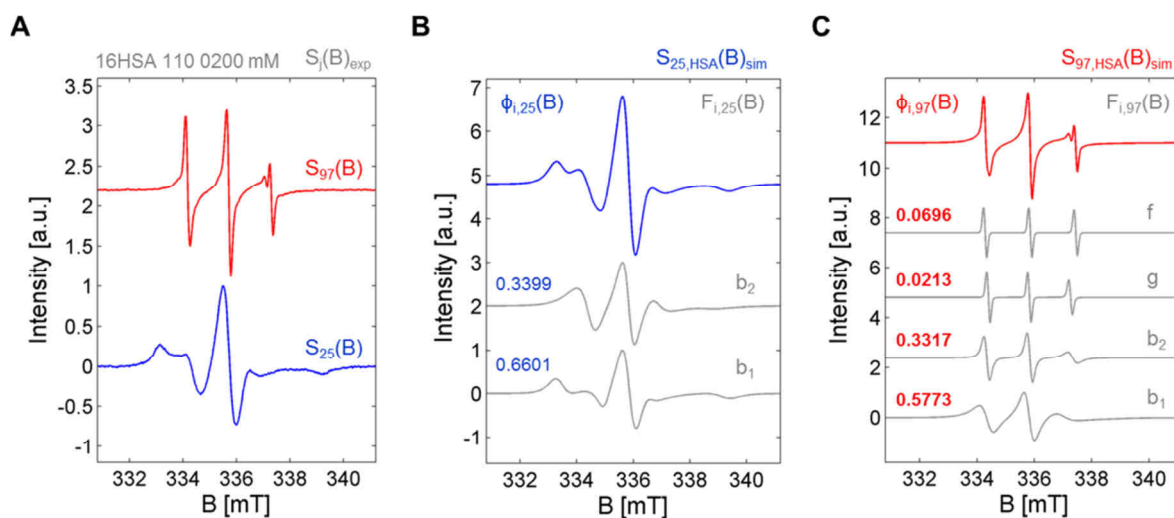
Figure 11.1 | Decomposition strategy of CW EPR spectra from 16-DSA-probed HSA solutions. (**A**) The temperature-dependent appearance of CW EPR spectra from 16-DSA-probed HSA is shown for $j = 25$ and $j = 97$ (16HSA 110 0200 mM). (**B**) A spectral simulation of HSA is shown at $j = 25$ (blue) composed of two subspectra $F_{i,25}(B)$ emerging in balanced dynamic fractions $\phi_{i,25}(B)$, in this case b_1 and b_2. (**C**) A spectral simulation of HSA is shown at $j = 97$ (red) composed of four components $F_{i,97}(B)$ emerging in balanced dynamic fractions $\phi_{i,97}(B)$, in this case b_1, b_2, g and f. All simulation traces are shown in gray color. All measurements were conducted in 0.137 M DPBS pH 7.4 at an equivalent concentration of $c_{16\text{-DSA}} = 0.204$ mM (with $c_H = 0.180$ mM).

The temperature response of EPR-active 16-DSA-probed HSA solutions was investigated in the range from $5 < j < 97$ and it was already shown in **Chapter 7** that several dynamic regimes of 16-DSA emerge when co-dissolved with HSA. Additionally, the thermodynamic terminology is largely transferred from **Chapter 10**. The applied fatty acid loading ratio of 1.13 : 1.00 at an equivalent concentration of $c_H = 0.18$ mM certifies that no micelles form throughout all investigated temperatures

($c_{16\text{-DSA}}$ < CMC = 0.285 mM, see also **Appendix H1**). In turn, this circumstance simplifies spectral simulation procedures decisively. Altogether four different subspectra were identified as it is graphically highlighted in **Figure 11.1**.

A list of appropriate simulation parameters for these two spectra is given in **Table I1** and all simulations are depicted in **Figure I1**. Here, the most important feature is that 16-DSA in HSA solutions exhibits two immobilized fractions b_1 and b_2 as it was observed for the C_6S_{32} and $C_{11}S_{14}$ polymers (**Chapter 10**).

From about 50°C onwards an additional free (*f*) and a hydrogel-like fraction (*g*) is observable, leading to a generally more complex appearance of spectra at higher temperatures. A complete set of recorded spectra $S_j(B)$ and all emerging fractions $\phi_{i,j}$ in the temperature range from $5 < j < 97$ are presented in **Figure 11.2**. The combined b_1 and b_2 fractions comprise 100% of HSA spectra below 50°C and constantly exceed 90% of the spectral fraction above this temperature ($\phi_{b,j} > 0.9$). Those two spectral components exhibit a highly non-trivial temperature course above 50°C that will be explicitly discussed in **Chapter 11.2.3**.

The b_1 fraction remains above and b_2 below 50% throughout all experimental temperatures ($\phi_{b1,j} > 0.5$ and $\phi_{b2,j} < 0.5$). The characteristic a_{iso} value denoting the probed polarity in b_1 and b_2 is 15.25 G (42.93 MHz) for 25°C as it was also found by Ge *et al.* for BSA[9] and decreases to 15.04 G (42.33 MHz, **Table I1**) at 97°C. The free (*f*) fraction emerges at 53°C and steadily increases in a sigmoidal fashion to about $\phi_{f,97} = 7.0$ % at 97°C. The very hydrophobic, hydrogel-like spectral component *g* with an a_{iso} value of 14.28 G (= 40.20 MHz) is assumed to emerge from about 50°C onwards. However, the hydrogel-like (*g*) fraction only develops clearly visible spectral characteristics well above 70°C and rises exponentially to a maximum value of $\phi_{g,97} = 2.1$ %. As it is well-known, HSA forms ordered macroscopic gel-structures by fibrillation at defined temperatures, pH, osmolality and protein concentrations giving fibrils of 15 – 30 nm in diameter and 0.1 – 2.0 µm in length.[31,32] A recent study in this regard was aiming for a thorough characterization of the formation of these gel-states in aqueous solutions of HSA and BSA.[33] This aspect will be considered in further analysis and discussions but is not specified in detail here.

The 16-DSA spin probe is thus assumed to intercalate with buried hydrophobic parts while the HSA fibril structures form. Since ϕ_f and ϕ_g are very small compared to ϕ_{b1} and ϕ_{b2}, the corresponding rotational correlation times τ_c and a_{iso} values were estimated from reference experiments on 16-DSA in pure DPBS buffer (see **Appendix H2** and **Appendix H3**).

Simulation parameters from the spectral *g* fraction that was also observed in the 16-DSA-probed C_3S_{32} polymer solution (**Figure 10.3A** and **Table H2**) were used as starting values for obtaining optimum simulation curves. The hydrodynamic properties of HSA solutions are again discussed with a combination of τ_c values from EPR spectroscopy and the results from temperature-dependent DLS experiments (**Figure 11.3**) as it was shown for the core-shell polymers in **Figure 10.4**.
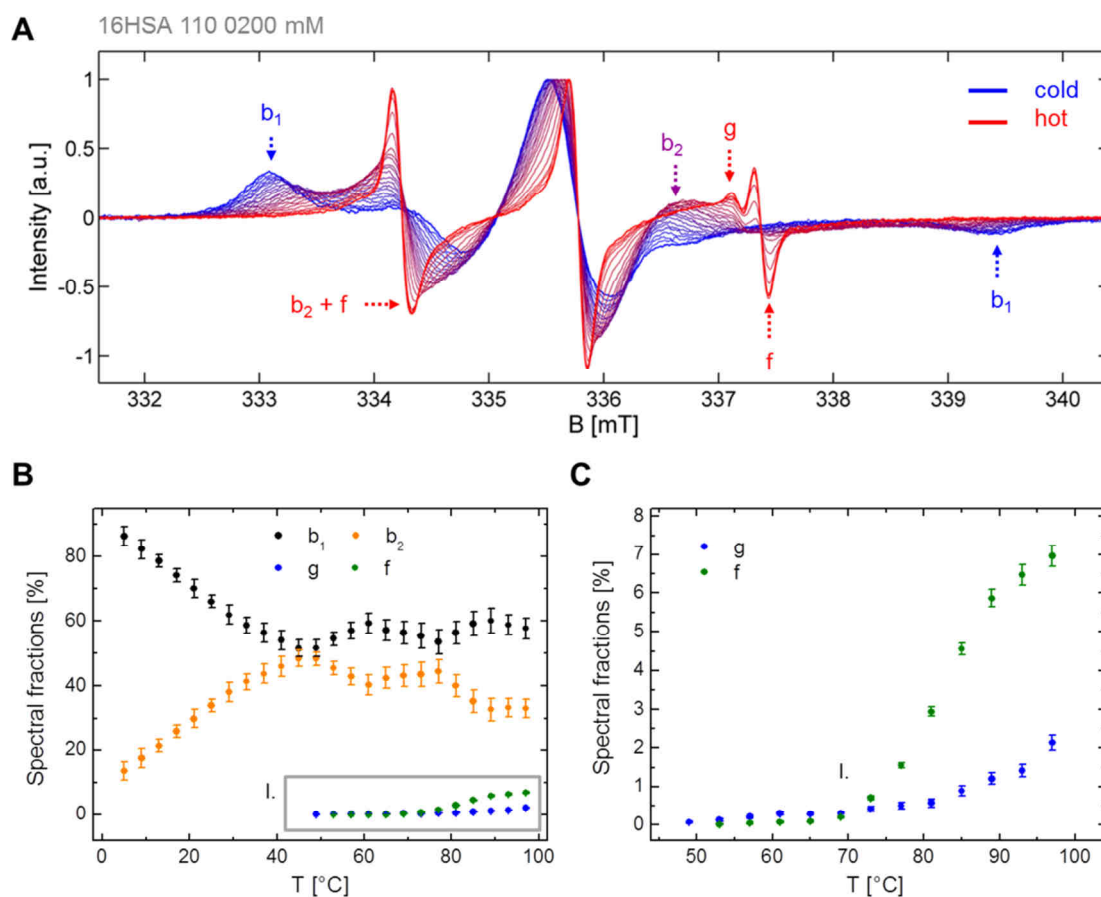
Figure 11.2 | CW EPR temperature responses $S_j(B)$ from 16-DSA interacting with HSA. EPR spectroscopic view from a 16-DSA-probed HSA solution (16HSA 110 0200 mM) that was measured in the temperature range from $5 < j < 97$ in steps of $\Delta T = 4$ K. The 16-DSA loading ratio of HSA is $1.13 : 1.00$ ($c_H = 0.18$ mM). (**A**) CW EPR spectra $S_j(B)$ of 16-DSA interacting with HSA. The most prominent spectral features of dynamic fractions f, b_1, b_2 and g are highlighted. The lowest (dark blue) and the highest (dark red) temperature curve is shown in bold to create an envelope effect. (**B**) Response curves of 16-DSA are here depicted as spectral fractions $\phi_{i,j}$. Immobilized fractions are shown in black (b_1) and orange (b_2), whereas hydrogel-like fractions (g) are shown in blue and free fractions (f) are shown in green. (**C**) A magnification of inset I is shown in (B) and all error margins have been determined from individual spectral simulations.

Principally, the $-\log \tau_{c,i,j}$ curves for the spectral components b_1 and b_2 both exhibit a sigmoidal shape (**Figure 11.3A**). The rotational correlation time ratio $\tau_{c,b1}/\tau_{c,b2}$ yields a value of 2.46 ± 0.18 when it is averaged across all temperatures j, again being very close to 2.65 as proposed for an interconversion from Brownian to free diffusion ($K_{IC,j}$, see also **Chapter 10.2.3**).[34,35] While the $\tau_{c,b1,j}$ values decrease from 14.3 ns ($j = 5$) to 2.9 ns ($j = 97$), $\tau_{c,b2,j}$ values decrease from 5.7 ns to 1.2 ns in the same temperature range. The most intriguing feature of the $-\log \tau_{c,i,j}$ curves for the spectral components b_1 and b_2 (**Figure 11.3A**) is that $\tau_{c,b1,j}$ shows a strong decrease from 50°C onwards, while $\tau_{c,b2,j}$ does not significantly decrease prior to 70°C. The reason for this decrease in τ_c can be directly assigned to the structural weakening of the protein due to its intrinsic temperature stability. This structural weakening is therefore detected by a decrease in ligand immobilization.

This temperature instability is also monitored by hydrodynamic radii $R_{H,j}$ from DLS experiments on 16-DSA-probed HSA (**Figure 11.3B**). Whereas the average particle size in the HSA solution does not change significantly until up to 70°C, a sudden significant size increase takes place above 75°C. This

is due to the emergence of self-association of HSA leading to oligomers of about 50 – 100 nm above 57°C and even larger aggregates above 81°C (**Figure 11.3C**, $R_{H,>81} > 100$ nm). Macroscopically, it could be confirmed that the investigated HSA solution indeed forms a gel, as the solution in the DLS cuvette was completely solidified after the experiment.
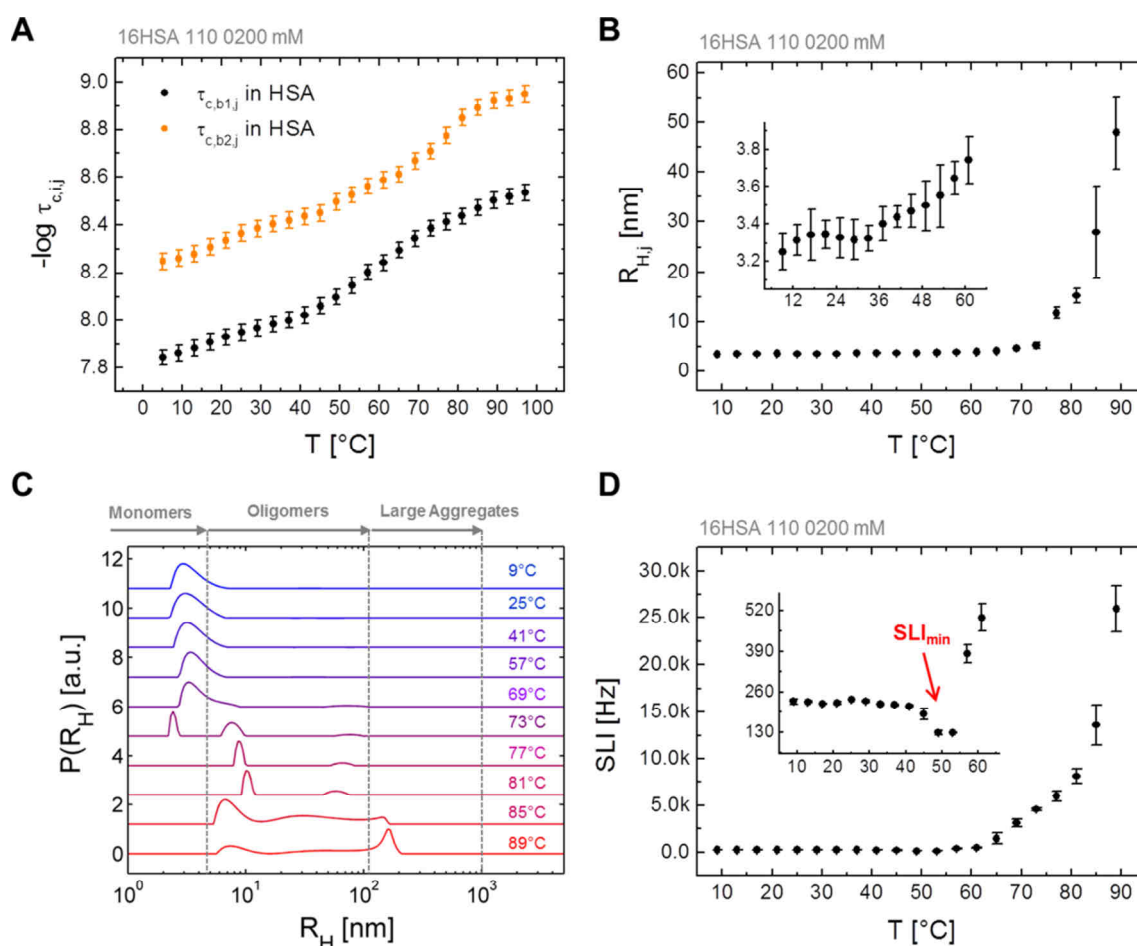
Figure 11.3 | Temperature-induced changes in spin probe and protein dynamics. Comparison of CW EPR and DLS data from a 16-DSA-probed HSA solution (16HSA 110 0200 mM) that was measured in the temperature range from $5 < j < 97$ ($9 < j < 89$ for DLS data) in steps of $\Delta T = 4$ K. (**A**) Semilogarithmic plot of the temperature-dependent rotational correlation times from CW EPR of spectral components b_1 (black) and b_2 (orange) of 16-DSA interacting with HSA. Error margins were estimated from spectral simulations to range about 8 %. (**B**) The temperature dependence of the main hydrodynamic radii $R_{H,j}$ is shown as detected in DLS experiments. Error bars are given as the fluctuation about the mean values of individual measurements at constant temperature. (**C**) The temperature-dependent particle size distributions $P(R_H)$ in spin probed HSA solutions are given here. Three different regimes are highlighted comprising monomers from $9 < j < 57$, oligomers for $j > 70$ and larger aggregates for $j > 80$. (**D**) The scattered light intensity (SLI) is given in count rates (in Hz) from temperature-dependent DLS experiments on 16-DSA-probed HSA with a clear minimum within $45 < j < 57$ (SLI$_{min}$). All experiments were conducted at pH 7.4 with 1:1 nominal equivalents of 16-DSA to HSA at 0.2 mM.

A closer examination of the temperature range from $9 < j < 63$ (see inset in **Figure 11.3B**) reveals that the particle size is largely constant at about 3.3 nm in the low-temperature range ($j < 40$). However, above 45°C a significant particle size increase takes place, still without any larger aggregates appearing in detectable quantities. The scattered light intensity (SLI, **Figure 11.3D**) was recorded simultaneously and gives a congruent view on the problem. Surprisingly, an identifiable drop in scattered light intensity is detected in between $45 < j < 57$ (SLI$_{min}$) that was associated with the

dissolution of polymer aggregates in the previous chapter (see also **Figure 10.4C**). Prior studies attributed this effect to a mere opening of the Cys34 crevice,[26,36] some reversible conformational changes,[37] or a change in compressibility.[38] According to Curry, the three globular albumin domains (I – III) rotate as rigid bodies relative to one another and fatty acids may stitch these domains together overtaking the role of lock pins.[39] This dynamic feature may also be modified by temperature.

As expected, the SLI significantly increases for $j > 60$, when also an increasing number of larger oligomeric particles forms. Therefore, the conclusion has to be drawn that HSA undergoes a structural rearrangement from a tight to a more loose organization of subdomains that finally leads to protein aggregation by mutual entanglement. Technically, this drop in SLI around 50°C can be understood in terms of an opening of globular HSA molecules forming a kind of three-winged boomerang or *boleadora*. In turn, the decrease of τ_c values of the spectral component b_1 (**Figure 11.3A**) monitoring the global Brownian diffusion confirm the picture of a structural softening of HSA at about 40 – 50°C. The τ_c values of the free diffusion process as monitored by b_2 do not exhibit this decrease to that extent. This circumstance indicates that the domains harboring the 16-DSA ligand remain largely unaffected up to about 70°C. It is concluded that indeed a temperature-induced rotational decoupling of the three HSA domains is the most probable reason for the observed dynamic effects.

11.2.2 | Temperature-dependent Ligand Uptake Capabilities of HSA

The 16-DSA binding capacity has been determined for HSA via a Scatchard plot analysis[40] after explicit simulation of CW EPR spectra. The results from the simulations can be found in **Figure I2**. For now, two different temperatures have been chosen to investigate the effect that temperature has on the ligand binding properties, one at room temperature (25°C) and another one at physiological temperature (37°C). Both Scatchard plots were constructed in the loading ratios from about 2:1 to 8:1 At 25°C a straightforward routine can be conducted as presented in **Chapter 7.3.1** and **Chapter 10.2.4**, that allows for extracting the number of equivalent binding sites N_E and the association (see equation 10.2, K_A) or dissociation constant (K_D, see **Figure 11.4A**). This plot reveals that HSA possesses $N_{E,25} = N_{T,25} = 8.1 \pm 0.3$ equivalent binding sites for 16-DSA with a macroscopic association constant $K_{A,25} = (1.66 \pm 0.04) \cdot 10^6$ M^{-1} corresponding to $K_{D,25} = 603 \pm 16$ nM (**Table 11.1**). However, at 37°C linearity in the Scatchard plot has vanished and again an exponentially decaying curve shape can be observed.[41,42] An arbitrary fit curve has been inserted in **Figure 11.4B** that allows the application of the Rosenthal method (blue, see also **Chapter 7.3.1**),[43] revealing a slight increase in the total number of binding sites ($N_{T,37} = 9.2 \pm 2.9$) that can be subdivided into two groups ($N_1 = N_{E,37,I}$ = 4.0 ± 1.3 and $N_2 = N_{E,37,II} = 5.2 \pm 1.6$) with different affinities each. In fact, this is a concept that was initially introduced by Karush[44] for exemplifying the cooperativity of ligand binding to albumins.

This approach seems to describe albumin behavior best.[45] Results from these Scatchard analyses are given in **Table 11.1**. It can be rationalized that the total number of binding sites is also slightly dependent on temperature. A cooperativity test according to the scheme given by Tanford[46] reveals

an interesting feature when both Scatchard plots are compared in terms of $\ln K_{A,int}^{*}$ (**Figure 11.4C**, see **Chapter 7.4.2** for details). In principle, the plot of $\ln K_{A,int}^{*}$ versus N_L yields the ligand concentration-dependent energy levels of association. The interpretation is again made according to the suggestion of De Meyts and Roth.[47] At 25°C, the typical non-cooperative (N.C.) region is identified up to $N_L \approx 6.5$, as it was similarly observed for unmodified BSA (**Figure 7.9**).
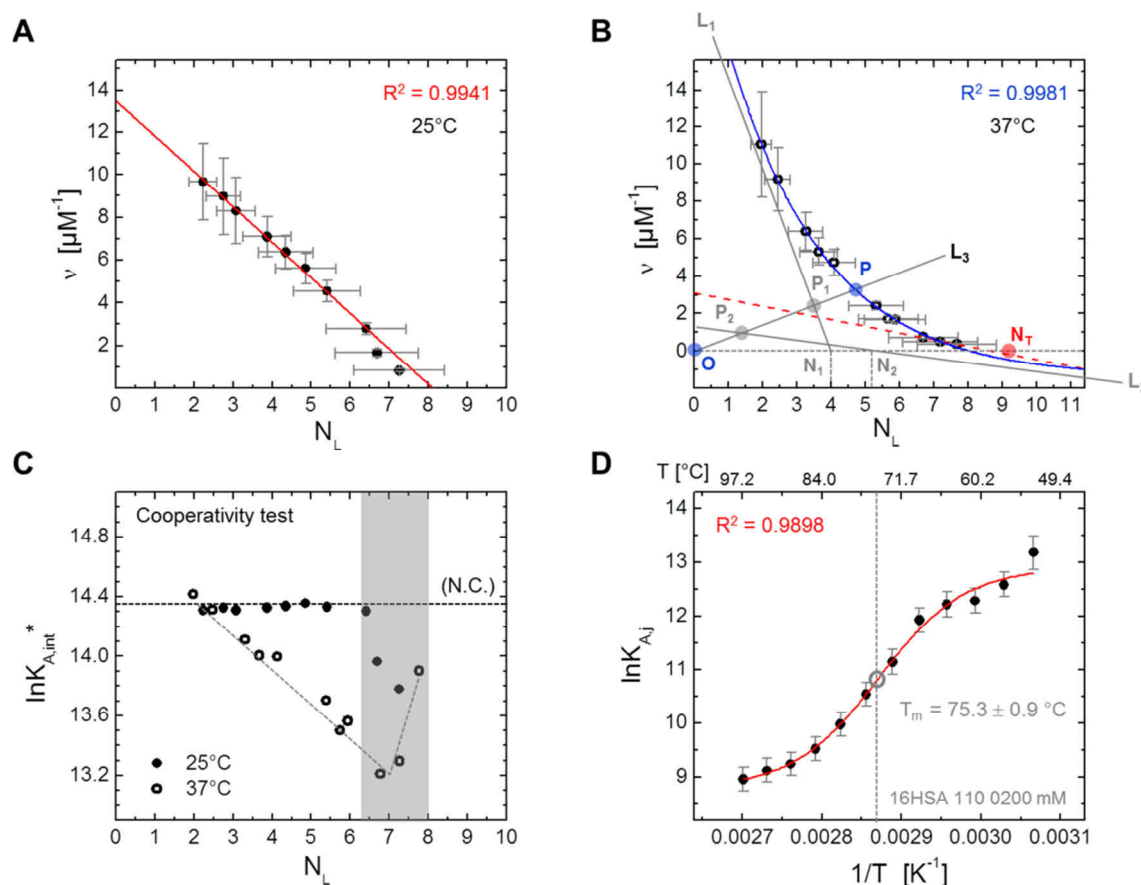
Figure 11.4 | Temperature-dependent 16-DSA binding affinity and capacity of HSA. Scatchard plots of 16-DSA interacting with HSA at (**A**) 25°C (black, full circles) with linear fit (red) and (**B**) at 37°C (black, open circles) with an arbitrary exponential fit curve for highlighting the exponential curve progression (blue). The Rosenthal method[43] was applied according to the procedure shown in **Figure 7.4** where the three lines (L_1, L_2, L_3) allow for the consideration of two groups of binding sites (N_1, N_2). A linear fit (red dotted line) to the last three data points typically gives the total number of binding sites (N_T). The Scatchard plots were constructed in the loading ratios from about 2:1 to 8:1. (**C**) A cooperativity test for both Scatchard plots was performed according to the scheme presented in **Chapter 7.4.2**. The region where the type of cooperativity changes in both curves is highlighted with a gray bar. The change from negative to positive cooperativity at 37°C (open circles) is retraced with gray dotted lines as an aid to the eye. (**D**) A van't Hoff plot of the association constant $K_{A,j}$ is shown that can be constructed from free (*f*) and bound (b_1, b_2, *g*) spectral fractions in **Figure 11.2B+C** (16HSA 110 0200 mM). A sigmoidal Boltzmann fit curve is shown together with the midpoint temperature T_m (= α_3^{-1}, see equation 11.1). The ligand-to-protein ratio for the van't Hoff plot is 1.13 : 1.00 at 0.18 mM equivalents. The quality (R^2) of respective fit curves is given in according colors.

However, there is a region of negative cooperativity for $N_L > 6.5$. At 37°C negative cooperativity is observed instead of the non-cooperative phase that switches to positive cooperativity for $N_L > 6.5$. It is therefore concluded that temperature affects the binding site cooperativity decisively and a really precise determination of N_T is only obtained at 25°C.

Additionally, a van't Hoff plot of the temperature-dependent association constant $K_{A,j}$ can be constructed from data shown in **Figure 11.2** (1.13 equivalents of 16-DSA per HSA). In this case equation 10.8 can be applied as the tight binding regime is also valid here ($[L]_t < [R]_t = N_{T,25} \cdot c_H$). However, for simplicity the total receptor concentration is assumed to remain constant at a value of $[R]_t = 1.46$ mM for all temperatures, as it is only of interest where the strongest change in affinity occurs. Additionally, the bound fraction is here constituted from the sum of dynamic regimes b_1, b_2 and g for simplicity ($\phi_b = \phi_{b1} + \phi_{b2} + \phi_g$).

As 16-DSA binding at lower temperatures is so strong that the free fractions (f) are overshadowed by noise ($\phi_{f,5-49} < 0.02$ %), a temperature-dependent van't Hoff plot of $K_{A,j}$ in this temperature range is unfortunately inaccessible ($5 < j < 53$). However, a fit function can be applied to the curve shape of $\ln K_{A,j}$ for $j \geq 53$ as shown in **Figure 11.4D** that reveals some more properties of the temperature-dependent ligand binding process. The general shape of $\ln K_{A,j}$ is best described by a Boltzmann function of the kind:

$$\ln K_{A,j} = -\ln\left[N_{T,25} \cdot c_H\left(\frac{[L]_t}{[L]_{b,j} + [L]_{g,j}}\right) - [L]_{f,j}\right] = \alpha_1 + \frac{\alpha_2 - \alpha_1}{(1 + e^{(x-\alpha_3)/\alpha_4})} \qquad (11.1)$$

where α_z ($z = 1 - 4$) are fit parameters that are given in **Table I4.** For clarity, the inverse temperature from the van't Hoff plots is from now on replaced by $x = T^{-1}$ in most mathematical expressions. From this indirect sigmoidal picture of a macroscopic ligand association constant $K_{A,j}$ it has to be initially assumed that HSA denaturation is a hypothetical two-state phase transition, e.g. from a solid (s) to a vapor (v) state.[48] The assignment of the meaning of fit parameters in equation 11.1 can be developed in the following way: the denaturation process of HSA occurs in a defined temperature range ΔT with a midpoint temperature $T_m = \alpha_3^{-1}$ between the states of energy $H_1 = \alpha_1$ and $H_2 = \alpha_2$.[49] The respective temperature range $\Delta T = (\alpha_3 - \alpha_4)^{-1} - \alpha_3^{-1} = 6.61$ K of the transition also defines the corresponding slope $k_{KA} = (\alpha_2 - \alpha_1)/(4\Delta T) = 0.155$ K^{-1} at T_m.[49,50] The midpoint temperature or melting temperature of HSA is therefore at $T_m = 75.3 \pm 0.9$ °C, as determined from the maximum change in ligand binding affinity. **Table 11.1** reveals that the most affected functional property of HSA upon temperature increase is the decrease of the macroscopic ligand association constant $K_{A,j}$ by more than two orders of magnitude (~ 200 times, assuming that $N_{T,j} = N_{T,25} = 8.1$ for all temperatures). Therefore, the free energy of 16-DSA association also decreases and the observed ligand binding process gets less exergonic ($\Delta G^\circ_{A,97} - \Delta G^\circ_{A,25} = 7.9$ kJ mol^{-1}).

These data are in nice resemblance with results obtained by Gantchev and Shopova,[8] who also reported $N_T = 8 \pm 1$ for HSA. Furthermore, an astonishing conformity is revealed by comparing free energies from palmitic acid binding to HSA. Spector *et al.*[41,51] also found two classes of binding sites with $\Delta G^\circ_{A,37,I} = -39.8$ kJ/mol and $\Delta G^\circ_{A,37,II} = -32.2$ kJ/mol. An ITC study by Aki and Yamamoto revealed similar results for palmitic acid interacting with HSA ($\Delta G^\circ_{A,37} = -38.8$ kJ/mol).[52]

Table 11.1 | Thermodynamic data from 16-DSA binding to HSA

j	$N_{T,j}$	p	$N_{E,j,p}$	$K_{A,j,p}$ [M^{-1}]	$K_{D,j,p}$ [M]	$\Delta G^{\bullet}_{A,j,p}{}^{d}$ [kJ/mol]	$C_{j,p}{}^{e}$
25[a]	8.1 ± 0.3	–	–	$(1.66 \pm 0.04)\cdot 10^{6}$	$(6.03 \pm 0.16)\cdot 10^{-7}$	-35.5 ± 0.9	(N.C and –)
37[b]	9.2 ± 2.9	I	4.0 ± 1.3	$(5.40 \pm 0.74)\cdot 10^{6}$	$(1.85 \pm 0.25)\cdot 10^{-7}$	-40.0 ± 5.5	(–)
		II	5.2 ± 1.6	$(2.50 \pm 0.60)\cdot 10^{5}$	$(4.00 \pm 1.01)\cdot 10^{-6}$	-32.0 ± 7.7	(– and +)
97[c]	–	–	–	$(7.84 \pm 0.49)\cdot 10^{3}$	$(1.27 \pm 0.03)\cdot 10^{-4}$	-27.6 ± 8.3	N.A.

[a]Values are obtained from the Scatchard plot in **Figure 11.4A**. [b]Values are obtained from the Rosenthal analysis that was applied to the Scatchard plot in **Figure 11.4B**, here with Scatchard phases p. [c]Values are obtained from the van't Hoff plot of $\ln K_{A,j}$ in **Figure 11.4D**.

11.2.3 | Thermodynamic Analysis of the Interconversion Process of 16-DSA Bound to HSA

The EPR spectroscopic view in terms of $K_{A,j}$ from **Chapter 11.2.2** is now further refined by examining the temperature-dependent interconversion process during the denaturation process of HSA from the bound ligands' point of view (ϕ_{bi}, see also **Chapter 10.2.8**). Values for $\ln K_{IC,j}$ are constructed from **Figure 11.2B** according to equation 10.4 ($K_{IC,j} = \phi_{b2,j}/\phi_{b1,j}$) and the corresponding temperature response of the system consisting of 16-DSA bound to HSA is shown in **Figure 11.5**.

According to the procedure that was shown for C_nS_m polymers, a fit function has been found for the van't Hoff plot of $\ln K_{IC,x}$ in HSA and is given as equation 11.2 ($x = T^{-1}$). It turns out that the sum of exponential (second term of equation 11.2) and a double Boltzmann expression (third term of equation 11.2 in parentheses) fits best to describe the temperature-dependent curve progression of the interconversion equilibrium:

$$\ln K_{IC,x} = \ln K_{IC,0} + \kappa_1 \cdot e^{\kappa_2 x} + \left(\frac{\kappa_3 \kappa_4}{1 + e^{(x-\kappa_5)/\kappa_6}} + \frac{\kappa_3(1-\kappa_4)}{1 + e^{(x-\kappa_7)/\kappa_8}} \right) \qquad . \qquad (11.2)$$

after all yielding a correlation coefficient of $R^2 = 0.9985$. Pure polynomial functions definitely fail in reproducing this $\ln K_{IC,j}$ curve shape. All corresponding fit parameter values of $\ln K_{IC,0}$ and κ_y ($y = 1 - 8$) are shown in **Table I5** (see **Appendix I3**). Optionally, the second term $\kappa_1 \cdot \exp(\kappa_2 \cdot x)$ can also be written as a polynomial equation $u \cdot x + v \cdot x^2$. The fit curve is given together with the $\ln K_{IC,j}$ values in **Figure 11.5A** and the rationale for separating individual contributions is given in **Figure 11.5B**. The application of a double Boltzmann term generally implies that two dynamic transitions may occur in HSA that affect the temperature course of $\ln K_{IC,j}$.

Again the parameters κ_3 and κ_4 can be understood as arbitrary step heights of the transitions and parameters κ_5 and κ_7 are the midpoint temperatures $T_{m,k}$ of the individual transitions k, while κ_6 and κ_8 are the individual transition widths. A straightforward thermodynamic analysis can be conducted for $\ln K_{IC,j}$ of 16-DSA interacting with HSA in accordance to the strategy developed in **Chapter 10.2.8** (see equations 10.11 – 10.13).
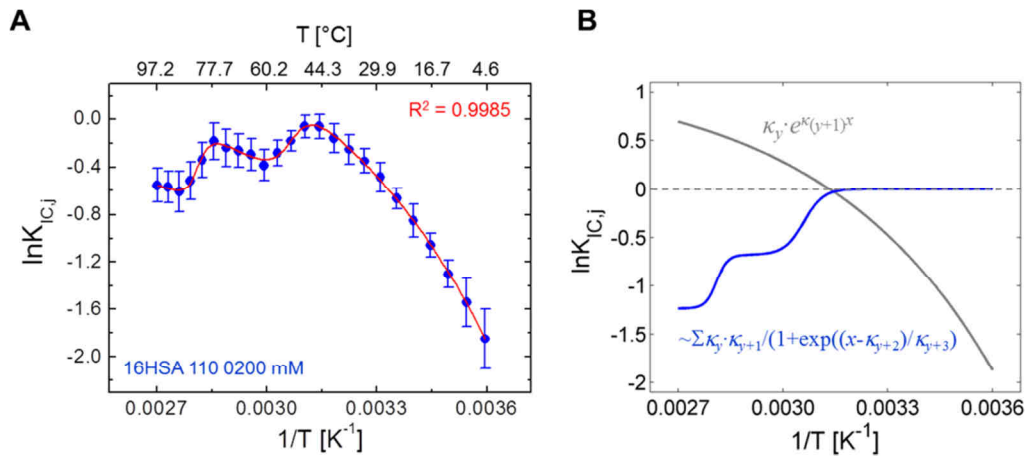
Figure 11.5 | A van't Hoff plot of $\ln K_{IC,j}$ from 16-DSA bound to HSA. (**A**) Individual data points of the van't Hoff plot for $\ln K_{IC,j}$ were calculated from equation 10.4 with the spectral fractions ϕ_{b1} and ϕ_{b2} of 16-DSA bound to HSA (blue) in the temperature range from $5 < j < 97$ (16HSA 110 0200 mM). A fit curve derived from equation 11.2 is shown in red. (**B**) Mathematical decomposition of the fit function for $\ln K_{IC,j}$ highlighting the second and third term of equation 11.2.

The temperature-dependent interconversion enthalpy change is obtained from equation 11.2 with the relation:

$$\Delta H^{\circ}_{IC,x} = -R \frac{\partial \ln K_{IC,x}}{\partial x} \qquad , \qquad (11.3)$$

resulting in:

$$\Delta H^{\circ}_{IC,x} = -R\left(\kappa_1 \kappa_2 \cdot e^{\kappa_2 x} - \frac{\kappa_3 \kappa_4}{\kappa_6} \cdot \frac{e^{(x-\kappa_5)/\kappa_6}}{(1+e^{(x-\kappa_5)/\kappa_6})^2} - \frac{\kappa_3(1-\kappa_4)}{\kappa_8} \cdot \frac{e^{(x-\kappa_7)/\kappa_8}}{(1+e^{(x-\kappa_7)/\kappa_8})^2} \right) . \qquad (11.4)$$

Together with the relation $\Delta G^{\circ}_{IC,x} = \Delta H^{\circ}_{IC,x} - T\Delta S^{\circ}_{IC,x} = -RT\ln K_{IC,x}$, the temperature-dependent molar interconversion entropy change may also be determined as:

$$
\begin{aligned}
\Delta S^{\circ}_{IC,x} &= x \cdot \Delta H^{\circ}_{IC,x} + R\ln K_{IC,x} \\
&= -R \cdot x\left(\kappa_1\kappa_2 e^{\kappa_2 x} - \frac{\kappa_3\kappa_4}{\kappa_6} \cdot \frac{e^{(x-\kappa_5)/\kappa_6}}{(1+e^{(x-\kappa_5)/\kappa_6})^2} - \frac{\kappa_3(1-\kappa_4)}{\kappa_8} \cdot \frac{e^{(x-\kappa_7)/\kappa_8}}{(1+e^{(x-\kappa_7)/\kappa_8})^2} \right) \\
&\quad + R\left(\ln K_{IC,0} + \kappa_1 \cdot e^{\kappa_2 x} + \frac{\kappa_3\kappa_4}{1+e^{(x-\kappa_5)/\kappa_6}} + \frac{\kappa_3(1-\kappa_4)}{1+e^{(x-\kappa_7)/\kappa_8}} \right)
\end{aligned} \qquad (11.5)
$$

In analogy to equation 10.13 the differential equation of the molar heat capacity change $\Delta C^{\circ}_{P,IC,j} = d\Delta H^{\circ}_{IC,j}/dT$ is best calculated by:

$$\Delta C^{\circ}_{P,IC,j} = \left(\frac{\partial \Delta H^{\circ}_{IC,j}}{\partial T}\right)_P = \frac{1}{T^2} \cdot \left(\frac{\partial \Delta H^{\circ}_{IC,j}}{\partial\left(\frac{1}{T}\right)}\right)_P \qquad (11.6a)$$

$$\Delta C^{\circ}_{P,IC,x} = x^2 \cdot \left(\frac{\partial \Delta H^{\circ}_{IC,x}}{\partial x}\right)_P = -Rx^2\left(\frac{\partial^2 \ln K_{IC,x}}{\partial x^2}\right)_P \qquad , \qquad (11.6b)$$

yielding:

$$\Delta C_{\mathrm{P,IC},x}^{\circ} = -Rx^2 \cdot \left(\frac{2\kappa_3\kappa_4}{\kappa_6^2} \cdot \frac{e^{2(x-\kappa_5)/\kappa_6}}{(e^{(x-\kappa_5)/\kappa_6}+1)^3} + \frac{2\kappa_3(1-\kappa_4)}{\kappa_8^2} \cdot \frac{e^{2(x-\kappa_7)/\kappa_8}}{(e^{(x-\kappa_7)/\kappa_8}+1)^3} \right.$$
$$\left. - \frac{\kappa_3\kappa_4}{\kappa_6^2} \cdot \frac{e^{(x-\kappa_5)/\kappa_6}}{(e^{(x-\kappa_5)/\kappa_6}+1)^2} - \frac{\kappa_3(1-\kappa_4)}{\kappa_8^2} \cdot \frac{e^{(x-\kappa_7)/\kappa_8}}{(e^{(x-\kappa_7)/\kappa_8}+1)^2} + \kappa_1\kappa_2^2 e^{\kappa_2 x} \right) . \tag{11.7}$$

In order to clarify the origin of these rather bulky thermodynamic expressions, explicit derivations are given in **Appendix I4**. In **Figure 11.6** all functions are plotted in the temperature range of $5 < j < 97$. First of all, it is worth to mention that the spectral fraction of b_1 does not decrease below $\phi_{b1,j} = 0.5$, thus leading to constantly negative $\ln K_{\mathrm{IC},j}$ values. In turn, this means that $\Delta G^{\circ}_{\mathrm{IC},j}$ is always endergonic and the interconversion process is therefore unfavorable throughout the whole observed temperature range. However, the $\Delta G^{\circ}_{\mathrm{IC},j}$ curve exhibits a global minimum at 47.4°C, where the free energy approaches zero ($\Delta G^{\circ}_{\mathrm{IC},j} \approx 0.11$ kJ/mol). Intriguingly, this is the temperature region in which also the onset of the HSA expansion, or structural opening can be observed in corresponding DLS data (SLI$_{\min}$, **Figure 11.3D**). For $j > 47.4$ the interconversion process of bound 16-DSA is again more unfavorable. Unlike free energy, the corresponding enthalpy changes $\Delta H^{\circ}_{\mathrm{IC},j}$ of the interconversion process strongly alternate between endothermic and exothermic interconversion conditions. Altogether, four enthalpy compensation temperatures are found, $T_{\mathrm{H,1}} = 47.4$°C, $T_{\mathrm{H,2}} = 61.1$°C, $T_{\mathrm{H,3}} = 76.5$°C and $T_{\mathrm{H,4}} = 89.7$°C. Therefore, it can be concluded that this process is entropy driven ($\Delta H^{\circ}_{\mathrm{IC},j} > 0$, $\Delta S^{\circ}_{\mathrm{IC},j} > 0$) and gains energy from its environment for $5 < j < 47.4$, from $61.1 < j < 76.5$, as well as for $j > 89.7$. Some energy is released in the intervals $47.4 < j < 61.1$ and $76.5 < j < 89.7$ where the dynamic interconversion process of 16-DSA is enthalpy driven ($\Delta H^{\circ}_{\mathrm{IC},j} < 0$, $\Delta S^{\circ}_{\mathrm{IC},j} < 0$). These characteristic temperatures are summarized in **Figure 11.6F** and were calculated according to equations 10.22 – 10.24.

The changes in molar heat capacity $\Delta C^{\circ}_{\mathrm{P,IC},j}$ in **Figure 11.6E** reveal a slight apolar hydration ($\Delta C^{\circ}_{\mathrm{P,IC},j} < 0$) for $j < 38$ before a significant increase is detected with a maximum at 49.7°C. This is again corroborated as a mere opening of the HSA structure that exposes some hydrophobic regions containing 16-DSA ligands to the solvent. The zero-crossing at $T_{\mathrm{AD,1}} = 53.6$°C terminates the apolar hydration temperature region. Note, that the solvent exposure of hydrophobic regions/ligand coincides with the onset of detectable free ligand fractions ϕ_f and the gel fraction ϕ_g. This means that protein aggregation is triggered and ligand binding becomes less favorable, as it was already shown for the C_6S_{32} polymers. Accordingly, the structural integrity of HSA can be expected to be noticeably deteriorated above $T_{\mathrm{AD,1}}$.

This loss in protein functionality is again converted into an apolar hydration process above $T_{\mathrm{AH,1}} = 69.4$°C. This (second) apolar hydration process above $j > 70$ is much more pronounced than the first one (from about $38 < j < 53$) with a maximum appearing at 80.0°C. This distinct temperature range from $70 < j < 80$ was already identified as the region with the strongest decrease in HSA's ligand binding affinity (**Figure 11.4D**, $\ln K_{\mathrm{A},j}$) and also embraces the corresponding midpoint temperature

$T_{\mathrm{m}} = 75.3 \pm 0.9°C$. At $T_{\mathrm{AD},2} = 82.7°C$ the apolar dehydration is re-established where the SLI from DLS experiments exhibits the strongest increase. This final apolar dehydration therefore coincides with the formation of larger HSA aggregates (**Figure 11.3C**). Thus, it is shown that the basic principles found in **Chapter 10.2.8** can be transferred in direct analogy to more complex systems as HSA.
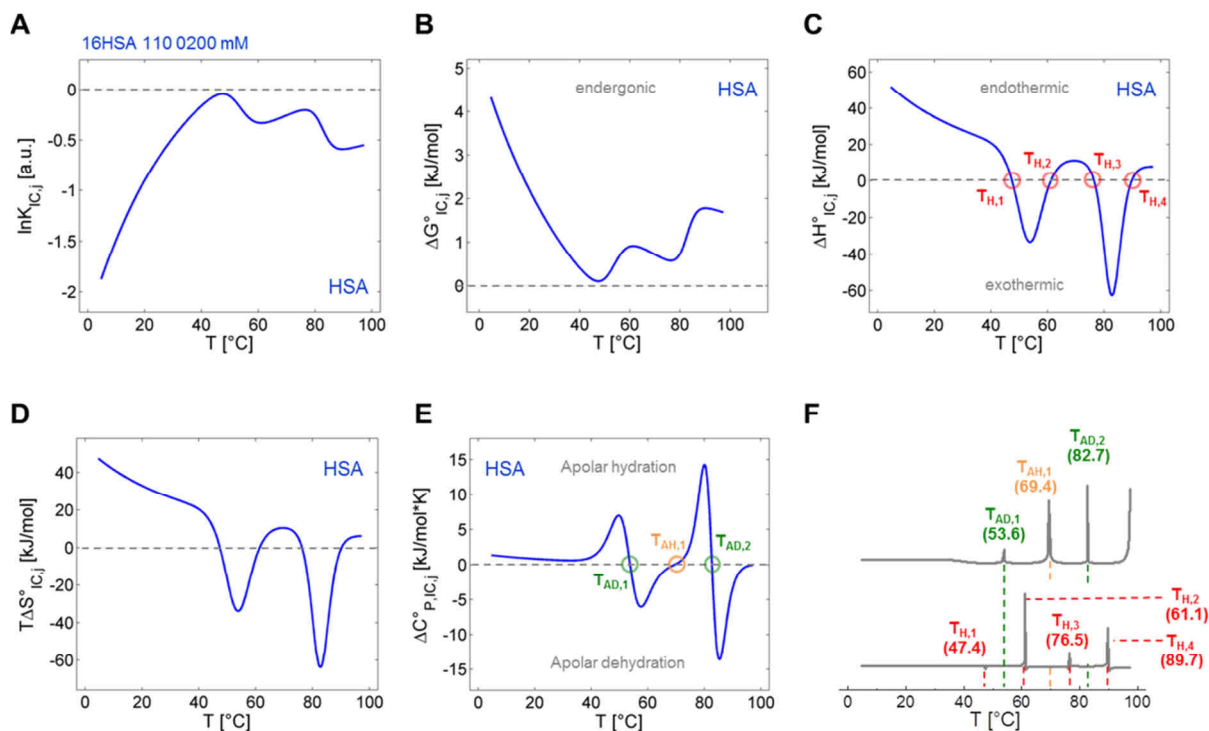

Figure 11.6 | Graphical representation of the thermodynamic functions from ln$K_{\mathrm{IC},j}$ with 16-DSA bound to HSA.
Continuous depiction of (**A**) ln$K_{\mathrm{IC},j}$ vs. T from equation 11.2, resulting in the (**B**) molar Gibbs free energy change $\Delta G°_{\mathrm{IC},j}$ that remains endergonic in the whole temperature range. (**C**) Temperature-induced change of molar enthalpy $\Delta H°_{\mathrm{IC},j}$ calculated from equation 11.4 comprising endothermic and exothermic regions and enthalpy compensation temperatures $T_{\mathrm{H},1} - T_{\mathrm{H},4}$ in red. (**D**) Temperature-dependent change in molar entropy $T\Delta S°_{\mathrm{IC},j}$ calculated from equation 11.5. (**E**) Change in molar heat capacity $\Delta C°_{\mathrm{P,IC},j}$ with apolar dehydration temperatures $T_{\mathrm{AD},1}$ and $T_{\mathrm{AD},2}$ in green and the apolar hydration temperature $T_{\mathrm{AH},1}$ in orange. The corresponding curve was calculated from equation 11.7. (**F**) Determination of enthalpy compensation temperatures $T_{\mathrm{H},i}$, apolar dehydration temperatures $T_{\mathrm{AD},i}$ and apolar hydration temperature $T_{\mathrm{AH},1}$ using equations 10.22 – 10.24. All curves are obtained from the interconversion process ln$K_{\mathrm{IC},j}$ as obtained from data presented in **Figure 11.2**. The results are shown in blue throughout (16HSA 110 0200 mM).

11.2.4 | Classification of the ln$K_{\mathrm{IC},j}$ Process in Comparison with Results from DSC

Here, a qualitative comparison is made in between the results from EPR-derived thermodynamic analyses of ln$K_{\mathrm{IC},j}$ and the changes in heat capacity of HSA itself as observed from DSC experiments. This approach delivers a combined view from the nanoscopic thermodynamic properties obtained from the fatty acid ligands together with the macroscopic heat signature of the bulk protein solution. Thus, samples have been prepared identically, each containing nominal 16-DSA-to-HSA equivalents of about 1.1 : 1.0 at $c_{\mathrm{H}} = 0.18$ mM.

The DSC thermogram in **Figure 11.7** (black) exhibits the classical bimodal appearance of albumin loaded with fatty acids[53,54] showing maxima at the two denaturation temperatures $T_{\mathrm{D},1} = 65.1°C$ and $T_{\mathrm{D},2} = 75.1°C$. This biphasic appearance of the thermogram was initially assigned to a ligand

redistribution process during denaturation.[54–56] According to this hypothesis the released fatty acids from molten HSA molecules are absorbed by still intact HSA, contributing their binding energy to internal protein stability.[54] This is a common phenomenon in ligand binding to macromolecules.[57,58] Here, EPR data do not reproduce the DSC thermogram shape but rather reveal some of the dynamic processes in HSA that exert an influence on the course of ligand interconversion thermodynamics. First of all, the two denaturation temperatures $T_{D,i}$ from DSC are not directly found in the parameters from thermodynamic analyses of $\ln K_{IC,j}$.
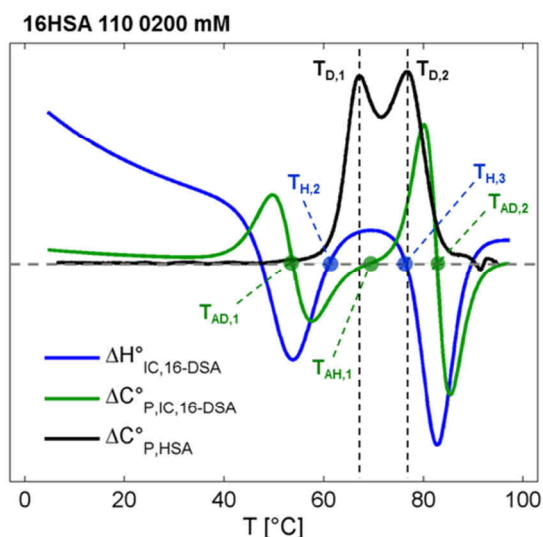

Figure 11.7 | Comparison of $\ln K_{IC,j}$ thermodynamics with a DSC thermogram of 16-DSA bound to HSA. Here, an overlap of EPR data together with a DSC thermogram is shown that represents heat capacity changes of HSA molecules ($\Delta C°_{P,HSA}$, black) comprising denaturation temperatures $T_{D,1}$ and $T_{D,2}$. EPR data are taken from **Figure 11.6C** ($\Delta H°_{IC,16-DSA}$, blue) as well as from **Figure 11.6E** ($\Delta C°_{P,IC,16-DSA}$, green) that highlights 16-DSA-based interconversion enthalpy compensation temperatures $T_{H,2}$ and $T_{H,3}$, as well as changes of ligand hydration at $T_{AD,1}$, $T_{AH,1}$ and $T_{AD,2}$. The exact ligand-to-protein ratio for both methods was quite close to 1.1 : 1.0.

Fit parameters for midpoint temperatures in **Figure 11.5** are again identified as the apolar dehydration temperatures $T_{AD,1}$ (κ_5^{-1}) and $T_{AD,2}$ (κ_7^{-1}) that represent zero-crossings of $\Delta C°_{P,IC,j}$, roughly coinciding with the onset and termination of heat capacity changes in HSA as detected in DSC experiments ($\Delta C°_{P,HSA}$). Consistently, $T_{AD,i}$ give the minima of the $\Delta H°_{IC,j}$ and $\Delta S°_{IC,j}$ curves. However, this direct correlation of DSC and EPR curves reveals that $T_{AH,1}$ is quite close to the minimum between $T_{D,1}$ and $T_{D,2}$, while $T_{H,3}$ almost exactly coincides with the second melting peak ($T_{D,2}$). Besides, the enthalpy compensation temperature $T_{H,3}$ also indicates the strongest increase or maximum slope in apolar hydration as observed from dynamic ligand interconversion.

On a more fundamental level of argumentation, the ligand interconversion changes to endothermic reaction conditions for $T_{H,2} < j < T_{H,3}$, while the first melting peak develops and ceases ($T_{D,1}$). This means that the interconversion process of 16-DSA gets energetically more favorable during the first phase transition in the HSA substrate when also interconversion entropy $T\Delta S°_{IC,j}$ starts to rise simultaneously. This behavior can only be understood when ligand and protein undergo a mutual energetic coupling, at least to a certain extent.

The conclusion can be drawn that apolar dehydration temperatures $T_{AD,i}$ from ligand interconversion coincide with fine-tuned structural rearrangements in albumin that trigger denaturation and aggregation. However, both $T_{AD,1}$ and $T_{AD,2}$ in HSA differ from the denaturation temperatures ($T_{D,i}$) and are not detected in DSC experiments as they rather confine the temperature range of the whole biphasic denaturation process (53.6 < j < 82.7). In contrast, the apolar hydration temperature $T_{AH,1}$

seems to represent the structural rearrangement that induces an increased structural stability in HSA. From an energetic viewpoint, fatty acids can be seen to be influenced by HSA denaturation and absorb heat in form of a favored interconversion that indicates the emergence and shift of the second melting peak ($T_{D,2}$). The simultaneous increase in interconversion entropy ($T_{AH,1}$ = 69.4°C) illustrates that the ligand obtains additional degrees of motional freedom.

The change in temperature stability upon 16-DSA loading was also investigated by DSC. A typical ligand induced conversion in the melting behavior (T_D) is seen in **Figure 11.8A** ranging from bimodality at lower fatty acid equivalents (up to ca. 5 equivalents) to a singular melting peak at higher loadings. The relative increase in melting temperatures is depicted in the scheme of Shrake and Ross.[54] While the first melting peak ($T_{D,1}$) is shifted linearly upon 16-DSA loading, the second melting peak position ($T_{D,2}$) shifts in a non-linear fashion to higher values that can be described by an exponential function.
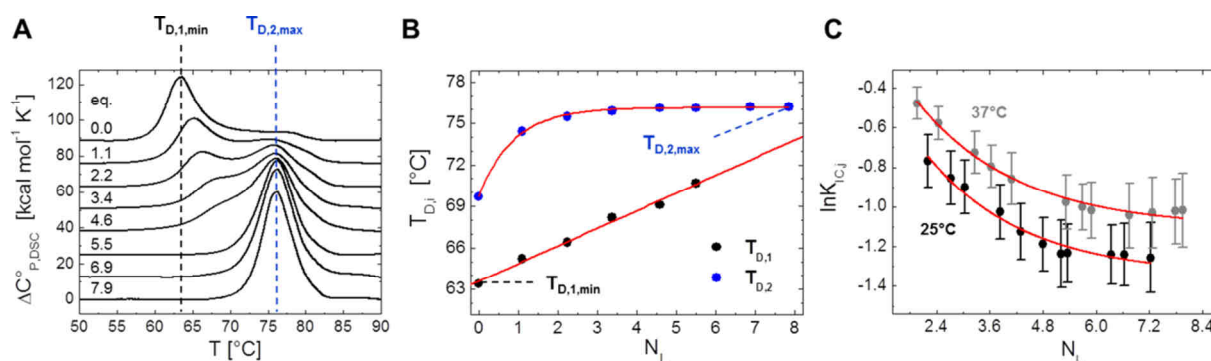

Figure 11.8 | Temperature stability shift of HSA by fatty acid loading in the view from DSC and EPR. (**A**) DSC thermograms of HSA loaded in the range from 0 to about 8 fatty acid equivalents. The melting temperatures $T_{D,1,min}$ and $T_{D,2,max}$ represent the minimum and maximum melting temperatures as induced by the absence or presence of 16-DSA, respectively. (**B**) Melting temperatures $T_{D,1}$ (black) and $T_{D,2}$ (blue) of HSA depending on fatty acid loading equivalents N_L. Individual values are taken from thermograms in (A). Linear and exponential fit curves are shown in red with characteristic values $T_{D,1,min}$ and $T_{D,2,max}$ highlighted. (**C**) Influence of fatty acid loading on $\ln K_{IC,j}$ for 25°C (black) and 37°C (gray). All $\ln K_{IC,j}$ values are taken from simulations that were used for Scatchard plot construction in **Figure 11.4A+B** with respective exponential fit curves shown in red.

All fit parameters can be found in **Table I6** and all extrapolation functions can be found in **Appendix I5**. Additionally, the fit functions for $T_{D,i}$ contribute a distinct lower ($T_{D,1,min}$ = 63.6°C) and upper ($T_{D,2,max}$ = 76.1°C) denaturation temperature limit that defines the maximum observed stability increase of $\Delta T_{D,i,max}$ = 12.5°C as induced by the presence of 16-DSA (**Figure 11.8B**). These values are in nice correspondence with former studies[59–61] and are also affirmative for a largely fatty acid-free protein lot that was used in this thesis.

Simulation data from both Scatchard plots (**Figure 11.4A+B)** provide the view on how 16-DSA loading leads to a global shift in the interconversion equilibrium ($K_{IC,j}$). Similar to results that are obtained from $T_{D,2}$ in DSC experiments, no further global change in $\ln K_{IC,j}$ is observed when HSA is loaded with about $N_L \geq 5$ fatty acids (**Figure 11.8C**). Intriguingly, not only temperature but also fatty acid loading defines to which extent the interconversion process is endergonic. While a temperature increase shifts this equilibrium to free diffusion (b_2), an increased fatty acid content of an HSA

monomer shifts the ligand interconversion back to Brownian diffusion (b_1), i.e. $\ln K_{IC}$ generally decreases when the b_1 fraction increases. Therefore, dynamic ligand interconversion gets more unfavorable with higher FA loading. Hence, fatty acid ligands can be truly seen as temperature equivalents for HSA as they contribute their free energy of binding to protein stability,[57] however, only partially.[58] In this regard, the slope $\partial T_{D,1}/\partial N_L$ from the linear fit to $T_{D,1}$ in **Figure 11.8B** gives a value of $k_{TD,1} = 1.28 \pm 0.06$ °C/FA. Thus, the first HSA monomer melting temperature is shifted for about +1.3 K with each additional 16-DSA molecule.

Both exponential fit curves from $\ln K_{IC,j}$ in **Figure 11.8C** exhibit an almost identical decay constant of about $B_{K,j} = 2.2 \pm 0.3$ FA, therefore being apparently more or less independent of temperature. This allows for the conclusion that temperature (here: $\Delta T = 37$°C $- 25$°C $= 12$ K) mainly shifts the ligand concentration-dependent $\ln K_{IC,j}$ isotherm along the y-axis. Accordingly, the difference $\Delta \ln K_{IC,\Delta T}$ is assumed to be largely constant for all loadings, sustaining a value of about 0.24 that corresponds to $\Delta \Delta G°_{IC} = 0.48$ kJ/mol (as it is determined by $\ln K_{IC,j,0}$ for the plateau at $N_L \rightarrow \infty$, see also **Table I7**). This EPR spectroscopic feature is also indicative of how fatty acid binding reduces internal flexibility in HSA with a simultaneous gain in temperature stability and indirectly confirms the picture of their lock pin task.[39] To this effect, 16-DSA, or fatty acids in general can be seen as natural pharmacoperones, i.e. small molecules that promote refolding of proteins that are exposed to disadvantageous circumstances as high temperature, or bear an intrinsic dysfunctionality due to missense mutations.[62,63]

11.2.5 | DEER Experiments – Screening for Ligand Redistribution Evidence

In case that the proposed stabilizing ligand redistribution[54] takes place during temperature-induced HSA denaturation, the binding site occupation of still intact protein should change to a certain extent. As CW EPR results have shown that a strong decrease in binding affinity towards 16-DSA takes place at temperatures $j > 53$, the redistribution process of bound ligands during HSA denaturation is not confirmed spatially so far. Additionally, in **Figure 11.4** it was confirmed that binding site cooperativity changes with temperature.[51] Therefore, it is tested in this section, whether DEER can provide further insights into these issues.

Several aspects have to be considered for this approach. It was already shown in Junk *et al.*[64] that HSA exhibits much smaller modulation depths for a 16-DSA loading ratio of 2:1 than derived from model biradicals, despite a similar number of coupled spins can be expected (see **Chapter 9**). Therefore, standard spin counting procedures that utilize standardized inversion efficiencies λ do not apply properly for this self-assembled system. In this regard, a recent study also emphasizes the effect that cooperativity may have on modulation depth.[65] Furthermore, the potential number of accessible binding sites in this study (here: $N_{T,25} = 8.1 \pm 0.3$, see **Table 11.1**) gives rise to tremendous multispin effects that leads to an overestimation of short distances and suppresses large distances. First, the previous experiments from Junk *et al.*[64] are here recapitulated with the 16-DSA-probed HSA system

(again in equivalents of $c_H = 0.18$ mM). In an initial step CW EPR is applied to a small volume fraction of the final DEER sample in order to determine the fatty acid concentration in the sample solution by double integration (**Figure 11.9A**). It can be seen that the free fraction f does not notably increase until a loading ratio of about $N_L = 3.5$ is reached.

As it was shown in **Chapter 9**, all binding pockets are occupied to a certain extent in the solution ensemble of HSA, even at a 1:1 loading ratio. This is indirectly confirmed by the Scatchard plot at 25°C in **Figure 11.4A** giving $N_{T,25} = 8.1 \pm 0.3$ equivalent, non-cooperative binding sites. Even at the highest loading ratios of about 1:7 ($N_L \approx 7$), more than 98.5 % of supplied 16-DSA is bound to HSA.

The corresponding DEER measurements of each CW EPR sample in this section exhibit the well-known increase in modulation depths up to values of about $\Delta \approx 0.7$ (**Figure 11.9B+C**). The resulting distance distributions in **Figure 11.9D** also exhibit an overestimation of short distances to quite some extent for $N_L > 2$, as it was also shown by Junk *et al.*[64] The main characteristics of these 16-DSA-derived distance distributions are now termed as $P_A(r)$ for the peak at $r_A = 3.5 \pm 0.1$ nm and $P_B(r)$ for the peak at $r_B = 2.2 \pm 0.2$ nm that are used for the construction of the relative intensity ratio $P_{AB}(r) = P_A(r)/P_B(r)$. As this $P_{AB}(r)$ value may cover a wide range of several orders of magnitude, it is depicted as its natural logarithm in **Figure 11.9E** ($\ln P_{AB}(r)$) together with the first moment $\langle r \rangle$ of the complete distance distribution. The latter one is given mandatory in the result files of the DeerAnalysis software[66] and can be used as a measure for rather broad and ambiguous distance distributions.[67]

The first moment $\langle r \rangle$ does not only contain information about the weight center of $P(r)$, but here also tells about the slight shifts of r_A and r_B for up to about 0.4 nm that might indicate slight allosteric reorganizations of individual binding pockets[39,68–70] upon 16-DSA ligand loading. As it was pointed out before, fatty acids are generally assumed to act as lock pins that increase the albumin diameter for about 0.5 nm by a relative rotation of domain I and II.[39] Instead, this effect is here observed as a general decrease of FA interspin distances acting like a bootlace that ties the domains together. Hence, $\ln P_{AB}(r)$ and $\langle r \rangle$ mainly represent the rise in relative intensity changes of $P_B(r)$, depending on the number of equivalent 16-DSA molecules per HSA. A quite smooth curve is obtained for $\ln P_{AB}(r)$ that can be fitted with an exponential function (equation I.34 in **Appendix I6**). Thus, an empirical formula can be derived that correlates $\ln P_{AB}(r)$ with the fatty acid content $N_{P(r)}$ by:

$$N_{P(r)} = -\ln\left(\frac{20 \cdot \ln P_{AB}(r) + 9}{17 \cdot N_{T,25}} \right) \tag{11.8}$$

where $\ln P_{AB}(r)$ is the experimental parameter from the distance distribution. A quick and intuitive derivation of equation 11.8 is shown in **Appendix I6**. The 16-DSA equivalent-dependent modulation depth Δ also increases in a non-linear fashion to a saturation-like state above $N_\Delta > 3.5$ (**Figure 11.9F**). A mathematical model is here adopted for 16-DSA adsorption to HSA in analogy to a Langmuir isotherm that is usually applied to describe gas absorption to energetically heterogeneous surfaces:[71]

$$\Delta = \frac{\Delta_{\max} \cdot b \cdot N_{\Delta}^{\eta}}{1 + b \cdot N_{\Delta}^{\eta}} \tag{11.9}$$

Thus, the number of 16-DSA molecules that are absorbed by HSA can be determined by modulation depths from DEER experiments using the following empirical expression:

$$N_{\Delta} = \left(\frac{\Delta}{b \cdot (\Delta_{\max} - \Delta)} \right)^{1/\eta} \tag{11.10}$$

Mathematically, the parameters $b = 0.503$ and $\Delta_{\max} = 0.712$ are equivalent to the Langmuir constants, and $\eta = 2.203$ is a stretching factor that originally considers energetic inhomogeneities on absorbing surfaces, or as it is here used in a more figurative sense for the ligand binding sites of HSA.
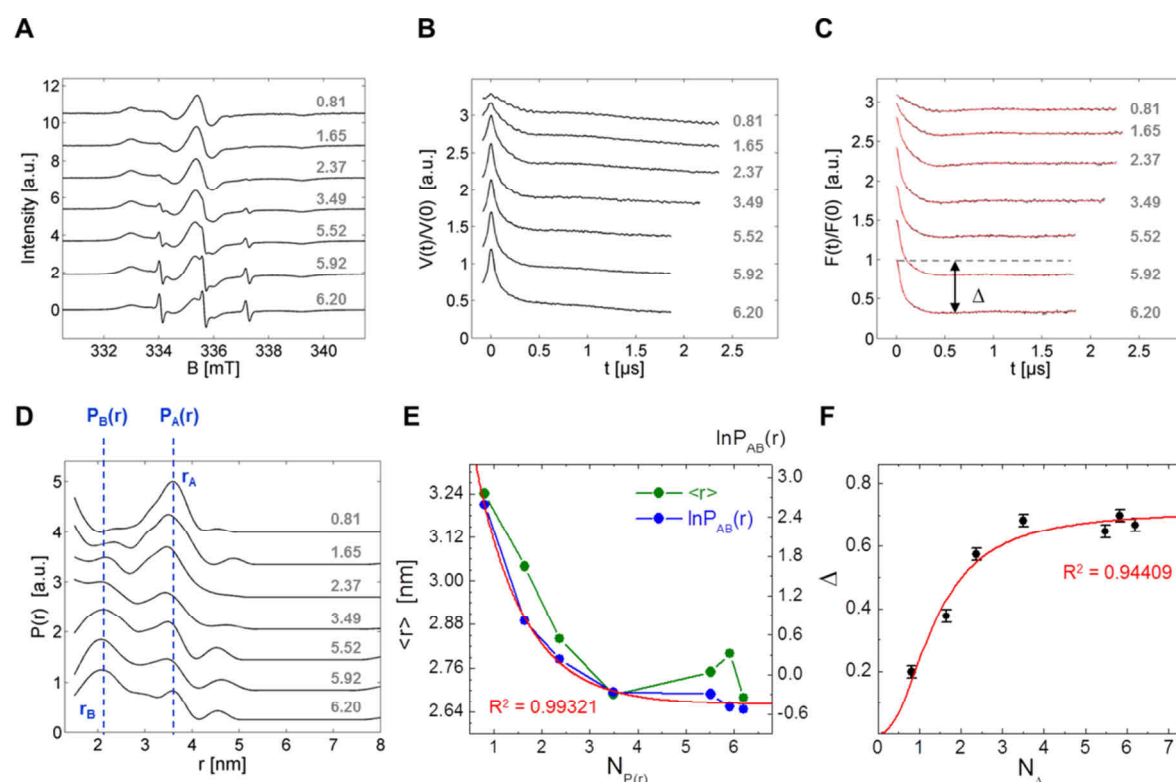
Figure 11.9 | Spin counting strategy for 16-DSA-probed HSA solutions in DEER. A quantitative determination of the co-dissolved 16-DSA molecules in HSA solutions is facilitated by indirect spin-counting utilizing double integration of CW EPR spectra that can be afterwards transferred to ligand concentration-dependent DEER data. (**A**) CW EPR data of HSA loaded in the ratio 0.81 to 6.20 at $c_H = 0.18$ mM equivalents. (**B**) Raw time domain DEER data $V(t)/V(0)$ of samples shown in (A) with corresponding (**C**) dipolar evolution functions $F(t)/F(0)$ with regularized fits (red), modulation depths Δ (gray dotted line, indicated for highest loading ratio 6.2) and (**D**) resulting distance distributions $P(r)$. The two most prominent features in $P(r)$ are denoted as $P_A(r)$ at $r_A = 3.5 \pm 0.1$ nm and $P_B(r)$ at about $r_B = 2.2 \pm 0.2$ nm. (**E**) The first moments $\langle r \rangle$ (green) of $P(r)$ and $\ln P_{AB}(r)$ (blue) are shown as functions of peak-ratio-derived 16-DSA concentration equivalents $N_{P(r)}$. An exponential fit curve is applied to the $\ln P_{AB}(r)$ curve (red) that finally yields equation 11.8. (**F**) The modulation depth Δ is presented as a function of 16-DSA equivalents N_{Δ} with a fit curve corresponding to equation 11.9.

However, these spin counting strategies are intrinsically restricted and are only applicable in the range of about $0 < N_L < 4$ equivalents 16-DSA due to the saturation-like behavior in the corresponding $\ln P_{AB}(r)$ and modulation depth (Δ) curves (**Figure 11.9E+F**). Thus, in combination with double

integration in CW EPR, equations 11.8 and 11.10 allow for spin counting in an empirical fashion, without using formulae that account for multispin contributions that arise in HSA,[64] or other systems.[72–74]

In order to check for the proposed ligand redistribution processes at temperatures $j > 64$,[54] a rather unconventional strategy was pursued, but its feasibility is demonstrated in the following. Aliquots from a single 16-DSA-probed HSA stock solution (16HSA 120 0200 mM) were incubated for 5 min at appropriate temperatures in the range from $9 < j < 81$ that are routinely shock frozen afterwards. The purpose of this approach is now to freeze a snapshot from each of the temperature-specific dynamic ensembles. The results from these experiments are shown in **Figure 11.10**. At first sight the DEER time traces and dipolar evolution functions in **Figure 11.10A+B** do not seem to change considerably upon heating. A further interesting aspect is that also the distance distributions do not change decisively (**Figure 11.10C**) even for higher temperatures. However, a closer inspection of the general distribution shape reveals a slight but traceable increase in $P_B(r)$. The empirical rules of thumb in equations 11.8 (and equation 11.10) that were devised from the loading study in **Figure 11.9** are now deliberately applied. The calculated values of $\ln P_{AB}(r)$ are shown in **Figure 11.10D**.

An average value of $\ln P_{AB}(r) = 1.13 \pm 0.12$ is obtained for "native" HSA ($\sim 9 < j < 65$) that provides a criterion for changes in each distance distribution and therefore essentially in fatty acid loading. Additionally, individual data points are almost entirely located above $\ln P_{AB}(r) > 1$, i.e. when the relative peak ratio is $P_{AB}(r) \approx 3$. For temperatures $j > 70$, all $\ln P_{AB}(r) < 1$, indicating an increase of the $P_B(r)$ feature (see also red traces (*) in the range of $73 < j < 81$ in **Figure 11.10C**). The minimum value for $\ln P_{AB}(r)$ is at 77°C indicating a maximum intensity in $P_B(r)$, almost directly coinciding with $T_{D,2}$ from DSC experiments. In contrast, the first moment $\langle r \rangle$ of $P(r)$ does not show significant changes apart from a slight decrease in the course of HSA temperature denaturation.

The calculation of individual, temperature-dependent $N_{P(r)}$ values is here conducted according to equation 11.8 and is shown in **Figure 11.10E**. An average value of $N_{P(r)} = 1.47 \pm 0.07$ is obtained in the temperature range from $9 < j < 65$. In analogy to $\ln P_{AB}(r)$, the maximum number of ligands per HSA is found at 77°C. This directly leads to $N_{P(r),max} = 2.03$ equivalents of 16-DSA molecules per HSA. This is now clearly associated with an increase in fatty acid loading in the still intact HSA molecules, or associated binding sites. The fit curves of the DSC-derived melting peaks in **Figure 11.8** allow here for extrapolation of 16-DSA equivalent-depending melting peak positions ($T_{D,1} = 65.5$°C and $T_{D,2} = 74.9$°C) and are shown as insets throughout **Figure 11.10D–F** where applicable. Whereas $N_{P(r)}$ and $\ln P_{AB}(r)$ represent $T_{D,2}$ quite well, the temperature-dependent modulation depths show some more subtle features.

An overall maximum modulation depth of $\Delta = 0.41$ is found at 25°C and at 45°C a first local minimum appears in the temperature range that coincides with the drop in SLI from DLS experiments ($SLI_{min} \approx 40 - 55$°C) confirming the loss in protein compactness. A slight kink is also seen for $T_{D,1}$ and for $j > 70$, Δ significantly decreases steadily, while passing $T_{D,2}$.
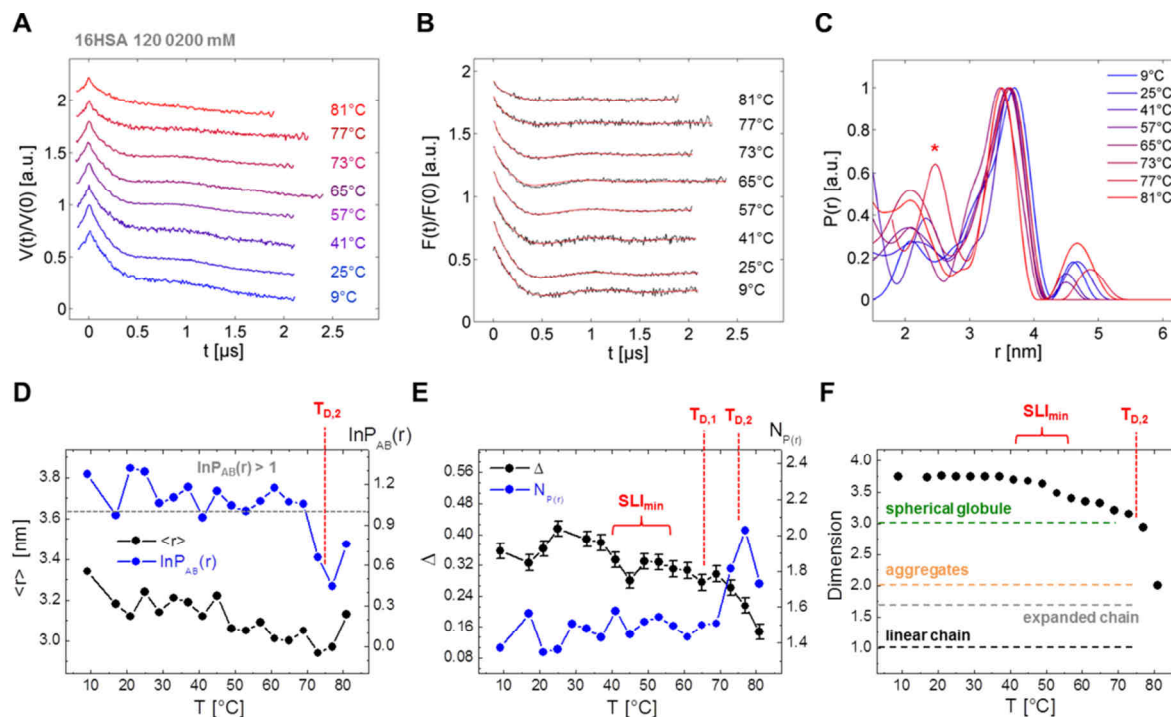
Figure 11.10 | DEER results from temperature denaturation of 16-DSA-probed HSA solutions. (**A**) Several temperature-dependent raw DEER time traces $V(t)/V(0)$ of 16-DSA-probed HSA (16HSA 120 0200 mM), incubated at selected temperatures with corresponding (**B**) dipolar evolution functions $F(t)/F(0)$ (black) with regularized fit curve (red) and (**C**) distance distributions $P(r)$. The red asterisk in (C) denotes the distribution shape at 77°C. (**D**) The first moments $\langle r \rangle$ (black) of $P(r)$ and $\ln P_{AB}(r)$ (blue) are shown as functions of temperature. The gray dotted line indicates $\ln P_{AB}(r) = 1$. (**E**) Experimental modulation depths Δ and $N_{P(r)}$ (from equation 11.8) are presented as functions of temperature. Error bars for individual modulation depths were chosen as $\Delta\Delta = 0.02$ as suggested in Bode *et al.*[72] (**F**) Temperature-dependent background dimensionality change of 16-DSA-probed HSA. The different dimensionality regimes are denoted to indicate shapes of homogenous and spherical globules ($D = 3$), aggregates ($D = 2$), expanded chains ($D = 1.67$) and linear chains.[66,75] The red items in **Figure 11.10D–F** indicate $T_{D,1} = 65.5$°C as the first and $T_{D,2} = 74.9$°C as the second melting temperature from DSC results, calculated from equations I.31 and I.32 in the corresponding loading ratio $N_{P(r)} = 1.47$. SLI_{min} is here given as the temperature range from DLS data in **Figure 11.3D** where HSA elongates and the subdomains are assumed to decouple.

The background dimensionality of the raw DEER time traces was also adjusted carefully to extract additional qualitative information. A typical value of $D = 3.74$ could be used for HSA at lower incubation temperatures ($j < 40$).[76,77] As this parameter is sensitive to changes in global shape and excluded volume (see also **Chapter 8**),[75,77] successful analyses of available DEER data is only guaranteed when dimensionality is lowered in between 3.0 and 3.7 for $40 < j < 70$. Besides the sharp dimensionality drop beyond $T_{D,2}$ ($D < 3$), that would indicate a more linearly stretched chain,[75,78] data evaluation is strongly hampered and spin echo formation vanishes, not least because of the accumulation of denatured protein in gel-like fractions (see also **Figure 11.2C** and **Figure 11.3C**).[33] Thereupon, it is concluded that inhomogenous vitrification of the heated sample, containing the desolate protein, renders DEER experiments at higher incubation temperatures impossible ($j > 81$). Note, that the dimensionality curve in **Figure 11.10F** resembles an inverted SLI curve (**Figure 11.3D**).

11.3 | Discussion

The observed dynamic processes from 16-DSA-probed HSA solutions from EPR spectroscopy, DLS and DSC are summarized in **Figure 11.11** (loading ratio 1:1). Overall six different dynamic rearrangement phases are encountered in this study. The compact and native state of HSA is clearly observed in the temperature range from about $5 < j < 40$ and is termed as Phase I. At $j > 33$ the protein structure starts to extend as detected by a drop in scattered light intensity (SLI) in DLS experiments (**Figure 11.3C**). Simultaneously, the Brownian diffusion component b_1 in corresponding EPR spectra shows a non-linear decrease in rotational correlation times (**Figure 11.3A**), unlike the free diffusion component b_2. Both applied methods, EPR and DLS confirm a protein-based structural extension or decoupling mechanism without any detectable phase transition in DSC. This phenomenon in Phase II is here termed as the *rotationally decoupled domain model* (RODEO model) of HSA forming a *boleadora*-type of domain arrangement. This temperature-induced domain decoupling was proposed in several other studies[79,80] that goes along with mild alterations in secondary structure.[37,38] The existence of a ligand-independent opened and closed state of albumin[81] cannot be confirmed from the obtained data, as the time scale of this process (300 ms)[82] by far exceeds the nanosecond timescale. However, the energetic contributions from fatty acid binding to HSA (**Figure 11.6**) are quite similar to values that were reported in the kinetic model of a two-step attachment profile given by Scheider.[83]

In phase III, the ligand association constant K_A experiences a detectable drop for $j > 53$ as the HSA molecule shows increased fatty acid release (f) being indicative for a structural weakening. At the same time a gel fraction (g) appears in CW EPR spectra, formed by aggregation of individual proteins as confirmed by a spontaneous increase in SLI for $j > 53$. It is here noteworthy that Banerjee and Pal[84] found a structural transition in BSA at 54°C by differential thermal analysis (DTA) that could be also related to slight changes in DLS data. Altogether four coexisting dynamic components are observed in EPR spectra (b_1, b_2, f and g) with the onset of phase III. Thus, the RODEO model shall describe the structural elongation/weakening that is the reason for an entanglement of domains. The HSA *boleadoras* get entangled, accumulate and form gel-like water-depleted regions that are here probed by 16-DSA ligand. In Phase IV that sets in for $j > 64$, the first denaturation process of HSA is triggered ($T_{D,1}$). While a fraction of HSA molecules weakens and denaturation proceeds, 16-DSA release is amplified accordingly.

This emerging free fraction of ligand is absorbed by still intact HSA molecules, however, with lower affinity, leading to a structural stabilization (Phase V) of HSA. Therefore, the protein experiences a shift in denaturation temperatures $T_{D,i}$ (**Figure 11.8A**) as a consequence of the pharmacoperone property[63] of the fatty acids (Phase VI). Finally, a macroscopic gel is formed that consists of a mixture of denatured protein and still intact domains that harbor 16-DSA ligands.

It is also intriguing to which extent the observed phenomena recur throughout different applied methods. Changes in rotational correlation times in CW EPR coincide with SLI effects in DLS data, as

well as changes in hydrodynamic radii ($R_{\mathrm{H},j}$). Additionally, even DEER data exhibit sensitivities to these observed hydrodynamic effects in CW EPR and DLS.
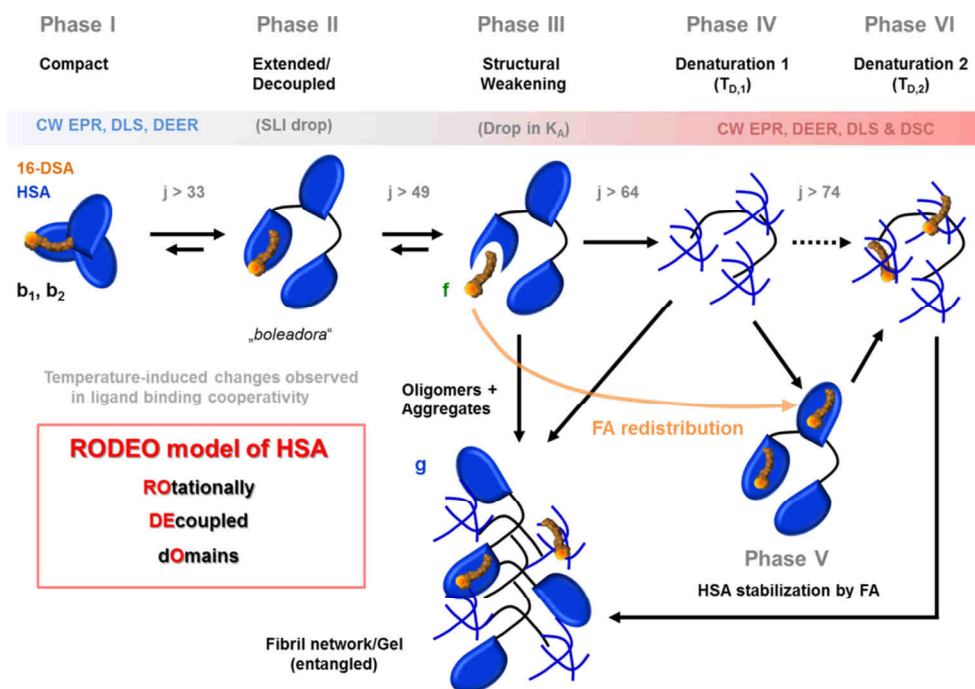

Figure 11.11 | Temperature-induced dynamic phases in HSA solutions containing 16-DSA. A model was devised from available data in this study that also corroborates prevalent literature. The model can be separated in six phases, whereas the first three phases belong to the proposed RODEO model in that globular HSA (Phase I) elongates/decouples to a kind of *boleadora*-like appearance for $j > 33$ (Phase II), decreases in structural integrity that leads to a drop in K_{A} (*f*) and the formation of a fibril network/gel phase for $j > 49$ (*g*, Phase III). During Phase I, changes in ligand binding cooperativity can be observed. The fibril network is presented according to the scheme given by Bhattacharya *et al.*[85] The first denaturation phase occurs in Phase IV for $j > 64$. The still intact HSA molecule fraction can be further stabilized (Phase V) by uptake of the 16-DSA ligands that are released from denatured HSA molecules during Phase III and Phase IV. Beyond $j > 74$, all HSA proteins are denatured and accumulate in the gel phase.

Besides the modulation depth (Δ) that can be seen to detect the overall compactness of the protein ensemble (**Figure 11.10E**), the background dimensionality (D) qualitatively resembles an inverted shape of the SLI curve from DLS results (**Figure 11.3D** and **Figure 11.10F**). Particularly, CW EPR data reveal sophisticated properties in the interconversion thermodynamics that indirectly reflect phase transitions as obtained from DSC, however, on the nanoscopic level of ligand solvation. Therefore, from this study, it can be stated confidently that the strategies that were developed for the calculation of interconversion processes (K_{IC}) in core-shell polymers can also contribute for a better understanding of more complex systems such as HSA.

Again, the clearest conclusions can be drawn from ligand hydration states as obtained from $\Delta C_{\mathrm{P,IC},j}$. As it was predicted earlier, such interactions based on hydrophobicity should exhibit complicated temperature dependences of ΔC_{P}.[86] This is in line with the findings made here (**Figure 11.6**). The obtained apolar dehydration temperatures $T_{\mathrm{AD,1}} = 53.6°C$ and $T_{\mathrm{AD,2}} = 82.7°C$ denote the onset and the termination of the denaturation process in HSA. Furthermore, the region around the apolar hydration temperature $T_{\mathrm{AH,1}} = 69.4°C$ most probably describes the thermodynamically stabilizing reorganization

process of the system that ultimately leads to the appearance of a second denaturation temperature $T_{D,2}$ (**Figure 11.7**). The temperature course in the derived thermodynamic quantities from the interconversion equilibrium elucidate how intricately ligand and protein are energetically coupled, particularly, the heat capacity curves from HSA ($\Delta C^\circ_{P,HSA}$, from DSC) and 16-DSA interconversion ($\Delta C^\circ_{P,IC}$, from CW EPR) interdigitate like cogwheels.

The predicted second denaturation temperature from DSC experiments ($T_{D,2} = 74.4°C$) coincides quite well with the value obtained from the van't Hoff plot of $\ln K_{A,j}$ ($T_m = 75.3 \pm 0.9°C$) for identical loading ratios (about 1.13 equivalents of 16-DSA). With increasing 16-DSA loading upon HSA, a plateau is established in $\ln K_{IC,j}$ from CW EPR data (**Figure 11.8C**), in Δ from DEER data (**Figure 11.9F**) and in $T_{D,2}$ from DSC experiments (**Figure 11.8B**), indicating that this structural stabilization experiences a saturation at about $3.5 < N_L < 5.0$ bound ligand equivalents. An ITC study of Fang *et al.*[87] revealed that only 5 binding sites contribute to structural changes that accompany fatty acid binding (in this case: myristate). It is therefore not far-fetched to conclude that these plateau-like regions above $N_L > 3.5$ illustrate allosteric reorganizations of HSA towards a state of reduced flexibility. The experimental parameters $\ln K_{IC,j}$, Δ, and also SLI values can be seen to truly probe for protein compactness and flexibility. The applied paramagnetic fatty acids can be understood to constitute intrinsic temperature equivalents ($T_{D,1,min} + 1.28°C \cdot N_L$). These fatty acids contribute to HSA's stability solely upon binding and are therefore considered as physiological pharmacoperones.

DEER data gave experimental proof for fatty acid ligand redistribution by a slight, however perceptible change in distance distribution characteristics ($\ln P_{AB}(r)$) that are strongly indicative for higher ligand binding site occupations per albumin ($\sim +40\%$). The established picture of weak and strong binding sites in HSA has to be extended and revised, as it was here shown on a more fundamental level that protein compactness strongly affects the mode of diffusion of ligand. It has to be further ascertained to which extent ligand binding cooperativity is affected by the rotational decoupling of HSA subdomains (RODEO model). From **Figure 11.4** it appears as if not only temperature, but also the associated domain proximity should have an effect on the nature of ligand binding cooperativity. A similar temperature effect was also observed in laurate and myristate binding to HSA by Pedersen *et al.*[51] The FA-lock pin hypothesis given by Curry[39] can be confirmed by $\ln K_{IC,j}$ at different 16-DSA loadings and temperatures (**Figure 11.8C**).

In summary, it should be emphasized that the stability of HSA is not only induced by the sheer presence of fatty acid ligands, but is also energetically driven from the interconvertible modes of intrinsic fatty acid diffusion that facilitate storage of thermal energy in form of rotational entropy.

11.4 | Materials and Methods

Materials. Lyophilized powder of HSA (>95%, Calbiochem), 16-DSA (Sigma-Aldrich) and 87 wt% glycerol (ACROS) were used without further purification. The 0.137 M DPBS buffer[88] pH 7.4 was prepared according to the procedure described in **Appendix C1**.

Sample Preparation. All experiments were conducted on HSA solutions loaded with 16-DSA equivalents of similar or varying ratios. Regardless of the applied method the protein concentration was kept constant at about $c_H = 0.18$ mM as calculated from equation 5.1. Therefore, as the stability of HSA is also dependent on protein concentration,[89] only the concentration of 16-DSA was varied by default throughout the whole study. All sample volumes were adjusted for device-specific requirements ranging from about 0.01 – 1.00 ml. HSA was dissolved in 0.137 M DPBS buffer pH 7.4 to a final stock concentration of 1 mM. Upon addition of a 8 mM stock solution 16-DSA dissolved in 0.1 M KOH the solution gained a slight alkaline pH change being compensated by titrating with appropriate alkaline and acidic 0.12 M DPBS-buffers (see **Appendix C2**) equipped with appropriate amounts of HCl and NaOH, so that final physiological values of pH 7.42 ± 0.06[28,90] could be obtained for all samples. The exact amounts of added 16-DSA was determined by double integration of corresponding CW EPR spectra throughout (**Appendix E3**).

Temperature steps for HSA denaturation with CW EPR (**Figure 11.2**) were set to increase in steps of $\Delta T = 4$ K and the molar ratio of HSA to 16-DSA was 1.00 to 1.13 with a 16-DSA concentration of $[L]_t = 204 \pm 6$ µM. About 15 µL of the final solutions were filled into appropriate EPR-silent capillaries (BLAUBRAND® IntraMARK) for this experiment.

In order to determine $K_{A,j}$ and $N_{E,j,p}$ from CW EPR-based Scatchard plots, the molar ratios of HSA to 16-DSA were individually varied in the range from 0 to 8 nominal equivalents at pH 7.4 to prevent ligand micelle formation[5,91] when the free ligand concentration $[L]_f$ would exceed about 0.3 mM (**Appendix H1**). This phenomenon was successfully prevented.

A single DEER sample was prepared as a 1 ml stock solution at pH 7.38 that was aliquoted in 0.05 ml fractions, so that each sample contains identical ingredients for temperature denaturation. Unlike in other experiments of this study, all DEER samples were equipped with 20% v/v glycerol to prevent crystallization upon freezing. The same accounts for individually prepared samples that were used in the 16-DSA loading study with DEER for extraction of reference data for the DEER temperature denaturation (**Figure 11.9**). All spin probed HSA samples were filled into 3 mm outer diameter quartz tubes (Heraeus Quarzschmelze) and the aliquots were additionally incubated for 5 min at individual temperatures in the range from $9 < j < 81$. The incubation temperatures were chosen to coincide with temperatures in all other experiments and were also conducted in steps of $\Delta T = 4$ K in a water bath that was set up with ultrapure water (MilliQ) in Eppendorf reaction tubes being pre-heated for sufficient time in a thermomixer (~ 5 min for each temperature in Eppendorf Thermomixer C). Afterwards, the samples were shock frozen in liquid nitrogen cooled 2-methylbutane (Sigma-Aldrich) for subsequent DEER measurements. The samples for 16-DSA loading studies with DEER were conveniently shock frozen at room temperature without further treatment.

EPR Spectroscopy. *CW EPR Experiments:* A Miniscope MS400 (Magnettech GmbH) benchtop spectrometer was employed for X-band CW EPR measurements operating at a microwave frequency of 9.4 GHz. All measurements were performed in the temperature range from $5 < j < 97$ utilizing modulation amplitudes of 1 G during a field sweep of 15 mT with an incident microwave power in the range of 3.16 mW. For precise temperature adjustments (intrinsic error is about 0.3 K) a temperature controller (Magnettech Temperature Controller H03) was used. EPR spectra for 16-DSA-based temperature response curves of HSA were recorded in steps of $\Delta T = 4$ K with a precautionary incubation time for each temperature step of about 2 – 3 min. The microwave frequency was recorded with a frequency counter (RACAL-DANA, model 2101).

DEER Experiments: The 4-pulse DEER sequence:[92,93]

$$\pm(\pi/2)_{obs}-\tau_1-(\pi)_{obs,1}-(t_d+t_0+N_t \cdot \Delta t)-(\pi)_{pump}-(t'-N_t \cdot \Delta t+t_d)-(\pi)_{obs,2}-\tau_2-echo$$

was used to obtain dipolar time evolution data from paramagnetic 16-DSA spin probes interacting with HSA at X-band frequencies of 9.1– 9.4 GHz with a BRUKER Elexsys E580 spectrometer equipped with a BRUKER

Flexline split-ring resonator ER4118X–MS3. The temperature was set to $T = 50$ K by cooling with a closed cycle cryostat (ARS AF204, customized for pulse EPR, ARS, Macungie, PA) and the resonator was overcoupled to $Q \approx 100$. The pump pulse position $t_d + t_0$ after the first observer π-pulse deadtime t_d was typically incremented for N_t timesteps of $\Delta t = 8$ ns in the range $t_0 + t' = \tau_1 + \tau_2 - 2t_d$, whereas τ_1 and τ_2 were kept constant. Proton modulation was averaged by addition of eight time traces of variable τ_1 starting with $\tau_{1,1} = 200$ ns, incrementing by $\Delta\tau_1 = 8$ ns and ending up at $\tau_{1,8} = 256$ ns. Additionally, a 2-step phase cycle ($\pm$) was applied to the first $\pi/2$ pulse of the observer frequency for cancelling out receiver offsets and unwanted echoes. The pump frequency ν_{pump} was set to the maximum of the field swept electron spin echo (ESE)-detected spectrum. The observer frequency ν_{obs} was set to $\nu_{pump} + \Delta\nu$ with $\Delta\nu$ being in the range of 65 MHz and therefore coinciding with the low field local maximum of the nitroxide ESE spectrum. The observer pulse lengths for each DEER experiment were set to 32 ns for both $\pi/2-$ and $\pi-$pulses and the pump pulse length was 12 ns.

Data Analysis: All EPR data have been evaluated exclusively in MATLAB 2008b. Spectral simulations of spin probed HSA samples for temperature denaturation and Scatchard plots were conducted with the MATLAB-based easyspin 5.0.2 software package.[94] All corresponding MATLAB codes have been optimized for 2- to 4-component nitroxide spectra. Individual subspectra were double-integrated to extract the spectral fraction concentrations $[L]_t \cdot \phi_{i,j}$ of corresponding dynamic populations for subsequent thermodynamic analysis. For an appropriate starter set of simulation parameters and the simulation approach the reader is referred to **Table I1** and **Appendix H5**. All spectral simulations can be found in **Figure I1** and **Figure I2**. Fit parameters that were obtained from temperature-dependent Scatchard plots[40] in **Figure 11.4A+B** are presented in **Table I2** and **Table I3**. Scatchard plots were analyzed according to strategies presented throughout **Chapter 7** using linear regressions as well as the Rosenthal method.[43] Temperature-dependent and ligand loading dependent $\ln K_{IC,j}$ values (**Figure 11.8C**) were also obtained in the course of Scatchard plot evaluation. These curves were reconstructed with exponential fit curves (see equation I.33 and **Table I7**). The cooperativity test for both Scatchard plots (see **Figure 11.4C**) was conducted as described in **Chapter 7.4.2**.

Thermodynamic analyses from CW EPR spectral simulations in this study are largely adopted from the strategies described in **Chapter 10.2.8** with several situational adjustments. All physical quantities that emerge from equilibrium constants $K_{A,j}$ and $K_{IC,j}$ have been calculated with fit parameters that were obtained from a sigmoidal fit curve ($\ln K_{A,j}$ in equation 11.1) and a home-written combination of exponential and double sigmoidal Boltzmann curve regression ($\ln K_{IC,j}$ in equation 11.2) in Microcal Origin (see **Table I4**, **Table I5** and **Appendix I3**). Fit parameters from the aforementioned curve regressions in Origin were incorporated in the home-written MATLAB codes that generate appropriate energy plots in **Figure 11.6**. All corresponding thermodynamic functions for $\ln K_{IC,j}$, $\Delta G^{\circ}_{IC,j}$, $\Delta H^{\circ}_{IC,j}$, $\Delta S^{\circ}_{IC,j}$ and $\Delta C^{\circ}_{P,IC,j}$ in this graph were computed in a quasi-continuous 500 point grid corresponding to about 0.19 K temperature resolution. Derivations of the expressions given in equations 11.4 – 11.7 are explicitly shown in **Appendix I4**. Characteristic temperatures as $T_{AH,i}$, $T_{AD,i}$ and $T_{H,i}$ were obtained from relations given in equations 10.22 – 10.24. Due to the complexity in $\Delta C^{\circ}_{P,IC,j}$, the apolar hydration temperature was introduced in analogy to $T_{AD,i}$ (see equation 10.23), when the zero-crossing changes from negative to positive values with increasing temperature.

The raw DEER time domain data as shown in **Figure 11.9B** and (partially) in **Figure 11.10A** were processed with the MATLAB-based program package DeerAnalysis2013.[66] For the DEER-derived 16-DSA loading study, all background dimensionalities were set to $D = 3.74$ throughout. These datasets serve as a reference for calculations of the average number of spins from the distribution shape ($N_{P(r)}$). The derivation of an empiric equation that enables to pursue this strategy is based on an exponential fit curve to $\ln P_{AB}(r)$ data shown in **Figure 11.9E** and is given in **Appendix I6** (equation I.34). As no spin dilution was applied to these samples, a Langmuir power law could be used for reproducing the modulation depths (Δ) best when 16-DSA loading to HSA varies in the range from about 0.8 – 6.2 equivalents (see **Figure 11.9F**).[71] Similarly an empirical relation was derived in **Appendix I6** that facilitates prediction of the average number of coupled spins based on modulation depth (N_Δ, see equation 11.10). Due to the change in shape and compactness of HSA with temperature, this approach is preliminary discouraged as the modulation depth experiences additional modification in this respect. All DEER time traces that were obtained from temperature incubated samples were background corrected with adjustable spin distribution dimensionalities ranging from $2.00 < D < 3.76$. These dimensionalities were obtained in a comparative iterative global analysis of all data sets prior to the final

Tikhonov regularization procedure. All first moments $\langle r \rangle$ of individual distance distributions $P(r)$ were obtained from the DeerAnalysis result files.

DLS Measurements. All DLS data were obtained with an ALV-NIBS high performance particle sizer (HPPS) equipped with an ALV-5000/EPP Multiple Tau Digital Correlator (ALV-Laser Vertriebsgesellschaft m. b. H.). The ALV-NIBS device facilitates HeNe-LASER irradiation with a typical wavelength of $\lambda = 632.8$ nm and a 3 mW output power source. Count rates were recorded in a backscattering detection angle of 173° relative to the incident monochromatic light. The sample cell temperatures were adjusted in the range of $9 < j < 89$ in steps of $\Delta T = 4$ K by a Peltier temperature control unit. HSA temperature denaturation was conducted on an individual sample in 1.5 mL PMMA semi-micro cuvettes (BRAND). For sustaining comparability, a nominal 1-to-1 ratio 16-DSA was used to equip the protein with the same fatty acid content as in respective CW EPR experiments, well below the CMC = (0.285 ± 0.029) mM. A sample volume of 0.4 – 0.6 ml was filtered through Rotilabo cellulose acetate (CA) syringe filters with a pore size of 0.2 µM (Rotilabo, Carl Roth) in order to minimize sample adhesion and therefore protein concentration loss.

HSA particle size data were extracted from the intensity correlation functions by a $g_2(t)$-DLS exponential and a mass weighted regularized fit in the ALV-NIBS software v.3.0 utilizing the CONTIN algorithm.[95] The refractive index was assumed to be constant at $n_{\text{H2O}} = 1.332$ for all temperatures (and $\lambda = 632.8$ nm),[96] the water (DPBS buffer, see also **Table 5.1**) viscosity was corrected for each applied temperature j [°C] according to equation 10.25,[97] assuming that $\eta_0 = 1.002$ mPa·s at $j = 20$.[97–99] Deviations in true viscosities from calculated values that are induced by the intrinsic viscosity of HSA are considered as marginal and do not exceed +7.7% at $c_{\text{H}} = 0.18$ mM = 12.0 mg/ml within $5 < j < 45$.[100] Each sample was measured at least four times at the same temperature for 30 s and was averaged at least over three individual values. The mean values $R_{\text{H},j}$ of the most prominent size peaks and their statistical fluctuations are given as the standard deviation as depicted in the error bars in **Figure 11.3B**. The duration of the whole heating procedure was about 8 – 9 h.

Differential Scanning Calorimetry (DSC) Measurements. All DSC experiments and data evaluations as presented in **Figure 11.7** and **Figure 11.8A+B** were performed by Dr. Christian Schwieger using a Microcal VP-DSC device (MicroCal Inc.). In all experiments a heating rate of 0.25 K/min was used. Data were recorded with a time resolution of 4 s in the temperature range of 5 – 95°C that covers the decisive regions of the corresponding EPR experiments. Two consecutive up- and down scans were performed for each sample. However, due to irreversible gelation of the HSA-containing samples at high temperature, only the first thermogram is presented and evaluated. In scan 2 – 4 only residual heats could be detected. All 16-DSA-probed HSA solutions were loaded to the sample cell and for comparability the HSA concentration was again set to $c_{\text{H}} = 0.18$ mM. The ligand-to-protein ratio was varied in the range from about 0 – 8 equivalents, so that altogether eight thermograms were obtained. Pure, degassed DPBS buffer was loaded to the reference cell. Therefore, from all presented thermograms of 16-DSA-probed HSA samples a buffer/buffer reference, as well as a thermogram of pure 16-DSA was subtracted before normalizing $\Delta C_{\text{P,HSA}}$ to the HSA concentrations. Afterwards, a cubic baseline was subtracted manually. Data processing was performed with the DSC module for Origin software (MicroCal Inc.). The obtained thermograms were fitted with two Gaussian curves in order to deconvolute both overlapping transitions ($T_{\text{D},1}$ and $T_{\text{D},2}$). The midpoints of the obtained Gaussians were finally used as transitions temperatures for the two HSA species and are given in the scheme according to Shrake and Ross[54] as presented in **Figure 11.8B**. A brief analytic rationalization of these results is given in **Appendix I5**.

12 | Conclusions and Outlook

12.1 | Conclusions

Hydrophobic and electrostatic forces are the main driving forces in systems of self-assembling nano-objects. In this regard, several albumin-based, or albumin-inspired model systems from polymer chemistry and biochemistry were used to investigate the impact that various physical and chemical alterations may have on functionality and structural integrity. Functionality is here understood as the capability to accommodate ligands in the interior of the substrate with defined capacity and affinity. Structural integrity is strongly related to functionality and can be seen as the reference solution shape of the respective compound. Both features are extensively studied with CW EPR and DEER spectroscopy. Where appropriate, data are supplemented with a combination of different methods in order to construct a more comprehensive view on the subject. The main purpose of this thesis was to show how the solution structure and functionality of such self-assembled systems can be obtained and rationalized in terms of amino acid sequence, chemical composition, posttranslational modifications, pH and temperature. Therefore, optimum control of experimental parameters is inevitable for proper data assessment, especially across different studies.

Optimum Experimental Parameters for Spin Probed Albumins in EPR Spectroscopy

For comparing eventually large data sets from e.g. extensive screening studies, the properties of albumin solutions have to be kept as constant as possible. Therefore, **Chapter 5** highlights several strategies that allow for appropriate adjustments of ionic strength, pH, viscosity, concentration and the prediction of the excluded volume fraction. It is shown that pH can be reliably adjusted in the range of $1 < \text{pH} < 13$. Some rules of thumb are given for EPR sample preparation that should *always* provide sufficient SNR for successful data evaluation, both in CW EPR and DEER experiments. Based on these results, the spin probe concentration should be chosen to a minimum of 0.2 mM for studies that compare 5-DSA- and 16-DSA-probed albumin samples. A quality parameter Γ was introduced for DEER experiments on albumins that predicted optimum comparability for 0.4 mM molar equivalents (HSA). The rather complex distance distributions that are typically obtained in DEER experiments on spin probed HSA are fully resolved for $t_{max} \geq 1.4$ µs, or experimental dipolar evolution times of $\tau_2 \geq 1.6$ µs. It is regarded essential to collect time traces with an SNR > 10 for 5-DSA and SNR > 20 for 16-DSA that is safely obtained for $X > 500$ scans.

It could be also shown that protein concentration has significant effects on data processing. The background dimensionality ($D > 3$) in DEER time traces of spin probed albumins is not necessarily a constant and can be considered as a pure crowding effect. For example, the consideration of excluded volume effects in CW EPR data leads to significant improvements in the results from Scatchard plots in subsequent chapters. Beyond that, a profound strategy is given for reducing spectrometer time without losing data quality.

Genetic Fingerprints of Albumins in DEER Experiments

The fatty acid-derived solution structures of HSA and BSA as presented in **Chapter 4** revealed some clear differences. As the available crystal structures of both proteins are almost congruent with a sequence similarity of 75.5%, it was investigated on the level of primary and tertiary structures where these differences come from. It turned out that many amino acids at decisive functional regions (FA1 and FA5 binding site, intersection region of subdomain IB and IIIA and loop region in subdomain IIB) show inverted hydropathy behavior. Therefore, both proteins exhibit several localized and opposite physicochemical solvent interactions with HSA being globally more hydrophobic compared to BSA. Whereas spin probed HSA exhibits the well-known symmetric fatty acid distribution on its surface (16-DSA), spin probed BSA unexpectedly resembles the crystal structure-derived solution structure of HSA. The justified conclusion is made that BSA is more rigid and crystal-like compared to HSA, with the latter one gaining its functional plasticity due to its more hydrophobic character.

In **Chapter 6** this genetic comparison was expanded to sheep (SSA), goat (GSA) and cat (FSA) serum albumins (74.5 – 81.8 % sequence similarity compared to HSA) using the optimized experimental parameters from **Chapter 5**. Astonishingly, the fatty acid-based distance distributions of SSA and GSA are very similar and furthermore strongly resemble data obtained from BSA. In contrast, data derived from FSA gave a completely different picture, however, with some recurrent features compared to SSA and GSA. Additionally, FSA overtook a misfit role as it precipitated at higher concentration (~ 2 mM) and also exhibited lower background dimensionalities in DEER time traces, however, still functional as it was proven by SDS PAGE and CW EPR.

After all, an intuitive, however, tentative conclusion can be made that the fatty acid-derived distribution shape should be linked to individual nutrition, as cattle, sheep and goats belong to the realm of herbivores, cats belong to carnivores and humans to omnivores. Therefore, the distribution becomes ever more symmetric, i.e. the protein gains plasticity and adaptability with increasing complexity of customary food supply. Trivially, accessible crystal structures from HSA, BSA and SSA are all more or less congruent (1.21 Å < RMSD < 1.54 Å) and the role that solvent (water) has in tuning albumins functionality should thus not be underestimated.

The Effect of Posttranslational Modifications (PTMs) on Albumins

The effect of PTMs on albumin functionality was tested on several systems as shown in **Chapter 7**. In the course of these projects, simulation-based Scatchard plots for fatty acid-probed albumins were established, emphasizing various routines that allow for extracting the total number of binding sites (N_T) and ligand binding affinities (K_A). These datasets can be either evaluated empirically (method A), with explicit simulations and Scatchard plot constructions (method B), or with a peak-picking routine that utilizes reference simulations facilitating fast Scatchard plot construction (method C).

The analytic strategies for biphasic and multiphasic (*p*) Scatchard plots are transferred to EPR spectroscopy from established biophysical routines that can also promote the identification of binding

site cooperativity (C_p). Modifications of HSA that were provided with positively charged PAMAM dendrimers (G2 and G3) decreased the fatty acid accessibility towards binding sites with increasing generation (Gy). A large fraction of the binding sites remained accessible, however, with lowered affinity. The provided advanced glycation endproducts (AGEs) of HSA with glyoxal (HSA-GLX10), that may partially form structural crosslinks between individual subdomains, revealed biphasic Scatchard plots with two types of non-interacting binding sites (N_1 and N_2) and therefore different affinity ($K_{A,1}$ and $K_{A,2}$). Compared to native HSA the total number of binding sites increases from $N_{T,N}$ = 6.5 to $N_{T,GLX10}$ = 9.5 upon glycation of the protein.

The number of equivalent, non-cooperative binding sites of native BSA ($N_{T,N,B}$ = 6.4) is almost identical to HSA ($N_{T,N,H}$ = 6.5). However, BSA exhibits a slightly lower 16-DSA affinity ($K_{A,B}$ = 7.5·10^5 M^{-1}) compared to HSA ($K_{A,H}$ = 1.9·10^6 M^{-1}). Furthermore, modified BSA samples were provided as macroinitiators (BSA-Ix) and polymerized core-shell structures (BSA-Pn) from a squaric acid-mediated "grafting from" approach using OEGMA$_{475}$ monomers. All modified BSA samples exhibited biphasic, or multiphasic Scatchard plots. With increasing degree of surface modification (x), the fatty acid capacity could be enhanced to a maximum of $N_{T,14,II}$ = 12.9 ± 0.9 for x = 14, coinciding with staggered alterations of phase-specific $K_{A,k,p}$ values. This artificially induced increase in N_T is shown to be equivalent to positive cooperativity effects. The BSA core-shell structures that primarily constitute the protein core less accessible still exhibited a minimum capacity of N_T > 3. Corresponding DEER experiments revealed that these surface modifications lead to a change in binding site preference and the site occupation gets shuffled to quite some extent. The adaptability or plasticity of the protein core gets restricted as observed from the more asymmetric fatty acid distance distributions in the modified samples. DLS and Zeta potential experiments confirmed that ligand affinity is influenced by diffusion, charge and size. A strategy was developed that allows to extract the effective dielectric constant of the solvent-pervaded polymer shell ($\varepsilon_{eff,Pn}$ ≈ 71). The net charges (Z_k) of the modified proteins are obtained by rationalizing the extent of surface modification with the corresponding Zeta potentials. Each modified lysine residue decreases the Zeta potential for about –1 mV and about 66% of the surface charges are screened by buffer ions.

Generally, sterical hindrance, solvent entanglement, structural plasticity and charge are considered as the main factors that govern induced changes in K_A and N_T, i.e. cooperativity in posttranslationally modified albumins.

pH Denaturation of HSA

Structural and dynamic changes in proteins due to pH are generally based on alterations of the net charge that finally leads to denaturation as a consequence of strong electrostatic repulsive forces. The combination of results from spin labeling and spin probing experiments on HSA were used in **Chapter 8** in order to shed light on various effects that occur in the range of 1 < pH < 13.

The application of empirical and established analytic strategies for CW EPR spectra reveals a wealth of information about structural and dynamic changes of HSA that also affect protein-ligand interactions. All pH-induced conformational isomers of HSA can be identified with CW EPR (E = elongated, F = fast migrating, N = norm, B = basic and A = aged form). The compact form (C) of HSA is maintained from $4.0 < \text{pH} < 11.2$ and can be detected either with spectral characteristics from bound or free ligands. Therefore, an empirical parameter I_{abf} was introduced that monitors relative changes in shape of free (f), bound (b_1, b_2) and micellar (a) spectral fractions and circumvents cumbersome spectral simulations. DLS and DEER experiments confirmed the pH range of the compact (C) form. A region of maximum ligand order (S_{max}) is found at physiological conditions ($\text{pH}_S = 7.6$) and maximum structural stability of HSA is found for $\text{pH}_{opt} = 9.6$ coinciding with bio-informatical calculations. These calculations also predict a collective lysine pK_a value at $pK_{a,Lys} = 10.3$ that could be confirmed experimentally by maximum lysine side-chain mobility in CW EPR on 5-MSL HSA. The loss in structural compactness and therefore stability of HSA leads to fatty acid release for $\text{pH}_a > \text{pH} > \text{pH}_f$, where $\text{pH}_f = 11.4$ is the basic and $\text{pH}_a = 4.3$ is the acidic onset of the release process. The maximum rate of micelle formation is found at $\text{pH}_{a,0} = 3.45$.

The most reliable parameter for molten globule state (MG) detection of HSA is the center-field linewidth ($\Delta B_{0,pp}$). This MG state can be observed at $\text{pH}_{MG} = 2.1 \pm 0.2$ and is characterized as a local minimum in ligand immobilization. A similar picture is obtained from order parameters (S) that show maximum angular fluctuations of bound ligands in this pH range.

All spin probing experiments in CW EPR and DEER revealed a recurrent feature at $\text{pH} = 6.1 \pm 0.2$. This feature can be rationalized as an intermediate decrease in fatty acid affinity ($\text{pH}_{f,0}$), a transition in fatty acid immobilization ($\text{pH}_{B,0}$, $\text{pH}_{b,0}$), or an electrophoretic migration due to slight changes in protein shape ($\text{pH}_{P,0}$) and protein net charge in the C form. A tentative conclusion would be an electrostatic activation (pH_{EA}) of ligand that should be related to the isoelectric point of HSA (pI).

Finally, a more generalized picture is given that expands the established viewpoint of pH-induced conformational isomerizations in HSA towards a pH-induced functional phase space as mainly derived from fatty acid ligand interactions.

Fatty Acid Triangulation in Albumins

A hybrid strategy was pursued in **Chapter 9** that encouraged a simultaneous spin probing and spin labeling approach of HSA and BSA. The insertion of a localized and covalently attached surveillance benchmark spin (SBS, in this case MTSSL) should facilitate the characterization of consecutive fatty acid entry and the localization of individual fatty acids.

MD simulations were used to generate all potential interspin distances in 8×8 matrices that may be observed in DEER-derived distance distributions. It was shown that mixture distributions are experimentally obtained from expanded interspin systems $P(r)$ that can be rationalized as the weighted sum of standard fatty acid-based interspin systems $P_{FA}(r)$ and a reduced interspin system $P_{SBS}(r)$.

Furthermore, the reduced interspin system is defined to only contain distance contributions that are exclusively directed from the SBS nitroxide towards individual fatty acid nitroxides. The relative weight of both distributions is mainly defined by the labeling efficiency of the used protein. The labeling efficiency was obtained with standard biochemical protocols or spin counting in DEER experiments. According to available data sets, fatty acid loading merely shifts the weight of both interspin system components in the mixture distribution. Compelling and direct experimental evidence is provided that all binding sites of the albumin ensemble are occupied even at the lowest fatty acid loading ratios that were applied (1:1).

Identification of individual fatty acids is slightly hampered by experimental restrictions and partially coinciding distances in $P_{SBS}(r)$. In a combined view, several features in the resulting distance distributions were assigned to singularities (FA1, FA2 and FA7), pairs (e.g. FA4 and FA7), or larger groupings (FA3 – FA6). It was shown that the choice of the spin probe has an additional effect on fatty acid discrimination. Several ideas are provided in an outlook that allow for strategic improvements and simplifications of this approach.

Amphiphilic Core-shell Polymers

Several brush-like polymers were provided with varying chemical composition. These core-shell-like cylindrical structures (C_nS_m) were grafted from amphiphilic macromonomers containing azido alkyl methacrylate cores with adjustable alkyl (C_n) and polyglycerol chain lengths (S_m). The cylindrical shape of the polymers was confirmed with electron microscopy (TEM).

The major object in **Chapter 10** was to use CW EPR spectroscopy for characterizing the tunability of polymer interactions with paramagnetic amphiphilic ligands (16-DSA). This amphiphilic self-assembly comprised several temperature-induced phenomena that were observed in EPR and DLS data in the liquid water range from 5 – 95°C. The results from this study can be rationalized in the scheme of tunable *dynamic hydrophobic attachment*. This scheme encompasses temperature-induced *dynamic hydrophobic binding* of fatty acid ligands (K_A), *dynamic hydrophobic aggregation* of the polymers and *dynamic hydrophobic interconversion* equilibria of bound ligands (K_{IC}).

It could be shown that ligand capacity (N_E) is proportional to the degree of polymerization and that the non-cooperative ligand binding affinity (K_A) depends on the size and polarity of the respective hydrophobic cores (n). Accessibility towards the hydrophobic cores is determined by the length of a hydrophilic polyglycerol shell (m). The S_{32} shell polymers were shown to trigger a temperature-induced optimum functional state by a *hydrophilic shell collapse* that is detected as a slight volume phase transition (VPT) with DLS. Interestingly, this slight transition occurs in the temperature range of mammalian body temperature. Additionally, this hydrophilic shell overtakes a camouflage property that may shield the hydrophobic core from solvent and regulates the aggregation behavior of the polymers. Ligand binding for polymers with n < 6 was not observed and it could be shown that a minimum of 14 grafted amphiphilic macromonomers is required to form a single longitudinal fatty

acid binding site. All observed amphiphilic interactions exhibited strong temperature dependencies and it was concluded that these polymers generally constitute an important model system for drug delivery and for basic investigations that may further unravel the nature of the hydrophobic effect.

Thermodynamic Calorimetry from Ligand Affinity and Interconversion Equilibria in CW EPR

In order to perform thermodynamic calorimetry from CW EPR data it is required that spectral simulations reveal at least free (*f*) and bound (*b*) spectral fractions that define the association equilibrium in case total ligand, substrate and receptor or binding site concentrations are known. The assumption of tight binding characteristics for spin probed macromolecules was found to be indispensable for correlating ligand binding affinities (K_A) from Scatchard isotherms with temperature-dependent affinities ($K_{A,j}$). The temperature course of $K_{A,j}$ may be linear throughout, or may change direction, depending on length scale and the emergence of a dynamic structural rearrangement. A model for dynamic hydrophobic interconversion equilibria (K_{IC}) was devised from the bimodality in 16-DSA immobilization. It is here proposed for the first time, that this bimodality is based on the temperature-induced interconversion from Brownian diffusion (b_1) towards free diffusion (b_2) of ligand. The strongest argument in this regard is found in the rotational correlation times τ_c from spectral simulations, yielding values for $\tau_{c,b1}/\tau_{c,b2}$ in the range from 2.4 – 3.4 that are very close to the theoretically predicted value ($7^{1/2} \approx 2.65$). The temperature dependence of K_{IC} yields non-linear van't Hoff plots that are indicative for changes in the heat capacity of this process ($\Delta C_{P,IC}$). These heat capacity changes in fatty acid interconversion can be rationalized to depict changes in the ligand hydration state. In turn, this ligand hydration state indirectly monitors temperature-induced structural rearrangements and intermolecular aggregation of the macromolecular substrates.

The interconversion equilibrium facilitates investigations on complex and dynamic macromolecular substrates from the bound ligands' point of view and provides a coherent interpretation based on its nanoscopic thermodynamic fingerprint. The transferability of this method is provided for HSA and works well, however, the scientific scope of its applicability has yet to be revealed.

Temperature Denaturation of HSA

The analytic strategies from EPR spectroscopic thermodynamic calorimetry that could be established with the core-shell polymers were successfully transferred to 16-DSA-probed HSA solutions as shown in **Chapter 11**. It was therefore proven that the principle of *dynamic hydrophobic attachment* also applies for the description of temperature-induced effects observed in HSA solutions. This concluding study on HSA collects and unifies several ideas and approaches that were explicitly tested in most previous chapters. The rather complicated temperature course of K_{IC} from 16-DSA spin probes interacting with HSA was observed in the temperature range of 5 – 97°C and was additionally confirmed and correlated with bimodal denaturation curves from DSC data. Appropriate analytical functions could be derived that enable the prediction of all important thermodynamic parameters.

Here, the major finding is that K_{IC} highlights the energetic interplay and entanglement of ligand and protein, yet, preliminary on a mainly qualitative level of argumentation.

The aggregation behavior of HSA was investigated by DLS and confirmed the effects observed in EPR data. It could be rationalized that HSA steadily changes its shape with increasing temperature before it aggregates and suffers from denaturation events. This slight change in native shape is observed in EPR and DLS and can be only understood as a transition from a more compact and globular state towards independently moving subdomains ("*boleadoras*"). This feature was summarized as the *rotationally decoupled domain* (RODEO) model. Scatchard plots at different temperatures in native HSA suggest that this RODEO scheme, and therefore also the subdomain proximity, may have an impact on the ligand binding cooperativity. The onset of HSA aggregation at about 50°C is accompanied by an enhanced release of ligand prior to denaturation. This aggregation process can be also seen as an entanglement of the rotationally decoupled domains in HSA.

At higher temperatures, the temporarily released fatty acids may accumulate in still native HSA molecules. Therefore, fatty acids overtake a function as natural pharmacoperones that induce protein stabilization by their quantitative redistribution. DSC data show, that each additional 16-DSA ligand increases the first melting temperature ($T_{D,1}$) for 1.3 K and may expand stability from $T_{D1,min} = 64$°C to temperatures as high as $T_{D2,max} = 76$°C. Thus, HSA may experience a total stability gain of about 12 K by consequent loading of 16-DSA. In this regard it was observed, that the interconversion equilibrium is either shifted by fatty acid loading or by temperature. This further substantiated and confirmed the role of fatty acids as protein-stabilizing temperature quanta.

The ligand redistribution process was also investigated with a spin counting strategy in DEER utilizing the impact that multispin effects have on the resulting distance distributions ($P_{AB}(r)$). Indeed, it could be shown that the fatty acid content of non-denatured HSA molecules increases for about 40% at 77°C and gives further experimental proof for this 30 year old hypothesis going beyond DSC data. It is here noteworthy that the background dimensionalities D and modulation depths Δ in DEER provide comparable features as obtained from scattered light intensities (SLI) in DLS experiments and therefore constitute a measure for shape and compactness. Finally, the observed effects and features from the applied methods strongly correlate with earlier findings that altogether corroborate a holistic dynamic picture of the process of HSA temperature denaturation.

Functional Cross-correlation

This thesis highlights several physicochemical aspects that affect functionality in albumins. Albumin proteins are highly complex and dynamic nano-objects that exhibit conformational entropy in terms of structural plasticity and adaptability. This feature is best represented by the coarse-grained solution structure that is here observed in DEER distance distributions from bound EPR-active fatty acids.

Ligand binding cooperativity is based on conformational entropy effects and can be routinely characterized from standard Scatchard isotherms. A fully functional native albumin protein (XSA)

provides $N_{T,X} = 7 \pm 1$ non-cooperative fatty acid binding sites at room temperature. It was explicitly shown, that a loss in conformational entropy can be induced by fatty acid binding, temperature decrease and posttranslational modifications. Providing native albumins with a defined degree of covalently attached PTMs leads to tunable changes in binding site cooperativity. This cooperativity comprises variations in the total number of binding sites and their individual ligand binding affinities.

The high mutual resemblance of available crystal structures and the experimentally observed differences in fatty acid alignments observed across several species suggests that water must play a decisive role in defining the solution structure, ligand binding affinity and therefore functionality.

Thus, albumins should be treated as multifunctional nano-objects that primarily evolve in the dimensions of space and time that again defines their time-averaged solution shape. Further distinct functional dimensions are constituted by temperature, pH (charge), amino acid composition, the degree of posttranslational modification and the associated binding site cooperativity. Dynamic properties as stability, ligand capacity and ligand affinity were shown to depend either on ligand supply, pH, temperature or the extent of PTMs.

Several functional aspects of albumins can be mimicked with synthetic amphiphilic core-shell polymers with tunable structural and dynamic properties. Thermodynamic calorimetry can be performed in a wide temperature range based on the equilibrium of rotational interconversion of bound fatty acid ligands. This provides a nanoscopic view on intricate temperature-induced macromolecular reorganizations on the level of ligand hydration. It was verified that this method can be applied for amphiphilic polymers as well as for albumins. Furthermore, the 16-DSA spin probe was shown to be sufficiently stable for all applied temperatures and pH regimes. This EPR-active probe reliably provides valuable dynamic information about itself and the probed substrates.

Finally, on a more fundamental level of argumentation, all these functional properties enable albumins to passively regulate functionality and therefore its transport properties that are required for specific physiological circumstances. Across all studies, the common basis of albumin functionality, especially its plasticity and adaptability for ligands, seems to be strongly driven by conformational entropy that is best represented by the degree of binding site cooperativity.

12.2 | Outlook

The studies ranging from **Chapter 4** to **Chapter 11** can be combined in a flowchart scheme that is shown in **Figure 12.1**. A combined manifold of applications is devised and demonstrated, based on the findings made in this thesis and several previous studies that also made use of the combination of CW EPR and DEER.[1–6] The intrinsic strategic potential that EPR spectroscopy provides in albumin research shall be highlighted. Reference experiments mentioned in this scheme can be regarded as being supplementary, however, emerging from experimental techniques and theoretical approaches with each bearing its own stand-alone value. Beyond that, this most recent flowchart is regarded to still constantly evolve and thus raises no claims for completeness.

The current level of awareness naturally does not coincide to previously published versions,[7] but the main scheme is conserved and is considered as still being valid.

Basically, this *EPR spectroscopic albumin research platform* emphasizes its inherent synergy as indicated by the gray arrows. One should not underrate the importance of choosing appropriate support from other disciplines in order to confirm occasionally ambiguous findings that may be encountered in EPR studies alone. Appropriate techniques comprise e.g. calorimetry (ITC, DSC), light scattering (DLS, SAXS), spectrophotometry (IR, UV/Vis), circular dichroism (UV/CD), electron microscopy (EM), rheology and theoretical approaches as e.g. MD simulations for just mentioning a few possibilities. For example, the comparison of hydrodynamic radii (R_H) from DLS and rotational correlation times (τ_c) that are obtained from spectral simulations in CW EPR, turned out to provide exceptional resemblances of phemomena based on shape and ligand immobilization. Furthermore, it turned out that several basic analytic strategies that were already refined in other disciplines can be adopted one-to-one. In case of Scatchard plot evaluations, this methodological transfer was found to be exceptionally fruitful. This research platform also reflects the various physicochemical aspects that govern albumin functionality. It might be used as a guideline for future scientists working in this field as to strategically simplify, or expand experiments according to the exclusion principle.
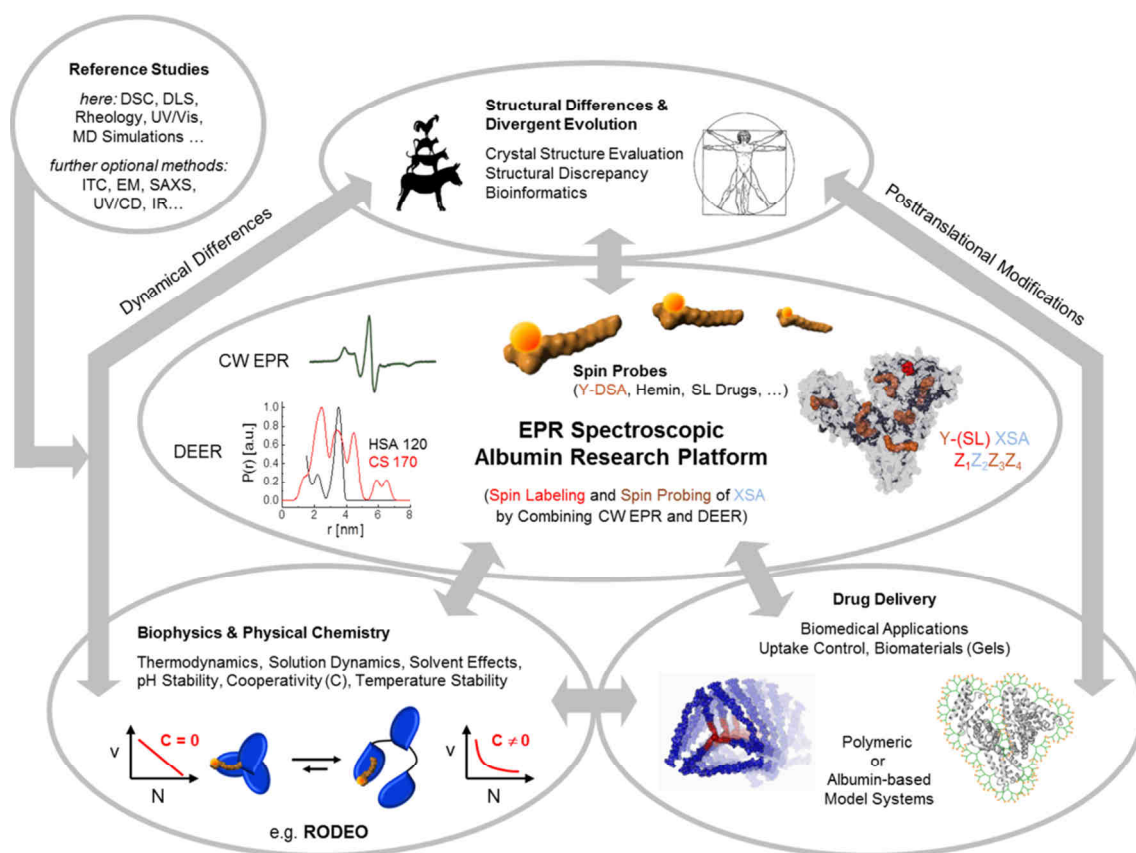
Figure 12.1 | An expandable EPR spectroscopic albumin research platform. A generalized flowchart is presented, aiming for experimental design strategies in the realm of spin probing and spin labeling experiments that were made accessible for albumins in EPR spectroscopy so far. This research platform accentuates the significance of combining CW EPR and DEER experiments. The relative interdependence of individual disciplines is highlighted in a synergistic scheme with gray arrows.

Several studies in this thesis demonstrate that the combinatory nature of experimental design and the often perplexing complexity of the dynamic response of albumins eventually can appear insurmountable. Such circumstances may quickly lead to larger-than-life tasks for individual experimentalists, especially in elaborate screening studies that comprise several albumins (XSA) in combination with several paramagnetic ligands (e.g. Y-DSA).

It can be confidently stated that the combined application of CW EPR and DEER on either spin probed or spin-labeled (SL) albumins still bear unforeseeable potential, ever revealing further complementary functional and structural insights to the albumin paradigm. In structural biology terms, this platform provides only coarse-grained information compared to the atomistic resolution in NMR and X-ray diffraction (XRD) studies. All so far available crystal structures can be deliberately used for structural alignments, some bioinformatics approaches and molecular modeling that in turn provide the accessibility of some insightful MD simulations.[8] In case of the DEER-derived genetic fingerprint of fatty acid alignments in spin probed albumins, pertinent conclusions about a nutrition-based distribution shape are self-evident as shown in **Chapter 6**. However, it should embrace an expanded viewpoint from some additional organisms as e.g. dog and monkey. This would complement the present data set for an additional carnivore and omnivore, respectively.

Although the experimental system is here reduced to a lowest possible level of detail, still a lot of structural and dynamic information is accessible simultaneously. For better rationalizing the experimental setup, an appropriate short notation identifier of each investigated system was developed within this thesis and is finally best described with the scheme:

$$Y\text{-(SL) XSA } Z_1Z_2Z_3Z_4\, c \qquad .$$

Here, Y is the chain position where the doxyl residue is attached to stearic acid backbone of the applied probe, SL may comprise any spin label that attaches to the Cys34 residue as e.g. MTSSL[9] or IAA,[10] X defines the respective organism (H = human, B = bovine, etc.) and c [mM] gives the basis concentration of the molar equivalents Z_i that are added relative to albumin. Most EPR spectroscopic studies in this thesis were performed at molar equivalent concentrations from $0.1\text{ mM} < c < 0.4\text{ mM}$, being relatively close to physiological values of albumin.[11] When applicable, according equivalents of the spin label (Z_1), albumin (Z_2), paramagnetic (Z_3) and diamagnetic, spin-diluted spin probes (Z_4) are then clearly indicated. This scheme had to be devised in **Chapter 9** for keeping an appropriate overview about the rather complex experimental system. Therefore, spin labels that are attached unspecifically (e.g. 5-MSL) should actually have an appropriate equivalent Z_1 value that can be obtained from MALDI spectra.

Certainly, for most conceivable studies it suffices to simply add one or two spin probes that already yield a wide variety of physicochemical information from albumins, or albumin-based model systems.

The term albumin-related or albumin-inspired model system emphasizes constructs of albumin-mimicking polymers, functional and purposeful PTMs attached to XSA, or e.g. biomaterials as functional albumin nanotubes[12] and gels[13] with adjustable and predictable properties. These experimental model systems can be used for drug delivery studies in case organism-specific biocompatibility[11] is provided.

Therefore, long-term objectives are generally targeted towards uptake control and release for novel biomedical applications. In case of blood tests, several approaches were already devised from the spin probing technique in CW EPR to distinguish various pathological implications.[14–17] Thus, it is self-explanatory that special attention should be dedicated to such kind of studies.

Beyond the paramagnetic fatty acid spin probes, several EPR-active drug-based alternatives were already successfully tested in terms of their binding properties[18–26] and can be deliberately adopted and incorporated in this research platform as well. It was proposed in **Chapter 9.3** that ligands with lower numbers of binding sites (N_T) may decisively reduce complexity of binding site identification when these ligands were triangulated with a surveillance benchmark spin (SBS). This should be of major interest for future studies, because each mammal albumin possesses a highly conserved Cys34 residue.[11,27] The Cys34 residue can be easily labeled with e.g. MTSSL, as it was exemplified for HSA and BSA. Most of the drugs that are bound to albumin exhibit affinities from $10^2\,\mathrm{M}^{-1} < K_A < 10^7\,\mathrm{M}^{-1}$ when they are unmodified i.e. native and EPR-silent.[11,28] Anyway, the binding properties of SL-derivatives are routinely accessible with Scatchard plots from CW EPR (see **Table 9.3**).[25] Beyond enabling the construction of binding isotherms that are exquisitely indicative for albumins' ADME properties,[29] these spin-labeled pharmaceuticals (SLP), or SL drugs should be accessible for optional physicochemical analyses as well.[19]

It was shown that the precision of extracting the total binding site number (N_T) is much higher in linear Scatchard plots (non-cooperative (N.C.) with $C = 0$, $\Delta N_T = 5 - 10\%$) than from multiphasic isotherms (cooperative, $C \neq 0$, $\Delta N_T = 20 - 30\%$). Therefore, experimental temperatures can be deliberately chosen to generate linear plots on native (globular) albumins that circumvent temperature-induced cooperativity effects (see **Chapter 11**). This may prevent the application of comparatively complicated and tedious analyses and the emergence of much larger uncertainties in the resulting dynamic parameters. Furthermore, only a minimum of about $q \geq 3$ data points are required for significant and linear Scatchard plots. For example, several studies regarding equilibrium dialysis employed way beyond 10^2 data points in a single Scatchard plot ($q = 133^{[30]}$ and $q = 220^{[31]}$) in order to resolve all fatty acid binding site affinities in terms of multiple equilibria models from multiphasic curves. This honorable approach is strongly discouraged for simulation-based Scatchard plot construction from CW EPR data, as it would simply take way too long (> 2 months). However, it could be ruled out that a minimum set of about $q \geq 6$ data points should be available in order to obtain appropriate results from multiphasic plots.

It was previously highlighted that different functional scenarios of proteins may follow the rules of game theory[32] that naturally also comprises cooperativity effects.[33–35] According to Kovacs, the non-cooperative state of albumin ($C = 0$) would then correspond to the optimum scenario for rigid globular proteins, whereas the cooperativity scenario ($C \neq 0$) introduces "unfairness" that is hence only observed for flexible proteins, or e.g. for albumins with decoupled domains. The number of participants with disproportionate interests in this game would then be given by the number N_T of fatty acid binding sites that are subjected to case-specific cooperativity. Of course, this is only an example of a different viewpoint on this problem. The result is primarily of pure statistical nature and was already described with the presence of multiple equilibria ($K_{A,i}$).[36,37] Beyond that, these multiple equilibria are commonly observed in complex self-organizing systems in case there are selection mechanisms of any kind involved.[38]

One distinct issue is that the simultaneous alteration of physicochemical parameters in a single study should be generally discouraged, as e.g. in a temperature-dependent pH denaturation.[39,40] Although there are some holistic studies available in this regard[41] and it always depends on what the author intends to show, it is primarily preferable to rigorously separate physicochemical impacts. Here, it was demonstrated for HSA that a vast variety of specific phenomena appears in each aspect (pH and temperature, $n = 2$). This combinatoric challenge soon appears unscalable, while the number of required experiments literally explodes ($\sim q^n$). This also accounts for the change of solvent properties, e.g. by applying ionic liquids (ILs) that were however not investigated here. It was already shown with CW EPR and DEER that solution properties and temperature responses are modified on a fundamental level of protein functionality,[4] as well as shape.[42]

The interconversion equilibrium (K_{IC}) of the bound spectral fractions (b_1 and b_2) is an entangled process that is exceptionally sensitive to hydration phenomena with its heat capacity ($\Delta C_{P,IC}$). Additionally, it is assumed that this process is ubiquitary in all fatty acid probed albumin samples and it would be therefore interesting to see how K_{IC} is affected by such changes in solvent composition. To this effect, the experimentalist should be aware about the interference of various simultaneous inherent processes and therefore the sample compositions should be thoughtfully selected. It is further noted that already on the level of glycerol addition some slight changes in solution properties are anticipated. Especially, the deviation of the isoelectric point (pI $\approx$ pH$_{EA}$ = 6.1) from experimental reference values (pI = 4.8 – 5.6)[43,44] in **Chapter 8** and the decrease in the number of accessible ligand binding sites (compare data in **Chapter 7.3.1** and **Chapter 11.2**) suggest that glycerol may block about 1 – 2 binding sites for 16-DSA. However, cooperativity and therefore functionality seems to remain unaffected and pI happens to be a complicated function of ionic strength, fatty acid loading and further solvent properties that mainly affect e.g. the dielectric constant (ε_r). Rheology is routinely conducted on albumins since the 1930s.[45] Meanwhile, intrinsic viscosities may be calculated from rules of thumb and physically reasonable models,[46–48] but it is here essential to become aware about the slight alterations in physicochemical properties of the samples when glycerol is added (see **Chapter 5**).

One distinct rule for albumins is that "the more precise you measure, the more you see". This is of course an immediate and intuitive aspect that makes albumin so popular among biologists, chemists and physicists. Currently, there seems to be no final truth to the physical origin of the intricate functional properties of this protein and it remains to be settled for each study which extent of experimental precision is appropriate.

A further critical view on this EPR-based method of investigating albumins is given in a quite early study by Gaffney and McConnell,[49] accentuating that the mere presence of a paramagnetic nitroxide group may already disturb the observed system. In this regard, it was proven that ligand binding affinities indeed varies when a doxyl group is attached to stearic acids (see **Table 3.1**).[50] This EPR spectroscopic research platform therefore does not provide access to native, unliganded or unmodified HSA as it is provided e.g. in DLS or DSC experiments. Beyond the disturbing nitroxide or doxyl group in EPR-active samples, the scientific curiosity for investigating a system with EPR spectroscopy typically introduces an observer effect similar to the superposition principle in quantum mechanics.[51] Such considerations are of decisive importance in case of albumin, as each additional EPR-active fatty acid additionally shifts the protein stability for +1.3 K as it was shown in **Chapter 11**.

Despite these critical remarks, EPR spectroscopy definitely helps to extrapolate blurry and ensemble-driven albumin properties on a tentative and coarse-grained argumentative level. For example, the picture of a hard asymmetric interior and soft symmetric surface[1] can be also largely confirmed for other albumins, based on data presented in **Figure 6.4**. The physical basis of this functional feature is still not very clear and should be further investigated from e.g. cooperativities that are obtained from Scatchard plots, or rotational correlation times of the applied spin probes. Generally, it is well-known that 5-DSA probes exhibit stronger immobilization compared to 16-DSA when bound to albumin (see also $A_\parallel$ values in **Chapter 8**).[52]

Actually, as it was shown in earlier studies, ligand immobilization is not necessarily a linear function of nitroxide immersion and probe penetration into the albumin interior.[53,54] In principle, this aspect can be further elucidated with 2-pulse ESEEM on Y-DSA ligands that already helped to reveal solvent accessibilities in the ligand binding sites of HSA,[55] as well as β-Lactoglobulin.[56] Characterizations of the immediate molecular environment of paramagnetic ligands and the atomistic mechanism of association should be also partially accessible by HYSCORE,[57] or ENDOR techniques,[58,59] e.g. for the copper porphyrin that was used by Junk *et al.*[3] It can be anticipated that a closer investigation of the spin dynamics (T_1, T_2) also reveals several interesting functional aspects,[60,61] especially in terms of micelle formation and ligand ordering in spin probed albumin samples (see **Chapter 8**). Such basic and actually important spin dynamic investigations were not tested in this thesis, but some primary studies are already available.[2]

Nowadays, several strategies are developed for increasing experimentally accessible t_{max} values beyond 80 μs with the potential to determine distances of up to 17 nm.[62] This can be achieved by extending experiments to higher frequencies (Q-band) in combination with high power travelling wave

tubes (TWT) for pulse power amplification.[62,63] Another strategy would be to increase the phase memory time T_m of the sample system by perdeuteration[64] in order to circumvent the strong hyperfine coupling to protons that causes spin diffusion within the immediate nitroxide environment.[65] A recent theoretical feasibility study about spin diffusion experiments highlighted that even distances of up to 20 – 30 nm may be extracted from biradicals.[66] Furthermore, an additional benefit of high-field EPR spectroscopy, or the application of rigid spin labels, is the orientation selectivity that adds the angular dependence of dipole-dipole interactions to data sets.[67–69] It should be therefore tested whether all emerging fatty acid distances, or even their relative angular alignments become accessible in tri-angulation experiments by these more elaborate experimental and theoretical approaches (**Chapter 9**).

There are significant implications for the validity of the LCW theory[70] for the investigated nano-objects, especially for the observed hydropathy differences between HSA and BSA (**Chapter 4**) and the length scales of the core-shell polymers (**Chapter 10**). It is highlighted by Chandler[71] and Cooper[72] that the hydrophobic effect is strongly temperature-dependent. Thus, the hydrophobic effect generally plays a significant role in amphipilic substrate-ligand interactions that may invert its thermodynamic nature with temperature. These fundamental principles and considerations should be integrated in future studies as they decisively contribute for understanding and predicting several functional aspects of self-assembly that were observed throughout this thesis.

It is furthermore generally suggested to decompose complex systems by simple kinetic models or equilibria for thermodynamical analysis that may help to unravel the internal mechanisms of self-organizing matter.[73] In a retrospective, it was not clear for a long time what all these spectral fractions emerging from simulations in CW EPR are good for. This irritation indeed dissipated when the interconversion equilibrium could be devised from existing physical models (K_{IC}). An expansion and adoption of the associated strategies occurred naturally later on. It appears that not until the complexity of the investigated EPR-active sample systems was decisively decreased to an attainable minimum (**Chapter 11**, 16HSA 110 0200 mM), these analyses finally became accessible. Therefore, evaluation could be expanded to much more intricate routes that provided a fresh way of looking inside the energetic gear box of albumin.

The general impact of the work that was done by Charles Tanford on albumins during the 1950s should not be underestimated by any researcher working in this field. Tanford left behind a fundamentally precious pool of experiments and results not least due to their collection in his monograph.[74] This book is more up to date than one would expect, despite its early year of publication. Especially, the intentional conjunction of common physicochemical principles in polymers and proteins was found to be of decisive importance for this thesis. Several unspoken constructive analytic feedback loops can be found and set up therein, as it is seen e.g. in the applicability of Scatchard plots to the core-shell polymers, though not being entirely unique in polymer science.[75]

The picture of structural adaptability and plasticity of albumins[36,76] is highly appealing and still appears to be the best description of how these proteins work. The term plasticity, or flexibility was also reconsidered by Junk *et al.*[1] For the first time, DEER experiments on HSA revealed that crystal structure and solution structure simply did not coincide. A recent article by Litus *et al.*[77] highlighted the IDP character of HSA and BSA in a quite thorough comparative view. Interestingly, the topological regions that are responsible for this high flexibility were found to be amenable for PTMs. Moreover, the majority of ligand binding sites (see **Figure 3.2**) exhibited a dual personality, displaying a combination of ordered and disordered amino acids with a supposed adaptive function. This issue was similarly anticipated in **Chapter 4** and could be redirected towards the LCW theory that suggests drying out zones with viscosity gradients around water exposed hydrophobic patches which increase side chain motility.[70,78] It was shown in **Chapter 7** that PTMs change binding site cooperativities in albumins. The intrinsic notion for structural disorder and non-cooperative fatty acid binding in native albumins may be a key for understanding its functional tunability by PTMs that modulate conformational entropy and therefore adaptability, plasticity and flexibility.

Albumin research has a strong intrinsic potential for dictating the research direction towards a modern view on the functionality of proteins that should go beyond the established rigid picture of fixed protein crystal structures.[79] This rather intuitive and straightforward classical view on proteins is meanwhile upheld for about 60 years. The Anfinsen dogma gives a more dynamic view on proteins and suggests that each protein adopts a minimum free energy state in its native state with a single native conformation.[80] The minimum energy state for albumins is clearly given by their crystal structures, however, these all look almost similar, or even identical (**Chapter 6**). In **Chapter 8** it was also clearly shown that the minimum energy state (ΔG_{el}) would rather occur at $pH_{opt} = 9.6$ instead at more physiological values. The same principle is seen in **Chapter 11**, where the decoupling of domains sets in at physiological temperatures (for $T > 33°C$) and not at room temperature. The desirable functional state of albumin is therefore a slightly unstable and mixed conformational ensemble at body temperature ($T = 37°C$). Such ensemble-related parameters were already shown to be accessible by MD simulations.[81,82] Thus, it seems that albumins are intrinsically tuned for escaping structural equilibrium in order to harness their functionality. In this regard, it can be stated that PTMs, charge, fatty acid content and temperature may each change the free energy level of albumins stability that leads to deviations from functional equilibrium conditions. A schematic representation of this correlation is visualized in **Figure 12.2**.

In recent years, it became more and more accepted that the crystal structure-based functional perception of proteins needs a fresh impetus that should be directed towards stochastic and time-resolved ensembles of proteins in general.[83] This novel viewpoint is also advocated by EPR spectroscopists,[84–86] not least as a consequence of the fact that structures which lack atomistic resolution often end up in EPR labs for obtaining some additional structural restraints. This is especially pronounced for systems where conformational entropy plays a functional role.[86]
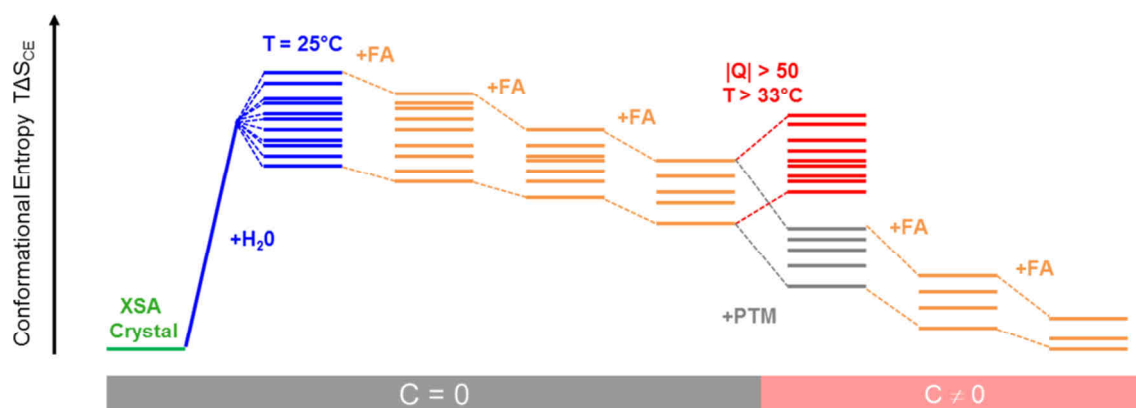
Figure 12.2 | Functional factors that modify conformational entropy in albumins. A qualitative schematic representation is given of the influence that various factors exert on intrinsic conformational entropy ($T\Delta S_{CE}$) and therefore plasticity of albumins. Assuming that a XSA crystal structure exhibits a minimum of conformational entropy (green), the addition of water (H_2O, blue) leads to a diversification of energetic states that are generally reduced in number by addition of fatty acids (FA, orange, **Chapter 4**). Cooperativity was shown to be zero at room temperature for native albumins (**Chapter 7** and **Chapter 11**). When temperature is raised, or charge is increased, the conformational entropy is naturally increased accordingly (**Chapter 8** and **Chapter 11**). Otherwise, when albumins are exposed to PTMs (gray), positive or negative cooperativity is introduced ($C \neq 0$). Typically, this is due to a simultaneously decreased flexibility of structural elements.

According to Tuszynski it is mainly the still prevalent lack of connectivity in between disciplines, especially biology and physics that are suspicious for preventing a further understanding of such intricate or ambiguous processes.[87] This lack of connectivity in between the natural sciences was already mentioned by Schrödinger in the 1940s. In his eyes there was an urgent need for upcoming explanations regarding the functionality of these biomacromolecules that he called "aperiodic crystals" being responsible for regulating most processes in living organisms.[88] However, it is obvious that bridging this interdisciplinary gap may often be accompanied with considerable effort.[38]

Several interesting approaches are nowadays encouraged in progressive textbooks,[87,89] where protein function is mathematically and physicochemically rigorously deconstructed in order to present fascinating new analytic perspectives. Therefore, it has to be emphasized that CW EPR, as it is used here, gives only a narrow window of timescale in the nanosecond to picosecond range. Yet, conformational exchange is in the timescale of microseconds and beyond that it is rather monitored by ST-EPR, or PELDOR techniques as DEER.[84] Intriguingly, there is also experimental evidence from e.g. time-domain dielectric relaxation[90] and low-frequency Raman spectroscopy[91] that there are collective albumin "breathing modes" or phonons[92,93] at timescales even in the millisecond timescale. The very same collective motions are suspected to provoke allosteric changes and cooperative effects.[92] Consequentially, these processes are hidden in timescale ranges that are either inaccessible, or have yet to be thoroughly explored with EPR spectroscopy or other methods.

Another way to approach protein functionality is given by the resonant recognition model (RRM)[94,95] that is based on the work of Davydov.[96,97] Particularly, the Davydov model assumes that electronic conduction along the polypeptide backbone facilitates shape alterations when proteins are exposed to

(strong) electromagnetic irradiation. In this regard it would be worth to investigate, whether microwave irradiation itself has already an impact on protein function.

The symmetric DEER distance distributions obtained from the protein surface (16-DSA-probed HSA) are strongly indicative that albumin function is eventually based on fundamental natural principles comprising entropy and symmetry in configurations. Junk *et al.*[1] described this phenomenon may emerge due to an almost octahedral alignment of 16-DSA-based interspin distances. The assumption nature will preferentially form tetrahedral and octahedral structures can be well justified with the symmetry principles that were already set up by Plato,[98] or Richard Buckminster Fuller.[99] Basically, there is a general notion that albumin functionality is intrinsically obscure and mysterious.[11]

All this indicates how important it is to tread unexplored scientific paths for albumin that are yet unknown. Setting up new functional ideas is generally considered as being the key for scientific progress, although upcoming ideas may lead to unpleasant paradigm shifts. However, science is often most fruitful when casual anarchistic methods are applied rigorously.[100] In terms of the radical constructivism of Heinz von Förster, it is suggested that the observer should rather choose a way of steady cybernetic simplification and iteration of problems, as well as being aware about his own social and scientific standpoint. The perception of problems and finding their solutions are almost exclusively subjective and are thus in turn limited by the respective observer.[101] This highly regarded philosophic statement is not thought to be offending to anyone, but it rather highlights the intrinsic individuality of scientific results and according interpretations, in turn closing the circle towards the quote that is given at the beginning of this thesis.

This thesis shows that albumin functionality is defined by an intricate interplay of charge, diffusion, shape, ligand affinity, cooperativity and therefore also allosteric modulation, solvent, PTMs and it would be pretentious to claim that this thesis or EPR spectroscopy alone completely clarifies the dynamic nature of this protein in solution. However, several new aspects, as well as experimental and analytic approaches have been picked up and refined that should help in designing new experiments for unraveling the underlying physicochemical principles of albumin function. Furthermore, the research platform has already been recognized and partially adopted by the EPR community[10,102] and it remains to be seen whereto it will evolve.

As Erwin Schrödinger stated, the main characteristics of living beings, or animated matter is the formation of orderliness from disorder.[88,103] In terms of fatty acid binding properties this definition could truly be applied for albumin.

13 | Summary

Several physicochemical aspects were investigated that govern the structural and dynamic properties of albumins, as well as albumin-inspired, self-organizing compounds. On the basis of previous EPR spectroscopic studies on albumins, the experimental setups and frameworks were optimized to gain reproducible and reliable results at about physiological conditions. Most of the studies are based on utilizing paramagnetic fatty acid spin probes that elucidate structural, as well as dynamic information about the investigated substrates.

Here, a strategy was pursued that guarantees optimum data quality and parameter control at X-band frequencies in CW EPR and DEER spectroscopy. It could be shown that already differences on the primary structure level of albumins exert a decisive influence on alignment patterns of bound fatty acids. Moreover, albumin functionality can be sensitively altered by posttranslational modifications. These slight changes in functionality are best characterized by the onset of fatty acid binding site cooperativity. The variation of pH in the range of $1 < pH < 13$ leads to various observable phenomena that were summarized in a pH-induced functional phase space model. The introduction of a covalently attached and thus localized surveillance spin in combination with appropriate MD simulations bears the potential to identify individual fatty acid binding sites, or groups of binding sites that are encountered as peaks in DEER distance distributions. The assessment of distinct spatial correlations of albumin-bound paramagnetic fatty acids is therefore significantly improved and becomes accessible in EPR spectroscopy in the first place.

The applied amphiphilic core-shell polymers can be seen as simplified albumin-inspired model systems that imitate some functional aspects of albumins. They constitute synthetic and strategic drug delivery devices with several tunable dynamic properties. Due to their complex dynamic, amphiphilic and brush-like structure and self-assembling properties with fatty acids, these polymers can be also used to confirm, or even to study yet unexplored aspects of the hydrophobic effect at work. Similar to albumins, the bound fatty acids exhibit intricate temperature-dependent interconversion equilibria of diffusion regimes that provide access to thermodynamic analyses based on the construction of non-linear van't Hoff plots. Particularly, the heat capacity changes of this diffusion interconversion process provide indirect information about the hydration state and the self-organizing properties of the macromolecular substrate.

Thermodynamic analyses that were established for the polymers were successfully transferred to the albumin system. The emerging thermodynamic profile of this fatty acid-based interconversion process can be directly correlated to calorimetric data from thermal denaturation of albumin itself. Thereupon, a holistic picture of the temperature denaturation of albumin is given that highlights protein solution dynamics, as well as ligand dynamics simultaneously. The fatty acid redistribution that typically occurs during thermal albumin denaturation, leads to structural stabilization of albumin. The associated quantitative change in binding site occupation can be directly monitored with appropriate DEER experiments.

In summary, the combined view of the results suggests that the structural and dynamic adaptability and therefore optimum functionality of albumin is intricately based on the presence of conformational entropy and binding site cooperativity. The physiological conditions, where albumins are typically situated in, provide a physicochemical environment that does not support maximum protein stability. Therefore, albumin functionality and its corresponding solution structure are based on physiological conditions causing slight structural instabilities. In turn, fatty acid uptake, or uptake of a variety of other ligands may partially compensate for this structural instability. The free energy of ligand association is transformed into a reduction of conformational entropy and therefore into a gain in stability of an experimental albumin ensemble.

14 | Zusammenfassung

Es wurden mehrere physikochemische Aspekte untersucht welche die strukturellen und dynamischen Eigenschaften von Albuminen, sowie von albuminbasierten, selbstorganisierenden Systemen regulieren. Basierend auf bisherigen EPR-spektroskopischen Albuminstudien wurden die experimentellen Rahmenbedingungen optimiert, um möglichst reproduzierbare und verlässliche Ergebnisse bei nahezu physiologischen Bedingungen zu erzielen. Für die meisten Studien wurden paramagnetische Fettsäuren als Spinsonden verwendet mit welchen sowohl strukturelle, als auch dynamische Daten bezüglich der untersuchten Substrate gewonnen werden können.

Hierbei wurde eine Strategie verfolgt die es ermöglicht optimale Datenqualität und Kontrolle bezüglich der entsprechenden Parameter in CW EPR und DEER Experimenten im X-band zu gewährleisten. Es konnte gezeigt werden, dass bereits die Primärstruktur von Albuminen einen entscheidenden Einfluß auf die Anlagerungsmuster von gebundenen Fettsäuren hat. Darüber hinaus kann die Funktionalität von Albumin durch posttranslationale Modifikationen geringfügig verändert werden. Diese Veränderung der Funktionalität läßt sich am besten durch eine einsetzende Kooperativität der Fettsäurebindungstaschen beobachten.

Die Variation des pH-Wertes im Bereich 1 < pH < 13 führt zu einer ganzen Reihe von Phänomenen welche in einem pH-induzierten funktionellen Phasenraummodell festgehalten wurden. Das Einführen eines kovalent gebundenen und daher lokalisierten Überwachungsspins, in Kombination mit geeigneten MD Simulationen, birgt das Potenzial individuelle Fettsäuren in ihren Bindungstaschen, oder einer bestimmten Gruppe von Bindungstaschen, auszumachen. Diese Fettsäuren tauchen dann jeweils als Maxima in entsprechenden DEER-Abstandsverteilungen auf. Das Aufspüren von diesbezüglichen räumlichen Korrelationen von albumingebundenen paramagnetischen Fettsäuren wird dadurch erheblich vereinfacht und mittels EPR Spektroskopie überhaupt erst zugänglich.

Die verwendeten amphiphilen core-shell Polymere können als vereinfachte Modellsysteme betrachtet werden, welche einige funktionelle Eigenschaften aufweisen die auch bei Albuminen zu finden sind. Diese Polymere stellen zudem synthetische und strategische pharmakokinetische Transporter dar, die eine Reihe von einstellbaren Eigenschaften besitzen. Durch Ihre komplexe dynamische, amphiphile und bürstenartige Struktur und ihre Fähigkeit der Selbstorganisation mit amphiphilen Fettsäuren, können diese Polymere sowohl für die experimentelle Überprüfung, als auch für eventuell weitere Untersuchungen von noch unbekannten Aspekten des hydrophoben Effekts herangezogen werden. Ähnlich den Albuminen weisen diese polymergebundenen Fettsäuren ein temperaturabhängiges Gleichgewicht der gegenseitigen Umwandlung von Diffusionsregimes auf. Dieses Gleichgewicht ermöglicht eine thermodynamische Analyse, welche auf der Konstruktion von nicht-linearen van't Hoff Diagrammen beruht. Insbesondere die Änderungen in der Wärmekapazität dieses Diffusionsumwandlungsprozesses liefern indirekte Informationen über den Hydratationszustand und die selbstorganisatorischen Eigenschaften der makromolekularen Substrate. Die thermodynamischen Analysen, welche für die Polymere erstellt wurden, konnten erfolgreich auf Albumin übertragen werden.

Das thermodynamische Profil dieses fettsäurebasierten Diffusionsumwandlungsprozesses kann direkt mit kalorimetrischen Daten aus der Temperaturdenaturierung von Albumin selbst korreliert werden. Es wurde daraufhin ein ganzheitliches Bild der Temperaturdenaturierung von Albumin erstellt, welches Protein- und Ligandendynamik simultan darzustellen vermag. Die üblicherweise während der Temperaturdenaturierung von Albuminen auftretende Fettsäureumverteilung führt zu einer strukturellen Stabilisierung des Proteins. Die quantitative Änderung der Fettsäurebeladung kann im Zuge dessen direkt mittels DEER Experimenten bestimmt werden.

Letztlich führt eine ganzheitliche Betrachtung der Ergebnisse dieser Arbeit zu dem Schluss, dass die strukturelle und dynamische Anpassungsfähigkeit und daher der Zustand optimaler Funktionalität von Albuminen auf komplizierte Weise mit der Konformationsentropie des Ensembles und auch mit der Kooperativität der Ligandenbindungstaschen zusammen hängt. Die physiologischen Gegebenheiten in welchen Albumine üblicherweise anzutreffen sind, stellen physikochemische Bedingungen bereit, welche ungünstig für die Stabilität des Proteins sind. Daher hängen die physiologische Funktionalität und damit auch die Lösungsstruktur der Albumine von Randbedingungen ab, die leichte strukturelle Instabilitäten verursachen. Durch die Aufnahme von Fettsäuren, oder einer ganzen Reihe weiterer Liganden, kann diese strukturelle Instabilität bis zu einem gewissen Maß wieder ausgeglichen werden. Die freie Energie der Ligandenbindung wird demnach in eine Reduktion der Konformationsentropie und daher in einen Stabilitätsgewinn des experimentellen Albuminensembles umgesetzt.

References by Chapter

Chapter 1

[1] Y. Xia, Y. Li, A. O. Burts, M. F. Ottaviani, D. A. Tirrell, J. A. Johnson, N. J. Turro, R. H. Grubbs, *J Am Chem Soc* **2011**, *133*, 19953–19959.

[2] D. Hinderberger, EPR spectroscopy in polymer science. In *EPR Spectroscopy: Applications in Chemistry and Biology*; Drescher, M., Jeschke, G., Eds.; Springer: Berlin, Heidelberg, **2012**, pp 67–89.

[3] D. Kurzbach, M. J. N. Junk, D. Hinderberger, *Macromol Rapid Commun* **2013**, *34*, 119–134.

[4] D. Kurzbach, W. Hassouneh, J. R. McDaniel, E. A. Jaumann, A. Chilkoti, D. Hinderberger, *J Am Chem Soc* **2013**, *135*, 11299–11308.

[5] R. Graf, M. R. Hansen, D. Hinderberger, K. Muennemann, H. W. Spiess, *Phys Chem Chem Phys* **2014**, *16*, 9700–9712.

[6] Y. H. Tang, M. Cangiotti, C. L. Kao, M. F. Ottaviani, *J Phys Chem B* **2017**, *121*, 10498–10507.

[7] W. L. Hubbell, C. Altenbach, *Curr Opin Struct Biol* **1994**, *4*, 566–573.

[8] O. Schiemann, T. F. Prisner, *Q Rev Biophys* **2007**, *40*, 1–53.

[9] W. L. Hubbell, C. J. Lopez, C. Altenbach, Z. Yang, *Curr Opin Struct Biol* **2013**, *23*, 725–733.

[10] S. Kucher, S. Korneev, S. Tyagi, R. Apfelbaum, D. Grohmann, E. A. Lemke, J. P. Klare, H. J. Steinhoff, D. Klose, *J Magn Reson* **2017**, *275*, 38–45.

[11] G. Jeschke, *Emerging Top Life Sci* **2018**, *2*, 9–18.

[12] D. Kurzbach, D. R. Kattnig, N. Pfaffenberger, W. Schärtl, D. Hinderberger, *ChemistryOpen* **2012**, *1*, 211–214.

[13] N. Van Eps, L. N. Caro, T. Morizumi, A. K. Kusnetzow, M. Szczepek, K. P. Hofmann, T. H. Bayburt, S. G. Sligar, O. P. Ernst, W. L. Hubbell, *Proc Natl Acad Sci USA* **2017**, *114*, E3268–E3275.

[14] T. Schmidt, M. A. Wälti, J. L. Baber, E. J. Hustedt, G. M. Clore, *Angew Chem Int Ed* **2016**, *128*, 16137–16141.

[15] V. N. Syryamina, M. De Zotti, C. Toniolo, F. Formaggio, S. A. Dzuba, *Phys Chem Chem Phys* **2018**, *20*, 3592–3601.

[16] J. Eisermann, L. Prager, D. Hinderberger, *Phys Chem Chem Phys* **2018**, *20*, 1421–1430.

[17] H. J. Steinhoff, A. Savitsky, C. Wegener, M. Pfeiffer, M. Plato, K. Möbius, *Biochim Biophys Acta* **2000**, *1457*, 253–262.

[18] K. Möbius, A. Savitsky, C. Wegener, M. Plato, M. Fuchs, A. Schnegg, A. A. Dubinskii, Y. A. Grishin, I. A. Grigorev, M. Kühn, D. Duche, H. Zimmermann, H. J. Steinhoff, *Magn Reson Chem* **2005**, *43*, S4–S19.

[19] M. J. N. Junk, U. Jonas, D. Hinderberger, *Small* **2008**, *4*, 1485–1493.

[20] M. J. N. Junk, W. Li, A. D. Schlüter, G. Wegner, H. W. Spiess, A. Zhang, D. Hinderberger, *Angew Chem Int Ed* **2010**, *49*, 5683–5687.

[21] K. Widder, S. R. MacEwan, E. Garanger, V. Nunez, S. Lecommandoux, A. Chilkoti, D. Hinderberger, *Soft Matter* **2017**, *13*, 1816–1822.

[22] A. Schweiger, G. Jeschke, *Principles of pulse electron paramagnetic resonance.* Oxford University Press Inc.: Oxford, **2001**.

[23] R. E. Martin, M. Pannier, F. Diederich, V. Gramlich, M. Hubrich, H. W. Spiess, *Angew Chem Int Ed* **1998**, *37*, 2834–2837.

[24] M. Pannier, S. Veit, A. Godt, G. Jeschke, H. W. Spiess, *J Magn Reson* **2000**, *142*, 331–340.

[25] G. Jeschke, *Annu Rev Phys Chem* **2012**, *63*, 419–446.

[26] S. S. Sinha, R. K. Mitra, S. K. Pal, *J Phys Chem B* **2008**, *112*, 4884–4891.

[27] D. Klose, J. P. Klare, D. Grohmann, C. W. M. Kay, F. Werner, H. J. Steinhoff, *PLoS One* **2012**, *7*, e39492.

[28] H. Takahashi, E. Ohmichi, H. Ohta, *Appl Phys Lett* **2015**, *107*, 182405.

[29] T. Okamoto, H. Takahashi, E. Ohmichi, H. Ohta, *J Infrared Milli Terahz Waves* **2016**, *37*, 1173–1184.

[30] P. P. Borbat, E. R. Georgieva, J. H. Freed, *J Phys Chem Lett* **2013**, *4*, 170–175.

[31] P. A. S. Cruickshank, D. R. Bolton, D. A. Robertson, R. I. Hunter, R. J. Wylde, G. M. Smith, *Rev Sci Instrum* **2009**, *80*, 103102.

[32] G. W. Reginsson, R. I. Hunter, P. A. S. Cruickshank, D. R. Bolton, S. T. Sigurdsson, G. M. Smith, O. Schiemann, *J Magn Reson* **2012**, *216*, 175–182.

[33] X. Wang, J. E. McKay, B. Lama, J. van Tol, T. Li, K. Kirkpatrick, Z. Gan, S. Hill, J. R. Long, H. C. Dorn, *Chem Commun* **2018**, *54*, 2425–2428.

[34] D. J. Schneider, J. H. Freed, Calculating slow motional magnetic resonance spectra: A user's guide. In *Spin Labeling: Theory and Applications*; L. J. Berliner, J. Reuben, Eds.; Plenum Press: New York, London, **1989**, Vol. 8, pp 1–76.

[35] H. J. Steinhoff, N. Radzwill, W. Thevis, V. Lenz, D. Brandenburg, A. Antson, G. Dodson, A. Wollmer, *Biophys J* **1997**, *73*, 3287–3298.

[36]   B. Barquera, J. E. Morgan, D. Lukoyanov, C. P. Scholes, R. B. Gennis, M. J. Nilges, *J Am Chem Soc* **2003**, *125*, 265–275.

[37]   T. Spalek, P. Pietrzyk, Z. Sojka, *J Chem Inf Model* **2005**, *45*, 18–29.

[38]   J. Strancar, T. Koklic, Z. Arsov, B. Filipic, D. Stopar, M. A. Hemminga, *J Chem Inf Model* **2005**, *45*, 394–406.

[39]   S. Stoll, A. Schweiger, *J Magn Reson* **2006**, *178*, 42–55.

[40]   G. Jeschke, V. Chechik, P. Ionita, A. Godt, H. Zimmermann, J. Banham, C. R. Timmel, D. Hilger, H. Jung, *Appl Magn Reson* **2006**, *30*, 473–498.

[41]   Y. Polyhach, E. Bordignon, G. Jeschke, *Phys Chem Chem Phys* **2011**, *13*, 2356–2366.

[42]   G. Jeschke, *Protein Sci* **2018**, *27*, 76–85.

[43]   G. Hagelueken, R. Ward, J. H. Naismith, O. Schiemann, *Appl Magn Reson* **2012**, *42*, 377–391.

[44]   http://www.biochemistry.ucla.edu/Faculty/Hubbell

[45]   http://www.epr.ethz.ch/software

[46]   J. N. Rao, C. C. Jao, B. G. Hedge, R. Langen, T. S. Ulmer, *J Am Chem Soc* **2010**, *132*, 8657–8668.

[47]   C. Engelhard, S. Raffelberg, Y. Tang, R. P. Diensthuber, A. Möglich, A. Losi, W. Gärtner, R. Bittl, *Photochem Photobiol Sci* **2013**, *12*, 1855–1863.

[48]   G. Fanali, P. Ascenzi, G. Bernardi, M. Fasano, *J Biomol Struct Dyn* **2012**, *29*, 1195–1205.

[49]   E. J. Cohn, L. E. Strong, W. L. Hughes Jr., D. J. Mulford, J. N. Ashworth, M. Melin, H. L. Taylor, *J Am Chem Soc* **1946**, *68*, 459–475.

[50]   T. Peters Jr., *All about Albumin: Biochemistry, Genetics and Medical Applications*. Academic Press, Inc.: San Diego, **1995**.

[51]   K. Weber, M. Osborn, *J Biol Chem* **1969**, *244*, 4406–4412.

[52]   U. K. Laemmli, *Nature* **1970**, *227*, 680–685.

[53]   E. Engvall, P. Perlmann, *Immunochemistry* **1971**, *8*, 871–874.

[54]   M. M. Bradford, *Anal Biochem* **1976**, *72*, 248–254.

[55]   P. K. Smith, R. I. Krohn, G. T. Hermanson, A. K. Mallia, F. H. Gartner, M. D. Provenzano, E. K. Fujimoto, N. M. Goeke, B. J. Olson, D. C. Klenk, *Anal Biochem* **1985**, *150*, 76–85.

[56]   B. J. S. C. Olson, J. Markwell, *Curr Protoc Protein Sci* **2007**, Unit 3.4, 1–29.

[57]   C. Tanford, *Physical Chemistry of Macromolecules.* John Wiley & Sons, Inc.: New York, **1961**.

[58]   G. Sudlow, D. J. Birkett, D. N. Wade, *Mol Pharmacol* **1975**, *11*, 824–832.

[59]   G. Sudlow, D. J. Birkett, D. N. Wade, *Mol Pharmacol* **1976**, *12*, 1052–1061.

[60]   U. Kragh-Hansen, *Pharmacol Rev* **1981**, *33*, 17–53.

[61]   S. Curry, *Drug Metab Pharmacokinet* **2009**, *24*, 342–357.

[62]   RCSB Protein Data Base Home Page. http://www.rcsb.org (accessed Jun 5, 2018)

[63]   T. J. Stone, T. Buckman, P. L. Nordio, H. M. McConnell, *Proc Natl Acad Sci USA* **1965**, *54*, 1010–1017.

[64]   O. H. Griffith, H. M. McConnell, *Proc Natl Acad Sci USA* **1966**, *55*, 8–11.

[65]   M. J. N. Junk, H. W. Spiess, D. Hinderberger, *Angew Chem Int Ed* **2010**, *49*, 8755–8759.

[66]   Y. Akdogan, M. J. N. Junk, D. Hinderberger, *Biomacromolecules* **2011**, *12*, 1072–1079.

[67]   Y. Shenberger, A. Shimshi, S. Ruthstein, *J Phys Chem B* **2015**, *119*, 4824–4830.

[68]   C. M. Gruian, C. Rickert, S. C. T. Nicklisch, E. Vanea, H. J. Steinhoff, S. Simon, *ChemPhysChem* **2017**, *18*, 634–642.

[69]   A. Pavicevic, J. Luo, A. Popovic-Bijelic, M. Mojovic, *Eur Biophys J* **2017**, 1–15.

[70]   M. J. N. Junk, H. W. Spiess, D. Hinderberger, *J Magn Reson* **2011**, *210*, 210–217.

[71]   M. J. N. Junk, H. W. Spiess, D. Hinderberger, *Biophys J* **2011**, *100*, 2293–2301.

[72]   Y. Akdogan, D. Hinderberger, *J Phys Chem B* **2011**, *115*, 15422–15429.

[73]   Y. Akdogan, Y. Wu, K. Eisele, M. Schaz, T. Weil, D. Hinderberger, *Soft Matter* **2012**, *8*, 11106–11114.

[74]   A. A. Bhattacharya, T. Grüne, S. Curry, *J Mol Biol* **2000**, *303*, 721–732.

[75]   J. A. Johnson, Y. Y. Lu, A. O. Burts, Y. H. Lim, M. G. Finn, J. T. Koberstein, N. J. Turro, D. A. Tirrell, R. H. Grubbs, *J Am Chem Soc* **2010**, *133*, 559–566.

[76]   Y. Bakkour, V. Darcos, F. Coumes, S. Li, J. Coudane, *Polymer* **2013**, *54*, 1746–1754.

[77]   R. Haag, F. Kratz, *Angew Chem Int Ed* **2006**, *45*, 1198–1215.

Chapter 2

[1]   C. P. Poole Jr.*,* H. A. Farach, Preparing the way for paramagnetic resonance. In *Foundations of Modern EPR*; G. R. Eaton, S. S. Eaton, K. M. Salikhov, Eds.; World Scientific Publishing Co. Pte. Ltd: Singapore, **1998**, pp 13–24.

[2]   S. Procopiu, *Bulletin scientifique de l'Académie roumaine de sciences,* Bucharest, **1913**.

[3]   N. Bohr, *Philos Mag* **1913**, *26*, 857–875.

[4]   I. I. Rabi, J. R. Zacharias, S. Millman, P. Kusch, *Phys Rev* **1938**, *53*, 318.

[5]   L. W. Alvarez, F. Bloch, *Phys Rev* **1940**, *57*, 111–122.

[6]   E. Zavoisky, *J Phys USSR* **1945**, *9*, 211–245.

[7]   B. Bleaney, K. W. H. Stevens, *Rep Prog Phys* **1953**, *16*, 108–159.

[8]   F. Bloch, *Phys Rev* **1946**, *70*, 460–474.

[9]   C. P. Poole Jr., H. A. Farach, The first sesquidecade of paramagnetic resonance. In *Foundations of Modern EPR*; G. R. Eaton, S. S. Eaton, K. M. Salikhov, Eds.; World Scientific Publishing Co. Pte. Ltd: Singapore, **1998**, pp 63–83.

[10]   J. A. Weil, J. R. Bolton, *Electron Paramagnetic Resonance: elementary theory and practical applications.* John Wiley & Sons Inc.: Hoboken, New Jersey, **2007**.

[11]   W. Demtröder, *Experimentalphysik 3: Atome, Moleküle und Festkörper.* Springer-Verlag: Berlin, Heidelberg, **2010**.

[12]   J. J. Hudson, D. M. Kara, I. J. Smallman, B. E. Sauer, M. R. Tarbutt, E. A. Hinds, *Nature* **2011**, *473*, 493–496.

[13]   S. J. Brodsky, S. D. Drell, *Phys Rev D: Part Fields* **1980**, *22*, 2236–2243.

[14]   D. Bourilkov, *Phys Rev D: Part Fields* **2001**, *64*, 071701.

[15]   P. Zeeman, *Philos Mag* **1897**, *44*, 55–60.

[16]   W. Gerlach, O. Stern, *Z Phys* **1922**, *9*, 349–352.

[17]   W. Gerlach, O. Stern, *Z Phys* **1922**, *9*, 353–355.

[18]   G. E. Uhlenbeck, S. Goudsmit, *Naturwissenschaften* **1925**, *13*, 953–954.

[19]   G. E. Uhlenbeck, S. Goudsmit, *Nature* **1926**, *117*, 264–265.

[20]   E. R. Andrew, A. Bradbury, R. G. Eades, *Nature* **1959**, *183*, 1802–1803.

[21]   I. J. Lowe, *Phys Rev Lett* **1959**, *2*, 285–287.

[22]   C. M. Sommerfield, *Phys Rev* **1957**, *107*, 328–329.

[23]   K. Möbius, A. Savitsky, *High-field EPR spectroscopy on proteins and their model systems: characterization of transient paramagnetic states.* Royal Society of Chemistry: Cambridge, UK, **2009**.

[24]   F. Schneider, M. Plato, *Elektronenspin-Resonanz: experimentelle Technik.* Verlag Karl Thiemig KG: München, **1971**.

[25]   P. L. Nordio, General magnetic resonance theory. In *Spin Labeling: Theory and Applications*; L. J. Berliner, Ed.; Academic Press: New York, **1976**, Vol. 1, pp 5–52.

[26]   W. Demtröder, *Experimentalphysik 2: Elektrizität und Optik.* Springer-Verlag: Berlin, Heidelberg, **2013**.

[27]   A. Schweiger, G. Jeschke, *Principles of pulse electron paramagnetic resonance.* Oxford University Press Inc.: Oxford, **2001**.

[28]   K. Schmidt-Rohr, H. W. Spiess, *Multidimensional solid-state NMR and polymers.* Academic Press: London, **1994**.

[29]   H. C. Torrey, *Phys Rev* **1956**, *104*, 563–565.

[30]   G. Jeschke, Instrumentation and experimental setup. In *ESR spectroscopy in membrane biophysics*; M. A. Hemminga, L. J. Berliner, Eds.; Springer Science+Business Media, LLC: New York, **2007**, Vol. 27, pp 17–47.

[31]   M. A. Hemminga, P. A. De Jager, Saturation transfer spectroscopy of spin labels: techniques and interpretation of spectra. In *Spin Labeling: Theory and Applications*; L. J. Berliner, J. Reuben, Eds.; Plenum Press: New York, **1989**, Vol. 8, pp 131–178.

[32]   A. Abragam, M. H. L. Pryce, *Proc R Soc London, Ser A* **1951**, *205*, 135–153.

[33]   B. R. McGarvey, *J Phys Chem* **1967**, *71*, 51–66.

[34]   T. Ando, N. Hirota, H. Wada, *Sci Technol Adv Mater* **2009**, *10*, 014609.

[35]   J. G. Ku, X. Y. Liu, H. H. Chen, R. D. Deng, Q. X. Yan, *AIP Adv* **2016**, *6*, 025004.

[36]   W. Demtröder, *Experimentalphysik 4: Kern-, Teilchen- und Astrophysik.* Springer-Verlag: Berlin, Heidelberg, **2014**.

[37]   C. H. Townes, B. P. Dailey, *J Chem Phys* **1952**, *20*, 35–40.

[38]   J. F. Baugher, P. C. Taylor, T. Oja, P. J. Bray, *J Chem Phys* **1969**, *50*, 4914–4925.

[39]   G. Likhtenstein, Depth of immersion of paramagnetic centers in biological systems. In *Distance measurements in biological systems by EPR*; L. J. Berliner, G. R. Eaton, S. S. Eaton, Eds.; Kluwer Academic Publishers: New York, Boston, **2002**, Vol. 19, pp 309–345.

[40]   Y. N. Molin, K. M. Salikhov, K. I. Zamaraev, *Spin exchange: Principles and applications in chemistry and biology.* Springer-Verlag: Berlin, Heidelberg, **1980**.

[41]   S. S. Eaton, G. R. Eaton, Distance measurements by CW and pulsed EPR. In *Distance measurements in biological systems by EPR*; L. J. Berliner, G. R. Eaton, S. S. Eaton, Eds.; Kluwer Academic Publishers: New York, Boston, **2002**, Vol. 19, pp 1–27.

[42]   Z. Ciecierska-Tworek, S. P. Van, O. H. Griffith, *J Mol Struct* **1973**, *16*, 139–148.

[43]   H. J. Steinhoff, *J Biochem Bioph Methods* **1988**, *17*, 237–247.

[44]   H. J. Steinhoff, K. Lieutenant, J. Schlitter, *Z Naturforsch* **1989**, *44c*, 280–288.

[45]   H. J. Steinhoff, N. Radzwill, W. Thevis, V. Lenz, D. Brandenburg, A. Antson, G. Dodson, A. Wollmer, *Biophys J* **1997**, *73*, 3287–3298.

[46] M. D. Rabenstein, Y. K. Shin, *Proc Natl Acad Sci USA* **1995**, *92*, 8239–8243.

[47] A. Kumar, R. R. Ernst, K. Wüthrich, *Biochem Biophys Res Commun* **1980**, *95*, 1–6.

[48] A. W. Overhauser, *Phys Rev* **1953**, *92*, 411–415.

[49] W. Braun, C. Bösch, L. R. Brown, N. Go, K. Wüthrich, *Biochim Biophys Acta, Protein Struct* **1981**, *667*, 377–396.

[50] M. H. Levitt, *Spin Dynamics: basics of nuclear magnetic resonance.* John Wiley & Sons, Ltd.: Chichester, UK, **2008**.

[51] G. Hanson, L. J. Berliner, *Metals in biology: applications of high resolution EPR to metalloenzymes.* Springer Science+Business Media, LLC: New York, **2010**.

[52] A. K. Hoffmann, A. T. Henderson, *J Am Chem Soc* **1961**, *83*, 4671–4672.

[53] A. K. Hoffmann, W. G. Hodgson, W. H. Jura, *J Am Chem Soc* **1961**, *83*, 4675–4676.

[54] N. Naik, R. Braslau, *Tetrahedron* **1998**, *54*, 667–696.

[55] W. L. Hubbell, C. Altenbach, *Curr Opin Struct Biol* **1994**, *4*, 566–573.

[56] S. I. Ohnishi, H. M. McConnell, *J Am Chem Soc* **1965**, *87*, 2293.

[57] T. J. Stone, T. Buckman, P. L. Nordio, H. M. McConnell, *Proc Natl Acad Sci USA* **1965**, *54*, 1010–1017.

[58] L. Stryer, O. H. Griffith, *Proc Natl Acad Sci USA* **1965**, *54*, 1785–1791.

[59] P. Törmälä, *J Macromol Sci, Rev Macromol Chem Phys* **1979**, *17*, 297–357.

[60] W. L. Hubbell, D. S. Cafiso, C. Altenbach, *Nat Struct Mol Biol* **2000**, *7*, 735–739.

[61] D. Hinderberger, H. W. Spiess, G. Jeschke, *J Phys Chem B* **2004**, *108*, 3698–3704.

[62] D. Hinderberger, O. Schmelz, M. Rehahn, G. Jeschke, *Angew Chem Int Ed* **2004**, *43*, 4616–4621.

[63] M. J. N. Junk, W. Li, A. D. Schlüter, G. Wegner, H. W. Spiess, A. Zhang, D. Hinderberger, *Macromol Chem Phys* **2011**, *212*, 1229–1235.

[64] D. Kurzbach, W. Hassouneh, J. R. McDaniel, E. A. Jaumann, A. Chilkoti, D. Hinderberger, *J Am Chem Soc* **2013**, *135*, 11299–11308.

[65] D. Kurzbach, M. J. N. Junk, D. Hinderberger, *Macromol Rapid Commun* **2013**, *34*, 119–134.

[66] W. L. Hubbell, C. J. Lopez, C. Altenbach, Z. Yang, *Curr Opin Struct Biol* **2013**, *23*, 725–733.

[67] J. H. Freed, Theory of slow tumbling ESR spectra for nitroxides. In *Spin Labeling: Theory and Applications*; L. J. Berliner, Ed.; Academic Press: New York, **1976**, Vol. 1, pp 53–132.

[68] M. Karplus, G. K. Fraenkel, *J Chem Phys* **1961**, *35*, 1312–1323.

[69] O. H. Griffith, P. C. Jost, Lipid spin labels in biological membranes. In *Spin Labeling: Theory and Applications*; L. J. Berliner, Ed.; Academic Press: New York, **1976**, Vol. 1, pp 453–523.

[70] H. M. McConnell, *J Chem Phys* **1956**, *24*, 764–766.

[71] H. M. McConnell, D. B. Chestnut, *J Chem Phys* **1958**, *28*, 107–117.

[72] A. M. Vasserman, A. L. Buchachenko, *J Struct Chem* **1966**, *7*, 633–638.

[73] B. M. Hoffman, T. B. Eames, *J Am Chem Soc* **1969**, *91*, 2169–2170.

[74] E. G. Rozantsev, V. D. Sholle, *Russ Chem Rev* **1971**, *40*, 233–246.

[75] O. H. Griffith, P. J. Dehlinger, S. P. Van, *J Membrane Biol* **1974**, *15*, 159–192.

[76] H. J. Steinhoff, A. Savitsky, C. Wegener, M. Pfeiffer, M. Plato, K. Möbius, *Biochim Biophys Acta, Bioenerg* **2000**, *1457*, 253–262.

[77] C. Wegener, A. Savitsky, M. Pfeiffer, K. Möbius, H. J. Steinhoff, *Appl Magn Reson* **2001**, *21*, 441–452.

[78] K. Möbius, A. Savitsky, C. Wegener, M. Plato, M. Fuchs, A. Schnegg, A. A. Dubinskii, Y. A. Grishin, I. A. Grigorev, M. Kühn, D. Duche, H. Zimmermann, H. J. Steinhoff, *Magn Reson Chem* **2005**, *43*, S4–S19.

[79] E. Bordignon, H. J. Steinhoff, Membrane protein structure and dynamics studied by site-directed spin-labeling ESR. In *ESR spectroscopy in membrane biophysics*; M. A. Hemminga, L. J. Berliner, Eds.; Springer Science+Business Media, LLC: New York, **2007**, Vol. 27, pp 129–164.

[80] L. Onsager, *J Am Chem Soc* **1936**, *58*, 1486–1493.

[81] O. Tapia, O. Goscinski, *Mol Phys* **1975**, *29*, 1653–1661.

[82] R. Owenius, M. Engström, M. Lindgren, M. Huber, *J Phys Chem A* **2001**, *105*, 10967–10977.

[83] S. Stoll, A. Schweiger, EasySpin: simulating cw ESR spectra. In *ESR spectroscopy in membrane biophysics*; M. A. Hemminga, L. J. Berliner, Eds.; Springer Science+Business Media, LLC: New York, **2007**, Vol. 27, pp 299–321.

[84] C. Tanford, *Physical Chemistry of Macromolecules*. John Wiley & Sons, Inc.: New York, **1961**.

[85] J. H. Freed, G. V. Bruno, C. F. Polnaszek, *J Phys Chem* **1971**, *75*, 3385–3399.

[86] D. Gamliel, H. Levanon, *Stochastic processes in magnetic resonance.* World Scientific Publishing Co. Pte. Ltd.: New York, **1995**.

[87] S. A. Goldman, G. V. Bruno, C. F. Polnaszek, J. H. Freed, *J Chem Phys* **1972**, *56*, 716–735.

[88] K. A. Earle, D. E. Budil, J. H. Freed, *J Phys Chem* **1993**, 97, 13289–13297.

[89] D. J. Schneider, J. H. Freed, Calculating slow motional magnetic resonance spectra: A user's guide. In *Spin Labeling: Theory and Applications*; L. J. Berliner, J. Reuben, Eds.; Plenum Press: New York, London, **1989**, Vol. 8, pp 1–76.

[90]   F. Perrin, *J Phys Radium* **1934**, *5*, 497–511.
[91]   F. Perrin, *J Phys Radium* **1936**, *7*, 1–11.
[92]   J. H. Freed, *J Chem Phys* **1964**, *41*, 2077–2083.
[93]   G. Breit, I. I. Rabi, *Phys Rev* **1931**, *38*, 2082–2083.
[94]   D. Kivelson, *J Chem Phys* **1960**, *33*, 1094–1106.
[95]   D. Marsh, Experimental methods in spin-label spectral analysis. In *Spin Labeling: Theory and Applications*; L. J. Berliner, J. Reuben, Eds.; Plenum Press: New York, London, **1989**, Vol. 8, pp 255–303.
[96]   S. Stoll, A. Schweiger, *Chem Phys Lett* **2003**, *380*, 464–470.
[97]   S. Stoll, A. Schweiger, *J Magn Reson* **2006**, *178*, 42–55.
[98]   W. L. Hubbell, H. M. McConnell, *J Am Chem Soc* **1971**, *93*, 314–326.
[99]   E. L. Hahn, *Phys Rev* **1950**, *80*, 580–594.
[100]   R. J. Blume, *Phys Rev* **1958**, *109*, 1867–1873.
[101]   L. G. Rowan, E. L. Hahn, W. B. Mims, *Phys Rev* **1965**, *137*, A61–A71.
[102]   W. B. Mims, *Phys Rev B* **1972**, *5*, 2409–2419.
[103]   W. B. Mims, *Proc R Soc London, Ser A* **1965**, *283*, 452–457.
[104]   E. R. Davies, *Phys Lett A* **1974**, *47*, 1–2.
[105]   P. Höfer, A. Grupp, H. Nebenführ, M. Mehring, *Chem Phys Lett* **1986**, *132*, 279–282.
[106]   J. W. Saalmüller, H. W. Long, G. G. Maresch, H. W. Spiess, *J Magn Reson, Ser A* **1995**, *117*, 193–208.
[107]   W. B. Mims, K. Nassau, J. D. McGee, *Phys Rev* **1961**, *123*, 2059–2069.
[108]   U. Fano, *Rev Mod Phys* **1957**, *29*, 74–93.
[109]   O. W. Sorensen, G. W. Eich, M. H. Levitt, G. Bodenhausen, R. R. Ernst, *Prog Nucl Magn Reson Spectrosc* **1983**, *16*, 163–192.
[110]   F. Lottspeich, J. W. Engels, *Bioanalytik.* Spektrum Akademischer Verlag: Heidelberg, **2009**.
[111]   H. V. Meinke, F. W. Gundlach, *Taschenbuch der Hochfrequenztechnik.* Springer-Verlag: Berlin, Heidelberg, **1986**.
[112]   R. L. Herndon, *Engineering and Design: Electromagnetic Pulse (EMP) and Tempest Protection for Facilities*. Pamphlet EP 1110-3-2, U.S. Army Corps of Engineers, Washington, D.C., USA, 31 December **1990**.
[113]   G. Jeschke, BlochSolver. http://www.epr.ethz.ch/software/blochsolver-older-version.html (accessed July 29, 2016).
[114]   J. K. M. Sanders, B. K. Hunter, *Modern NMR Spectroscopy: A Guide for Chemists*. Oxford University Press: Oxford, **1993**.
[115]   P. G. Fajer, L. Brown, L. Song, Practical pulsed dipolar ESR (DEER). In *ESR spectroscopy in membrane biophysics*; M. A. Hemminga, L. J. Berliner, Eds.; Springer Science+Business Media, LLC: New York, **2007**, Vol. 27, pp 95–128.
[116]   M. J. N. Junk, Assessing the Functional Structure of Molecular Transporters by EPR Spectroscopy. Ph.D. Thesis, Johannes Gutenberg-Universität Mainz, **2010**.
[117]   S. S. Eaton, G. R. Eaton, Relaxation times of organic radicals and transition metal ions. In *Distance measurements in biological systems by EPR*; L. J. Berliner, G. R. Eaton, S. S. Eaton, Eds.; Kluwer Academic Publishers: New York, Boston, **2002**, Vol. 19, pp 29–154.
[118]   J. R. Klauder, P. W. Anderson, *Phys Rev* **1962**, *125*, 912–932.
[119]   G. Bodenhausen, H. Kogler, R. R. Ernst, *J Magn Reson* **1984**, *58*, 370–388.
[120]   R. T. Weber, *E580 User's Manual*, Bruker BioSpin Corporation: Billerica, MA, USA, **2005**.
[121]   A. Godt, M. Schulte, H. Zimmermann, G. Jeschke, *Angew Chem Int Ed* **2006**, *118*, 7722–7726.
[122]   V. V. Kurshev, A. M. Raitsimring, Y. D. Tsvetkov, *J Magn Reson* **1989**, *81*, 441–454.
[123]   Z. Levi, A. M. Raitsimring, D. Goldfarb, *J Phys Chem* **1991**, *95*, 7830–7838.
[124]   S. Saxena, J. H. Freed, *Chem Phys Lett* **1996**, *251,* 102–110.
[125]   S. Saxena, J. H. Freed, *J Chem Phys* **1997**, *107*, 1317–1340.
[126]   P. P. Borbat, J. H. Freed, *Chem Phys Lett* **1999**, *313*, 145–154.
[127]   G. Jeschke, M. Pannier, A. Godt, H. W. Spiess, *Chem Phys Lett* **2000**, *331*, 243–252.
[128]   K. D. Bowers, W. B. Mims, *Phys Rev* **1959**, *115*, 285–295.
[129]   A. D. Milov, K. M. Salikhov, M. D. Shirov, *Fiz Tverd Tela* **1981**, *23*, 975–982.
[130]   A. D. Milov, A. B. Ponomarev, Y. D. Tsvetkov, *Chem Phys Lett* **1984**, *110*, 67–72.
[131]   R. G. Larsen, D. J. Singel, *J Chem Phys* **1993**, *98*, 5134–5146.
[132]   V. Pfannebecker, H. Klos, M. Hubrich, T. Volkmer, A. Heuer, U. Wiesner, H. W. Spiess, *J Phys Chem* **1996**, *100*, 13428–13432.
[133]   D. E. Kaplan, E. L. Hahn, *J Phys Radium* **1958**, *19*, 821–825.
[134]   M. Emshwiller, E. L. Hahn, D. Kaplan, *Phys Rev* **1960**, *118*, 414–424.
[135]   P. K. Wang, C. P. Slichter, *Phys Rev Lett* **1984**, *53*, 82–85.
[136]   R. E. Martin, M. Pannier, F. Diederich, V. Gramlich, M. Hubrich, H. W. Spiess, *Angew Chem Int Ed* **1998**, *37*, 2834–2837.

[137] M. Pannier, S. Veit, A. Godt, G. Jeschke, H. W. Spiess, *J Magn Reson* **2000**, *142*, 331–340.
[138] A. D. Milov, Y. D. Tsvetkov, *Appl Magn Reson* **1997**, *12*, 495–504.
[139] G. Jeschke, V. Chechik, P. Ionita, A. Godt, H. Zimmermann, J. Banham, C. R. Timmel, D. Hilger, H. Jung, *Appl Magn Reson* **2006**, *30*, 473–498.
[140] G. Strobl, *The Physics of Polymers: Concepts for Understanding Their Structures and Behavior.* Springer-Verlag: Berlin, Heidelberg, **2007**.
[141] G. Jeschke, *ChemPhysChem* **2002**, *3*, 927–932.
[142] G. Jeschke, Y. Polyhach, *Phys Chem Chem Phys* **2007**, *9*, 1895–1910.
[143] G. Jeschke, *Annu Rev Phys Chem* **2012**, *63*, 419–446.
[144] G. Jeschke, G. Panek, A. Godt, A. Bender, H. Paulsen, *Appl Magn Reson* **2004**, *26*, 223–244.
[145] A. N. Tikhonov, V. Y. Arsenin, *Solution of ill-posed problems.* V. H. Winston & Sons, **1977**.
[146] P. C. Hansen, *SIAM Rev* **1992**, *34*, 561–580.
[147] M. T. Nair, S. V. Pereverzev, U. Tautenhahn, *Inverse Prob* **2005**, *21*, 1851–1869.
[148] E. Parzen, *Ann Math Statist* **1962**, *33*, 1065–1076.
[149] G. Jeschke, A. Koch, U. Jonas, A. Godt, *J Magn Reson* **2002**, *155*, 72–82.
[150] B. E. Bode, D. Margraf, J. Plackmeyer, G. Dürner, T. F. Prisner, O. Schiemann, *J Am Chem Soc* **2007**, *129*, 6736–6745.
[151] D. Hilger, H. Jung, E. Padan, C. Wegener, K. P. Vogel, H. J. Steinhoff, G. Jeschke, *Biophys J* **2005**, *89*, 1328–1338.

Chapter 3

[1] T. Peters Jr., *All about Albumin: Biochemistry, Genetics, and Medical Applications.* Academic Press, Inc.: San Diego, **1995**.
[2] N. A. Kratochwil, W. Huber, F. Müller, M. Kansy, P. R. Gerber, *Biochem Pharmacol* **2002**, *64*, 1355–1374.
[3] A. A. Bhattacharya, T. Grüne, S. Curry, *J Mol Biol* **2000**, *303*, 721–732.
[4] A. A. Spector, *J Lipid Res* **1975**, *16*, 165–179.
[5] M. Anraku, V. T. G. Chuang, T. Maruyama, M. Otagiri, *Biochim Biophys Acta, Gen Subj* **2013**, *1830*, 5465–5472.
[6] G. Paris, S. Kraszewski, C. Ramseyer, M. Enescu, *Biopolymers* **2012**, *97*, 889–898.
[7] T. J. Stone, T. Buckman, P. L. Nordio, H. M. McConnell, *Proc Natl Acad Sci USA* **1965**, *54*, 1010–1017.
[8] D. Kivelson, *J Chem Phys* **1960**, *33*, 1094–1106.
[9] J. H. Freed, G. K. Fraenkel, *J Chem Phys* **1963**, *39*, 326–348.
[10] J. H. Freed, *J Chem Phys* **1964**, *41*, 2077–2083.
[11] D. Wallach, *J Chem Phys* **1967**, *47*, 5258–5268.
[12] O. H. Griffith, H. M. McConnell, *Proc Natl Acad Sci USA* **1966**, *55*, 8–11.
[13] H. H. Hull, R. Chang, L. J. Kaplan, *Biochim Biophys Acta, Protein Struct* **1975**, *400*, 132–136.
[14] A. Alonso, W. P. dos Santos, S. J. Leonor, J. G. dos Santos, M. Tabak, *Biophys J* **2001**, *81*, 3566–3576.
[15] J. L. V. Anjos, P. S. Santiago, M. Tabak, A. Alonso, *Colloids Surf, B* **2011**, *88*, 463–470.
[16] A. Pavicevic, J. Luo, A. Popovic-Bijelic, M. Mojovic, *Eur Biophys J* **2017**, 1–15.
[17] A. H. Beth, R. C. Perkins Jr., S. D. Venkataramu, D. E. Pearson, C. R. Park, J. H. Park, L. R. Dalton, *Chem Phys Lett* **1980**, *69*, 24–28.
[18] P. Graceffa, *Arch Biochem Biophys* **1983**, *225*, 802–808.
[19] L. J. Berliner, J. Grunwald, H. O. Hankovszky, K. Hideg, *Anal Biochem* **1982**, *119*, 450–455.
[20] D. S. Park, C. E. Petersen, C. E. Ha, K. Harohalli, J. B. Feix, N. V. Baghavan, *IUBMB Life* **1999**, *48*, 169–174.
[21] Y. Shenberger, A. Shimshi, S. Ruthstein, *J Phys Chem B* **2015**, *119*, 4824–4830.
[22] C. M. Gruian, C. Rickert, S. C. T. Nicklisch, E. Vanea, H. J. Steinhoff, S. Simon, *ChemPhysChem* **2017**, *18*, 634–642.
[23] V. V. Khramtsov, L. M. Weiner, S. I. Eremenko, O. I. Belchenko, P. V. Schastnev, I. A. Grigor'ev, V. A. Reznikov, *J Magn Reson* **1985**, *61*, 397–408.
[24] V. V. Khramtsov, D. Marsh, L. Weiner, V. A. Reznikov, *Biochim Biophys Acta, Biomembr* **1992**, *1104*, 317–324.
[25] A. I. Smirnov, A. Ruuge, V. A. Reznikov, M. A. Voinov, I. A. Grigor'ev, *J Am Chem Soc* **2004**, *126*, 8872–8873.
[26] S. Thetiot-Laurent, G. Gosset, J. L. Clement, M. Cassien, A. Mercier, D. Siri, A. Gaudel-Siri, A. Rockenbauer, M. Culcasi, S. Pietri, *ChemBioChem* **2017**, *18*, 300–315.
[27] F. E. Kendall, *J Biol Chem* **1941**, *138*, 97–109.
[28] A. D. Keith, A. S. Waggoner, O. H. Griffith, *Proc Natl Acad Sci USA* **1968**, *61*, 819–826.
[29] A. S. Waggoner, T. J. Kingzett, S. Rottschaeffer, O. H. Griffith, *Chem Phys Lipids* **1969**, *3*, 245–253.

[30] W. L. Hubbell, H. M. McConnell, *J Am Chem Soc* **1971**, *93*, 314–326.
[31] C. J. Scandella, P. Devaux, H. M. McConnell, *Proc Natl Acad Sci USA* **1972**, *69*, 2056–2060.
[32] H. Träuble, E. Sackmann, *Nature* **1973**, *245*, 210–211.
[33] E. Sackmann, H. Träuble, *J Am Chem Soc* **1972**, *94*, 4482–4491.
[34] E. Sackmann, H. Träuble, *J Am Chem Soc* **1972**, *94*, 4492–4498.
[35] A. S. Waggoner, A. D. Keith, O. H. Griffith, *J Phys Chem* **1968**, *72*, 4129–4132.
[36] O. H. Griffith, A. S. Waggoner, *Acc Chem Res* **1969**, *2*, 17–24.
[37] B. J. Gaffney, H. M. McConnell, *J Magn Reson* **1974**, *16*, 1–28.
[38] J. D. Morrisett, H. J. Pownall, A. M. Gotto, *J Biol Chem* **1975**, *250*, 2487–2494.
[39] G. Scatchard, *Ann NY Acad Sci* **1949**, *51*, 660–672.
[40] A. V. Hill, *J Physiol* **1910**, *40*, 4–7.
[41] J. Barcroft, *Biochem J* **1913**, *7*, 481–491.
[42] A. N. Kuznetsov, B. Ebert, G. Lassmann, A. B. Shapiro, *Biochim Biophys Acta, Protein Struct* **1975**, *379*, 139–146.
[43] H. H. Ruf, M. Gratzl, *Biochim Biophys Acta, Protein Struct* **1976**, *446*, 134–142.
[44] S. J. Rehfeld, D. J. Eatough, W. Z. Plachy, *J Lipid Res* **1978**, *19*, 841–849.
[45] N. A. Abumrad, R. C. Perkins, J. H. Park, C. R. Park, *J Biol Chem* **1981**, *256*, 9183–9191.
[46] R. C. Perkins Jr., N. Abumrad, K. Balasubramanian, L. R. Dalton, A. H. Beth, J. H. Park, C. R. Park, *Biochemistry* **1982**, *21*, 4059–4064.
[47] T. G. Gantchev, M. B. Shopova, *Biochim Biophys Acta, Protein Struct Mol Enzymol* **1990**, *1037*, 422–434.
[48] M. Ge, S. B. Rananavare, J. H. Freed, *Biochim Biophys Acta, Gen Subj* **1990**, *1036*, 228–236.
[49] D. Tatlidil, M. Ucuncu, Y. Akdogan, *Phys Chem Chem Phys* **2015**, *17*, 22678–22685.
[50] M. L. Sheely, *Ind Eng Chem* **1932**, *24*, 1060–1064.
[51] K. C. Chou, *Biophys Chem* **1988**, *30*, 3–48.
[52] I. Bertini, C. Luchinat, M. S. Viezzoli, L. Banci, S. H. Koenig, H. T. Leung, J. E. Coleman, *Inorg Chem* **1989**, *28*, 352–358.
[53] S. S. Eaton, G. R. Eaton, Relaxation times of organic radicals and transition metal ions. In *Distance Measurements in Biological Systems by EPR*; L. J. Berliner, G. R. Eaton, S. S. Eaton, Eds.; Kluwer Academic Publishers: New York, Boston, **2002**, Vol. 19, pp 29–154.
[54] S. Krause, C. T. O'Konski, *J Am Chem Soc* **1959**, *81*, 5082–5088.
[55] F. Winter, R. Kimmich, *Biochim Biophys Acta, Gen Subj* **1982**, *719*, 292–298.
[56] I. Munro, I. Pecht, L. Stryer, *Proc Natl Acad Sci USA* **1979**, *76*, 56–60.
[57] M. Gentin, M. Vincent, J. C. Brochon, A. K. Livesey, N. Cittanova, J. Gallay, *Biochemistry* **1990**, *29*, 10405–10412.
[58] P. Marzola, E. Gratton, *J Phys Chem* **1991**, *95*, 9488–9495.
[59] J. R. Lakowicz, I. Gryczynski, *Biophys Chem* **1992**, *45*, 1–6.
[60] M. K. Helms, C. E. Petersen, N. V. Baghavan, D. M. Jameson, *FEBS Lett* **1997**, *408*, 67–70.
[61] W. Qiu, L. Zhang, O. Okobiah, Y. Yang, L. Wang, D. Zhong, A. H. Zewail, *J Phys Chem B* **2006**, *110*, 10540–10549.
[62] M. L. Ferrer, R. Duchowicz, B. Carrasco, J. G. de la Torre, A. U. Acuna, *Biophys J* **2001**, *80*, 2422–2430.
[63] V. A. Livshits, D. Marsh, *Biochim Biophys Acta, Biomembr* **2000**, *1466*, 350–360.
[64] R. Dulbecco, M. Vogt, *J Exp Med* **1954**, *99*, 167–182.
[65] D. S. Goodman, *J Am Chem Soc* **1958**, *80*, 3892–3898.
[66] J. D. Ashbrook, A. A. Spector, E. C. Santos, J. E. Fletcher, *J Biol Chem* **1975**, *250*, 2333–2338.
[67] J. D. Morrisett, The use of spin labels for studying the structure and function of enzymes. In *Spin Labeling: Theory and Applications*; L. J. Berliner, Ed.; Academic Press: New York, **1976**, Vol. 1, pp 273–338.
[68] A. R. Berengian, M. Parfenova, H. S. Mchaourab, *J Biol Chem* **1999**, *274*, 6305–6314.
[69] A. Cotton, *J Phys Theor Appl* **1896**, *5*, 237–244.
[70] L. Velluz, M. Legrand, *Angew Chem Int Ed* **1965**, *4*, 838–845.
[71] D. Madge, E. Elson, W. W. Webb, *Phys Rev Lett* **1972**, *29*, 705–708.
[72] D. K. Sasmal, T. Mondal, S. S. Mojumdar, A. Choudhury, R. Banerjee, K. Bhattacharyya, *J Phys Chem B* **2011**, *115*, 13075–13083.
[73] E. S. Watson, M. J. O'Neill, J. Justin, N. Brenner, *Anal Chem* **1964**, *36*, 1233–1238.
[74] S. Gumpen, P. O. Hegg, H. Martens, *Biochim Biophys Acta, Lipids Lipid Metab* **1979**, *574*, 189–196.
[75] S. B. Dubin, J. H. Lunacek, G. B. Benedek, *Proc Natl Acad Sci USA* **1967**, *57*, 1164–1171.
[76] S. E. Harding, *Biophys Chem* **1995**, *55*, 69–93.
[77] A. I. Luik, Y. N. Naboka, S. E. Mogilevich, T. O. Hushcha, N. I. Mischenko, *Spectrochim Acta, Part A* **1998**, *54*, 1503–1507.
[78] C. Honda, H. Kamizono, K. I. Matsumoto, K. Endo, *J Colloid Interface Sci* **2004**, *278*, 310–317.

[79]   M. Tabak, D. de Sousa Neto, C. E. G. Salmon, *Braz J Phys* **2006**, *36*, 83–89.
[80]   D. de Sousa Neto, C. E. G. Salmon, A. Alonso, M. Tabak, *Colloids Surf, B* **2009**, *70*, 147–156.
[81]   Y. Akdogan, M. J. N. Junk, D. Hinderberger, *Biomacromolecules* **2011**, *12*, 1072–1079.
[82]   Y. Akdogan, D. Hinderberger, *J Phys Chem B* **2011**, *115*, 15422–15429.
[83]   W. Scheider, *Proc Natl Acad Sci USA* **1979**, *76*, 2283–2287.
[84]   W. Scheider, *J Phys Chem* **1980**, *84*, 925–928.
[85]   D. P. Cistola, D. M. Small, J. A. Hamilton, *J Biol Chem* **1987**, *262*, 10971–10979.
[86]   D. P. Cistola, D. M. Small, J. A. Hamilton, *J Biol Chem* **1987**, *262*, 10980–10985.
[87]   S. Curry, H. Mandelkow, P. Brick, N. Franks, *Nat Struct Biol* **1998**, *5*, 827–835.
[88]   S. Curry, P. Brick, N. P. Franks, *Biochim Biophys Acta, Mol Cell Biol Lipids* **1999**, *1441*, 131–140.
[89]   A. A. Spector, J. E. Fletcher, J. D. Ashbrook, *Biochemistry* **1971**, *10*, 3229–3232.
[90]   R. B. Simpson, J. D. Ashbrook, E. C. Santos, A. A. Spector, *J Lipid Res* **1974**, *15*, 415–422.
[91]   J. R. Simard, P. A. Zunszain, C. E. Ha, J. S. Yang, N. V. Baghavan, I. Petitpas, S. Curry, J. A. Hamilton, *Proc Natl Acad Sci USA* **2005**, *102*, 17958–17963.
[92]   J. R. Simard, P. A. Zunszain, J. A. Hamilton, S. Curry, *J Mol Biol* **2006**, *361*, 336–351.
[93]   G. J. van der Vusse, *Drug Metab Pharmacokinet* **2009**, *24*, 300–307.
[94]   C. Tanford, *Physical Chemistry of Macromolecules.* John Wiley & Sons, Inc.: New York, **1961**.
[95]   J. E. Fletcher, J. D. Ashbrook, A. A. Spector, *Ann NY Acad Sci* **1973**, *226*, 69–81.
[96]   V. P. Dole, *J Clin Invest* **1956**, *35*, 150–154.
[97]   E. Shafrir, *J Clin Invest* **1958**, *37*, 1775–1782.
[98]   C. M. Mendel, P. H. Frost, R. R. Cavalieri, *J Clin Endocrinol Metab* **1986**, *63*, 1394–1399.
[99]   R. J. Havel, A. Naimark, C. F. Borchgrevink, *J Clin Invest* **1963**, *42*, 1054–1063.
[100]   M. F. Oliver, *Circulation* **1972**, *45*, 491–500.
[101]   P. Taggart, M. Carruthers, *Lancet* **1971**, *297*, 363–366.
[102]   S. Laurell, *Scand J Clin Lab Invest* **1956**, *8*, 81–82.
[103]   A. H. Kissebah, S. Alfarsi, P. W. Adams, V. Wynn, *Diabetologia* **1976**, *12*, 563–571.
[104]   C. B. Berde, B. S. Hudson, R. D. Simoni, L. A. Sklar, *J Biol Chem* **1979**, *254*, 391–400.
[105]   T. Oida, *J Biochem* **1986**, *100*, 1533–1542.
[106]   A. Svenson, E. Holmer, L. O. Andersson, *Biochim Biophys Acta, Protein Struct* **1974**, *342*, 54–59.
[107]   P. J. Tummino, R. A. Copeland, *Biochemistry* **2008**, *47*, 5481–5492.
[108]   J. A. Hamilton, D. P. Cistola, J. D. Morrisett, J. T. Sparrow, D. M. Small, *Proc Natl Acad Sci USA* **1984**, *81*, 3718–3722.
[109]   F. De Simone, R. Guzzi, L. Sportelli, D. Marsh, R. Bartucci, *Biochim Biophys Acta, Biomembr* **2007**, *1768*, 1541–1549.
[110]   D. P. Cistola, D. M. Small, *J Clin Invest* **1991**, *87*, 1431–1441.
[111]   A. Gurachevsky, S. C. Kazmierczak, A. Jörres, V. Muravsky, *Clin Chem Lab Med* **2008**, *46*, 1203–1210.
[112]   E. S. Krenzel, Z. Chen, J. A. Hamilton, *Biochemistry* **2013**, *52*, 1559–1567.
[113]   P. Seidel, A. Gurachevsky, V. Muravsky, K. Schnurr, G. Seibt, G. Matthes, *Z Med Phys* **2005**, *15*, 265–272.
[114]   S. C. Kazmierczak, A. Gurachevsky, G. Matthes, V. Muravsky, *Clin Chem* **2006**, *52*, 2129–2134.
[115]   A. Gurachevsky, E. Muravskaya, T. Gurachevskaya, L. Smirnova, V. Muravsky, *Cancer Invest* **2007**, *25*, 378–383.
[116]   C. Schmidt, C. Krumbiegel, K. Waterstradt, G. Petznick, H. Schäfer, K. Schnurr, In *Expectation-Maximization-Estimation of Mixture Densities for Electron-Spin-Resonance-Analysis of Albumin*, IEEE International Workshop on Genomic Signal Processing and Statistics (GENSIPS), Minneapolis, MN, USA, May 17–19, pp 1–4, **2009**.
[117]   R. Jalan, K. Schnurr, R. P. Mookerjee, S. Sen, L. Cheshire, S. Hodges, V. Muravsky, R. Williams, G. Matthes, N. A. Davies, *Hepatology* **2009**, *50*, 555–564.
[118]   M. Gelos, D. Hinderberger, E. Welsing, J. Belting, K. Schnurr, B. Mann, *Int J Colorectal Dis* **2010**, *25*, 119–127.
[119]   G. Sudlow, D. J. Birkett, D. N. Wade, *Mol Pharmacol* **1975**, *11*, 824–832.
[120]   G. Sudlow, D. J. Birkett, D. N. Wade, *Mol Pharmacol* **1976**, *12*, 1052–1061.
[121]   I. Petitpas, C. E. Petersen, C. E. Ha, A. A. Bhattacharya, P. A. Zunszain, J. Ghuman, N. V. Baghavan, S. Curry, *Proc Natl Acad Sci USA* **2003**, *100*, 6440–6445.
[122]   S. Y. Cheng, G. Rakhit, F. Erard, J. Robbins, C. F. Chignell, *J Biol Chem* **1981**, *256*, 831–836.
[123]   T. Hauenschild, Spinmarkierung pharmazeutischer Wirkstoffe sowie deren Bindungseigenschaften an Serum Albumin vom Menschen, Diploma Thesis, Johannes Gutenberg-Universität Mainz, **2013**.
[124]   T. Hauenschild, J. Reichenwallner, V. Enkelmann, D. Hinderberger, *Chem Eur J* **2016**, *22*, 12825–12838.
[125]   Y. Akdogan, M. Emrullahoglu, D. Tatlidil, M. Ucuncu, G. Cakan-Akdogan, *Phys Chem Chem Phys* **2016**, *18*, 22531–22539.

[126] A. A. Pavicevic, A. D. Popovic-Bijelic, M. D. Mojovic, S. V. Susnjar, G. G. Bacic, *J Phys Chem B* **2014**, *118*, 10898–10905.

[127] J. Ghuman, P. A. Zunszain, I. Petitpas, A. A. Bhattacharya, M. Otagiri, S. Curry, *J Mol Biol* **2005**, *353*, 38–52.

[128] RCSB Protein Data Base Home Page. http://www.rcsb.org (accessed Jun 5, 2018).

[129] A. Shrake, P. D. Ross, *J Biol Chem* **1988**, *263*, 15392–15399.

[130] A. Shrake, D. Frazier, F. P. Schwarz, *Biopolymers* **2006**, *81*, 235–248.

[131] W. Scheider, J. K. Fuller, *Biochim Biophys Acta* **1970**, *221*, 376–378.

[132] D. D. Thomas, L. R. Dalton, J. S. Hyde, *J Chem Phys* **1976**, *65*, 3006–3024.

[133] M. A. Hemminga, P. A. De Jager, Saturation transfer spectroscopy of spin labels: techniques and interpretation of spectra. In *Spin Labeling: Theory and Applications*; L. J. Berliner, J. Reuben, Eds.; Plenum Press: New York, **1989**, Vol. 8, pp 131–178.

[134] V. V. Khramtsov, D. Marsh, *Biochim Biophys Acta, Biomembr* **1991**, *1068*, 257–260.

[135] J. M. Berg, J. L. Tymoczko, L. Stryer, *Biochemie*. Spektrum Akademischer Verlag: Heidelberg, **2007**.

[136] C. Tanford, J. G. Buzzell, *J Phys Chem* **1956**, *60*, 225–231.

[137] M. Maruthamuthu, S. Kishore, *Proc Indian Acad Sci, Chem Sci* **1988**, *100*, 525–533.

[138] V. D. Trivedi, I. Saxena, M. U. Siddiqui, M. A. Qasim, *Biochem Mol Biol Int* **1997**, *43*, 1–8.

[139] G. Fanali, P. Ascenzi, G. Bernardi, M. Fasano, *J Biomol Struct Dyn* **2012**, *29*, 1195–1205.

[140] M. R. Salaman, J. Warwicker, *Proteins Struct Funct Bioinf* **2005**, *61*, 468–472.

[141] A. Ohkubo, *J Biochem* **1969**, *65*, 879–888.

[142] A. Gurachevsky, E. Shimanovitch, T. Gurachevskaya, V. Muravsky, *Biochem Biophys Res Commun* **2007**, *360*, 852–856.

[143] V. Muravsky, T. Gurachevskaya, S. Berezenko, K. Schnurr, A. Gurachevsky, *Spectrochim Acta, Part A* **2009**, *74*, 42–47.

[144] W. B. Mims, J. Peisach, *Biochemistry* **1976**, *15*, 3863–3869.

[145] L. G. Rowan, E. L. Hahn, W. B. Mims, *Phys Rev* **1965**, *137*, A61–A71.

[146] M. J. N. Junk, H. W. Spiess, D. Hinderberger, *Angew Chem Int Ed* **2010**, *49*, 8755–8759.

[147] S. S. Sinha, R. K. Mitra, S. K. Pal, *J Phys Chem B* **2008**, *112*, 4884–4891.

[148] D. Klose, J. P. Klare, D. Grohmann, C. W. M. Kay, F. Werner, H. J. Steinhoff, *PLoS One* **2012**, *7*, e39492.

[149] R. Klinke, S. Silbernagl, *Lehrbuch der Physiologie.* Georg Thieme Verlag: Stuttgart, **1996**.

[150] J. F. Carpenter, J. H. Crowe, *Cryobiology* **1988**, *25*, 244–255.

[151] R. V. Rariy, A. M. Klibanov, *Proc Natl Acad Sci USA* **1997**, *94*, 13520–13523.

[152] J. L. Dashnau, N. V. Nucci, K. A. Sharp, J. M. Vanderkooi, *J Phys Chem B* **2006**, *110*, 13670–13677.

[153] A. Godt, M. Schulte, H. Zimmermann, G. Jeschke, *Angew Chem Int Ed* **2006**, *118*, 7722–7726.

[154] B. E. Bode, D. Margraf, J. Plackmeyer, G. Dürner, T. F. Prisner, O. Schiemann, *J Am Chem Soc* **2007**, *129*, 6736–6745.

[155] K. Sale, L. Song, Y. S. Liu, E. Perozo, P. Fajer, *J Am Chem Soc* **2005**, *127*, 9334–9335.

[156] J. Reichenwallner, M. Chakour, S. Indu, R. Varadarajan, W. E. Trommer, *Appl Magn Reson* **2013**, *44*, 983–995.

[157] A. R. Balo, H. Feyrer, O. P. Ernst, *Biochemistry* **2016**, *55*, 5256–5263.

[158] S. V. Gulla, G. Sharma, P. Borbat, J. H. Freed, H. Ghimire, M. R. Benedikt, N. L. Holt, G. A. Lorigan, K. Rege, C. Mavroidis, D. E. Budil, *J Am Chem Soc* **2009**, *131*, 5374–5375.

[159] G. Jeschke, M. Sajid, M. Schulte, A. Godt, *Phys Chem Chem Phys* **2009**, *11*, 6580–6591.

[160] T. von Hagens, Y. Polyhach, M. Sajid, A. Godt, G. Jeschke, *Phys Chem Chem Phys* **2013**, *15*, 5854–5866.

[161] M. J. N. Junk, H. W. Spiess, D. Hinderberger, *J Magn Reson* **2011**, *210*, 210–217.

[162] C. M. Paleos, P. Dais, *J Chem Soc, Chem Commun* **1977**, 345–346.

[163] D. C. Carter, X. M. He, *Science* **1990**, *249*, 302–303.

[164] X. M. He, D. C. Carter, *Nature* **1992**, *358*, 209–215.

[165] S. Sugio, A. Kashima, S. Mochizuki, M. Noda, K. Kobayashi, *Protein Eng* **1999**, *12*, 439–446.

[166] M. J. N. Junk, Assessing the Functional Structure of Molecular Transporters by EPR Spectroscopy. Ph.D. Thesis, Johannes Gutenberg-Universität Mainz, **2010**.

[167] G. Jeschke, V. Chechik, P. Ionita, A. Godt, H. Zimmermann, J. Banham, C. R. Timmel, D. Hilger, H. Jung, *Appl Magn Reson* **2006**, *30*, 473–498.

[168] E. Krieger, G. Koraimann, G. Vriend, *Proteins Struct Funct Genet* **2002**, *47*, 393–402.

[169] R. B. Fuller, *Synergetics: Explorations in the Geometry of Thinking.* Macmillan Publishing Co., Inc.: New York, **1975**.

[170] F. Karush, *J Am Chem Soc* **1950**, *72*, 2705–2713.

[171] F. Karush, *J Am Chem Soc* **1954**, *76*, 5536–5542.

[172] M. J. N. Junk, H. W. Spiess, D. Hinderberger, *Biophys J* **2011**, *100*, 2293–2301.

[173] P. A. Zunszain, J. Ghuman, T. Komatsu, E. Tsuchida, S. Curry, *BMC Struct Biol* **2003**, *3*, 6.

[174] P. Ascenzi, A. Bocedi, S. Notari, E. Menegatti, M. Fasano, *Biochem Biophys Res Commun* **2005**, *334*, 481–486.
[175] M. Jupin, P. J. Michiels, F. C. Girard, M. Spraul, S. S. Wijmenga, *J Magn Reson* **2013**, *228*, 81–94.
[176] P. Wasserscheid, W. Keim, *Angew Chem Int Ed* **2000**, *39*, 3772–3789.
[177] V. I. Parvulescu, C. Hardacre, *Chem Rev* **2007**, *107*, 2615–2665.
[178] X. Chen, J. Liu, J. Wang, *Anal Methods* **2010**, *2*, 1222–1226.
[179] D. Constantinescu, C. Herrmann, H. Weingärtner, *Phys Chem Chem Phys* **2010**, *12*, 1756–1763.
[180] Y. Shu, M. Liu, S. Chen, X. Chen, J. Wang, *J Phys Chem B* **2011**, *115*, 12306–12314.
[181] E. A. Litus, S. E. Permyakov, V. N. Uversky, E. A. Permyakov, *Cell Biochem Biophys* **2017**, 1–19.
[182] Y. Akdogan, Y. Wu, K. Eisele, M. Schaz, T. Weil, D. Hinderberger, *Soft Matter* **2012**, *8*, 11106–11114.
[183] C. Tanford, *J Am Chem Soc* **1950**, *72*, 441–451.
[184] R. E. Martin, M. Pannier, F. Diederich, V. Gramlich, M. Hubrich, H. W. Spiess, *Angew Chem Int Ed* **1998**, *37*, 2833–2837.
[185] M. Pannier, S. Veit, A. Godt, G. Jeschke, H. W. Spiess, *J Magn Reson* **2000**, *142*, 331–340.
[186] J. Reichenwallner, D. Hinderberger, *Biochim Biophys Acta, Gen Subj* **2013**, *1830*, 5382–5393.

Chapter 4

[1] A. Ben-Naim, *Curr Opin Struct Biol* **1994**, *4*, 264–268.
[2] J. G. Kirkwood, *J Polym Sci, Part B: Polym Phys* **1954**, *12*, 1–14.
[3] W. Kauzmann, *Adv Protein Chem* **1959**, *14*, 1–63.
[4] A. Ben-Naim, A. M. Navarro, J. M. Leal, *Phys Chem Chem Phys* **2008**, *10*, 2451–2460.
[5] A. Cooper, *Proc Natl Acad Sci USA* **1976**, *73*, 2740–2741.
[6] K. Lum, D. Chandler, J. D. Weeks, *J Phys Chem B* **1999**, *103*, 4570–4577.
[7] A. Ben-Naim, *J Chem Phys* **2006**, *125*, 024901.
[8] A. Ben-Naim, *J Chem Phys* **2008**, *129*, 104506.
[9] N. V. Nucci, M. S. Pometun, A. J. Wand, *Nat Struct Mol Biol* **2011**, *18*, 245–250.
[10] A. J. Patel, P. Varilly, S. N. Jamadagni, M. F. Hagan, D. Chandler, S. Garde, *J Phys Chem B* **2012**, *116*, 2498–2503.
[11] C. Tanford, J. G. Buzzell, *J Phys Chem* **1956**, *60*, 225–231.
[12] M. L. Ferrer, R. Duchowicz, B. Carrasco, J. G. de la Torre, A. U. Acuna, *Biophys J* **2001**, *80*, 2422–2430.
[13] D. B. Heidorn, J. Trewhella, *Biochemistry* **1988**, *27*, 909–915.
[14] V. D. Trivedi, I. Saxena, M. U. Siddiqui, M. A. Qasim, *Biochem Mol Biol Int* **1997**, *43*, 1–8.
[15] M. J. N. Junk, H. W. Spiess, D. Hinderberger, *Angew Chem Int Ed* **2010**, *49*, 8755–8759.
[16] Y. Akdogan, M. J. N. Junk, D. Hinderberger, *Biomacromolecules* **2011**, *12*, 1072–1079.
[17] M. J. N. Junk, H. W. Spiess, D. Hinderberger, *J Magn Reson* **2011**, *210*, 210–217.
[18] Y. Akdogan, D. Hinderberger, *J Phys Chem B* **2011**, *115*, 15422–15429.
[19] M. J. N. Junk, H. W. Spiess, D. Hinderberger, *Biophys J* **2011**, *100*, 2293–2301.
[20] H. Chen, M. Deere, J. T. Hecht, J. Lawler, *J Biol Chem* **2000**, *275*, 26538–26544.
[21] S. Watkins, Y. Sakamoto, J. Madison, E. Davis, D. G. Smith, J. Dwulet, F. W. Putnam, *Proc Natl Acad Sci USA* **1993**, *90*, 2409–2413.
[22] R. G. Efremov, A. O. Chugunov, T. V. Pyrkov, J. P. Priestle, A. S. Arseniev, E. Jacoby, *Curr Med Chem* **2007**, *14*, 393–415.
[23] A. A. Polyansky, B. Zagrovic, *J Phys Chem Lett* **2012**, *3*, 973–976.
[24] A. A. Bhattacharya, T. Grüne, S. Curry, *J Mol Biol* **2000**, *303*, 721–732.
[25] G. Jeschke, M. Sajid, M. Schulte, A. Godt, *Phys Chem Chem Phys* **2009**, *11*, 6580–6591.
[26] T. G. Gantchev, M. B. Shopova, *Biochim Biophys Acta, Protein Struct Mol Enzymol* **1990**, *1037*, 422–434.
[27] K. A. Majorek, P. J. Porebski, A. Dayal, M. D. Zimmerman, K. Jablonska, A. J. Stewart, M. Chruszcz, W. Minor, *Mol Immunol* **2012**, *52*, 174–182.
[28] S. Sugio, A. Kashima, S. Mochizuki, M. Noda, K. Kobayashi, *Protein Eng* **1999**, *12*, 439–446.
[29] A. S. Konagurthu, J. C. Whisstock, P. J. Stuckey, A. M. Lesk, *Proteins Struct Funct Bioinf* **2006**, *64*, 559–574.
[30] D. M. Huang, D. Chandler, *Proc Natl Acad Sci USA* **2000**, *97*, 8324–8327.
[31] D. M. Engelman, T. A. Steitz, A. Goldman, *Ann Rev Biophys Biophys Chem* **1986**, *15*, 321–353.
[32] D. Eisenberg, E. Schwarz, M. Komaromy, R. Wall, *J Mol Biol* **1984**, *179*, 125–142.
[33] H. Naderi-Manesh, M. Sadeghi, S. Arab, A. A. M. Movahedi, *Proteins Struct Funct Genet* **2001**, *42*, 452–459.
[34] J. Kyte, R. F. Doolittle, *J Mol Biol* **1982**, *157*, 105–132.
[35] S. Kawashima, H. Ogata, M. Kanehisa, *Nucleic Acids Res* **1999**, *27*, 368–369.
[36] S. Kawashima, M. Kanehisa, *Nucleic Acids Res* **2000**, *28*, 374.

[37]   AAindex database Home Page. http://www.genome.jp/aaindex/ (accessed July, 2012)
[38]   D. L. Nelson, M. M. Cox, A. L. Lehninger, *Biochemie*. Springer-Verlag: Berlin, **2009**.
[39]   M. Billeter, R. Riek, G. Wider, S. Hornemann, R. Glockshuber, K. Wüthrich, *Proc Natl Acad Sci USA* **1997**, *94*, 7281–7285.
[40]   J. R. Simard, P. A. Zunszain, C. E. Ha, J. S. Yang, N. V. Baghavan, I. Petitpas, S. Curry, J. A. Hamilton, *Proc Natl Acad Sci USA* **2005**, *102*, 17958–17963.
[41]   W. Kabsch, C. Sander, *Proc Natl Acad Sci USA* **1984**, *81*, 1075–1078.
[42]   W. L. Hubbell, C. Altenbach, *Curr Opin Struct Biol* **1994**, *4*, 566–573.
[43]   H. J. Steinhoff, *Front Biosci* **2002**, *7*, c97–110.
[44]   M. Kim, Q. Xu, D. Murray, D. S. Cafiso, *Biochemistry* **2008**, *47*, 670–679.
[45]   M. S. Marlow, J. Dogan, K. K. Frederick, K. G. Valentine, A. J. Wand, *Nat Chem Biol* **2010**, *6*, 352–358.
[46]   J. M. Berg, J. L. Tymoczko, L. Stryer, *Biochemie*. Spektrum Akademischer Verlag: Heidelberg, **2007**.
[47]   C. Sander, R. Schneider, *Proteins Struct Funct Genet* **1991**, *9*, 56–68.
[48]   D. R. Booth, M. Sunde, V. Bellotti, C. V. Robinson, W. L. Hutchinson, P. E. Fraser, P. N. Hawkins, C. M. Dobson, S. E. Radford, C. C. F. Blake, M. B. Pepys, *Nature* **1997**, *385*, 787–793.
[49]   H. Inouye, J. Bond, M. A. Baldwin, H. L. Ball, S. B. Prusiner, D. A. Kirschner, *J Mol Biol* **2000**, *300*, 1283–1296.
[50]   C. M. Dobson, *Nature* **2003**, *426*, 884–890.
[51]   W. Scheider, *J Phys Chem* **1980**, *84*, 925–928.
[52]   P. W. Atkins, *Physikalische Chemie*. Wiley VCH: Weinheim, **2001**.
[53]   A. Cooper, *Biophys Chem* **2005**, *115*, 89–97.
[54]   M. J. N. Junk, Assessing the Functional Structure of Molecular Transporters by EPR Spectroscopy. Ph.D. Thesis, Johannes Gutenberg-Universität Mainz, **2010**.
[55]   R. E. Martin, M. Pannier, F. Diederich, V. Gramlich, M. Hubrich, H. W. Spiess, *Angew Chem Int Ed* **1998**, *37*, 2834–2837.
[56]   M. Pannier, S. Veit, A. Godt, G. Jeschke, H. W. Spiess, *J Magn Reson* **2000**, *142*, 331–340.
[57]   G. Jeschke, V. Chechik, P. Ionita, A. Godt, H. Zimmermann, J. Banham, C. R. Timmel, D. Hilger, H. Jung, *Appl Magn Reson* **2006**, *30*, 473–498.
[58]   E. Krieger, G. Koraimann, G. Vriend, *Proteins Struct Funct Genet* **2002**, *47*, 393–402.

Chapter 5

[1]   T. Peters Jr., *All about Albumin: Biochemistry, Genetics and Medical Applications*. Academic Press, Inc.: San Diego, **1995**.
[2]   S. Ringer, *J Physiol* **1882**, *3*, 380–393.
[3]   S. Ringer, *J Physiol* **1885**, *6*, 361–381.
[4]   R. Klinke, S. Silbernagl, *Lehrbuch der Physiologie*. Georg Thieme Verlag: Stuttgart, **1996**.
[5]   R. Dulbecco, M. Vogt, *J Exp Med* **1954**, *99*, 167–182.
[6]   Z. Adamczyk, A. Bratek, B. Jachimska, T. Jasinski, P. Warszynski, *J Phys Chem B* **2006**, *110*, 22426–22435.
[7]   C. Tanford, J. G. Buzzell, *J Phys Chem* **1956**, *60*, 225–231.
[8]   C. Tanford, J. G. Kirkwood, *J Am Chem Soc* **1957**, *79*, 5333–5339.
[9]   G. S. Manning, *Acc Chem Res* **1979**, *12*, 443–449.
[10]   V. V. Khramtsov, D. Marsh, L. Weiner, V. A. Reznikov, *Biochim Biophys Acta, Biomembr* **1992**, *1104*, 317–324.
[11]   G. Lamm, G. R. Pack, *Biopolymers* **2010**, *93*, 619–639.
[12]   O. H. Lowry, N. J. Rosebrough, A. L. Farr, R. J. Randall, *J Biol Chem* **1951**, *193*, 265–275.
[13]   P. K. Smith, R. I. Krohn, G. T. Hermanson, A. K. Mallia, F. H. Gartner, M. D. Provenzano, E. K. Fujimoto, N. M. Goeke, B. J. Olson, D. C. Klenk, *Anal Biochem* **1985**, *150*, 76–85.
[14]   M. M. Bradford, *Anal Biochem* **1976**, *72*, 248–254.
[15]   B. J. S. C. Olson, J. Markwell, *Curr Protoc Protein Sci* **2007**, Unit 3.4, 1–29.
[16]   K. J. Wiechelman, R. D. Braun, J. D. Fitzpatrick, *Anal Biochem* **1988**, *175*, 231–237.
[17]   C. Tanford, *Physical Chemistry of Macromolecules*. John Wiley & Sons, Inc.: New York, **1961**.
[18]   C. Chafer-Pericas, A. Balaguer, A. Maquieira, R. Puchades, *Anal Biochem* **2013**, *432*, 31–37.
[19]   A. Einstein, *Ann Phys* **1906**, *324*, 289–306.
[20]   A. Polson, *Kolloid Z* **1939**, *88*, 51–61.
[21]   J. W. Mehl, J. L. Oncley, R. Simha, *Science* **1940**, *92*, 132–133.
[22]   J. T. Yang, J. F. Foster, *J Am Chem Soc* **1954**, *76*, 1588–1595.
[23]   R. Simha, *J Phys Chem* **1940**, *44*, 25–34.
[24]   G. Strobl, *The Physics of Polymers: Concepts for Understanding Their Structures and Behavior*. Springer-Verlag: Berlin, Heidelberg, **2007**.

[25] G. B. Jeffery, *Proc R Soc London, Ser A* **1922**, *102*, 161–179.
[26] H. A. Scheraga, *J Chem Phys* **1955**, *23*, 1526–1532.
[27] H. A. Scheraga, L. Mandelkern, *J Am Chem Soc* **1953**, *75*, 179–184.
[28] K. A. Majorek, P. J. Porebski, A. Dayal, M. D. Zimmerman, K. Jablonska, A. J. Stewart, M. Chruszcz, W. Minor, *Mol Immunol* **2012**, *52*, 174–182.
[29] E. W. Lemmon, Thermophysical properties of water and steam. In *CRC Handbook of Chemistry and Physics*; W. M. Haynes, D. R. Lide, T. J. Bruno, Eds.; CRC Press: Boca Raton, FL, **2014**, Vol. 95, p 6–1.
[30] M. L. Sheely, *J Ind Eng Chem* **1932**, *24*, 1060–1064.
[31] R. C. Perkins Jr., N. Abumrad, K. Balasubramanian, L. R. Dalton, A. H. Beth, J. H. Park, C. R. Park, *Biochemistry* **1982**, *21*, 4059–4064.
[32] M. Ge, S. B. Rananavare, J. H. Freed, *Biochim Biophys Acta, Gen Subj* **1990**, *1036*, 228–236.
[33] T. G. Gantchev, M. B. Shopova, *Biochim Biophys Acta, Protein Struct Mol Enzymol* **1990**, *1037*, 422–434.
[34] P. D. Ross, A. Shrake, *J Biol Chem* **1988**, *263*, 11196–11202.
[35] A. Shrake, P. D. Ross, *J Biol Chem* **1988**, *263*, 15392–15399.
[36] D. P. Cistola, J. A. Hamilton, D. Jackson, D. M. Small, *Biochemistry* **1988**, *27*, 1881–1888.
[37] S. J. Rehfeld, D. J. Eatough, W. Z. Plachy, *J Lipid Res* **1978**, *19*, 841–849.
[38] A. A. Bhattacharya, T. Grüne, S. Curry, *J Mol Biol* **2000**, *303*, 721–732.
[39] Y. N. Molin, K. M. Salikhov, K. I. Zamaraev, *Spin exchange: Principles and applications in chemistry and biology*. Springer-Verlag: Berlin, Heidelberg, **1980**.
[40] M. Fasano, S. Curry, E. Terreno, M. Galliano, G. Fanali, P. Narciso, S. Notari, P. Ascenzi, *IUBMB Life* **2005**, *57*, 787–796.
[41] H. J. Steinhoff, *Biol Chem* **2004**, *385*, 913–920.
[42] D. Hilger, H. Jung, E. Padan, C. Wegener, K. P. Vogel, H. J. Steinhoff, G. Jeschke, *Biophys J* **2005**, *89*, 1328–1338.
[43] K. Sale, L. Song, Y. S. Liu, E. Perozo, P. Fajer, *J Am Chem Soc* **2005**, *127*, 9334–9335.
[44] G. E. Fanucci, D. S. Cafiso, *Curr Opin Struct Biol* **2006**, *16*, 644–653.
[45] G. Jeschke, G. Panek, A. Godt, A. Bender, H. Paulsen, *Appl Magn Reson* **2004**, *26*, 223–244.
[46] A. Godt, M. Schulte, H. Zimmermann, G. Jeschke, *Angew Chem Int Ed* **2006**, *118*, 7722–7726.
[47] A. D. Milov, Y. D. Tsvetkov, *Appl Magn Reson* **1997**, *12*, 495–504.
[48] J. E. Banham, C. M. Baker, S. Ceola, I. J. Day, G. H. Grant, E. J. J. Groenen, C. T. Rodgers, G. Jeschke, C. R. Timmel, *J Magn Reson* **2008**, *191*, 202–218.
[49] G. Jeschke, *ChemPhysChem* **2002**, *3*, 927–932.
[50] G. Jeschke, A. Koch, U. Jonas, A. Godt, *J Magn Reson* **2002**, *155*, 72–82.
[51] G. Jeschke, Y. Polyhach, *Phys Chem Chem Phys* **2007**, *9*, 1895–1910.
[52] G. Jeschke, *Annu Rev Phys Chem* **2012**, *63*, 419–446.
[53] G. Jeschke, V. Chechik, P. Ionita, A. Godt, H. Zimmermann, J. Banham, C. R. Timmel, D. Hilger, H. Jung, *Appl Magn Reson* **2006**, *30*, 473–498.
[54] M. J. N. Junk, H. W. Spiess, D. Hinderberger, *J Magn Reson* **2011**, *210*, 210–217.
[55] S. Brandon, A. H. Beth, E. J. Hustedt, *J Magn Reson* **2012**, *218*, 93–104.
[56] D. R. Kattnig, J. Reichenwallner, D. Hinderberger, *J Phys Chem B* **2013**, *117*, 16542–16557.
[57] Y. E. Kutsovsky, A. G. Mariasov, Y. I. Aristov, V. N. Parmon, *React Kinet Catal Lett* **1990**, *42*, 19–24.
[58] A. D. Milov, A. G. Maryasov, Y. D. Tsvetkov, *Appl Magn Reson* **1998**, *15*, 107–143.
[59] O. U. Uche, F. H. Stillinger, S. Torquato, *Physica A* **2006**, *360*, 21–36.
[60] J. K. Percus, G. J. Yevick, *Phys Rev* **1958**, *110*, 1–13.
[61] D. Henderson, *Condens Matter Phys* **2009**, *12*, 127–135.
[62] M. A. Kiselev, I. A. Gryzunov, G. E. Dobretsov, M. N. Komarova, *Biofizika* **2001**, *46*, 423–427.
[63] J. L. Baber, J. M. Louis, G. M. Clore, *Angew Chem Int Ed* **2015**, *54*, 5336–5339.
[64] M. J. N. Junk, H. W. Spiess, D. Hinderberger, *Angew Chem Int Ed* **2010**, *49*, 8755–8759.
[65] G. Jeschke. *DeerAnalysis2011*. User manual: Zürich, Switzerland, March **2012**.
[66] P. G. Fajer, L. Brown, L. Song, Practical pulsed dipolar ESR (DEER). In *ESR spectroscopy in membrane biophysics*; M. A. Hemminga, L. J. Berliner, Eds.; Springer Science+Business Media, LLC: New York, **2007**, Vol. 27, pp 95–128.
[67] G. Jeschke, M. Sajid, M. Schulte, N. Ramezanian, A. Volkov, H. Zimmermann, A. Godt, *J Am Chem Soc* **2010**, *132*, 10107–10117.
[68] P. Schöps, J. Plackmeyer, A. Marko, *J Magn Reson* **2016**, *269*, 70–77.
[69] M. R. Cannon, R. E. Manning, J. D. Bell, *Anal Chem* **1960**, *32*, 355–358.
[70] T. Mezger, *Das Rheologie-Handbuch: Für Anwender von Rotations- und Oszillations-Rheometern*. Curt R. Vincentz Verlag: Hannover, **2000**.
[71] F. He, G. W. Becker, J. R. Litowski, L. O. Narhi, D. N. Brems, V. I. Razinkov, *Anal Biochem* **2010**, *399*, 141–143.

[72]   M. Wagner, K. Reiche, A. Blume, P. Garidel, *Pharm Dev Technol* **2013**, *18*, 963–970.
[73]   E. Krieger, G. Koraimann, G. Vriend, *Proteins Struct Funct Genet* **2002**, *47*, 393–402.
[74]   R. E. Martin, M. Pannier, F. Diederich, V. Gramlich, M. Hubrich, H. W. Spiess, *Angew Chem Int Ed* **1998**, *37*, 2833–2837.
[75]   M. Pannier, S. Veit, A. Godt, G. Jeschke, H. W. Spiess, *J Magn Reson* **2000**, *142*, 331–340.

Chapter 6

[1]   T. Peters Jr., *All about Albumin: Biochemistry, Genetics and Medical Applications*. Academic Press, Inc.: San Diego, **1995**.
[2]   M. Chruszcz, K. Mikolajczak, N. Mank, K. A. Majorek, P. J. Porebski, W. Minor, *Biochim Biophys Acta, Gen Subj* **2013**, *1830*, 5375–5381.
[3]   S. Watkins, Y. Sakamoto, J. Madison, E. Davis, D. G. Smith, J. Dwulet, F. W. Putnam, *Proc Natl Acad Sci USA*, **1993**, *90*, 2409–2413.
[4]   G. Fanali, P. Ascenzi, G. Bernardi, M. Fasano, *J Biomol Struct Dyn* **2012**, *29*, 1195–1205.
[5]   M. J. N. Junk, H. W. Spiess, D. Hinderberger, *Angew Chem Int Ed* **2010**, *49*, 8755–8759.
[6]   Universal Protein Resource Home Page. http://www.uniprot.org (accessed March, 2017).
[7]   S. F. Altschul, T. L. Madden, A. A. Schäffer, J. Zhang, Z. Zhang, W. Miller, D. J. Lipman, *Nucleic Acids Res* **1997**, *25*, 3389–3402.
[8]   S. F. Altschul, J. C. Wootton, E. M. Gertz, R. Agarwala, A. Morgulis, A. A. Schäffer, Y. K. Yu, *FEBS J* **2005**, *272*, 5101–5109.
[9]   Basic Local Alignment Search Tool Home Page. https://blast.ncbi.nlm.nih.gov/Blast.cgi (accessed March, 2017)
[10]   Science Gateway Home Page. http://www.sciencegateway.org/tools/proteinmw.htm (accessed March, 2017)
[11]   K. Oettl, G. Marsche, *Methods Enzymol* **2010**, *474*, 181–195.
[12]   G. Paris, S. Kraszewski, C. Ramseyer, M. Enescu, *Biopolymers* **2012**, *97*, 889–898.
[13]   M. Anraku, V. T. G. Chuang, T. Maruyama, M. Otagiri, *Biochim Biophys Acta, Gen Subj* **2013**, *1830*, 5465–5472.
[14]   J. Bonanata, L. Turell, L. Antmann, G. Ferrer-Sueta, S. Botasini, E. Mendez, B. Alvarez, E. L. Coitino, *Free Radical Biol Med* **2017**, *108*, 952–962.
[15]   Public Domain Vectors Home Page. https://publicdomainvectors.org (accessed March 12, 2017).
[16]   Y. Akdogan, J. Reichenwallner, D. Hinderberger, *PLoS One* **2012**, *7*, e45681.
[17]   D. Hilger, H. Jung, E. Padan, C. Wegener, K. P. Vogel, H. J. Steinhoff, G. Jeschke, *Biophys J* **2005**, *89*, 1328–1338.
[18]   S. Milikisiyants, S. Wang, R. A. Munro, M. Donohue, M. E. Ward, D. Bolton, L. S. Brown, T. I. Smirnova, V. Ladizhansky, A. I. Smirnov, *J Mol Biol* **2017**, *429*, 1903–1920.
[19]   D. R. Kattnig, J. Reichenwallner, D. Hinderberger, *J Phys Chem B* **2013**, *117*, 16542–16557.
[20]   J. A. Hamilton, D. P. Cistola, J. D. Morriset, J. T. Sparrow, D. M. Small, *Proc Natl Acad Sci USA* **1984**, *81*, 3718–3722.
[21]   D. P. Cistola, D. M. Small, J. A. Hamilton, *J Biol Chem* **1987**, *262*, 10971–10979.
[22]   M. J. N. Junk, Assessing the Functional Structure of Molecular Transporters by EPR Spectroscopy. Ph.D. Thesis, Johannes Gutenberg-Universität Mainz, **2010**.
[23]   G. Jeschke, *Annu Rev Phys Chem* **2012**, *63*, 419–446.
[24]   A. A. Bhattacharya, T. Grüne, S. Curry, *J Mol Biol* **2000**, *303*, 721–732.
[25]   A. Bujacz, J. A. Talaj, A. J. Pietrzyk. http://www.rcsb.org/pdb/explore/explore.do?structureId=4LUF (accessed Oct 16, 2017).
[26]   S. Sugio, A. Kashima, S. Mochizuki, M. Noda, K. Kobayashi, *Protein Eng* **1999**, *12*, 439–446.
[27]   K. A. Majorek, P. J. Porebski, A. Dayal, M. D. Zimmerman, K. Jablonska, A. J. Stewart, M. Chruszcz, W. Minor, *Mol Immunol* **2012**, *52*, 174–182.
[28]   A. S. Konagurthu, J. C. Whisstock, P. J. Stuckey, A. M. Lesk, *Proteins Struct Funct Bioinf* **2006**, *64*, 559–574.
[29]   K. Alba, R. J. Bingham, V. Kontogiorgos, *Biopolymers* **2017**, *107*, e23016.
[30]   B. Jachimska, M. Wasilewska, Z. Adamczyk, *Langmuir* **2008**, *24*, 6866–6872.
[31]   B. Jachimska, A. Pajor, *Bioelectrochemistry* **2012**, *87*, 138–146.
[32]   F. Karush, *J Am Chem Soc* **1950**, *72*, 2705–2713.
[33]   F. Karush, *J Am Chem Soc* **1954**, *76*, 5536–5542.
[34]   E. A. Litus, S. E. Permyakov, V. N. Uversky, E. A. Permyakov, *Cell Biochem Biophys* **2017**, 1–19.
[35]   T. G. Gantchev, M. B. Shopova, *Biochim Biophys Acta, Protein Struct Mol Enzymol* **1990**, *1037*, 422–434.
[36]   J. D. Ashbrook, A. A. Spector, E. C. Santos, J. E. Fletcher, *J Biol Chem* **1975**, *250*, 2333–2338.
[37]   M. J. N. Junk, H. W. Spiess, D. Hinderberger, *J Magn Reson* **2011**, *210*, 210–217.

[38] R. Dulbecco, M. Vogt, *J Exp Med* **1954**, *99*, 167–182.
[39] E. Krieger, G. Koraimann, G. Vriend, *Proteins Struct Funct Genet* **2002**, *47*, 393–402.
[40] R. E. Martin, M. Pannier, F. Diederich, V. Gramlich, M. Hubrich, H. W. Spiess, *Angew Chem Int Ed* **1998**, *37*, 2833–2837.
[41] M. Pannier, S. Veit, A. Godt, G. Jeschke, H. W. Spiess, *J Magn Reson* **2000**, *142*, 331–340.
[42] G. Jeschke, V. Chechik, P. Ionita, A. Godt, H. Zimmermann, J. Banham, C. R. Timmel, D. Hilger, H. Jung, *Appl Magn Reson* **2006**, *30*, 473–498.
[43] U. K. Laemmli, *Nature* **1970**, *227*, 680–685.

Chapter 7

[1] V. Pejaver, W. L. Hsu, F. Xin, A. K. Dunker, V. N. Uversky, P. Radivojac, *Protein Sci* **2014**, *23*, 1077–1093.
[2] T. Peters Jr, *All about Albumin: Biochemistry, Genetics and Medical Applications*. Academic Press, Inc.: San Diego **1995**.
[3] E. A. Litus, S. E. Permyakov, V. N. Uversky, E. A. Permyakov, *Cell Biochem Biophys* **2017**, 1–19.
[4] J. M. Berg, J. L. Tymoczko, L. Stryer, *Biochemie*. Spektrum Akademischer Verlag: Heidelberg, **2007**.
[5] M. Hochstrasser, *Nature* **2009**, *458*, 422–429.
[6] B. D. Strahl, C. D. Allis, *Nature* **2000**, *403*, 41–45.
[7] J. F. Day, S. R. Thorpe, J. W. Baynes, *J Biol Chem* **1979**, *254*, 595–597.
[8] R. Dolhofer, O. H. Wieland, *FEBS Lett* **1979**, *103*, 282–286.
[9] D. Hawkins, R. N. Pinckard, R. S. Farr, *Science* **1968**, *160*, 780–781.
[10] G. E. Means, M. L. Bender, *Biochemistry* **1975**, *14*, 4989–4994.
[11] K. Oettl, R. E. Stauber, *Br J Pharmacol* **2007**, *151*, 580–590.
[12] K. Oettl, G. Marsche, *Methods Enzymol* **2010**, *474*, 181–195.
[13] M. Anraku, V. T. G. Chuang, T. Maruyama, M. Otagiri, *Biochim Biophys Acta, Gen Subj* **2013**, *1830*, 5465–5472.
[14] J. Bonanata, L. Turell, L. Antmann, G. Ferrer-Sueta, S. Botasini, E. Mendez, B. Alvarez, E. L. Coitino, *Free Radical Biol Med* **2017**, *108*, 952–962.
[15] P. Thordarson, B. Le Droumaguet, K. Velonia, *Appl Microbiol Biotechnol* **2006**, *73*, 243–254.
[16] M. A. Gauthier, H. A. Klok, *Chem Commun* **2008**, 2591–2611.
[17] S. Ko, S. Gunasekaran, *J Microencapsulation* **2006**, *23*, 887–898.
[18] C. Wa, R. L. Cerny, W. A. Clarke, D. S. Hage, *Clin Chim Acta* **2007**, *385*, 48–60.
[19] A. Abuchowski, T. van Es, N. C. Palczuk, F. F. Davis, *J Biol Chem* **1977**, *252*, 3578–3581.
[20] E. M. D'Urso, G. Fortier, *Biotechnol Tech* **1994**, *8*, 71–76.
[21] F. Wurm, T. Steinbach, H. A. Klok, *Chem Commun* **2013**, *49*, 7815–7817.
[22] T. J. Stone, T. Buckman, P. L. Nordio, H. M. McConnell, *Proc Natl Acad Sci USA* **1965**, *54*, 1010–1017.
[23] O. H. Griffith, H. M. McConnell, *Proc Natl Acad Sci USA* **1966**, *55*, 8–11.
[24] D. Wallach, *J Chem Phys* **1967**, *47*, 5258–5268.
[25] R. M. Broyer, G. N. Grover, H. D. Maynard, *Chem Commun* **2011**, *47*, 2212–2226.
[26] M. A. Gauthier, H. A. Klok, *Polym Chem* **2010**, *1*, 1352–1373.
[27] F. E. Kendall, *J Biol Chem* **1941**, *138*, 97–109.
[28] D. S. Goodman, *J Am Chem Soc* **1958**, *80*, 3892–3898.
[29] A. D. Keith, A. S. Waggoner, O. H. Griffith, *Proc Natl Acad Sci USA* **1968**, *61*, 819–826.
[30] O. H. Griffith, A. S. Waggoner, *Acc Chem Res* **1969**, *2*, 17–24.
[31] A. S. Waggoner, T. J. Kingzett, S. Rottschaeffer, O. H. Griffith, *Chem Phys Lipids* **1969**, *3*, 245–253.
[32] B. J. Gaffney, H. M. McConnell, *J Magn Reson* **1974**, *16*, 1–28.
[33] J. D. Morrisett, H. J. Pownall, A. M. Gotto, *J Biol Chem* **1975**, *250*, 2487–2494.
[34] J. Reichenwallner, D. Hinderberger, *Biochim Biophys Acta, Gen Subj* **2013**, *1830*, 5382–5393.
[35] Y. Akdogan, Y. Wu, K. Eisele, M. Schaz, T. Weil, D. Hinderberger, *Soft Matter* **2012**, *8*, 11106–11114.
[36] S. L. Kuan, B. Stöckle, J. Reichenwallner, D. Y. W. Ng, Y. Wu, M. Doroshenko, K. Koynov, D. Hinderberger, K. Müllen, T. Weil, *Biomacromolecules* **2013**, *14*, 367–376.
[37] F. Karush, *J Am Chem Soc* **1950**, *72*, 2705–2713.
[38] F. Karush, *J Am Chem Soc* **1954**, *76*, 5536–5542.
[39] D. A. Windrem, W. Z. Plachy, *Biochim Biophys Acta, Biomembr* **1980**, *600*, 655–665.
[40] S. J. Rehfeld, D. J. Eatough, W. Z. Plachy, *J Lipid Res* **1978**, *19*, 841–849.
[41] A. A. Bhattacharya, T. Grüne, S. Curry, *J Mol Biol* **2000**, *303*, 721–732.
[42] M. J. N. Junk, H. W. Spiess, D. Hinderberger, *Angew Chem Int Ed* **2010**, *49*, 8755–8759.
[43] Y. Akdogan, J. Reichenwallner, D. Hinderberger, *PLoS One* **2012**, *7*, e45681.
[44] D. A. Tomalia, H. Baker, J. Dewald, M. Hall, G. Kallos, S. Martin, J. Roeck, J. Ryder, P. Smith, *Polym J* **1985**, *17*, 117–132.

[45]   A. K. Patri, A. Myc, J. Beals, T. P. Thomas, N. H. Bander, J. R. Baker, Jr., *Bioconjugate Chem* **2004**, *15*, 1174–1181.

[46]   I. van Baal, H. Malda, S. A. Synowski, J. L. J. van Dongen, T. M. Hackeng, M. Merkx, E. W. Meijer, *Angew Chem Int Ed* **2005**, *44*, 5052–5057.

[47]   X. Wang, R. Inapagolla, S. Kannan, M. Lieh-Lai, R. M. Kannan, *Bioconjugate Chem* **2007**, *18*, 791–799.

[48]   M. A. Kostiainen, J. Kotimaa, M. L. Laukkanen, G. M. Pavan, *Chem Eur J* **2010**, *16*, 6912–6918.

[49]   M. A. Kostiainen, G. R. Szilvay, J. Lehtinen, D. K. Smith, M. B. Linder, A. Urtti, O. Ikkala, *ACS Nano* **2007**, *1*, 103–113.

[50]   G. Bansal, J. E. I. Wright, C. Kucharski, H. Uludag, *Angew Chem Int Ed* **2005**, *44*, 3710–3714.

[51]   W. Ke, Y. Zhao, R. Huang, C. Jiang, Y. Pei, *J Pharm Sci* **2008**, *97*, 2208–2216.

[52]   H. L. Crampton, E. E. Simanek, *Polym Int* **2007**, *56*, 489–496.

[53]   A. D'Emanuele, D. Attwood, *Adv Drug Delivery Rev* **2005**, *57*, 2147–2162.

[54]   J. C. Roberts, M. K. Bhalgat, R. T. Zera, *J Biomed Mater Res* **1996**, *30*, 53–65.

[55]   N. Malik, R. Wiwattanapatapee, R. Klopsch, K. Lorenz, H. Frey, J. W. Weener, E. W. Meijer, W. Paulus, R. Duncan, *J Controlled Release* **2000**, *65*, 133–148.

[56]   S. Parimi, T. J. Barnes, D. F. Callen, C. A. Prestidge, *Biomacromolecules* **2010**, *11*, 382–389.

[57]   L. Albertazzi, M. Serresi, A. Albanese, F. Beltram, *Mol Pharmaceutics* **2010**, *7*, 680–688.

[58]   K. Jain, P. Kesharwani, U. Gupta, N. K. Jain, *Int J Pharm* **2010**, *394*, 122–142.

[59]   R. Duncan, L. Izzo, *Adv Drug Delivery Rev* **2005**, *57*, 2215–2237.

[60]   E. Froehlich, J. S. Mandeville, C. J. Jennings, R. Sedaghat-Herati, H. A. Tajmir-Riahi, *J Phys Chem B* **2009**, *113*, 6986–6993.

[61]   J. W. Lee, J. H. Kim, H. J. Kim, S. C. Han, J. H. Kim, W. S. Shin, S. H. Jin, *Bioconjugate Chem* **2007**, *18*, 579–584.

[62]   E. D. Goddard-Borger, R. V. Stick, *Org Lett* **2007**, *9*, 3797–3800.

[63]   S. F. M. van Dongen, R. L. M. Teeuwen, M. Nallani, S. S. van Berkel, J. J. L. M. Cornelissen, R. J. M. Nolte, J. C. M. van Hest, *Bioconjugate Chem* **2009**, *20*, 20–23.

[64]   D. W. Nicholson, N. A. Thornberry, *Trends Biochem Sci* **1997**, *22*, 299–306.

[65]   R. U. Jänicke, M. L. Sprengart, M. R. Wati, A. G. Porter, *J Biol Chem* **1998**, *273*, 9357–9360.

[66]   R. H. Blum, S. K. Carter, *Ann Intern Med* **1974**, *80*, 249–259.

[67]   S. K. Carter, R. H. Blum, *CA Cancer J Clin* **1974**, *24*, 322–331.

[68]   M. Ge, S. B. Rananavare, J. H. Freed, *Biochim Biophys Acta, Gen Subj* **1990**, *1036*, 228–236.

[69]   R. A. Copeland, *Enzymes: A Practical Introduction to Structure, Mechanism, and Data Analysis.* Wiley-VCH: New York, **2000**.

[70]   S. I. F. S. Martins, W. M. F. Jongens, M. A. J. S. van Boekel, *Trends Food Sci Technol* **2001**, *11*, 364–373.

[71]   E. H. Ajandouz, A. Puigserver, *J Agric Food Chem* **1999**, *47*, 1786–1793.

[72]   P. J. Thornalley, A. Langborg, H. S. Minhas, *Biochem J* **1999**, *344*, 109–116.

[73]   C. Henning, M. A. Glomb, *Glycoconj J* **2016**, *33*, 499–512.

[74]   J. W. Baynes, S. R. Thorpe, M. H. Murtiashaw, *Methods Enzymol* **1984**, *106*, 88–98.

[75]   D. V. Zyzak, J. M. Richardson, S. R. Thorpe, J. W. Baynes, *Arch Biochem Biophys* **1995**, *316*, 547–554.

[76]   E. Schleicher, O. H. Wieland, *Biochim Biophys Acta, Gen Subj* **1986**, *884*, 199–205.

[77]   A. Lapolla, R. Reitano, R. Seraglia, G. Sartore, E. Ragazzi, P. Traldi, *Mol Nutr Food Res* **2005**, *49*, 685–690.

[78]   S. Agalou, N. Ahmed, P. J. Thornalley, A. Dawnay, *Ann NY Acad Sci* **2005**, *1043*, 734–739.

[79]   D. R. Sell, M. A. Lane, W. A. Johnson, E. J. Masoro, O. B. Mock, K. M. Reiser, J. F. Fogarty, R. G. Cutler, D. K. Ingram, G. S. Roth, V. M. Monnier, *Proc Natl Acad Sci USA* **1996**, *93*, 485–490.

[80]   O. Nedic, S. I. S. Rattan, T. Grune, I. P. Trougakos, *Free Radical Res* **2013**, *47*, 28–38.

[81]   D. R. McCance, D. G. Dyer, J. A. Dunn, K. E. Bailie, S. R. Thorpe, J. W. Baynes, T. J. Lyons, *J Clin Invest* **1993**, *91*, 2470–2478.

[82]   M. P. Vitek, K. Bhattacharya, J. M. Glendening, E. Stopa, H. Vlassara, R. Bucala, K. Manogue, A. Cerami, *Proc Natl Acad Sci USA* **1994**, *91*, 4766–4770.

[83]   M. A. Smith, S. Taneda, P. L. Richey, S. Miyata, S. D. Yan, D. Stern, L. M. Sayre, V. M. Monnier, G. Perry, *Proc Natl Acad Sci* **1994**, *91*, 5710–5714.

[84]   V. M. Monnier, A. Cerami, *Science* **1981**, *211*, 491–493.

[85]   F. Bahmani, S. Z. Bathaie, S. J. Aldavood, A. Ghahghaei, *Molecules* **2016**, *21*, 143.

[86]   H. Vlassara, H. Fuh, Z. Makita, S. Krungkrai, A. Cerami, R. Bucala, *Proc Natl Acad Sci USA* **1992**, *89*, 12043–12047.

[87]   S. Horiuchi, *Trends Cardiovasc Med* **1996**, *6*, 163–168.

[88]   H. Vlassara, M. Brownlee, A. Cerami, *Proc Natl Acad Sci USA* **1985**, *82*, 5588–5592.

[89]   S. Bongarzone, V. Savickas, F. Luzi, A. D. Gee, *J Med Chem* **2017**, *60*, 7213–7232.

[90]   H. Vlassara, Y. M. Li, F. Imani, D. Wojciechowicz, Z. Yang, F. T. Liu, A. Cerami, *Mol Med* **1995**, *1*, 634–646.

[91]   L. J. Sparvero, D. Asafu-Adjei, R. Kang, D. Tang, N. Amin, J. Im, R. Rutledge, B. Liu, A. A. Amoscato, H. J. Zeh, M. T. Lotze, *J Transl Med* **2009**, *7*, 17.

[92]   C. Esposito, H. Gerlach, J. Brett, D. Stern, H. Vlassara, *J Exp Med* **1989**, *170*, 1387–1407.

[93]   R. Salazar, R. Brandt, S. Krantz, *Biochim Biophys Acta, Mol Cell Res* **1995**, *1266*, 57–63.

[94]   R. Salazar, R. Brandt, S. Krantz, *Glycoconj J* **2001**, *18*, 769–777.

[95]   S. Schaarschmidt. Charakterisierung der biologischen und molekularen Eigenschaften von Maillard-modifiziertem Serumalbumin. Diploma Thesis, Martin-Luther-Universität Halle-Wittenberg, **2015**.

[96]   S. C. Kazmierczak, A. Gurachevsky, G. Matthes, V. Muravsky, *Clin Chem* **2006**, *52*, 2129–2134.

[97]   A. Gurachevsky, E. Shimanovitch, T. Gurachevskaya, V. Muravsky, *Biochem Biophys Res Commun* **2007**, *360*, 852–856.

[98]   V. Muravsky, T. Gurachevskaya, S. Berezenko, K. Schnurr, A. Gurachevsky, *Spectrochim Acta, Part A* **2009**, 74, 42–47.

[99]   A. A. Pavicevic, A. D. Popovic-Bijelic, M. D. Mojovic, S. V. Susnjar, G. G. Bacic, *J Phys Chem B* **2014**, *118*, 10898–10905.

[100]   P. Jost, O. H. Griffith, Instrumental aspects of spin labeling. In *Spin Labeling: Theory and Applications*; L. J. Berliner, Ed.; Academic Press: New York, **1976**, Vol. 1, pp 251–272.

[101]   G. Scatchard, *Ann NY Acad Sci* **1949**, *51*, 660–672.

[102]   A. A. Spector, *J Lipid Res* **1975**, *16*, 165–179.

[103]   T. G. Gantchev, M. B. Shopova, *Biochim Biophys Acta, Protein Struct Mol Enzymol* **1990**, *1037*, 422–434.

[104]   H. H. Ruf, M. Gratzl, *Biochim Biophys Acta, Protein Struct* **1976**, *446*, 134–142.

[105]   R. C. Perkins Jr., N. Abumrad, K. Balasubramanian, L. R. Dalton, A. H. Beth, J. H. Park, C. R. Park, *Biochemistry* **1982**, *21*, 4059–4064.

[106]   T. Hauenschild, Spinmarkierung pharmazeutischer Wirkstoffe sowie deren Bindungseigenschaften an Serum Albumin vom Menschen, Diploma Thesis, Johannes Gutenberg-Universität Mainz, **2013**.

[107]   T. Hauenschild, J. Reichenwallner, V. Enkelmann, D. Hinderberger, *Chem Eur J* **2016**, *22*, 12825–12838.

[108]   H. E. Rosenthal, *Anal Biochem* **1967**, *20*, 525–532.

[109]   H. E. Hart, *Bull Math Biophys* **1965**, *27*, 87–98.

[110]   A. A. Schreier, P. R. Schimmel, *J Mol Biol* **1974**, *86*, 601–620.

[111]   J. G. Norby, P. Ottolenghi, J. Jensen, *Anal Biochem* **1980**, *102*, 318–320.

[112]   M. J. Roberts, M. D. Bentley, J. M. Harris, *Adv Drug Delivery Rev* **2012**, *64*, 116–127.

[113]   J. F. Lutz, *J Polym Sci, Part A: Polym Chem* **2008**, *46*, 3459–3470.

[114]   A. L. Sisson, D. Steinhilber, T. Rossow, P. Welker, K. Licha, R. Haag, *Angew Chem Int Ed* **2009**, *48*, 7540–7545.

[115]   J. Khandare, A. Mohr, M. Calderon, P. Welker, K. Licha, R. Haag, *Biomaterials* **2010**, *31*, 4268–4277.

[116]   K. Matyjaszewski, *Macromolecules* **2012**, *45*, 4015–4039.

[117]   K. L. Heredia, D. Bontempo, T. Ly, J. T. Byers, S. Halstenberg, H. D. Maynard, *J Am Chem Soc* **2005**, *127*, 16955–16960.

[118]   D. Bontempo, H. D. Maynard, *J Am Chem Soc* **2005**, *127*, 6508–6509.

[119]   J. Nicolas, V. San Miguel, G. Mantovani, D. M. Haddleton, *Chem Commun* **2006**, 4697–4699.

[120]   B. Le Droumaguet, K. Velonia, *Angew Chem Int Ed* **2008**, *120*, 6359–6362.

[121]   B. Le Droumaguet, J. Nicolas, *Polym Chem* **2010**, *1*, 563–598.

[122]   B. S. Sumerlin, *ACS Macro Lett* **2012**, *1*, 141–145.

[123]   S. Averick, A. Simakova, S. Park, D. Konkolewicz, A. J. D. Magenau, R. A. Mehl, K. Matyjaszewski, *ACS Macro Letters* **2011**, *1*, 6–10.

[124]   D. Konkolewicz, A. J. D. Magenau, S. E. Averick, A. Simakova, H. He, K. Matyjaszewski, *Macromolecules* **2012**, *45*, 4461–4468.

[125]   M. S. Strozyk, M. Chanana, I. Pastoriza-Santos, J. Perez–Juste, L. M. Liz-Marzan, *Adv Funct Mater* **2012**, *22*, 1436–1444.

[126]   H. Charan, J. Kinzel, U. Glebe, D. Anand, T. M. Garakani, L. Zhu, M. Bocola, U. Schwaneberg, A. Böker, *Biomaterials* **2016**, *107*, 115–123.

[127]   C. S. Cummings, K. Fein, H. Murata, R. L. Ball, A. J. Russell, K. A. Whitehead, *J Controlled Release* **2017**, *255*, 270–280.

[128]   T. Steinbach, F. Wurm, H. A. Klok, *Polym Chem* **2014**, *5*, 4039–4047.

[129]   U. K. Laemmli, *Nature* **1970**, *227*, 680–685.

[130]   A. Thomas, Heterofunctional Polyether Building Blocks: From Diverse Macromonomer Structures to Bioinspired Nanoparticle Coatings. Ph.D. Thesis, Johannes Gutenberg-Universität Mainz, **2013**.

[131]   K. A. Majorek, P. J. Porebski, A. Dayal, M. D. Zimmerman, K. Jablonska, A. J. Stewart, M. Chruszcz, W. Minor, *Mol Immunol* **2012**, *52*, 174–182.

[132]   C. Tanford, J. G. Buzzell, *J Phys Chem* **1956**, *60*, 225–231.

[133]   B. Jachimska, M. Wasilewska, Z. Adamczyk, *Langmuir* **2008**, *24*, 6866–6872.

[134]   B. J. Berne, R. Pecora, *Dynamic light scattering – with applications to chemistry, biology, and physics*. Dover Publications, Inc.: New York, **2000**.

[135]   C. Chafer-Pericas, A. Balaguer, A. Maquieira, R. Puchades, *Anal Biochem* **2013**, *432*, 31–37.

[136]   A. Salis, M. Boström, L. Medda, F. Cugia, B. Barse, D. F. Parsons, B. W. Ninham, M. Monduzzi, *Langmuir* **2011**, *27*, 11597–11604.

[137]   S. Salgin, U. Salgin, S. Bahadir, *Int J Electrochem Sci* **2012**, *7*, 12404–12414.

[138]   B. Jachimska, A. Pajor, *Bioelectrochemistry* **2012**, *87*, 138–146.

[139]   E. W. Lemmon, Thermophysical properties of water and steam. In *CRC Handbook of Chemistry and Physics*; W. M. Haynes, D. R. Lide, T. J. Bruno, Eds.; CRC Press: Boca Raton, FL, **2014**, Vol. 95, p 6–1.

[140]   M. L. Sheely, *Ind Eng Chem* **1932**, *24*, 1060–1064.

[141]   R. F. Atmeh, I. M. Arafa, M. Al-Khateeb, *Jordan J Chem* **2007**, *2*, 169–182.

[142]   B. Derjaguin, L. Landau, *Acta Physicochim URSS* **1941**, *14*, 633–662.

[143]   S. Honary, M. Jahanshahi, P. Golbayani, P. Ebrahimi, K. Ghajar, *J Nanosci Nanotechnol* **2010**, *10*, 7752–7757.

[144]   M. Larsson, A. Hill, J. Duffy, *Ann T Nord Rheol Soc* **2012**, *20*, 209–214.

[145]   Z. Adamczyk, A. Bratek, B. Jachimska, T. Jasinski, P. Warszynski, *J Phys Chem B* **2006**, *110*, 22426–22435.

[146]   C. Tanford, S. A. Swanson, W. S. Shore, *J Am Chem Soc* **1955**, *77*, 6414–6421.

[147]   G. S. Manning, *Acc Chem Res* **1979**, *12*, 443–449.

[148]   G. S. Manning, *J Phys Chem B* **2007**, *111*, 8554–8559.

[149]   G. Lamm, G. R. Pack, *Biopolymers* **2010**, *93*, 619–639.

[150]   U. Böhme, U. Scheler, *Chem Phys Lett* **2007**, *435*, 342–345.

[151]   P. R. Bergethon, *The Physical Basis of Biochemistry: The Foundations of Molecular Biophysics*. Springer Science+Business Media, LLC: New York, **2010**.

[152]   W. Demtröder, *Experimentalphysik 2: Elektrizität und Optik*. Springer-Verlag: Berlin, Heidelberg, **2013**.

[153]   C. Tanford, *J Phys Chem* **1955**, *59*, 788–793.

[154]   D. Shoup, A. Szabo, *Biophys J* **1982**, *40*, 33–39.

[155]   O. G. Berg, P. H. von Hippel, *Ann Rev Biophys Biophys Chem* **1985**, *14*, 131–160.

[156]   P. De Meyts, J. Roth, *Biochem Biophys Res Commun* **1975**, *66*, 1118–1126.

[157]   C. Tanford, *Physical Chemistry of Macromolecules*, John Wiley & Sons, Inc.: New York, **1961**.

[158]   I. M. Klotz, G. P. Royer, A. R. Sloniewsky, *Biochemistry* **1969**, *8*, 4752–4756.

[159]   M. I. Stefan, N. Le Novere, *PLoS Comput Biol* **2013**, *9*, e1003106.

[160]   A. A. Spector, K. John, J. E. Fletcher, *J Lipid Res* **1969**, *10*, 56–67.

[161]   A. A. Spector, J. E. Fletcher, J. D. Ashbrook, *Biochemistry* **1971**, *10*, 3229–3232.

[162]   D. P. Cistola, D. M. Small, J. A. Hamilton, *J Biol Chem* **1987**, *262*, 10971–10979.

[163]   M. J. N. Junk, H. W. Spiess, D. Hinderberger, *Biophys J* **2011**, *100*, 2293–2301.

[164]   RCSB Protein Data Base Home Page. http://www.rcsb.org (accessed Mar 1, 2018).

[165]   R. Dulbecco, M. Vogt, *J Exp Med* **1954**, *99*, 167–182.

[166]   R. E. Martin, M. Pannier, F. Diederich, V. Gramlich, M. Hubrich, H. W. Spiess, *Angew Chem Int Ed* **1998**, *37*, 2833–2837.

[167]   M. Pannier, S. Veit, A. Godt, G. Jeschke, H. W. Spiess, *J Magn Reson* **2000**, *142*, 331–340.

[168]   G. Jeschke, *Annu Rev Phys Chem* **2012**, *63*, 419–446.

[169]   S. Stoll, A. Schweiger, *J Magn Reson* **2006**, *178*, 42–55.

[170]   J. H. Freed, Theory of slow tumbling ESR spectra for nitroxides. In *Spin Labeling: Theory and Applications*; L. J. Berliner, Ed.; Academic Press: New York, **1976**, Vol. 1, pp 53–132.

[171]   D. J. Schneider, J. H. Freed, Calculating slow motional magnetic resonance spectra: A user's guide. In *Spin Labeling: Theory and Applications*; L. J. Berliner, J. Reuben, Eds.; Plenum Press: New York, London, **1989**, Vol. 8, pp 1–76.

[172]   G. Jeschke, V. Chechik, P. Ionita, A. Godt, H. Zimmermann, J. Banham, C. R. Timmel, D. Hilger, H. Jung, *Appl Magn Reson* **2006**, *30*, 473–498.

[173]   D. R. Kattnig, J. Reichenwallner, D. Hinderberger, *J Phys Chem B* **2013**, *117*, 16542–16557.

[174]   S. W. Provencher, *Comput Phys Commun* **1982**, *27*, 213–227.

[175]   H. Noack, C. Moitzi, Modulator Monitoring During Measuring Electromobility, U.S. Patent: US 20140144780 A1, May 29, **2014**.

[176]   P. Schiebener, J. Straub, J. M. H. Levelt Sengers, J. S. Gallagher, *J Phys Chem Ref Data* **1990**, *19*, 677–717.

[177]   J. W. Swan, E. M. Furst, *J Colloid Interface Sci* **2012**, *388*, 92–94.

Chapter 8

[1]   S. Bugarszky, L. Liebermann, *Pflug Arch Eur J Phy* **1898**, *72*, 51–74.
[2]   K. Linderström-Lang, *Trans Faraday Soc* **1935**, *31*, 324–335.
[3]   C. Tanford, *Physical Chemistry of Macromolecules*. John Wiley & Sons, Inc.: New York, **1961**.
[4]   A. S. Yang, B. Honig, *J Mol Biol* **1993**, *231*, 459–474.
[5]   A. Onufriev, D. A. Case, G. M. Ullmann, *Biochemistry* **2001**, *40*, 3413–3419.
[6]   A. V. Finkelstein, O. B. Ptitsyn, *Protein physics: a course of lectures.* Academic Press: London, San Diego, **2002**.
[7]   J. M. Berg, J. L. Tymoczko, L. Stryer, *Biochemie*. Spektrum Akademischer Verlag: Heidelberg, **2007**.
[8]   H. Li, A. D. Robertson, J. H. Jensen, *Proteins Struct Funct Bioinf* **2005**, *61*, 704–721.
[9]   F. Oosawa, *Polyelectrolytes.* Marcel Dekker, Inc.: New York, **1971**.
[10]   Y. Goto, Y. Hagihara, D. Hamada, M. Hoshino, I. Nishii, *Biochemistry* **1993**, *32*, 11878–11885.
[11]   C. B. Anfinsen, *Biochem J* **1972**, *128*, 737–749.
[12]   P. S. Kim, R. L. Baldwin, *Annu Rev Biochem* **1982**, *51*, 459–489.
[13]   O. B. Ptitsyn, *J Protein Chem* **1987**, *6*, 273–293.
[14]   K. A. Dill, *Biochemistry* **1990**, *29*, 7133–7155.
[15]   M. Ohgushi, A. Wada, *FEBS Lett* **1983**, *164*, 21–24.
[16]   O. B. Ptitsyn, V. N. Uversky, *FEBS Lett* **1994**, *341*, 15–18.
[17]   D. A. Dolgikh, R. I. Gilmanshin, E. V. Brazhnikov, V. E. Bychkova, G. V. Semisotnov, S. Y. Venyaminov, O. B. Ptitsyn, *FEBS Lett* **1981**, *136*, 311–315.
[18]   P. A. Jennings, P. E. Wright, *Science* **1993**, *262*, 892–896.
[19]   L. Stryer, *J Mol Biol* **1965**, *13*, 482–495.
[20]   G. V. Semisotnov, N. A. Rodionova, O. I. Razgulyaev, V. N. Uversky, A. F. Gripas, R. I. Gilmanshin, *Biopolymers* **1991**, *31*, 119–128.
[21]   S. Sheshadri, G. M. Lingaraju, R. Varadarajan, *Protein Sci* **1999**, *8*, 1689–1695.
[22]   K. Kuwajima, *FASEB J* **1996**, *10*, 102–109.
[23]   V. S. Pande, D. S. Rokhsar, *Proc Natl Acad Sci USA* **1998**, *95*, 1490–1494.
[24]   L. J. Calciano, W. A. Escobar, G. L. Millhauser, S. M. Miick, J. Rubaloff, A. P. Todd, A. L. Fink, *Biochemistry* **1993**, *32*, 5644–5649.
[25]   J. Reichenwallner, M. Chakour, S. Indu, R. Varadarajan, W. E. Trommer, *Appl Magn Reson* **2013**, *44*, 983–995.
[26]   W. L. Hubbell, C. Altenbach, *Curr Opin Struct Biol* **1994**, *4*, 566–573.
[27]   W. L. Hubbell, D. S. Cafiso, C. Altenbach, *Nat Struct Mol Biol* **2000**, *7*, 735–739.
[28]   J. D. Morrisett, C. A. Broomfield, *J Am Chem Soc* **1971**, *93*, 7297–7304.
[29]   A. R. Berengian, M. Parfenova, H. S. Mchaourab, *J Biol Chem* **1999**, *274*, 6305–6314.
[30]   S. Muzammil, Y. Kumar, S. Tayyab, *Eur J Biochem* **1999**, *266*, 26–32.
[31]   M. Dockal, D. C. Carter, F. Rüker, *J Biol Chem* **2000**, *275*, 3042–3050.
[32]   P. Sen, B. Ahmad, R. H. Khan, *Eur Biophys J* **2008**, *37*, 1303–1308.
[33]   J. T. Yang, J. F. Foster, *J Am Chem Soc* **1954**, *76*, 1588–1595.
[34]   T. J. Stone, T. Buckman, P. L. Nordio, H. M. McConnell, *Proc Natl Acad Sci USA* **1965**, 54, 1010–1017.
[35]   A. Sali, E. Shakhnovich, M. Karplus, *Nature* **1994**, *369*, 248–251.
[36]   M. J. N. Junk, H. W. Spiess, D. Hinderberger, *Angew Chem Int Ed* **2010**, *49*, 8755–8759.
[37]   M. J. N. Junk, H. W. Spiess, D. Hinderberger, *Biophys J* **2011**, *100*, 2293–2301.
[38]   M. J. N. Junk, H. W. Spiess, D. Hinderberger, *J Magn Reson* **2011**, *210*, 210–217.
[39]   Y. Akdogan, M. J. N. Junk, D. Hinderberger, *Biomacromolecules* **2011**, *12*, 1072–1079.
[40]   Y. Akdogan, D. Hinderberger, *J Phys Chem B* **2011**, *115*, 15422–15429.
[41]   Y. Akdogan, Y. Wu, K. Eisele, M. Schaz, T. Weil, D. Hinderberger, *Soft Matter* **2012**, *8*, 11106–11114.
[42]   K. Wallevik, *J Biol Chem* **1973**, *248*, 2650–2655.
[43]   T. Peters Jr., *All about Albumin: Biochemistry, Genetics and Medical Applications*. Academic Press, Inc.: San Diego, **1995**.
[44]   W. Qiu, L. Zhang, O. Okobiah, Y. Yang, L. Wang, D. Zhong, A. H. Zewail, *J Phys Chem B* **2006**, *110*, 10540–10549.
[45]   O. H. Griffith, H. M. McConnell, *Proc Natl Acad Sci USA* **1966**, *55*, 8–11.
[46]   H. H. Hull, R. Chang, L. J. Kaplan, *Biochim Biophys Acta, Protein Struct* **1975**, *400*, 132–136.
[47]   V. A. Livshits, D. Marsh, *Biochim Biophys Acta, Biomembr* **2000**, *1466*, 350–360.
[48]   A. Alonso, W. P. dos Santos, S. J. Leonor, J. G. dos Santos, M. Tabak, *Biophys J* **2001**, *81*, 3566–3576.
[49]   F. De Simone, R. Guzzi, L. Sportelli, D. Marsh, R. Bartucci, *Biochim Biophys Acta, Biomembr* **2007**, *1768*, 1541–1549.
[50]   J. L. V. Anjos, P. S. Santiago, M. Tabak, A. Alonso, *Colloids Surf, B* **2011**, *88*, 463–470.
[51]   A. Pavicevic, J. Luo, A. Popovic-Bijelic, M. Mojovic, *Eur Biophys J* **2017**, 1–15.

[52] D. C. Bas, D. M. Rogers, J. H. Jensen, *Proteins Struct Funct Bioinf* **2008**, *73*, 765–783.

[53] M. H. M. Olsson, C. R. Sondergaard, M. Rostkowski, J. H. Jensen, *J Chem Theory Comput* **2011**, *7*, 525–537.

[54] S. Sugio, A. Kashima, S. Mochizuki, M. Noda, K. Kobayashi, *Protein Eng* **1999**, *12*, 439–446.

[55] A. A. Bhattacharya, T. Grüne, S. Curry, *J Mol Biol* **2000**, *303*, 721–732.

[56] S. Gumpen, P. O. Hegg, H. Martens, *Biochim Biophys Acta, Lipids Lipid Metab* **1979**, *574*, 189–196.

[57] A. Shrake, P. D. Ross, *J Biol Chem* **1988**, *263*, 15392–15399.

[58] M. A. Evenson, H. F. Deutsch, *Clin Chim Acta* **1978**, *89*, 341–354.

[59] M. Dockal, D. C. Carter, F. Rüker, *J Biol Chem* **1999**, *274*, 29303–29310.

[60] K. Langer, S. Balthasar, V. Vogel, N. Dinauer, H. von Briesen, D. Schubert, *Int J Pharm* **2003**, *257*, 169–180.

[61] B. Jachimska, M. Wasilewska, Z. Adamczyk, *Langmuir* **2008**, *24*, 6866–6872.

[62] M. D. Barratt, A. P. Davies, M. T. A. Evans, *Eur J Biochem* **1971**, *24*, 280–283.

[63] W. L. Hubbell, H. M. McConnell, *J Am Chem Soc* **1971**, *93*, 314–326.

[64] C. Wa, R. L. Cerny, W. A. Clarke, D. S. Hage, *Clin Chim Acta* **2007**, *385*, 48–60.

[65] K. Oettl, G. Marsche, *Methods Enzymol* **2010**, *474*, 181–195.

[66] M. Anraku, V. T. G. Chuang, T. Maruyama, M. Otagiri, *Biochim Biophys Acta, Gen Subj* **2013**, *1830*, 5465–5472.

[67] J. Bonanata, L. Turell, L. Antmann, G. Ferrer-Sueta, S. Botasini, E. Mendez, B. Alvarez, E. L. Coitino, *Free Radical Biol Med* **2017**, *108*, 952–962.

[68] F. Wurm, T. Steinbach, H. A. Klok, *Chem Commun* **2013**, *49*, 7815–7817.

[69] C. N. Cornell, L. J. Kaplan, *Biochemistry* **1978**, *17*, 1750–1754.

[70] C. N. Cornell, L. J. Kaplan, *Biochemistry* **1978**, *17*, 1755–1758.

[71] J. Applequist, P. Doty, α-helix Formation in Poly-ε-Carbobenzoxy-L-Lysine and Poly-L-Lysine. In *Polyamino Acids, Polypeptides and Proteins*; M. A. Stahmann, Ed.; University of Wisconsin Press, Madison, WI, **1962**, pp 161–177.

[72] M. Ge, S. B. Rananavare, J. H. Freed, *Biochim Biophys Acta, Gen Subj* **1990**, *1036*, 228–236.

[73] V. Muravsky, T. Gurachevskaya, S. Berezenko, K. Schnurr, A. Gurachevsky, *Spectrochim Acta, Part A* **2009**, *74*, 42–47.

[74] D. P. Cistola, D. M. Small, J. A. Hamilton, *J Lipid Res* **1982**, *23*, 795–799.

[75] D. P. Cistola, D. M. Small, J. A. Hamilton, *J Biol Chem* **1987**, *262*, 10980–10985.

[76] P. S. Sukhija, D. L. Palmquist, *J Dairy Sci* **1990**, *73*, 1784–1787.

[77] K. de la Caba, C. Pena, E. M. Ciannamea, P. M. Stefani, I. Mondragon, R. A. Ruseckaite, *J Appl Polym Sci* **2012**, *124*, 1796–1807.

[78] W. Scheider, J. K. Fuller, *Biochim Biophys Acta* **1970**, *221*, 376–378.

[79] Y. N. Molin, K. M. Salikhov, K. I. Zamaraev, *Spin Exchange: Principles and applications in chemistry and biology.* Springer-Verlag: Berlin, Heidelberg, **1980**.

[80] C. Tanford, J. G. Buzzell, *J Phys Chem* **1956**, *60*, 225–231.

[81] J. Seelig, Anisotropic motion in liquid crystalline structures. In *Spin Labeling: Theory and Applications*; L. J. Berliner, Ed.; Academic Press: New York, **1976**, Vol. 1, pp 373–409.

[82] J. A. Nelder, *Biometrics* **1966**, *22*, 128–141.

[83] R. A. Sutherland, C. C. Wright, L. M. J. Verstraeten, D. J. Greenwood, *Fert Res* **1986**, *10*, 251–262.

[84] G. Catillo, N. P. P. Macciotta, A. Carretta, A. Cappio-Borlino, *J Dairy Sci* **2002**, *85*, 1298–1306.

[85] O. H. Griffith, P. C. Jost, Lipid spin labels in biological membranes. In *Spin Labeling: Theory and Applications*; L. J. Berliner, Ed.; Academic Press: New York, **1976**, Vol. 1, pp 453–523.

[86] O. H. Griffith, P. J. Dehlinger, S. P. Van, *J Membr Biol* **1974**, *15*, 159–192.

[87] H. J. Steinhoff, A. Savitsky, C. Wegener, M. Pfeiffer, M. Plato, K. Möbius, *Biochim Biophys Acta* **2000**, *1457*, 253–262.

[88] J. J. Caramelo, O. A. Castro, L. G. Alonso, G. de Prat-Gay, A. J. Parodi, *Proc Natl Acad Sci USA* **2003**, *100*, 86–91.

[89] E. J. Gumbel, *J Am Stat Assoc* **1961**, *56*, 335–349.

[90] A. Saupe, W. Maier, *Z Naturforsch A* **1961**, *16*, 816–824.

[91] A. Saupe, *Z Naturforsch A* **1964**, *19*, 161–171.

[92] J. H. Chin, D. B. Goldstein, *Science* **1977**, *196*, 684–685.

[93] Y. K. Shin, J. H. Freed, *Biophys J* **1989**, *55*, 537–550.

[94] Y. K. Shin, J. K. Moscicki, J. H. Freed, *Biophys J* **1990**, *57*, 445–459.

[95] W. Birmachu, J. C. Voss, C. F. Louis, D. D. Thomas, *Biochemistry* **1993**, *32*, 9445–9453.

[96] R. E. Glover, R. R. Smith, M. V. Jones, S. K. Jackson, C. C. Rowlands, *FEMS Microbiol Lett* **1999**, *177*, 57–62.

[97] B. A. I. van den Bergh, P. W. Wertz, H. E. Junginger, J. A. Bouwstra, *Int J Pharm* **2001**, *217*, 13–24.

[98] M. B. Cassera, A. M. Silber, A. M. Gennaro, *Biophys Chem* **2002**, *99*, 117–127.

[99] W. K. Subczynski, J. Widomska, J. B. Feix, *Free Radical Bio Med* **2009**, *46*, 707–718.

[100] P. Stepien, A. Polit, A. Wisniewska-Becker, *Biochim Biophys Acta, Biomembr* **2015**, *1848*, 60–66.

[101] J. H. K. Rozenfeld, E. L. Duarte, T. R. Oliviera, M. T. Lamy, *Biophys Rev* **2017**, *9*, 633–647.

[102] E. D. Vieria, L. G. M. Basso, A. J. Costa-Filho, *Biochim Biophys Acta, Biomembr* **2017**, *1859*, 1133–1143.

[103] B. J. Gaffney, H. M. McConnell, *J Magn Reson* **1974**, *16*, 1–28.

[104] J. D. Morrisett, H. J. Pownall, A. M. Gotto, *J Biol Chem* **1975**, *250*, 2487–2494.

[105] T. G. Gantchev, M. B. Shopova, *Biochim Biophys Acta, Protein Struct Mol Enzymol* **1990**, *1037*, 422–434.

[106] D. S. Goodman, *J Am Chem Soc* **1958**, *80*, 3892–3898.

[107] A. A. Spector, *J Lipid Res* **1975**, *16*, 165–179.

[108] S. J. Rehfeld, D. J. Eatough, W. Z. Plachy, *J Lipid Res* **1978**, *19*, 841–849.

[109] A. A. Pavicevic, A. D. Popovic-Bijelic, M. D. Mojovic, S. V. Susnjar, G. G. Bacic, *J Phys Chem B* **2014**, *118*, 10898–10905.

[110] P. Jost, L. J. Libertini, V. C. Hebert, O. H. Griffith, *J Mol Biol* **1971**, *59*, 77–98.

[111] S. P. Van, G. B. Birrell, O. H. Griffith, *J Magn Reson* **1974**, *15*, 444–459.

[112] J. Israelachvili, J. Sjösten, L. E. G. Eriksson, M. Ehrström, A. Gräslund, A. Ehrenberg, *Biochim Biophys Acta, Biomembr* **1974**, *339*, 164–172.

[113] R. E. Martin, M. Pannier, F. Diederich, V. Gramlich, M. Hubrich, H. W. Spiess, *Angew Chem Int Ed* **1998**, *37*, 2833–2837.

[114] M. Pannier, S. Veit, A. Godt, G. Jeschke, H. W. Spiess, *J Magn Reson* **2000**, *142*, 331–340.

[115] D. R. Kattnig, J. Reichenwallner, D. Hinderberger, *J Phys Chem B* **2013**, *117*, 16542–16557.

[116] D. Hilger, H. Jung, E. Padan, C. Wegener, K. P. Vogel, H. J. Steinhoff, G. Jeschke, *Biophys J* **2005**, *89*, 1328–1338.

[117] Q. Mao, S. Schleidt, H. Zimmermann, G. Jeschke, *Phys Chem Chem Phys* **2008**, *10*, 1156–1167.

[118] B. E. Bode, R. Dastvan, T. F. Prisner, *J Magn Reson* **2011**, *211*, 11–17.

[119] D. R. Kattnig, D. Hinderberger, *J Magn Reson* **2012**, *230*, 50–63.

[120] B. E. Bode, D. Margraf, J. Plackmeyer, G. Dürner, T. F. Prisner, O. Schiemann, *J Am Chem Soc* **2007**, *129*, 6736–6745.

[121] J. Rescic, V. Vlachy, A. Jamnik, O. Glatter, *J Colloid Interface Sci* **2001**, *239*, 49–57.

[122] P. Taboada, M. Gutierrez-Pichel, V. Mosquera, *Biomacromolecules* **2004**, *5*, 1116–1123.

[123] W. Wang, J. Tang, X. Peng, Z. Hu, X. Chen, *Sci China, Ser B Chem* **2006**, *49*, 332–337.

[124] C. Tanford, J. G. Buzzell, D. G. Rands, S. A. Swanson, *J Am Chem Soc* **1955**, *77*, 6421–6428.

[125] F. Booth, *Proc R Soc London, Ser A* **1950**, *203*, 533–551.

[126] M. Kaszuba, D. McKnight, M. T. Connah, F. K. McNeil-Watson, U. Nobbmann, *J Nanopart Res* **2008**, *10*, 823–829.

[127] H. A. Saroff, *J Phys Chem* **1957**, *61*, 1364–1368.

[128] D. F. H. Wallach, S. P. Verma, E. Weidekamm, V. Bieri, *Biochim Biophys Acta, Biomembr* **1974**, *356*, 68–81.

[129] S. Curry, H. Mandelkow, P. Brick, N. Franks, *Nat Struct Biol* **1998**, *5*, 827–835.

[130] S. Curry, P. Brick, N. P. Franks, *Biochim Biophys Acta, Mol Cell Biol Lipids* **1999**, *1441*, 131–140.

[131] G. Jeschke, *Annu Rev Phys Chem* **2012**, *63*, 419–446.

[132] G. Lamm, G. R. Pack, *Biopolymers* **2010**, *93*, 619–639.

[133] A. Michnik, K. Michalik, Z. Drzazga, *J Therm Anal Calorim* **2005**, *80*, 399–406.

[134] S. H. Arabi, B. Aghelnejad, C. Schwieger, A. Meister, A. Kerth, D. Hinderberger, *Biomater Sci* **2018**, *6*, 478–492.

[135] V. V. Khramtsov, L. M. Weiner, S. I. Eremenko, O. I. Belchenko, P. V. Schastnev, I. A. Grigor'ev, V. A. Reznikov, *J Magn Reson* **1985**, *61*, 397–408.

[136] M. A. Voinov, I. A. Kirilyuk, A. I. Smirnov, *J Phys Chem B* **2009**, *113*, 3453–3460.

[137] V. V. Khramtsov, D. Marsh, L. Weiner, V. A. Reznikov, *Biochim Biophys Acta, Biomembr* **1992**, *1104*, 317–324.

[138] A. I. Smirnov, A. Ruuge, V. A. Reznikov, M. A. Voinov, I. A. Grigor'ev, *J Am Chem Soc* **2004**, *126*, 8872–8873.

[139] S. Thetiot-Laurent, G. Gosset, J. L. Clement, M. Cassien, A. Mercier, D. Siri, A. Gaudel-Siri, A. Rockenbauer, M. Culcasi, S. Pietri, *ChemBioChem* **2017**, *18*, 300–315.

[140] M. Tian, X. Peng, J. Fan, J. Wang, S. Sun, *Dyes Pigm* **2012**, *95*, 112–115.

[141] F. Gao, L. Tang, L. Dai, L. Wang, *Spectrochim Acta, Part A* **2007**, *67*, 517–521.

[142] H. T. Uyeda, I. L. Medintz, J. K. Jaiswal, S. M. Simon, H. Mattoussi, *J Am Chem Soc* **2005**, *127*, 3870–3878.

[143] R. Dulbecco, M. Vogt, *J Exp Med* **1954**, *99*, 167–182.

[144] M. M. Bradford, *Anal Biochem* **1976**, *72*, 248–254.

[145] P. K. Smith, R. I. Krohn, G. T. Hermanson, A. K. Mallia, F. H. Gartner, M. D. Provenzano, E. K. Fujimoto, N. M. Goeke, B. J. Olson, D. C. Klenk, *Anal Biochem* **1985**, *150*, 76–85.

[146]   M.-T. Oehmichen, Biophysikalische Untersuchung der pH-abhängigen Struktur und Dynamik von Serumalbumin, Bachelor Thesis, Martin-Luther-Universität Halle-Wittenberg, **2015**.
[147]   S. W. Provencher, *Comput Phys Commun* **1982**, *27*, 213–227.
[148]   P. Schiebener, J. Straub, J. M. H. Levelt Sengers, J. S. Gallagher, *J Phys Chem Ref Data* **1990**, *19*, 677–717.
[149]   M. L. Sheely, *Ind Eng Chem* **1932**, *24*, 1060–1064.
[150]   H. J. Steinhoff, K. Lieutenant, J. Schlitter, *Z Naturforsch, C: Biosci* **1989**, *44*, 280–288.
[151]   A. S. Waggoner, O. H. Griffith, C. R. Christensen, *Proc Natl Acad Sci USA* **1967**, *57*, 1198–1205.
[152]   P. Marzola, C. Pinzino, C. A. Veracini, *Langmuir* **1991**, *7*, 238–242.
[153]   E. Meirovitch, J. H. Freed, *J Phys Chem* **1984**, *88*, 4995–5004.
[154]   F. Navari-Izzo, M. F. Quartacci, C. Pinzino, N. Rascio, C. Vazzana, C. L. M. Sgherri, *Plant Physiol* **2000**, *124*, 1427–1436.
[155]   S. Stoll, A. Schweiger, *J Magn Reson* **2006**, *178*, 42–55.
[156]   G. Jeschke, V. Chechik, P. Ionita, A. Godt, H. Zimmermann, J. Banham, C. R. Timmel, D. Hilger, H. Jung, *Appl Magn Reson* **2006**, *30*, 473–498.

Chapter 9

[1]   M. J. N. Junk, H. W. Spiess, D. Hinderberger, *Angew Chem Int Ed* **2010**, *49*, 8755–8759.
[2]   M. J. N. Junk, H. W. Spiess, D. Hinderberger, *J Magn Reson* **2011**, *210*, 210–217.
[3]   M. J. N. Junk, H. W. Spiess, D. Hinderberger, *Biophys J* **2011**, *100*, 2293–2301.
[4]   A. A. Bhattacharya, T. Grüne, S. Curry, *J Mol Biol* **2000**, *303*, 721–732.
[5]   T. J. Stone, T. Buckman, P. L. Nordio, H. M. McConnell, *Proc Natl Acad Sci USA* **1965**, *54*, 1010–1017.
[6]   O. H. Griffith, H. M. McConnell, *Proc Natl Acad Sci USA* **1966**, *55*, 8–11.
[7]   F. De Simone, R. Guzzi, L. Sportelli, D. Marsh, R. Bartucci, *Biochim Biophys Acta, Biomembr* **2007**, *1768*, 1541–1549.
[8]   T. Peters Jr., *All about Albumin: Biochemistry, Genetics, and Medical Applications.* Academic Press, Inc.: San Diego, **1995**.
[9]   T. Hauenschild, Spinmarkierung pharmazeutischer Wirkstoffe sowie deren Bindungseigenschaften an Serum Albumin vom Menschen, Diploma Thesis, Johannes Gutenberg-Universität Mainz, **2013**.
[10]   D. S. Park, C. E. Petersen, C. E. Ha, K. Harohalli, J. B. Feix, N. V. Baghavan, *IUBMB Life* **1999**, *48*, 169–174.
[11]   Y. Shenberger, A. Shimshi, S. Ruthstein, *J Phys Chem B* **2015**, *119*, 4824–4830.
[12]   C. M. Gruian, C. Rickert, S. C. T. Nicklisch, E. Vanea, H. J. Steinhoff, S. Simon, *ChemPhysChem* **2017**, *18*, 634–642.
[13]   D. S. Goodman, *J Am Chem Soc* **1958**, *80*, 3892–3898.
[14]   J. E. Fletcher, A. A. Spector, J. D. Ashbrook, *Biochemistry* **1970**, *9*, 4580–4587.
[15]   A. A. Spector, J. E. Fletcher, J. D. Ashbrook, *Biochemistry* **1971**, *10*, 3229–3232.
[16]   J. D. Ashbrook, A. A. Spector, E. C. Santos, J. E. Fletcher, *J Biol Chem* **1975**, *250*, 2333–2338.
[17]   A. A. Spector, *J Lipid Res* **1975**, *16*, 165–179.
[18]   S. J. Rehfeld, D. J. Eatough, W. Z. Plachy, *J Lipid Res* **1978**, *19*, 841–849.
[19]   J. A. Hamilton, D. P. Cistola, J. D. Morrisett, J. T. Sparrow, D. M. Small, *Proc Natl Acad Sci USA* **1984**, *81*, 3718–3722.
[20]   D. P. Cistola, D. M. Small, J. A. Hamilton, *J Biol Chem* **1987**, *262*, 10971–10979.
[21]   J. A. Hamilton, S. Era, S. P. Bhamidipati, R. G. Reed, *Proc Natl Acad Sci USA* **1991**, *88*, 2051–2054.
[22]   S. Curry, H. Mandelkow, P. Brick, N. Franks, *Nat Struct Biol* **1998**, *5*, 827–835.
[23]   S. Curry, P. Brick, N. P. Franks, *Biochim Biophys Acta, Mol Cell Biol Lipids* **1999**, *1441*, 131–140.
[24]   J. R. Simard, P. A. Zunszain, C. E. Ha, J. S. Yang, N. V. Baghavan, I. Petitpas, S. Curry, J. A. Hamilton, *Proc Natl Acad Sci USA* **2005**, *102*, 17958–17963.
[25]   J. R. Simard, P. A. Zunszain, J. A. Hamilton, S. Curry, *J Mol Biol* **2006**, *361*, 336–351.
[26]   G. L. Ellman, *Arch Biochem Biophys* **1959**, *82*, 70–77.
[27]   P. K. Smith, R. I. Krohn, G. T. Hermanson, A. K. Mallia, F. H. Gartner, M. D. Provenzano, E. K. Fujimoto, N. M. Goeke, B. J. Olson, D. C. Klenk, *Anal Biochem* **1985**, *150*, 76–85.
[28]   L. J. Berliner, J. Grunwald, H. O. Hankovszky, K. Hideg, *Anal Biochem* **1982**, *119*, 450–455.
[29]   J. Janatova, J. K. Fuller, M. J. Hunter, *J Biol Chem* **1968**, *243*, 3612–3622.
[30]   K. Oettl, R. E. Stauber, *Br J Pharmacol* **2007**, *151*, 580–590.
[31]   K. Oettl, G. Marsche, *Methods Enzymol* **2010**, *474*, 181–195.
[32]   M. Anraku, V. T. G. Chuang, T. Maruyama, M. Otagiri, *Biochim Biophys Acta, Gen Subj* **2013**, *1830*, 5465–5472.
[33]   J. Bonanata, L. Turell, L. Antmann, G. Ferrer-Sueta, S. Botasini, E. Mendez, B. Alvarez, E. L. Coitino, *Free Radical Biol Med* **2017**, *108*, 952–962.

[34]   I. D. Pavicevic, V. B. Jovanovic, M. M. Takic, A. Z. Penezic, J. M. Acimovic, L. M. Mandic, *Chem Biol Interact* **2014**, *224*, 42–50.

[35]   C. K. Riener, G. Kada, H. J. Gruber, *Anal Bioanal Chem* **2002**, *373*, 266–276.

[36]   D. R. Kattnig, J. Reichenwallner, D. Hinderberger, *J Phys Chem B* **2013**, *117*, 16542–16557.

[37]   C. Tanford, J. G. Buzzell, *J Phys Chem* **1956**, *60*, 225–231.

[38]   G. Jeschke, *Annu Rev Phys Chem* **2012**, *63*, 419–446.

[39]   G. Jeschke, V. Chechik, P. Ionita, A. Godt, H. Zimmermann, J. Banham, C. R. Timmel, D. Hilger, H. Jung, *Appl Magn Reson* **2006**, *30*, 473–498.

[40]   J. Ghuman, P. A. Zunszain, I. Petitpas, A. A. Bhattacharya, M. Otagiri, S. Curry, *J Mol Biol* **2005**, *353*, 38–52.

[41]   M. A. Kiselev, I. A. Gryzunov, G. E. Dobretsov, M. N. Komarova, *Biofizika* **2001**, *46*, 423–427.

[42]   I. Tkach, S. Pornsuwan, C. Hobärtner, F. Wachowius, S. T. Sigurdsson, T. Y. Baranova, U. Diederichsen, G. Sicoli, M. Bennati, *Phys Chem Chem Phys* **2013**, *15*, 3433–3437.

[43]   A. Marko, V. Denysenkov, D. Margraf, P. Cekan, O. Schiemann, S. T. Sigurdsson, T. F. Prisner, *J Am Chem Soc* **2011**, *133*, 13375–13379.

[44]   J. E. Lovett, A. M. Bowen, C. R. Timmel, M. W. Jones, J. R. Dilworth, D. Caprotti, S. G. Bell, L. L. Wong, J. Harmer, *Phys Chem Chem Phys* **2009**, *11*, 6840–6848.

[45]   C. Abe, D. Klose, F. Dietrich, W. H. Ziegler, Y. Polyhach, G. Jeschke, H. J. Steinhoff, *J Magn Reson* **2012**, *216*, 53–61.

[46]   A. Marko, T. F. Prisner, *Phys Chem Chem Phys* **2013**, *15*, 619–627.

[47]   F. Karush, *J Am Chem Soc* **1950**, *72*, 2705–2713.

[48]   R. A. Redner, H. F. Walker, *SIAM Rev* **1984**, *26*, 195–239.

[49]   J. G. Morel, N. K. Nagaraj, *Biometrika* **1993**, *80*, 363–371.

[50]   A. Godt, M. Schulte, H. Zimmermann, G. Jeschke, *Angew Chem Int Ed* **2006**, *118*, 7722–7726.

[51]   S. Y. Cheng, G. Rakhit, F. Erard, J. Robbins, C. F. Chignell, *J Biol Chem* **1981**, *256*, 831–836.

[52]   B. Neises, W. Steglich, *Angew Chem Int Ed* **1978**, *17*, 522–524.

[53]   T. Hauenschild, J. Reichenwallner, V. Enkelmann, D. Hinderberger, *Chem Eur J* **2016**, *22*, 12825–12838.

[54]   G. Scatchard, *Ann NY Acad Sci* **1949**, *51*, 660–672.

[55]   X. M. He, D. C. Carter, *Nature* **1992**, *358*, 209–215.

[56]   F. Yang, C. Bian, L. Zhu, G. Zhao, Z. Huang, M. Huang, *J Struct Biol* **2007**, *157*, 348–355.

[57]   I. Sjöholm, B. Ekman, A. Kober, I. Ljungstedt-Pahlman, B. Seiving, T. Sjödin, *Mol Pharmacol* **1979**, *16*, 767–777.

[58]   P. Daneshgar, A. A. Moosavi-Movahedi, P. Norouzi, M. R. Ganjali, A. Madadkar-Sobhani, A. A. Saboury, *Int J Biol Macromol* **2009**, *45*, 129–134.

[59]   J. M. Chamouard, J. Barre, S. Urien, G. Houin, J. P. Tillement, *Biochem Pharmacol* **1985**, *34*, 1695–1700.

[60]   G. Sudlow, D. J. Birkett, D. N. Wade, *Mol Pharmacol* **1976**, *12*, 1052–1061.

[61]   I. Petitpas, A. A. Bhattacharya, S. Twine, M. East, S. Curry, *J Biol Chem* **2001**, *276*, 22804–22809.

[62]   A. Varlan, M. Hillebrand, *Cent Eur J Chem* **2011**, *9*, 624–634.

[63]   A. A. Bhattacharya, S. Curry, N. P. Franks, *J Biol Chem* **2000**, *275*, 38731–38738.

[64]   U. Kragh-Hansen, L. Minchiotti, S. O. Brennan, O. Sugita, *Eur J Biochem* **1990**, *193*, 169–174.

[65]   T. Hauenschild, ESR-basierte Entwicklung neuer, postmodifizierter Albumin-gebundener ß-Blockerderivate sowie neuartiger Nitroxidradikale zur systematischen Charakterisierung supramolekularer Systeme, Ph.D. Thesis. Martin-Luther-Universität Halle-Wittenberg, **2018**.

[66]   G. Jeschke, A. Koch, U. Jonas, A. Godt, *J Magn Reson* **2002**, *155*, 72–82.

[67]   M. Fasano, S. Curry, E. Terreno, M. Galliano, G. Fanali, P. Narciso, S. Notari, P. Ascenzi, *IUBMB Life* **2005**, *57*, 787–796.

[68]   G. Jeschke, H. Zimmermann, A. Godt, *J Magn Reson* **2006**, *180*, 137–146.

[69]   D. Kurzbach, D. R. Kattnig, B. Zhang, A. D. Schlüter, D. Hinderberger, *Chem Sci* **2012**, *3*, 2550–2558.

[70]   M. M. Bradford, *Anal Biochem* **1976**, *72*, 248–254.

[71]   J. A. Burns, J. C. Butler, J. Moran, G. M. Whitesides, *J Org Chem* **1991**, *56*, 2648–2650.

[72]   E. B. Getz, M. Xiao, T. Chakrabarty, R. Cooke, P. R. Selvin, *Anal Biochem* **1999**, *273*, 73–80.

[73]   Thermo Scientific. *Ellman's reagent.* Instructions manual, **2013**.

[74]   R. E. Martin, M. Pannier, F. Diederich, V. Gramlich, M. Hubrich, H. W. Spiess, *Angew Chem Int Ed* **1998**, *37*, 2834–2837.

[75]   M. Pannier, S. Veit, A. Godt, G. Jeschke, H. W. Spiess, *J Magn Reson* **2000**, *142*, 331–340.

[76]   G. Jeschke, M. Sajid, M. Schulte, N. Ramezanian, A. Volkov, H. Zimmermann, A. Godt, *J Am Chem Soc* **2010**, *132*, 10107–10117.

[77]   E. Krieger, G. Koraimann, G. Vriend, *Proteins Struct Funct Genet* **2002**, *47*, 393–402.

Chapter 10

[1] M. Zhang, T. Breiner, H. Mori, A. H. E. Müller, *Polymer* **2003**, *44*, 1449–1458.

[2] B. H. Tan, H. Hussain, Y. Liu, C. B. He, T. P. Davis, *Langmuir* **2009**, *26*, 2361–2368.

[3] Y. Y. Yuan, Q. Du, Y. C. Wang, J. Wang, *Macromolecules* **2010**, *43*, 1739–1746.

[4] C. Porsch, S. Hansson, N. Nordgren, E. Malmström, *Polym Chem* **2011**, *2*, 1114–1123.

[5] A. Thomas, F. K. Wolf, H. Frey, *Macromol Rapid Commun* **2011**, *32*, 1910–1915.

[6] Y. L. Luo, W. Yu, F. Xu, L. L. Zhang, *Polym Chem* **2012**, *50*, 2053–2067.

[7] A. Thomas, K. Niederer, F. Wurm, H. Frey, *Polym Chem* **2014**, *5*, 899–909.

[8] J. F. Lutz, *J Polym Sci Part A* **2008**, *46*, 3459–3470.

[9] J. F. Lutz, *Adv Mater* **2011**, *23*, 2237–2243.

[10] F. Herbst, D. Döhler, P. Michael, W. H. Binder, *Macromol Rapid Commun* **2013**, *34*, 203–220.

[11] D. Döhler, P. Michael, W. H. Binder, Principles of self-healing polymers. In *Self-Healing Polymers: From Principles to Applications*; W. H. Binder, Ed.; Wiley-VCH: Weinheim, Germany, **2013**, pp 5–60.

[12] J. Z. Du, L. Y. Tang, W. J. Song, Y. Shi, J. Wang, *Biomacromolecules* **2009**, *10*, 2169–2174.

[13] O. G. Schramm, M. A. R. Meier, R. Hoogenboom, H. P. van Erp, J. F. Gohy, U. S. Schubert, *Soft Matter* **2009**, *5*, 1662–1667.

[14] J. A. Johnson, Y. Y. Lu, A. O. Burts, Y. H. Lim, M. G. Finn, J. T. Koberstein, N. J. Turro, D. A. Tirrell, R. H. Grubbs, *J Am Chem Soc* **2010**, *133*, 559–566.

[15] Y. Bakkour, V. Darcos, F. Coumes, S. Li, J. Coudane, *Polymer* **2013**, *54*, 1746–1754.

[16] S. J. Rehfeld, D. J. Eatough, W. Z. Plachy, *J Lipid Res* **1978**, *19*, 841–849.

[17] R. C. Perkins Jr., N. Abumrad, K. Balasubramanian, L. R. Dalton, A. H. Beth, J. H. Park, C. R. Park, *Biochemistry* **1982**, *21*, 4059–4064.

[18] T. G. Gantchev, M. B. Shopova, *Biochim Biophys Acta, Protein Struct Mol Enzymol* **1990**, *1037*, 422–434.

[19] M. Ge, S. B. Rananavare, J. H. Freed, *Biochim Biophys Acta, Gen Subj* **1990**, *1036*, 228–236.

[20] S. Y. Cheng, G. Rakhit, F. Erard, J. Robbins, C. F. Chignell, *J Biol Chem* **1981**, *256*, 831–836.

[21] T. Hauenschild, J. Reichenwallner, V. Enkelmann, D. Hinderberger, *Chem Eur J* **2016**, *22*, 12825–12838.

[22] D. Kurzbach, D. R. Kattnig, B. Zhang, A. D. Schlüter, D. Hinderberger, *Chem Sci* **2012**, *3*, 2550–2558.

[23] D. Kurzbach, W. Hassouneh, J. R. McDaniel, E. A. Jaumann, A. Chilkoti, D. Hinderberger, *J Am Chem Soc* **2013**, *135*, 11299–11308.

[24] D. Kurzbach, M. N. Reh, D. Hinderberger, *ChemPhysChem* **2011**, *12*, 3566–3572.

[25] D. Kivelson, *J Chem Phys* **1960**, *33*, 1094–1106.

[26] J. H. Freed, G. K. Fraenkel, *J Chem Phys* **1963**, *39*, 326–348.

[27] J. H. Freed, *J Chem Phys* **1964**, *41*, 2077–2083.

[28] T. J. Stone, T. Buckman, P. L. Nordio, H. M. McConnell, *Proc Natl Acad Sci USA* **1965**, *54*, 1010–1017.

[29] J. H. Freed, Theory of slow tumbling ESR spectra for nitroxides. In *Spin Labeling: Theory and Applications*; L. J. Berliner, Ed.; Academic Press: New York, **1976**, Vol. 1, pp 53–132.

[30] W. L. Hubbell, C. Altenbach, *Curr Opin Struct Biol* **1994**, *4*, 566–573.

[31] O. H. Griffith, P. J. Dehlinger, S. P. Van, *J Membrane Biol* **1974**, *15*, 159–192.

[32] H. J. Steinhoff, A. Savitsky, C. Wegener, M. Pfeiffer, M. Plato, K. Möbius, *Biochim Biophys Acta, Bioenerg* **2000**, *1457*, 253–262.

[33] D. Hinderberger, EPR spectroscopy in polymer science. In *EPR Spectroscopy: Applications in Chemistry and Biology*; Drescher, M., Jeschke, G., Eds.; Springer: Berlin, Heidelberg, **2012**, pp 67–89.

[34] A. S. Waggoner, T. J. Kingzett, S. Rottschaefer, O. H. Griffith, A. D. Keith, *Chem Phys Lipids* **1969**, *3*, 245–253.

[35] M. J. N. Junk, W. Li, A. D. Schlüter, G. Wegner, H. W. Spiess, A. Zhang, D. Hinderberger, *Angew Chem Int Ed* **2010**, *49*, 5683–5687.

[36] J. Reichenwallner, A. Thomas, L. Nuhn, T. Johann, A. Meister, H. Frey, D. Hinderberger, *Polym Chem* **2016**, *7*, 5783–5798.

[37] K. C. Waterman, R. C. Adami, *Int J Pharm* **2005**, *293*, 101–125.

[38] N. Maltar-Strmecki, B. Rakvin, *Appl Radiat Isot* **2005**, *63*, 375–380.

[39] M. J. N. Junk, U. Jonas, D. Hinderberger, *Small* **2008**, *4*, 1485–1493.

[40] M. J. N. Junk, W. Li, A. D. Schlüter, G. Wegner, H. W. Spiess, A. Zhang, D. Hinderberger, *Macromol Chem Phys* **2011**, *212*, 1229–1235.

[41] D. Kurzbach, M. J. N. Junk, D. Hinderberger, *Macromol Rapid Commun* **2013**, *34*, 119–134.

[42] C. Tanford, *J Mol Biol* **1972**, *67*, 59–74.

[43] W. J. Simmonds, *Aust J Exp Biol Med Sci* **1972**, *50*, 403–421.

[44] C. Tanford, *Science* **1978**, *200*, 1012–1018.

[45] E. Fuguet, C. Rafols, M. Roses, E. Bosch, *Anal Chim Acta* **2005**, *548*, 95–100.

[46]   S. W. Provencher, *Comput Phys Commun* **1982**, *27*, 213–227.

[47]   P. R. Majhi, A. Blume, *J Phys Chem B* **2002**, *106*, 10753–10763.

[48]   P. J. Tummino, R. A. Copeland, *Biochemistry* **2008**, *47*, 5481–5492.

[49]   J. F. W. Keana, New aspects of nitroxide chemistry. In *Spin labeling: Theory and applications*; L. J. Berliner, Ed.; Academic Press: New York, **1979**, Vol. 2, pp 115–172.

[50]   Y. Ma, C. Loyns, P. Price, V. Chechik, *Org Biomol Chem* **2011**, *9*, 5573–5578.

[51]   E. A. Haidasz, D. Meng, R. Amorati, A. Baschieri, K. U. Ingold, L. Valgimigli, L. A. Pratt, *J Am Chem Soc* **2016**, *138*, 5290–5298.

[52]   A. Gurachevsky, E. Shimanovitch, T. Gurachevskaya, V. Muravsky, *Biochem Biophys Res Commun* **2007**, *360*, 852–856.

[53]   T. Peters Jr., *All about Albumin: Biochemistry, Genetics and Medical Applications*. Academic Press, Inc.: San Diego, **1995**.

[54]   J. A. Hamilton, *J Lipid Res* **1998**, *39*, 467–481.

[55]   J. A. Hamilton, *Prog Lipid Res* **2004**, *43*, 177–199.

[56]   W. Scheider, *Proc Natl Acad Sci USA* **1979**, *76*, 2283–2287.

[57]   W. Scheider, *J Phys Chem* **1980**, *84*, 925–928.

[58]   F. Kamp, J. A. Hamilton, *Prostaglandins, Leukotrienes Essent Fatty Acids* **2006**, *75*, 149–159.

[59]   J. A. Hamilton, *Prostaglandins, Leukotrienes Essent Fatty Acids* **2007**, *77*, 355–361.

[60]   E. Barta, *J Membr Biol* **2015**, *248*, 783–793.

[61]   E. Sackmann, H. Träuble, *J Am Chem Soc* **1972**, *94*, 4482–4491.

[62]   E. Sackmann, H. Träuble, *J Am Chem Soc* **1972**, *94*, 4492–4498.

[63]   C. J. Scandella, P. Devaux, H. M. McConnell, *Proc Natl Acad Sci USA* **1972**, *69*, 2056–2060.

[64]   H. Träuble, E. Sackmann, *Nature* **1973**, *245*, 210–211.

[65]   B. N. Brockhouse, *Il Nuovo Cimento* **1958**, *9*, 45–71.

[66]   B. N. Brockhouse, N. K. Pope, *Phys Rev Lett* **1959**, *3*, 259–262.

[67]   C. T. Chudley, R. J. Elliott, *Proc Phys Soc* **1961**, *77*, 353–361.

[68]   P. A. Egelstaff, *J Chem Phys* **1970**, *53*, 2590–2598.

[69]   S. A. Goldman, G. V. Bruno, C. F. Polnaszek, J. H. Freed, *J Chem Phys* **1972**, *56*, 716–735.

[70]   K. A. Valiev, E. N. Ivanov, *Phys Usp* **1973**, *16*, 1–16.

[71]   G. V. Bruno, J. H. Freed, *J Phys Chem* **1974**, *78*, 935–940.

[72]   K. A. Earle, D. E. Budil, J. H. Freed, *J Phys Chem* **1993**, *97*, 13289–13297.

[73]   G. Scatchard, *Ann NY Acad Sci* **1949**, *51*, 660–672.

[74]   C. Tanford, *Physical Chemistry of Macromolecules*. John Wiley & Sons, Inc.: New York, **1961**.

[75]   R. A. Copeland, *Enzymes: A Practical Introduction to Structure, Mechanism, and Data Analysis*. Wiley-VCH: New York, **2000**.

[76]   T. Hauenschild, J. Reichenwallner, V. Enkelmann, D. Hinderberger, *Chem Eur J* **2016**, *22*, 12825–12838.

[77]   J. Matsui, Y. Miyoshi, O. Doblhoff-Dier, T. Takeuchi, *Anal Chem* **1995**, *67*, 4404–4408.

[78]   H. Hussain, K. Y. Mya, C. He, *Langmuir* **2008**, *24*, 13279–13286.

[79]   K. A. Sharp, A. Nicholls, R. F. Fine, B. Honig, *Science* **1991**, *252*, 106–109.

[80]   I. Tunon, E. Silla, J. L. Pascual-Ahuir, *Protein Eng* **1992**, *5*, 715–716.

[81]   N. C. Woodward, B. Z. Chowdhry, M. J. Snowden, S. A. Leharne, P. C. Griffiths, A. L. Winnington, *Langmuir* **2003**, *19*, 3202–3211.

[82]   C. D. Jones, L. A. Lyon, *Macromolecules* **2003**, *36*, 1988–1993.

[83]   R. A. Ramli, W. A. Laftah, S. Hashim, *RSC Adv* **2013**, *3*, 15543–15565.

[84]   P. L. Privalov, O. B. Ptitsyn, *Biopolymers* **1969**, *8*, 559–571.

[85]   J. M. Sturtevant, *Proc Natl Acad Sci USA* **1977**, *74*, 2236–2240.

[86]   K. Vuignier, J. Schappler, J. L. Veuthey, P. A. Carrupt, S. Martel, *Anal Bioanal Chem* **2010**, *398*, 53–98.

[87]   R. I. Boysen, A. J. O. Jong, J. A. Wilce, G. F. King, M. T. W. Hearn, *J Biol Chem* **2002**, *277*, 23–31.

[88]   J. F. Brandts, *J Am Chem Soc* **1964**, *86*, 4291–4301.

[89]   W. Bode, A. Blume, *FEBS Lett* **1973**, *36*, 318–322.

[90]   D. J. W. Grant, M. Mehdizadeh, A. H. L. Chow, J. E. Fairbrother, *Int J Pharm* **1984**, *18*, 25–38.

[91]   N. V. Prabhu, K. A. Sharp, *Annu Rev Phys Chem* **2005**, *56*, 521–548.

[92]   A. Vailaya, C. Horvath, *Ind Eng Chem Res* **1996**, *35*, 2964–2981.

[93]   T. Galaon, V. David, *J Sep Sci* **2011**, *34*, 1423–1428.

[94]   P. R. Majhi, A. Blume, *Langmuir* **2001**, *17*, 3844–3851.

[95]   R. I. Boysen, A. J. O. Jong, M. T. W. Hearn, *J Chromatogr A* **2005**, *1079*, 173–186.

[96]   E. D. Vieira, L. G. M. Basso, A. J. Costa-Filho, *Biochim Biophys Acta, Biomembr* **2017**, *1859*, 1133–1143.

[97]   T. Y. Kao, C. J. Tsai, Y. J. Lan, Y. W. Chiang, *Phys Chem Chem Phys* **2017**, *19*, 9584–9591.

[98]   G. I. Makhatadze, P. L. Privalov, *J Mol Biol* **1990**, *213*, 375–384.

[99]   P. L. Privalov, G. I. Makhatadze, *J Mol Biol* **1990**, *213*, 385–391.
[100]   S. Paula, W. Süs, J. Tuchtenhagen, A. Blume, *J Phys Chem* **1995**, *99*, 11742–11751.
[101]   A. G. Kozlov, T. M. Lohman, *Biochemistry* **1999**, *38*, 7388–7397.
[102]   W. Y. Chen, H. M. Huang, C. C. Lin, F. Y. Lin, Y. C. Chan, *Langmuir* **2003**, *19*, 9395–9403.
[103]   C. N. Pace, *Trends Biochem Sci* **1990**, *15*, 14–17.
[104]   D. Chandler, *Nature* **2005**, *437*, 640–647.
[105]   E. Meirovitch, A. Nayeem, J. H. Freed, *J Phys Chem* **1984**, *88*, 3454–3465.
[106]   J. L. V. Anjos, P. S. Santiago, M. Tabak, A. Alonso, *Colloids Surf, B* **2011**, *88*, 463–470.
[107]   Y. K. Shin, J. H. Freed, *Biophys J* **1989**, *56*, 1093–1100.
[108]   Y. K. Shin, D. E. Budil, J. H. Freed, *Biophys J* **1993**, 1283–1294.
[109]   S. Yamabe, Y. Furumiya, K. Hiraoka, K. Morise, *Chem Phys Lett* **1986**, *131*, 261–266.
[110]   E. D. Sprague, C. E. Larrabee Jr., H. B. Halsall, *Anal Biochem* **1980**, *101*, 175–181.
[111]   T. L. Kirley, E. D. Sprague, H. B. Halsall, *Biophys Chem* **1982**, *15*, 209–216.
[112]   Y. Liu, J. M. Sturtevant, *Biophys Chem* **1997**, *64*, 121–126.
[113]   P. W. Atkins, *Physikalische Chemie.* Wiley VCH: Weinheim, **2001**.
[114]   A. V. Finkelstein, O. B. Ptitsyn, *Protein physics: a course of lectures.* Academic Press: London, San Diego, **2002**.
[115]   W. J. Becktel, J. A. Schellman, *Biopolymers* **1987**, *26*, 1859–1877.
[116]   J. D. Dunitz, *Chem Biol* **1995**, *2*, 709–712.
[117]   D. H. Leung, R. G. Bergman, K. N. Raymond, *J Am Chem Soc* **2008**, *130*, 2798–2805.
[118]   T. Keleti, *Biochem J* **1983**, *209*, 277–280.
[119]   H. Naghibi, A. Tamura, J. M. Sturtevant, *Proc Natl Acad Sci USA* **1995**, *92*, 5597–5599.
[120]   G. Weber, *J Phys Chem* **1995**, *99,* 1052–1059.
[121]   J. Tellinghuisen, *Biophys Chem* **2006**, *120*, 114–120.
[122]   A. Cooper, *Biophys Chem* **2005**, *115*, 89–97.
[123]   K. Lum, D. Chandler, J. D. Weeks, *J Phys Chem B* **1999**, *103*, 4570–4577.
[124]   N. Choudhury, B. M. Pettitt, *J Am Chem Soc* **2005**, *127*, 3556–3567.
[125]   A. Ben-Naim, *J Chem Phys* **2006**, *125*, 024901.
[126]   C. N. Pace, B. A. Shirley, M. McNutt, K. Gajiwala, *FASEB J* **1996**, *10*, 75–83.
[127]   L. Pauling, *Proc Natl Acad Sci USA* **1928**, *14*, 359–362.
[128]   L. Pauling, *J Am Chem Soc* **1932**, *54*, 3570–3582.
[129]   R. Parajuli, *Curr Sci* **2016**, *110*, 495–498.
[130]   R. Dinarvand, A. D'Emanuele, *J Controlled Release* **1995**, *36*, 221–227.
[131]   R. Haag, *Angew Chem Int Ed* **2004**, *43*, 278–282.
[132]   R. Haag, F. Kratz, *Angew Chem Int Ed* **2006**, *45*, 1198–1215.
[133]   R. Dulbecco, M. Vogt, *J Exp Med* **1954**, *99*, 167–182.
[134]   S. Stoll, A. Schweiger, *J Magn Reson* **2006**, *178*, 42–55.
[135]   D. J. Schneider, J. H. Freed, Calculating slow motional magnetic resonance spectra: A user's guide. In *Spin Labeling: Theory and Applications*; L. J. Berliner, J. Reuben, Eds.; Plenum Press: New York, London, **1989**, Vol. 8, pp 1–76.
[136]   P. Schiebener, J. Straub, J. M. H. Levelt Sengers, J. S. Gallagher, *J Phys Chem Ref Data* **1990**, *19*, 677–717.
[137]   J. Kestin, M. Sokolov, W. A. Wakeham, *J Phys Chem Ref Data* **1978**, *7*, 941–948.
[138]   J. F. Swindells, J. R. Coe Jr., T. B. Godfrey, *J Res Nat Bur Stand* **1952**, *48*, 1–31.
[139]   L. Korson, W. Drost-Hansen, F. J. Millero, *J Phys Chem* **1969**, *73*, 34–39.
[140]   E. Krieger, G. Koraimann, G. Vriend, *Proteins Struct Funct Genet* **2002**, *47*, 393–402.

Chapter 11

[1]   D. F. H. Wallach, S. P. Verma, E. Weidekamm, V. Bieri, *Biochim Biophys Acta, Biomembr* **1974**, *356*, 68–81.
[2]   J. D. Morrisett, H. J. Pownall, A. M. Gotto, *J Biol Chem* **1975**, *250*, 2487–2494.
[3]   H. H. Ruf, M. Gratzl, *Biochim Biophys Acta, Protein Struct* **1976**, *446*, 134–142.
[4]   A. N. Kuznetsov, B. Ebert, G. Lassmann, A. B. Shapiro, *Biochim Biophys Acta, Protein Struct* **1975**, *379*, 139–146.
[5]   S. J. Rehfeld, D. J. Eatough, W. Z. Plachy, *J Lipid Res* **1978**, *19*, 841–849.
[6]   N. A. Abumrad, R. C. Perkins, J. H. Park, C. R. Park, *J Biol Chem* **1981**, *256*, 9183–9191.
[7]   R. C. Perkins Jr., N. Abumrad, K. Balasubramanian, L. R. Dalton, A. H. Beth, J. H. Park, C. R. Park, *Biochemistry* **1982**, *21*, 4059–4064.
[8]   T. G. Gantchev, M. B. Shopova, *Biochim Biophys Acta, Protein Struct Mol Enzymol* **1990**, *1037*, 422–434.
[9]   M. Ge, S. B. Rananavare, J. H. Freed, *Biochim Biophys Acta, Gen Subj* **1990**, *1036*, 228–236.

[10]   B. J. Gaffney, H. M. McConnell, *J Magn Reson* **1974**, *16*, 1–28.

[11]   A. Alonso, W. P. dos Santos, S. J. Leonor, J. G. dos Santos, M. Tabak, *Biophys J* **2001**, *81*, 3566–3576.

[12]   G. Matthes, G. Seibt, V. Muravsky, G. Hersmann, G. Dornheim, *Transfus Apher Sci* **2002**, *27*, 129–135.

[13]   A. Alonso, J. V. da Silva, M. Tabak, *Biochim Biophys Acta, Proteins Proteomics* **2003**, *1646*, 32–41.

[14]   S. C. Kazmierczak, A. Gurachevsky, G. Matthes, V. Muravsky, *Clin Chem* **2006**, *52*, 2129–2134.

[15]   A. Gurachevsky, E. Muravskaya, T. Gurachevskaya, L. Smirnova, V. Muravsky, *Cancer Invest* **2007**, *25*, 378–383.

[16]   A. Gurachevsky, E. Shimanovitch, T. Gurachevskaya, V. Muravsky, *Biochem Biophys Res Commun* **2007**, *360*, 852–856.

[17]   V. Muravsky, T. Gurachevskaya, S. Berezenko, K. Schnurr, A. Gurachevsky, *Spectrochim Acta, Part A* **2009**, *74*, 42–47.

[18]   D. de Sousa Neto, C. E. G. Salmon, A. Alonso, M. Tabak, *Colloids Surf, B* **2009**, *70*, 147–156.

[19]   C. Schmidt, C. Krumbiegel, K. Waterstradt, G. Petznick, H. Schäfer, K. Schnurr, In *Expectation-Maximization-Estimation of Mixture Densities for Electron-Spin-Resonance-Analysis of Albumin*, IEEE International Workshop on Genomic Signal Processing and Statistics (GENSIPS), Minneapolis, MN, USA, May 17–19, pp 1–4, **2009**.

[20]   M. Gelos, D. Hinderberger, E. Welsing, J. Belting, K. Schnurr, B. Mann, *Int J Colorectal Dis* **2010**, *25*, 119–127.

[21]   J. L. V. Anjos, P. S. Santiago, M. Tabak, A. Alonso, *Colloids Surf, B* **2011**, *88*, 463–470.

[22]   A. A. Pavicevic, A. D. Popovic-Bijelic, M. D. Mojovic, S. V. Susnjar, G. G. Bacic, *J Phys Chem B* **2014**, *118*, 10898–10905.

[23]   D. Tatlidil, M. Ucuncu, Y. Akdogan, *Phys Chem Chem Phys* **2015**, *17*, 22678–22685.

[24]   Y. Akdogan, M. Emrullahoglu, D. Tatlidil, M. Ucuncu, G. Cakan-Akdogan, *Phys Chem Chem Phys* **2016**, *18*, 22531–22539.

[25]   T. Hauenschild, J. Reichenwallner, V. Enkelmann, D. Hinderberger, *Chem Eur J* **2016**, *22*, 12825–12838.

[26]   A. Pavicevic, J. Luo, A. Popovic-Bijelic, M. Mojovic, *Eur Biophys J* **2017**, 1–15.

[27]   J. Strancar, T. Koklic, Z. Arsov, B. Filipic, D. Stopar, M. A. Hemminga, *J Chem Inf Model* **2005**, *45*, 394–406.

[28]   T. Peters Jr., *All about Albumin: Biochemistry, Genetics and Medical Applications*. Academic Press, Inc.: San Diego, **1995**.

[29]   S. Curry, P. Brick, N. P. Franks, *Biochim Biophys Acta, Mol Cell Biol Lipids* **1999**, *1441*, 131–140.

[30]   J. D. Morrisett, The use of spin labels for studying the structure and function of enzymes. In *Spin Labeling: Theory and Applications*; L. J. Berliner, Ed.; Academic Press: New York, **1976**, Vol. 1, pp 273–338.

[31]   J. Juarez, P. Taboada, V. Mosquera, *Biophys J* **2009**, *96*, 2353–2370.

[32]   J. Juarez, P. Taboada, S. Goy-Lopez, A. Gambon, M. B. Madec, S. G. Yeates, V. Mosquera, *J Phys Chem B* **2009**, *113*, 12391–12399.

[33]   S. H. Arabi, B. Aghelnejad, C. Schwieger, A. Meister, A. Kerth, D. Hinderberger, *Biomater Sci* **2018**, *6*, 478–492.

[34]   J. H. Freed, Theory of slow tumbling ESR spectra for nitroxides. In *Spin Labeling: Theory and Applications*; L. J. Berliner, Ed.; Academic Press: New York, **1976**, Vol. 1, pp 53–132.

[35]   K. A. Earle, D. E. Budil, J. H. Freed, *J Phys Chem* **1993**, *97*, 13289–13297.

[36]   M. Pantusa, L. Sportelli, R. Bartucci, *Eur Biophys J* **2008**, *37*, 961–973.

[37]   M. Rezaei-Tavirani, S. H. Moghaddamnia, B. Ranjbar, M. Amani, S. A. Marashi, *J Biochem Mol Biol* **2006**, *39*, 530–536.

[38]   R. K. Mitra, S. S. Sinha, S. K. Pal, *Langmuir* **2007**, *23*, 10224–10229.

[39]   S. Curry, *Vox Sang* **2002**, *83*, 315–319.

[40]   G. Scatchard, *Ann NY Acad Sci* **1949**, *51*, 660–672.

[41]   A. A. Spector, K. John, J. E. Fletcher, *J Lipid Res* **1969**, *10*, 56–67.

[42]   J. D. Ashbrook, A. A. Spector, E. C. Santos, J. E. Fletcher, *J Biol Chem* **1975**, *250*, 2333–2338.

[43]   H. E. Rosenthal, *Anal Biochem* **1967**, *20*, 525–532.

[44]   F. Karush, *J Am Chem Soc* **1950**, *72*, 2705–2713.

[45]   A. A. Spector, *J Lipid Res* **1975**, *16*, 165–179.

[46]   C. Tanford, *Physical Chemistry of Macromolecules*. John Wiley & Sons, Inc.: New York, **1961**.

[47]   P. De Meyts, J. Roth, *Biochem Biophys Res Commun* **1975**, *66*, 1118–1126.

[48]   V. S. Pande, D. S. Rokhsar, *Proc Natl Acad Sci USA* **1998**, *95*, 1490–1494.

[49]   A. V. Finkelstein, O. B. Ptitsyn, *Protein physics: a course of lectures.* Academic Press: London, San Diego, **2002**.

[50]   A. A. Saboury, A. A. Moosavi-Movahedi, *Biochem Educ* **1994**, *22*, 210–211.

[51]   A. O. Pedersen, B. Honore, R. Brodersen, *Eur J Biochem* **1990**, *190*, 497–502.

[52]   H. Aki, M. Yamamoto, *J Pharm Sci* **1994**, *83*, 1712–1716.

[53] S. Gumpen, P. O. Hegg, H. Martens, *Biochim Biophys Acta, Lipids Lipid Metab* **1979**, *574*, 189–196.
[54] A. Shrake, P. D. Ross, *J Biol Chem* **1988**, *263*, 15392–15399.
[55] A. Shrake, P. D. Ross, *J Biol Chem* **1990**, *265*, 5055–5059.
[56] A. Shrake, P. D. Ross, *Biopolymers* **1992**, *32*, 925–940.
[57] J. A. Schellman, *Biopolymers* **1975**, *14*, 999–1018.
[58] J. D. McGhee, *Biopolymers* **1976**, *15*, 1345–1375.
[59] G. A. Pico, *Int J Biol Macromol* **1997**, *20*, 63–73.
[60] B. Farruggia, G. A. Pico, *Int J Biol Macromol* **1999**, *26*, 317–323.
[61] B. E. Lang, K. D. Cole, *Biotechnol Progr* **2015**, *31*, 62–69.
[62] J. A. Janovick, M. Goulet, E. Bush, J. Greer, D. G. Wettlaufer, P. M. Conn, *J Pharmacol Exp Ther* **2003**, *305*, 608–614.
[63] J. A. Janovick, M. D. Stewart, D. Jacob, L. D. Martin, J. M. Deng, C. A. Stewart, Y. Wang, A. Cornea, L. Chavali, S. Lopez, S. Mitalipov, E. Kang, H. S. Lee, P. R. Manna, D. M. Stocco, R. R. Behringer, P. M. Conn, *Proc Natl Acad Sci USA* **2013**, *110*, 21030–21035.
[64] M. J. N. Junk, H. W. Spiess, D. Hinderberger, *J Magn Reson* **2011**, *210*, 210–217.
[65] A. Giannoulis, K. Ackermann, P. E. Spindler, C. Higgins, D. B. Cordes, A. M. Z. Slawin, T. F. Prisner, B. E. Bode, *Phys Chem Chem Phys* **2018**, *20*, 11196–11205.
[66] G. Jeschke, V. Chechik, P. Ionita, A. Godt, H. Zimmermann, J. Banham, C. R. Timmel, D. Hilger, H. Jung, *Appl Magn Reson* **2006**, *30*, 473–498.
[67] G. Jeschke, G. Panek, A. Godt, A. Bender, H. Paulsen, *Appl Magn Reson* **2004**, *26*, 223–244.
[68] J. Ghuman, P. A. Zunszain, I. Petitpas, A. A. Bhattacharya, M. Otagiri, S. Curry, *J Mol Biol* **2005**, *353*, 38–52.
[69] P. Ascenzi, A. Bocedi, S. Notari, G. Fanali, R. Fesce, M. Fasano, *Mini Rev Med Chem* **2006**, *6*, 483–489.
[70] P. Ascenzi, M. Fasano, *Biophys Chem* **2010**, *148*, 16–22.
[71] A. Kapoor, J. A. Ritter, R. T. Yang, *Langmuir* **1990**, *6*, 660–664.
[72] B. E. Bode, D. Margraf, J. Plackmeyer, G. Dürner, T. F. Prisner, O. Schiemann, *J Am Chem Soc* **2007**, *129*, 6736–6745.
[73] G. Jeschke, M. Sajid, M. Schulte, A. Godt, *Phys Chem Chem Phys* **2009**, *11*, 6580–6591.
[74] T. von Hagens, Y. Polyhach, M. Sajid, A. Godt, G. Jeschke, *Phys Chem Chem Phys* **2013**, *15*, 5854–5866.
[75] G. Strobl, *The Physics of Polymers: Concepts for Understanding Their Structures and Behavior.* Springer-Verlag: Berlin, Heidelberg, **2007**.
[76] M. J. N. Junk, Assessing the Functional Structure of Molecular Transporters by EPR Spectroscopy. Ph.D. Thesis, Johannes Gutenberg-Universität Mainz, **2010**.
[77] D. R. Kattnig, J. Reichenwallner, D. Hinderberger, *J Phys Chem B* **2013**, *117*, 16542–16557.
[78] D. Hinderberger, H. W. Spiess, G. Jeschke, *J Phys Chem B* **2004**, *108*, 3698–3704.
[79] T. A. McCarty, P. M. Page, G. A. Baker, F. V. Bright, *Ind Eng Chem Res* **2008**, *47*, 560–569.
[80] T. A. Page, N. D. Kraut, P. M. Page, G. A. Baker, F. V. Bright, *J Phys Chem B* **2009**, *113*, 12825–12830.
[81] V. A. Livshits, D. Marsh, *Biochim Biophys Acta, Biomembr* **2000**, *1466*, 350–360.
[82] W. Scheider, *J Phys Chem* **1980**, *84*, 925–928.
[83] W. Scheider, *Proc Natl Acad Sci USA* **1979**, *76*, 2283–2287.
[84] D. Banerjee, S. K. Pal, *Photochem Photobiol* **2008**, *84*, 750–757.
[85] M. Bhattacharya, N. Jain, S. Mukhopadhyay, *J Phys Chem B* **2011**, *115*, 4195–4205.
[86] A. Cooper, *Biophys Chem* **2005**, *115*, 89–97.
[87] Y. Fang, G. C. Tong, G. E. Means, *Biochim Biophys Acta, Proteins Proteomics* **2006**, *1764*, 285–291.
[88] R. Dulbecco, M. Vogt, *J Exp Med* **1954**, *99*, 167–182.
[89] P. D. Ross, A. Shrake, *J Biol Chem* **1988**, *263*, 11196–11202.
[90] R. Klinke, S. Silbernagl, *Lehrbuch der Physiologie.* Georg Thieme Verlag: Stuttgart, **1996**.
[91] F. Wu, B. J. Gaffney, *Biochemistry* **2006**, *45*, 12510–12518.
[92] R. E. Martin, M. Pannier, F. Diederich, V. Gramlich, M. Hubrich, H. W. Spiess, *Angew Chem Int Ed* **1998**, *37*, 2833–2837.
[93] M. Pannier, S. Veit, A. Godt, G. Jeschke, H. W. Spiess, *J Magn Reson* **2000**, *142*, 331–340.
[94] S. Stoll, A. Schweiger, *J Magn Reson* **2006**, *178*, 42–55.
[95] S. W. Provencher, *Comput Phys Commun* **1982**, *27*, 213–227.
[96] P. Schiebener, J. Straub, J. M. H. Levelt Sengers, J. S. Gallagher, *J Phys Chem Ref Data* **1990**, *19*, 677–717.
[97] J. Kestin, M. Sokolov, W. A. Wakeham, *J Phys Chem Ref Data* **1978**, *7*, 941–948.
[98] J. F. Swindells, J. R. Coe Jr., T. B. Godfrey, *J Res Nat Bur Stand* **1952**, *48*, 1–31.
[99] L. Korson, W. Drost-Hansen, F. J Millero, *J Phys Chem* **1969**, *73*, 34–39.
[100] K. Monkos, *Biochim Biophys Acta, Proteins Proteomics* **2004**, *1700*, 27–34.

Chapter 12

[1] M. J. N. Junk, H. W. Spiess, D. Hinderberger, *Angew Chem Int Ed* **2010**, *49*, 8755–8759.

[2] M. J. N. Junk, H. W. Spiess, D. Hinderberger, *J Magn Reson* **2011**, *210*, 210–217.

[3] M. J. N. Junk, H. W. Spiess, D. Hinderberger, *Biophys J* **2011**, *100*, 2293–2301.

[4] Y. Akdogan, M. J. N. Junk, D. Hinderberger, *Biomacromolecules* **2011**, *12*, 1072–1079.

[5] Y. Akdogan, D. Hinderberger, *J Phys Chem B* **2011**, *115*, 15422–15429.

[6] Y. Akdogan, Y. Wu, K. Eisele, M. Schaz, T. Weil, D. Hinderberger, *Soft Matter* **2012**, *8*, 11106–11114.

[7] J. Reichenwallner, D. Hinderberger, *Biochim Biophys Acta, Gen Subj* **2013**, *1830*, 5382–5393.

[8] S. I. Fujiwara, T. Amisaki, *Biochim Biophys Acta, Gen Subj* **2013**, *1830*, 5427–5434.

[9] D. S. Park, C. E. Petersen, C. E. Ha, K. Harohalli, J. B. Feix, N. V. Baghavan, *IUBMB Life* **1999**, *48*, 169–174.

[10] C. M. Gruian, C. Rickert, S. C. T. Nicklisch, E. Vanea, H. J. Steinhoff, S. Simon, *ChemPhysChem* **2017**, *18*, 634–642.

[11] T. Peters Jr., *All about Albumin: Biochemistry, Genetics and Medical Applications*. Academic Press, Inc.: San Diego, **1995**.

[12] T. Komatsu, *Nanoscale* **2012**, *4*, 1910–1918.

[13] S. H. Arabi, B. Aghelnejad, C. Schwieger, A. Meister, A. Kerth, D. Hinderberger, *Biomater Sci* **2018**, *6*, 478–492.

[14] G. Matthes, G. Seibt, V. Muravsky, G. Hersmann, G. Dornheim, *Transfus Apher Sci* **2002**, *27*, 129–135.

[15] S. C. Kazmierczak, A. Gurachevsky, G. Matthes, V. Muravsky, *Clin Chem* **2006**, *52*, 2129–2134.

[16] A. Gurachevsky, E. Muravskaya, T. Gurachevskaya, L. Smirnova, V. Muravsky, *Cancer Invest* **2007**, *25*, 378–383.

[17] M. Gelos, D. Hinderberger, E. Welsing, J. Belting, K. Schnurr, B. Mann, *Int J Colorectal Dis* **2010**, *25*, 119–127.

[18] M. Basset, G. Defaye, E. M. Chambaz, *Biochim Biophys Acta, Protein Struct* **1977**, *491*, 434–446.

[19] M. Basset, E. M. Chambaz, G. Defaye, B. Metz, *Biochimie* **1978**, *60*, 715–724.

[20] S. Y. Cheng, G. Rakhit, F. Erard, J. Robbins, C. F. Chignell, *J Biol Chem* **1981**, *256*, 831–836.

[21] M. D. Barratt, D. M. Rickwood, *Biophys Chem* **1984**, *19*, 69–73.

[22] T. Hauenschild, Spinmarkierung pharmazeutischer Wirkstoffe sowie deren Bindungseigenschaften an Serum Albumin vom Menschen, Diploma Thesis, Johannes Gutenberg-Universität Mainz, **2013**.

[23] D. Tatlidil, M. Ucuncu, Y. Akdogan, *Phys Chem Chem Phys* **2015**, *17*, 22678–22685.

[24] Y. Akdogan, M. Emrullahoglu, D. Tatlidil, M. Ucuncu, G. Cakan-Akdogan, *Phys Chem Chem Phys* **2016**, *18*, 22531–22539.

[25] T. Hauenschild, J. Reichenwallner, V. Enkelmann, D. Hinderberger, *Chem Eur J* **2016**, *22*, 12825–12838.

[26] T. Hauenschild, ESR-basierte Entwicklung neuer, postmodifizierter Albumin-gebundener ß-Blocker-derivate sowie neuartiger Nitroxidradikale zur systematischen Charakterisierung supramolekularer Systeme, Ph.D. Thesis. Martin-Luther-Universität Halle-Wittenberg, **2018**.

[27] R. Glowacki, H. Jakubowski, *J Biol Chem* **2004**, *279*, 10864–10871.

[28] U. Kragh-Hansen, *Pharmacol Rev* **1981**, *33*, 17–53.

[29] S. Curry, *Drug Metab Pharmacokinet* **2009**, *24*, 342–357.

[30] J. D. Ashbrook, A. A. Spector, E. C. Santos, J. E. Fletcher, *J Biol Chem* **1975**, *250*, 2333–2338.

[31] A. O. Pedersen, B. Hust, S. Andersen, F. Nielsen, R. Brodersen, *Eur J Biochem* **1986**, *154*, 545–552.

[32] I. A. Kovacs, M. S. Szalay, P. Csermely, *FEBS Lett* **2005**, *579*, 2254–2260.

[33] J. von Neumann, *Math Ann* **1928**, *100*, 295–320.

[34] J. Nash, *Ann Math* **1951**, *54*, 286–295.

[35] J. Nash, *Econometrica* **1953**, *21*, 128–140.

[36] F. Karush, *J Am Chem Soc* **1950**, *72*, 2705–2713.

[37] J. E. Fletcher, A. A. Spector, J. D. Ashbrook, *Biochemistry* **1970**, *9*, 4580–4587.

[38] M. Eigen, *Naturwissenschaften* **1971**, *58*, 465–523.

[39] A. K. Shaw, S. K. Pal, *J Photochem Photobiol, B* **2008**, *90*, 69–77.

[40] V. Muravsky, T. Gurachevskaya, S. Berezenko, K. Schnurr, A. Gurachevsky, *Spectrochim Acta, Part A* **2009**, *74*, 42–47.

[41] K. Wallevik, *J Biol Chem* **1973**, *248*, 2650–2655.

[42] D. K. Sasmal, T. Mondal, S. S. Mojumdar, A. Choudhury, R. Banerjee, K. Bhattacharyya, *J Phys Chem B* **2011**, *115*, 13075–13083.

[43] M. A. Evenson, H. F. Deutsch, *Clin Chim Acta* **1978**, *89*, 341–354.

[44] B. Jachimska, M. Wasilewska, Z. Adamczyk, *Langmuir* **2008**, *24*, 6866–6872.

[45] A. Polson, *Kolloid Z* **1939**, *88*, 51–61.

[46] K. Monkos, B. Turczynski, *Int J Biol Macromol* **1991**, *13*, 341–344.

[47] K. Monkos, *Int J Biol Macromol* **1996**, *18*, 61–68.

[48]   K. Monkos, *Biochim Biophys Acta, Proteins Proteomics* **2004**, *1700*, 27–34.
[49]   B. J. Gaffney, H. M. McConnell, *J Magn Reson* **1974**, *16*, 1–28.
[50]   S. J. Rehfeld, D. J. Eatough, W. Z. Plachy, *J Lipid Res* **1978**, *19*, 841–849.
[51]   M. Schlosshauer, *Rev Mod Phys* **2004**, *76*, 1267–1305.
[52]   T. G. Gantchev, M. B. Shopova, *Biochim Biophys Acta, Protein Struct Mol Enzymol* **1990**, *1037*, 422–434.
[53]   R. C. Perkins Jr., N. Abumrad, K. Balasubramanian, L. R. Dalton, A. H. Beth, J. H. Park, C. R. Park, *Biochemistry* **1982**, *21*, 4059–4064.
[54]   M. Ge, S. B. Rananavare, J. H. Freed, *Biochim Biophys Acta, Gen Subj* **1990**, *1036*, 228–236.
[55]   F. De Simone, R. Guzzi, L. Sportelli, D. Marsh, R. Bartucci, *Biochim Biophys Acta, Biomembr* **2007**, *1768*, 1541–1549.
[56]   R. Guzzi, B. Rizzuti, R. Bartucci, *J Phys Chem B* **2012**, *116*, 11608–11615.
[57]   P. Höfer, A. Grupp, H. Nebenführ, M. Mehring, *Chem Phys Lett* **1986**, *132*, 279–282.
[58]   W. B. Mims, *Proc R Soc London, Ser A* **1965**, *283*, 452–457.
[59]   E. R. Davies, *Phys Lett A* **1974**, *47*, 1–2.
[60]   S. A. Dzuba, *J Struct Chem* **2013**, *54*, S1–S15.
[61]   D. Marsh, *J Magn Reson* **2018**, *290*, 38–45.
[62]   T. Schmidt, M. A. Wälti, J. L. Baber, E. J. Hustedt, G. M. Clore, *Angew Chem Int Ed* **2016**, *128*, 16137–16141.
[63]   P. P. Borbat, E. R. Georgieva, J. H. Freed, *J Phys Chem Lett* **2013**, *4*, 170–175.
[64]   P. P. Borbat, J. H. Freed, *Methods Enzymol* **2007**, *423*, 52–116.
[65]   R. Ward, A. Bowman, E. Sozudogru, H. El-Mkami, T. Owen-Hughes, D. G. Norman, *J Magn Reson* **2010**, *207*, 164–167.
[66]   A. Blank, *Phys Chem Chem Phys* **2017**, *19*, 5222–5229.
[67]   O. Schiemann, P. Cekan, D. Margraf, T. F. Prisner, S. T. Sigurdsson, *Angew Chem Int Ed* **2009**, *48*, 3292–3295.
[68]   P. A. S. Cruickshank, D. R. Bolton, D. A. Robertson, R. I. Hunter, R. J. Wylde, G. M. Smith, *Rev Sci Instrum* **2009**, *80*, 103102.
[69]   G. W. Reginsson, R. I. Hunter, P. A. S. Cruickshank, D. R. Bolton, S. T. Sigurdsson, G. M. Smith, O. Schiemann, *J Magn Reson* **2012**, *216*, 175–182.
[70]   K. Lum, D. Chandler, J. D. Weeks, *J Phys Chem B* **1999**, *103*, 4570–4577.
[71]   D. Chandler, *Nature* **2005**, *437*, 640–647.
[72]   A. Cooper, *Biophys Chem* **2005**, *115*, 89–97.
[73]   C. Tanford, *Science* **1978**, *200*, 1012–1018.
[74]   C. Tanford, *Physical Chemistry of Macromolecules*. John Wiley & Sons, Inc.: New York, **1961**.
[75]   J. Matsui, Y. Miyoshi, O. Doblhoff-Dier, T. Takeuchi, *Anal Chem* **1995**, *67*, 4404–4408.
[76]   F. Karush, *J Am Chem Soc* **1954**, *76*, 5536–5542.
[77]   E. A. Litus, S. E. Permyakov, V. N. Uversky, E. A. Permyakov, *Cell Biochem Biophys* **2017**, 1–19.
[78]   A. J. Patel, P. Varilly, S. N. Jamadagni, M. F. Hagan, D. Chandler, S. Garde, *J Phys Chem B* **2012**, *116*, 2498–2503.
[79]   J. C. Kendrew, G. Bodo, H. M. Dintzis, R. G. Parrish, H. Wyckoff, D. C. Phillips, *Nature* **1958**, *181*, 662–666.
[80]   C. B. Anfinsen, *Science* **1973**, *181*, 223–230.
[81]   A. Kitao, N. Go, *Curr Opin Struct Biol* **1999**, *9*, 164–169.
[82]   S. I. Fujiwara, T. Amisaki, *Proteins Struct Funct Bioinf* **2006**, *64*, 730–739.
[83]   M. Kurzynski, *Prog Biophys Mol Biol* **1998**, *69*, 23–82.
[84]   W. L. Hubbell, C. J. Lopez, C. Altenbach, Z. Yang, *Curr Opin Struct Biol* **2013**, *23*, 725–733.
[85]   I. Hänelt, D. Wunnicke, E. Bordignon, H. J. Steinhoff, D. J. Slotboom, *Nat Struct Mol Biol* **2013**, *20*, 210–214.
[86]   G. Jeschke, *Emerging Top Life Sci* **2018**, *2*, 9–18.
[87]   J. A. Tuszynski, M. Kurzynski, *Introduction to Molecular Biophysics*. CRC Press: Boca Raton, **2003**.
[88]   E. Schrödinger, *What is life ?: with Mind and Matter and Autobiographical Sketches*. Cambridge University Press: Cambridge, UK, **1944**.
[89]   R. Phillips, *Physical Biology of the Cell*. Garland Science, Taylor & Francis Group, LLC: New York, **2013**.
[90]   W. Scheider, *J Phys Chem* **1980**, *84*, 925–928.
[91]   P. C. Painter, L. E. Mosher, C. Rhoads, *Biopolymers* **1982**, *21*, 1469–1472.
[92]   K. C. Chou, *Biophys Chem* **1988**, *30*, 3–48.
[93]   P. Martel, *Prog Biophys Mol Biol* **1992**, *57*, 129–179.
[94]   I. Cosic, A. N. Hodder, M. I. Aguilar, M. T. W. Hearn, *Eur J Biochem* **1991**, *198*, 113–119.
[95]   I. Cosic, *IEEE Trans Biomed Eng* **1994**, *41*, 1101–1114.
[96]   A. S. Davydov, *J Theor Biol* **1973**, *38*, 559–569.

[97]   A. S. Davydov, N. I. Kislukha, *Phys Status Solidi B* **1973**, *59*, 465–470.

[98]   W. Demtröder, *Experimentalphysik 3: Atome, Moleküle und Festkörper*. Springer-Verlag: Berlin, Heidelberg, **2010**.

[99]   R. B. Fuller, *Synergetics: Explorations in the Geometry of Thinking*. Macmillan Publishing Co., Inc.: New York, **1975**.

[100]   P. Feyerabend, *Wider den Methodenzwang*. Suhrkamp Verlag: Frankfurt am Main, **1986**.

[101]   R. K. Aggrawala, *Kybernetes* **2015**, *44*, 1193–1206.

[102]   A. Pavicevic, J. Luo, A. Popovic-Bijelic, M. Mojovic, *Eur Biophys J* **2017**, 1–15.

[103]   H. von Förster, *Understanding Understanding: Essay on Cybernetics and Cognition*. Springer-Verlag: New York, Berlin, Heidelberg, **2003**.

Appendix

Appendix A | Serum Albumin – A Model System in EPR Spectroscopy

A1 | Construction of Fatty Acid Distance Distributions from a Crystal Structure

In Junk *et al.*[A1] an approach was introduced for calculating theoretical distance distributions of doxyl stearic acids bound to HSA as obtained from the crystal structure of seven octadecanoic (stearic) acids complexed with HSA (PDB ID: 1e7i).[A2] Those theoretical distance distributions were originally generated for 3-dimensional and topological reference assignments of stearic acid-associated nitroxides, that are buried in fatty acid binding sites 1 – 7, with all being prone for potentially being occupied when albumin is spin probed. An original set of the crystal structure-derived $N_{r,\mathrm{FA}} = (N_{\mathrm{FA}}^2 - N_{\mathrm{FA}})/2 = 21$ individual distances $r_{i,j}$ is given in a symmetric 7×7 matrix form from extrapolated nitroxide positions at the methylene chain, either at C5- or C16-position (CY with $Y \in$ 5,16, **Table A1**).[A3] When read out, the individual distances $r_{Y,i,j}$ are then broadened and summed up with a gaussian function of the approximate form:[A1,A3]

$$P_{\mathrm{MD}}(r_{i,j}, Y) = \frac{1}{|A|} \cdot \sum_{i \neq j}^{N_{r,Y,\mathrm{FA}}} \exp\left(-\frac{(r - r_{Y,i,j})}{2\sigma} \right)^2 \tag{A.1}$$

with $|A|$ being a normalization constant, r is the mean distance and σ is the Gaussian broadening of individual distances $r_{Y,i,j}$. The resulting distance distribution $P_{\mathrm{MD}}(r_{i,j}, Y)$ from this kind of analysis can be used for correlating the distance distributions to individual fatty acid binding sites that are obtained experimentally by DEER experiments (see **Figure 3.3C+D**). A general assumption is made, that all association constants $K_{\mathrm{A},i} = K_{\mathrm{A}}$ of individual binding sites 1–7 are identical. A more elaborate strategy of this subject is presented in **Appendix G7**.

Table A1 | The 7×7 distance matrices of C5 and C16 atoms from stearic acid models bound to HSA

$r_{5,ij}$ [a]	1	2	3	4a	5	6	7		$r_{16,ij}$ [a]	1	2	3	4a	5	6	7
1	0	2.48	3.42	3.10	3.25	4.18	2.92		1	0	2.23	2.54	2.64	4.41	3.54	2.06
2	2.48	0	3.63	3.71	5.00	3.29	1.35		2	2.23	0	4.64	4.26	6.53	3.83	3.38
3	3.42	3.63	0	0.89	2.68	1.82	2.59		3	2.54	4.64	0	2.13	3.17	3.17	1.76
4a	3.10	3.71	0.89	0	2.14	2.18	2.92		4a	2.64	4.26	2.13	0	2.59	3.70	2.44
5	3.25	5.00	2.68	2.14	0	4.31	4.54		5	4.41	6.53	3.17	2.59	0	5.90	4.52
6	4.18	3.29	1.82	2.18	4.31	0	2.18		6	3.54	3.83	3.17	3.70	5.90	0	1.32
7	2.92	1.35	2.59	2.92	4.54	2.18	0		7	2.06	3.38	1.76	2.44	4.52	1.32	0

[a]Distances $r_{Y,i,j}$ are given in nanometers [nm] and as a symmetric matrix.[A3]

A2 | References

[A1]   M. J. N. Junk, H. W. Spiess, D. Hinderberger, *Angew Chem Int Ed* **2010**, *49*, 8755–8759.
[A2]   A. A. Bhattacharya, T. Grüne, S. Curry, *J Mol Biol* **2000**, *303*, 721–732.
[A3]   M. J. N. Junk, Assessing the Functional Structure of Molecular Transporters by EPR Spectroscopy. Ph.D. Thesis, Johannes Gutenberg-Universität Mainz, **2010**.

Appendix B | Evidence for Water-tuned Structural Differences in Albumins

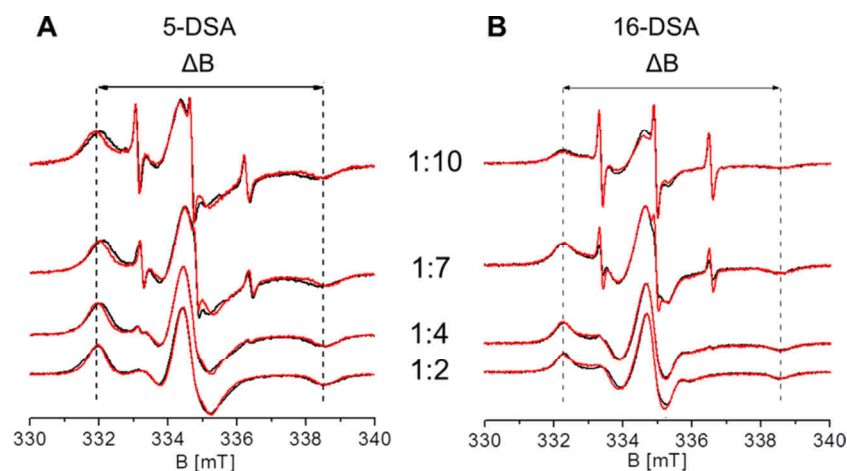## B1 | Complementary CW EPR data from samples in DEER experiments

Figure B1 | CW EPR measurements on spin probed HSA and BSA. CW EPR spectra of (**A**) 5-DSA in HSA (red) and BSA (black). (**B**) 16-DSA probed HSA (red) and BSA (black) with different nominal ratios (Albumin:DSA) recorded at $T = 25°C$. Dashed lines (---) point at the outer spectral extrema ($\Delta B = 2A_\parallel$) values, adapted from Akdogan et al.[B1]
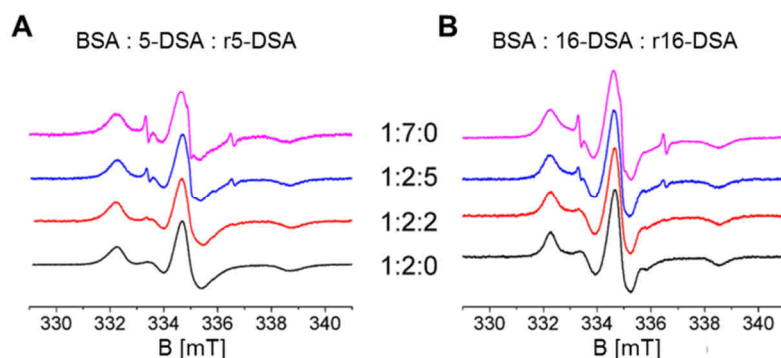
Figure B2 | CW EPR experiments of spin probed BSA. CW EPR spectra of (**A**) 5-DSA and r5-DSA and (**B**) 16-DSA and r16-DSA in BSA with different BSA : DSA : r-DSA ratios 1:2:0, 1:2:2, 1:2:5 and 1:7:0 recorded at $T = 25°C$, adapted from Akdogan et al.[B1]

The binding pocket occupation in HSA and BSA by DSA and r-DSA can be monitored indirectly by CW EPR measurements as shown in **Figure B1** and **Figure B2**. Independent of according individual equilibrium dissociation constants $K_{D,i}$ (**Table 3.1**) of each binding pocket, the fatty acid loading of albumin will approach a saturation state. This can be monitored when free fatty acid species emerge, as e.g. for a nominal loading of 1:2:5 and 1:7:0 with the spin dilution approach (**Figure B2**).[B2]

Figure 4.1 of the main text shows the intramolecular parts of the DEER time domain data and all corresponding distance distributions when BSA is loaded with exclusively seven paramagnetic 5-DSA or 16-DSA ligands. The modulation depths Δ of the all-spin systems (1:7:0) are much larger than those obtained with spin-diluted BSA-fatty acid systems as Δ is a intramolecular measure of the number of coupled spins as described in **Chapter 2.5.5**.[B3,B4] Systems with more than two spins cause artifacts such as broadening of the distance peaks, overestimation of small distances and suppression of large

distances. Hence, the all-spin system (1:7:0) has a distance distribution with strongly broadened distance peaks and an increased population of short distances compared to the results of spin-diluted BSA-fatty acid (1:2:5) systems (also shown in **Figure 4.1**).

B2 | Determination of RMSD Values Between Two Distance Distribution Curves

The determination of RMSD values between different curves shown in **Figure 4.2** was carried out for 5-DSA and 16-DSA bound to HSA and BSA using experimental distance distribution files (X_{exp}) and the distance distributions from the HSA crystal structures (HSA$_{cs}$). Those individual sets of $N_{r,FA} = 21$ single distances (**Table A1**) of the crystal structures were again artificially broadened ($\sigma = 0.18$) with a MATLAB code as in Junk *et al.* (see **Appendix A1**).[B2] The maximum peaks of the distance distributions $P(r)$ were normalized, and in case the datasets did not contain equal amounts of data points, they were interpolated to contain the same amount of values by the corresponding Microcal Origin interpolation tool. The informative distance range was kept constant at 1.5 to 8.0 nm for comparison. Each data point of the two curves was treated as follows to achieve the RMSD value:

$$\text{RMSD} = \sqrt{\frac{\sum_{i=1}^{N_t}(y_{1,i} - y_{2,i})^2}{N_t}} \quad , \quad (B.1)$$

where $y_{j,i}$ is the ordinate value of each of both datasets $j = 1,2$, while i is the i-th data point of the dataset and N_t the total number of accessible data points. All calculated RMSD-values from according distance distributions are summarized in **Table B1**.

Table B1 | RMSD analysis of fatty acid distance distributions

Ligand	Comparison	RMSD
5-DSA	HSA$_{cs}$ vs. BSA$_{exp}$	0.243
	HSA$_{exp}$ vs. BSA$_{exp}$	0.171
	HSA$_{exp}$ vs. HSA$_{cs}$	0.200
16-DSA	HSA$_{cs}$ vs. BSA$_{exp}$	0.201
	HSA$_{exp}$ vs. BSA$_{exp}$	0.272
	HSA$_{exp}$ vs. HSA$_{cs}$	0.317

B3 | Mutual Structure Alignment of HSA and BSA with the MUSTANG Algorithm

Both fatty acid-free crystal structures of HSA (PDB ID: 1BM0)[B5] and BSA (PDB ID: 3v03)[B6] that are aligned with the MUSTANG algorithm[B7] fit surprisingly well in their 3D-topology (**Figure 4.3** and **Figure B3**) as it is usually anticipated for proteins with corresponding functions.[B8] The RMSD value is 1.361 Å and sequence identity is 75.52 % among 572 aligned residues. Distracting atomic, molecular and excess macromolecular objects of e.g. dimers were removed before the alignment procedure was started. All ribbon style illustrations have been created using the aforementioned

YASARA Structure software.[B9] However, the graphical comparison between HSA and BSA for hydropathy analyses was carried out in the framework of HSA with seven FAs bound (PDB ID: 1e7i)[B10] in order to obtain an additional functional view on both crystal structures (**Figure 4.4** and **Figure 4.5**). In this case, no molecular modeling was applied on the stearic acids, so that individual ligand molecules may appear clipped when not fully resolved in the crystal structure. For all depictions, HSA's backbone matrix was kept in blue, whereas mutual differences in amino acid sequences of HSA and BSA are highlighted in red (**Figure B3**).
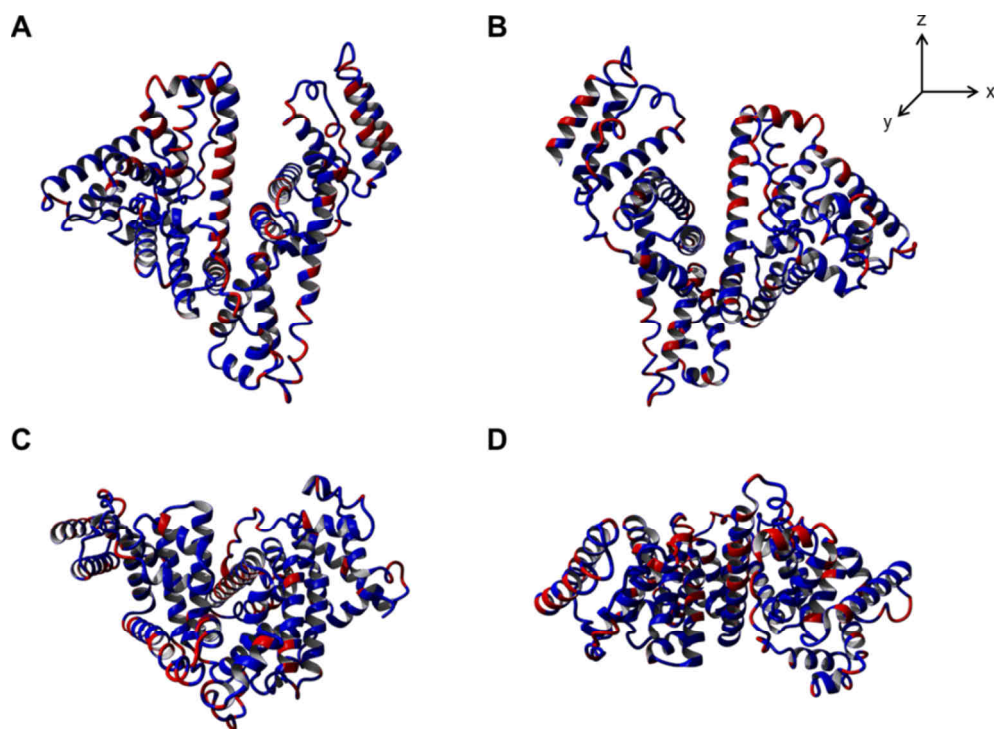
Figure B3 | 3D rotation of aligned structures of HSA and BSA. Different angular viewpoints on the MUSTANG-aligned structures of HSA (blue, PDB ID: 1BM0)[B5] and BSA (red, PDB ID: 3v03).[B6] HSA and BSA structures are shown (**A**) in front view (0, 0, 0), (**B**) rotated for an 180° angle around z-axis (0, 0, 180°), (**C**) rotated for an –90° angle around x-axis (–90°, 0, 0), and (**D**) rotated for an +90° angle around x-axis (+90°, 0, 0). Red regions denote areas where HSA and BSA contain different sets of amino acids.

B4 | Amino Acid and Hydropathy Alignment of Selected Topological Regions of HSA and BSA

The corresponding amino acid sequence alignment was constructed from the according sequences in FASTA-format (again PDB ID: 1BM0[B5] and PDB ID: 3v03[B6], see **Table B2**) obtained from the RCSB homepage.[B11] BSA was found to lack a valin at position 116, shifting the whole working frame of this protein for one amino acid. Therefore, in direct comparison to the HSA sequence, the original BSA sequence positions exceeding residue 116 are thus denoted as (i – 1).

Details on 3D-Hydropathy analysis of HSA and BSA

Hydropathy values (HI = Hydropathy Index) in **Table B2** were adopted from the original hydropathy scale of Kyte and Doolittle.[B12] Unlike their SOAP program that facilitates discrimination of hydrophobic and hydrophilic regions in proteins by applying sliding average window ranges, here the window range was deliberately set to "one" amino acid residue for getting rid of generalizations and difficult decisions emerging from this approach. The hydropathy difference (ΔHI) values are determined due to:

$$\Delta HI_i = HI_{HSA,i} - HI_{BSA,i} \qquad\qquad (B.2)$$

and the overall hydropathies are:

$$\Omega_x = \sum_i^{N(x)} HI_{x,i} \qquad\qquad , \qquad\qquad (B.3)$$

where *x* can be an arbitrary polypeptide chain of length $N(x)$ of a protein *x* and *i* denotes the respective amino acid with respect to its chain position, disregarding 3D topology in terms of surface exposition. The histograms below **Figure 4.4** and **Figure 4.5** illustrate the difference in hydropathy by the corresponding ΔHI values between HSA and BSA. Additionally, the common noisy lines appearing at low window ranges are overcome with this approach. Furthermore, amino acids are kept in the common one letter code, if no further notice is given.

Comparison of Kyte & Doolittle with other hydropathy scales

The comparison of four different normalized hydropathy scales of completely independent origin was carried out for consistency check. The Kyte and Doolittle hydropathy scale (**KD**)[B12] is based on water-vapor-transfer energies and interior/exterior amino acid distributions. The hydropathy scale from Engelman *et al.* (**GES**)[B13] is based on the amino acid free energy transfer from water to oil, including hydrophobic (surface area calculations) and hydrophilic (hydrogen bonding and pK_a) considerations. The Eisenberg hydropathy scale (**ES**)[B14] is a normalized consensus scale, that was calculated from hydrophobic dipole moments, based on five other hydropathy scales. Finally, the hydropathy scale from Naderi-Manesh (**NM**)[B15] utilizes information theory to predict solvent accessibility from the propensity of amino acids to take over certain conformations, depending on the according local environment. A quantitative estimate of mutual correlations between different hydropathy scales is given by the "Pearson's R" value, this value delivers a scalar number for cross correlations and linear dependencies. For strong correlations "Pearson's R" lies in the range:

$$R \in \left\{ \, |\pm\, 1.0\,| \leq x \leq /\pm\, 0.5/ \, \right\}$$

Table B2 | Sequence and hydropathy alignment of HSA and BSA for residues 118–582[a]

res	118	119	120	121	122	123	124	125	126	127	128	129	130	131	132	133	134	135	136	137
aa HSA	P	E	V	D	V	M	C	T	A	F	H	D	N	E	E	T	F	L	K	K
HI	-1.6	-3.5	4.2	-3.5	4.2	1.9	2.5	-0.7	1.8	2.8	-3.2	-3.5	-3.5	-3.5	-3.5	-0.7	2.8	3.8	-3.9	-3.9
aa BSA	P	D	P	N	T	L	C	D	E	F	K	A	D	E	K	K	F	W	G	K
HI	-1.6	-3.5	-1.6	-3.5	-0.7	3.8	2.5	-3.5	-3.5	2.8	-3.9	1.8	-3.5	-3.5	-3.9	-3.9	2.8	-0.9	-0.4	-3.9

res	155	156	157	158	159	160	161	162	163	164	165	166	167
aa HSA	L	F	F	A	K	R	Y	K	A	A	F	T	E
HI	3.8	2.8	2.8	1.8	-3.9	-4.5	-1.3	-3.9	1.8	1.8	2.8	-0.7	-3.5
aa BSA	L	Y	Y	A	N	K	Y	N	G	V	F	Q	E
HI	3.8	-1.3	-1.3	1.8	-3.5	-3.9	-1.3	-3.5	-0.4	4.2	2.8	-3.5	-3.5

res	180	181	182	183	184	185	186	187	188	189	190	191	192	193	194
aa HSA	P	K	L	D	E	L	R	D	E	G	K	A	S	S	A
HI	-1.6	-3.9	3.8	-3.5	-3.5	3.8	-4.5	-3.5	-3.5	-0.4	-3.9	1.8	-0.8	-0.8	1.8
aa BSA	P	K	I	E	T	M	R	E	K	V	L	T	S	S	A
HI	-1.6	-3.9	4.5	-3.5	-0.7	1.9	-4.5	-3.5	-3.9	4.2	3.8	-0.7	-0.8	-0.8	1.8

res	195	196	197	198	199	200
aa HSA	K	Q	R	L	K	C
HI	-3.9	-3.5	-4.5	3.8	-3.9	2.5
aa BSA	R	Q	R	L	R	C
HI	-4.5	-3.5	-4.5	3.8	-3.9	2.5

res	293	294	295	296	297	298	299	300	301	302	303	304	305	306	307	308
aa HSA	V	E	N	D	E	M	P	A	D	L	P	S	L	A	A	D
HI	4.2	-3.5	-3.5	-3.5	-3.5	1.9	-1.6	1.8	-3.5	3.8	-1.6	-0.8	3.8	1.8	1.8	-3.5
aa BSA	V	E	K	D	A	I	P	E	N	L	P	P	L	T	A	D
HI	4.2	-3.5	-3.9	-3.5	1.8	4.5	-1.6	-3.5	-3.5	3.8	-1.6	-1.6	3.8	-0.7	1.8	-3.5

res	309	310	311	312	313	314	315	316	317	318	319	320	321	322	323
aa HSA	F	V	E	S	K	D	V	C	K	N	Y	A	E	A	K
HI	2.8	4.2	-3.5	-0.8	-3.9	-3.5	4.2	2.5	-3.9	-3.5	-1.3	1.8	-3.5	1.8	-3.9
aa BSA	F	A	E	D	K	D	V	C	K	N	Y	Q	E	A	K
HI	2.8	1.8	-3.5	-3.5	-3.9	-3.5	4.2	2.5	-3.9	-3.5	-1.3	-3.5	-3.5	1.8	-3.9

res	351	352	353	354	355	356	357	358	359	360	361	362	363	364	365	366
aa HSA	K	T	Y	E	T	T	L	E	K	C	C	A	A	A	D	P
HI	-3.9	-0.7	-1.3	-3.5	-0.7	-0.7	3.8	-3.5	-3.9	2.5	2.5	1.8	1.8	1.8	-3.5	-1.6
aa BSA	K	E	Y	E	A	T	L	E	E	C	C	A	K	D	D	P
HI	-3.9	-3.5	-1.3	-3.5	1.8	-0.7	3.8	-3.5	-3.5	2.5	2.5	1.8	-3.9	-3.5	-3.5	-1.6

res	367	368	369	370	371	372	373	374	375	376	377	378	379	380
aa HSA	H	E	C	Y	A	K	V	F	D	E	F	K	P	L
HI	-3.2	-3.5	2.5	-1.3	1.8	-3.9	4.2	2.8	-3.5	-3.5	2.8	-3.9	-1.6	3.8
aa BSA	H	A	C	Y	S	T	V	F	D	K	L	K	H	L
HI	-3.2	1.8	2.5	-1.3	-0.8	-0.7	4.2	2.8	-3.5	-3.9	3.8	-3.9	-3.2	3.8

res	453	454	455	456	457	458	459	460	461
aa HSA	L	S	V	V	L	N	Q	L	C
HI	3.8	-0.8	4.2	4.2	3.8	-3.5	-3.5	3.8	2.5
aa BSA	L	S	L	I	L	N	R	L	C
HI	3.8	-0.8	3.8	4.5	3.8	-3.5	-4.5	3.8	2.5

res	500	501	502	503	504	505	506	507
aa HSA	K	E	F	N	A	E	T	F
HI	-3.9	-3.5	2.8	-3.5	1.8	-3.5	-0.7	2.8
aa BSA	K	A	F	D	E	K	L	F
HI	-3.9	1.8	2.8	-3.5	-3.5	-3.9	3.8	2.8

res	559	560	561	562	563	564	565	566	567	568	569	570	571	572	573	574
aa HSA	C	K	A	D	D	K	E	T	C	F	A	E	E	G	K	K
HI	2.5	-3.9	1.8	-3.5	-3.5	-3.9	-3.5	-0.7	2.5	2.8	1.8	-3.5	-3.5	-0.4	-3.9	-3.9
aa BSA	C	A	A	D	D	K	E	A	C	F	A	V	E	G	P	K
HI	2.5	1.8	1.8	-3.5	-3.5	-3.9	-3.5	1.8	2.5	2.8	1.8	4.2	-3.5	-0.4	-1.6	-3.9

res	575	576	577	578	579	580	581	582
aa HSA	L	V	A	A	S	Q	A	A
HI	3.8	4.2	1.8	1.8	-0.8	-3.5	1.8	1.8
aa BSA	L	V	V	S	T	Q	T	A
HI	3.8	4.2	4.2	-0.8	-0.7	-3.5	-0.7	1.8

[a]The results of this Kyte and Doolittle[B12] hydropathy index (HI) analysis of individual amino acid (aa) can also be found in the ΔHI plots in **Figure 4.4** and **Figure 4.5**.

The Pearson R values for a comparative analysis of hydropathy scales were obtained from the AAindex database[B16–B18] and are listed in **Table 4.1**. Furthermore, each scale was renormalized to KD values in the interval range [–4.5, +4.5], so that all scales can be compared graphically (**Figure 4.4** and **Figure 4.5**). A full set of original and normalized hydropathy values from all four scales is given in **Table B3**.

Table B3 | List of original and normalized (*) hydropathy values

Amino acid[a]	3-letter	1-letter	KD	GES	GES*	ES	ES*	NM	NM*
Isoleucine	**Ile**	**I**	4.5	–3.1	1.744	1.38	3.176	106	2.789
Valine	**Val**	**V**	4.2	–2.6	1.463	1.08	2.486	108	2.842
Leucine	**Leu**	**L**	3.8	–2.8	1.575	1.06	2.440	103	2.711
Phenylalanine	**Phe**	**F**	2.8	–3.7	2.081	1.19	2.739	108	2.842
Cysteine	**Cys**	**C**	2.5	–2.0	1.125	0.29	0.668	137	3.605
Methionine	**Met**	**M**	1.9	–3.4	1.913	0.64	1.473	73	1.921
Alanine	**Ala**	**A**	1.8	–1.6	0.900	0.62	1.427	51	1.342
Glycine	**Gly**	**G**	–0.4	–1.0	0.563	0.48	1.105	–13	–0.342
Threonine	**Thr**	**T**	–0.7	–1.2	0.675	–0.05	–0.115	–3	–0.079
Tryptophane	**Trp**	**W**	–0.9	–1.9	1.069	0.81	1.864	69	1.816
Serine	**Ser**	**S**	–0.8	–0.6	0.338	–0.18	–0.414	–26	–0.684
Tyrosine	**Tyr**	**Y**	–1.3	0.7	–0.394	0.26	0.598	11	0.289
Proline	**Pro**	**P**	–1.6	0.2	–0.113	0.12	0.276	–79	–2.079
Histidine	**His**	**H**	–3.2	3	–1.688	–0.40	–0.921	–55	–1.447
Glutamic acid	**Glu**	**E**	–3.5	8.2	–4.613	–0.74	–1.703	–115	–3.026
Glutamine	**Gln**	**Q**	–3.5	4.1	–2.306	–0.85	–1.957	–128	–3.368
Aspartic acid	**Asp**	**D**	–3.5	9.2	–5.175	–0.90	–2.072	–78	–2.053
Asparagine	**Asn**	**N**	–3.5	4.8	–2.700	–0.78	–1.795	–84	–2.211
Lysine	**Lys**	**K**	–3.9	8.8	–4.950	–1.50	–3.453	–205	–5.395
Arginine	**Arg**	**R**	–4.5	12.3	–6.919	–2.53	–5.824	–144	–3.789

[a]Hydropathy values from all four hydropathy scales (KD, GES, ES, NM). For a direct comparison three of the scales (GES, ES, NM) were renormalized (*) to the KD scale. All proteinogenic amino acids are given with full names, 3-letter and 1-letter codes. The normalized value ranges are GES* = [–6.919, +2.081], ES* = [+3.176, –5.824] and NM* = [+3.605, –5.395].

The resulting excess hydropathy points across the full primary sequences sum up according to the relation:

$$\Delta\Omega_k = \Omega_{k,\text{HSA}} - \Omega_{k,\text{BSA}} \qquad , \qquad (B.4)$$

yielding $\Delta\Omega_{\text{KD}} = 48.4$, $\Delta\Omega_{\text{NM}} = 34.8$, $\Delta\Omega_{\text{ES}} = 16.8$ and $\Delta\Omega_{\text{GES}} = 9.4$, where k is the applied normalized hydropathy scale from **Table B3**. All normalized scales give the same qualitative result with HSA being more hydrophobic along its entire polypeptide chain compared to BSA. In **Figure B4** the Kyte

and Doolittle scale itself is scaled to a range from [+0.5, –0.5] as well as the unity-normalized hydropathy values from **Table B3** are set out graphically and show intriguing similarity.
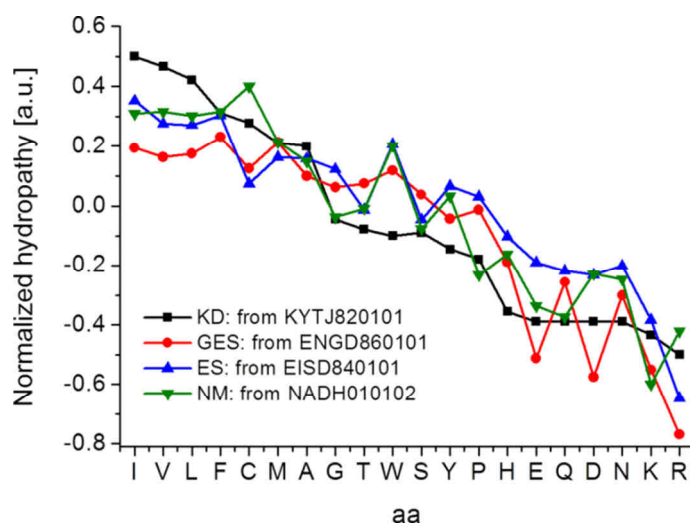
Figure B4 | Graphical comparison of unity-normalized hydropathy scales from Table B3. The hydropathy scales GES, ES and NM are again normalized to the KD scale that has been restricted to range in the interval [+0.5, –0.5]. Additionally, the 10-letter-code of AAindex entries are given as insets together with the individual hydropathy scale acronyms (aa = amino acid).

B5 | Reduction of Doxyl Stearic Acids (DSA) with Phenylhydrazine for Spin Dilution

The experimental requirement for successful distance measurements in DEER is to keep the number of paramagnetic species per macromolecular unit at about two. In case of spin probed albumin it was therefore established[B2,B19] to convert the nitroxide group of additional electron spin-bearing 5-DSA and 16-DSA molecules into an EPR-silent hydroxylamines (r5-DSA or r16-DSA) by reduction with phenylhydrazine in the scheme of Lee and Keana.[B20] This strategy facilitates the suppression of multispin-effects,[B4] although an albumin loading (FA:Albumin) equivalent of 2:1 may be exceeded. An exemplary reduction scheme of 5-DSA is shown in **Figure B5**.
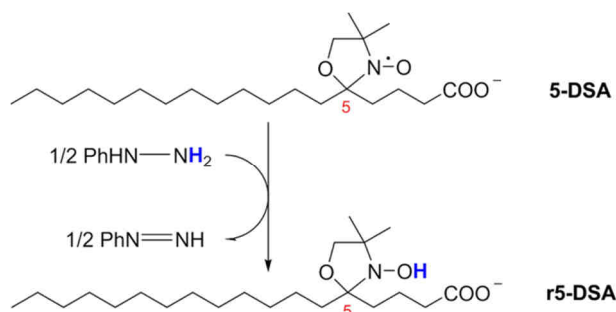
Figure B5 | Exemplary reduction of 5-DSA with phenylhydrazine.

The procedure for reduction of doxyl stearic acids (DSA) was slightly modified compared to Junk *et al.*[B2] The procedure is therefore given briefly. 1 mg of DSA powder (Sigma-Aldrich) was dissolved

in 80 µl of 0.1 M KOH (32.5 mM) and stirred from time to time with gentle agitation, yielding a yellowish and slightly opaque stock solution, partly due to micelle formation. Before each reduction procedure a fresh colorless solution of 66.2 mM phenylhydrazine (97%, Sigma-Aldrich) in 0.1 M KOH was prepared and mixed thoroughly. 12.5 µl of this phenylhydrazine stock solution was added to 50 µl of 32.5 mM DSA in 0.1 M KOH so that the reaction solution was equipped with phenylhydrazine (0.51 eq) and 26 mM DSA. This reaction was allowed to proceed under argon atmosphere at room temperature. A thorough observation of the reduction procedure was made in the time course of 1.0 – 1.5 hours (**Figure B6**) by a quantitative approach utilizing a double integration routine.
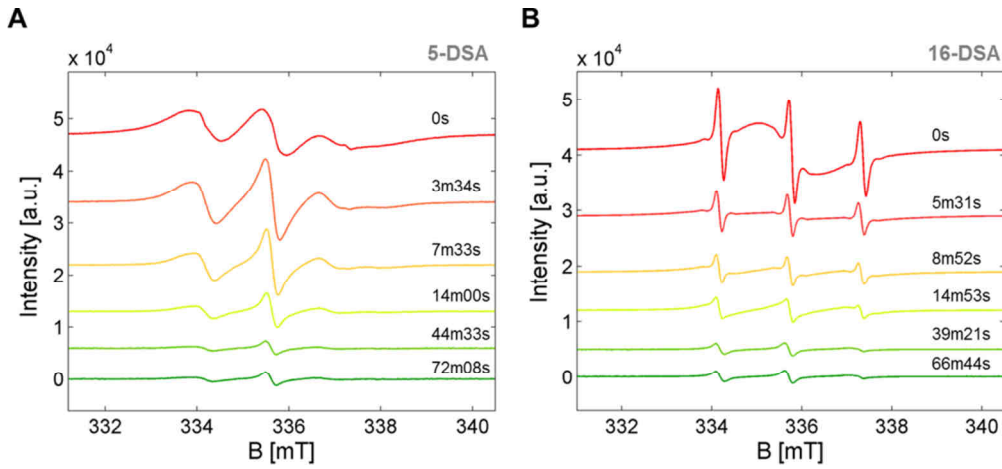
Figure B6 | CW EPR spectra of Y-DSA during the reduction with phenylhydrazine. Selected spectra $S_{i,j}(t_{i,j},B)$ at distinct times in minutes (m) and seconds (s) during the reduction of (**A**) 5-DSA and (**B**) 16-DSA in the time range of about 1.5 h. Predominant micellar species can be observed at $t_0 = 0$ s that vanish with time.

The curves in **Figure B6** were analyzed in terms of their reduction kinetics assuming the general form of first order reaction kinetics for single ($p = 1$) and double ($p = 2$) exponential shapes, similar to Pavicevic *et al.*:[B21]

$$\frac{\mathrm{DI}_{i,j}(t_{i,j})}{\mathrm{DI}_{0,i}} = \frac{\iint S_{i,j}(t_{i,j},B)\,\mathrm{d}^2B}{\iint S_{0,i}(t_0,B)\,\mathrm{d}^2B} = A_{0,i} + \sum_p^2 A_{p,i}\cdot e^{-k_{p,i}\cdot t} \quad , \tag{B.5}$$

where the i-th sample (5-DSA or 16-DSA) at each individual time $t_{i,j}$ yields the corresponding time–dependent spectrum $S_{i,j}(t_{i,j},B)$ giving the double integral $\mathrm{DI}_{i,j}(t_{i,j})$ that is normalized to the double integral $\mathrm{DI}_{0,i}$ at $t_0 = 0$ s. The time-course of the initial signal strength $S_{0,i}(t_0,B)$ during reduction is therefore extrapolated ($A_{0,i}$) with an pre-exponential factor $A_{p,i}$ and a reduction rate constant $k_{p,i}$. Data that are shown in **Table B4** suggest that 5-DSA and 16-DSA follow different reduction kinetics. 5-DSA is reduced with first order kinetics and 95% of the initial signal strength has vanished after $t_{0.95} = 22$ min, with a half-life of $t_{1/2} = \ln2/k_{1,\text{5-DSA}} = 3.78$ min $= 227$ s. 16-DSA exhibits a two-

component first order reduction process, that shows a fast ($k_{1,16\text{-DSA}}$) and a slow ($k_{2,16\text{-DSA}}$) component, leading to a faster initial reduction and a subsequent slower reduction after ca. 8 – 10 min. Regarding the value of $t_{0.95} = 39$ min, 16-DSA is therefore reduced about twice as slow as 5-DSA, giving rise to the assumption that the nitroxide group in 5-DSA is a bit more vulnerable during phenylhydrazine exposition, inverse, but similar to the findings of Junk.[B19]
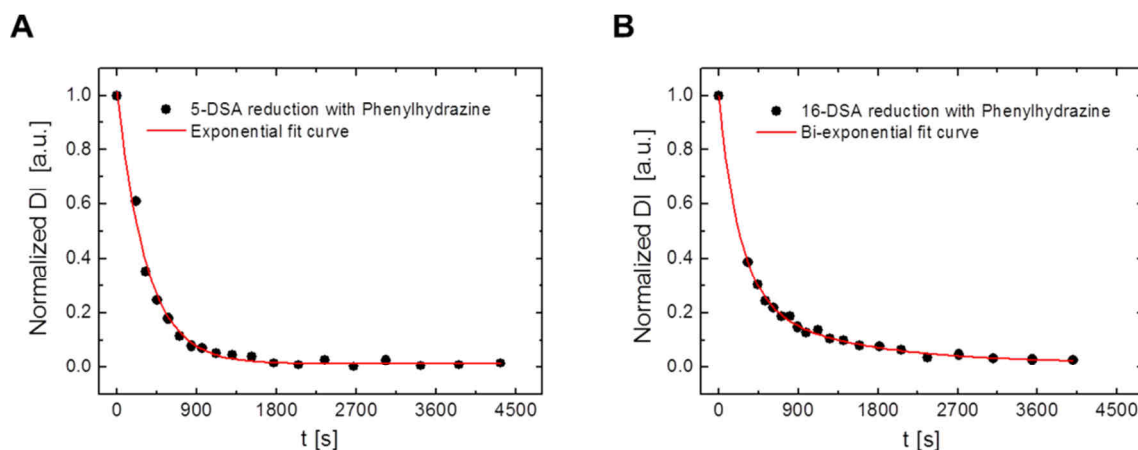
Figure B7 | Reduction kinetics of Y-DSA exposed to phenylhydrazine. EPR spectra from (**A**) 5-DSA and (**B**) 16-DSA were double integrated (black dots) and fitted (red curve) according to equation B.5. The time course of signal reduction differs for both spin probes and was recorded in the range of about 1.0 – 1.5 hours.

The reduction efficiency η_{red} is about 96 – 98 % for both spin probes, so that after 22 and 39 minutes only 2 – 4 % of the nitroxides are still EPR active. Additionally, the parameter $A_{0,i}$ indicates that in case of $t \rightarrow \infty$ about 98.3 – 98.5 % of the originally paramagnetic spin probes can be converted into diamagnetic species. This is largely sufficient for the spin dilution approach on albumin and the resulting sample solutions were used without further purification.

Table B4 | Results of the kinetic analysis of the phenylhydrazine reduction on DSA

	k	5-DSA	16-DSA
	R^2	0.99215	0.99843
	$A_{0,i}$	0.01486 ± 0.00706	0.01689 ± 0.0115
$p = 1$	$A_{1,i}$	1.00202 ± 0.02213	0.72104 ± 0.05673
	$k_{1,i}$ [min^{-1}]	0.1829 ± 0.0074	0.2633 ± 0.0241
$p = 2$	$A_{2,i}$	–	0.26242 ± 0.04781
	$k_{2,i}$ [min^{-1}]	–	0.0509 ± 0.0132
	$t_{0.95,i}$ [min]	22	39
	η_{red} [%]	97.9 ± 1.4	96.4 ± 0.8

B6 | References

[B1]   Y. Akdogan, J. Reichenwallner, D. Hinderberger, *PLoS One* **2012**, *7*, e45681.

[B2]   M. J. N. Junk, H. W. Spiess, D. Hinderberger, *Angew Chem Int Ed* **2010**, *49*, 8755–8759.

[B3]   G. Jeschke, M. Sajid, M. Schulte, A. Godt, *Phys Chem Chem Phys* **2009**, *11*, 6580–6591.

[B4]   M. J. N. Junk, H. W. Spiess, D. Hinderberger, *J Magn Reson* **2011**, *210*, 210–217.

[B5]   S. Sugio, A. Kashima, S. Mochizuki, M. Noda, K. Kobayashi, *Protein Eng* **1999**, *12*, 439–446.

[B6]   K. A. Majorek, P. J. Porebski, A. Dayal, M. D. Zimmerman, K. Jablonska, A. J. Stewart, M. Chruszcz, W. Minor, *Mol Immunol* **2012**, *52*, 174–182.

[B7]   A. S. Konagurthu, J. C. Whisstock, P. J. Stuckey, A. M. Lesk, *Proteins Struct Funct Bioinf* **2006**, *64*, 559–574.

[B8]   J. M. Berg, J. L. Tymoczko, L. Stryer, *Biochemie*. Spektrum Akademischer Verlag: Heidelberg, **2007**.

[B9]   E. Krieger, G. Koraimann, G. Vriend, *Proteins Struct Funct Genet* **2002**, *47*, 393–402.

[B10]   A. A. Bhattacharya, T. Grüne, S. Curry, *J Mol Biol* **2000**, *303*, 721–732.

[B11]   RCSB Protein Data Base Home Page. http://www.rcsb.org (accessed Mar 9, 2012).

[B12]   J. Kyte, R. F. Doolittle, *J Mol Biol* **1982**, *157*, 105–132.

[B13]   D. M. Engelman, T. A. Steitz, A. Goldman, *Ann Rev Biophys Biophys Chem* **1986**, *15*, 321–353.

[B14]   D. Eisenberg, E. Schwarz, M. Komaromy, R. Wall, *J Mol Biol* **1984**, *179*, 125–142.

[B15]   H. Naderi-Manesh, M. Sadeghi, S. Arab, A. A. M. Movahedi, *Proteins Struct Funct Genet* **2001**, *42*, 452–459.

[B16]   S. Kawashima, H. Ogata, M. Kanehisa, *Nucleic Acids Res* **1999**, *27*, 368–369.

[B17]   S. Kawashima, M. Kanehisa, *Nucleic Acids Res* **2000**, *28*, 374.

[B18]   AAindex database Home Page. http://www.genome.jp/aaindex (accessed July, 2012)

[B19]   M. J. N. Junk, Assessing the Functional Structure of Molecular Transporters by EPR Spectroscopy. Ph.D. Thesis, Johannes Gutenberg-Universität Mainz, **2010**.

[B20]   T. D. Lee, J. F. W. Keana, *J Org Chem* **1975**, *40*, 3145–3147.

[B21]   A. A. Pavicevic, A. D. Popovic-Bijelic, M. D. Mojovic, S. V. Susnjar, G. G. Bacic, *J Phys Chem B* **2014**, *118*, 10898–10905.

Appendix C | Optimum Control of the Albumin System for EPR Spectroscopy

C1 | Preparation of a 0.137 M DPBS Buffer Solution at pH 7.4

The accomplishment of producing 1000 ml DPBS buffer[C1] at pH 7.4 as an essential isotonic ingredient for all samples is given in the following. Initially, three different solutions are prepared referred to as solution A – C. Preparation of solution A comprises dissolving 8.00 g of sodium chloride (NaCl, Sigma-Aldrich), 0.20 g potassium chloride (KCl, Merck), 1.15 g disodium phosphate (Na_2HPO_4, Sigma-Aldrich) and 0.20 g potassium dihydrogenphosphate (KH_2PO_4, Fluka) in 700 ml ultrapure water (Milli-Q). Solution B contains 0.10 g calcium chloride ($CaCl_2$, Carl Roth) and solution C contains 0.10 g magnesium chloride hexahydrate ($MgCl_2·6H_20$, Santa Cruz Biotechnology). Both solutions B and C are then separately prepared by dissolving each salt in 100 ml of ultrapure water (Milli-Q). All three solutions were filtered over 0.45 µm Millex-LCR PTFE membranes (Merck Millipore®) before they were autoclaved separately to prevent precipitation of these salts. After cooling, solutions A – C are mixed (900 ml) and titrated to pH 7.4 with 1 M hydrochloric acid (HCl, Fisher Scientific) or 1 M sodium hydroxide (NaOH, Fisher Scientific), while the solution is stirred with gentle agitation. Again, about 100 ml of ultrapure water is added and a final pH measurement is taken. The ready-made solution is stored at 4°C and may be used for up to 12 months without any concern. The solution may be regarded as expired, when cloudy aggregates have formed. The final osmolality (310.6 mosmol/l) is considered as the sum concentration of all osmotically active ion particles in the solution, i.e. 136.89 mM NaCl, 2.68 mM KCl, 8.1 mM Na_2HPO_4, 1.47 mM KH_2PO_4, 0.90 mM $CaCl_2$ and 0.49 mM $MgCl_2·6H_2O$.

C2 | Preparation of Acidic and Alkaline 0.12 M DPBS Titration Buffers

Before any acidic or alkaline buffer is prepared the pH microelectrode (InLab® Micro pH 0 – 14, Mettler-Toledo) is calibrated with a two-point calibration using reference buffers at pH 4.00 and pH 10.00 that have been found to yield the best linear dependence in the whole investigated pH range. This was tested with references buffers in the range from pH 1 – 12 (ROTI® CALIPURE, Carl Roth) that yield values as given in **Table C1**.

Table C1 | Several calibration results of the pH microelectrode in the range from pH 1 – 12

Reference pH	Test 1	Test 2	Test 3	mean	σ
1.00	0.87	0.98	0.85	0.90	0.07
4.00	3.99	4.00	3.96	3.98	0.02
7.00	6.97	6.94	7.03	6.98	0.05
10.00	10.04	10.00	9.99	10.01	0.03
12.00	11.86	12.03	12.06	11.98	0.11

with individual errors of $\Delta pH_{4-10} = 0.02 - 0.06$, $\Delta pH_{1-4} = 0.07 - 0.15$ and an error of $\Delta pH_{10-12} = 0.11 - 0.14$. As each albumin sample may slightly vary in pH, a titration buffer concept has been established comprising a set of individual buffers in the range from pH 0.2 – 13.5 with $V = 14$ ml. An

example is given in **Table C2**. From preparations of the buffers the volume fraction of 0.137 M DPBS buffer is about 87.3 ± 1.6 % corresponding to 119.6 mM $\approx$ 0.12 M of electrolytes.

Table C2 | Preparation of 0.12 M DPBS buffers with acidic and alkaline pH

solution	DPBS pH 7.4 0.137 M	H₂O 55.6 M	HCl 1 M	HCl 12.08 M[a]	NaOH 1 M	NaOH 2.5 M[b]	
no	[ml]	[ml]	[ml]	[ml]	[ml]	[ml]	pH
1	12.0	1.316	–	0.684	–	–	0.20
2	12.0	1.671	–	0.329	–	–	0.55
3	12.0	–	2.000	–	–	–	0.80
4	12.0	1.000	1.000	–	–	–	1.13
5	12.0	1.500	0.500	–	–	–	1.57
6	12.0	1.800	0.200	–	–	–	2.25
7	12.0	1.900	0.100	–	–	–	4.41
8	12.0	1.950	0.050	–	–	–	6.62
9	12.0	1.980	–	–	0.020	–	8.47
10	12.0	1.950	–	–	0.050	–	10.81
11	12.0	1.900	–	–	0.100	–	11.41
12	12.0	1.800	–	–	0.200	–	11.86
13	12.0	1.700	–	–	–	0.300	12.54
14	12.0	1.500	–	–	–	0.500	12.81
15	12.0	1.000	–	–	–	1.000	13.17
16	12.0	–	–	–	–	2.000	13.46

[a]37 % = 12.08 M fuming HCl (Fisher Scientific) and [b]10 wt% in H₂O = 2.5 M NaOH (Fisher Scientific) were used.

C3 | Buffer Capacity Check

Upon addition of various amounts of hydrochloric acid (HCl, Fisher Scientific) and sodium hydroxide (NaOH, Fisher Scientific) the buffer pH is changed according to its buffer capacity. In **Figure C1** the resulting 0.12 M DPBS buffer pH values from **Table C2** are plotted versus the negative logarithmic concentrations $c_{m,i}$ [M].
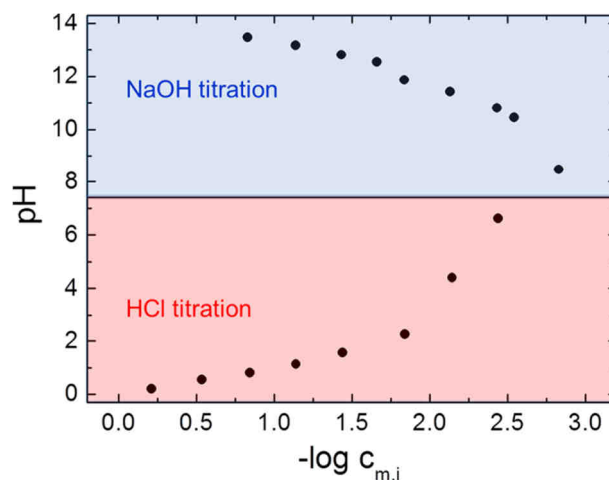
Figure C1 | Buffer capacity of 0.12 M DPBS buffer of varying pH. The change in pH of 0.12 M DPBS buffer is obtained from HCl and NaOH titrations as shown in **Table C2**.

C4 | Preparation of an EPR-active Albumin Sample Loaded with Fatty Acids at pH 7.4

An appropriate EPR-active albumin sample with paramagnetic fatty acids or other EPR-active ligands[C2] is usually made up of several components. Therefore, a general procedure for successful albumin sample preparations is described in the following. In the simplest case, e.g. for CW EPR and subsequent DEER measurements on the same sample, the nominal target concentration of albumin is here chosen to be 0.2 mM and the Albumin:FA ratio is 1:2, with a glycerol content of 20% v/v at pH 7.4. The minimum required sample volume is 100 µl where typically 20 µl are required for CW EPR and 80 µl for DEER.

An exemplary 1 mM HSA stock solution in 0.137 M DPBS (66.572 mg/ml HSA, MW(HSA) = 66572 Da[C3]) is prepared in an Eppendorf reaction tube by dissolving 20 mg of lyophilized protein powder (>95%, Calbiochem) in 300 µl DPBS buffer pH 7.4. HSA is completely dissolved upon centrifugation for 1 min at 12.000 rpm (~ 10.000 g for the Heraeus Pico 17 centrifuge) and exhibits a slightly yellowish void-free solution.

Here, an exemplary 8 mM 16-DSA stock solution is obtained by dissolving 1 mg of the dry yellowish 16-DSA powder (Sigma-Aldrich) in 325 µl of 0.1 M KOH (3.077 mg/ml, MW(16-DSA) = 384.57 Da). After gentle stirring for 2 – 3 min the powder is dispersed in a yellowish opaque liquid. Centrifugation of this solution should be prevented, leading to a bulk 16-DSA concentration loss due to sedimentation of micellar solution components that consequentially also contain 16-DSA.

The final sample solution is now split into several functional volume compartments according to **Table C3**. The sample assembly is shown in an optimized order and individual volumes and stock solution concentrations may be adjusted depending on the purpose of a study. Here, the primary sample volume is chosen as 90 µl (buffer, HSA stock, 16-DSA stock and glycerol, assembly order 1 – 4). The remaining 10 µl void is reserved as the sample titration volume. After each step of assembly the sample has to be stirred thoroughly and in case of blister formation it has to be centrifuged again for 1 min at 12 krpm. The sample volume is prepared with 0.137 M DPBS buffer at pH 7.4 so that all subsequently added components (HSA stock and 16-DSA stock) can be directly injected to the bulk liquid without any volume deficiencies. The addition of 20% v/v glycerol (87% in water, ACROS), serves as a protein cryoprotectant[C4] in later sample vitrification for pulse EPR measurements. In this naive example, the sample is at pH 7.52 after addition of all components. In order to obtain the desired sample pH 7.40, an optional set of titration buffers may be applied. The best choice is to use DPBS buffers at pH 1–2 for acidic and pH 12–13 for alkaline sample titration to prevent exceeding the default sample volume.

With this approach almost any sample composition may be obtained regarding HSA and 16-DSA concentration (or any other paramagnetic ligand as in Hauenschild et al.[C2]) and pH. For higher 16-DSA (or 5-DSA) loadings, or spin dilution experiments, it is recommended to rather prepare 26 mM 16-DSA in 0.1 M KOH stock solutions (10 mg/ml 16-DSA). The final buffered solution has a residual

0.097 M DPBS content and an osmolality of about 220 – 250 mosmol/l, depending on the amount and strength of added DPBS titration buffer.

Table C3 | Composition of an EPR-active albumin sample with fatty acids at pH 7.4

Assembly order	Component	Volume [µl]	pH
1	0.137 M DPBS pH 7.4	42.0	–
2	1 mM HSA in DPBS	20.0	–
3	8 mM 16-DSA in 0.1 M KOH	5.0	–
4	87% glycerol in water	23.0	7.52
5	0.120 M DPBS pH 1.13	0.5	7.47
6	0.120 M DPBS pH 1.13	0.7	7.36
7	0.137 M DPBS pH 7.40	8.8	**7.38**

C5 | Identification of Protein Content from an Albumin Solution

Bradford reagent – qualitative registration of protein content

This protein reagent was prepared very similar to the original description given by M. M. Bradford.[C5] 49.53 mg Coomassie Brilliant Blue G-250 (CBBG, AppliChem) were dissolved in 24 ml ethanol absolute (>99.8%, Riedel-de Haen) and complemented with 1 ml ultrapure H_2O (= 25 ml). The resulting solution was equipped with 50 ml of phosphoric acid (85% H_3PO_4, J.T.Baker) to provide an acidic milieu that is essential for protein binding of CBBG. Upon addition of 425 ml ultrapure water, a final solution with a total volume of 500 ml was obtained. Thus, the final concentrations are 0.1 mg/ml CBBG (116 µM), 4.8% v/v ethanol and 1.46 M H_3PO_4.

A qualitative estimate whether protein is present in a solution was gained by adding 40 µl of Bradford reagent to 40 µl of a protein test solution. In case proteins are present, the color of the test solution will turn to maximum bright blue intensity after 2 – 5 minutes at room temperature. This method is mainly employed in spin labeling procedures of albumin or during centrifugation processes to check the eluate for protein content.

Bicinchoninic acid (BCA) assay – quantitative registration of protein content

This method serves as a procedure yielding quantitative estimates about the protein content of albumin solutions and is based on a protocol first published by Smith *et al.*[C6] A common procedure is also given in the provided Thermo Scientific BCA Protein Assay Kit instruction.[C7] The kit contains three predefined solutions: BCA reagent A (some ingredients: Na_2CO_3 and BCA in 0.1 M NaOH), BCA reagent B (4% copper(II)sulfate = $CuSO_4(H_2O)_x$) and 2 mg/ml albumin standard (BSA).

The albumin standard is used to generate a calibration line that correlates absorption values A_{562} with test protein concentrations according to **Table C4**. Therefore, 0.1 ml of the albumin standard is diluted with 0.7 ml ultrapure water to yield a 0.25 mg/ml BSA stock solution. The calibration samples also contain a blank without any coloration to get a reference blank value $A_{562,0}$. The BCA reagent is obtained by mixing BCA reagent A with BCA reagent B in the ratio 50(A):1(B). The amount of

required BCA reagent is calculated by multiplying the desired number of samples times 1.0 ml to get some backup volume. The test samples are prepared in a dilution row. For example, a test sample containing approximately 1 mM of BSA affords a harsh predilution of 1:100 to hit the valid range of the calibration line (typically: $0.02 < A_{562} < 1.10$). Therefore 0.01 ml of the 1 mM BSA solution should be diluted in 0.99 ml of ultrapure H_2O and stirred thoroughly.

Table C4 | Established scheme for preparing a calibration line for BCA tests

Calibration sample[a]	1	2	3	4	5	6	7	8
0.25 mg/ml BSA [µl]	0	10	20	30	40	50	60	70
H_2O [µl]	100	90	80	70	60	50	40	30
c_{BSA} [µg/ml]	0	2.5	5.0	7.5	10.0	12.5	15.0	17.5

[a]Preparation takes place in duplicate

The 1:100 predilution stock (BSA_{PD} = 10 µM) is again diluted upon addition of ultrapure water for 3 – 5 test samples with a dilution of ca. 500 – 5000 giving a set of test solutions of 0.1 ml. A typical scheme (H_2O:BSA_{PD} = 80 µl : 20 µl (1:500), 90 µl : 10 µl (1:1000), 95 µl : 5 µl (1:2000), 98 µl : 2µl (1:5000) in duplicate) would give at least 2 – 3 duplicate values that can be later averaged to a meaningful concentration number. Each of the 16 calibration samples and the 8 test samples are then equipped with 0.9 ml BCA reagent and are directly put on ice to block the room temperature reaction. This preparative step again increases the dilution for a factor of about 10 (to 5000, 10000, 20000 and 50000). All 24 samples are finally incubated on 65°C for 10 min at 300 rpm on a thermomixer (ThermoMixer C, Eppendorf) in favor for the high temperature coloration reaction of the BCA reagent. After the coloration reaction has reached an optimum, all samples are again put on ice in order to stop the reaction and the absorption values are subsequently measured at λ_{BCA} = 562 nm on an UV/Vis spectrophotometer (Hewlett-Packard HP 8453 in combination with HP 89090A). The calibration line as shown in **Figure C2** is then utilized to extrapolate a precise concentration to the test samples from the slope (b), dilution (d), blank absorption ($A_{562,0}$) and the averaged duplicate ($N = 2$) absorption values $A_{562,i}$ according to the relation:

$$c = \frac{d}{b} \cdot \left(\frac{1}{N} \sum_{i}^{N} A_{562,i} - A_{562,0} \right) \qquad . \qquad (C.1)$$

Generally, Thermo Scientific gives a protein specific sensitivity variation in BCA assay results with a standard deviation of σ_{BCA} = 14.7 %.[C7] The sensitivity of albumin-based results is found to be a much smaller with a value of $\sigma_{Albumin}$ = 6.9 % as it can be retrieved from two independently obtained data sets as shown in **Table C5**. Additionally, it can be claimed, that this test is not sensitive enough to

reveal clear differences among bovine (BSA), human (HSA), goat (GSA) and sheep (SSA) albumins. The emergence of lower concentrations than expected (~ 1 mM) are discussed in **Chapter 5.2** and can be traced back to a commercial least powder sample purity (P_{ALP}) in combination with excluded volume effects ($\phi(c)$).
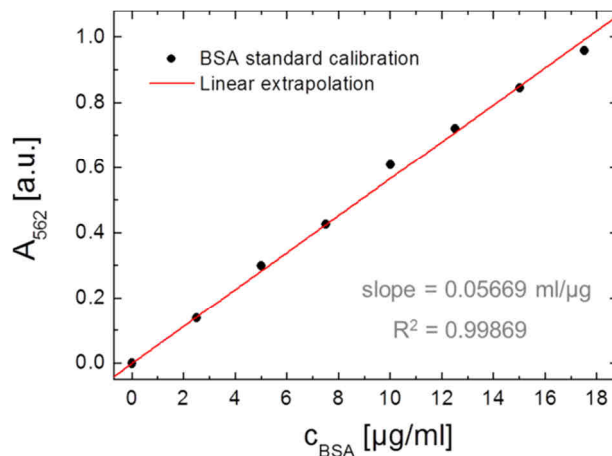
Figure C2 | Calibration of a BSA standard dilution. Multiplication of the slope with the obtained absorption value A_{562} of a test sample yields the desired protein concentration.

Table C5 | Results from BCA assays on several 1 mM stock solutions of various albumins

Albumin	V1[a]	V2[a]
BSA [mM]	0.9361 ± 0.0984	0.7916 ± 0.0013
HSA [mM]	0.8181 ± 0.0445	0.7863 ± 0.0009
GSA [mM]	0.9137 ± 0.0658	0.7869 ± 0.0245
SSA [mM]	0.8702 ± 0.0490	0.7886 ± 0.0321

[a]Both BCA assays, V1 and V2, were prepared independently but each from 1 mM albumin stock solutions.

C6 | Rheological Data

Some supplementary and comparative data for viscometric results as shown in **Table 5.1** were obtained from a rheometer with cone-plate geometry (Physica MCR 301, Anton Paar). The dynamic viscosities η_{dyn} were recorded as functions of the applied shear rate with increasing complexity of the solution (**Figure C3**). The actual viscosities η were back-extrapolated from the linear regime of shear-tickening (see linear extrapolations (red)) as described by Mezger.[C8] The pure 0.137 M DPBS buffer pH 7.4 shows a slightly increased viscosity compared to pure deionized water (H_2O). Upon addition of 20% v/v glycerol the solution gains a decreased ionic strength and a viscosity that is approximately twice as high compared to pure H_2O and pure 0.137 M DPBS buffer (0.1 M DPBS pH 7.4 with 20% v/v glycerol). The presence of a nominal albumin concentration of $c_{nom} = 32$ mg/ml in a sample solution again increases the viscosity for 20 – 30 %. The exact protein concentration corresponds to

c_{BSA} = 29.7 mg/ml as the used BSA stock solution contains 88.7 mg/ml BSA stock solution in DPBS ($\phi(c)$ = 0.0721 (equation 5.1), 32 mg/ml BSA in 20% v/v glycerol and 0.1 M DPBS buffer at pH 7.4).
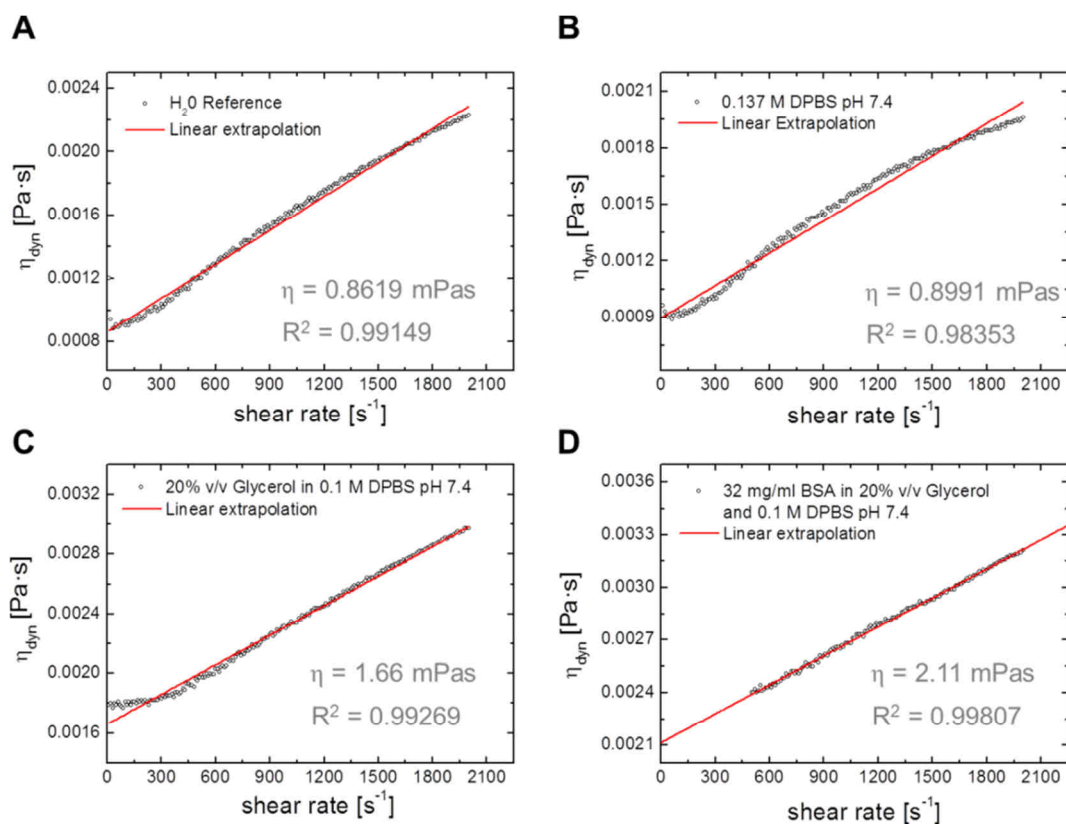
Figure C3 | Rheological data from a systematic increase in solution complexity. A comparison of shear curves is given for T = 25°C from solutions made up of (**A**) deionized H_2O, (**B**) 0.137 M DPBS buffer at pH 7.4, (**C**) 0.1 M DPBS buffer at pH 7.4 equipped with 20% v/v glycerol and (**D**) 0.1 M DPBS buffer at pH 7.4 equipped with 20% v/v glycerol and a nominal BSA concentration of c_{nom} = 32 mg/ml (c_{BSA} = 29.7 mg/ml).

C7 | Determination of the Modulation Depth Parameter λ of the Pulse EPR Spectrometer

Oligo(*para*-phenylene-ethynylene)s (OligoPPEs) are monodisperse rod-shaped compounds.[C9] Their accessibility to EPR spectroscopy can be provided by attaching free radicals (3-carboxy-proxyl) at each end of the PPE backbone that allows either for extraction of label-to-label or backbone end-to-end distances aided by MD Simulations.[C10] The spectrometer specific modulation depth parameter λ that is e.g. necessary for spin counting procedures[C11–C15] can be determined by such model biradicals with just $\langle n \rangle$ = 2 electron spins per molecule. Their adjustable length has been utilized in ample studies to define their intrinsic flexibility as well as the boundary of accessible distances in dipolar spectroscopy from EPR as SIFTER[C16] or in particular DEER.[C10,C14,C17] Here, two different types of OligoPPE compounds are used (**Figure C4A+C**) in combination with perdeuterated ortho-terphenyl (OTP-d$_{14}$, **Figure C4B**) as an optimal glass forming matrix similar to the strategy that was already described in previous studies.[C10,C17]
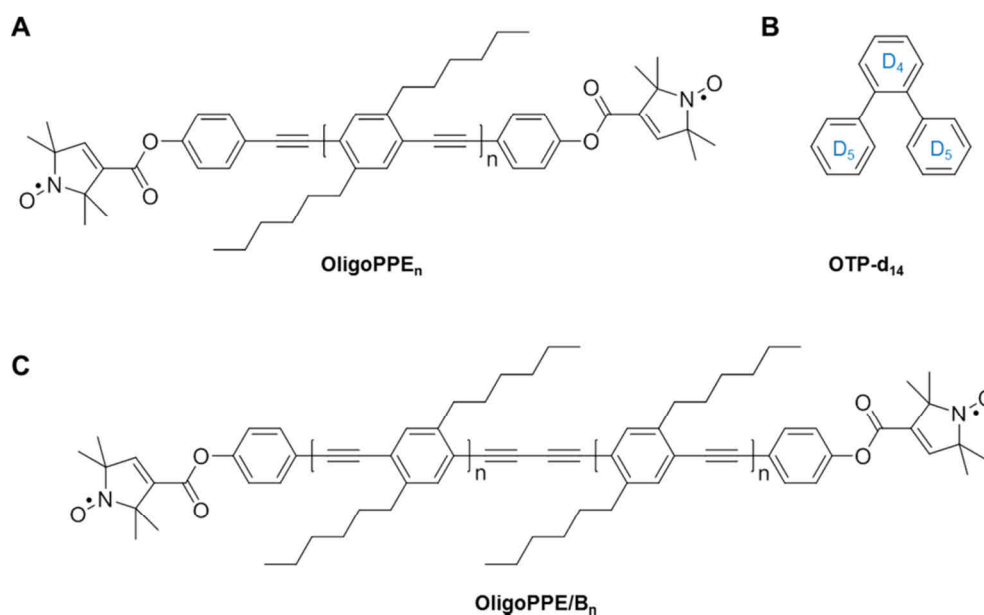
Figure C4 | Chemical structures of biradicals and the glass forming compound. Chemical composition of (**A**) OligoPPE$_n$, (**B**) perdeuterated ortho-terphenyl (OTP-d$_{14}$) and (**C**) OligoPPE/B$_n$. The blue insets (D_i) in (B) are the respective numbers of deuterons per aromatic ring.

Preparation of biradical samples

The pure biradical powders of altogether six different samples (**Table C6**) were obtained in round-bottom flasks kindly provided from Prof. Dr. Adelheid Godt and Miriam Hülsmann from Bielefeld University, Germany. Each flask contained 0.1 mg of yellowish biradical powder that was dissolved in 500 µl toluene (>99.9%, ROTISOLV HPLC, Carl Roth) for transferring it into screw neck vials (Macherey-Nagel). Afterwards, the toluene volume was vaporized in a lab fume hood overnight at room temperature yielding a homogenous laminar layer of evenly spread biradical. About 100 – 150 mg of perdeuterated ortho-terphenyl (OTP-d$_{14}$, 98 atom % D, C/D/N Isotopes) was added to the transferred powder. A heat gun (HL 2010 E electronic, STEINEL) was adjusted to 90 – 100°C air temperature for melting the OTP-d$_{14}$ powder (melting point of OTP-d$_{14}$ = 57 – 59°C).[C18] The hot liquid OTP-d$_{14}$/biradical mixture was then gently stirred with a scoop or a vortex mixer for obtaining an even biradical distribution (IKA vortex genius 3). The biradical concentrations in **Table C6** were calculated with the carefully weighed masses of OTP-d$_{14}$ (Mettler AT261 DeltaRange) assuming an OTP density of ρ_{OTP} = 1.14 g/l.[C19] Additionally, the initial biradical 1 stock solution (1.301 mM) was diluted to 0.10 mM, 0.30 mM and 0.75 mM following the same procedure. During EPR sample preparation a heater plate (IKA RCT basic) was adjusted to 70 – 80°C ensuring that all obtained OTP-d$_{14}$-based liquids do not solidify and that all air bubbles in the bulk solution have vanished. Softly preheated Eppendorf pipet tips were used to transfer 50 – 80 µl of the solutions to a smaller snap-cap vial. Finally, an EPR sample tube (Heraeus Quarzglas, inner diameter Ø = 3 mm) was filled with a sterile soda-lime glas Pasteur pipette (Carl Roth, outer diameter Ø = 1.3 mm). Assuring a constant flow of hot air certified that almost the complete treated sample volume (30 – 50 µl) could be transferred inside the EPR sample tube. Again, the heat gun was used to remove all bubbles from the

bulk solution. The samples were then either stored at –20°C or were vitrified in nitrogen-cooled 2-methylbutane for subsequent DEER distance measurements.

Table C6 | Specifications of the received biradical samples

Biradical	Synthesis no[a]	OligoX-identifier	MW [Da]	c [mM]	Reference
1	MS57/2	PPE_1	811.058	0.300	C10
2	AG555	PPE/B_1	1103.516	0.850	C10
3	NR119/2/2	PPE_3	1347.931	0.595	C17
4	AG565/2	PPE/B_2	1640.389	0.537	C10
5	MS29	PPE/B_3	2177.261	0.400	C10
6	AG745/7-11	PPE/B_4	2714.134	0.274	C10

[a]Provided samples were equipped with a short characterization and an according synthesis number.

Experimental details are given in the main manuscript and all experimental and analytic results as obtained from DeerAnalysis2013[C13] are shown in **Figure C5**.
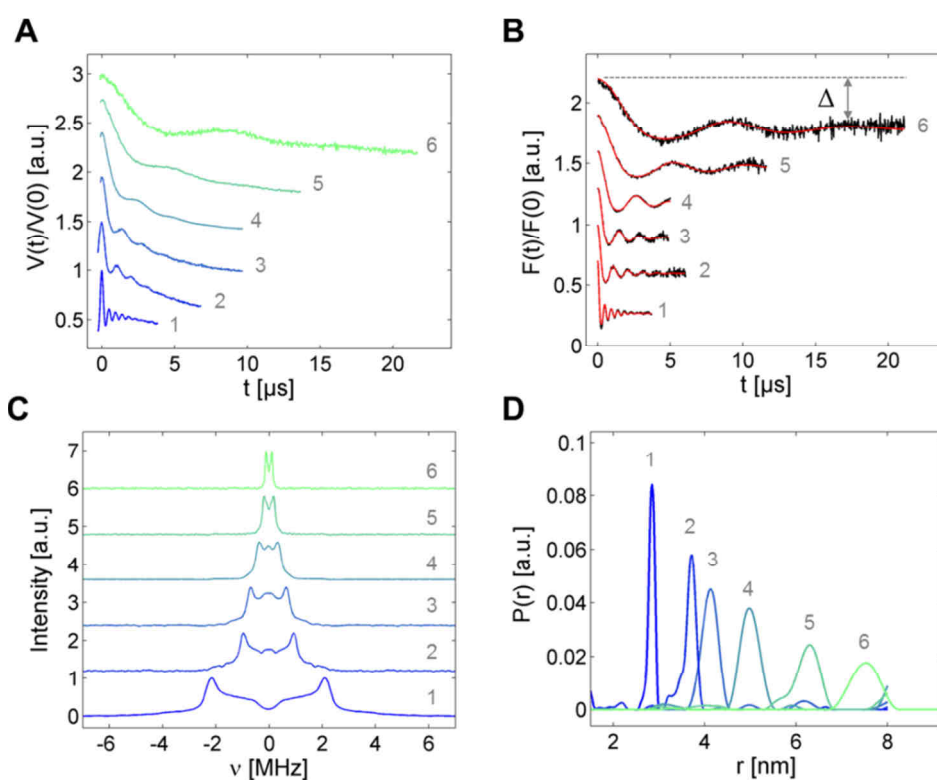
Figure C5 | Results from DEER experiments and data analyses of all biradicals. (**A**) Raw experimental time domain data $V(t)/V(0)$, (**B**) dipolar evolution functions $F(t)/F(0)$ with modulation depths Δ (only indicated for biradical 6), (**C**) dipolar spectra (Pake patterns) and (**D**) distance distributions $P(r)$ are shown for all biradicals (1–6) from **Table C6**. The presented datasets were obtained from Tikhonov regularization as implemented in DeerAnalysis2013.[C13]

Table C7 | Distance results from DEER experiments on model biradicals

Biradical	1	2	3	4	5	6
α	0.1	1	100	100	100	1000
r [nm]	2.848	3.707	4.121	4.968	6.299	7.524
Δ	0.430	0.407	0.409	0.425	0.428	0.402

According to equation 1.103 the modulation depth parameter can be described by the expression $\lambda = -\ln(1-\Delta)$ for $\langle n \rangle = 2$.[C13] Therefore, an artificial quantity $p = r \cdot \lambda$ is introduced here that allows for a zero intercept linear regression of distance r versus p (**Figure C6**). Error bars for p have been calculated due to the propagation of uncertainty assuming an intrinsic modulation depth error $\Delta\Delta = 0.02$[C14] and a maximum distance error $\Delta r = 0.04$ nm:[C20]

$$\Delta p = \left| \frac{\partial p}{\partial r} \right| \cdot \Delta r + \left| \frac{\partial p}{\partial \Delta} \right| \cdot \Delta\Delta = -\Delta r \cdot \ln(1-\Delta) + \frac{r \cdot \Delta\Delta}{(1-\Delta)} \qquad . \qquad (C.2)$$

Consequently, the λ parameter can be extracted from the slope of the linear fit curve. The distance-independent value of the modulation depth parameter of the used BRUKER Elexsys E580 pulse EPR machine equipped with the Flexline split-ring resonator ER4118X–MS3 is therefore expected to assume the value $\lambda = 0.5342 \pm 0.0092$. This is in nice agreement with a previously reported value for the same spectrometer ($\lambda = 0.52$).[C21]
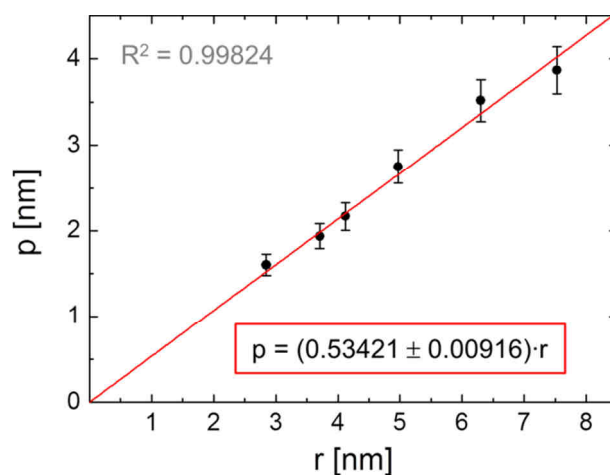
Figure C6 | Determination of the distance-independent modulation depth parameter λ. The slope of the linear regression can be regarded as λ.

C8 | References

[C1]   R. Dulbecco, M. Vogt, *J Exp Med* **1954**, *99*, 167–182.

[C2]   T. Hauenschild, J. Reichenwallner, V. Enkelmann, D. Hinderberger, *Chem Eur J* **2016**, *22*, 12825–12838.

[C3]   A. Lapolla, D. Fedele, R. Seraglia, S. Catinella, L. Baldo, R. Aronica, P. Traldi, *Diabetologia* **1995**, *38*, 1076–1081.

[C4]   J. L. Dashnau, N. V. Nucci, K. A. Sharp, J. M. Vanderkooi, *J Phys Chem B* **2006**, *110*, 13670–13677.

[C5]   M. M. Bradford, *Anal Biochem* **1976**, *72*, 248–254.

[C6]   P. K. Smith, R. I. Krohn, G. T. Hermanson, A. K. Mallia, F. H. Gartner, M. D. Provenzano, E. K. Fujimoto, N. M. Goeke, B. J. Olson, D. C. Klenk, *Anal Biochem* **1985**, *150*, 76–85.

[C7]   Thermo Scientific. *Pierce BCA Protein Assay Kit.* Instructions manual, **2013**.

[C8]   T. Mezger, *Das Rheologie-Handbuch: Für Anwender von Rotations- und Oszillations-Rheometern.* Curt R. Vincentz Verlag: Hannover, **2000**.

[C9]   A. Godt, C. Franzen, S. Veit, V. Enkelmann, M. Pannier, G. Jeschke, *J Org Chem* **2000**, *65*, 7575–7582.

[C10]   A. Godt, M. Schulte, H. Zimmermann, G. Jeschke, *Angew Chem Int Ed* **2006**, *118*, 7722–7726.

[C11]   A. D. Milov, A. B. Ponomarev, Y. D. Tsvetkov, *Chem Phys Lett* **1984**, *110*, 67–72.

[C12]   D. Hilger, H. Jung, E. Padan, C. Wegener, K. P. Vogel, H. J. Steinhoff, G. Jeschke, *Biophys J* **2005**, *89*, 1328–1338.

[C13]   G. Jeschke, V. Chechik, P. Ionita, A. Godt, H. Zimmermann, J. Banham, C. R. Timmel, D. Hilger, H. Jung, *Appl Magn Reson* **2006**, *30*, 473–498.

[C14]   B. E. Bode, D. Margraf, J. Plackmeyer, G. Dürner, T. F. Prisner, O. Schiemann, *J Am Chem Soc* **2007**, *129*, 6736–6745.

[C15]   G. Jeschke, M. Sajid, M. Schulte, A. Godt, *Phys Chem Chem Phys* **2009**, *11*, 6580–6591.

[C16]   G. Jeschke, M. Pannier, A. Godt, H. W. Spiess, *Chem Phys Lett* **2000**, *331*, 243–252.

[C17]   G. Jeschke, M. Sajid, M. Schulte, N. Ramezanian, A. Volkov, H. Zimmermann, A. Godt, *J Am Chem Soc* **2010**, *132*, 10107–10117.

[C18]   *o-Terphenyl-d₁₄*; MSDS No. D-4165; C/D/N Isotopes Inc.: Pointe-Claire, Quebec. March 3, 2017. https://cdnisotopes.com/nf/o-terphenyl-d14 (accessed Nov 5, 2017).

[C19]   Gefahrstoffinformationssystem (GESTIS), density, ZVG No.: 492452, CAS No.: 84-15-1, www.dguv.de/ifa/gestis/gestis-stoffdatenbank/index.jsp (accessed Nov 5, 2017).

[C20]   G. Jeschke, *Annu Rev Phys Chem* **2012**, *63*, 419–446.

[C21]   M. J. N. Junk, H. W. Spiess, D. Hinderberger, *J Magn Reson* **2011**, *210*, 210–217.

Appendix D | The Genetic Fingerprint of Spin Probed Albumins

D1 | Concentration Effect on DEER Data of SSA

The impact of concentration on t_{max} and $P(r)$ is exemplified here.
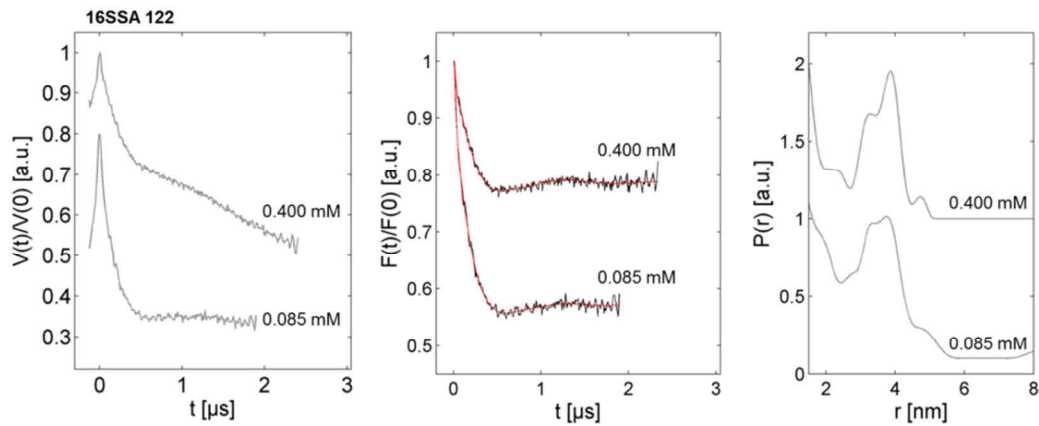
Figure D1 | Impact of concentration on t_{max} and $P(r)$ in DEER. DEER experiments were conducted with SSA (gray) in the albumin-to-ligand ratio 1:2:2 (16SSA 122). All original raw DEER time traces are shown on the left, dipolar evolution functions (black) with fit curves (red) are shown in the middle and the resulting distance distributions after Tikhonov regularization can be seen on the right. The fatty acid and albumin equivalent concentrations were $c_1 = 0.085$ mM ($t_{max} = 1.9$ µs) and $c_2 = 0.400$ mM ($t_{max} = 2.3$ µs). Note that the individual features in $P(r)$ are resolved much clearer for 0.400 mM.

D2 | Representative CW EPR Spectra of Spin Probed XSA 120 Samples

Slight differences in between XSA samples can be already observed in CW EPR spectra.
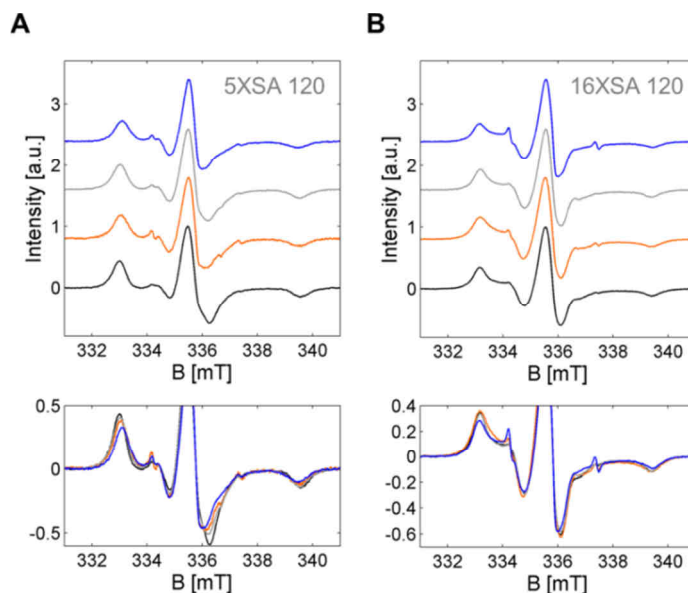
Figure D2 | CW EPR results from several spin probed mammal albumins (XSA) loaded in the ratio 1:2:0. CW EPR experiments were conducted consistently with HSA (black), GSA (orange), SSA (gray) and FSA (blue) for (**A**) 5-DSA and (**B**) 16-DSA in the albumin-to-ligand ratio 1:2:0 (1 eq = 0.4 mM for 5XSA 120 and 16XSA 120). Additionally, a superimposed depiction is given in the lower trace for highlighting slight differences in diffusion tensors. The slight kink at 336.5 mT in the spectra for GSA and SSA loaded with 5-DSA is from electronic noise intrinsic to the Miniscope MS200 CW EPR spectrometer (see also **Figure 5.3**).

D3 | SDS PAGE as a Quality Control for FSA Functionality

The FSA stock solution was tested for impurities with a SDS PAGE.
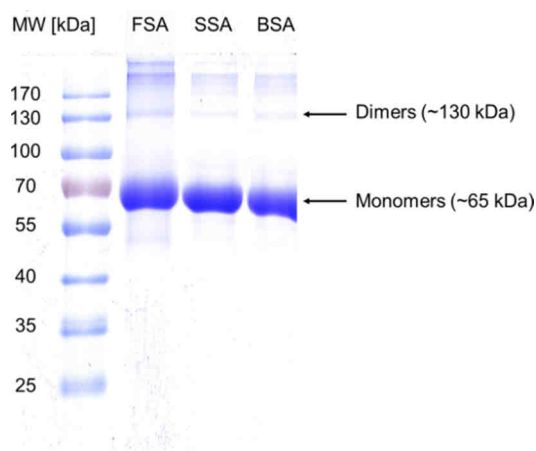
Figure D3 | SDS PAGE of some of the investigated albumins. FSA was sedimenting at a stock solution concentration of 2 mM in DPBS pH 7.4. The result of this SDS PAGE elucidates that FSA (~ 65 kDa) behaves normal compared to the other albumins with a few more aggregates appearing beyond the dimer bands at about 130 kDa.

D4 | Reference DEER Data of Spin Probed XSA 110 Samples

Dipolar modulation is already observable for a nominal albumin:FA loading ratio of 1:1.
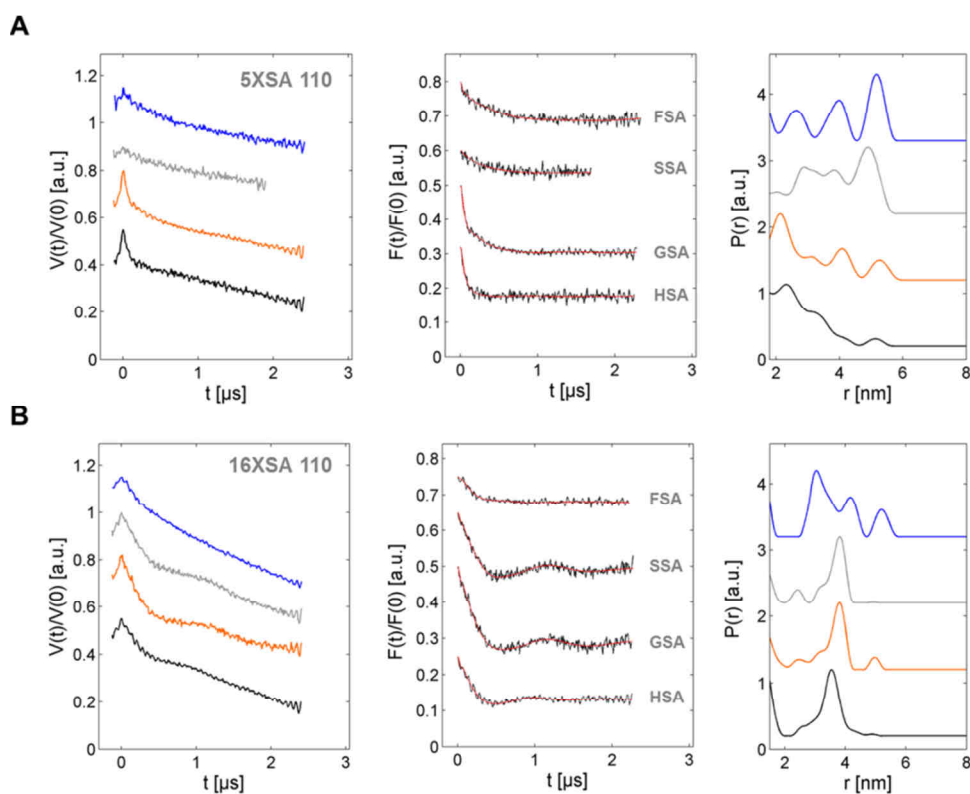
Figure D4 | DEER results from several spin probed mammal albumins (XSA) loaded in the ratio 1:1:0. DEER experiments were conducted with HSA (black), GSA (orange), SSA (gray) and FSA (blue) in the albumin-to-ligand ratio 1:1:0 (1 eq = 0.4 mM). All original raw DEER time traces are shown on the left, dipolar evolution functions (black) with fit curves (red) are shown in the middle and the distance distributions can be seen on the right for (**A**) all four albumins loaded with 5-DSA and r5-DSA and (**B**) 16-DSA and r16-DSA. All samples have been prepared at pH 7.4 and with 20% v/v glycerol.

D5 | Low-concentration DEER Data of Several Spin Probed 5XSA 120 Samples

Experimental DEER data for distance distributions shown in **Figure 6.5A** are given here.
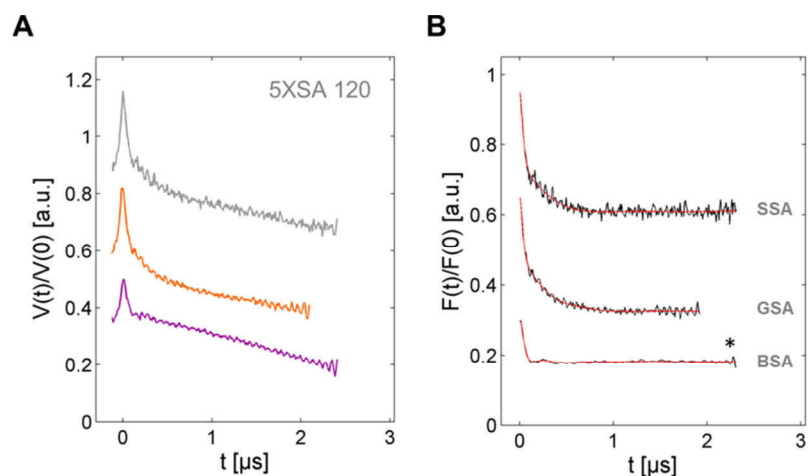
Figure D5 | Time domain data from DEER experiments on lower-concentrated albumins BSA, GSA and SSA. Additional time domain data for distance distributions of ruminant albumins BSA (deep purple), GSA (orange) and SSA (gray) at 0.17 mM loaded with 5-DSA in the ratio 1:2:0 (from **Figure 6.5A**). (**A**) Raw time domain data of DEER experiments and (**B**) corresponding dipolar evolution functions. The asterisk (*) indicates that the long pass filter was switched on during data analysis for BSA.

Appendix E | Posttranslational Modifications in Albumin Molecules

E1 | Simulations of CW EPR Spectra from HSA-N and G*y*-DHSA Interacting with 16-DSA

An overview of simulation parameters that were used to construct spectral simulations in **Figure 7.2** from individual fractions ϕ_i are given in **Table E1**. All *g*-values for simulations were chosen equally as $g_{\mathrm{iso}} = (1/3)\cdot\sum g_{kl} = 2.00617$ with $\boldsymbol{g}_J = [g_{xx}\ g_{yy}\ g_{zz}] = [2.0087\ 2.0067\ 2.0031]$. For a more elaborate description of spectral simulations the reader is referred to **Appendix E2**.

Table E1 | Empiric simulation parameters of the 16-DSA spin probe interacting with G*y*-DHSA

sample	ratio	A_{xx}^{a} [G]	A_{yy}^{a} [G]	A_{zz}^{a} [G]	$a_{\mathrm{iso},b}^{\mathrm{b}}$ [G]	$\tau_{\mathrm{c},b}^{\mathrm{c}}$ [ns]	$a_{\mathrm{iso},f}^{\mathrm{b}}$ [G]	$\tau_{\mathrm{c},f}^{\mathrm{c}}$ [ns]	$a_{\mathrm{iso},a}^{\mathrm{b}}$ [G]	$J_{\mathrm{AB}}^{\mathrm{d}}$ [MHz]
HSA-N	2:1	6.5	7.1	33.5	15.7	16.7	15.9	0.123	–	–
	4:1	7.2	7.4	33.3	16.0	16.7	15.8	0.139	–	–
	8:1	6.5	9.2	33.3	16.2	16.2	15.8	0.112	15.8	45
G2-DHSA	2:1	6.5	9.2	32.9	16.2	16.2	15.9	0.139	–	–
	4:1	6.5	9.2	33.3	16.3	16.2	15.8	0.140	–	–
	8:1	6.5	9.2	33.3	16.3	16.2	15.9	0.128	15.9	45
G3-DHSA	2:1	6.5	9.2	33.3	16.3	17.9	15.8	0.139	–	–
	4:1	6.5	9.2	33.3	16.3	16.2	15.9	0.131	–	–
	8:1	6.5	9.2	33.3	16.3	16.2	15.9	0.136	15.8	45

[a] A_{kl} = hyperfine coupling tensor components of immobilized subspectra. [b] $a_{\mathrm{iso},i}$ = isotropic hyperfine coupling constant of spectral fraction i with $a_{\mathrm{iso}} = (1/3)\cdot\sum A_{kl}$. [c] $\tau_{\mathrm{c},i}$ = rotational correlation time of spectral fraction i. [d] J_{AB} = effective Heisenberg spin exchange frequency.[E1,E2] Spectral simulations have been conducted in EasySpin.[E3]

E2 | Simulations of Multi-component CW EPR Spectra of 16-DSA Interacting with Albumins

The basis for a simulation approach in EasySpin[E3] is now to choose a set of appropriate starting parameters for the *g*-tensors and hyperfine coupling tensors *A* that enable a (global) manual iterative fitting procedure that guarantees a largely consistent analysis. The EasySpin software package comprises routines that operate due to the theory of slow tumbling nitroxides.[E1,E4] This simulation procedure is of decisive importance for reconstruction of the ligand-loading-dependent multi-component CW EPR spectra. The strategy is therefore optimized here for comparing different albumin samples at varying 16-DSA loading ratios exhibiting experimental spectra $S(B)$ comprising N subspectra $F_i(B)$ of dynamical regimes i that appear in the relative population fractions ϕ_i. Appropriate starting values for spectral simulations of 16-DSA interacting with albumin in general can be found in Ge *et al.*[E5] Optimum results were obtained for rhombic *g*-tensor values $[g_{xx}\ g_{yy}\ g_{zz}]$ and slightly rhombic hyperfine coupling *A*-tensors $[A_{xx}\ A_{yy}\ A_{zz}]$. In **Table E2** the values of the main components are given as individual and isotropic values $g_{\mathrm{iso}} = Tr(\boldsymbol{g}) = (g_{xx}+g_{yy}+g_{zz})/3$ and $a_{\mathrm{iso}} = Tr(\boldsymbol{A}) = (A_{xx}+A_{yy}+A_{zz})/3$ as a summary. All values are given for HSA-N as well as for BSA-N. Rotational correlation times $\tau_{\mathrm{c},i}$ have been calculated as the geometric average of the diffusion tensor elements $\boldsymbol{D}_r = [D_x\ D_y\ D_z]$ according to the relation:

$$\tau_{c,i} = \frac{1}{6\sqrt[3]{D_x D_y D_z}} \quad , \tag{E.1}$$

assuming a 3D Stokes-Einstein rotational diffusion process. Slightly rhombic diffusion tensor values have been adjusted to $D_x < D_y \approx D_z$ in the respective ratio of about $1 : 6 : 7$ for 16-DSA giving an overall axial character to the employed model. Individual subspectra $F_i(B)$ of experiments $S(B)$ have been simulated to yield the intrinsic dynamics and population fractions ϕ_i by following equation:

$$\phi_i = \frac{A_S}{A_{F,i}} \cdot \frac{\iint F_i(B)\mathrm{d}^2 B}{\iint S(B)\mathrm{d}^2 B} \tag{E.2}$$

Here, the scalar values of A_S and $A_{F,i}$ are normalization constants from the double integration process. Subspectra emerging from different dynamic regimes of 16-DSA are termed f, b_1, b_2 and a. Hence, $S(B)$ is the complete experimental spectrum that can be reconstructed with $S(B)_{\mathrm{sim}}$ by N optional components $F_i(B)$. This is facilitated by following relation:

$$S(B)_{\mathrm{sim}} = \sum_i^N \phi_i \cdot \iint F_i(B) = A_S \sum_i^N \frac{1}{A_{F,i}} \cdot \frac{\iint F_i(B)\mathrm{d}^2 B}{\iint S(B)\mathrm{d}^2 B} \tag{E.3}$$

The intrinsic error of g_{iso} was determined by a Mn-Standard sample (Magnettech GmbH) yielding $\Delta g_{\mathrm{iso}} = 4.4 \cdot 10^{-4}$, so that the values given for g_{iso} in **Table E2** are only of a qualitative and relative character. For more detailed values of g and A, spectra should be measured at Q-band or W-band frequencies.

Table E2 | Simulation parameters of the 16-DSA spin probe interacting with HSA-N and BSA-N

albumin	$F_i(B)$	ϕ_i [%]	g_{xx}	g_{yy}	g_{zz}	g_{iso}	A_{xx} [G]	A_{yy} [G]	A_{zz} [G]	a_{iso} [G]	$\tau_{c,i}$ [ns]	β_i [°]
HSA-N[a]	b_1	67.587	2.0089	2.0064	2.0025	2.00593	6.3	5.6	34.5	15.48	15.382	24
	b_2	32.355	2.0089	2.0064	2.0025	2.00593	6.3	5.6	34.5	15.48	7.415	53
	f	0.0577	2.0086	2.0064	2.0025	2.00583	6.5	6.1	34.7	15.79	0.120	45
	a[b]	32.663	2.0089	2.0064	2.0025	2.00593	6.3	5.6	34.5	15.48	–	45
BSA-N[c]	b_1	70.875	2.0089	2.0064	2.0025	2.00593	5.9	5.5	34.4	15.26	13.506	16
	b_2	28.931	2.0089	2.0064	2.0025	2.00593	5.9	5.5	34.4	15.26	5.652	45
	f	0.1944	2.0087	2.0063	2.0024	2.00580	6.6	6.0	34.7	15.77	0.136	45

[a]Values are taken from a simulation of a 16-DSA to HSA-N loading ratio of 1.40 : 1 (**Figure 7.3**). [b]Micellar subspectrum $F_a(B)$ for a 16-DSA to HSA loading ratio of 11.72 : 1 with $J_{\mathrm{AB}} = 45$ MHz (Heisenberg spin exchange frequency).[E1,E2] Spectral simulations have been conducted in EasySpin.[E3] [c]Values are taken from a simulation of a 16-DSA to BSA loading ratio of 1.59 : 1 (**Figure E5A**).

The Euler angles β_i are the tilt angles between the molecular coordinate system ($\boldsymbol{D}$) and the coordinate system of the magnetic parameters of the nitroxide moiety ($\boldsymbol{g},\boldsymbol{A}$).[E3,E6] The values were set to $\beta_f = 45°$ and $\beta_{bi} = 16 - 53°$. However, the validity of the β-values can also be considered as of only a qualitative nature. An exemplary collection of simulation parameters for HSA-N and BSA-N is given in **Table E2** for an albumin-to-16-DSA loading of about 1.0 : 1.5. As micelles do not appear at such low 16-DSA equivalent concentrations, according simulation parameters (*a*) are additionally given for a 1.00 : 11.72 loading ratio of 16-DSA interacting with HSA (**Figure 7.3**) where about 32.7 % of the 16-DSA molecules reside in micelles.

E3 | Double Integration of CW EPR Spectra

A manual double integration routine has turned out to be inevitable in some cases in order to quantify the amount of added 16-DSA molecules. Therefore, as it is also implied in the multi-component simulation routine (**Appendix E2**), double integration (DI) was employed for quantitative assessment of spin concentration[E7] in a rather rough approach for CW EPR spectra that are shown in **Figure 7.3** and **Figure 7.4**. The determination of individual 16-DSA concentrations was conducted by simply relating the signal strength of an individual sample to its according stock solution by the relation:

$$c_{\text{16-DSA}} = [\text{L}] = \frac{\iint S_{j,k}(B)\, \mathrm{d}^2 B}{\iint S_{\text{stock}}(B)\, \mathrm{d}^2 B} \cdot c_{\text{16-DSA}}^{\text{stock}} \qquad (E.4)$$

The computation of ligand concentration [L] by double integration can be simplified by using a spectrometer constant C_{DI} in case of constant experimental parameter setups. The receiver gain (V_{out}) for values $100 < V_{\text{out}} < 900$ and modulation amplitude values (MA) for $0.2\,\text{G} < \text{MA} < 1.4\,\text{G}$ are almost perfectly linear with DI value increase ($R^2(V_{\text{out}}) = 0.99997$ and $R^2(\text{MA}) = 0.99952$) and can therefore be changed in the specified range without concern (see **Figure E1**).
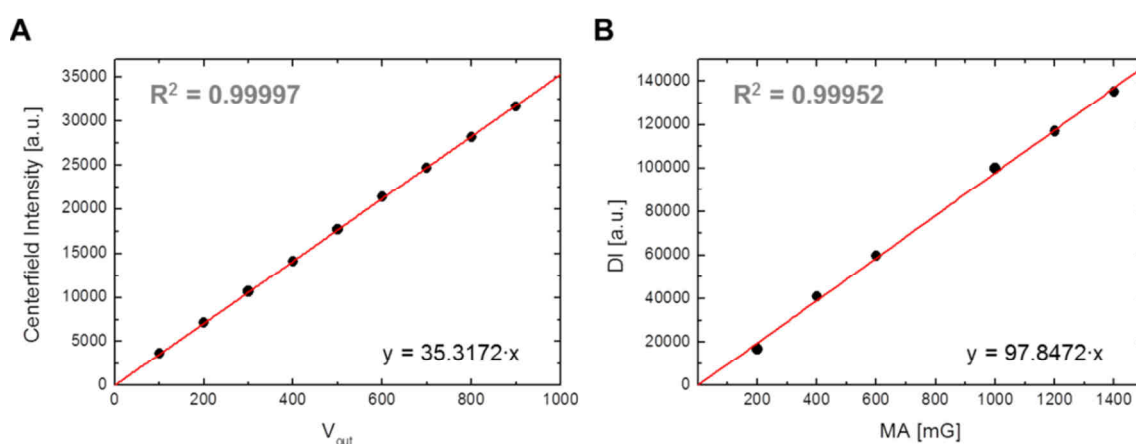
Figure E1 | Calibration of gain (V_{out}) and modulation amplitude (MA) for double integration (DI). A sample containing 0.29 mM of 16-DSA in DPBS pH 7.4 was subject to different experimental parameters in CW EPR. The changed parameters are (**A**) V_{out} at MA = 500 mG and (**B**) MA at V_{out} = 300 at the Miniscope MS400 spectrometer.

The comparison of several stock solutions gives an approximate 16-DSA-specific spectrometer constant of e.g. $C_{DI} = 8.65 \cdot \mu M^{-1} \, G^{-1}$. Application of equation E.5 therefore incorporates variations of modulation amplitudes and gain values for constant microwave power:

$$c_{16-DSA} \;=\; [L] \;=\; \frac{DI}{C_{DI} \cdot V_{out} \cdot MA} \tag{E.5}$$

With this method adequate and reliable values for 16-DSA concentration can be obtained. When the double integration routine fails due to e.g. a low SNR, the center-field intensity or the nominal concentration was taken as a quantitative measure of 16-DSA concentration.

E4 | MALDI-TOF Mass Spectra of BSA-based Macroinitiators (BSA-I*x*)

As a proof of the degree of squaric acid modification of BSA the determination of individual MWs was conducted by MALDI-TOF MS, as conventional SDS PAGE usually does not provide sufficient mass resolution to observe the expected weight increase of an attached residue ($MW_{SA} = 288.11$ Da, see **Figure E3**). The results of corresponding MALDI experiments on all available BSA-I*x* and their native precursor BSA are shown in **Figure E2** and **Table 7.3**. The determination of the rounded *x*-values is straightforward and can be obtained from the relation $x = (MW_{Ix} - MW_N)/MW_{SA}$ (see also **Chapter 7.6**).
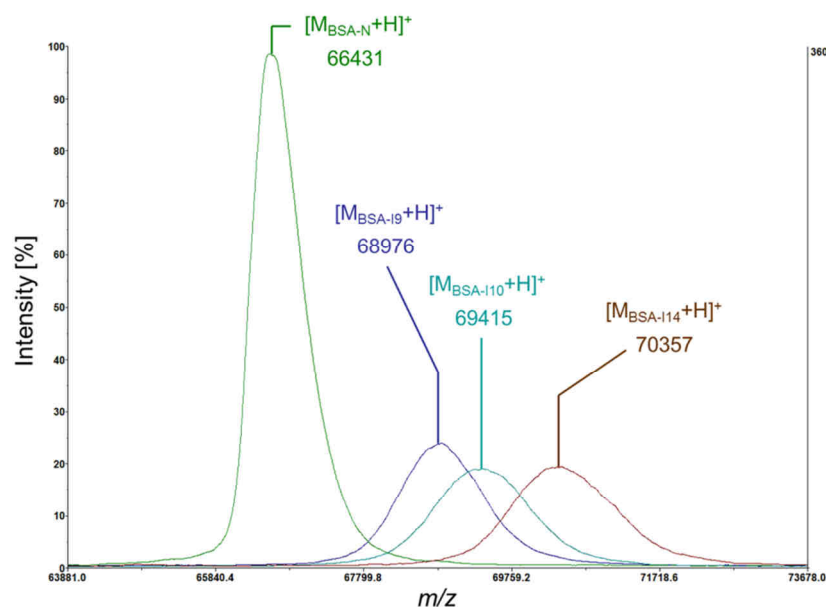
Figure E2 | MALDI-TOF spectra of BSA and BSA-I*x* macroinitiators. Mass spectra of samples *k* as BSA-N (green), BSA-I9 (blue), BSA-I10 (cyan) and BSA-I14 (brown) are presented as singly charged ions $[M_k+H]^+$. The colored inset numbers are the corresponding molecular weights in Da.

E5 | SDS PAGE of Different Stages of BSA Polymer-protein Conjugation (BSA-P*n*)

The effect of the grafting reaction on the molecular weight of native BSA (BSA-N, lane 3) was tested with a SDS PAGE.[E8] Whereas the slight change in molecular weight of the BSA-I10 macroinitiator (+2984 Da ≈ 10.4 squaric acid initiators, lane 4) is hardly detectable, the grafting reaction with OEGMA$_{475}$ leads to broad bands in both cases of polymer-protein conjugation (BSA-*g*-P(OEGMA)$_n$) leading to samples BSA-P11 (lane 5) and BSA-P18 (lane 6). Note, that the bands of BSA-I10 completely vanished in lanes 5 and 6 indicating a high initiation efficiency of the grafting reaction. The features in between 130 and 180 kDa in lanes 3 and 4 can be attributed to BSA dimer and trimer fractions.
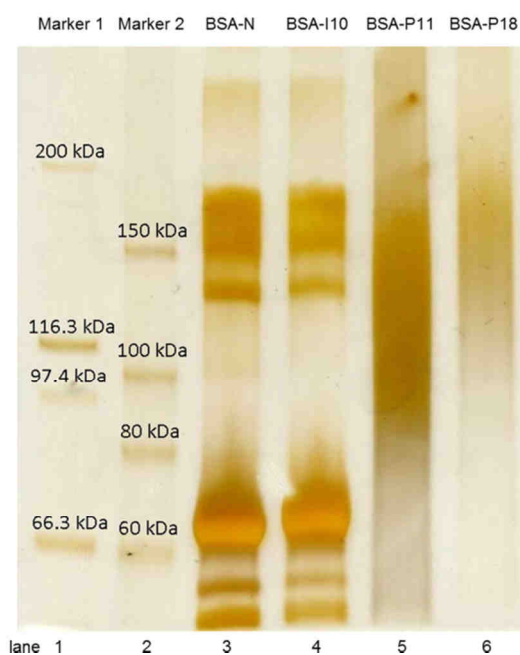
Figure E3 | SDS PAGE of BSA-N, the BSA-I10 macro-initiator and the resulting BSA-P*n* polymer-protein conjugates. Different stages of posttranslational modifications of BSA are shown: lanes 1 and 2: Marker 1 and Marker 2, lane 3: native BSA (BSA-N), lane 4: macroinitiator BSA-I10, lane 5: polymer-protein conjugates BSA-*g*-P(OEGMA)$_{11}$ = BSA-P11 and lane 6: BSA-*g*-P(OEGMA)$_{18}$ = BSA-P18. For details about the preparation of the SDS PAGE the reader is referred to the PhD thesis of Dr. Anja Thomas.[E8]

The determination of the rounded *n*-values is straightforward and is obtained from the corresponding relation $MW_{Pn} = MW_N + x \cdot MW_{SA} + x \cdot n \cdot MW_{OEG}$ (see also **Chapter 7.6**), so that $n = 11$ for the sample in lane 5 and $n = 18$ for the sample in lane 6 (see **Table 7.3**).

E6 | Characterization of Modified BSA Samples by Zeta Potentials

(*i*) *Calculation of the net charge of BSA samples*

Zeta potentials (ζ) do not only serve as a measure of the system's stability,[E9–E11] but may also reveal some functional properties that provide further insights into the complex interplay of protein, surrounding ions and solvent. The ionic strength of 0.137 M DPBS buffer[E12] can be calculated with the well-known relation:

$$I = \frac{1}{2} \sum_{i=1}^{n} c_i z_i^2 \qquad , \qquad (E.6)$$

giving a value of $I = 169.528$ mM = mol·m^{-3} with a summation across all buffer ion components i. The corresponding screening, or Debye length (λ_D) at $T = 25°C$ is defined as:

$$\lambda_D = \sqrt{\frac{\varepsilon_0 \varepsilon_r k_B T}{2e^2 I \cdot N_A}} = \sqrt{\frac{\varepsilon_0 \varepsilon_r k_B T}{N_A e^2 \sum c_i z_i^2}} \qquad (E.7)$$

giving an estimate for the double layer thickness, or the interaction radius around the electrolyte particles. Here, $\varepsilon_0 = 8.854 \cdot 10^{-12}$ A·s·V^{-1}·m^{-1} is the vacuum permittivity, $\varepsilon_r = 78.4$ the dielectric constant for water,[E13] $k_B = 1.3806 \cdot 10^{-23}$ J K^{-1} the Boltzmann constant, $e = 1.6022 \cdot 10^{-19}$ C the elementary charge and $N_A = 6.0221 \cdot 10^{23}$ mol^{-1} is Avogadro's number. Although multivalent ions ($Y^{\pm Z}$) may exhibit a more complicated behavior of this intrinsic decay length,[E14] the expression in equation E.7 shall suffice here. The calculated value for a 0.05 M DPBS buffer as it was employed in the Zeta potential experiments is $\lambda_D = 1.222$ nm. Usually, the inverse Debye length $\kappa = \lambda_D^{-1}$ is used as a parameter that indicates the double layer thickness around a charged sphere of radius a. For large particles with a thin layer the product $\kappa a \gg 1$. In case of BSA-N this value is $\kappa a_N = 2.65$ with $a_N = 3.24$ nm. The experimentally determined Zeta potential of 0.10 g/l BSA-N in 0.05 M DPBS buffer is $\zeta_N = -18.6$ mV (**Table 7.4** and **Table E3**) with a conductivity of $\kappa_{el,N} = 6.52$ mS cm^{-1}. The electrophoretic mobility $\mu_{e,k}$ of any BSA sample k is then defined as:[E15]

$$\mu_{e,k} = \frac{2\varepsilon_0 \varepsilon_r \zeta_k F(\kappa a_k)}{3\eta} \qquad , \qquad (E.8)$$

where $\eta = 0.89$ mPa·s is the dynamic viscosity and $F(\kappa a_k)$ is the individual Henry function. An appropriate mathematical expression for individual Henry functions was recently presented by Swan *et al.*:[E16]

$$F(\kappa a_k) = F_{SF}(\kappa a_k) = \frac{16 + 18\kappa a_k + 3(\kappa a_k)^2}{16 + 18\kappa a_k + 2(\kappa a_k)^2} \qquad (E.9)$$

yielding a value of $F_{SF}(\kappa a_N) = 1.0904$ for BSA-N. This Henry function value can be computed prior to experiments on the Zetasizer^{TM} 500 device for considering differences in Henry's functions during operation ($a_N = R_{H,N} = 3.24$ nm). For calculated values of κa_k and $F_{SF}(\kappa a_k)$ from all five other samples the reader is referred to **Table E3**. The number of uncompensated charges $N_{c,k}$ of each sample can be obtained with the assumption that the charge Q_k in uniform electric fields (as it is supposed to exist in the Omega cuvette) is defined as:[E17]

$$Q_k = N_{c,k} \cdot e = 6\pi\eta a_k \mu_{e,k} \qquad . \qquad (E.10)$$

With equation E.8 and E.10 an expression can be derived that directly correlates the Zeta potential to the number $N_{c,k}$ of uncompensated charges:

$$N_{c,k} = \frac{4\pi a_k \varepsilon_0 \varepsilon_r \zeta_k F(\kappa a_k)}{e} \qquad (E.11)$$

Table E3 | Parameters from DLS and Zeta potential measurements

k	$\mu_{e,k}{}^a$ [$10^{-8}m^2V^{-1}s^{-1}$]	$\kappa_{el,k}{}^a$ [mS cm^{-1}]	$\kappa a_k{}^b$	$F_{SF}(\kappa a_k)^c$	$\zeta_k{}^a$ [mV]	$N_{c,k}{}^d$	$Z_k{}^e$
N	-1.05 ± 0.13	6.522	2.651	1.0904	-18.584 ± 1.504	-3.573 ± 0.554	-10.461 ± 2.250
I9	-1.55 ± 0.07	6.623	3.151	1.1072	-27.409 ± 1.479	-6.359 ± 0.936	-18.617 ± 3.857
I10	-1.63 ± 0.05	6.549	3.232	1.1099	-28.740 ± 1.054	-6.858 ± 0.858	-20.076 ± 3.718
I14	-1.75 ± 0.09	6.582	3.584	1.1210	-30.893 ± 0.882	-8.255 ± 1.083	-24.168 ± 4.622
P11	-0.70 ± 0.05	6.595	6.367	1.1915	-12.392 ± 1.572	-6.252 ± 1.621	-18.304 ± 5.845
P18	-0.75 ± 0.10	7.269	6.342	1.1910	-13.191 ± 1.335	-6.627 ± 1.607	-19.400 ± 5.869

[a]Experimental values of Zeta potentials (ζ_k), electrophoretic mobilities ($\mu_{e,k}$) with corresponding conductivities ($\kappa_{el,k}$) are shown. [b]Calculated from equation E.7 and a_k values from **Table 7.3**. [c]The Henry factor $F_{SF}(\kappa a_k)$ according to Swan *et al.*[E15] was calculated from equation E.9. [d]The numbers of uncompensated charges $N_{c,k}$ and their errors $\Delta N_{c,k}$ were calculated from equation E.11 and E.12. [e]The net charges Z_k and their errors ΔZ_k were calculated from equation E.15 and E.16.

giving $N_{c,N} = -3.6 \pm 0.6$ for BSA-N (**Table E3**). The corresponding errors were calculated with the relation:

$$\Delta N_{c,k} = \frac{4\pi \varepsilon_0 \varepsilon_r}{e} \cdot \left(\left| \zeta_k \cdot F(\kappa a_k) \cdot \Delta a_k \right| + \left| a_k \cdot F(\kappa a_k) \cdot \Delta \zeta_k \right| + \left| a_k \cdot \zeta_k \cdot \Delta F(\kappa a_k) \right| \right) , \qquad (E.12)$$

whereas $\Delta F(\kappa a_k) = F(\kappa a_k) - F(\kappa a_N)$ is the difference of sample k to the BSA-N reference.
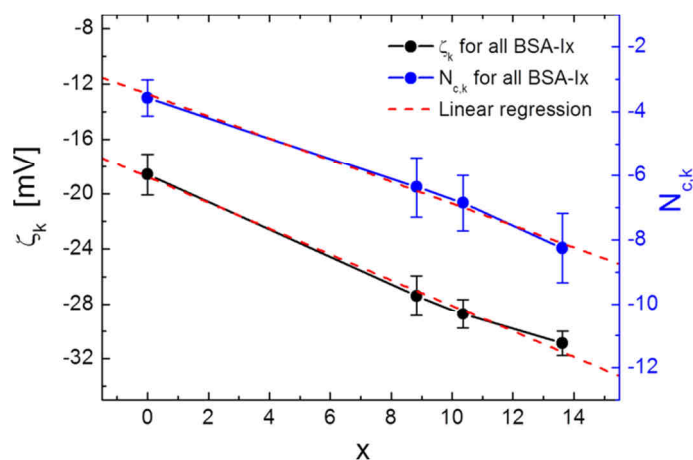
Figure E4 | Linear decrease of ζ_k and $N_{c,k}$ with increasing squaric acid modification x. The decreases in Zeta potential (ζ_k, black) and the number of uncompensated charges ($N_{c,k}$, blue) are considered as being linear functions of the degree of squaric acid modifications in BSA-Ix macroinitiators ($x = 0, 9, 10$ and 14, here: BSA-N = BSA-I0).

The changes in the number of uncompensated charges ($N_{c,k}$) and Zeta potential (ζ_k) can be plotted versus the degree x of squaric acid modification (**Figure E2** and **Table 7.3**) for all macroinitiators (BSA-Ix) that also comprise the native BSA sample (BSA-N = BSA-I0). Following expressions are found from linear regression analyses:

$$\zeta_k(x) = k_\zeta x + \zeta_N = -0.93792 \cdot x - 18.75643 \tag{E.13}$$

$$N_{c,k}(x) = k_Q x + N_{c,N} = -0.34157 \cdot x - 3.45536 \quad , \tag{E.14}$$

where $\zeta_N = -(18.75643 \pm 0.46119)$ mV and $N_{c,N} = -(3.45536 \pm 0.21194)$ are the reference values for unmodified BSA ($x = 0$, $k = N$, **Table E3**) and $k_\zeta = -(0.93792 \pm 0.05165)$ mV SA^{-1}, as well as $k_Q = -(0.34157 \pm 0.02051)$ SA^{-1} are the slopes of these linear extrapolations (the correlation quality is $R^2 > 0.989$ for both obtained parameters). Assuming that each squaric acid initiator blocks exactly one accessible surface lysine, then $\sigma = 1 - k_Q = 0.65843$ is the fraction of screened charges and the net charge $Z_k \pm \Delta Z_k$ of the BSA samples k can be calculated from the relations:

$$Z_k = -\frac{4\pi a_k \varepsilon_0 \varepsilon_r \zeta_k F(\kappa a_k)}{e k_Q} \tag{E.15}$$

$$\Delta Z_k = \frac{4\pi \varepsilon_0 \varepsilon_r}{e k_Q} \cdot \left(\left| \zeta_k F(\kappa a_k) \Delta a_k \right| + \left| a_k F(\kappa a_k) \Delta \zeta_k \right| + \left| a_k \zeta_k \Delta F(\kappa a_k) \right| + \left| -\frac{a_k \zeta_k F(\kappa a_k)}{k_Q} \Delta k_Q \right| \right). \tag{E.16}$$

The results for Z_k from all samples can be found in **Table E3** and **Table 7.4**.

(*ii*) *Determination of the effective dielectric constant $\varepsilon_{eff,Pn}$ of the polymer layer in BSA-Pn*

The electric field $E(R)$ of a charged sphere (BSA) of radius a surrounded by a medium with $\varepsilon_r > 1$ and $R \geq a$ is given as:

$$E(R) = -\frac{Ze}{4\pi \varepsilon_0 \varepsilon_r R^2} \quad , \tag{E.17}$$

when the charge $Q = Z \cdot e$ is assumed to reside in the origin of the coordinate system.[E18] The corresponding distance-dependent potential $V(R)$ is given as:

$$V(R) = \int E(R) dR = \frac{Ze}{4\pi \varepsilon_0 \varepsilon_r R} \tag{E.18}$$

The voltage in this polymer layer is the difference in the potential of two respective points in the distances $R_1 < R_2$:

$$U = V(R_2) - V(R_1) = \int_{R_1}^{R_2} E(R)\,dR = \frac{Ze}{4\pi\varepsilon_0\varepsilon_r}\left(\frac{1}{R_2} - \frac{1}{R_1}\right) \qquad . \qquad (E.19)$$

In case of the posttranslationally modified protein samples BSA-Pn ($R_2 = a_{Pn}$) the reference substance is the macroinitiator BSA-I10 ($R_1 = a_{I10}$) with almost equivalent numbers of uncompensated charges $N_{c,k}$ that generate the potential with an average value $N_c = (1/3)\cdot\sum N_{c,k} = -6.578 \pm 0.306$. This allows for calculating the potentials for each substance at its slipping plane (SP) surface with the relation:

$$V_k(a_k) = \frac{N_c \cdot e}{4\pi\varepsilon_0\varepsilon_r} \cdot \frac{1}{a_k} \qquad . \qquad (E.20)$$

By combining equation E.20 with equation 7.7 it follows, that:

$$\mu_{e,k} = \frac{2\varepsilon_0\varepsilon_r V_k(a_k)}{3\eta} \qquad (E.21)$$

and therefore it can be concluded from equation E.8 that $V_k(a_k) = \zeta_k \cdot F(\kappa a_k)$. This leads to a modified version of equation E.20 that again predicts the radius-dependent Zeta potential:

$$\zeta_k(a_k) = \frac{N_c \cdot e}{4\pi\varepsilon_0\varepsilon_r} \cdot \frac{1}{a_k F(\kappa a_k)} \qquad , \qquad (E.22)$$

giving $V_{I10} = -27.6$ mV, $V_{P11} = -13.0$ mV and $V_{P18} = -13.1$ mV. This reasonable correspondence (deviation $< 5\%$) to experimental values (**Table 7.4** and **Table E3**) proves the validity of the derived approach when using $\varepsilon_r = 78.4$. Thus, a rough approximation of the radius-dependent Zeta potential decrease as claimed in **Chapter 7.4.1** can be obtained with equation E.22 from the fraction:

$$\phi_\zeta = \frac{\zeta_{Pn}}{\zeta_{I10}} = \frac{a_{I10}F(\kappa a_{I10})}{a_{Pn}F(\kappa a_{Pn})} \approx \frac{a_{I10}}{a_{Pn}} \qquad , \qquad (E.23)$$

while it is here generously assumed that $F(\kappa a_{I10})/F(\kappa a_{Pn}) = 0.932 \approx 1.000$. As the voltage difference $\Delta\zeta_n$ is stretched from a_{I10} to a_{Pn} the effective medium is now the P(OEGMA)$_n$ polymer shell (pervaded by solvent/DPBS buffer). As the protein samples BSA-Pn with their reference macroinitiator-core (BSA-I10) have an (almost) equivalent number of uncompensated charges N_c it is possible to calculate

the effective dielectric constant $\varepsilon_{\text{eff},\text{P}n}$ of the polymer shell with the experimentally observed difference in the Zeta potentials of BSA-I10 and BSA-Pn. Therefore, a modified version of equation E.19 rearranged with equation E.22 is used:

$$\Delta\zeta_n = \zeta_{\text{P}n} - \zeta_{\text{I}10} = \frac{N_c \cdot e}{4\pi\varepsilon_0\varepsilon_{\text{eff},\text{P}n}}\left(\frac{1}{a_{\text{P}n}F(\kappa a_{\text{P}n})} - \frac{1}{a_{\text{I}10}F(\kappa a_{\text{I}10})}\right) \tag{E.24a}$$

that allows for an estimation of the effective dielectric constant $\varepsilon_{\text{eff},\text{P}n}$ of the water-pervaded polymer layer with:

$$\varepsilon_{\text{eff},\text{P}n} = \frac{N_c \cdot e}{4\pi\varepsilon_0\Delta\zeta_n} \cdot \left(\frac{1}{a_{\text{P}n}F(\kappa a_{\text{P}n})} - \frac{1}{a_{\text{I}10}F(\kappa a_{\text{I}10})}\right) \quad , \tag{E.24b}$$

when replacing the term $\zeta_{\text{P}n} - \zeta_{\text{I}10}$ with $\Delta\zeta_n$ (see equation 7.11 in the main manuscript). Therefore, the error of propagation is given as:

$$\Delta\varepsilon_{\text{eff},\text{P}n} = \frac{e}{4\pi\varepsilon_0}\cdot\left(\frac{\Delta N_c}{\Delta\zeta_n}\cdot\delta + \frac{N_c\Delta\Delta\zeta_n}{\Delta\zeta_n^2}\cdot\delta + \frac{N_c}{\Delta\zeta_n}\cdot\left(\frac{\Delta a_{\text{P}n}}{a_{\text{P}n}^2 F(\kappa a_{\text{P}n})} + \frac{\Delta a_{\text{I}10}}{a_{\text{I}10}^2 F(\kappa a_{\text{I}10})}\right)\right) \tag{E.25}$$

with the abbreviation:

$$\delta = \left(\frac{1}{a_{\text{P}n}F(\kappa a_{\text{P}n})} - \frac{1}{a_{\text{I}10}F(\kappa a_{\text{I}10})}\right) \quad . \tag{E.26}$$

E7 | Determination of k_{L} for Simulation-free Scatchard Plot Construction

It is here shown that the correlation of several spectral characteristics with results from explicit simulations of EPR spectra can be facilitated by a correlation constant k_{L}. First, a reference data set of various BSA samples loaded with different molar ratios of 16-DSA in the range from 1.6 to 5.3 is explicitly simulated according to the procedure given in **Appendix E2** (see **Figure E5A**). In the absence of micellar spectral components in albumin solutions this is usually done with a 3-component approach comprising one free fraction (f) and two immobilized fractions (b_1 and b_2).[E19–E21] From these data, a Scatchard[E22] graph can be constructed by plotting $v = [\text{L}]_b/([\text{L}]_f \cdot c_{\text{B}})$ versus the number of bound ligands N_{L} when the total concentrations of BSA protein (c_{B}) and ligand $[\text{L}]_t$ are known (**Figure E5B**). Upon applying equation 7.1, this Scatchard plot yields the number $N_{\text{E}} = N_{\text{T}} = 6.4 \pm 0.3$ of equivalent ligand binding sites and the macroscopic association constant $K_{\text{A}} = (7.5 \pm 0.2)\cdot10^5 \text{ M}^{-1}$ of 16-DSA ligands in a single BSA molecule (see also **Table 7.5**). Furthermore, the obtained simulation parameters (see **Table E2**) henceforth allow that the ratio of free (f) to bound ($b = b_1 + b_2$) spectral fractions ϕ_i can be arbitrarily varied in simulations that are free of experimental spectra and the relative

increase of spectral features can be extracted from the resulting simulations. By now, the usually observed slight changes in linewidths of the immobilized fractions $b = b_1 + b_2$ are not taken into account in this strategy.[E23,E24] Here, the low-field peak height of the free fraction ($h_{+1,f}$) was compared to the center-field peak of the bound fraction ($h_{0,b}$) that are both clearly visible throughout all applied experimental 16-DSA loading ratios in this study (**Figure E5C**). An almost perfect linear relationship is found in between the ratio of low-field peak of the free fraction and the center-field peak of the bound fraction ($h_{+1,f}/h_{0,b}$) that can be described by the relation:

$$\phi_f = k_L \cdot \frac{h_{+1,f}}{h_{0,b}} \tag{E.27}$$

where $k_L = (2.486 \pm 0.015) \cdot 10^{-2}$ is the desired correlation constant from the linear fit in **Figure E5C** (logarithmic plot). From equation E.27 the free or bound ligand concentration $[L]_i$ is then obtained without any spectral simulation as pointed out in equation 7.12 and 7.13 of the main manuscript.
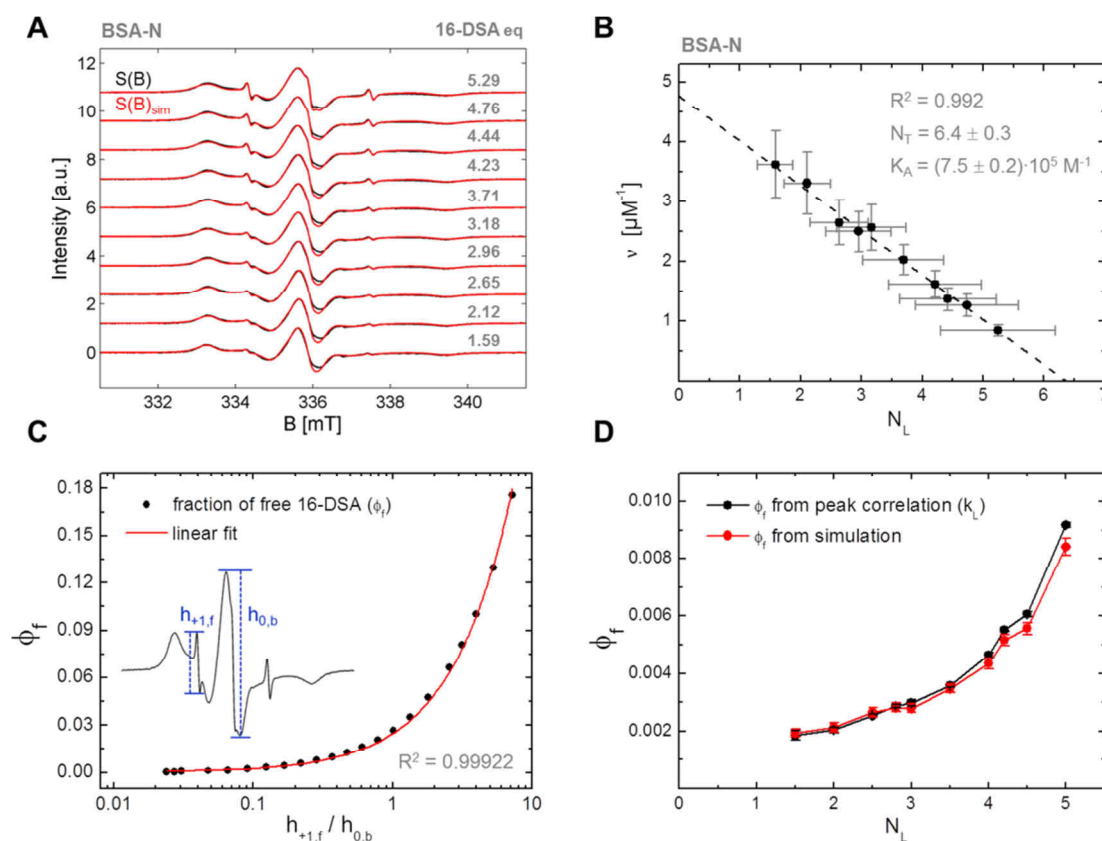
Figure E5 | Scatchard plot construction from the simulation-free peak correlation approach (k_L). (**A**) CW EPR spectra of 16-DSA loaded on native BSA (BSA-N) in the ratio of 1.59 – 5.29 molar equivalents (see gray inset numbers). Experimental data ($S(B)$, black) are equipped with according spectral simulations ($S(B)_{sim}$, red). (**B**) A Scatchard plot for 16-DSA interacting with BSA-N was constructed from simulation data in (A) with a linear fit (black dotted line). (**C**) Correlation of peak characteristics $h_{+1,f}$ and $h_{0,b}$ to the free fraction ϕ_f of 16-DSA ligand from arbitrary simulations. A linear relation (red curve, $R^2 = 0.99922$) is obtained in between the peak ratio and the free fraction ϕ_f in the range of about three orders of magnitude. For better visibility of individual data points a logarithmic axis has been chosen for $h_{+1,f}/h_{0,b}$. (**D**) Comparison of the obtained free fractions ϕ_f depending on the amount of bound 16-DSA ligand equivalents (N_L) from spectral simulation (red) and from the correlation approach (black) according to a visualization strategy pursued in Perkins *et al.*[E23]

A complete Scatchard plot can therefore be constructed just by knowledge of the total ligand concentration $[L]_t$:

$$[L]_t = \phi_f [L]_t + \phi_b [L]_t \qquad\qquad\qquad\qquad (E.28)$$

and by extraction of the individual ratios $h_{+1,f}/h_{0,b}$ from a consistent set of experimental spectra. A comparison of the results from spectral simulations and the peak-correlation method is shown in **Figure E5D** and shows nice correspondence with individual deviations ranging only from about $2-9$ %. In this case, the 16-DSA equivalent loading ratios were extracted by dividing the nominal 16-DSA concentrations by the real BSA concentration as given in equation 5.5 (eq $= c_{16\text{-DSA}}/c_{r,\text{BSA}}$).

E8 | CW EPR Spectra for Scatchard Plot Construction of BSA-I*x* and BSA-P*n*

Due to the large amount of spectra, the Scatchard plots in **Figure 7.8** were all constructed according to the scheme presented in **Appendix E7**. The underlying CW EPR raw data are presented in **Figure E5A** and **Figure E6**. As the noise in several spectra was comparatively high at lower loading ratios, Double integration partially failed and therefore the 16-DSA equivalent loading ratios are extracted from sample preparation protocols (added solution volumes) and by dividing the nominal 16-DSA concentrations by the experimentally adjusted BSA concentration (eq = $c_{16\text{-DSA}}/c_{\text{BSA},i}$).
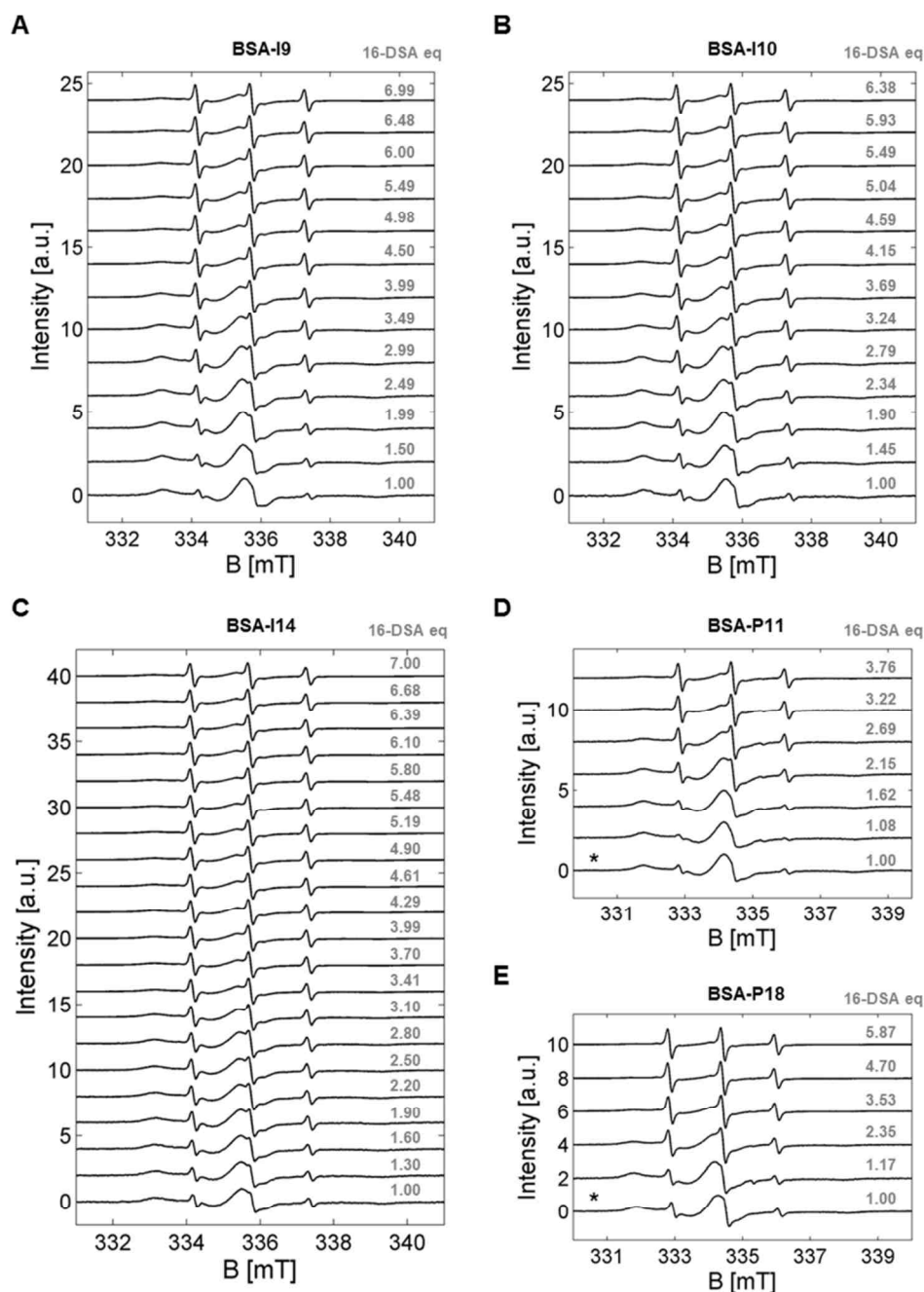
Figure E6 | CW EPR data for Scatchard plot construction of BSA-I*x* and BSA-P*n*. All CW EPR data sets are given with their respective 16-DSA ligand loading equivalent ratio (16-DSA eq) for macroinitiators (**A**) BSA-I8, (**B**) BSA-I11 and (**C**) BSA-I12 at $c_{\text{B,I}x} = 0.1$ mM each and polymer-protein conjugates (**D**) BSA-P11 and (**E**) BSA-P18 ($c_{\text{B,P}n} = 0.06 – 0.32$ mM). Spectra from **Figure 7.7** were partially employed in this analysis and are highlighted with an asterisk in (D) and (E).

E9 | Fit Parameters from Linear Regressions in Scatchard Plots of BSA-Ix and BSA-Pn

Equation 7.14 was used to extract phase-specific numbers of equivalent binding sites ($N_{E,k,p}$) and association constants ($K_{A,k,p}$). The association constants are simply the inverse of the dissociation constants ($K_{A,k,p} = K_{D,k,p}^{-1}$, k = sample, p = Scatchard phase: I, Ia, Ib, Ic or II).[E25] Following relation served as an appropriate linear regression function in Origin:

$$y = \alpha_{k,p} \cdot x + \beta_{k,p} = v = -K_{A,k,p} \cdot \left(N_L - N_{E,k,p} \right) + v_{k,p,N_L \to 0} \qquad , \qquad \text{(E.29)}$$

whereas $\alpha_{k,p}$ and $\beta_{k,p}$ are individual fit parameters that are listed with their relative uncertainties (Δ) in **Table E4**. Additionally, the phase-specific fit ranges and numbers of fit-employed data points q are given, indicating the used data for an individual linear regression in a specific Scatchard plot ($\forall_q \geq 3$).

Table E4 | Fit parameters from phase-specific (p) linear regressions in Scatchard plots

k	p	$\alpha_{k,p}$ [µM^{-1}]	$\Delta\alpha_{k,p}$ [µM^{-1}]	$\beta_{k,p}$ [µM^{-1}]	$\Delta\beta_{k,p}$ [µM^{-1}]	R^2	Fit range	q
BSA-N	I§	−0.74911	0.02262	4.76466	0.10486	0.99185	1 – 10	10
	I	−0.83835	0.02816	5.06010	0.10287	0.98993	1 – 10	10
BSA-I9	Ia	−0.75800	0.14263	2.13657	0.19885	0.93161	1 – 3	3
	Ib	−0.25211	0.01036	1.19836	0.02945	0.99162	3 – 8	6
BSA-I10	Ia	−0.15056	0.01316	0.94437	0.02459	0.98484	2 – 4	3
	Ib	−0.28692	0.03184	1.25206	0.09319	0.95249	4 – 8	5
	II	−0.03198	0.00302	0.28459	0.01468	0.95688	8 – 13	6
BSA-I14	Ia	−0.25643	0.02200	0.96423	0.03595	0.96423	1 – 6	6
	Ib	−0.51495	4.60719E–4	1.79002	0.00134	1.00000	7 – 9	3
	Ic	−0.05893	0.00646	0.40420	0.03073	0.95363	13 – 17	5
	II	−0.01509	7.85326E–4	0.19341	0.00410	0.98133	9 – 12, 18 – 21	8
BSA-P11	Ia	−0.42030	0.02335	1.21969	0.03710	0.99080	2 – 5	4
BSA-P18	Ia	−0.28956	0.01449	0.82393	0.03100	0.99500	1 – 3	3
	Ib	−0.06343	0.00578	0.31248	0.01727	0.98352	3 – 5	3

§Fit parameters for simulation data of the (native) BSA-N samples loaded with 16-DSA (**Figure E5A**).

E10 | References

[E1] J. H. Freed, Theory of slow tumbling ESR spectra for nitroxides. In *Spin Labeling: Theory and Applications*; L. J. Berliner, Ed.; Academic Press: New York, **1976**, Vol. 1, pp 53–132.

[E2] E. Meirovitch, D. Igner, E. Igner, G. Moro, J. H. Freed, *J Chem Phys* **1982**, *77*, 3915–3938.

[E3] S. Stoll, A. Schweiger, *J Magn Reson* **2006**, *178*, 42–55.

[E4] D. J. Schneider, J. H. Freed, Calculating slow motional magnetic resonance spectra: A user's guide. In *Spin Labeling: Theory and Applications*; L. J. Berliner, J. Reuben, Eds.; Plenum Press: New York, London, **1989**, Vol. 8, pp 1–76.

[E5] M. Ge, S. B. Rananavare, J. H. Freed, *Biochim Biophys Acta, Gen Subj* **1990**, *1036*, 228–236.

[E6] A. R. Edmonds, *Angular momentum in quantum mechanics*. Princeton University Press: Princeton, **1996**.

[E7] G. R. Eaton, S. S. Eaton, D. P. Barr, R. T. Weber, *Quantitative EPR*. Springer-Verlag: Wien, New York, **2010**.

[E8] A. Thomas, Heterofunctional Polyether Building Blocks: From Diverse Macromonomer Structures to Bioinspired Nanoparticle Coatings. Ph.D. Thesis, Johannes Gutenberg-Universität Mainz, **2013**.

[E9] B. Derjaguin, L. Landau, *Acta Physicochim URSS* **1941**, *14*, 633–662.

[E10] S. Honary, M. Jahanshahi, P. Golbayani, P. Ebrahimi, K. Ghajar, *J Nanosci Nanotechnol* **2010**, *10*, 7752–7757.

[E11] M. Larsson, A. Hill, J. Duffy, *Ann T Nord Rheol Soc* **2012**, *20*, 209–214.

[E12] R. Dulbecco, M. Vogt, *J Exp Med* **1954**, *99*, 167–182.

[E13] E. W. Lemmon, Thermophysical properties of water and steam. In *CRC Handbook of Chemistry and Physics*; W. M. Haynes, D. R. Lide, T. J. Bruno, Eds.; CRC press: Boca Raton, FL, **2014**, Vol. 95, p 6–1.

[E14] M. M. Kohonen, M. E. Karaman, R. M. Pashley, *Langmuir* **2000**, *16*, 5749–5753.

[E15] B. Jachimska, A. Pajor, *Bioelectrochemistry* **2012**, *87*, 138–146.

[E16] J. W. Swan, E. M. Furst, *J Colloid Interface Sci* **2012**, *388*, 92–94.

[E17] Z. Adamczyk, A. Bratek, B. Jachimska, T. Jasinski, P. Warszynski, *J Phys Chem B* **2006**, *110*, 22426–22435.

[E18] W. Demtröder, *Experimentalphysik 2: Elektrizität und Optik*. Springer-Verlag: Berlin, Heidelberg, **2013**.

[E19] A. Gurachevsky, E. Shimanovitch, T. Gurachevskaya, V. Muravsky, *Biochem Biophys Res Commun* **2007**, *360*, 852–856.

[E20] V. Muravsky, T. Gurachevskaya, S. Berezenko, K. Schnurr, A. Gurachevsky, *Spectrochim Acta, Part A* **2009**, *74*, 42–47.

[E21] A. A. Pavicevic, A. D. Popovic-Bijelic, M. D. Mojovic, S. V. Susnjar, G. G. Bacic, *J Phys Chem B* **2014**, *118*, 10898–10905.

[E22] G. Scatchard, *Ann NY Acad Sci* **1949**, *51*, 660–672.

[E23] R. C. Perkins Jr., N. Abumrad, K. Balasubramanian, L. R. Dalton, A. H. Beth, J. H. Park, C. R. Park, *Biochemistry* **1982**, *21*, 4059–4064.

[E24] T. G. Gantchev, M. B. Shopova, *Biochim Biophys Acta, Protein Struct Mol Enzymol* **1990**, *1037*, 422–434.

[E25] R. A. Copeland, *Enzymes: A Practical Introduction to Structure, Mechanism, and Data Analysis*. Wiley-VCH: New York, **2000**.

Appendix F | Exploring the pH-induced Functional Phase Space of HSA

F1 | Data Extraction from CW EPR Spectra

In order to extract apparent hyperfine coupling constants $A_{//}$[F1] and collective rotational correlation times τ_c from CW EPR spectra of 5-MSL HSA a scheme is presented in **Figure F1** of how the corresponding data in **Figure 8.2B** were obtained. According to a strategy presented by Meirovitch and Freed[F2] the A-tensor components (A_{xx}, A_{yy}, A_{zz}) are extracted from low-temperature X-band CW EPR spectra (A_{zz}) in combination with room temperature spectra (a_{iso}), assuming an overall axial nitroxide geometry with $A_{xx} = A_{yy}$. The pure A_{zz} tensor value can be extracted from CW EPR spectra below about 200 K, as the strongly restricted rotational freedom leads $A_{//}$ to approach A_{zz}.[F3] This is the characteristic threshold temperature when intramolecular motions with $\tau_c < 100$ ns become visible from a protein sample. The isotropic hyperfine coupling constant:

$$a_{iso} = Tr(\boldsymbol{A}) = \tfrac{1}{3}\left(A_{xx} + A_{yy} + A_{zz}\right) = \tfrac{1}{3}\left(2A_{xx} + A_{zz}\right) \tag{F.1}$$

from 5-MSL is here taken from an extremely basic room temperature sample at pH 11.96, where the freely rotating component with its typical three-line spectra is dominant and clearly identifiable. **Figure F1A** shows the spectral positions of specific features that were extracted ($x_i \in A_i$, a_i). However, besides the straightforward peak-picking procedure, a Manganese standard (Magnettech GmbH) has been used to take device-specific uncertainties in relative line-positions into account and a sweep-width correction factor $k_{SW} = 0.9965$ could be determined for experiments with the 5-MSL spin label and $k_{SW} = 0.9923$ for 5-DSA and 16-DSA (average value: $k_{SW} = 0.9944$). The corrected values for A_{zz}, $A_{//}$ and a_{iso} are therefore generally obtained with following expression:

$$x = \frac{k_{SW}}{2}\left(B(x_2) - B(x_1)\right) \quad , \tag{F.2}$$

where $B(x_i)$ are the corresponding magnetic field positions in Gauss [G]. Errors for A_{zz} and $A_{//}$ are determined by the relation (**Figure F1B**):

$$\Delta x = \frac{k_{SW}}{2}\left(\Delta B(x_2) + \Delta B(x_1)\right) \quad , \tag{F.3}$$

as obtained from the propagation of uncertainty. The respective error in individual $\Delta B(x_i)$ are determined during data readouts (here in **Figure F1**: $\Delta A_{zz} = 0.20$ G). Furthermore, this strategy was pursued for all manual data extraction procedures in this study (x-axis values derived from 5-DSA and 16-DSA spectra are: $A_{\parallel}$, $A_{\perp}$, A_{zz}, $\Delta B_{0,pp}$, see **Figure 8.4A**). The error for a_{iso} is related to the magnetic field resolution $\Delta B(x_i) = B_{max}/N_{max} = 3.66$ μT $= 0.0366$ G with $B_{max} = 15$ mT being the sweep width

and the number of recorded data points $N_{max} = 4096$, so that $\Delta a_{iso} = k_{SW} \cdot \Delta B(a_i) = 0.0365$ G. If necessary, values and their errors for y-axis values (e.g. h_0, $h_\perp$ and h_{-1}, see **Figure 8.4A**) were extracted with:

$$y = \tfrac{1}{2}\left(y_2 - y_1\right) \qquad , \qquad \text{(F.4)}$$

and

$$\Delta y = \tfrac{1}{2}\left(\Delta y_2 + \Delta y_1\right) \qquad . \qquad \text{(F.5)}$$
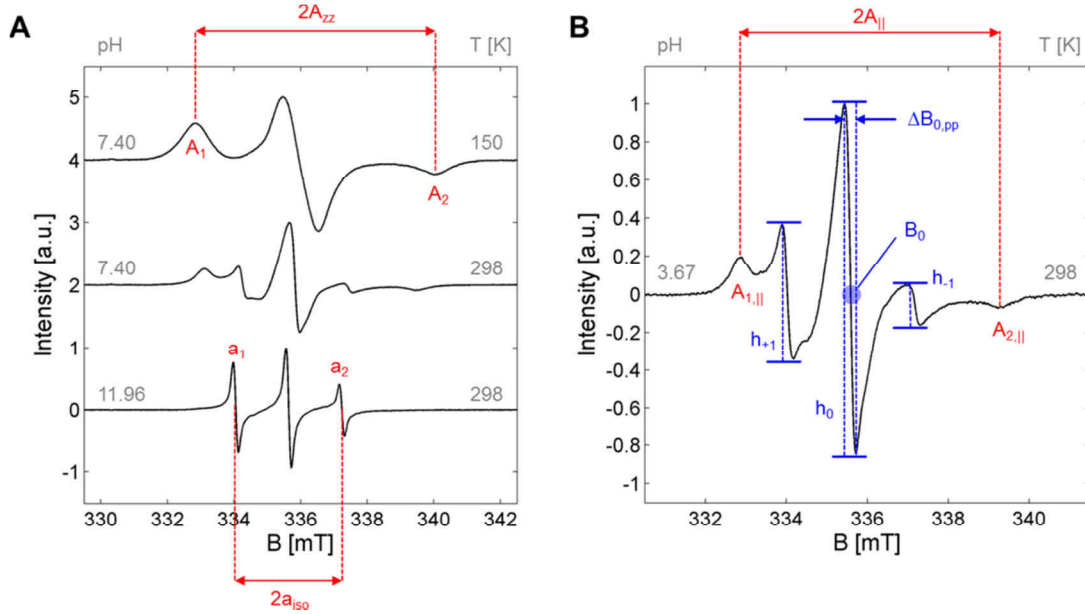
Figure F1 | Exemplary data extraction from CW EPR spectra of 5-MSL HSA. (**A**) Determination of A_{zz} from peak positions A_i in a $T = 150$ K low-temperature spectrum of 1.35 mM 5-MSL HSA in DPBS buffer pH 7.4 (top lane), directly after the concentration step of the purification procedure. The a_{iso} value is taken from value (a_i) of a 0.09 mM 5-MSL HSA sample at pH 11.96 with clearly distinguishable isotropic three-line components of 5-MSL (bottom lane, room temperature, $T = 298$ K). Additionally, a room temperature spectrum of the sample in the top lane is shown in the middle lane. (**B**) Determination of $A_{//}$ from peak positions $A_{i,//}$ in a room temperature ($T = 298$ K) spectrum of 0.09 mM 5-MSL HSA at pH 3.67. The parameters h_{+1}, h_0, h_{-1}, B_0 and $\Delta B_{0,pp}$ are extracted for calculations of collective rotational correlation times τ_c (see equations F.8 and F.9).

According to the method from Meirovitch,[F2] equations F.1 – F.3 can be combined to yield an expression for A_{xx} and A_{yy}:

$$A_{xx} = A_{yy} = \frac{k_{SW}}{4}\left(3 \cdot (B(a_2) - B(a_1)) - (B(A_2) - B(A_1))\right) = \frac{k_{SW}}{2}\left(3 \cdot a_{iso} - A_{zz}\right) \qquad \text{(F.6)}$$

with the uncertainties:

$$\Delta A_{xx} = \Delta A_{yy} = \frac{k_{SW}}{4}\left(6\Delta B(a_i) + \Delta B(A_2) + \Delta B(A_1)\right) \qquad . \qquad \text{(F.7)}$$

Finally, the A-tensor values of 5-MSL can be determined as $A_{zz} = (35.78 \pm 0.20)$ G, $A_{xx} = A_{yy} = (5.91 \pm 0.13)$ G and $a_{iso} = (15.863 \pm 0.037)$ G. The well-known semi-empirical approach for calculations of pH-dependent rotational correlation times τ_c was also tested.[F4,F5] As multi-component CW EPR spectra can be observed throughout all pH values for 5-MSL HSA, the precise extraction of individual rotational components is only accessible by thorough spectral simulation. Therefore, the calculated values are termed as collective rotational correlation times τ_c. The magnetic parameters for g- and A-tensors were used, with the former one being regarded as principally inaccessible without simulations at X-band frequencies. Therefore, the g-tensor values given in Marzola et $al.$[F6] with $g_{xx} = 2.0084$, $g_{yy} = 2.0061$, $g_{zz} = 2.0025$ were used here. Explicit formulae from lineshape theory (see also **Chapter 2.4.2.2**, equation 2.70) were used as given in equation F.8 and F.9. Furthermore, the τ_c values are usually obtained by calculating the arithmetic average of both values $\tau_{c,1}$ and $\tau_{c,2}$ that are defined as:[F4,F5,F7]

$$\tau_{c,1} = -\frac{45\sqrt{3}}{32} \cdot \frac{\hbar}{\mu_B (A_{zz} - A_{xx}) \cdot (g_{zz} - \frac{1}{2}(g_{xx} + g_{yy}))} \cdot \frac{\Delta B_{0,pp}}{B_0} \cdot \left(\sqrt{\frac{h_0}{h_{-1}}} - \sqrt{\frac{h_0}{h_{+1}}} \right) \qquad \text{(F.8)}$$

$$\tau_{c,2} = \frac{9\sqrt{3}}{4\pi} \cdot \frac{\Delta B_{0,pp}}{(A_{zz} - A_{xx})^2} \cdot \left(\sqrt{\frac{h_0}{h_{+1}}} + \sqrt{\frac{h_0}{h_{-1}}} - 2 \right) \qquad , \qquad \text{(F.9)}$$

whereas μ_B is the Bohr magneton, $\hbar$ is the reduced Planck constant, B_0 is the center-field in Tesla, $\Delta B_{0,pp}$ is the peak-to-peak linewidth of the central nitroxide resonance line ($m_I = 0$) given in s^{-1}, and h_0, h_{-1} and h_{+1} are the relative line heights of the three nuclear transitions ($m_I = -1, 0, +1$) in isotropic nitroxide spectra as shown in **Figure F1B.** The result from this analysis is given in **Figure 8.2B** (dark yellow). Error bars were not calculated for τ_c.

F2 | Collective Lysine pK$_a$ Estimation from pH-dependent EPR Experiments on 5-MSL HSA

The significant pH-dependence of the high-field (h_{-1}) and low-field (h_{+1}) peaks in CW EPR spectra from 5-MSL HSA that are also used to calculate rotational correlation times τ_c in **Appendix F1** exhibit an odd maximum feature at about pH 10.4 (see **Figure F2**). Therefore, the results from PROPKA 3.0 calculations[F8–F10] on the fatty acid-free HSA structure (PDB ID: 1BM0)[F11] were tested for lysine pK$_a$ values. Overall, $N_{Lys} = 58$ lysine residues have been considered in the charge calculation, apart from the Lys4 residue. Individual lysine pK$_{a,i}$ values ranged from 6.36 – 11.59 with an average:

$$\text{pK}_{a,Lys} = \frac{1}{N_{Lys}} \sum_{i=1}^{N_{Lys}} \text{pK}_{a,i} \qquad \text{(F.10)}$$

that yields pK$_{a,Lys}$ = 10.28 $\pm$ 0.89. This unexpected correspondence (**Figure F2**) may facilitate the estimation of a collective lysine pK$_a$ value (pK$_{a,Lys}$) from CW EPR spectra of 5-MSL HSA alone.
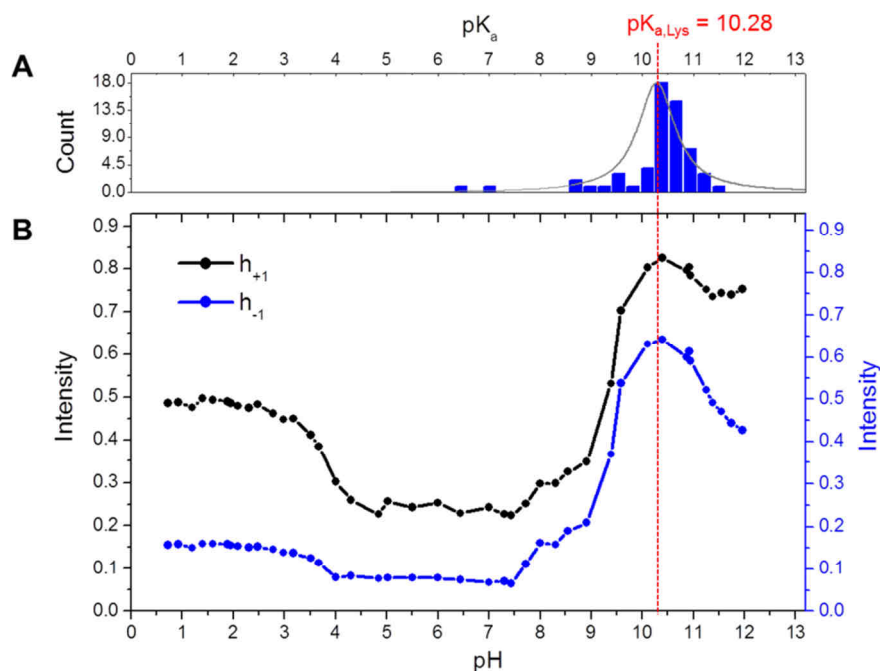
Figure F2 | Correlation of lysine pK$_a$ values and EPR spectral features of 5-MSL HSA. (**A**) Histogram of individual pK$_{a,i}$ values (blue) that were calculated with PROPKA 3.0.[F8–F10] The histogram has been equipped with a Lorentz distribution envelope curve (gray). (**B**) pH-dependent intensities of high-field (h$_{-1}$, blue) and low-field (h$_{+1}$, black) peaks are shown that appear in CW EPR spectra of 5-MSL HSA. The calculated average value pK$_{a,Lys}$ is highlighted as a red dotted line to indicate correspondence with EPR spectroscopic data.

F3 | Exemplary Simulation of 16-DSA Alone and Interacting with HSA

Two spectra were simulated with EasySpin[F12] that contain 16-DSA either in its free form (010 loading), or while interacting with HSA (120 loading, see **Figure F3**). The observed subspectra $F_i(B)$ comprise 16-DSA in micelles (*a*), free in solution (*f*), or bound to albumin (*b$_1$*, *b$_2$*) in the relative fractions ϕ_i.
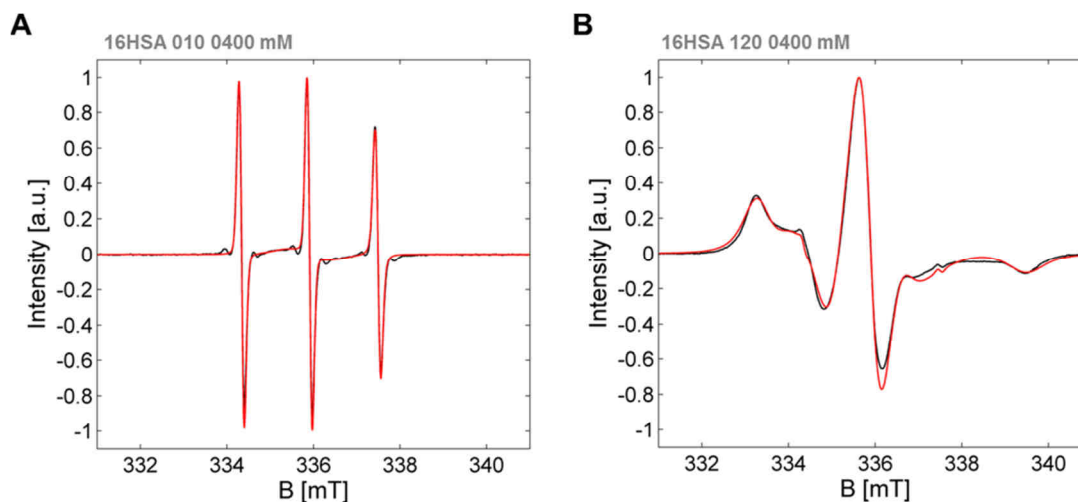
Figure F3 | Exemplary spectral simulations from samples containing 16-DSA. Spectral simulations of (**A**) 0.4 mM 16-DSA-probed DPBS buffer with 20% v/v glycerol at pH 7.4 and (**B**) 16-DSA probed HSA in a 2:1 loading ratio (1 eq = 0.4 mM) in DPBS buffer at pH 7.4 and 20% v/v glycerol. Experimental spectra are shown in black and simulations in red.

A thorough description of a procedure for spectral simulations is given in **Appendix E2**. The obtained simulation parameters are listed in **Table F1**. In order to facilitate a comparison of the simulation parameters with the extracted spectral features $A_{\parallel}$, A_{zz} and $\Delta B_{0,pp}$, all original values $A_{ii,sim}$ are multiplied with the sweep-field correction factor that was determined as $k_{SW} = 0.9923$ for all spin probe experiments, so that here $A_{ii} = A_{ii,sim} \cdot k_{SW}$.

Table F1 | Simulation parameters from 16-DSA alone and 16-DSA-probed HSA

	$F_i(B)$	ϕ_i [%]	g_{xx}	g_{yy}	g_{zz}	$A_{xx}{}^a$ [G]	$A_{yy}{}^a$ [G]	$A_{zz}{}^a$ [G]	a_{iso} [G]	$\tau_{c,i}$ [ns]	β_i [°]
16HSA 010	f	63.421	2.0087	2.0064	2.0025	6.58	5.91	34.48	15.66	0.117	45
	a	36.579	2.0087	2.0064	2.0025	6.58	5.91	34.48	15.66	–	45
16HSA 120	f	0.071	2.0087	2.0064	2.0025	6.58	5.91	34.48	15.66	0.117	45
	b_1	62.081	2.0089	2.0064	2.0025	5.91	5.42	34.34	15.22	14.232	16
	b_2	37.848	2.0089	2.0064	2.0025	5.91	5.42	34.34	15.22	5.837	45

^{a}Values were corrected with $k_{SW} = 0.9923$ as simulations were conducted on experimental spectra.

Exemplary subspectra $F_i(B)$ for graphical representation of the emerging dynamic regimes were calculated according to values given in **Table F1** and are presented in **Figure 8.3D**. 16-DSA in micelles (a) was simulated with an effective Heisenberg spin exchange frequency $J_{AB} = 45$ MHz as it is shown in **Appendix E1**.

F4 | Rationalization and Analyses of I_{abf} curves

All I_{abf} values were calculated according to equation 8.1 and corresponding errors were therefore obtained with:

$$\Delta I_{abf} = \left| \frac{\Delta h_{\perp} + \Delta h_{-1}}{h_0} \right| + \left| \frac{h_{\perp} \Delta h_0}{h_0^2} \right| \qquad . \qquad \text{(F.11)}$$

The different transition zones of 16-DSA-probed HSA in I_{abf} curves were extrapolated by fit curves for a better extraction of decisive pH values. The curve shape reproduction for pH regions from pH 1 – 4 (16-DSA micellation ($j = a$)) and pH 4 – 9 (slight changes in $h_{\perp}$ ($j = b$)) is facilitated best with the use of Boltzmann functions of the kind:

$$I_{abf} = I_{j,max} + \frac{(I_{j,max} - I_{j,min})}{1 + e^{(pH - pH_{j,0})/dpH_j}} \qquad . \qquad \text{(F.12)}$$

This allows for an estimation of individual transition heights $I_j = I_{j,max} - I_{j,min}$, transition midpoints $pH_{j,0}$ and corresponding widths dpH_j. The resulting fit curves are presented in **Figure F4A–D** and the fit parameters can be found in **Table F2**.

Table F2 | Boltzmann fit parameters obtained from I_{abf} curves (16-DSA)

Parameter	16HSA 110		16HSA 120	
j	a	b	a	b
pH fit range	0.98 – 4.39	3.94 – 8.51	0.89 – 4.79	3.99 – 10.27
$I_{j,max}$	0.07422 ± 0.0049	–0.17543 ± 0.01191	0.24243 ± 0.00975	–0.19986 ± 0.0015
$I_{j,min}$	–0.17316 ± 0.00431	–0.07242 ± 0.00548	–0.20042 ± 0.00323	-0.08952 ± 0.000848146
$pH_{j,0}$	3.43628 ± 0.02649	5.60005 ± 0.21366	3.44529 ± 0.02797	6.18825 ± 0.03318
dpH_j	0.18916 ± 0.02135	0.6654 ± 0.19488	0.15777 ± 0.01544	0.5639 ± 0.028
R^2	0.99386	0.97507	0.99323	0.99755

The relative amount of free ligand can be observed in **Figure 8.4D** by monitoring the ratio h_{-1}/h_0. The emergence of the bump feature from pH 4.5 to about pH 8.5 indicates a clear increase in free ligand. The bump can be described by a conventional Gaussian curve shape of the form:

$$\frac{h_{-1}}{h_0} = I_{f,0} + I_f \cdot e^{-\frac{1}{2}\left(\frac{pH - pH_{f,0}}{\sigma_{f,0}}\right)^2}$$

(F.13)

and the fit curves are given in **Figure F4E+F**. Obviously the inflection point $pH_{a,0}$ is at pH 3.45 and the maximum at $pH_{f,0}$ is located around pH 6.2 for both 16-DSA loading ratios.
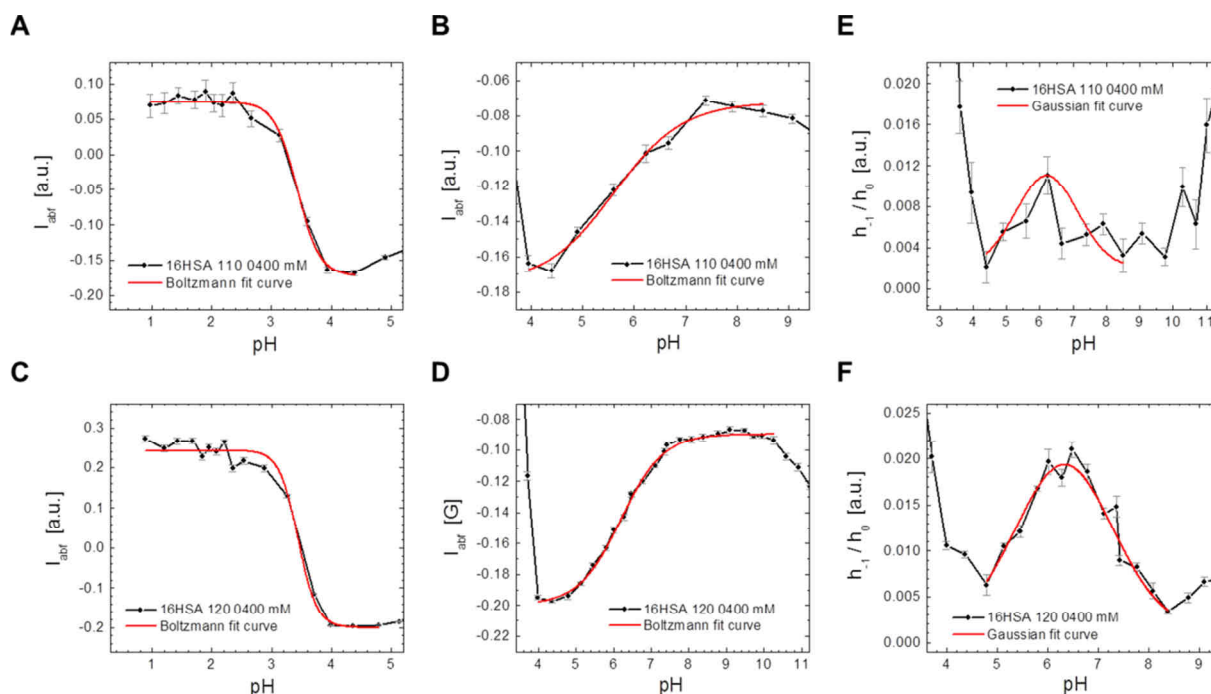
Figure F4 | Fit curves from pH-dependent I_{abf} and h_{-1}/h_0 parameters. Boltzmann fit curves (equation F.12) to I_{abf} for 16-DSA-probed HSA (110 loading ratio) (**A**) in the acidic (pH 1 – 4) and (**B**) in the neutral pH range (pH 4 – 9). Boltzmann fit curves to I_{abf} for 16-DSA-probed HSA (120 loading ratio) (**C**) in the acidic (pH 1 – 4) and (**D**) in the neutral pH range (pH 4 – 9). Gaussian fit curves (equation F.13) to the relative high-field peak heights h_{-1}/h_0 for 16-DSA-probed HSA are given in the range from pH 4.5 – 8.5 for (**E**) 110 and (**F**) 120 loading. Results are shown in **Table F2** and **Table F3**.

Table F3 | Gaussian fit parameters obtained from h_{-1}/h_0 curves (16-DSA)

Parameter	110	120
pH fit range	4.39 – 8.51	4.79 – 8.38
$I_{f,0}$	0.00214	0.00160 ± 0.00123
$pH_{f,0}$	6.20419 ± 0.20889	6.32685 ± 0.0368
$\sigma_{f,0}$	0.92868 ± 0.1548	0.97151 ± 0.09145
I_f	0.00891	0.01775 ± 0.00114
FWHM	2.18688	2.28774
Area	0.02073	0.04322
R^2	0.66013	0.97085

The curve shape for minima in I_{abf} that occur around $pH_a \approx 4$ and $pH_f \approx 11$ is of a more intricate mathematical nature. Here, a rational Nelder model function[F13] is used that facilitates the reproduction of such curves containing asymmetric extrema. The applied function:

$$I_{abf} = \frac{pH + \alpha}{\beta_0 + \beta_1(pH + \alpha) + b_2(pH + \alpha)^2}$$

(F.14)

allows for this circumstance here.

Table F4 | Nelder fit parameters obtained from I_{abf} curves (16-DSA)

Parameter	110		120	
pH fit range	3.14 – 6.67	9.08 – 12.38	3.26 – 6.28	9.96 – 12.24
α	-3.24123 ± 0.03178	-12.07377 ± 0.01134	-3.41752 ± 0.02594	-12.10222 ± 0.01786
β_0	-3.11757 ± 0.45248	1.70672 ± 0.07087	-1.45843 ± 0.16545	1.82273 ± 0.17503
β_1	0.16922 ± 0.7431	-1.92667 ± 0.19557	-1.95748 ± 0.3745	-1.67417 ± 0.80685
β_2	-3.00233 ± 0.28495	3.39413 ± 0.16743	-1.54115 ± 0.1817	4.46325 ± 0.72271
R^2	0.97704	0.99369	0.96297	0.96664

In order to detect these extrema from the curve fits, a general derivation according to the quotient rule gives:

$$\frac{\partial I_{abf}}{\partial pH} = \frac{1}{\beta_0 + \beta_1(pH + \alpha) + \beta_2(pH + \alpha)^2} - \frac{(pH + \alpha) \cdot (2\beta_2(pH + \alpha) + \beta_1}{(\beta_0 + \beta_1(pH + \alpha) + \beta_2(pH + \alpha)^2)^2} = 0$$

(F.15)

Obtaining the zeros of this function is straightforward and reveals that:

$$pH_{min} = -\alpha \pm \sqrt{\frac{\beta_0}{\beta_2}}$$

(F.16)

with the errors:

$$\Delta pH_{min} = \frac{\Delta\beta_0}{2\beta_2\sqrt{\frac{\beta_0}{\beta_2}}} + \frac{\beta_0\Delta\beta_2}{2\beta_2^2\sqrt{\frac{\beta_0}{\beta_2}}} + \Delta\alpha \qquad . \qquad (F.17)$$

Therefore, the β_1 parameter is of obvious inferior importance. It is found that the sign depends on the curve symmetry, so that the acidic minimum is located at $pH_a = -\alpha + (\beta_0/\beta_2)^{-1/2}$ and the basic minimum $pH_f = -\alpha - (\beta_0/\beta_2)^{-1/2}$. The corresponding fit curves are given in **Figure F5**.
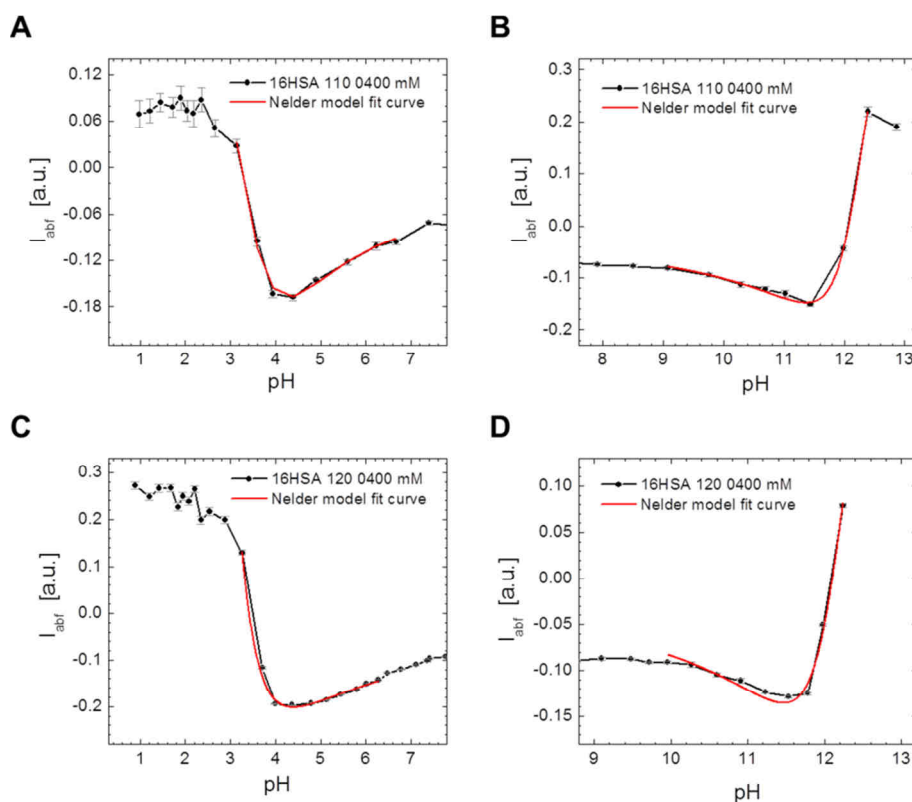
Figure F5 | Nelder fit curves from pH-dependent I_{abf} values. Nelder fit curves (equation F.14) to I_{abf} for 16-DSA-probed HSA (110 loading) (**A**) in the acidic (pH 3 – 6) and (**B**) in the basic pH range (pH 9 – 12). Nelder fit curves to I_{abf} for 16-DSA probed HSA (120 loading) (**C**) in the acidic (pH 3 – 6) and (**D**) in the basic pH range (pH 9 – 12). Results ($R^2 > 0.962$) from the curve regressions are given in **Table F4**.

F5 | Analysis of pH-dependent Apparent Hyperfine Coupling Constants $A_\parallel$

The obtained curves for $A_\parallel$ values (**Figure 8.5B**) in the region around pH 2 were fitted with Gaussian functions:

$$A_\parallel = A_{\parallel,0} + I_{A,MG} \cdot e^{-\frac{1}{2}z^2} \qquad (F.18)$$

with

$$z = (pH - pH_{MG})/\sigma_{MG} \qquad (F.19)$$

for 5-DSA-probed HSA (120 loading) and with an extreme value distribution function for 16-DSA-probed HSA (110 loading) according to Gumbel:[F14]

$$A_{//} = A_{//,0} + I_{A,\text{MG}} \cdot e^{(e^{-z} - z + 1)} \qquad . \qquad \text{(F.20)}$$

Here, $A_{\|,0}$ is the ambient value around the indentation around pH 2.0 and $I_{A,\text{MG}}$ is the fitted indentation depth of a corresponding feature.
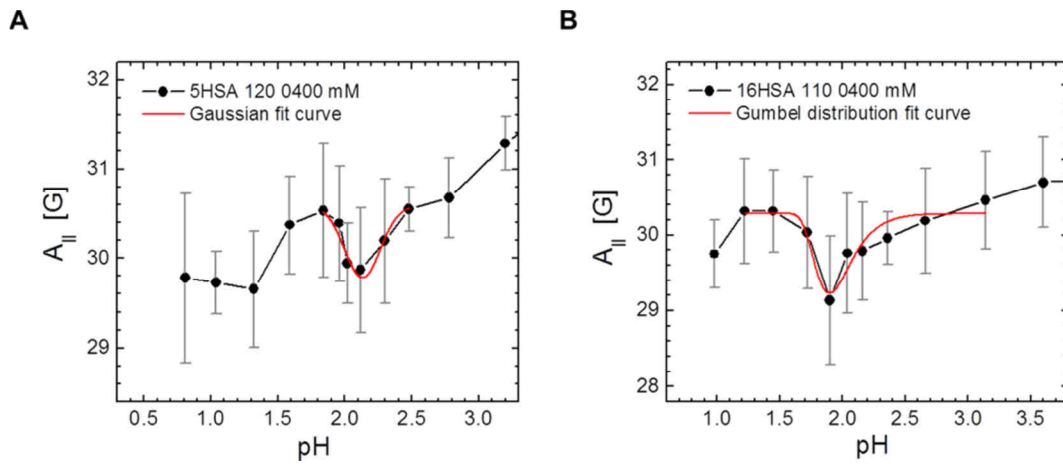
Figure F6 | Fit curves of pH-dependent $A_\|$ values in the range from pH 1 – 3. A Gaussian fit curve was applied to reproduce (**A**) $A_\|$ values from 5-DSA-probed HSA (120 loading) in the acidic range from pH 1.8 – 2.5 and a Gumbel[F14] distribution was used to reproduce (**B**) $A_\|$ values from 16-DSA-probed HSA (110 loading) in the acidic range from pH 1.2 – 3.1. Results are shown in **Table F5**.

Table F5 | Gaussian Fit parameters obtained from $A_{//}$ curves

Parameter	5-DSA 120	16-DSA 110
Fit range	1.84 – 2.48	1.22 – 3.14
Model	Gauss (eq. F.18)	Gumbel (eq. F.19)
$A_{//,0}$	30.58344 ± 0.08901	30.28436 ± 0.08572
pH_{MG}	2.13381 ± 0.02565	1.89827 ± 0.02927
σ_{MG}	0.13282 ± 0.03678	0.14185 ± 0.02845
$I_{A,\text{MG}}$	−0.80224 ± 0.015556	−1.05386 ± 0.18346
FWHM	0.31278	–
R^2	0.87299	0.81192

F6 | Determination of Low-temperature A_{zz} Values at $T = 150$ K from Spin Probed HSA

The g_{xx} and A_{zz} tensor values are the most sensitive quantities when changes in polarity are to be detected.[F15,F16] In a straightforward procedure, outer extrema separations of spectra at $T = 150$ K were used as it was already shown for 5-MSL HSA at pH 7.4 (see **Appendix F1**). $A_{zz,k}$ from spin probes k is here observed as a function of pH and the corresponding individual experimental findings are summarized in **Figure F7** and **Table F6**. Individual values of $A_{zz,k}$ and their uncertainties have been obtained by using equation F.2 and F.3.
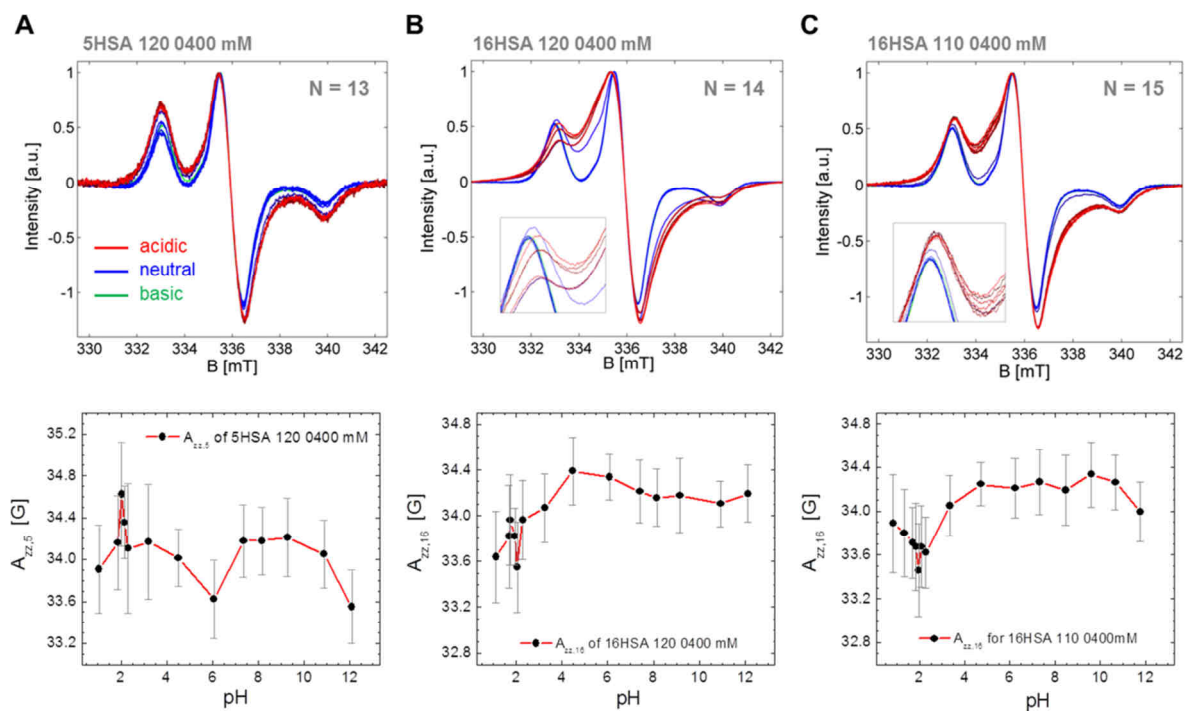
Figure F7 | A_{zz} parameters from low-temperature CW EPR spectra at T = 150 K. Here, color-coded experimental spectra are presented in terms of the pH region of interest. The acidic range is shown in red (pH < 4), the neutral range in blue (4 < pH < 11) and the basic range is shown in green (pH > 11). CW EPR spectra (top) are given together with the extracted $A_{zz,k}$ values (bottom) for (**A**) 5-DSA-probed HSA (120 loading, N = 13), (**B**) 16-DSA-probed HSA (120 loading, N = 14) and (**C**) with 110 loading (N = 15). Inset graphs are given for 16-DSA-probed HSA samples and highlight regions where strong spectral changes appear.

Table F6 | A_{zz} values from spin probed HSA as a function of pH[a]

	5-DSA 120		16-DSA 120		16-DSA 110		
pH	$A_{zz,5}$ **[G]**	**pH**	$A_{zz,16}$ **[G]**	**pH**	$A_{zz,16}$ **[G]**	**pH[b]**	δA_{zz}**[c] [G]**
1.04	33.91 ± 0.42	1.13	33.64 ± 0.40	0.83	33.89 ± 0.45	1.09 ± 0.06	0.27 ± 0.41
1.87	34.16 ± 0.45	1.71	33.82 ± 0.45	1.33	33.80 ± 0.40	1.79 ± 0.11	0.34 ± 0.45
2.03	34.62 ± 0.50	1.75	33.96 ± 0.40	1.70	33.71 ± 0.32	2.05 ± 0.02	1.07 ± 0.45
2.16	34.35 ± 0.35	1.96	33.82 ± 0.25	1.85	33.68 ± 0.40	2.31 ± 0.01	0.14 ± 0.48
2.31	34.10 ± 0.62	2.06	33.55 ± 0.40	1.97	33.46 ± 0.42	3.23 ± 0.04	0.10 ± 0.42
3.20	34.17 ± 0.55	2.30	33.96 ± 0.35	2.08	33.68 ± 0.37	4.50 ± 0.02	–0.38 ± 0.29
4.51	34.02 ± 0.27	3.26	34.07 ± 0.30	2.28	33.62 ± 0.32	6.08 ± 0.01	–0.71 ± 0.29
6.07	33.62 ± 0.37	4.48	34.39 ± 0.30	3.35	34.05 ± 0.27	7.39 ± 0.04	–0.04 ± 0.31
7.36	34.18 ± 0.35	6.08	34.34 ± 0.20	4.72	34.25 ± 0.20	8.16 ± 0.01	0.02 ± 0.29
8.17	34.18 ± 0.32	7.41	34.21 ± 0.27	6.24	34.21 ± 0.27	9.22 ± 0.09	0.04 ± 0.35
9.28	34.21 ± 0.37	8.15	34.16 ± 0.25	7.32	34.27 ± 0.30	10.90 ± 0.04	–0.05 ± 0.26
10.87	34.05 ± 0.32	9.15	34.18 ± 0.32	8.48	34.19 ± 0.32	12.11 ± 0.02	–0.64 ± 0.30
12.09	33.55 ± 0.35	10.93	34.10 ± 0.20	9.61	34.34 ± 0.30		
–	–	12.12	34.19 ± 0.25	10.68	34.27 ± 0.25		
–	–	–	–	11.78	34.00 ± 0.27		
$A_{zz,k,\text{pH}}$**[d] [G]**	**34.09 ± 0.28**		**34.03 ± 0.25**		**33.96 ± 0.29**		

[a]Values are taken from spectra in **Figure F7**. [b]5-DSA and 16-DSA experiments with 120 loading and approximate overlapping pH values are summarized by an average pH value together with its mean deviation. [c]δA_{zz} values are given together with an averaged error from $A_{zz,5}$ and $A_{zz,16}$ (see equation F.21 and **Figure 8.5C**). [d]$A_{zz,k,\text{pH}}$ = averaged $A_{zz,k}$ values across all pH are given with their standard deviation.

Differences in between $A_{zz,5}$ and $A_{zz,16}$ in the 120 loading status are detected by the differences at similar or identical pH values with:

$$\delta A_{zz} = A_{zz,5} - A_{zz,16} \qquad\qquad (F.21)$$

and are listed on the right hand side of **Table F6**. Additionally, a pH-independent average value is given by $A_{zz,k,\mathrm{pH}}$ in the bottom line.

F7 | Analysis of $\Delta B_{0,\mathrm{pp}}$ Curves

The obtained curve sections for $\Delta B_{0,\mathrm{pp}}$ in **Figure 8.6B** were fitted with Gaussian functions:

$$\Delta B_{0,\mathrm{pp}} = \Delta B_{0,\mathrm{pp,min},j} + \Delta B_{0,\mathrm{pp,max},j} \cdot e^{-\frac{1}{2}\left(\frac{\mathrm{pH}-\mathrm{pH}_j}{\sigma_j}\right)^2} \qquad\qquad (F.22)$$

in the range from about pH 0.9 – 3.3 (j = MG) for all spin probes and additionally from pH 3.9 – 8.5 for 5-DSA (j = B,0). The obtained fit parameters are given in **Table F7**. The resulting Gauss fit curves are shown in **Figure F8A–D**.

Table F7 | Gaussian fit parameters obtained from $\Delta B_{0,\mathrm{pp}}$ curves

Parameter	5-DSA 120		16-DSA 120	16-DSA 110
j	MG	B,0	MG	MG
pH fit range	1.76 – 2.78	3.87 – 8.52	0.89 – 3.26	1.22 – 2.66
$\Delta B_{0,\mathrm{pp,min},j}$	–	7.829	–	4.22214 ± 0.00673
pHj	2.16438 ± 0.02421	6.24516 ± 0.07607	1.86558 ± 0.07226	2.00736 ± 0.00993
σ_j	0.36869 ± 0.03152	0.95372 ± 0.08149	0.94832 ± 0.49595	0.12667 ± 0.01224
$\Delta B_{0,\mathrm{pp,max},j}$	–	-0.75519 ± 0.05393	–	-0.19596 ± 0.01319
FWHM	0.86819	2.24585	2.23313	0.2983
R^2	0.89973	0.88973	0.8198	0.9714

The transition region from about pH 3 – 9 for 16-DSA was reproduced best with the use of Boltzmann functions of the kind:

$$\Delta B_{0,\mathrm{pp}} = \Delta B_{0,\mathrm{pp,max}} + \frac{(\Delta B_{0,\mathrm{pp,min}} - \Delta B_{0,\mathrm{pp,max}})}{1 + e^{(\mathrm{pH}-\mathrm{pH}_{B,0})/\mathrm{dpH}_{B,0}}} \qquad . \qquad (F.23)$$

This allows for an estimation of the transition height $I_{B,j} = \Delta B_{0,\mathrm{pp,max}} - \Delta B_{0,\mathrm{pp,min}}$, the transition midpoint $\mathrm{pH}_{B,0}$ and its corresponding width $\mathrm{dpH}_{B,0}$. The fit curves are presented in **Figure F8E–F** with the respective parameters in **Table F8**.
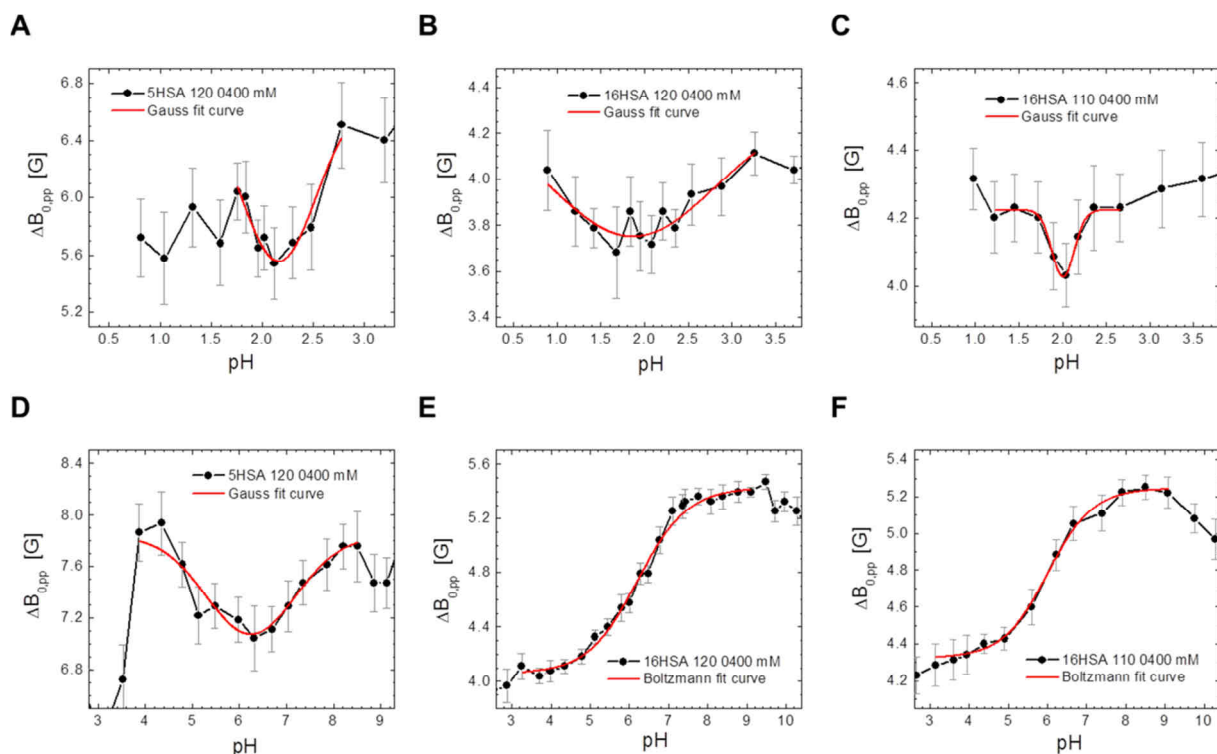
Figure F8 | Fit curves from $\Delta B_{0,pp}$. Gaussian fit curves were applied to reproduce $\Delta B_{0,pp}$ values from (**A**) 5-DSA-probed HSA (120 loading) in the acidic range from pH 1.8 – 2.8, (**B**) 16-DSA-probed HSA (120 loading) in the acidic range from pH 0.9 – 3.3, (**C**) 16-DSA-probed HSA (110 loading) in the acidic range from pH 1.2 – 2.7 and (**D**) 5-DSA-probed HSA (120 loading) in the neutral range from pH 3.9 – 8.5. All corresponding parameters are given in **Table F7**. Boltzmann fit curves were applied to reproduce $\Delta B_{0,pp}$ values from (**E**) 16-DSA-probed HSA (120 loading) in the neutral range from pH 3.3 – 9.1 and (**F**) 16-DSA-probed HSA (110 loading) in the neutral range from pH 3.1 – 9.1 with parameters given in **Table F8**.

Table F8 | Boltzmann fit parameters obtained from $\Delta B_{0,pp}$ curves (16-DSA)

Parameter	16HSA 120	16HSA 110
Fit range	3.26 – 9.10	3.14 – 9.08
$\Delta B_{0,pp,min}$	4.05486 ± 0.03264	4.32322 ± 0.02539
$\Delta B_{0,pp,max}$	5.42791 ± 0.02457	5.24575 ± 0.01961
$pH_{B,0}$	6.20903 ± 0.06045	6.00845 ± 0.07364
$dpH_{B,0}$	0.634 ± 0.05898	0.57317 ± 0.0698
R^2	0.99289	0.99445

F8 | Further Information about Order Parameters S and Wobbling Angles γ

The setup of an order parameter S (see equation 8.3, **Figure 8.7**) for HSA requires knowledge about the "crystalline" hyperfine coupling tensor values (A_{ii}) that can be extracted from spectral simulations of the bound ligand subspectra (b_1 and b_2, see **Table F1**). It is here insufficient to only use the low-temperature A_{zz} values given in **Table F6**. However, experimental ($A_{zz,16,exp}$ = 34.21 G, pH 7.40) values compare well to the simulated ($A_{zz,16,sim}$ = 34.34 G, pH 7.41) ones of bound fatty acids at physiological pH. With these simulations the denominator expression ($A_{zz} - A_{xx}$) = 28.43 G in equation 8.3 becomes accessible. For simplicity it is kept constant at all pH values as the relative changes in the

expression $(A_{zz} - A_{xx})$ for bound fatty acids with pH can be considered as small (well below 6 %). The errors for pH-dependent order parameters S were determined by propagation of uncertainty:

$$\Delta S = \left|\frac{\partial S}{\partial x}\right| \Delta x = \left(\frac{a_{\text{iso},b}}{a_{\text{iso},S}} \cdot \frac{1}{(A_{zz} - A_{xx})}\right) \cdot (\Delta A_\parallel + \Delta A_\perp) + \left(\frac{a_{\text{iso},b}}{a_{\text{iso},S}} \cdot \frac{(A_\parallel - A_\perp)}{(A_{zz} - A_{xx})^2}\right) \cdot (\Delta A_{zz} + \Delta A_{xx})$$
$$+ \left(\frac{1}{a_{\text{iso},S}} \frac{(A_\parallel - A_\perp)}{(A_{zz} - A_{xx})}\right) \cdot \left(\Delta a_{\text{iso},b} + \frac{a_{\text{iso},b}}{a_{\text{iso},S}} \cdot \Delta a_{\text{iso},S}\right)$$

$$(F.24)$$

with $\Delta A_{ii} = \Delta a_{\text{iso},b} = 0.1$ G, $\Delta a_{\text{iso},b} = 0.14 - 0.53$ G, $\Delta A_\parallel = 0.12 - 0.94$ G and $\Delta A_\perp = 0.12 - 0.57$ G. The derivation of equation 8.4b is facilitated straightforward from equation 8.4a. Thus, substitution of $\cos\gamma$ with x leads to the quadratic expression:

$$2S = \cos\gamma + \cos^2\gamma = x + x^2$$

$$(F.25)$$

that yields:

$$x_1 = \frac{\sqrt{8S+1} - 1}{2} = \cos\gamma_1 = \cos\gamma$$

$$(F.26)$$

and therefore:

$$\gamma = \arccos\left(\frac{\sqrt{8S+1} - 1}{2}\right)$$

$$(F.27)$$

From equation F.27 the error $\Delta\gamma$ of the wobbling angle is obtained as:

$$\Delta\gamma = \left|\frac{\partial\gamma}{\partial S}\right| \Delta S = \left| -\frac{2}{\sqrt{8S+1} \cdot \sqrt{1 - \left(\frac{\sqrt{8S+1}-1}{2}\right)^2}} \right| \cdot \Delta S$$

$$(F.28)$$

Again, the region from pH 1.2 – 3.6 can be fitted best with appropriate Gaussian functions, both for the order parameter (**Figure F9**):

$$S = S_0 + I_{S,\text{MG}} \cdot e^{-\frac{1}{2}z^2}$$

$$(F.29)$$

as well as for the wobbling angle:

$$\gamma = \gamma_0 + I_{\gamma,\text{MG}} \cdot e^{-\frac{1}{2}z^2}$$

$$(F.30)$$
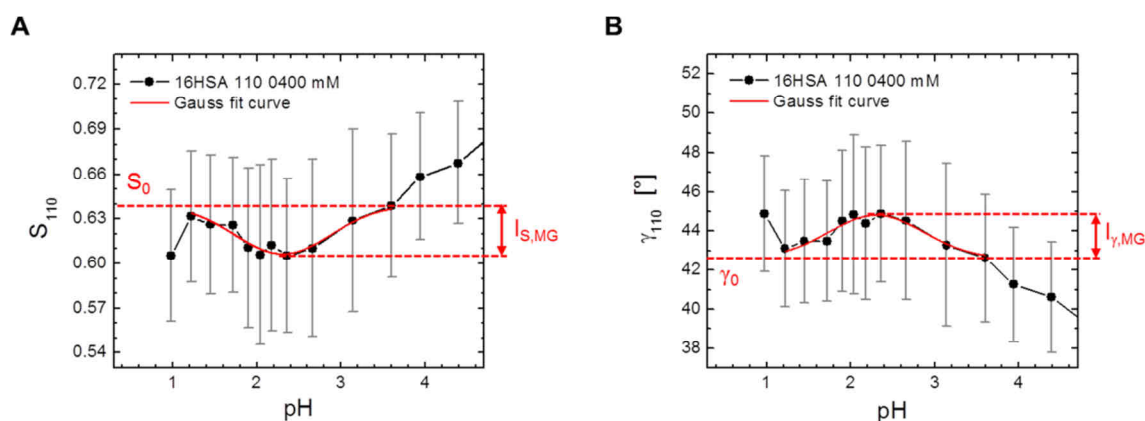
Figure F9 | Fit curves from pH-dependent order parameters *S* and wobbling angles *γ*. Gaussian fit curves were applied to the pH region from 1.2 – 3.6 of 16-DSA-probed HSA (110 loading) in order to reproduce values from (**A**) order parameter *S* and (**B**) wobbling angle *γ* best. Here, the indentation depths $I_{S,MG}$ and $I_{\gamma,MG}$ are highlighted in red.

The parameter *z* corresponds to the expression in equation F.19 and the corresponding fit parameters are given in **Table F9**.

Table F9 | Gaussian fit parameters derived from order parameter (*S*) and wobbling angle (*γ*) curves

Parameter	16-DSA 110	Parameter	16-DSA 110
Fit range	1.22 – 3.60	Fit range	1.22 – 3.60
S_0	0.63898 ± 0.00655	γ_0	42.59609 ± 0.45239
pH_{MG}	2.30774 ± 0.0681	pH_{MG}	2.30744 ± 0.068
σ_{MG}	0.56642 ± 0.15068	σ_{MG}	0.56902 ± 0.15239
$I_{S,MG}$	-0.03251 ± 0.0062	$I_{\gamma,MG}$	2.20901 ± 0.42722
FWHM	1.33382	FWHM	1.33993
R^2	0.86851	R^2	0.86873

F9 | Shift of $P_{max}(r)$ in DEER Data from pH Denaturation of HSA Spin Probed with 16-DSA

The assessment of background dimensionalities in DEER spectroscopy is a delicate subject and is here only given as a qualitative estimate in **Figure F10**. However, the pH-dependent peak shift of $P_{max}(r)$ is clearly detectable in **Figure 8.8E+F** and is depicted in **Figure 8.9A**. The corresponding curve shape was reconstructed by a Boltzmann-type function in Origin with a sigmoidal fit curve that yields values presented in **Table F10** for equation 8.5 in the main text.

Table F10 | Fit parameters from equation 8.5 in the main text

Parameter	16HSA 120
r_{min}	3.45496 ± 0.00751
r_{max}	3.96435 ± 0.02411
$pH_{P,0}$	6.16128 ± 0.12999
$dpH_{P,0}$	1.15562 ± 0.10845
R^2	0.99715
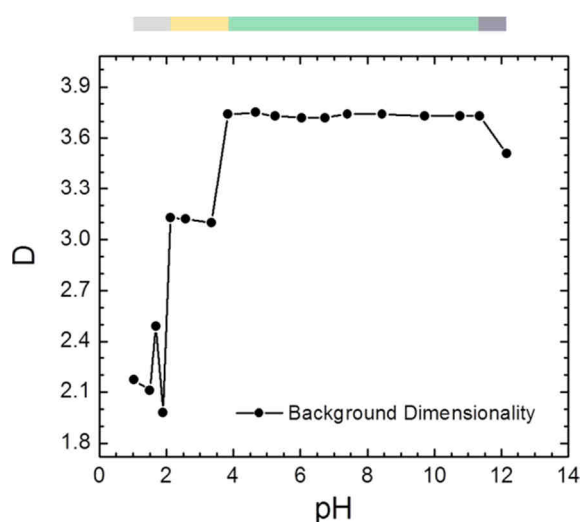
Figure F10 | DEER background of 16-DSA-probed HSA as a function of pH (120 loading). Background dimensionalities D from DEER time traces of 0.17 mM HSA in **Figure 8.8** are shown as a function of pH. The corresponding extended (E), fast migrating (F), compact (C) and aged (A) conformers are given in the phase space bar (top lane).

F10 | Functional Phase Space of HSA as Obtained from EPR Spectroscopy and DLS

The construction of **Figure 8.11** was facilitated by a combined set of pH ranges that were obtained from different parameters from CW EPR (5-MSL HSA, 5-DSA and 16-DSA-probed HSA), DEER (16-DSA) and DLS experiments that are summarized in **Table F11**.

Table F11 | Functional phase onsets of HSA from pH-dependent EPR and DLS experiments[a]

Method	Reporter	Quantity	MG	F	pH$_{a,0}$	C or N	pH$_a$	pI	S_{max}	B	pH$_{opt}$	A	pH$_f$
CW EPR	5-MSL	$A_{//}$	–	2.78	–	3.67	–	–	–	–	–	> 10.87	–
		τ_c	–	2.78	–	4.01	–	–	–	7.44	9.58	(> 9.58)	–
	5-DSA 120	$A_{//}$	2.13	2.78	–	3.87	–	–	–	7.86	9.84	(> 9.84)	–
		A_{zz}	2.03	–	–	–	–	–	–	–	–	–	–
		$\Delta B_{0,pp}$	2.16	2.78	–	3.87	–	6.25	–	8.21	9.43	> 11.19	–
	16-DSA 120	$A_{//}$	–	3.26	–	4.79	–	–	–	–	–	> 11.23	–
		A_{zz}	2.06	–	–	–	–	–	–	–	–	–	–
		$\Delta B_{0,pp}$	1.87	3.26	–	–	–	6.21	–	(7.11)	(9.48)	(> 9.48)	–
		I_{abf}	–	–	3.45	–	4.39	6.19	–	–	–	–	11.46
		h_{-1}/h_0	–	–	–	–	–	6.33	–	–	–	–	–
		S/γ	–	–	–	–	–	–	7.76	–	–	–	–
	16-DSA 110	$A_{//}$	1.90	2.66	–	3.60	–	–	–	–	–	> 11.02	–
		A_{zz}	1.97	–	–	–	–	–	–	–	–	–	–
		$\Delta B_{0,pp}$	2.01	3.14	–	–	–	6.01	–	(6.67)	(9.76)	> 11.02	–
		I_{abf}	–	–	3.44	–	4.26	5.60	–	–	–	–	11.36
		h_{-1}/h_0	–	–	–	–	–	6.20	–	–	–	–	–
		S/γ	2.31	–	–	–	–	–	7.40	–	–	–	–
DEER	16-DSA 120	Δ	–	2.57	–	3.83	–	–	–	–	–	> 11.35	–
		D	–	2.12	–	3.83	–	–	–	–	–	≥ 11.35	–
		r	–	–	–	3.83	–	6.16	–	–	–	≥ 11.35	–
DLS	–	R_H	–	3.53	–	4.29	–	–	–	–	–	≥ 11.70	–
		(A.M.)	**2.05**	**2.88**	**3.45**	**3.96**	**4.33**	**6.12**	**7.58**	**7.84**	**9.62**	**11.23**	**11.41**
		(S.D.)	0.14	0.39	0.01	0.35	0.09	0.23	0.21	0.39	0.21	0.25	0.07

[a]Values in parentheses are either experimental singularities or were not used for calculations of an arithmetic mean (A.M.) or a standard deviation (S.D.). Values from PROPKA calculations were not considered in this list.

An averaged value was determined across all experiments that contain reasonable peculiarities (values without parentheses). The E form is assumed to occur at pH values below the onset of the F form ($\leq$ pH 2.9) and comprises the emergence of the molten globule (MG) state. Therefore an E form is not explicitly mentioned. The compact form (C) reaches from the onset of the N form to the onset of the A form and can be subdivided in three compartments, the N_1, B and N_2 form.

F11 | References

[F1]   W. L. Hubbell, H. M. McConnell, *J Am Chem Soc* **1971**, *93*, 314–326.
[F2]   E. Meirovitch, J. H. Freed, *J Phys Chem* **1984**, *88*, 4995–5004.
[F3]   H. J. Steinhoff, K. Lieutenant, J. Schlitter, *Z Naturforsch, C: Biosci* **1989**, *44*, 280–288.
[F4]   T. J. Stone, T. Buckman, P. L. Nordio, H. M. McConnell, *Proc Natl Acad Sci USA* **1965**, *54*, 1010–1017.
[F5]   A. S. Waggoner, O. H. Griffith, C. R. Christensen, *Proc Natl Acad Sci USA* **1967**, *57*, 1198–1205.
[F6]   P. Marzola, C. Pinzino, C. A. Veracini, *Langmuir* **1991**, *7*, 238–242.
[F7]   I. Bulla, P. Törmälä, J. J. Lindberg, *Acta Chem Scand Ser A* **1975**, *29*, 89–92.
[F8]   H. Li, A. D. Robertson, J. H. Jensen, *Proteins Struct Funct Bioinf* **2005**, *61*, 704–721.
[F9]   D. C. Bas, D. M. Rogers, J. H. Jensen, *Proteins Struct Funct Bioinf* **2008**, *73*, 765–783.
[F10]   M. H. M. Olsson, C. R. Sondergaard, M. Rostkowski, J. H. Jensen, *J Chem Theory Comput* **2011**, *7*, 525–537.
[F11]   S. Sugio, A. Kashima, S. Mochizuki, M. Noda, K. Kobayashi, *Protein Eng* **1999**, *12*, 439–446.
[F12]   S. Stoll, A. Schweiger, *J Magn Reson* **2006**, *178*, 42–55.
[F13]   J. A. Nelder, *Biometrics* **1966**, *22*, 128–141.
[F14]   E. J. Gumbel, *J Am Stat Assoc* **1961**, *56*, 335–349.
[F15]   H. J. Steinhoff, A. Savitsky, C. Wegener, M. Pfeiffer, M. Plato, K. Möbius, *Biochim Biophys Acta, Bioenerg* **2000**, *1457*, 253–262.
[F16]   K. Möbius, A. Savitsky, C. Wegener, M. Plato, M. Fuchs, A. Schnegg, A. A. Dubinskii, Y. A. Grishin, I. A. Grigorev, M. Kühn, D. Duche, H. Zimmermann, H. J. Steinhoff, *Magn Reson Chem* **2005**, *43*, S4–S19.

Appendix G | Fatty Acid Triangulation in Albumins Using a Surveillance Benchmark Spin

G1 | Spin Labeling of Albumin

The general spin labeling procedure of albumin is an established method[G1–G8] and from a combination of some of these different strategies a procedure has been conceived that is described in the following. This spin labeling protocol can be employed for albumin at unspecific lysine and cysteine-specific labeling conditions employing the 5-MSL spin label (see **Chapter 8.2.2**),[G9] as well as for exclusively cysteine-specific (Cys34) conditions using MTSSL.[G10] Here, an exemplary labeling procedure for albumin is described by exclusively using MTSSL.

The protein stock solution is prepared by dissolving 120 mg of lyophilized albumin powder in 906 µl 0.137 M DPBS buffer pH 7.4 in order to obtain a nominal concentration of 2 mM. This protein stock solution should be subject to an Ellman's test (see **Appendix G2**) for quantitative determination of free sulfhydryl (-SH) content of each albumin (ϕ_{SH}). Additionally, 2.5 mg of MTSSL (Enzo Life Sciences) are dissolved in 94.6 µl ethanol yielding a final stock concentration of 100 mM. Both preparations are stirred until clear yellowish solutions are observable. Finally, 7.12 ml of 0.137 M DPBS buffer pH 7.4, 0.80 ml of the 2 mM albumin stock solution and 0.08 ml of 100 mM MTSSL in ethanol are arranged to a total of 8.00 ml incubation solution, exhibiting a 5-fold molar excess of MTSSL at pH 7.3 ± 0.1. The final ethanol concentration of 1% actually stabilizes the native state of albumin,[G11] while it might partially occupy binding pockets.[G12]
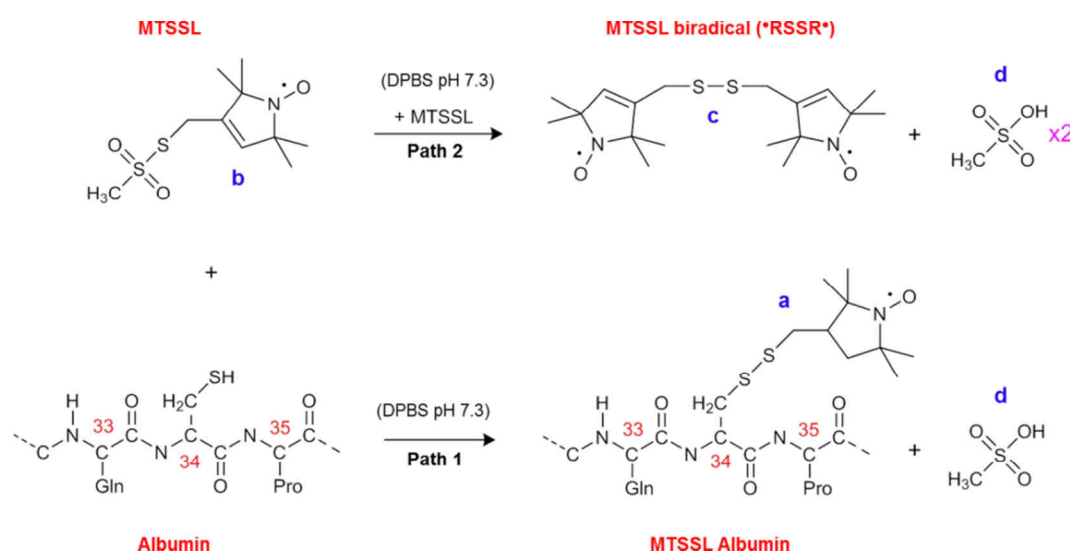
Figure G1 | Cys34-specific spin labeling of albumin with MTSSL. In path 1 the desired reaction[G13] is described that leads here to the formation of MTSSL albumin (a). In path 2 a side reaction is shown in the approximate scheme of Khramtsov *et al.,*[G14] leading to the formation of a MTSSL biradical (•RSSR•) (c) and two equivalents of the cleavage product methanesulfonic acid (d, here given as the protonated (–OH form at pH 7.3). The neighboring amino acids at position 33 (Gln) and 35 (Pro) are conserved in HSA and BSA.[G15]

The incubation solution is continuously but gently stirred for 16 – 24 hours at room temperature (PMR-30 Mini Rocker-Shaker, Grant Instruments Ltd.) under light exclusion. During this step MTSSL is covalently attached to the fraction of reduced Cys34 moieties (R-SH) of albumin according to the scheme shown in **Figure G1** (path 1, a). The typical addition of DTT to the incubation solution to increase accessibility of Cys34 is discouraged here because the functional and structural integrity of albumin already slightly changes at one DTT equivalent as observed with 16-DSA (**Figure G2A**). At 100 DTT equivalents, strong decreases in affinity to 16-DSA are observed and a macroscopic flocculation of the protein can be seen in the reaction tube. However, there is also a certain propensity of MTSSL (b) to form biradical dimers (path 2, see **Figure G1**, c) during DTT-free incubation, as it was also shown in Bleicken *et al.*[G16]
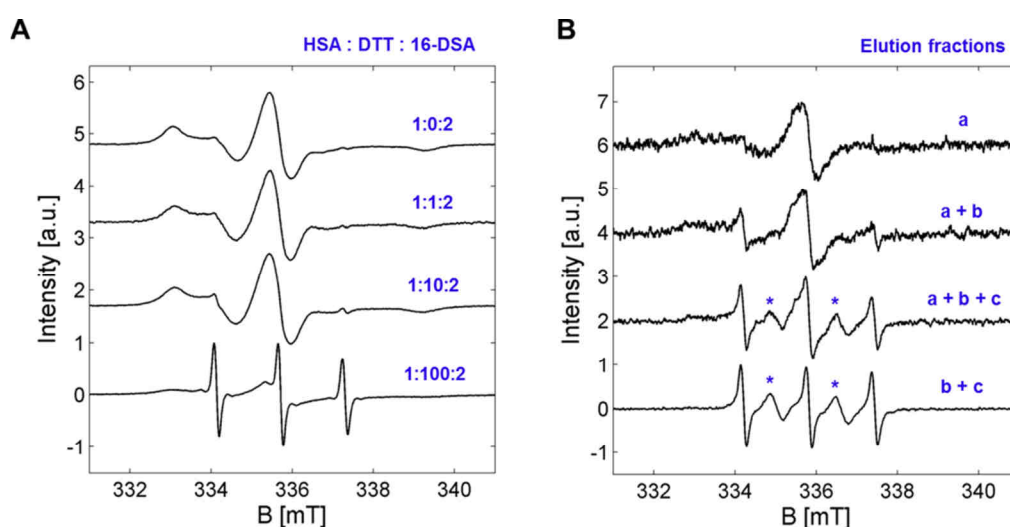
Figure G2 | Influence of DTT and observable elution fractions during protein purification. The effect that DTT exerts on albumin was tested on 16-DSA-probed HSA (loading ratio: 120) solutions in equivalents of 0.16 mM at pH 7.4. (**A**) CW EPR spectra of the tested ratios ranged from 1 to 100 equivalents DTT. (**B**) Elution fractions of an incubation solution containing albumin and MTSSL showing pure MTSSL albumin (a), MTSSL albumin with some unreacted MTSSL (a + b), MTSSL albumin with unreacted MTSSL and MTSSL biradicals (a + b + c) and a mixture of unreacted MTSSL and MTSSL biradicals (b + c) that exhibit characteristic exchange peaks highlighted with an asterisk (*).

The separation of spin-labeled albumin from unreacted label is facilitated via gravity flow size exclusion chromatography utilizing PD-10 columns (GE Healthcare) that contain Sephadex G-25 resins. In a first step the PD-10 column is washed with 20 – 30 ml DPBS buffer pH 7.4 for removing the 0.15% Kathon biocide in the storage solution. 2 ml of the incubation solution and 0.5 ml DPBS buffer are allowed to enter the resin until it is completely absorbed (V_0 = 2.5 ml). The next step is crucial for the separation as the flow-through has to be collected.

Upon filling 3.5 ml of DPBS buffer on the column the initial flow-through will contain the spin-labeled albumin. Thus, individual drops are carefully collected in test tubes (1 drop ~ 40 µl) and fraction tubes (9 drops ~ 360 µl) in an alternating fashion. When the whole solution has passed the column and all fractions are available, the test tubes are each equipped with 40 µl Bradford reagent (see also **Appendix C5**)[G17] indicating where protein is most abundant. The fractions belonging to the

bluish stained test tubes are subject to a further refinement procedure of this purification process that is performed by CW EPR spectroscopy. The resulting CW EPR spectra contain initial information whether the labeling procedure was successful.

In **Figure G2B**, a typical EPR spectroscopic view on the purification process can be observed. Several fractions may contain pure MTSSL albumin (a) that can be pooled and collected without hesitation. However, at a certain point of purification, free unreacted MTSSL (b) and MTSSL biradical (c) is admixed to the elution fractions. The two additional peaks (*) are due to pairwise spin exchange between overlapping orbitals of free radical subunits.[G18] Whereas fractions with a combination of free and biradical MTSSL can be directly discarded (b + c), fractions that still exhibit immobilized, or bound MTSSL characteristics in their EPR spectra (a + b and a + b + c) are collected separately and are subject to a second separation procedure to increase the yield of this protocol. This procedure is repeated four times for the complete incubation solution (4 × 2 ml) and the final pooled MTSSL albumin-containing solution is concentrated via spin columns (Vivaspin® 2 and Vivaspin® 4, 10.000 MWCO, Sartorius) in a benchtop centrifuge (Centrifuge 5810 R, Eppendorf AG) to a final volume of about 0.3 – 0.5 ml.

The protein content of this final solution is finally tested with a BCA assay (**Appendix C5**)[G19] and it was found that this procedure attains a yield of about $\phi_{\text{prep}} = 50 - 60$ % albumin (in other words: $\phi_{\text{MTSSL XSA}} = \phi_{\text{SH}} \cdot \phi_{\text{prep}} = 15 - 33\%$, see **Table 9.1**) compared to the initial amount of applied protein in the incubation solution.

G2 | Quantification of Accessible Thiol Groups in Albumin – Ellman's Test

The amount of accessible thiol groups (Cys34) in albumin during a cysteine-specific spin labeling procedure can be determined with DTNB (5,5'-dithiobis-(2-nitrobenzoic acid)), a reagent that has been devised by G. L. Ellman in 1958.[G20] In principle, this reagent may be employed for various purposes as the determination of glutathione or thiol content in blood or more generally in proteins. The following protocol is based on a generalized standard procedure[G21] that has been modified for own purposes regarding available sample quantities and concentrations.

The functionality of Ellman's reagent is based on the thiol-triggered cleavage of its disulfide bond. During this reaction, a stochiometric equivalent of exactly one TNB^{2-} (**Figure G3**) is generated that exhibits strong light absorbance at $\lambda_{\text{Ellman}} = 412$ nm and therefore constitutes a quantitative measure for thiol content[G22] of a test solution at pH > 7.3.[G23] Although this procedure should provide straight-forward results it is worth mentioning that albumins exhibit a heterogenous nature regarding the extent of thiol content,[G24] depending on various physiological conditions.[G25] So, each albumin preparation has to be assigned to a fresh thiol content determination with an Ellman's test as it is described in the following.
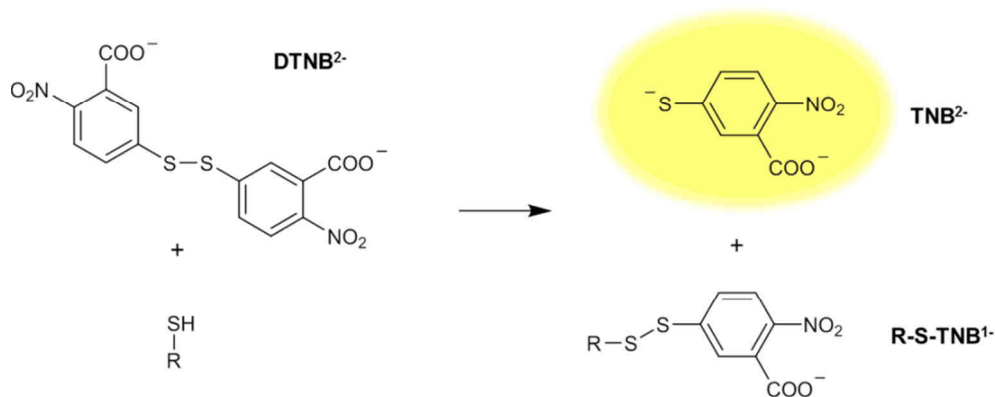
Figure G3 | Functionality of Ellman's reagent. The reaction of a thiol (here: R = albumin, R–SH) with Ellman's reagent (DTNB^{2-}) leads to the formation of the products R-S-TNB^{1-} and the yellow colored TNB^{2-}.

The 0.1 M phosphate reaction buffer pH 8.0 was prepared by dissolving 30.54 g Na$_2$HPO$_4$ (disodium hydrogen phosphate, Sigma-Aldrich) in 215.2 ml ultrapure water (MilliQ) yielding a clear 1 M phosphate solution after 2 hours of continuous stirring at 50°C. Additionally, 1.208 g EDTA Na$_2$·H$_2$O (Ethylenediaminetetraacetic acid disodium salt dihydrate, Sigma-Aldrich) were dissolved in 32.5 ml ultrapure water (MilliQ) for a 0.1 M EDTA stock solution. In a next step, 50 ml of the 1 M phosphate and 5 ml of 0.1 M EDTA stock solutions were filled to a preliminary volume of 400 ml at pH 8.49. Subsequently, a titration was conducted using 1 M HCl (Fisher Scientific) to a desired alkaline value of pH 8.01. The total volume of 500 ml was again adjusted with ultrapure water yielding a 0.1 M phosphate buffer with 1 mM EDTA at pH 8.00. This buffer was filtered with a syringe (BRAUN) and a hydrophilic sterile filter (0.45 µM Millex-LCR PTFE membrane, Merck Millipore®).

The 10 mM cysteine reference standard stock solution was prepared by dissolving 47.57 mg L-Cysteine HCl·H$_2$O (L-Cysteine Hydrochloride Monohydrate, Carl Roth) in 27.1 ml reaction buffer. The last preparation is the Ellman's reagent solution itself, where 3.25 mg DTNB (AppliChem) were dissolved in 812 µl reaction buffer (4.0 mg/ml). The cysteine standards for an Ellman's test are prepared in the concentration range from 0.0 to 1.0 mM and the procedure is described in **Table G1**.

Table G1 | Optimized scheme for preparing a calibration line for an Ellman's test

Calibration sample[a]	1	2	3	4	5	6	7	8	9	10	11
10 mM L-Cysteine [µl]	0	2	4	6	8	10	12	14	16	18	20
Reaction buffer [µl]	200	198	196	194	192	190	188	186	184	182	180
c_{Cys} [mM]	0	0.1	0.2	0.3	0.4	0.5	0.6	0.7	0.8	0.9	1.0

[a]Preparations take place in duplicate.

Finally, 75 µl of each calibration standard (and unknown albumin sample) is transferred to 750 µl reaction buffer and 15 µl Ellman's reagent solution is added. This incubation is prepared in duplicate and is allowed to advance for 15 min at room temperature before absorbance is measured at λ_{Ellman} =

412 nm on an UV/Vis spectrometer (Hewlett Packard HP 8453 and HP 89090A). In **Figure G4** an example of a resulting calibration line is shown that results from the preparation given in **Table G1**.
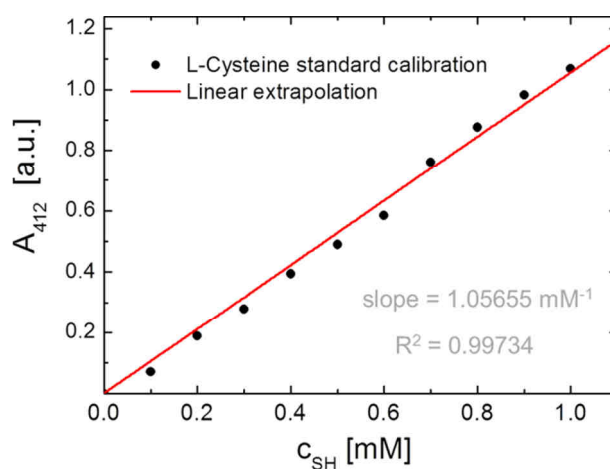
Figure G4 | Calibration curve from L-cysteine standard dilutions for an Ellman's test. Multiplication of the slope with the obtained absorption value A_{412} of a test sample yields the desired concentration (c_{SH}) of accessible Cys34 residues in unknown albumin samples.

This facilitates an estimate of the fraction of MTSSL-accessible thiol groups in each albumin lot. Therefore, the fraction $\phi_{SH} = c_{SH}/c_{BCA}$ can be regarded as the labeling efficiency. Another measure for the labeling efficiency is represented by the spin counting routine (see **Appendix G5**).

G3 | MALDI-TOF Mass Spectra of MTSSL Albumins

A further proof of a successful labeling procedure is the MW determination by MALDI-TOF mass spectrometry as conventional SDS PAGE usually does not provide sufficient mass resolution to observe the expected weight increase of an attached MTSSL residue (ΔMW = 184.28 Da, see also **Chapter 7.4.1**). The results of corresponding MALDI experiments on MTSSL HSA, MTSSL BSA and their native precursors HSA and BSA are shown in **Figure G5–G8**.
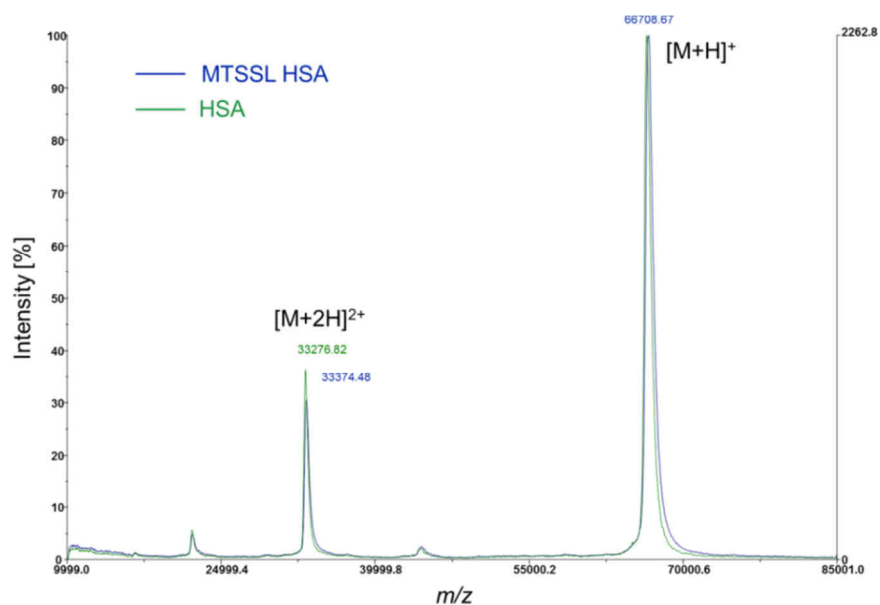
Figure G5 | MALDI-TOF spectra of HSA and MTSSL HSA. The full mass spectrum of HSA (green) and MTSSL HSA (blue) is shown with singly [M+H]$^+$ and doubly [M+2H]$^{2+}$ charged ions.
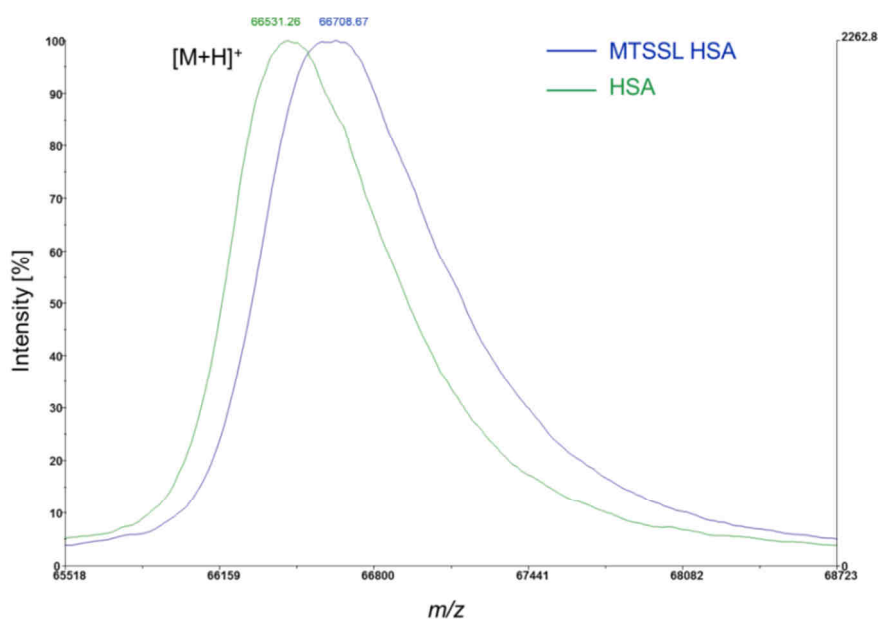
Figure G6 | Molecular weights of HSA and MTSSL HSA. The masses of the singly charged ions [M+H]$^+$ of HSA (green) and MTSSL HSA (blue) are highlighted.
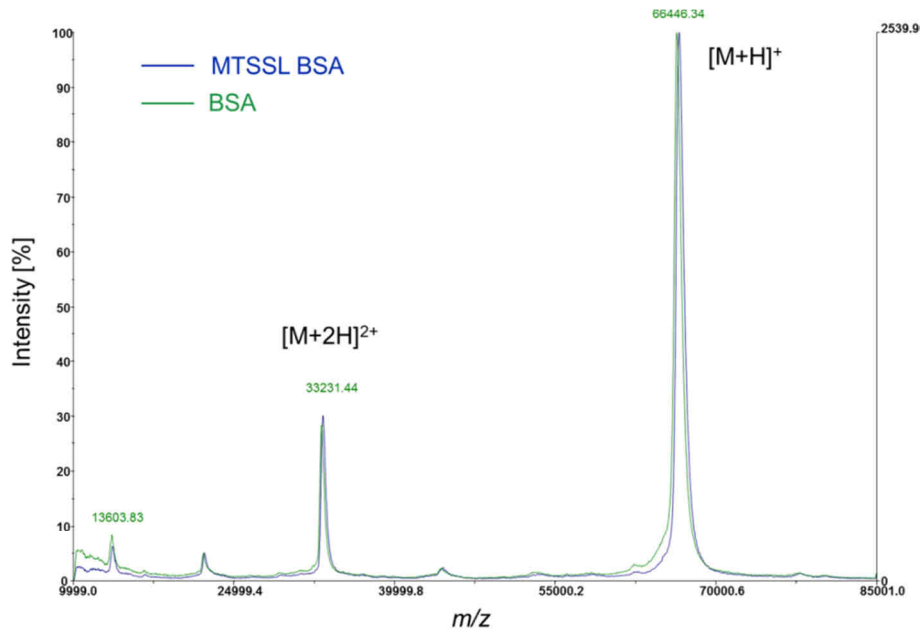
Figure G7 | MALDI-TOF spectra of BSA and MTSSL BSA. The full mass spectrum of BSA (green) and MTSSL BSA (blue) is shown with singly [M+H]$^+$ and doubly [M+2H]$^{2+}$ charged ions.
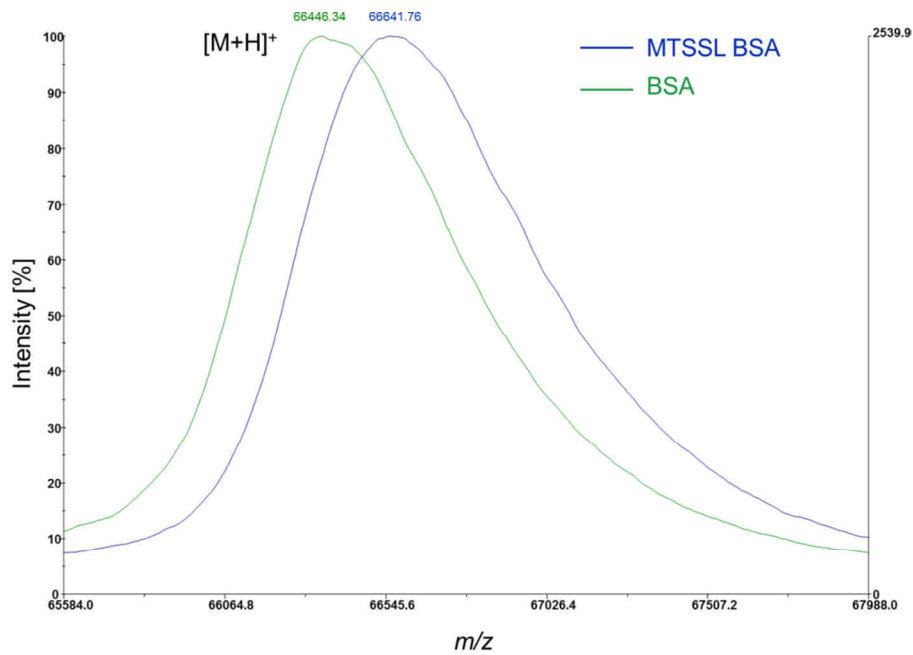
Figure G8 | Molecular weights of BSA and MTSSL BSA. The masses of the singly charged ions [M+H]$^+$ of BSA (green) and MTSSL BSA (blue) are highlighted.

G4 | CW EPR Spectra of Fatty Acid-loaded MTSSL Albumins

The graph shown in **Figure G9** depicts CW EPR spectra that were recorded prior to corresponding DEER experiments. It can be easily seen, that apart from some residual free MTSSL signals, all 5-DSA and 16-DSA probes are bound to HSA and BSA for at least 99 %. These data merely serve as a quality control for the results that will be shown in the following.
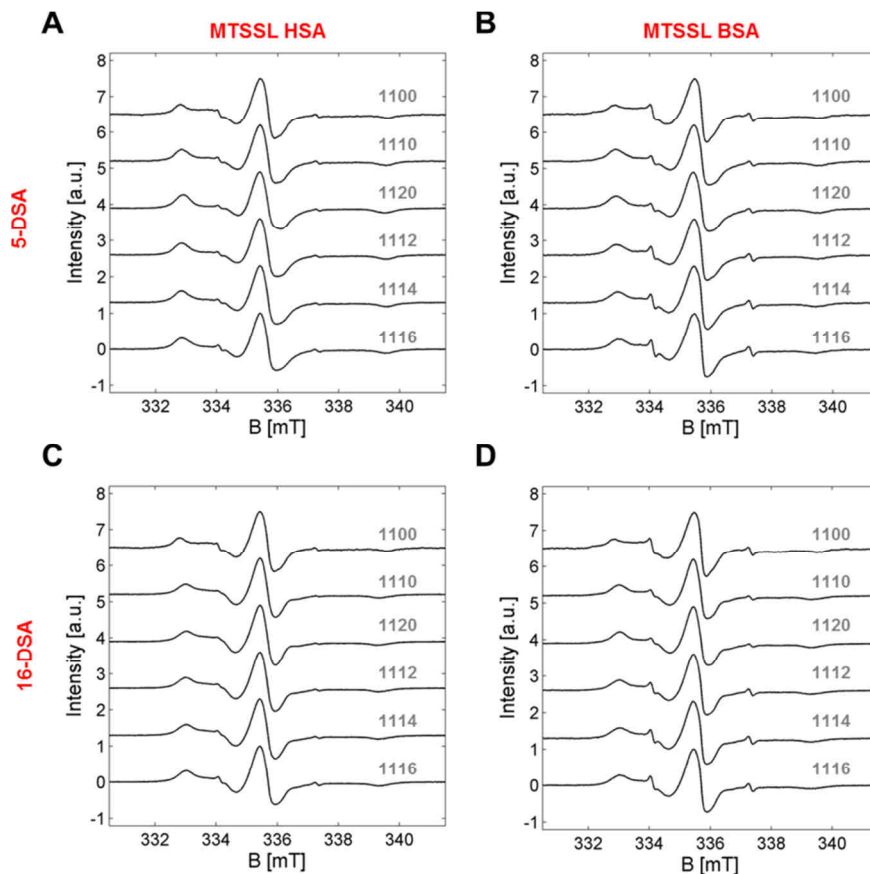
Figure G9 | CW EPR spectra of spin probed MTSSL XSA. This collection of CW EPR spectroscopic results originates from fatty acid loadings on (**A**) MTSSL HSA loaded with 5-DSA, (**B**) MTSSL BSA loaded with 5-DSA, (**C**) MTSSL HSA loaded with 16-DSA and (**D**) MTSSL BSA loaded with 16-DSA. The $11Z_3Z_4$ samples were equipped with paramagnetic (Z_3) to reduced (Z_4) fatty acid ratios of 0:0, 1:0, 2:0, 1:2, 1:4 and 1:6. The MTSSL concentration was set to 0.1 M corresponding to $c_H = 0.336$ mM and $c_B = 0.183$ mM. Samples were prepared in DPBS buffer equipped with 20% v/v glycerol at pH 7.4.

G5 | Dipolar Evolution Functions from DEER Experiments on MTSSL Albumins

All modulation depths Δ can be determined from dipolar evolution functions in **Figure G10** and are shown in **Figure G11A** directly after Tikhonov regularization in DeerAnalysis2013.[G26] The spin counting procedure applied here, is based on using the modulation depth parameter $\lambda \pm \Delta\lambda = 0.53421 \pm 0.00916$ that was determined in **Appendix C7**.
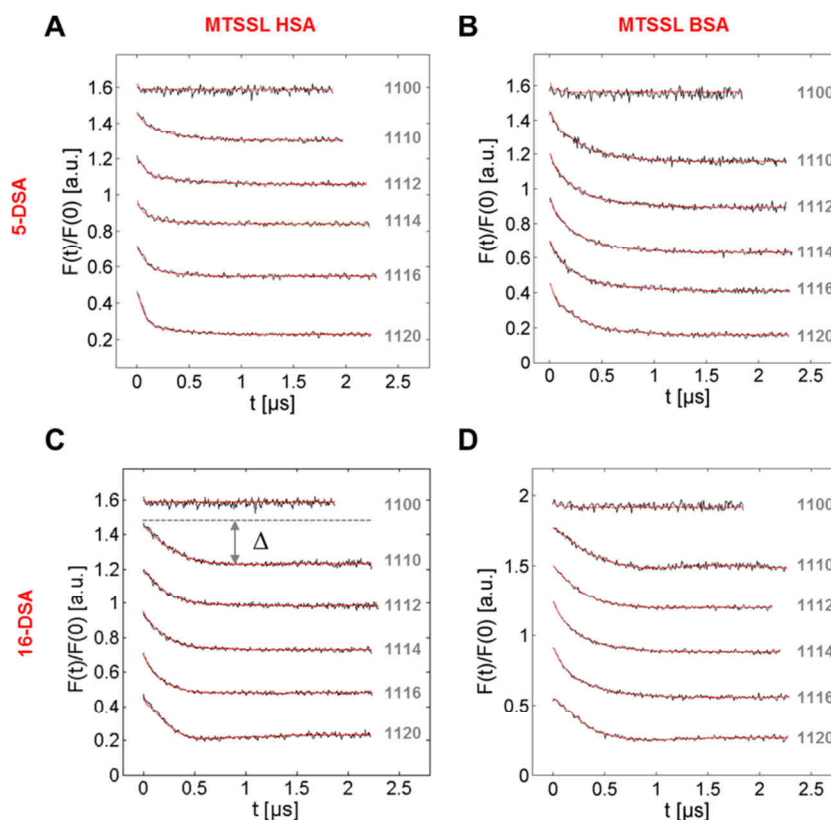
Figure G10 | DEER-derived dipolar evolution functions of spin probed MTSSL XSA. This collection of DEER-derived dipolar evolution functions $F(t)/F(0)$ originates from fatty acid alignments in (**A**) MTSSL HSA loaded with 5-DSA, (**B**) MTSSL BSA loaded with 5-DSA, (**C**) MTSSL HSA loaded with 16-DSA and (**D**) MTSSL BSA loaded with 16-DSA from the CW EPR samples shown in **Figure G9**. The $11Z_3Z_4$ samples were equipped with paramagnetic (Z_3) to reduced (Z_4) fatty acid ratios of 0:0, 1:0, 1:2, 1:4, 1:6 and 2:0. The modulation depth Δ is schematically shown for 16-MTSSL HSA 1110 in (C). The MTSSL concentration was set to 0.1 mM corresponding to $c_H = 0.336$ mM and $c_B = 0.183$ mM. All samples were prepared in DPBS buffer equipped with 20% v/v glycerol at pH 7.4.

Therefore, the familiar relation $\langle n \rangle = 1 - \ln(1 - \Delta)/\lambda$ (see equation 2.103) gives approximate values for the number of coupled spins $\langle n \rangle$ in MTSSL albumin samples. Error bars for modulations depths Δ were assumed to be constant at $\Delta\Delta = 0.020$[G27] and the error for the number of coupled spins $\Delta\langle n \rangle$ is calculated according to the propagation of uncertainty:

$$\Delta\langle n \rangle = \frac{\Delta\lambda \cdot \ln(1 - \Delta)}{\lambda^2} + \frac{\Delta\Delta}{\lambda \cdot (1 - \Delta)} \qquad . \tag{G.1}$$

Results from this analysis are shown in **Figure G11B**. Note, that the nominal number of loaded fatty acids is $N_L = 0$ for MTSSL XSA 1100 and for all other samples $N_L = Z_3 + Z_4$. From individual

modulation depths the average number of coupled spins is determined as $\langle n \rangle_{HSA} = 1.39 \pm 0.10$ and $\langle n \rangle_{BSA} = 1.69 \pm 0.09$. The difference in $\langle n \rangle_X \approx 1 + \phi_{SH}$ for Y-MTSSL XSA is therefore assumed to occur due to the different labeling efficiencies and gives a nice resemblance to values that were already determined with Ellman's tests (ϕ_{SH}, see **Table 9.1**)).
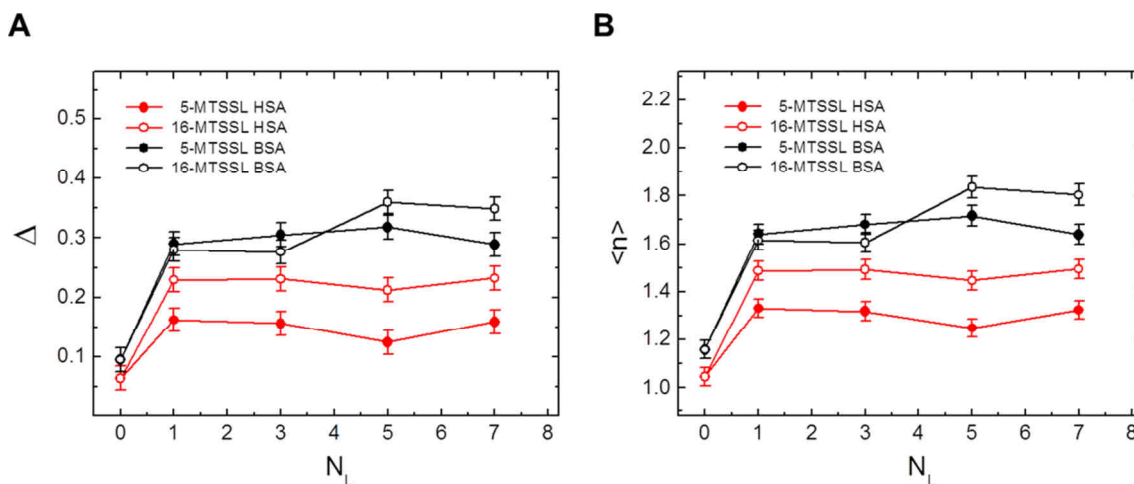
Figure G11 | Spin counting from spin probed MTSSL XSA samples. The DEER-derived dipolar evolution functions of 5-DSA- (●) and 16-DSA-probed (○) MTSSL HSA (red) and MTSSL BSA (black) in **Figure G10** provide further information about (**A**) the individual modulation depths Δ and (**B**) the number of coupled spins $\langle n \rangle$ as derived from modulation depths shown in (A). The nominal number of loaded fatty acids is here conventionally denoted as $N_L = Z_3 + Z_4$.

G6 | Molecular Dynamics (MD) Simulations with YASARA Structure

A general procedure for performing appropriate MD simulations with YASARA Structure[G28] is provided in the following. All MD simulations were primarily conducted with a second generation force-field AMBER03,[G29] being especially well-suited to predict protein structures and interactions of small organic molecules with proteins. The protocol can be subdivided in several distinct strategic steps. A single setup of a MD simulation can be executed in a few hours and the individual steps presented here have turned out to work quite well. Without immersing too much into MD simulation theory,[G30] a straightforward routine is presented in appropriate order as a general ruler for simulating the solution structure of e.g. proteins:

(*i*)   **Definition of a simulation cell.** The modeled structure is equipped with a simulation cell with periodic boundaries and a size usually surrounding each atom at a distance of 10 Å.

(*ii*)   **Force field selection.** By choosing the AMBER03 force field, an automatic cutoff radius of $r_{cut} = 7.86$ Å is adjusted with a particle mesh Ewald (PME) algorithm considering long range electrostatics.

(*iii*)   **Initialize simulator.** All atoms in the simulation cell are equipped with adequate force field parameters.

(*iv*)   **Set temperature.** The structure shall be calculated at $T = 298$ K.

(*v*)   **Cell neutralization and pK$_a$ prediction.** The simulation cell is now filled with water molecules and the solvent properties are chosen (pH 7.4, $c(\text{NaCl}) = 0.9$ %, $\rho_{\text{H20}} = 0.997$ g/ml). While pK$_a$ shifts are calculated, atoms are again parametrized. Then a steepest descent minimization is started without electrostatics, before counter ions are placed in a simulated annealing minimization procedure of the solvent in order to neutralize the simulation cell.

(*vi*)   **Energy minimization.** A preliminary energy minimization of the whole simulation cell is conducted starting with a steepest descent algorithm until the kinetic energy of the fastest atom has dropped below 3000 m/s (after 1 – 2 ps) indicating that conformational stress is gone. Then a simulated annealing experiment is started until the temperature drops below 10 K, indicating convergence.

(*vii*)   **Running the MD simulation.** The simulation is started and should proceed in timesteps of $\Delta t_{\text{MD}} = 1$ fs by rescaling atom velocities. The simulation cell pressure is kept constant at $p = 1$ bar and the solvent molecules are automatically adjusted to a density of 0.997 g/ml.

With this strategy 1.5 – 2.0 ns runtime may be calculated for 10^5 atoms per day with a contemporary desktop computer. Optionally, simulation snapshots can be saved and analyzed, however, it turned out that only advanced Python programming capabilities permit full access to the construction of any parameter trajectory and therefore this strategy was for now not pursued exhaustively.

G7 | Prediction of Distance Distributions from MTSSL Albumin by MD Simulations

A further refinement of the method for theoretical predictions of DEER-derived distance distributions from fatty acid alignments (see **Appendix A1**) can be achieved by explicit molecular modeling. As several decisive atoms in the seven stearic acids' methylene chains (C1 – C18) are not resolved in the associated crystal structure (PDB ID: 1e7i),[G31] the doxyl groups and the missing atoms can be artificially replaced in the topology file (missing chain segments in Ste1001: C14–C18; Ste1002, Ste1003, Ste1006: C18; Ste1007: C12–C18). The implementation of nitroxides in MD simulations usually affords special parametrization, but may also be modeled as a keto (C=O) group due to a similar bond length ($r((\text{C}^*)_2\text{–C=O}) = 1.210$ Å, $r((\text{C}^*)2\text{–N}^+\text{–O}^-) = 1.304$ Å).[G32] As an example the nitroxide bond length for Fremy's salt was found to range about 1.275 ± 0.024 Å.[G33] Thus, all nitroxides were modeled to contain a keto group that represents sterical and spatial requirements of the paramagnetic nitroxide moiety.

In order to obtain a crystal structure reference distance matrix as in **Table A1**,[G34] the protein object is first kept fixed and the modeled doxyl stearic acid molecules are subjected to an energy minimization that allows for reducing conformational stress and ligand accomodation to the protein interior. Regarding the necessity of simulated HSA structures that are required for this study, a simultaneous

extraction of FA and MTSSL-FA distance distributions is presented. Therefore, the modeled crystalline structure of HSA is equipped with a modeled MTSSL residue at position Cys34 as it is experimentally obtained from the spin labeling procedure described in **Appendix G1**.

Simulations were conducted according to the general procedure that is described in **Appendix G6** for MTSSL HSA equipped with 5-DSA as well as 16-DSA. The values for $r_{i,k}$ in between the nitrogen (or keto carbon) atoms of MTSSL and Y-DSA are taken from individual snapshots of the simulations. The results are summarized in **Figure G12** indicating the distances from MTSSL to each individual fatty acid (FAi). All obtained distance matrices were determined in between the (keto) carbon atoms replacing the nitrogen atoms. However, the nitroxide radical is actually located in between the nitrogen and oxygen nucleus as it has been pointed out in **Chapter 2.4.2.1**, giving an estimated intrinsic distance error of this approach not larger than $r_{NO} \approx 1.3$ Å $= 0.13$ nm.

Although this kind of approach has been conceived to simplify the peak assignment for purely spin probed albumin molecules,[G34] the addition of a covalently attached spin label extends the number of all experimentally observable nitroxides to $N_{SBS} = N_{FA} + N_{MTSSL} = 8$, yielding a total amount of combined distances $N_{r,SBS} = (N_{SBS}^2 - N_{SBS})/2 = 28$ in a 8×8 matrix instead of $N_{r,FA} = 21$ (**Table A1**).

The purpose of this approach is to simulate an explicit theoretical nitroxide-based solution structure of albumin as it is obtained from the coarse-grained viewpoint of aligned fatty acids. Henceforth, these fatty acids are additionally observed from the surveillance benchmark spin (SBS) that is here represented by MTSSL. The indices i and j denote individual fatty acid interaction numbers and k represents the MTSSL residue (i,j = FA interspin distances contributing to $P_{FA}(r)$, i,k = FA–MTSSL distances ($P_{SBS}(r)$) and i,j,k gives the complete correlation of all spins ($P(r)$)).

The assignment of distribution peaks to the binding site locations of the nitroxide groups is here facilitated best by correlating the obtained spin distributions from different standpoints. In the following, the resulting 8×8 matrices have been explicitly checked at simulation runtimes of about 0.0 ns, 3.4 ns and 9.4 ns and are shown in **Tables G2–G4** with all emerging matrix components. The diagonal ($r_{Y,i,j,k} = 0$ nm for $i = i$, $j = j$, $k = k$) and commutable matrix components ($r_{Y,j,i,k} = r_{Y,i,j,k}$) are given for completeness. The matrices can be rationalized in terms of a full distribution $P(r)$ for each applied probe ($Y \in 5,16$) with $N_{r,SBS} = 28$:

$$P(r) = P_{MD}(r_{i,j,k}, Y, t_{MD}) = \frac{1}{|A|} \cdot \sum_{i \neq j \neq k}^{N_{r,Y,SBS}} \exp\left(-\frac{(r - r_{Y,i,j,k})}{2\sigma}\right)^2 \qquad , \qquad (G.2)$$

a fatty acid based distribution with $N_{r,FA} = 21$:

$$P_{FA}(r) = P_{MD}(r_{i,j}, Y, t_{MD}) = \frac{1}{|A|} \cdot \sum_{i \neq j}^{N_{r,Y,FA}} \exp\left(-\frac{(r - r_{Y,i,j})}{2\sigma}\right)^2 \qquad (G.3)$$

and individual distances from MTSSL to each fatty acid with $N_{SBS} = 7$:

$$P_{SBS}(r) = P_{MD}(r_{i,k}, Y, t_{MD}) = \frac{1}{|A|} \cdot \sum_{i \neq k}^{N_{Y,SBS}} \exp\left(-\frac{(r - r_{Y,i,k})}{2\sigma}\right)^2 \qquad . \qquad (G.4)$$

The resulting distance distributions ($P(r)$, $P_{FA}(r)$ and $P_{SBS}(r)$) are shown in **Figures G13 – G15**. The Gaussian widths were set to $\sigma = 0.17$ for all distributions that were calculated herein.
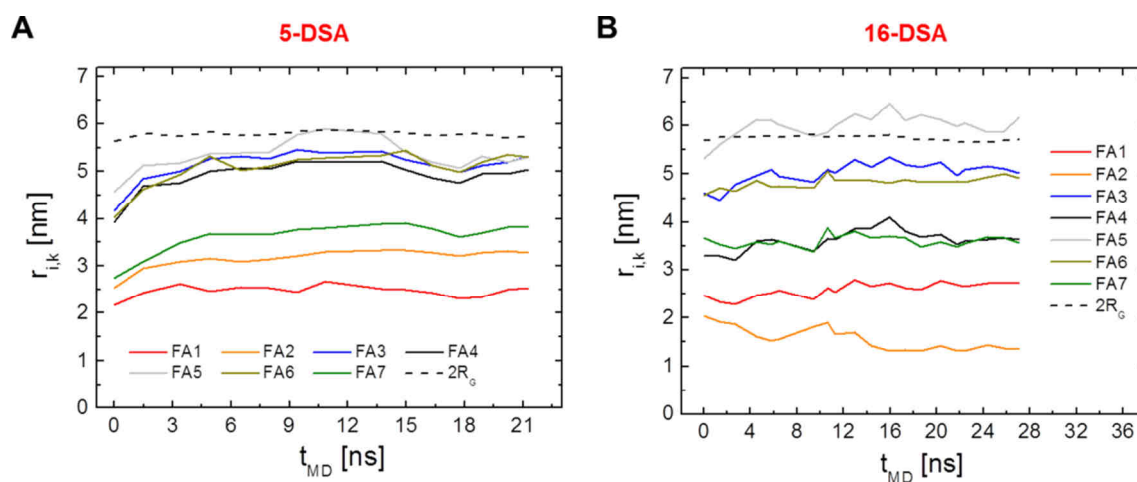
Figure G12 | Distance trajectories from MD simulations on molecular models of MTSSL HSA. Here, trajectories from the seven interspin distances $r_{i,k}$ of the reduced interspin system (SBS) are shown during 20 – 27 ns simulation runtime (t_{MD}) that represent (SBS-) distances between nitrogen (keto carbon) atoms of MTSSL and (**A**) 5-DSA as well as (**B**) 16-DSA. Therefore, individual fatty acids FA1 (red), FA2 (orange), FA3 (blue), FA4 (black), FA5 (light gray), FA6 (dark yellow) and FA7 (green) represent the different binding sites in HSA from their respective nitroxide positions. Additionally, the gyration diameter $2R_G = 5.76 \pm 0.07$ nm (black dotted line) is taken as an estimate for the protein diameter and refers to the geometric center of HSA. After 3 – 9 ns simulation runtime, significant changes vanish in the observed interspin distances.

Table G2 | The 8×8 distance matrices for MTSSL XSA loaded with 5- and 16-DSA after 0.0 ns[a]

$r_{5,ijk}$ [nm]	MTSSL	1	2	3	4a	5	6	7
MTSSL	0	2.63	2.92	4.45	4.13	4.66	4.30	3.04
1	2.63	0	2.44	3.43	3.26	3.19	4.10	2.40
2	2.92	2.44	0	3.69	3.79	4.93	3.26	1.18
3	4.45	3.43	3.69	0	0.60	2.59	1.89	2.55
4a	4.13	3.26	3.79	0.60	0	2.27	2.09	2.68
5	4.66	3.19	4.93	2.59	2.27	0	4.32	4.12
6	4.30	4.10	3.26	1.89	2.09	4.32	0	2.18
7	3.04	2.40	1.18	2.55	2.68	4.12	2.18	0

$r_{16,ijk}$ [nm]	MTSSL	1	2	3	4a	5	6	7
MTSSL	0	2.48	2.05	4.61	3.29	5.32	4.56	3.67
1	2.48	0	2.02	2.48	2.23	4.09	3.32	1.65
2	2.05	2.02	0	4.28	3.84	6.01	3.47	2.67
3	4.61	2.48	4.28	0	1.96	2.96	3.29	1.96
4a	3.29	2.23	3.84	1.96	0	2.56	3.77	2.59
5	5.32	4.09	6.01	2.96	2.56	0	5.95	4.58
6	4.56	3.32	3.47	3.29	3.77	5.95	0	1.89
7	3.67	1.65	2.67	1.96	2.59	4.58	1.89	0

[a]Numbers on gray background denote individual fatty acid binding sites, numbers on green background give the reduced interspin system (FA–MTSSL distances, $P_{SBS}(r)$) and numbers with white background give the fatty acid correlations (FA–FA distances, $P_{FA}(r)$).

Table G3 | The 8×8 distance matrices for MTSSL XSA loaded with 5- and 16-DSA after 3.8 ns[b]

$r_{5,ijk}$ [nm]	MTSSL	1	2	3	4a	5	6	7
MTSSL	0	2.63	3.08	5.18	4.76	5.00	4.93	3.49
1	2.63	0	2.45	3.27	3.11	3.05	4.06	2.62
2	3.08	2.45	0	3.40	3.60	4.79	3.17	1.16
3	5.18	3.27	3.40	0	0.67	2.67	1.79	2.40
4a	4.76	3.11	3.60	0.67	0	2.25	2.06	2.63
5	5.00	3.05	4.79	2.67	2.25	0	4.29	4.23
6	4.93	4.06	3.17	1.79	2.06	4.29	0	2.02
7	3.49	2.62	1.16	2.40	2.63	4.23	2.02	0

$r_{16,ijk}$ [nm]	MTSSL	1	2	3	4a	5	6	7
MTSSL	0	2.68	1.55	5.19	3.84	6.46	4.95	4.22
1	2.68	0	2.11	2.70	1.88	4.49	3.53	2.14
2	1.55	2.11	0	4.56	3.71	6.51	3.88	3.07
3	5.19	2.70	4.56	0	1.81	3.18	3.20	2.24
4a	3.84	1.88	3.71	1.81	0	2.96	3.77	2.80
5	6.46	4.49	6.51	3.18	2.96	0	6.21	5.24
6	4.95	3.53	3.88	3.20	3.77	6.21	0	1.73
7	4.22	2.14	3.07	2.24	2.80	5.24	1.73	0

[b]Numbers on gray background denote individual fatty acid binding sites, numbers on green background give the reduced interspin system (FA–MTSSL distances, $P_{SBS}(r)$) and numbers with white background give the fatty acid correlations (FA–FA distances, $P_{FA}(r)$).

Table G4 | The 8×8 distance matrices for MTSSL XSA loaded with 5- and 16-DSA after 9.4 ns[c]

$r_{5,ijk}$ [nm]	MTSSL	1	2	3	4a	5	6	7
MTSSL	0	2.45	3.20	5.45	5.21	5.76	5.25	3.77
1	2.45	0	2.63	3.58	3.35	3.49	4.08	2.86
2	3.20	2.63	0	3.46	3.73	4.96	3.03	1.11
3	5.45	3.58	3.46	0	0.85	2.59	1.70	2.55
4a	5.21	3.35	3.73	0.85	0	2.11	2.05	2.86
5	5.76	3.49	4.96	2.59	2.11	0	4.12	4.43
6	5.25	4.08	3.03	1.70	2.05	4.12	0	1.92
7	3.77	2.86	1.11	2.55	2.86	4.43	1.92	0

$r_{16,ijk}$ [nm]	MTSSL	1	2	3	4a	5	6	7
MTSSL	0	2.75	1.48	5.18	3.70	6.24	5.09	4.31
1	2.75	0	2.38	2.62	1.86	4.17	3.86	2.51
2	1.48	2.38	0	4.45	3.50	6.31	3.81	3.09
3	5.18	2.62	4.45	0	2.19	3.40	3.19	2.19
4a	3.70	1.86	3.50	2.19	0	2.96	3.80	3.00
5	6.24	4.17	6.31	3.40	2.96	0	6.22	5.35
6	5.09	3.86	3.81	3.19	3.80	6.22	0	1.64
7	4.31	2.51	3.09	2.19	3.00	5.35	1.64	0

[c]Numbers on gray background denote individual fatty acid binding sites, numbers on green background give the reduced interspin system (FA–MTSSL distances, $P_{SBS}(r)$) and numbers with white background give the fatty acid correlations (FA–FA distances, $P_{FA}(r)$).
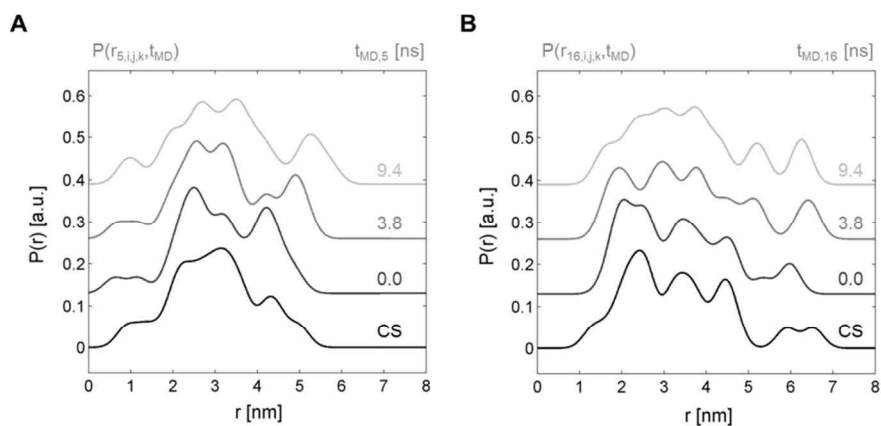
Figure G13 | Distance distributions $P(r,t_{MD})$ from MD simulations on molecular models of MTSSL HSA. Here, full distributions $P(r)$ are shown in shades of grey as calculated from equation G.2 using $\sigma = 0.17$. The underlying matrices for the crystal structure data (CS)[G34] can be found in **Table A1** and **Table G2–G4** giving the 8×8 matrices (green and white background) for $t_{MD} = 0.0$ ns, 3.8 ns and 9.4 ns simulation runtime from 5- and 16-DSA (see **Figure G12**).
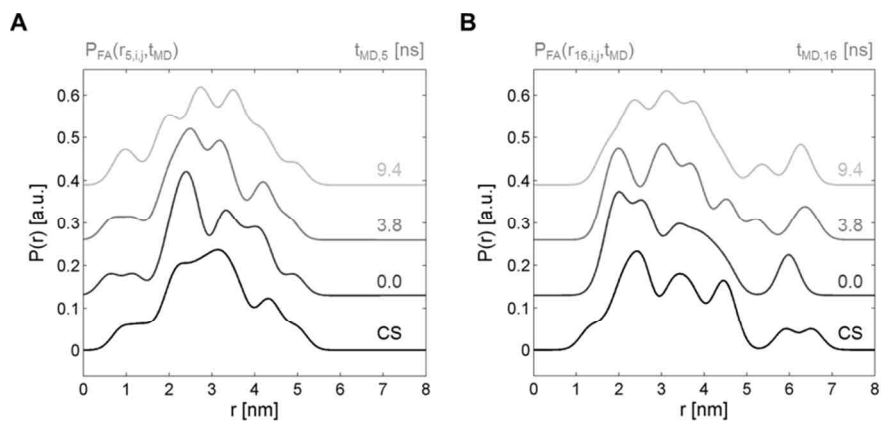
Figure G14 | Distance distributions $P_{FA}(r,t_{MD})$ from MD simulations on molecular models of MTSSL HSA. Here, the distributions $P_{FA}(r)$ are shown in shades of grey as calculated from equation G.3 using $\sigma = 0.17$. The underlying matrices for the crystal structure data (CS)[G34] can be found in **Table A1** and **Table G2–G4** giving the 7×7 matrices (white background) for $t_{MD} = 0.0$ ns, 3.8 ns and 9.4 ns simulation runtime from 5- and 16-DSA (see **Figure G12**).
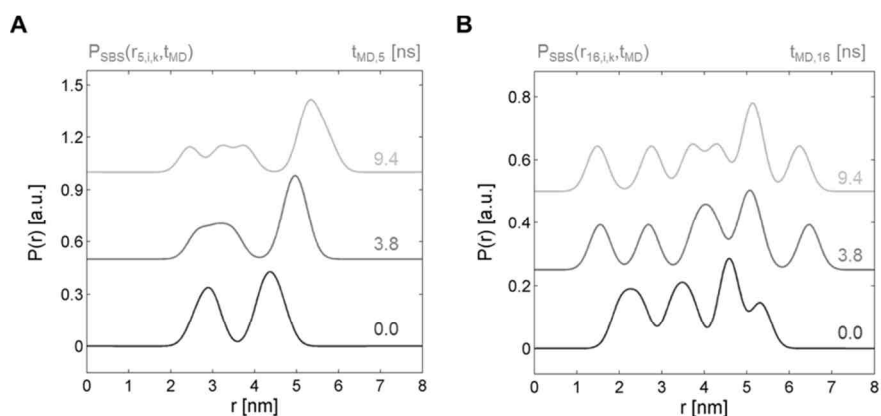
Figure G15 | Distance distribution $P_{SBS}(r,t_{MD})$ from MD simulations on molecular models of MTSSL HSA. Here, the reduced distributions $P_{SBS}(r)$ are shown in shades of grey as calculated from equation G.4 using $\sigma = 0.17$. The underlying matrices can be found in **Table G2–G4**. Here, only the column values (green) were used for the calculation of distributions at $t_{MD} = 0.0$ ns, 3.8 ns and 9.4 ns simulation runtime from 5- and 16-DSA (see **Figure G12**).

G8 | DEER Reference Data from Exclusively Fatty Acid-loaded HSA and BSA

In **Figure 9.4**, a comparison is made in between fatty acid loaded MTSSL XSA and precursor XSA (X ∈ H,B) with one (0110) or two (0120) equivalents of paramagnetic species that are used for identification of experimental contributions of $P_{SBS}(r)$. The results from the reference experiments are shown in **Figure G16A+B**. Due to excluded volume (see **Chapter 5.2**) and ligand distribution effects (**Chapter 3.3**), a nominal loading ratio of 0110 may already lead to dipolar modulation in the time traces (see also **Appendix D4**). Despite the low modulation depths for 0110 loadings (**Figure G16C+D**), distinct distance distributions can be obtained (**Figure G16E+F**).
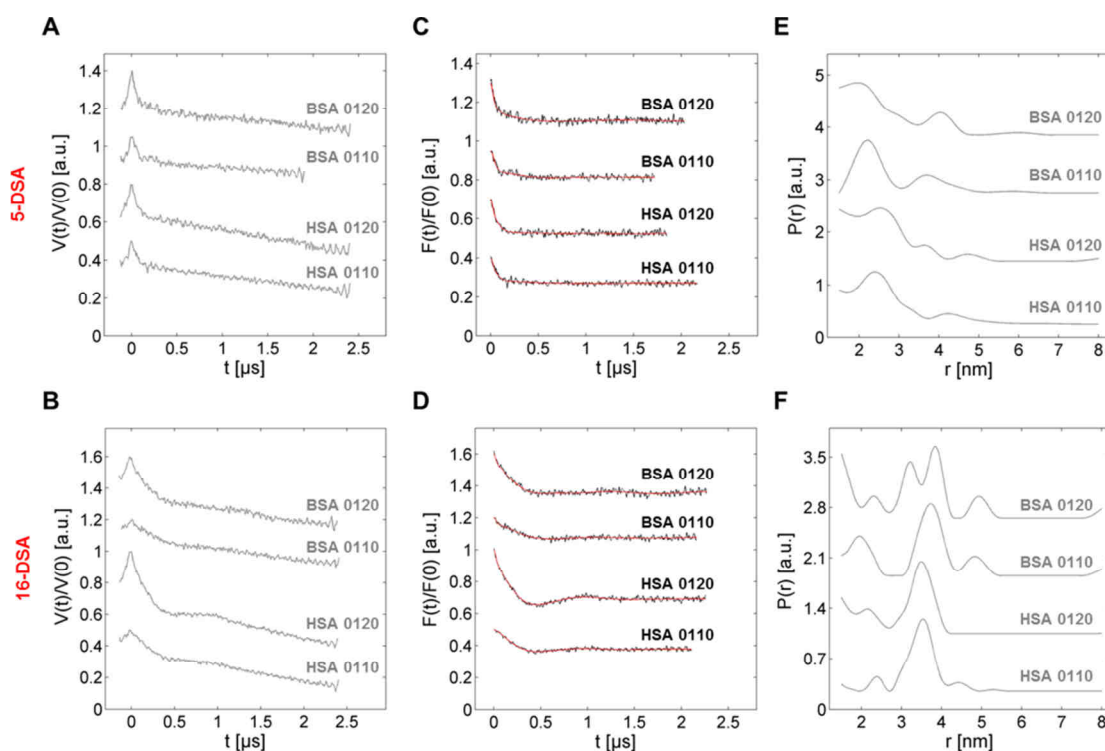
Figure G16 | Reference DEER data from spin probed XSA samples. This data set was recorded as a reference to MTSSL HSA and MTSSL BSA at identical equivalent concentrations of $c_H = 0.336$ mM and $c_B = 0.183$ mM, loaded with one (0110) or two (0120) paramagnetic species. Raw DEER time traces $V(t)/V(0)$ (gray) of HSA and BSA spin probed with (**A**) 5-DSA and (**B**) 16-DSA. Dipolar evolution functions $F(t)/F(0)$ (black) with regularized fits (red) of HSA and BSA spin probed with (**C**) 5-DSA and (**D**) 16-DSA and corresponding distance distributions $P_{FA}(r)$ (gray) are also given in (**E**) for 5-DSA and (**F**) 16-DSA. These experimental fatty acid-based distance distributions are used in **Figure 9.4** for identifying contributions from $P_{SBS}(r)$. All samples were prepared in DPBS buffer equipped with 20% v/v glycerol at pH 7.4.

G9 | References

[G1]   O. H. Griffith, H. M. McConnell, *Proc Natl Acad Sci USA* **1966**, *55*, 8–11.

[G2]   V. A. Livshits, D. Marsh, *Biochim Biophys Acta, Biomembr* **2000**, *1466*, 350–360.

[G3]   A. Alonso, W. P. dos Santos, S. J. Leonor, J. G. dos Santos, M. Tabak, *Biophys J* **2001**, *81*, 3566–3576.

[G4]   F. De Simone, R. Guzzi, L. Sportelli, D. Marsh, R. Bartucci, *Biochim Biophys Acta, Biomembr* **2007**, *1768*, 1541–1549.

[G5]   J. L. V. Anjos, P. S. Santiago, M. Tabak, A. Alonso, *Colloids Surf, B* **2011**, *88*, 463–470.

[G6]   D. S. Park, C. E. Petersen, C. E. Ha, K. Harohalli, J. B. Feix, N. V. Baghavan, *IUBMB Life* **1999**, *48*, 169–174.

[G7]   Y. Shenberger, A. Shimshi, S. Ruthstein, *J Phys Chem B* **2015**, *119*, 4824–4830.

[G8]   C. M. Gruian, C. Rickert, S. C. T. Nicklisch, E. Vanea, H. J. Steinhoff, S. Simon, *ChemPhysChem* **2017**, *18*, 634–642.

[G9]   Marie-Therese Oehmichen, Biophysikalische Untersuchung der pH-abhängigen Struktur und Dynamik von Serumalbumin. Bachelor Thesis. Martin-Luther-Universität Halle-Wittenberg, **2015**.

[G10]   L. J. Berliner, J. Grunwald, H. O. Hankovszky, K. Hideg, *Anal Biochem* **1982**, *119*, 450–455.

[G11]   A. Michnik, Z. Drzazga, *J Therm Anal Calorim* **2007**, *88*, 449–454.

[G12]   A. Michnik, *J Therm Anal Calorim* **2007**, *87*, 91–96.

[G13]   J. B. Feix, C. S. Klug, Site-directed spin labeling of membrane proteins and peptide-membrane interactions. In *Spin Labeling: The Next Millenium*; L. J. Berliner, Ed.; Kluwer Academic Publishers: New York, Boston, **2002**, Vol. 14, pp 251–281.

[G14]   V. V. Khramtsov, I. A. Grigor'ev, M. A. Foster, D. J. Lurie, *Antioxid Redox Signaling* **2004**, *6*, 667–676.

[G15]   T. Peters Jr., *All about Albumin: Biochemistry, Genetics, and Medical Applications.* Academic Press, Inc.: San Diego, **1995**.

[G16]   S. Bleicken, A. J. Garcia-Saez, E. Conte, E. Bordignon, *PLoS One* **2012**, *7*, e35910.

[G17]   M. M. Bradford, *Anal Biochem* **1976**, *72*, 248–254.

[G18]   V. V. Khramtsov, L. B. Volodarsky, Use of imidazoline nitroxides in studies of chemical reactions: ESR measurements of the concentration and reactivity of protons, thiols, and nitric oxide. In *Spin Labeling: The Next Millenium*; L. J. Berliner, Ed.; Kluwer Academic Publishers: New York, Boston, **2002**, Vol. 14, pp 109–180.

[G19]   P. K. Smith, R. I. Krohn, G. T. Hermanson, A. K. Mallia, F. H. Gartner, M. D. Provenzano, E. K. Fujimoto, N. M. Goeke, B. J. Olson, D. C. Klenk, *Anal Biochem* **1985**, *150*, 76–85.

[G20]   G. L. Ellman, *Arch Biochem Biophys* **1959**, *82*, 70–77.

[G21]   Thermo Scientific. *Ellman's reagent.* Instructions manual, **2013**.

[G22]   C. K. Riener, G. Kada, H. J. Gruber, *Anal Bioanal Chem* **2002**, *373*, 266–276.

[G23]   P. W. Riddles, R. L. Blakeley, B. Zerner, *Anal Biochem* **1979**, *94*, 75–81.

[G24]   J. Janatova, J. K. Fuller, M. J. Hunter, *J Biol Chem* **1968**, *243*, 3612–3622.

[G25]   K. Oettl, R. E. Stauber, *Br J Pharmacol* **2007**, *151*, 580–590.

[G26]   G. Jeschke, V. Chechik, P. Ionita, A. Godt, H. Zimmermann, J. Banham, C. R. Timmel, D. Hilger, H. Jung, *Appl Magn Reson* **2006**, *30*, 473–498.

[G27]   B. E. Bode, D. Margraf, J. Plackmeyer, G. Dürner, T. F. Prisner, O. Schiemann, *J Am Chem Soc* **2007**, *129*, 6736–6745.

[G28]   E. Krieger, G. Koraimann, G. Vriend, *Proteins Struct Funct Genet* **2002**, *47*, 393–402.

[G29]   W. D. Cornell, P. Cieplak, C. I. Bayly, I. R. Gould, K. M. Merz, Jr., D. M. Ferguson, D. C. Spellmeyer, T. Fox, J. W. Caldwell, P. A. Kollman, *J Am Chem Soc* **1995**, *117*, 5179–5197.

[G30]   A. R. Leach, *Molecular modelling: principles and applications.* Pearson Education, Ltd.: Harlow, England, **2001**.

[G31]   A. A. Bhattacharya, T. Grüne, S. Curry, *J Mol Biol* **2000**, *303*, 721–732.

[G32]   F. H. Allen, O. Kennard, D. G. Watson, L. Brammer, A. G. Orpen, R. Taylor, *J Chem Soc, Perkin Trans 2* **1987**, S1–S19.

[G33]   H. Elgabarty, M. Wolff, A. Glaubitz, D. Hinderberger, D. Sebastiani, *Phys Chem Chem Phys* **2013**, *15*, 16082–16089.

[G34]   M. J. N. Junk, H. W. Spiess, D. Hinderberger, *Angew Chem Int Ed* **2010**, *49*, 8755–8759.

Appendix H | Tunable Attachment of Ligands in Amphiphilic Core-shell Polymers

H1 | Critical Micelle Concentration (CMC) of 16-DSA in DPBS pH 7.4 at $T = 25°C$

It has been shown in earlier publications that obtaining CMC values for 16-DSA is challenging due to the highly complex solution behavior of this molecule.[H1] Generally, the 16-DSA spin probe is added to buffer solutions to detect CMCs and polarity effects of host molecules[H2–H4] by determination of the rotational correlation time τ_c. This value is most sensitive to changes in microviscosity, which can change drastically upon structural rearrangements in solution at reasonable host concentrations. Here, microviscosity is not altered considerably when 16-DSA concentration is increased and micelle formation is triggered (τ_c = 68 ps for 32 µM 16-DSA to τ_c = 99 ps for 2980 µM 16-DSA), so an alternative way of interpreting data has to be figured out.

As 5-DSA was reported to have a CMC of 0.035 mM in saline phosphate buffer at 37°C,[H5] 16-DSA can be expected to have a very similar value as it also contains stearic acid as an identical molecular matrix. Here, the commonly accepted inherent spectroscopic problems associated with spin-labeled DSA molecules are surmounted by insistent sample preparation until an adequate set of measurements is obtained. CW EPR spectra were obtained here in the concentration range from 13 – 3098 µM without a reasonable gap between individual data points that would give rise to a lack of information about the onset of micelle formation (**Figure H1A**). Unlike in Rehfeld *et al.*[H5] an alternative semi-empirical method of detecting the abundance of micelles in our samples is employed. As the exchange-broadened micellar spectral component grows with increasing 16-DSA concentration,[H6] the relative peak intensities of the center-field peak of freely tumbling 16-DSA (h_0) and micellar spectral components of 16-DSA (h_M) are compared. As all experimental parameters are kept constant in the sample (T, pH, ionic strength, solvent), the reproducibility of individual measurements is still overwhelmingly restricted. Therefore, double integration of individual CW EPR spectra was used as a quantitative spin counting tool (see **Appendix E3**). While the micellar spectral component h_M may partially overlap with the ^{13}C-satellite signals at the central ^{14}N-nitroxide line ($m_I = 0$), the ^{13}C intensity (h_C) is subtracted by default to obtain $h_{M,0} = h_M - h_C$ that allows to build the formal ratio $h_{M,0}/h_0$ (**Figure H1B**). Thereupon, this value is plotted versus the 16-DSA concentration as extracted from double integration.

As it is not always possible to prepare all the samples from the same stock solution it is strongly recommended to double integrate all stock solution CW EPR spectra additionally and normalize them against each other. The reason is that obviously not all supplier lots contain similar amounts of spin-bearing 16-DSA molecules. In this case an exemplary procedure would be to calculate:

$$r_{DI} = \frac{\iint S_{stock1}^{16\text{-DSA}}(B)\mathrm{d}^2B}{\iint S_{stock2}^{16\text{-DSA}}(B)\mathrm{d}^2B} = 0.69 \tag{H.1}$$

.

This routine applied well here to align independent measurements from two different stock solutions by an appropriate signal strength normalization factor r_{DI}. It can be shown in **Figure H1C** that a concise kink is emerging in the curve at the onset of micelle formation, as it is generally encountered in e.g. surface tension measurements.[H7] Linear fits of data points lying on straight lines following the relation $c_i = c_{k,i} \cdot x + c_{0,i}$ enable to extrapolate an intercept point of both lines that directly yields the CMC value for 16-DSA. In this case it can be shown that the relation:

$$CMC = c_{k,1} \cdot \left(\frac{c_{0,2} - c_{0,1}}{c_{k,1} - c_{k,2}} \right) + c_{0,1} \tag{H.2}$$

holds, if $i = 1$ corresponds to the low concentration line ($c_{16\text{-DSA}} < CMC$) and $i = 2$ corresponds to the high concentration line ($c_{16\text{-DSA}} > CMC$), whereas $c_{k,i}$ and $c_{0,i}$ are the individual slopes and y-axis intercepts, respectively.
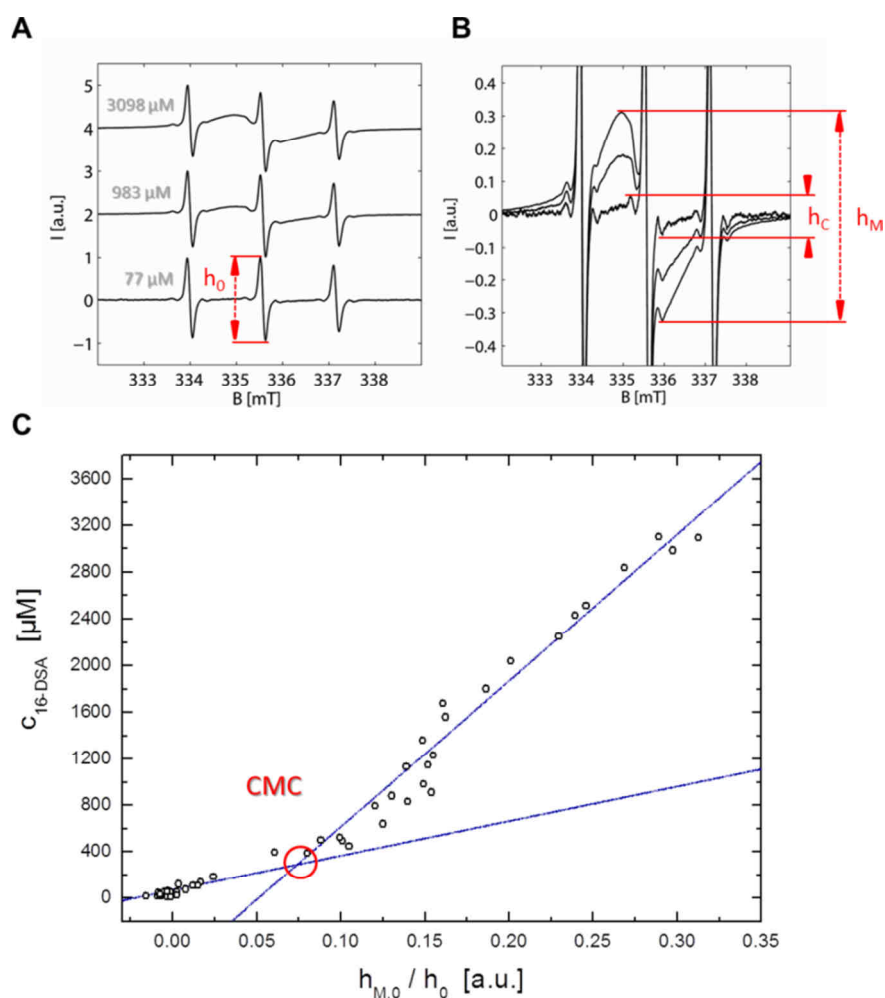
Figure H1 | Graphical determination of the CMC of 16-DSA. Micelle formation propensity gets ever stronger with increasing 16-DSA concentration. Therefore some exemplary CW EPR spectra are shown for 16-DSA concentrations at (**A**) 77 µM, 983 µM and 3098 µM. Here, the center-field line height (h_0) is highlighted in red. (**B**) Due to micelle formation broad spectral characteristics appear that can be characterized with the micelle feature (h_M). Additionally, the ^{13}C signal height (h_C) is subtracted from h_M, so that $h_{M,0} = h_M - h_C$. (**C**) Plot of $c_{16\text{-DSA}}$ versus the ratio $h_{M,0}/h_M$. The intersection region of both lines is defined as the critical micelle concentration (CMC, red circle).

The formation of 16-DSA micelles in 0.137 M DPBS buffer at pH 7.4 and $T = 25°C$ as determined from **Figure H1C** is therefore CMC = (285 ± 29) µM. Most of the subsequent samples were therefore supplied with about 0.2 mM 16-DSA to prevent micelle formation and unnecessary complication of spectral analysis, while a still sufficiently strong signal can be obtained from the sample. However, the determination of an exchange constant k_e leading to a line broadening as described in Molin *et al.*[H6] is not accessible by this method. Upon keeping the DPBS buffer concentration constant the influence of electrolyte concentration on the CMC value[H8] is largely excluded.

H2 | CW EPR Simulations of 16-DSA in DPBS pH 7.4 from 5 – 95°C

An intrinsic reference 16-DSA was simulated alone at a concentration of 0.2 mM in 0.137 M DPBS buffer pH 7.4, while temperature was raised in steps of $\Delta T = 5K$ from $5°C < T < 95°C$. The decrease in rotational correlation times τ_c (see also **Figure H3B**) is mirrored as an increase in relative resonance line intensities with temperature. Particularly, the high-field resonance peak ($m_I = -1$) at about 337.5 mT is strongly affected. Some exemplary simulation parameters can be found in **Table H2**.
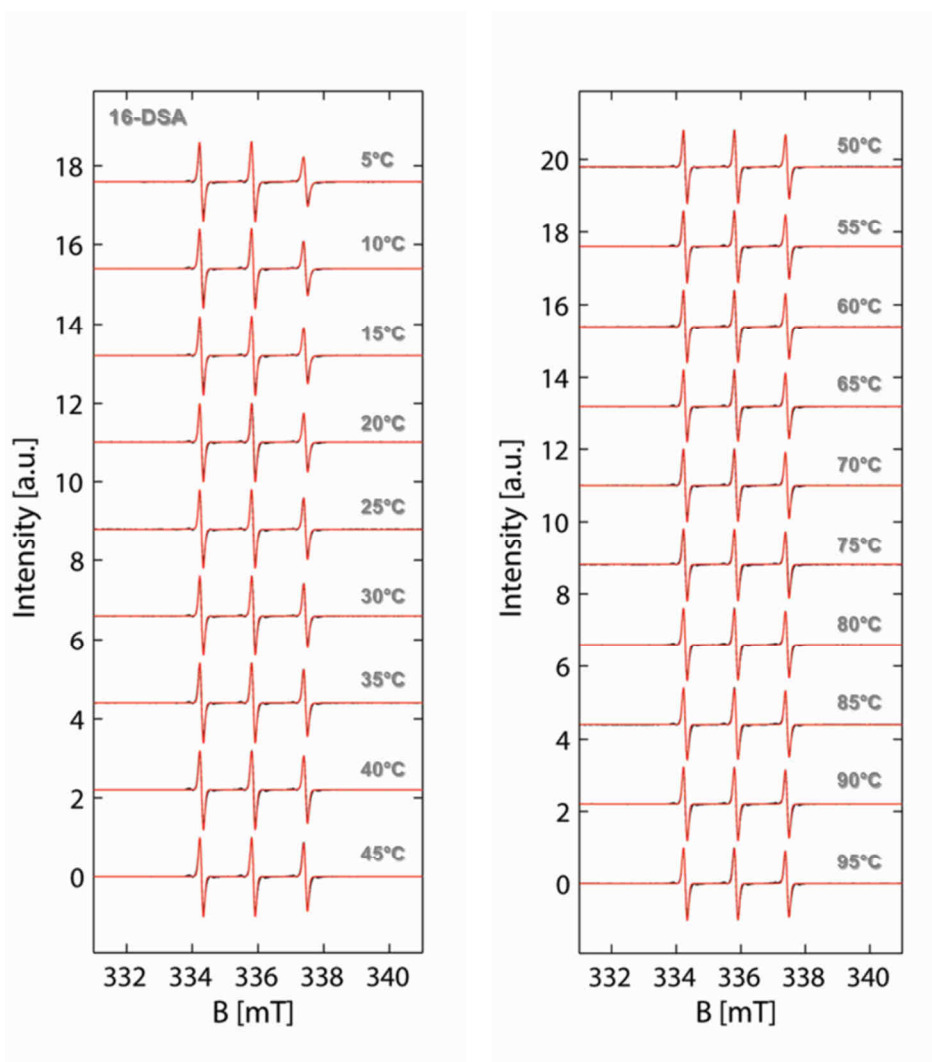
Figure H2 | CW EPR simulations of 16-DSA in DPBS at pH 7.4 from 5 – 95°C. All experimental data (black) have been simulated (red) and are shown in the temperature range from 5 – 95°C.

H3 | Rotational Dynamics (τ_c) of 16-DSA in DPBS at pH 7.4 from 5 – 95°C

As the dynamic environments of macromolecules are observed from a ligands' point of view in this study it is essential to have an in-depth view on the intrinsic behavior of the ligand towards a steady temperature increase. The well-known semi-empirical approach for calculations of rotational correlation times τ_c (here: temperature-dependent) was explicitly figured out in Stone *et al.*[H9] and Waggoner *et al.*[H10] Primarily, common rules of thumb[H11,H12] for this kind of evaluation gave strongly deviating values from simulations. Therefore, explicit formulae and strategies were employed from lineshape analysis as it is also described in **Appendix F1** (equations F.8 and F.9) and specific *g* and *A* tensor values were used from spectral simulations in **Appendix H2**.

Typical values are $\boldsymbol{g} = [g_{xx}\ g_{yy}\ g_{zz}] = [2.0087\ 2.0064\ 2.0025]$ with an optimum rhombic hyperfine coupling tensor $\boldsymbol{A} = [A_{xx}\ A_{yy}\ A_{zz}] = [18.6\ 17.4\ 97.4]$ MHz, or in Gauss: $[6.6\ 6.2\ 34.7]$ G (see also **Table H2**). For further information about magnetic tensors of 16-DSA see also Ge *et al.*[H13] Again, the typical relative line heights h_0, h_{-1} and h_{+1} of the three nuclear transitions ($m_I = -1, 0, +1$) and the center-field linewidth $\Delta B_{0,pp}$ ($m_I = 0$) in isotropic nitroxide spectra (see **Figure H3A**) were used to calculate rotational correlation times τ_c. Results from this analysis are compared to the simulated values of τ_c as presented in **Figure H3B**. No detectable phase transition occurs in the whole observed temperature range.
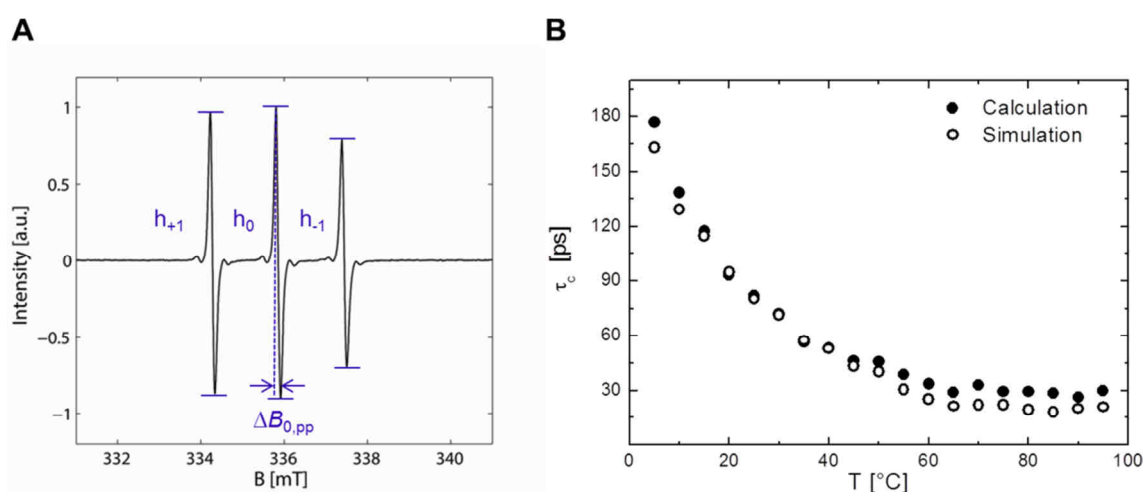
Figure H3 | Lineshape analysis of 16-DSA in DPBS at pH 7.4 from 5 – 95°C. All EPR spectral simulations and calculations of rotational correlation times τ_c of 16-DSA in DPBS pH 7.4 are shown in the temperature range 5 – 95°C. (**A**) Readout scheme from experimental spectra. (**B**) Calculated data are shown in full black circles (●) and simulations in black open circles (○).

As the viscosity of water decreases significantly with temperature,[H14] the temperature-dependent rotational correlation times $\tau_c(T)$ were extracted from spectral simulations according to equation E.1, showing a decrease from 163 ps at 5°C to a plateau of about 20 ps above 65°C. It has been taken into account that the isotropic hyperfine splitting (a_{iso}) is not constant over the whole temperature range. Due to slight changes of water polarity it decreases from 44.50 MHz at 5°C to 44.28 MHz at 95°C (see **Figure H6**), whereas g_{iso} was assumed to be constant at a value of 2.00587 at X-band frequencies.

The lineshape analysis reveals that the plateau originates from the lack of a detectable change of the relative peak heights above 70°C, so 16-DSA is only sensitive to values of $\tau_c > 20$ ps. As the relative viscosity decrease of water can be represented by a polynomial[H14,H15] it was found accordingly that:

$$\frac{\tau_c}{\tau_{c,0}} = a + b\left(\frac{T_0}{T}\right) + c\left(\frac{T_0}{T}\right)^2 + d\left(\frac{T_0}{T}\right)^3 \qquad , \qquad (H.3)$$

as $\tau_c \propto \eta$. Here, $\tau_{c,0} = 80.2$ ps is the rotational correlation time of 16-DSA at $T_0 = 25$°C, with $a = 0.242$, $b = 19.742$, $c = -47.399$ and $d = 28.443$ being the corresponding polynomial coefficients. A fit curve to the $\tau_c/\tau_{c,0}$ curve can be found in **Figure H4**. In principle, equation H.3 facilitates the calculation of rotational correlation times $\tau_c(T)$ and microviscosities $\eta(T)$ for any temperature.
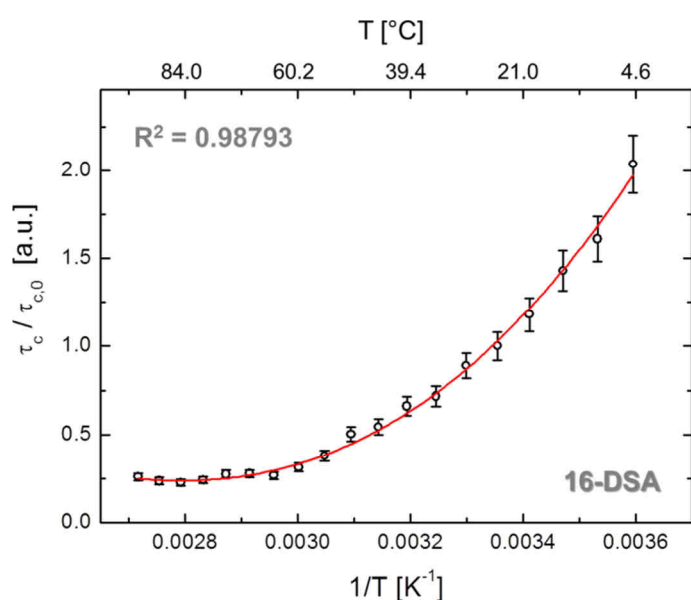
Figure H4 | Temperature behavior of τ_c from 16-DSA in DPBS pH 7.4 in the range from 5°C to 95°C. (A) Relative rotational correlation time $\tau_c/\tau_{c,0}$ of 16-DSA versus inverse temperature T^{-1}. The polynomial fit of $\tau_c/\tau_{c,0}$ versus 1/T (equation H.3) is shown in red. The probe concentration is $c_{16\text{-DSA}} = 0.2$ mM.

In **Chapter 5** it could be shown that the 16-DSA spin probe bears higher intrinsic signal strength than 5-DSA and it is also chemically more stable during phenylhydrazine reduction (**Appendix B5**). The spin probe stability towards temperature is discussed in the next section.

H4 | Accelerated Aging of 16-DSA in DPBS Buffer at pH 7.4

In pharmacological studies, the stability of compounds is of decisive importance for their individual shelf-life and potential toxicity. In order to determine the stability of a chemical compound, the reaction rate can be artificially sped up by increasing the temperature.[H16] Therefore, the stability of a compound can be extrapolated for any temperature of interest. Here, the thermal stability of the 16-DSA nitroxide is tested as its properties are of major interest in this study. All aging experiments are here conducted at identical 16-DSA concentrations (0.4 mM) and pH 7.4 to certify sufficient signal strength at high temperatures. All experimental results of this accelerated aging study on 16-DSA are summarized in **Figure H5**. All high temperature curves ($T_i > 83$°C) were fitted with exponential

functions. However, the linear regression in **Figure H5A** (green) is constructed with the assumption that this exponential function can be described as a power series:

$$e^z = \sum_{p=0}^{\infty} \frac{z^p}{p!} = 1 + z + \frac{z^2}{2} + \frac{z^3}{6} + ... \qquad , \qquad \text{(H.4)}$$

whereas $z = -kt$. The first order expansion is given as $e^{-kt} \approx 1 - kt$ and can be analyzed as a zero-order reaction in a straightforward fashion.[H16] Consistently, all applied CW EPR spectral analyses have been conducted similar to **Appendix B5** utilizing the normalized double integral:

$$\frac{\mathrm{DI}_j(t)}{\mathrm{DI}_{0,j}} = \frac{\iint S_j(t,B)\mathrm{d}^2B}{\iint S_{0,j}(t_0,B)\mathrm{d}^2B} = I_j \cdot e^{-k_j t} + I_{0,j} \qquad \text{(H.5a)}$$

and its linear approximation:

$$\lim_{T \to 0} \frac{\mathrm{DI}_j(t)}{\mathrm{DI}_{0,j}} = I_j(1 - k_j t) \qquad \text{(H.5b)}$$

in case the signal decay curve adopts a linear shape. Here, $I_{0,j}$ is the lower limit of the decay curve, I_j is the maximum value and k_j is the temperature specific rate constant of the signal decay.
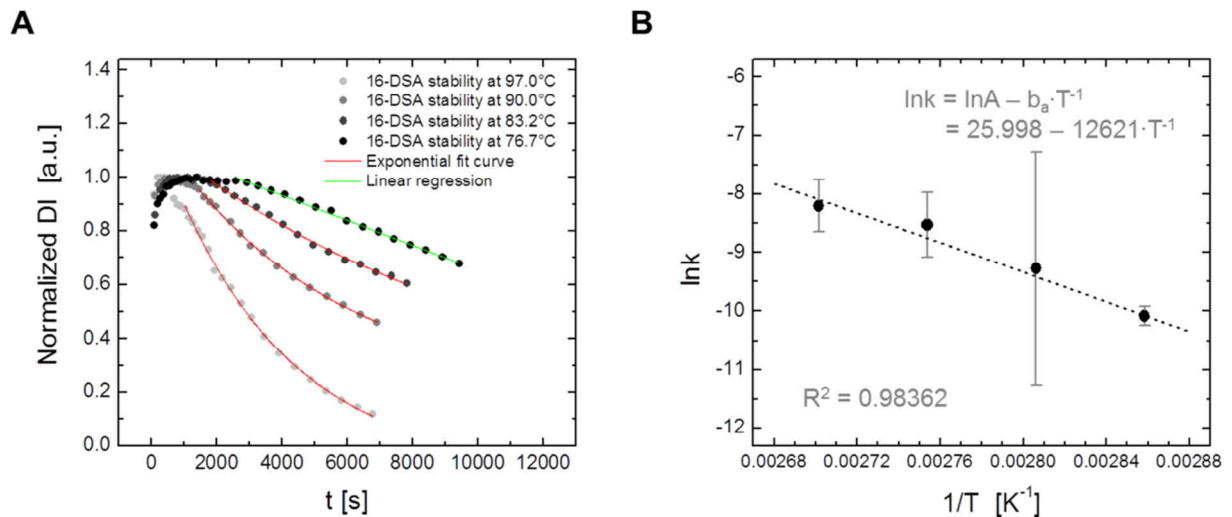
Figure H5 | Accelerated aging of 16-DSA in DPBS buffer at pH 7.4. (**A**) The decay in EPR signal strength (normalized double integral (DI)) is here given as a function of time. The temperatures were set to $T_1 = 76.7°C$ (black), $T_2 = 83.2°C$ (dark gray), $T_3 = 90.0°C$ (gray) and $T_4 = 97°C$ (light gray). Linear regressions are given in green and exponential fit curves are given in red. (**B**) An Arrhenius plot is constructed from the temperature-dependent rate constants of EPR signal decays (black) with linear extrapolations (red). All 16-DSA samples were prepared at concentrations of 0.4 mM to certify sufficient signal strength at high temperatures.

Finally, the four temperature-dependent rate constants are aligned in an Arrhenius plot that exhibits linear behavior (**Figure H5B**). From this plot the activation energy (E_a) of the signal reduction reaction can be obtained from the relation:

$$\ln k = \ln A - \frac{E_a}{R} \cdot \frac{1}{T} = \ln A - \frac{b_a}{T} \qquad , \qquad \text{(H.6)}$$

where $\ln A = 25.999 \pm 2.659$ is the $\ln k$ value for $1/T = 0$ and R is the gas constant. All corresponding fit parameters are given in **Table H1**.

Table H1 | Fit parameters from accelerated aging studies

$j = T$ [°C]	R^2	I_j	$I_{0,j}$	k_j [s^{-1}]
76.7	0.99639	1.11997 ± 0.0045	–	$(4.171 \pm 0.0726) \cdot 10^{-5}$
83.2	0.99631	1.06561 ± 0.13381	$+0.08972 \pm 0.14827$	$(9.3941 \pm 2.0131) \cdot 10^{-5}$
90.0	0.99891	0.99482 ± 0.02035	$+0.20975 \pm 0.03009$	$(1.9820 \pm 0.1281) \cdot 10^{-4}$
97.0	0.99822	1.30517 ± 0.01693	-0.09287 ± 0.02791	$(2.7401 \pm 0.1487) \cdot 10^{-4}$

The slope ($b_a = (12621 \pm 938)$ K) of the linear regression in **Figure H5B** yields the corresponding activation energy ($E_a = R \cdot b_a = (104.9 \pm 7.8)$ kJ/mol). This is in the range of commonly reported values for reduction reactions as observed in EPR spectroscopy.[H17,H18] Another landmark parameter is the half-life ($t_{1/2}$) of the radical that can be obtained from the relation:

$$t_{1/2} = \frac{\ln 2}{k} = \ln 2 \cdot e^{(\frac{b_a}{T} - \ln A)} \qquad . \qquad \text{(H.7)}$$

This expression facilitates predictions about the stability of 16-DSA, so that the half-life is about $t_{1/2} = 100$ days at room temperature and $t_{1/2} = 29$ min at the boiling point of water (~ 100°C).

H5 | Simulations of Temperature-dependent CW EPR Spectra of 16-DSA Probed Substrates

The basis for a temperature-dependent simulation approach was to choose a set of appropriate starting parameters for the g-tensors and hyperfine coupling tensors A for 16-DSA which can be found e.g. in Ge *et al.*[H13] As it was pointed out in **Appendix H3**, optimum rhombic g-tensor values e. g. for subspectrum f at $T = 25$°C can be chosen as $g = [g_{xx} \ g_{yy} \ g_{zz}] = [2.0087 \ 2.0064 \ 2.0025]$ and an optimum rhombic hyperfine coupling tensor would be $A = [A_{xx} \ A_{yy} \ A_{zz}] = [6.6 \ 6.2 \ 34.7]$ G.

In **Table H2** only the traces of the main components are given as isotropic values $g_{iso} = Tr(g) = (g_{xx} + g_{yy} + g_{zz})/3$ and $a_{iso} = Tr(A) = (A_{xx} + A_{yy} + A_{zz})/3$. Rotational correlation times τ_c were calculated as the geometric average of the diffusion tensor elements $D = [D_x \ D_y \ D_z]$ for a 3D-Stokes-Einstein rotational diffusion process (equation E.1). The slightly rhombic diffusion tensor values have been

adjusted to $D_x < D_y \approx D_z$ in the ratio $1 : 6 : 7$ and give an overall axial character to the employed model. Individual subspectra $F_{i,j,k}(B)$ of an individual temperature-specific measurement $S_{j,k}(B)$ have been simulated to yield intrinsic dynamics and population fractions $\phi_{i,j,k}$ by following equation:

$$\phi_{i,j,k} = \frac{A_{S,j,k}}{A_{F,i,j,k}} \cdot \frac{\iint F_{i,j,k}(B)\mathrm{d}^2 B}{\iint S_{j,k}(B)\mathrm{d}^2 B} \quad . \tag{H.8}$$

Here, the scalar values of $A_{S,j,k}$ and $A_{F,i,j,k}$ are normalization constants from the double integration process. Therefore, the EasySpin software package was used,[H19] which comprises routines that work according to the theory of slow tumbling nitroxides.[H20,H21] Hence, $S_{j,k}(B)$ is the complete experimental spectrum k at temperature j that can be reconstructed with $S_{i,j,k}(B)_{\mathrm{sim}}$ by N optional components $F_{i,j,k}(B)$ as f, b_1, b_2, a and g. This is facilitated by following relation:

$$S_{i,j,k}(B)_{\mathrm{sim}} = \sum_i^N \phi_{i,j,k} \cdot \iint F_{i,j,k}(B) = A_{S,j,k} \sum_i^N \frac{1}{A_{F,i,j,k}} \frac{\iint F_{i,j,k}(B)\mathrm{d}^2 B}{\iint S_{j,k}(B)\mathrm{d}^2 B} \quad . \tag{H.9}$$

The according simulation curves $S_{i,j,k}(B)_{\mathrm{sim}}$ are shown in **Figure H2**, **Figure H7–H10** and **Figure H14** in red. All potential emerging subspectra $F_{i,j,k}(B)$ are exemplary shown in **Figure 10.2B** in gray.

From these EPR spectroscopic simulations the errors for dynamic fractions $\Delta\phi_{i,j,k}$ have been imposed generously with $\Delta a_{\mathrm{iso}} = 0.036$ MHz and $\Delta\tau_{\mathrm{c}} = 8$ %. The error of g_{iso} was determined by a Mn-Standard sample (Magnettech GmbH) to be $\Delta g_{\mathrm{iso}} = 4.4 \cdot 10^{-4}$, so the values given for g_{iso} in **Table H2** are only of a qualitative character. The simulated a_{iso} values were also corrected for all values in **Table H2** with an intrinsic experimental field sweep correction factor $k_{\mathrm{SW}} = 0.99592$ similar to **Appendix F1**.

For more detailed values of g and A, spectra should be measured at Q-band or W-band frequencies. The Euler angle β is the tilt angle between the molecular coordinate system (D_r) and the coordinate system of the magnetic parameters of the nitroxide moiety (g,A).[H19,H22] This value was set to $\beta = 45°$ throughout, however, the validity of the β-values can only be considered as of purely qualitative nature. An ample collection of representative EPR simulation parameters for all spectral components $F_{i,j,k}(B)$ as f, b_1, b_2, a and g, as well as for the fractions of $\phi_{i,j,k}$ as g_{iso}, a_{iso} and τ_{c} is given in **Table H2** for $T = 25°$C. The gel fraction (g) only appears for $T \geq 45°$C and therefore only the value from the simulation at 95°C is shown where g is most abundant at a fractional value of $\phi_{i,j,k} = 13.14$ %.

Furthermore, a graphical representation of temperature-dependent $a_{\mathrm{iso,sim}}$ values that 16-DSA may adopt in DPBS buffer pH 7.4 and in solution with C_3S_{32}, C_6S_{32} and $C_{11}S_{14}$ polymers in the temperature range from $5 - 95°$C is given in **Figure H6**. Temperature-dependent τ_{c} values can be found in **Figure H3B**, **Figure H4** and **Figure 10.4A**.
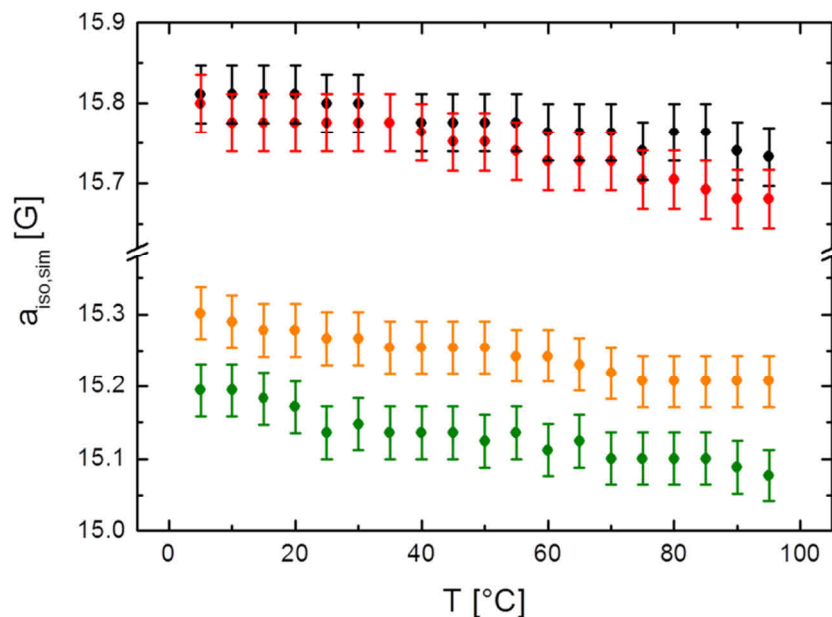
Figure H6 | Temperature-dependent a_{iso} values of 16-DSA interacting with polymers C_nS_m. Plot of simulated a_{iso} values for fractions f, b_1 and b_2 as observed from 16-DSA. Here the fraction f of 16-DSA in DPBS-buffer at pH 7.4 (black), fraction f of polymer C_3S_{32} in water (red), fraction b_1 (and b_2) of polymer C_6S_{32} in water (orange) and fraction b_1 (and b_2) of polymer $C_{11}S_{14}$ (green) are shown from simulations in the temperature range from 5 – 95°C. Due to the small differences of a_{iso} in unique fractions and the large differences in a_{iso} between the polymers, the y-axis has been cut in between 15.3 G and 15.7 G.

In the following, all CW EPR spectral simulations of 16-DSA interacting with the amphiphilic core-shell polymers are presented in **Figure H7–H10** with representative parameters at $T = 25°C$ given in **Table H2**.

Table H2 | Simulation parameters for spectral components $F_{i,j,k}(B)$ at $T = 25°C$

Sample	$F_{i,j,k}(B)$	$\phi_{i,j,k}$ [%]	g_{iso}	a_{iso} [MHz]	a_{iso} [G]	τ_c [ns]
16-DSA	f	100.000	2.00587	44.29	15.80	0.080
C_3S_{32}	f	32.995	2.00587	44.23	15.78	0.117
	a	67.005	2.00593	–	–	–
(95°C)	g	13.140	2.00603	40.22	14.35	0.472
C_6S_{32}	f	3.321	2.00587	44.26	15.79	0.136
	b_1	57.671	2.00590	42.80	15.27	6.618
	b_2	39.008	2.00590	42.80	15.27	1.989
$C_{11}S_{14}$	f	0.270	2.00587	44.23	15.78	0.080
	b_1	21.956	2.00593	42.44	15.14	6.614
	b_2	77.774	2.00593	42.44	15.14	2.556
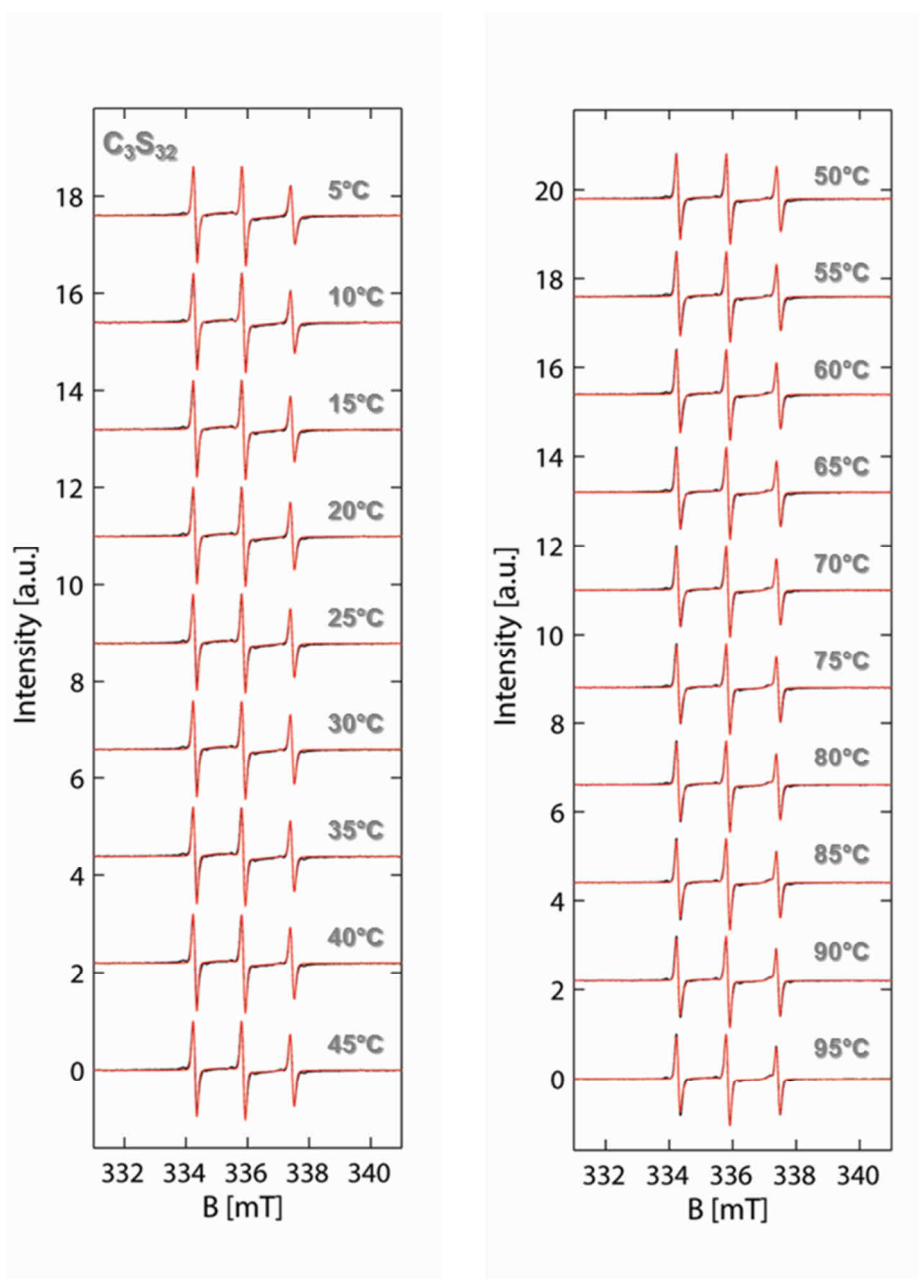
Figure H7 | Polymer C$_3$S$_{32}$ loaded with 16-DSA at 5 – 95°C. All EPR spectral simulations of polymer C$_3$S$_{32}$ loaded with 16-DSA are shown in the temperature range from 5 – 95°C. Experimental data are shown in black and simulations in red.
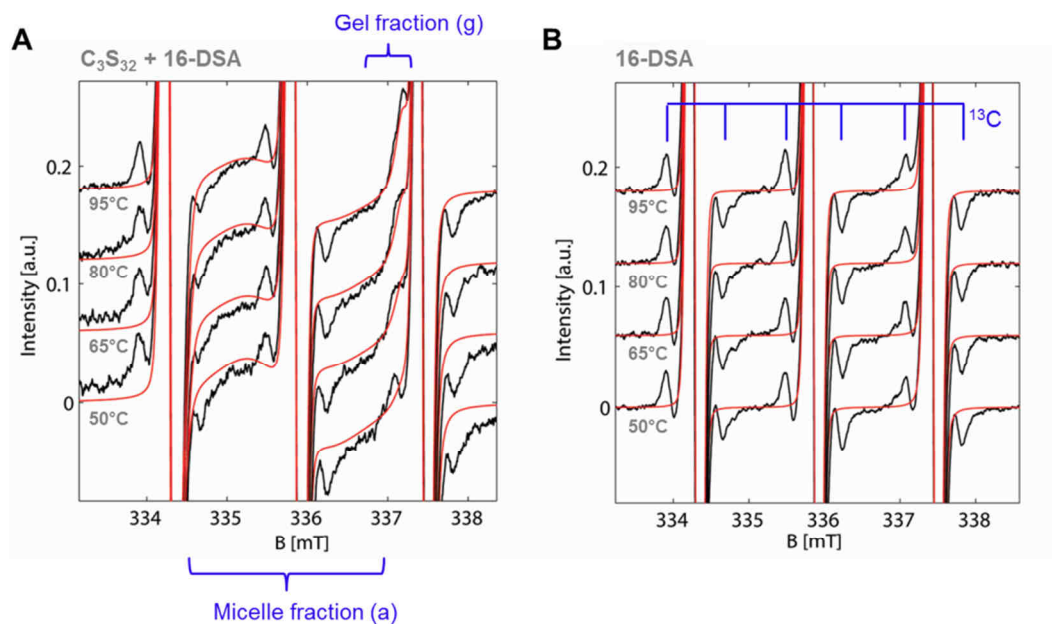
Figure H8 | Polymer C₃S₃₂ loaded with 16-DSA in comparison with pure 16-DSA at $T \geq 50°C$. Closeup view of selected EPR spectral simulations of the C_3S_{32} polymer loaded with 16-DSA and 16-DSA alone in DPBS-buffer at pH 7.4. (**A**) The 16-DSA-probed polymer C_3S_{32}, comprising micelle fractions (*a*) and temperature-induced gel fractions (*g*) are shown for $T \geq 50°C$. (**B**) 16-DSA alone in DPBS pH 7.4 at exactly the same temperatures ($T \geq 50°C$). Experimental data are shown in black and simulations are shown in red. Decisive spectral features as micelle fractions (*a*), gel fractions (*g*) in (A) and ^{13}C-satellite signals from the doxyl group itself in (B) are highlighted in blue.
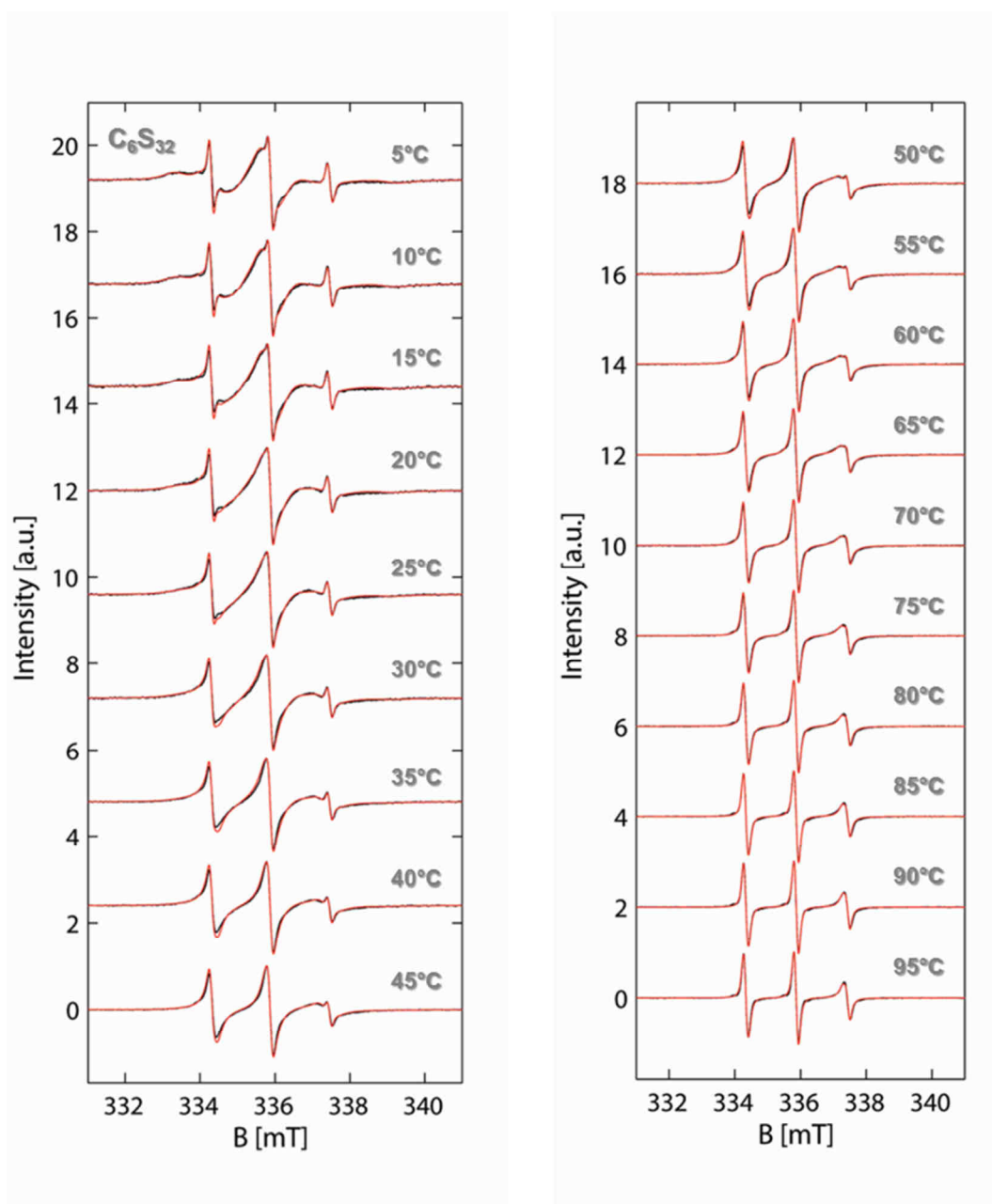
Figure H9 | Polymer C$_6$S$_{32}$ loaded with 16-DSA at 5 – 95°C. All EPR spectral simulations of polymer C$_6$S$_{32}$ loaded with 16-DSA are shown in the temperature range from 5 – 95°C. Experimental data are shown in black and simulations in red.
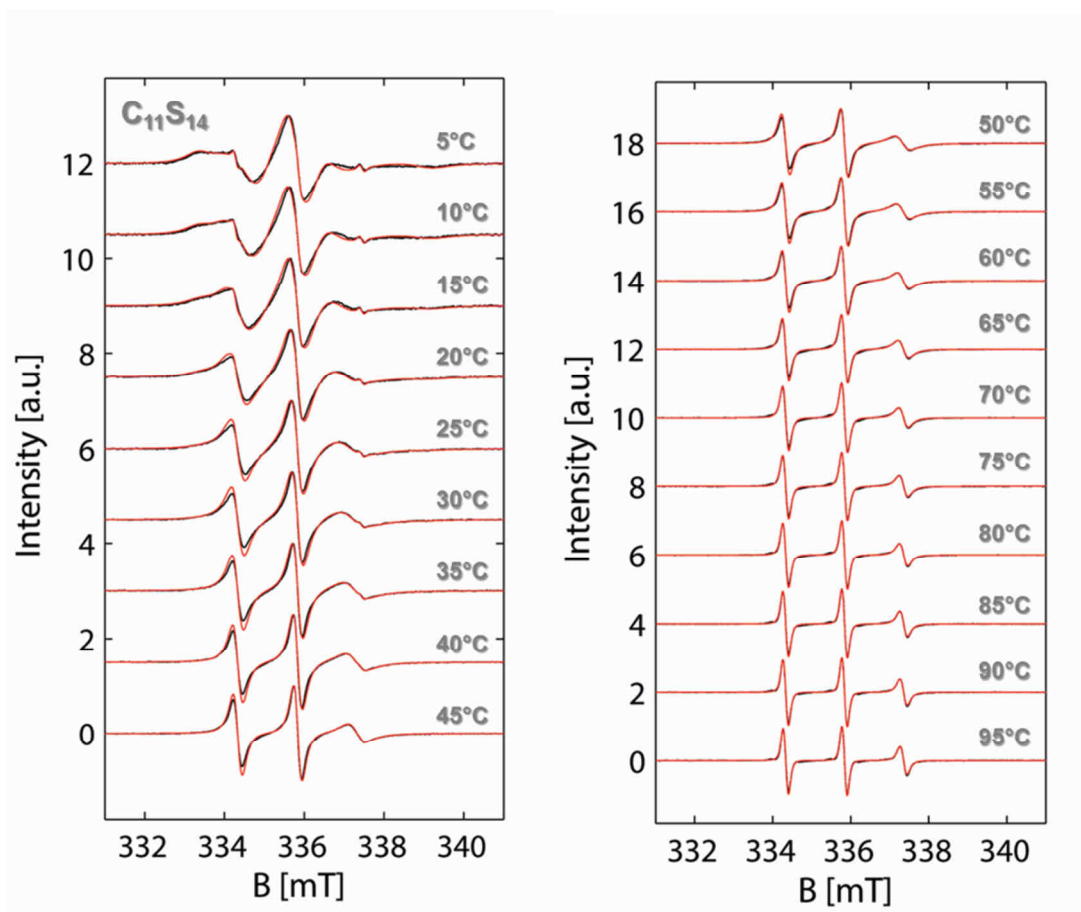
Figure H10 | Polymer C$_{11}$S$_{14}$ loaded with 16-DSA at 5 – 95°C. All EPR spectral simulations of polymer C$_{11}$S$_{14}$ loaded with 16-DSA are shown in the temperature range from 5 – 95°C. Experimental data are shown in black and simulations in red.

H6 | Particle Size Distributions from DLS Measurements
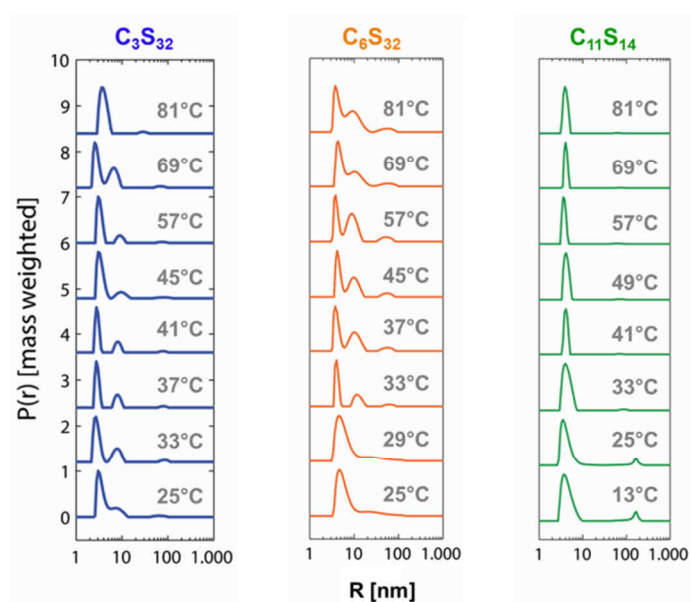
Figure H11 | Particle size distributions of all three polymer solutions for decisive temperatures. While C$_3$S$_{32}$ and C$_{11}$S$_{14}$ exhibit vanishing clusters above 50 nm with increasing temperature, the larger-sized particles get slightly more prominent for C$_6$S$_{32}$ with increasing temperature as also mirrored in the count rates in **Figure 10.4C**.

H7 | Temperature Stability of 16-DSA in Polymer Solutions – Mild Scavenger Activity

As the spin probe might be reduced to an EPR-silent fatty acid species during temperature increase as shown in **Appendix H4**, it is tested whether the signal strength is decreased differently in each polymer solution. A quantitative approach in this case again requires double integration of each spectrum $S_{j,k}(B)$ and a normalization step that is referenced to the maximum intensity. The relative signal intensity I_{rel} is therefore given as:

$$I_{rel} = \frac{\iint S_{j,k}(B)\,\mathrm{d}^2 B}{\iint S_{j,k}(B)_{max}\,\mathrm{d}^2 B} \approx \frac{h_0(T)}{h_0} \qquad . \qquad (H.10)$$

As successful double integration is strongly dependent on SNR, experimental spectra of 16-DSA alone in DPBS pH 7.4 were only evaluated by their temperature-dependent center-field peak height ($m_I = 0$, $h_0(T)$, see also **Figure H3**). The duration of collecting a set of 19 spectra over the temperature range of 5 to 95°C is about two hours for each sample. A strong time dependence as the cause for the different traces in **Figure H12** is therefore excluded and was not further investigated. Due to the principally fast exchange of ligand with polymer and solution as compared to the duration of a single experiment (~ 5 min), it is safely assumed that only the signal intensity decreases and not the intensity of an individual fraction $F_{i,j,k}(B)$. This is further substantiated as also the spectral shape remains the same. Apparently, reduction of the 16-DSA signal gets stronger when the C_n spacer length increases.
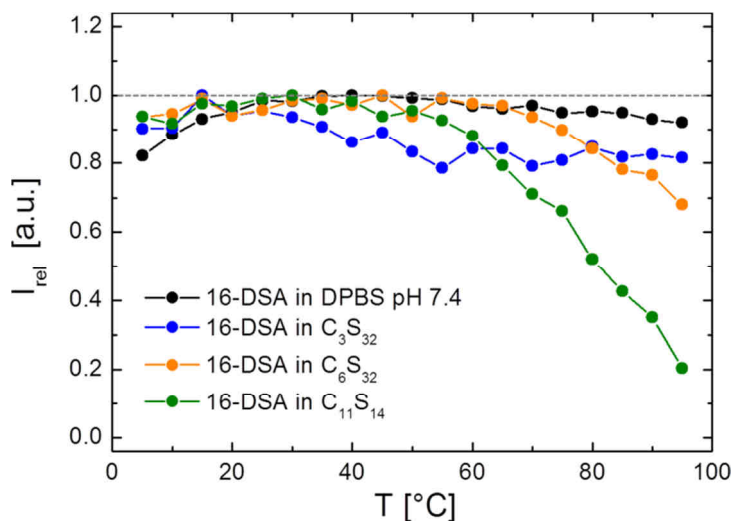
Figure H12 | Reduction of the relative signal intensity I_{rel} of 16-DSA and 16-DSA-probed polymer solutions. The different polymers are color-coded in full circles (●) according to the scheme in the main manuscript with free 16-DSA (black), 16-DSA-probed C_3S_{32} (blue), C_6S_{32} (orange) and $C_{11}S_{14}$ (green). Underlying CW EPR spectra are identical with those that were simulated. The gray dotted line indicates 100% signal strength. The 16-DSA concentrations of the three individual samples were 147 ± 15 µM (16-DSA alone in DPBS pH 7.4), 105 ± 5 µM (C_3S_{32}), 160 ± 4 µM (C_6S_{32}) and 204 ± 6 µM ($C_{11}S_{14}$) as it is also shown in **Figure 10.3**.

For polymer C_3S_{32}, the signal reduction of 16-DSA at high temperatures is $\Delta I_{rel} = 19.2\%$, for polymer C_6S_{32} $\Delta I_{rel} = 32.1\%$, and for polymer $C_{11}S_{14}$ it is 79.6%. 16-DSA alone is only reduced for about 8% in DPBS buffer. Reversibility studies are thus not possible for the spin probed polymers due to this radical scavenger behavior.

H8 | Results from MD Simulations of Modeled C_nS_m Structures

A straightforward analysis of three modeled molecular C_nS_m structures (**Figure H13**) reveals several properties that substantiate findings from DLS and EPR spectroscopy. All corresponding results from simulations with the YASARA Structure software[H23] can be found in **Table H3**.
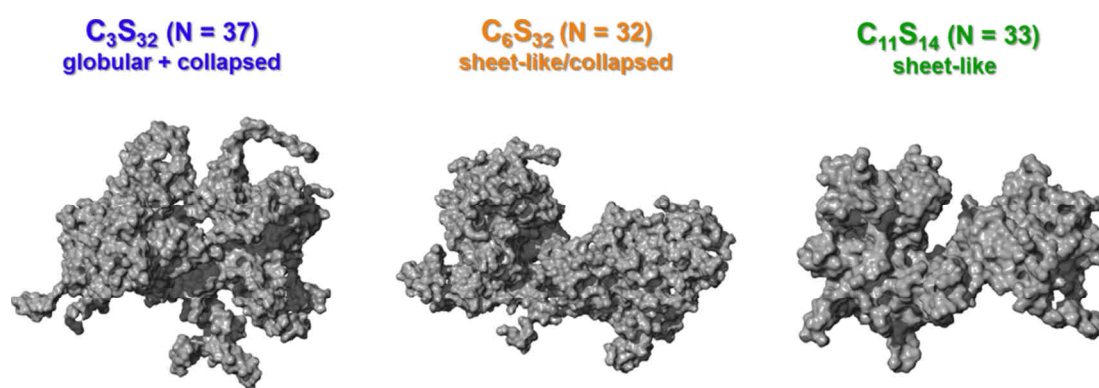
Figure H13 | Molecular models of C_nS_m polymers. C_3S_{32}, C_6S_{32} and $C_{11}S_{14}$ polymers were modeled with similar degrees of polymerization N. The snapshots are taken from the end of the simulation after about $t_{MD} = 12 – 13$ ns runtime at $T = 298K$.

Table H3 | Parameters from structural analysis of the molecular models in **Figure H13**

Parameter	Symbol[a,b]	C_3S_{32}	C_6S_{32}	$C_{11}S_{14}$
Model polymerization	$N_{M,k}$	37	32	33
Molecular weight	$MW_{M,k}$ [kDa]	99.2	87.2	48.2
Radius of gyration	$R_{G,M,k}$ [nm]	3.59	3.84	2.80
Molecular volume	$V_{M,k}$ [nm³]	99.983	89.361	52.073
Density	$MW_{M,k}/V_{M,k}$ [kDa nm⁻³]	0.9922	0.9758	0.9256
compactness	$R_{G,M,k}/MW_{M,k}$ [nm kDa⁻¹]	0.03619	0.04403	0.0580
Diameter	$d_{M,k}$ [nm]	6.7 – 9.5	4.0 – 7.6	2.0 – 6.8

[a]index M refers to the modeled nature of the underlying structures and k refers to the type of polymer. [b]Values were extracted from YASARA Structure software.[H23]

H9 | CW EPR Spectra for Scatchard Plot Construction of Polymers C₆S₃₂ and C₁₁S₁₄

Construction of a Scatchard plot[H24] is best achieved with knowledge about the real concentrations of ligand. The ligand concentrations were obtained by double integration as described in **Appendix E3**, however, in **Figure H14** the nominal 16-DSA concentrations are shown from sample preparation. The real ligand concentration values are as follows: 100 µM = 99.8 µM, 200 µM = 201 µM, 300 µM = 327 µM, 400 µM = 438 µM and 500 µM = 562 µM. Those real concentration values were used for both sets of Scatchard plot spectra, as double integration only worked partially for spectra from polymer C₆S₃₂ (**Figure H14A**) due to a slightly higher level of noise (see lowest trace at 100 µM). Sample preparation of both sets of spectra was moreover completely identical and all experiments were performed at $T = 25$°C.
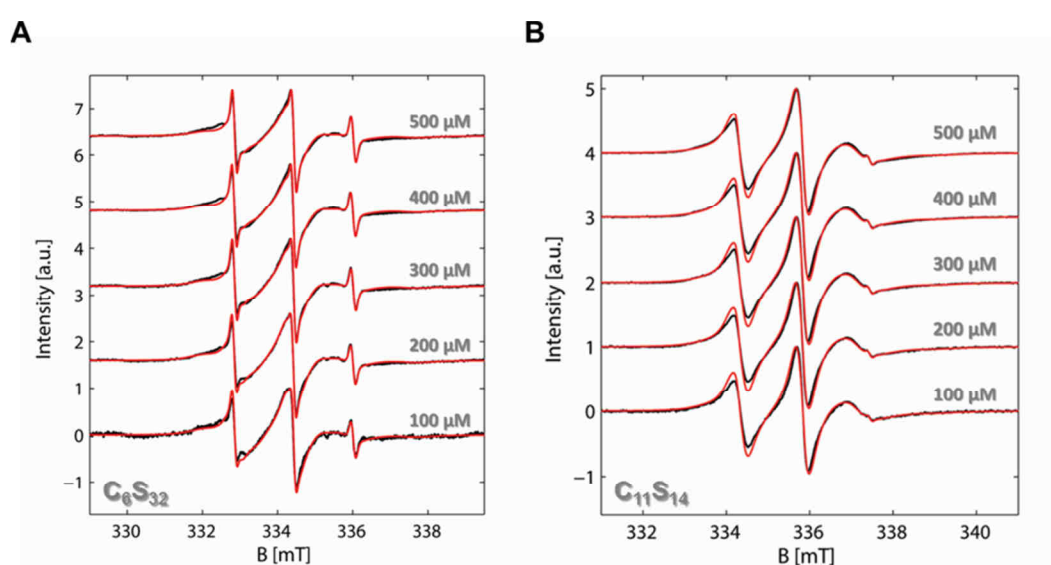
Figure H14 | Simulations of CW EPR spectra for Scatchard plot construction. (**A**) Stacked representation of C₆S₃₂ loaded with 16-DSA. (**B**) Stacked representation of C₁₁S₁₄ loaded with 16-DSA. The nominal 16-DSA concentrations are given in gray [µM]. Experimental spectra at $T = 25$°C are shown in black, whereas spectral simulations $S_{i,j,k}(B)_{sim}$ are again shown in red.

H10 | Explicit Derivation of Equation 10.8

The combination of a receptor R with ligand L towards a receptor-ligand complex RL is best described by the chemical equation:[H25]

$$R + L \xrightleftharpoons[k_d]{k_a} RL \quad .$$
(H.11)

The reaction rate constants facilitate the description of either ligand association (k_a), or dissociation (k_d). The total receptor concentration $[R]_{t,k}$ and the total ligand concentration $[L]_{t,k}$ are described as:

$$[R]_{t,k} = [RL]_{j,k} + [R]_{f,j,k}$$
(H.12)

$$[L]_{t,k} = [RL]_{j,k} + [L]_{f,j,k} \quad ,$$
(H.13)

where $[RL]_{j,k}$ is the ligand-receptor complex concentration, $[R]_{f,j,k}$ is the concentration of vacant receptors and $[L]_{f,j,k}$ is the concentration of free ligand. The law of mass action gives an equilibrium association constant $K_{A,j,k}$ by the relation:

$$K_{A,j,k} = \frac{\prod [x]_{p,i,j,k}}{\prod [x]_{e,i,j,k}} = \frac{[RL]_{j,k}}{[R]_{f,j,k}[L]_{f,j,k}} \quad .$$
(H.14)

The product of $[x]_{p,i,j,k}$ can be considered as the molecular complex $[RL]_{j,k}$ when educts $[x]_{e,i,j,k}$ described as $[R]_{f,j,k}$ and $[L]_{f,j,k}$ associate. With equation H.12 and H.13, equation H.14 can be rewritten for the case of tight binding interactions where $[L]_{f,j,k} << [L]_{t,k}$ and the value of the dissociation constant $K_{D,j,k}$ is in the range of the total receptor concentration ($[R]_{t,k} \approx K_{D,j,k} = K_{A,j,k}^{-1}$). Therefore, the $K_{A,j,k}$ value is initially expressed as:[H25]

$$K_{A,j,k} = \frac{[RL]_{j,k}}{([R]_{t,k} - [RL]_{j,k}) \cdot ([L]_{t,k} - [RL]_{j,k})} \quad .$$
(H.15)

The receptor-ligand complex concentration $[RL]_{j,k}$ is now termed as the bound fraction of ligand $[L]_{b,j,k}$. For this derivation no differentiation between Brownian and free diffusion of ligand has to be taken into account. Generally, $[L]_{b,j,k}$ is the sum of $[L]_{b1,j,k}$ and $[L]_{b2,j,k}$. The total receptor concentration $[R]_{t,k}$ is the product of the polymer concentration $c_{P,k}$ and the number of ligand binding sites $N_{E,k}$, so that:

$$[R]_{t,k} = N_{E,k} c_{P,k} \quad .$$
(H.16)

Collecting the aforementioned assumptions, equation H.15 can be rewritten as:

$$K_{A,j,k} = \frac{[L]_{b,j,k}}{(N_{E,k}c_{P,k} - [L]_{b,j,k}) \cdot ([L]_{t,k} - [L]_{b,j,k})}$$

$$= \frac{1}{\left(\dfrac{N_{E,k}c_{P,k}}{[L]_{b,j,k}} - 1\right) \cdot \left(\dfrac{[L]_{t,k}}{[L]_{b,j,k}} - 1\right)} \qquad . \qquad \text{(H.17)}$$

Expanding the right-hand side of equation H.17 leads to the expression:

$$K_{A,j,k} = \frac{1}{\left(\dfrac{N_{E,k}c_{P,k}[L]_{t,k}}{[L]_{b,j,k}} - N_{E,k}c_{P,k} - [L]_{t,k} + [L]_{b,j,k}\right)} \qquad \text{(H.18)}$$

that further simplifies to:

$$K_{A,j,k} = \frac{1}{\left(\dfrac{N_{E,k}c_{P,k}[L]_{t,k}}{[L]_{b,j,k}} - N_{E,k}c_{P,k} - [L]_{f,j,k}\right)}$$

$$= \frac{1}{\left([R]_{t,k}\left(\dfrac{[L]_{t,k}}{[L]_{b,j,k}} - 1\right) - [L]_{f,j,k}\right)} \qquad , \qquad \text{(H.19)}$$

when applying equation H.13 in the form of $[L]_{t,k} = [L]_{b,j,k} + [L]_{f,j,k}$ (equation H.19 corresponds to equation 10.8 in the main manuscript). The $[R]_{t,k}$ value can be calculated from the product of $N_{E,k}$ as determined from according Scatchard plots (see **Figure 10.5**) and $c_{P,k}$ that is already known from sample preparation (see **Table 10.3**). The total ligand concentration $[L]_{t,k}$ is obtained from double integration and therefore $[L]_{f,j,k}$, as well as $[L]_{b,j,k}$ can be obtained from the fractions $\phi_{i,j,k}$ emerging from EPR spectral simulations in the form of $\phi_{i,j,k} \cdot [L]_{t,k}$ as it is described in **Chapter 7.4.2**.

H11 | Fit Parameters for Temperature-dependent Equilibria

Extrapolation of $\ln K_{A,j,k}$ curves from equation 10.8

The linear regression of decisive parts from the van't Hoff plots of $\ln K_{A,j,k}$ in **Figure 10.10A** was conducted with following equation:

$$y_{j,k} = a_{j,k} + b_{j,k} \cdot x = \frac{\Delta S^{\circ}_{A,j,k}}{R} - \frac{\Delta H^{\circ}_{A,j,k}}{R} \cdot \frac{1}{T} = \ln K_{A,j,k} \qquad , \qquad \text{(H.20)}$$

so that $\Delta H^\circ_{A,j,k} = -R \cdot b_{j,k}$ and $\Delta S^\circ_{A,j,k} = R \cdot a_{j,k}$ where R is the universal gas constant. The fit curves can be found in **Figure H15A–C**. The fit parameters $p_1 = a_{j,k}$ and $p_2 = b_{j,k}$ are given together with their errors ($\Delta p_1 = \Delta a_{j,k}$ and $\Delta p_2 = \Delta b_{j,k}$) in **Table H4** and error limits for thermodynamic quantities θ are calculated according to the propagation of uncertainty:

$$\Delta \theta = \sum_i \left| \frac{\partial \theta}{\partial p_i} \right| \cdot \Delta p_i \qquad , \tag{H.21}$$

so that:

$$\Delta \Delta H^\circ_{A,j,k} = -\Delta b_{j,k} R \qquad , \tag{H.22}$$

$$\Delta \Delta S^\circ_{A,j,k} = \Delta a_{j,k} R \tag{H.23}$$

and

$$\Delta \Delta G^\circ_{A,j,k} = R \cdot \left(\Delta b_{j,k} + T \Delta a_{j,k} \right) \qquad . \tag{H.24}$$

Table H4 | Fit parameters $a_{j,k}$ and $b_{j,k}$ for $\ln K_{A,j,k}$

Polymer k	j	R^2	$a_{j,k} \pm \Delta a_{j,k}$	$b_{j,k} \pm \Delta b_{j,k}$
C_6S_{32}	≤ 25	0.98411	13.90997 ± 0.22731	-1031.69593 ± 65.41604
	≥ 55	0.99540	0.69999 ± 0.22443	3264.23482 ± 78.46214
$C_{11}S_{14}$	≤ 45	0.99894	19.87061 ± 0.08536	-2108.28452 ± 24.31021

Extrapolation of $\ln K_{IC,j,k}$ curves from equations 10.14 and 10.18

The polynomial (equation 10.14) and exponential (equation 10.18) curve regressions of the van't Hoff plots of $\ln K_{IC,j,k}$ in **Figure 10.10B** are shown in **Figure H15D–E** and corresponding fit parameters are shown in **Table H5**. Reliable error limits could not be determined from the applied multi-parameter non-linear curve fits.

Table H5 | Fit parameters α_z and κ_y for $\ln K_{IC,j,k}$

Polymer k	j	fit	R^2	z	y	α_z	κ_y
C_6S_{32}	$5-95$	Poly.	0.99407	1		303.78682	–
				2		-473108.6302	–
				3		$2.68781 \cdot 10^8$	–
				4		$-6.60985 \cdot 10^{10}$	–
				5		$5.95024 \cdot 10^{12}$	–
$C_{11}S_{14}$	$5-45$	Exp.	0.99587		1	–	$3.819 \cdot 10^8$
					2	–	$-1.68608 \cdot 10^{-4}$
					3	–	0.29148

H12 | Fit Curves from Thermodynamic Parameters K_A and K_{IC}

The original curve fits (red) from equation 10.10 (**Figure H15A–C**), equation 10.14 (**Figure H15D**) and equation 10.18 (**Figure H15E**) of the main manuscript are shown as the basis for all consequent thermodynamic analyses in the main text.
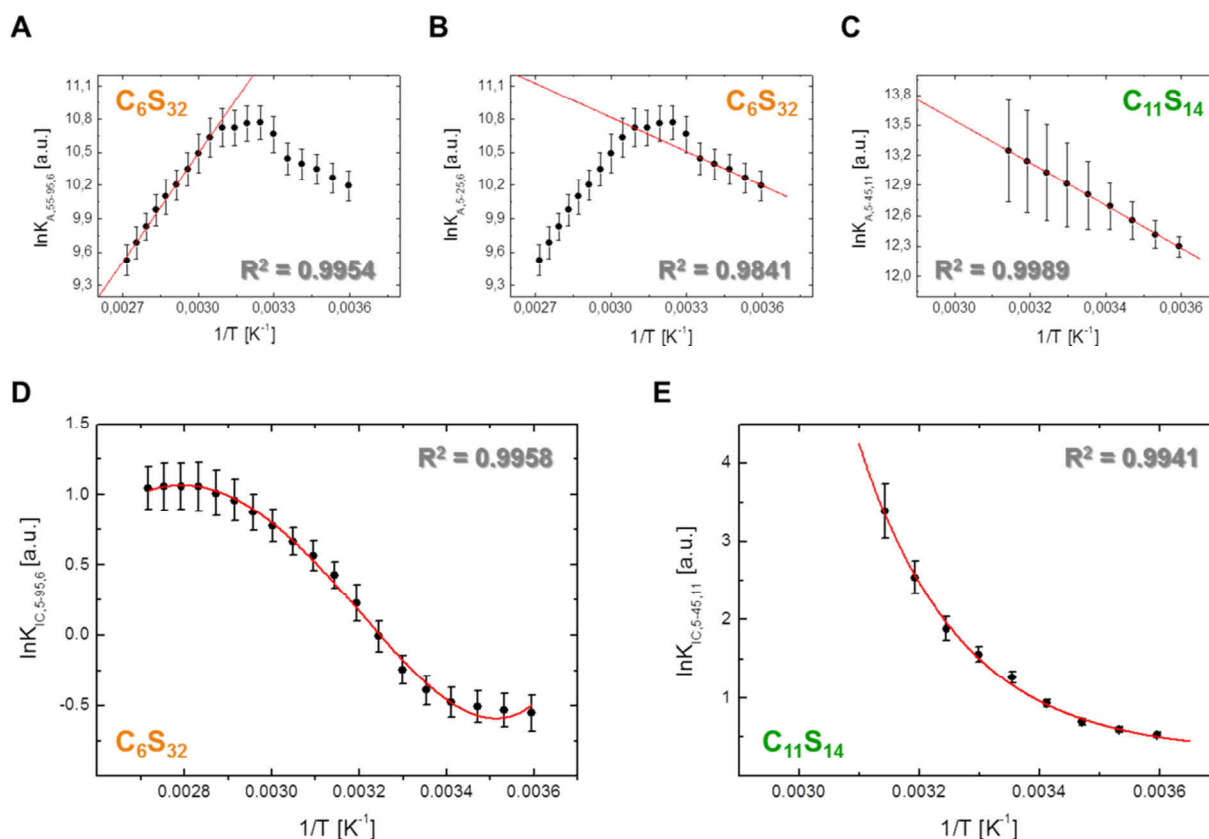
Figure H15 | Curve fits for $\ln K_{A,j,k}$ and $\ln K_{IC,j,k}$. (**A**) Linear fit of $\ln K_{A,55-95,6}$ of polymer C_6S_{32} in the temperature range from 55 – 95°C. (**B**) Linear fit of $\ln K_{A,5-25,6}$ of polymer C_6S_{32} in the temperature range from 5 – 25°C. (**C**) Linear fit of $\ln K_{A,5-45,11}$ of polymer $C_{11}S_{14}$ in the temperature range from 5 – 45°C. (**D**) Polynomial fit of $\ln K_{IC,5-95,6}$ of polymer C_6S_{32} in the temperature range from 5 – 95°C. (**E**) Exponential fit of $\ln K_{IC,5-45,11}$ of polymer $C_{11}S_{14}$ in the temperature range from 5 – 45°C. Calculated data points and error bars are shown in black, fit curves are shown in red. All corresponding fit parameters can be found in **Table H4** and **Table H5**.

H13 | DSC Curves from Polymers C_6S_{32} and $C_{11}S_{14}$ Loaded with 16-DSA
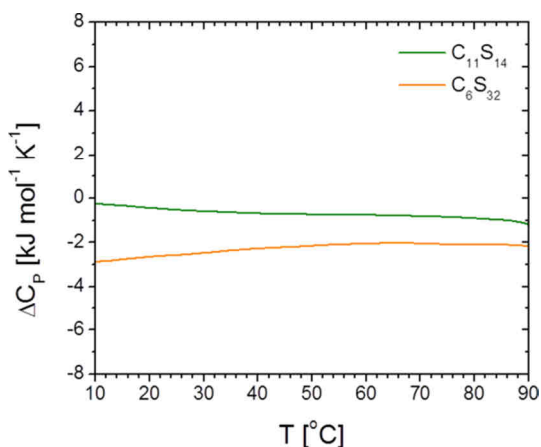
Figure H16 | DSC thermograms of both C_nS_m polymers loaded with 16-DSA. This graph shows the differential heat capacity per mol of macromonomer (ΔC_P) of $C_{11}S_{14}$ (1.66 mM + 29.1 μM 16-DSA, green) and C_6S_{32} (1.78 mM + 18.4 μM 16-DSA, orange). The presented heat capacity traces are corrected for buffer and 16-DSA contributions.

H14 | References

[H1]   F. Wu, B. J. Gaffney, *Biochemistry* **2006**, *45*, 12510–12518.

[H2]   A. M. Wasserman, V. A. Kasaikin, V. P. Timofeev, *Spectrochim Acta, Part A* **1998**, *54*, 2295–2308.

[H3]   A. Lewinska, K. A. Wilk, A. Jezierski, *J Solution Chem* **2012**, *41*, 1210–1223.

[H4]   M. Chin, P. Somasundaran, *Photochem Photobiol* **2014**, *90*, 455–462.

[H5]   S. J. Rehfeld, D. J. Eatough, W. Z. Plachy, *J Lipid Res* **1978**, *19*, 841–849.

[H6]   Y. N. Molin, K. M. Salikhov, K. I. Zamaraev, *Spin exchange: Principles and applications in chemistry and biology*. Springer-Verlag: Berlin, Heidelberg, **1980**.

[H7]   H. D. Dörfler, *Grenzflächen und kolloid-disperse Systeme: Physik und Chemie*. Springer-Verlag: Berlin, Heidelberg, **2002**.

[H8]   E. Fuguet, C. Rafols, M. Roses, E. Bosch, *Anal Chim Acta* **2005**, *548*, 95–100.

[H9]   T. J. Stone, T. Buckman, P. L. Nordio, H. M. McConnell, *Proc Natl Acad Sci USA* **1965**, *54*, 1010–1017.

[H10]   A. S. Waggoner, O. H. Griffith, C. R. Christensen, *Proc Natl Acad Sci USA* **1967**, *57*, 1198–1205.

[H11]   F. Lottspeich, J. W. Engels, *Bioanalytik*. Spektrum Akademischer Verlag: Heidelberg, **2009**.

[H12]   N. Beghein, L. Rouxhet, M. Dinguizli, M. E. Brewster, A. Arien, V. Preat, J. L. Habib, B. Gallez, *J Controlled Release* **2007**, *117*, 196–203.

[H13]   M. Ge, S. B. Rananavare, J. H. Freed, *Biochim Biophys Acta, Gen Subj* **1990**, *1036*, 228–236.

[H14]   J. Kestin, M. Sokolov, W. A. Wakeham, *J Phys Chem Ref Data* **1978**, *7*, 941–948.

[H15]   J. Kestin, N. Imaishi, S. H. Nott, J. C. Nieuwoudt, J. V. Sengers, *Physica A* **1985**, *134*, 38–58.

[H16]   K. C. Waterman, R. C. Adami, *Int J Pharm* **2005**, *293*, 101–125.

[H17]   J. A. Peterson, R. E. Ebel, D. H. O'Keeffe, T. Matsubara, R. W. Estabrook, *J Biol Chem* **1976**, *251*, 4010–4016.

[H18]   N. Maltar-Strmecki, B. Rakvin, *Appl Radiat Isot* **2005**, *63*, 375–380.

[H19]   S. Stoll, A. Schweiger, *J Magn Reson* **2006**, *178*, 42–55.

[H20]   J. H. Freed, Theory of slow tumbling ESR spectra for nitroxides. In *Spin Labeling: Theory and Applications*; L. J. Berliner, Ed.; Academic Press: New York, **1976**, Vol. 1, pp 53–132.

[H21]   D. J. Schneider, J. H. Freed, Calculating slow motional magnetic resonance spectra: A user's guide. In *Spin Labeling: Theory and Applications*; L. J. Berliner, J. Reuben, Eds.; Plenum Press: New York, London, **1989**, Vol. 8, pp 1–76.

[H22]   A. R. Edmonds, *Angular momentum in quantum mechanics*, Princeton University Press: Princeton, **1996**.

[H23]   E. Krieger, G. Koraimann, G. Vriend, *Proteins Struct Funct Genet* **2002**, *47*, 393–402.

[H24]   G. Scatchard, *Ann NY Acad Sci* **1949**, *51*, 660–672.

[H25]   R. A. Copeland, *Enzymes: A Practical Introduction to Structure, Mechanism, and Data Analysis*. Wiley-VCH: New York, **2000**.

Appendix I | Temperature-induced Solution Dynamics of the Spin Probed HSA System

I1 | Spectral Simulations of CW EPR Data from 16-DSA-probed HSA Solutions

A representative selection of parameters from spectral simulations of temperature-dependent 16-DSA-probed HSA solutions as shown in **Figure 11.1**, **Figure 11.2** and **Figure I1** are given in **Table I1**. The general strategy for simulations of such temperature-dependent multi-component EPR spectra is thoroughly described in **Appendix H5**.

Table I1 | Simulation parameters of 16-DSA-probed HSA solutions

Sample	j [°C]	$F_{i,j}$	$\phi_{i,j}$ [%]	g_{iso}	a_{iso} [MHz]	a_{iso} [G]	τ_c [ns]	β [°]
HSA	25	b_1	66.009	2.00593	42.93	15.25	11.262	16
		b_2	33.991	2.00593	42.93	15.25	4.319	45
	37	b_1	56.302	2.00593	42.87	15.23	9.982	16
		b_2	43.698	2.00593	42.87	15.23	3.808	45
	97	b_1	57.734	2.00593	42.33	15.04	2.928	16
		b_2	33.172	2.00593	42.33	15.04	1.119	45
		f	6.960	2.00587	44.33	15.75	0.021	45
		g	2.133	2.00607	40.20	14.28	0.137	45
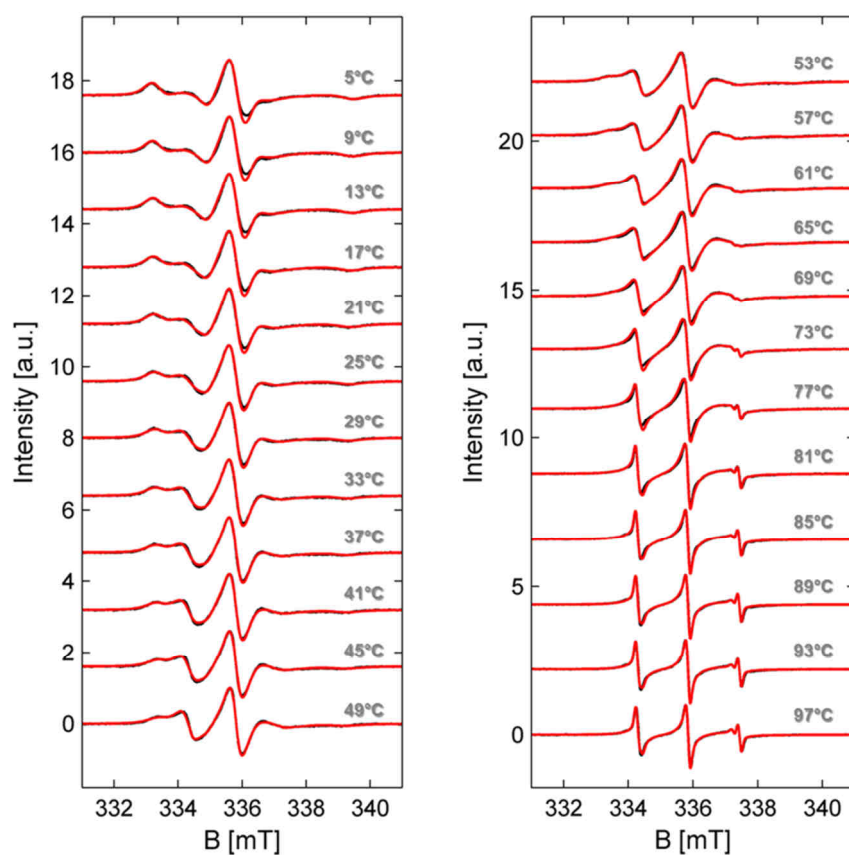
Figure I1 | Temperature-dependent spectral simulations of 16-DSA-probed HSA solutions. All CW EPR simulations of 16-DSA-probed HSA solutions are shown in the temperature range from $5 < j < 97$. Experimental data are shown in black and simulations in red.

I2 | Spectral Simulations of CW EPR Data for Scatchard Plot Construction

All spectral simulations for temperature-dependent Scatchard plots[II] of 16-DSA-probed HSA solutions in **Figure 11.4A+B** and **Figure 11.8C** are shown in **Figure I2**. A starting set of simulation parameters is given in **Table I1**.
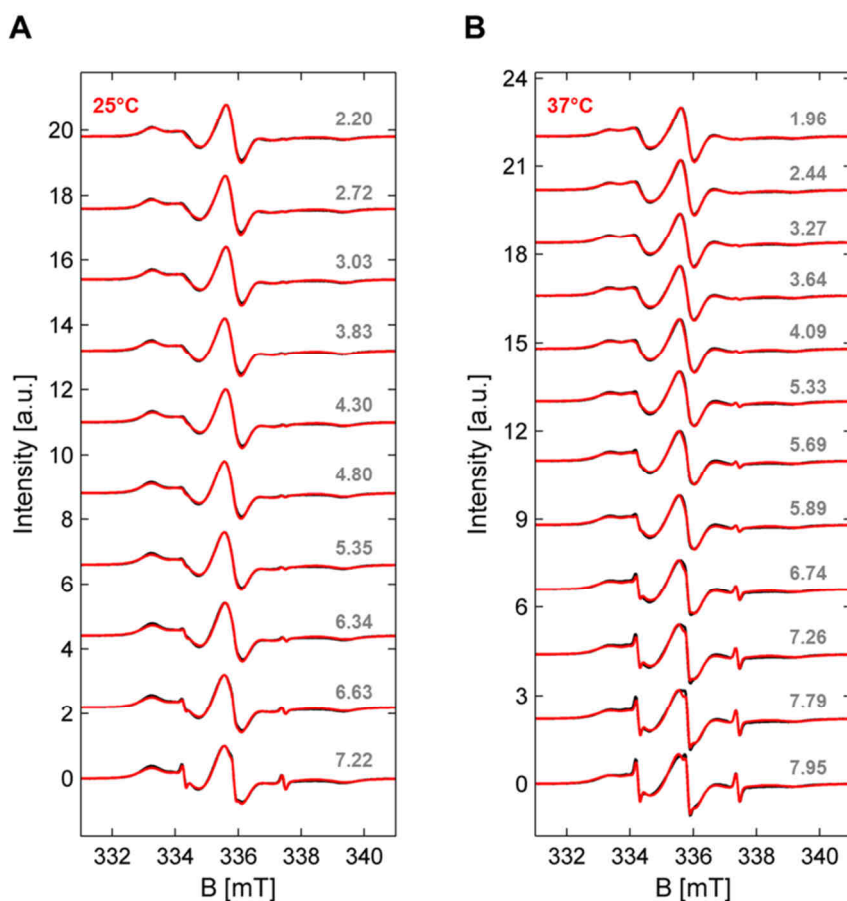
Figure I2 | Temperature-dependent spectral simulations of 16-DSA-probed HSA solutions. All CW EPR spectral simulations of 16-DSA-probed HSA solutions are shown in the loading range from about 2:1 to 8:1 at (**A**) 25°C and (**B**) 37°C. Experimental data are shown in black and simulations in red.

The Scatchard evaluation in **Figure 11.4A** was conducted according to equation 10.2. Parameters from the linear fit in **Figure 11.4A** were obtained with equation I.1 and are shown in **Table I2**:

$$y = v = b \cdot x + a = -K_A \cdot (N_L - N_E) + v_{N_L \to 0} \qquad . \qquad (I.1)$$

Table I2 | Fit parameters from linear Scatchard plot phases of 16-DSA interacting with HSA

Parameter	K_A [M^{-1}]	$v_{N_L \to 0} = N_E \cdot K_A$ [μM^{-1}]	q^a	R^2
$j = 25$	$(1.65889 \pm 0.04274) \cdot 10^6$	13.46333 ± 0.15949	1–10	0.99406
$j = 37$	$(3.5565 \pm 0.6295) \cdot 10^5$	3.08908 ± 0.45300	9–11	0.93925

$^a q$ = data point range in **Figure 11.4A** where the fit curve was adjusted to.

A linear Scatchard evaluation of **Figure 11.4B** was not conducted as no linearity was observed in the whole data range. Due to the exponential shape an empirical fit curve was used in order to reproduce the general shape according to the relation:

$$v = v_{N_L \to 0} \cdot e^{-N_L/B_v} + v_{N_L \to \infty} \qquad . \qquad (I.2)$$

Parameters from this exponential fit curve are shown in **Table I3** and the biphasic Scatchard plot in **Figure 11.4B** was evaluated according to the Rosenthal method[I2] as presented in **Chapter 7.3.1**. The results from this approach are summarized in **Table 11.1**.

Table I3 | Fit parameters from Scatchard plot of 16-DSA interacting with HSA at 37°C

Parameter	$v_{NL \to 0}$ [µM^{-1}]	$v_{NL \to \infty}$ [µM^{-1}]	B_v	q^a	R^2
$j = 37$	25.19168 ± 0.67608	-1.42223 ± 0.29311	2.79927 ± 0.15579	1–11	0.9981

$^a q$ = data point range in **Figure 11.4B** where the fit curve was adjusted to.

The van't Hoff plot of $\ln K_{A,j}$ in **Figure 11.4D** was fitted with a Boltzmann-type sigmoidal function as shown in equation 11.1. The parameters from this fit are given in **Table I4**.

Table I4 | Fit parameters from $\ln K_{A,j}$ of 16-DSA interacting with HSA from equation 11.1

Parameter	Value	Physical implication
α_1	8.80431 ± 0.17671	lower bound $\ln K_{A,j}$
α_2	12.89806 ± 0.17763	upper bound $\ln K_{A,j}$
α_3 [K^{-1}]	$(2.87000000 \pm 0.00737929) \cdot 10^{-3}$	midpoint temperature T_m
α_4 [K^{-1}]	$(5.34239 \pm 0.820633) \cdot 10^{-5}$	width of transition

I3 | Assessing Appropriate Fit Parameters from $\ln K_{IC,x}$ of 16-DSA Bound to HSA

A non-linear curve fit procedure was applied to the van't Hoff plot of $\ln K_{IC,j}$ of 16-DSA bound to HSA as shown in **Figure 11.5**. Best fits were obtained for a curve shape composed from an exponential and a double Boltzmann function. According fit parameters were obtained with a non-standard home-written origin code:

$$y = y_0 + B \cdot \exp(x / t_1) + A(\text{frac}(1 + \exp((x - x_{0,1}) / k_1)) + (1 - \text{frac})/(1 + \exp((x - x_{0,2}) / k_2))) \quad . \quad (I.3)$$

The resulting fit parameters from equation I.3 were renamed for equation 11.2 and the corresponding values are listed in **Table I5**. Due to the high amount of fit parameters no error margins could be determined.

Table I5 | Fit parameters from $\ln K_{IC,x}$ of 16-DSA bound to HSA

Parameter	Fit parameter	Value	SI unit	Physical implication
$\ln K_{IC,0}$	y_0	1.16783	–	y-intercept
κ_1	B	–0.0019	–	–
κ_2	$1/t_1$	2049.524715	K	–
κ_3	A	–1.23637	–	total step width
κ_4	frac	0.54918	–	partial step width
κ_5	$x_{0,1}$	0.00306	K^{-1}	midpoint temperature $T_{m,1} = T_{AD,1}$
κ_6	k_1	$2.80139 \cdot 10^{-5}$	K^{-1}	width of transition 1
κ_7	$x_{0,2}$	0.00281	K^{-1}	midpoint temperature $T_{m,2} = T_{AD,2}$
κ_8	k_2	$1.58927 \cdot 10^{-5}$	K^{-1}	width of transition 2

I4 | Derivation of Thermodynamic Functions from $\ln K_{IC,j}$ in equation 11.2

In principle, the derivation of equations 11.4, 11.5 and 11.7 is straightforward. The main calculation rules are restricted to the following mathematical rules, as the quotient rule:

$$\frac{d}{dx}\left[\frac{u(x)}{v(x)}\right] = \frac{u'(x) \cdot v(x) - u(x) \cdot v'(x)}{v(x)^2} \quad , \tag{I.4}$$

the reciprocal rule:

$$\frac{d}{dx}\left[\frac{1}{u(x)}\right] = -\frac{u'(x)}{u(x)^2} \quad , \tag{I.5}$$

the chain rule:

$$\frac{d}{dx}\left[e^{u(x)}\right] = e^{u(x)} \cdot u'(x) \tag{I.6}$$

and the power rule:

$$\frac{d}{dx}\left[u(x)^n\right] = n \cdot u(x)^{n-1} \cdot u'(x) \quad . \tag{I.7}$$

According to equation 11.3 the calculation of $\Delta H^\circ_{IC,x}$ proceeds in the following way:

$$\Delta H^\circ_{IC,x} = -R \cdot \frac{d}{dx}\left[\ln K_{IC,x}\right] \quad , \tag{I.8}$$

whereas

$$\ln K_{IC,x} = \ln K_{IC,0} + \kappa_1 \cdot e^{\kappa_2 x} + \frac{\kappa_3 \kappa_4}{1 + e^{(x-\kappa_5)/\kappa_6}} + \frac{\kappa_3(1-\kappa_4)}{1 + e^{(x-\kappa_7)/\kappa_8}} \quad , \tag{I.9}$$

as it is shown alternatively in equation I.3. Differentiation of $\ln K_{IC,x}$ with respect to x leads to:

$$\frac{d}{dx}\left[\ln K_{IC,x}\right] = \underbrace{\frac{d}{dx}\left[\ln K_{IC,0}\right]}_{0} + \underbrace{\frac{d}{dx}\left[\kappa_1 \cdot e^{\kappa_2 x}\right]}_{\text{scheme 1}} + \underbrace{\frac{d}{dx}\left[\frac{\kappa_3 \kappa_4}{1 + e^{(x-\kappa_5)/\kappa_6}}\right]}_{\text{scheme 2}} + \underbrace{\frac{d}{dx}\left[\frac{\kappa_3(1-\kappa_4)}{1 + e^{(x-\kappa_7)/\kappa_8}}\right]}_{\text{scheme 2}} \quad , \tag{I.10}$$

where the first term is zero and the second term can be calculated according to scheme 1 that utilizes the chain rule for exponential functions (equation I.6):

$$\frac{d}{dx}\left[\kappa_1 \cdot e^{\kappa_2 x}\right] = \kappa_1 \cdot \frac{d}{dx}\left[e^{\kappa_2 x}\right] = \kappa_1\left[\kappa_2 e^{\kappa_2 x}\right] = \kappa_1\kappa_2 e^{\kappa_2 x}. \tag{I.11}$$

The third term is calculated according to scheme 2 using the reciprocal rule (equation I.5):

$$\frac{d}{dx}\left[\frac{\kappa_3\kappa_4}{1+e^{(x-\kappa_5)/\kappa_6}}\right] = \kappa_3\kappa_4 \frac{d}{dx}\left[\frac{1}{1+e^{(x-\kappa_5)/\kappa_6}}\right] = \kappa_3\kappa_4 \frac{d}{dx}\left[\frac{1}{u_1(x)}\right], \tag{I.12}$$

where

$$u_1(x) = 1 + e^{(x-\kappa_5)/\kappa_6}, \tag{I.13}$$

$$u_1'(x) = \frac{d}{dx}[1] + \frac{d}{dx}\left[e^{(x-\kappa_5)/\kappa_6}\right], \tag{I.14}$$

and

$$u_2(x) = \frac{x-\kappa_5}{\kappa_6} \quad \text{and} \quad u_2'(x) = \frac{1}{\kappa_6}\left(\frac{d}{dx}[x] + \frac{d}{dx}[-\kappa_5]\right) = \frac{1}{\kappa_6}. \tag{I.15}$$

This leads to:

$$u_1'(x) = \frac{d}{dx}\left[e^{(x-\kappa_5)/\kappa_6}\right] = \frac{e^{(x-\kappa_5)/\kappa_6}}{\kappa_6} \tag{I.16a}$$

and finally itturns out, that:

$$\frac{d}{dx}\left[\frac{\kappa_3\kappa_4}{1+e^{(x-\kappa_5)/\kappa_6}}\right] = \kappa_3\kappa_4 \frac{d}{dx}\left[\frac{1}{u_1(x)}\right] = \kappa_3\kappa_4\left[-\frac{u_1'(x)}{u_1(x)^2}\right] = -\kappa_3\kappa_4\left[\frac{\frac{1}{\kappa_6}(e^{(x-\kappa_5)/\kappa_6})}{(1+e^{(x-\kappa_5)/\kappa_6})^2}\right]$$

$$= -\frac{\kappa_3\kappa_4}{\kappa_6} \cdot \frac{e^{(x-\kappa_5)/\kappa_6}}{(1+e^{(x-\kappa_5)/\kappa_6})^2}. \tag{I.17a}$$

The same procedure applies to the fourth term with the result:

$$\frac{d}{dx}\left[\frac{\kappa_3(1-\kappa_4)}{1+e^{(x-\kappa_7)/\kappa_8}}\right] = \kappa_3(1-\kappa_4)\frac{d}{dx}\left[\frac{1}{u_1(x)}\right] = \kappa_3(1-\kappa_4)\left[-\frac{u_1'(x)}{u_1(x)^2}\right] = \kappa_3(1-\kappa_4)\left[-\frac{\frac{1}{\kappa_8}(e^{(x-\kappa_7)/\kappa_8})}{(1+e^{(x-\kappa_7)/\kappa_8})^2}\right]$$

$$= -\frac{\kappa_3(1-\kappa_4)}{\kappa_8} \cdot \frac{e^{(x-\kappa_7)/\kappa_8}}{(1+e^{(x-\kappa_7)/\kappa_8})^2}. \tag{I.17b}$$

Finally the expression in equation 11.4 is obtained:

$$\Delta H^\circ_{IC,x} = -R\left(\kappa_1\kappa_2 \cdot e^{\kappa_2 x} - \frac{\kappa_3\kappa_4}{\kappa_6} \cdot \frac{e^{(x-\kappa_5)/\kappa_6}}{(1+e^{(x-\kappa_5)/\kappa_6})^2} - \frac{\kappa_3(1-\kappa_4)}{\kappa_8} \cdot \frac{e^{(x-\kappa_7)/\kappa_8}}{(1+e^{(x-\kappa_7)/\kappa_8})^2}\right). \tag{I.18}$$

The free energy of interconversion is given by:

$$\Delta G^{\circ}_{\text{IC},j} = \Delta H^{\circ}_{\text{IC},j} - T\Delta S^{\circ}_{\text{IC},j} = -RT \cdot \ln K_{\text{IC},j} \quad . \tag{I.19}$$

Dividing by T and separation of $\Delta S^{\circ}_{\text{IC},j}$ leads to:

$$S^{\circ}_{\text{IC},j} = \frac{\Delta H^{\circ}_{\text{IC},j}}{T} + R \cdot \ln K_{\text{IC},j} \quad . \tag{I.20a}$$

When temperature is substituted with $x = T^{-1}$, following equivalent relation is obtained:

$$S^{\circ}_{\text{IC},x} = x \cdot \Delta H^{\circ}_{\text{IC},x} + R \cdot \ln K_{\text{IC},x} \quad . \tag{I.20b}$$

The temperature-dependent molar interconversion entropy (equation 11.5) is then set up by simply inserting equation 11.2 and 11.4 into equation I.20b, so that:

$$
\begin{aligned}
\Delta S^{\circ}_{\text{IC},x} &= x \cdot \Delta H^{\circ}_{\text{IC},x} + R\ln K_{\text{IC},x} \\
&= -R \cdot x \left(\kappa_1 \kappa_2 e^{\kappa_2 x} - \frac{\kappa_3 \kappa_4}{\kappa_6} \cdot \frac{e^{(x-\kappa_5)/\kappa_6}}{(1+e^{(x-\kappa_5)/\kappa_6})^2} - \frac{\kappa_3(1-\kappa_4)}{\kappa_8} \cdot \frac{e^{(x-\kappa_7)/\kappa_8}}{(1+e^{(x-\kappa_7)/\kappa_8})^2} \right) \\
&\quad + R\left(\ln K_{\text{IC},0} + \kappa_1 \cdot e^{\kappa_2 x} + \frac{\kappa_3 \kappa_4}{1+e^{(x-\kappa_5)/\kappa_6}} + \frac{\kappa_3(1-\kappa_4)}{1+e^{(x-\kappa_7)/\kappa_8}} \right)
\end{aligned} \tag{I.21}
$$

An expression for the molar interconversion heat capacity $\Delta C^{\circ}_{\text{P,IC},j}$ was found by applying the basic principle given in equation 10.13, again by substitution of $T^{-1} = x$:

$$\Delta C^{\circ}_{\text{P,IC},j} = \left(\frac{\partial \Delta H^{\circ}_{\text{IC},j}}{\partial T} \right)_P = \frac{1}{T^2} \cdot \left(\frac{\partial \Delta H^{\circ}_{\text{IC},j}}{\partial \left(\frac{1}{T}\right)} \right)_P \tag{I.22a}$$

and

$$\Delta C^{\circ}_{\text{P,IC},x} = x^2 \cdot \left(\frac{\partial \Delta H^{\circ}_{\text{IC},x}}{\partial x} \right)_P = -Rx^2 \left(\frac{\partial^2 \ln K_{\text{IC},x}}{\partial x^2} \right)_P \quad . \tag{I.22b}$$

Therefore, $\Delta H_{\text{IC},x}$ has to be differentiated with respect to x:

$$\frac{d}{dx}\left[\Delta H^{\circ}_{\text{IC},x} \right] = -R \left(\underbrace{\frac{d}{dx}\left[\kappa_1 \kappa_2 \cdot e^{\kappa_2 x} \right]}_{\text{scheme 1}} + \underbrace{\frac{d}{dx}\left[-\frac{\kappa_3 \kappa_4}{\kappa_6} \cdot \frac{e^{(x-\kappa_5)/\kappa_6}}{(1+e^{(x-\kappa_5)/\kappa_6})^2} \right]}_{\text{scheme 3}} + \underbrace{\frac{d}{dx}\left[-\frac{\kappa_3(1-\kappa_4)}{\kappa_8} \cdot \frac{e^{(x-\kappa_7)/\kappa_8}}{(1+e^{(x-\kappa_7)/\kappa_8})^2} \right]}_{\text{scheme 3}} \right) . \tag{I.23}$$

According to scheme 1 the first bracketed term is given as:

$$\frac{d}{dx}\left[\kappa_1\kappa_2 \cdot e^{\kappa_2 x}\right] = \kappa_1\kappa_2\frac{d}{dx}\left[e^{\kappa_2 x}\right] = \kappa_1\kappa_2^2 e^{\kappa_2 x} . \qquad (I.24)$$

The second and third terms are calculated by scheme 3 that utilizes a more interlaced routine:

$$\frac{d}{dx}\left[-\frac{\kappa_3\kappa_4}{\kappa_6} \cdot \frac{e^{(x-\kappa_5)/\kappa_6}}{(1+e^{(x-\kappa_5)/\kappa_6})^2}\right] = -\frac{\kappa_3\kappa_4}{\kappa_6}\frac{d}{dx}\left[\frac{e^{(x-\kappa_5)/\kappa_6}}{(1+e^{(x-\kappa_5)/\kappa_6})^2}\right] = -\frac{\kappa_3\kappa_4}{\kappa_6}\frac{d}{dx}\left[\frac{u(x)}{v(x)}\right], \qquad (I.25)$$

where $u_1(x)$, $u_1{}'(x)$, $u_2(x)$ and $u_2{}'(x)$ are here identical to the expressions given in scheme 2 (see also equation I.16b). Additionally:

$$v_1(x) = \left(1+e^{(x-\kappa_5)/\kappa_6}\right)^2 = v_2(x)^2 \qquad (I.26)$$

and therefore it follows that:

$$v_2{}'(x) = u_1{}'(x) = \frac{d}{dx}\left[1\right] + \frac{d}{dx}\left[e^{(x-\kappa_5)/\kappa_6}\right] = \frac{e^{(x-\kappa_5)/\kappa_6}}{\kappa_6} \qquad (I.16b)$$

with:

$$v_1{}'(x) = \frac{d}{dx}\left[v_2(x)^n\right] = n \cdot v_2(x)^{n-1} \cdot v_2{}'(x) = \frac{2}{\kappa_6} \cdot (1+e^{(x-\kappa_5)/\kappa_6}) \cdot e^{(x-\kappa_5)/\kappa_6} . \qquad (I.27)$$

The quotient rule gives the expression:

$$\frac{d}{dx}\left[\frac{u(x)}{v(x)}\right] = \frac{u_1{}'(x) \cdot v_1(x) - u_1(x) \cdot v_1{}'(x)}{v_1(x)^2}$$

$$= \frac{\frac{1}{\kappa_6} \cdot e^{(x-\kappa_5)/\kappa_6} \cdot \left(1+e^{(x-\kappa_5)/\kappa_6}\right)^2 - \frac{2}{\kappa_6} \cdot e^{(x-\kappa_5)/\kappa_6} \cdot \left(1+e^{(x-\kappa_5)/\kappa_6}\right) \cdot e^{(x-\kappa_5)/\kappa_6}}{\left(1+e^{(x-\kappa_5)/\kappa_6}\right)^4}$$

$$= \frac{e^{(x-\kappa_5)/\kappa_6}}{\kappa_6 \cdot \left(1+e^{(x-\kappa_5)/\kappa_6}\right)^2} - \frac{2 \cdot e^{2(x-\kappa_5)/\kappa_6}}{\kappa_6 \cdot \left(1+e^{(x-\kappa_5)/\kappa_6}\right)^3} \qquad (I.28)$$

and consistently, upon combination of equation I.25 and equation I.28 it follows that:

$$\frac{d}{dx}\left[-\frac{\kappa_3\kappa_4}{\kappa_6} \cdot \frac{e^{(x-\kappa_5)/\kappa_6}}{(1+e^{(x-\kappa_5)/\kappa_6})^2}\right] = -\frac{\kappa_3\kappa_4}{\kappa_6}\frac{d}{dx}\left[\frac{u(x)}{v(x)}\right]$$

$$= -\frac{\kappa_3\kappa_4}{\kappa_6^2} \cdot \frac{e^{(x-\kappa_5)/\kappa_6}}{\left(1+e^{(x-\kappa_5)/\kappa_6}\right)^2} + \frac{2\kappa_3\kappa_4}{\kappa_6^2} \cdot \frac{e^{2(x-\kappa_5)/\kappa_6}}{\left(1+e^{(x-\kappa_5)/\kappa_6}\right)^3} \qquad (I.29a)$$

The third term in equation I.23 can be treated in analogy, so that:

$$\frac{d}{dx}\left[-\frac{\kappa_3(1-\kappa_4)}{\kappa_8}\cdot\frac{e^{(x-\kappa_7)/\kappa_8}}{(1+e^{(x-\kappa_7)/\kappa_8})^2}\right]=-\frac{\kappa_3(1-\kappa_4)}{\kappa_8^2}\cdot\frac{e^{(x-\kappa_7)/\kappa_8}}{\left(1+e^{(x-\kappa_7)/\kappa_8}\right)^2}+\frac{2\kappa_3(1-\kappa_4)}{\kappa_8^2}\cdot\frac{e^{2(x-\kappa_7)/\kappa_8}}{\left(1+e^{(x-\kappa_7)/\kappa_8}\right)^3}. \qquad \text{(I.29b)}$$

Finally, an expression for $\Delta C^{\circ}_{\text{P,IC},x}$ can be put together by using equation I.22b:

$$\Delta C^{\circ}_{\text{P,IC},x}=-Rx^2\cdot\left(\kappa_1\kappa_2^2 e^{\kappa_2 x}-\frac{\kappa_3\kappa_4}{\kappa_6^2}\cdot\frac{e^{(x-\kappa_5)/\kappa_6}}{\left(1+e^{(x-\kappa_5)/\kappa_6}\right)^2}+\frac{2\kappa_3\kappa_4}{\kappa_6^2}\cdot\frac{e^{2(x-\kappa_5)/\kappa_6}}{\left(1+e^{(x-\kappa_5)/\kappa_6}\right)^3}\right.$$
$$\left.-\frac{\kappa_3(1-\kappa_4)}{\kappa_8^2}\cdot\frac{e^{(x-\kappa_7)/\kappa_8}}{\left(1+e^{(x-\kappa_7)/\kappa_8}\right)^2}+\frac{2\kappa_3(1-\kappa_4)}{\kappa_8^2}\cdot\frac{e^{2(x-\kappa_7)/\kappa_8}}{\left(1+e^{(x-\kappa_7)/\kappa_8}\right)^3}\right). \qquad \text{(I.30)}$$

I5 | Fit Curves from Temperature Stability Shifts in DSC and $\ln K_{\text{IC},j}$

For successful predictions of denaturation temperatures $T_{\text{D},i}$ for any 16-DSA loading on HSA at 0.18 mM equivalents, the peak positions of the biphasic thermograms in **Figure 11.8A** were additionally plotted in **Figure 11.8B** and fitted with linear ($T_{\text{D},1}$) and exponential functions ($T_{\text{D},2}$). The according parameters were obtained from expressions for $T_{\text{D},1}$:

$$T_{\text{D},1}=T_{\text{D},1,\text{min}}+k_{T_{\text{D},1}}\cdot N_{\text{L}} \qquad \text{(I.31)}$$

and for $T_{\text{D},2}$:

$$T_{\text{D},2}=A_T\cdot e^{-N_{\text{L}}/B_T}+T_{\text{D},2,\text{max}}\quad . \qquad \text{(I.32)}$$

The corresponding results are summarized in **Table I6**.

Table I6 | Fit parameters for denaturation temperature prediction depending on 16-DSA loading

Parameter	Value	SI unit	Physical implication
N_{L}	(variable)	n.a.	no. of 16-DSA per HSA
$k_{\text{TD},1}$	1.2763 ± 0.0583	°C/FA	slope of $T_{\text{D},1}$ increase with N_{L}
$T_{\text{D},1,\text{min}}$	63.58913 ± 0.19760	°C	$T_{\text{D},1}$ for HSA without 16-DSA
A_T	-6.4112 ± 0.1053	°C	–
B_T	0.87377 ± 0.03867	n.a.	–
$T_{\text{D},2,\text{max}}$	76.12554 ± 0.04564	°C	$T_{\text{D},2}$ for HSA saturated with 16-DSA

The $\ln K_{\text{IC},j}$ curves that depend on temperature as well as on the 16-DSA loading ratio are presented in **Figure 11.8C** and were constructed from fit parameters that can be obtained from Scatchard plots in **Figure 11.4A+B** and **Figure I2**. Best fits were achieved with exponential fit curves according to

following equation:

$$\ln K_{IC,j} = \ln K_{IC,j,0} + A_{K,j} \cdot e^{-N_L / B_{K,j}} \quad .$$

(I.33)

All parameters from these exponential fit curves are shown in **Table I7**.

Table I7 | Fit parameters for $\ln K_{IC,j}$ depending on 16-DSA loading and temperature

Parameter	Value	SI unit	Physical implication
N_L	(variable)	n.a.	no. of 16-DSA per HSA
$\ln K_{IC,25,0}$	-1.34514 ± 0.05279	n.a.	Asymptotic value for $N_L \rightarrow \infty$
$\ln K_{IC,37,0}$	-1.10525 ± 0.02677	n.a.	Asymptotic value for $N_L \rightarrow \infty$
$A_{K,25}$	1.63636 ± 0.26177	n.a.	–
$A_{K,37}$	1.50332 ± 0.10046	n.a.	–
$B_{K,25}$	2.20156 ± 0.46068	n.a.	Decay constant of $\ln K_{IC,25}$ with N_L
$B_{K,37}$	2.28617 ± 0.23768	n.a.	Decay constant of $\ln K_{IC,37}$ with N_L

I6 | Fit Curves from DEER-derived Parameters $\ln P_{AB}(r)$ and Δ as Functions of 16-DSA Loading

In **Chapter 11.2.5** the $\ln P_{AB}(r)$ parameter was introduced that describes the change of characteristic peaks $P_A(r)$ and $P_B(r)$ in loading and temperature-dependent distance distributions from 16-DSA-probed HSA solutions ($P_{AB}(r) = P_A(r)/P_B(r)$). The $\ln P_{AB}(r)$ curve in **Figure 11.9E** can be described with an exponential function of the type:

$$\ln P_{AB}(r) = A_P \cdot e^{-N_{P(r)} / B_P} + \ln P_{AB,0}(r) \quad .$$

(I.34)

Table I8 | Fit parameters from $\ln P_{AB}(r)$ in DEER experiments

Parameter	Value	SI unit	Physical implication
$N_{P(r)}$	(variable)	n.a.	no. of 16-DSA per HSA from $P(r)$
A_P	6.83177 ± 0.50259	n.a.	–
B_P	0.99962 ± 0.08071	n.a.	Decay constant for $\ln P_{AB}(r)$ with N_L
$\ln P_{AB,0}(r)$	-0.45459 ± 0.05489	n.a.	Asymptotic value for $\ln P_{AB}(r)$

A shortcut to a more convenient expression can be found when parameter A_P is related to the maximum number of binding sites $N_{T,25}$ in HSA with $A_P/N_{T,25} = 0.841 \approx 17/20$, $\ln P_{AB,0}(r)$ is replaced by the value $-9/20$ and parameter B_P is set to 1. After variable separation of $N_{P(r)}$ following expression can be obtained:

$$N_{P(r)} = -B_P \cdot \ln \left(\frac{\ln P_{AB}(r) - \ln P_{AB,0}(r)}{A_P} \right) \quad .$$

(I.35)

With these aforementioned assumptions, equation I.35 can be simplified to:

$$N_{P(r)} \approx -\ln\left(\frac{\ln P_{AB}(r) + \frac{9}{20}}{\frac{17}{20} \cdot N_{T,25}}\right) = -\ln\left(\frac{20 \cdot \ln P_{AB}(r) + 9}{17 \cdot N_{T,25}}\right) \quad , \tag{I.36}$$

corresponding to equation 11.8 of the main text. The Langmuir isotherm analogue expression that was found to reproduce the curve shape of Δ versus N_Δ best was fitted with the expression:[I3]

$$\Delta = \frac{\Delta_{max} \cdot b \cdot N_\Delta^{(1-c)}}{1 + b \cdot N_\Delta^{(1-c)}} \quad , \tag{I.37}$$

where $(1 - c) = \eta$. A similar strategy was used by Sirotkin et al.[I4] for modeling enthalpy changes during HSA immersion in aliphatic alcohols. Replacing $(1 - c)$ with η and variable separation for N_Δ leads to equation 11.10 in the main text. The fit parameters of equation I.37 can be found in **Table I9**.

Table I9 | Fit parameters from Δ as a function of 16-DSA loading in DEER experiments

Parameter	Value	SI unit	Physical implication
N_Δ	(variable)	n.a.	no. of 16-DSA per HSA
Δ_{max}	0.71244 ± 0.04262	n.a.	Maximum attainable Δ-value
b	0.44382 ± 0.11462	n.a.	Langmuir parameter analogue
c	-1.20267 ± 0.52500	n.a.	Exponential stretch parameter

I7 | References

[I1]   G. Scatchard, *Ann NY Acad Sci* **1949**, *51*, 660–672.
[I2]   H. E. Rosenthal, *Anal Biochem* **1967**, *20*, 525–532.
[I3]   A. Kapoor, J. A. Ritter, R. T. Yang, *Langmuir* **1990**, *6*, 660–664.
[I4]   V. A. Sirotkin, M. D. Borisover, B. N. Solomonov, *Biophys Chem* **1997**, *69*, 239–248.

Acknowledgments

This work is the outcome of a wealth of discussions, ideas, work, effort, support, delegation, cooperation, help, suggestions, trials, failures, criticisms, quests for answers, troubleshooting and whatever it may be called. In fact it would not have been possible to finally accomplish this thesis without the following list of people that guided me during the last few years, as …

… PROF. DR. DARIUSH HINDERBERGER for initially inviting me to his research group at the MPIP, still as a project leader. During the time we spent together, there were of course many ups and downs and obstacles of any kind, but his positive attitude, curiosity and creativity convinced me to constantly immerse myself into an intense journey in order to find further clues and solutions of sometimes seemingly unsolvable problems. Thank you also for your patience with the realization of our ideas, your continued interest and support, as well as for all the opportunities and freedoms you gave me in the course of time and especially during the writing process of this thesis.

… PROF. DR. WOLFGANG E. TROMMER, who was actually the first one that ignited the flame for my interest in EPR spectroscopy with his catching passion for this scientific discipline. Thank you also for the friendly invitation back to Kaiserslautern and for also sending curious people to the MPIP and the MLU. I am also thankful to PROF. DR. HANS-WOLFGANG SPIESS for giving me the opportunity to start my thesis in his soon disbanding magnetic resonance group at the MPIP. The smooth transition in moving from Halle to Mainz with a minimum loss of productivity was also kindly guaranteed by the esteemed patience of PROF. DR. PAUL BLOM who permitted to further keep up the former EPR lab at the MPIP after overtaking the position of Spiess.

… CHRISTIAN BAUER, who was also a background key person for this thesis to whom I feel greatly indebted. He was very patient with the many questions about the EPR spectrometers that I had in the beginning. His help in moving the lab from Mainz to Halle was inestimable. Presumably, there are not many people that can build up a pulse X-band spectrometer (that actually works) faster than him.

… DR. YASAR AKDOGAN for introducing me to the state of the art albumin project at the very beginning of this thesis from where everything else could naturally evolve from.

… TILL HAUENSCHILD for many, many shared night shifts and weekends, countless hours of common work, discussions, ideas and mutual encouragement in situations of seemingly insurmountable problems. It was a big motivation and pleasure for me to have you around at the MPIP, as well as at the MLU. Thank you also for giving me these deep insights into your own work. At certain points you almost made me feel like a synthetic chemist by myself.

… DR. ANDREAS KERTH for his reliable and perpetual availability from the first day onwards in Halle and his helpful, patient, friendly and ever competent advice, especially with good books !

… DR. CHRISTIAN SCHWIEGER for his friendly, patient and enthusiastic participation, especially in some of the thermodynamic aspects of this thesis. His advice and his experimental contributions (DSC) also had a priceless impact on my thoughts and ideas about several contexts.

… the postdocs in Halle: DR. NADICA MALTAR-STRMECKI and DR. HALEH H. HAERI for their support, tips and tricks, endurance, patience and their always amicable and honest advice.

… KATHARINA WIDDER and SOMAYEH KHAZAEI for their critical, compassionate and warm words that often contributed to keep up my inner balance and serenity.

Publications

I | Original Research

1.   Y. Akdogan, J. Reichenwallner, D. Hinderberger, Evidence for Water-Tuned Structural Differences in Proteins: An Approach Emphasizing Variations in Local Hydrophilicity. *PLoS One* **2012**, *7*, e45681.

2.   S. L. Kuan, B. Stöckle, J. Reichenwallner, D. Y. W. Ng, Y. Wu, M. Doroshenko, K. Koynov, D. Hinderberger, K. Müllen, T. Weil, Dendronized Albumin Core-Shell Transporters with High Drug Loading Capacity. *Biomacromolecules* **2013**, *14*, 367–376.

3.   J. Reichenwallner, D. Hinderberger, Using bound fatty acids to disclose the functional structure of serum albumin. *Biochim Biophys Acta, Gen Subj* **2013**, *1830*, 5382–5393.

4.   J. Reichenwallner, M. Chakour, S. Indu, R. Varadarajan, W. E. Trommer, Maltose Binding Protein Is Partially Structured in Its Molten Globule State. *Appl Magn Reson* **2013**, *44*, 983–995.

5.   D. R. Kattnig, J. Reichenwallner, D. Hinderberger, Modeling Excluded Volume Effects for the Faithful Description of the Background Signal in Double Electron-Electron Resonance. *J Phys Chem B* **2013**, *117*, 16542–16557.

6.   T. Hauenschild, J. Reichenwallner, V. Enkelmann, D. Hinderberger, Characterizing Active Pharmaceutical Ingredient Binding to Human Serum Albumin by Spin-Labeling and EPR Spectroscopy. *Chem Eur J* **2016**, *22*, 12825–12838.

7.   J. Reichenwallner, A. Thomas, L. Nuhn, T. Johann, A. Meister, H. Frey, D. Hinderberger, Tunable dynamic hydrophobic attachment of guest molecules in amphiphilic core-shell polymers. *Polym Chem* **2016**, *7*, 5783–5798.

8.   J. Reichenwallner, C. Schwieger, D. Hinderberger, Probing the Nanoscopic Thermodynamic Fingerprint of Paramagnetic Ligands Interacting with Amphiphilic Macromolecules. *Polymers* **2017**, *9*, 324.

9.   J. Reichenwallner, M. T. Oehmichen, C. E. H. Schmelzer, T. Hauenschild, A. Kerth, D. Hinderberger, Exploring the pH-induced Functional Phase Space of Human Serum Albumin by EPR Spectroscopy, *in preparation*.

10.   J. Reichenwallner, A. Thomas, T. Steinbach, J. Eisermann, C. E. H. Schmelzer, F. Wurm, D. Hinderberger, Ligand-Binding Cooperativity Effects in Polymer-Protein Conjugation, *in preparation*.

11.   J. Reichenwallner, T. Hauenschild, C. E. H. Schmelzer, M. Hülsmann, A. Godt, D. Hinderberger, Fatty Acid Triangulation in Albumins Using a Landmark Spin Label, *in preparation*.

II | Conferences and Workshops

1.   EPR workshop 2011 in the group of H. J. Steinhoff, Physics Department, Osnabrück, 23th – 25th November 2011, attended.

2.   EUROMAR 2012 at University College Dublin (UCD), Dublin, Ireland, 1st – 5th July 2012, attended.

3.   J. Reichenwallner, Y. Akdogan, D. Hinderberger. *Evidence for local and allosteric water-tuned structural differences in proteins using DEER: monitoring the hydrophobic effect at the nanoscale*, Fachgruppentagung Magnetresonanz (FGMR 2012), 17th – 20th September 2012, in Halle (Saale), Germany, Poster presentation.

4.   J. Reichenwallner, D. Hinderberger. *Using bound fatty acids to disclose the functional structure of serum albumin*, EUROMAR 2013, 30th June – 5th July 2013 in Hersonissos, Crete, Poster presentation.

5.   J. Reichenwallner, D. Hinderberger, *Using bound fatty acids to disclose the functional structure of albumin,* CSCEC 2014, MPI for chemical energy conversion, 23th – 25th July 2014, Mülheim (Ruhr), Germany, Poster presentation.

6.   J. Reichenwallner, D. Hinderberger, *Using bound fatty acids to disclose the solution structure of serum albumin,* Joint Conference APES-IES-SEST 2014, 12th – 16th November 2014, Nara, Japan, Poster presentation.

7.   J. Reichenwallner, Marie-Therese Oehmichen, Dariush Hinderberger, *EPR-Spectroscopic Detection of pH-induced Molten Globules of Albumins*, 26th Faltertage, 23th – 25th October 2015, in Halle (Saale), Germany, poster presentation.

8.   J. Reichenwallner, A. Thomas, L. Nuhn, T. Johann, A. Meister, H. Frey, D. Hinderberger. *Adjustable Dynamic Hydrophobic Attachment of Fatty Acids in Amphiphilic Core-Shell Polymers*, Fachgruppentagung Magnetresonanz (FGMR 2016), 12th – 15th September 2016, in Düsseldorf, Germany, Poster presentation.

III | Oral Contributions

1.   J. Reichenwallner, D. Kurzbach, D. Hinderberger. *Studying Cooperative Effects, Structural Ensembles, and Dynamics in Proteins Using EPR Spectroscopy*, 26th Faltertage, 23th – 25th October 2015, in Halle (Saale), Germany, oral presentation.

PERSONAL INFORMATION

Permanent Address	**Campus Address**
Jörg Reichenwallner	MLU Halle-Wittenberg
Thomasius-Str. 27	Institute for Physical and Theoretical Chemistry
D-06110, Halle (Saale), Germany	Von-Danckelmann-Platz 4
	D-06120, Halle (Saale), Germany
E-mail: joerg.reichenwallner@chemie.uni-halle.de	Web: http://www.epr.uni-halle.de

TIMELINE

October 2013 – present	**PhD student** at Martin Luther University Halle-Wittenberg, Germany (MLU Halle), group of Prof. Dariush Hinderberger.
November 2011 – October 2013	**PhD student** at Johannes Gutenberg University Mainz, Germany, (JGU Mainz) at the Institute for Pharmacy and Biochemistry (group of Prof. Dirk Schneider) and scientific assistant at the Max Planck Institute for Polymer research (MPIP) in Mainz supervised by project leader PD Dr. D. Hinderberger in the group of Prof. H. W. Spiess.
September 2011 – October 2011	Graduate research assistant for practical courses in Physics at the Department of Physics, Technical University Kaiserslautern (TU KL).
June 2011 – September 2011	Graduate research assistant to Prof. W. E. Trommer at the Department of Chemistry, TU KL, Germany.
25th March, 2011	**Diploma in Biophysics**, received from the Departments of Chemistry, Biology and Physics, TU KL, Germany.
<u>Title of Diploma thesis (German)</u>:	*„Strukturuntersuchungen am Maltose-Bindungsprotein mit Hilfe der gepulsten Elektron-Elektron-Doppelresonanz Spektroskopie"*
October 2004 – March 2011	Studies of Biophysics, TU KL.
October 2003 – July 2004	Employed as a postman at DHL parcel service freight center Möglingen, Germany. Parcel delivery on time.
October 2002 – July 2003	National service at DRK for outpatient care in Ludwigsburg, Germany. Non-military national service with nursing and caring jobs.
2000 – 2002	Friedrich-Schiller-Gymnasium (Grammar school), Ludwigsburg, Germany. Matriculation standard (Abitur) in 2002.
1992 – 2000	Otto-Hahn-Gymnasium (Grammar school), Ludwigsburg.
1988 – 1992	Jakobschule (Primary school), Stuttgart, Germany.

PRIZES AND AWARDS

September 2011   GBM-Diploma/Masterprize for outstanding work from:
Gesellschaft für Biochemie und Molekularbiologie (GBM).

TEACHING EXPERIENCE

The following list comprises the drafting, assessment and grading of students work or research studies conducted at different institutes as a student or graduate research assistant.

October 2013 – present   **MLU Halle, Germany.**

Establishment of an EPR practical course (2014). Supervision of one Bachelor thesis (Marie-Therese Oehmichen, 2015) and two student trainees (Marie-Therese Oehmichen and Sophie Jost from 2014 – 2016). Teaching exercises of the subject Physical Chemistry I (2013/2014 and 2014/2015).

November 2011 – October 2013   **JGU and MPIP Mainz, Germany.**

Teaching practical courses in Biochemistry at the Institute of Pharmacy and Biochemistry in 2012 and 2013. Supervision of two student trainees (Eva Jaumann and Dmitri Spetter in 2012), as well as technical and organizational assistance of a Diploma thesis (Till Hauenschild in 2012/2013).

September 2009 – October 2011   **TU KL, Germany.**

Teaching practical courses in Physics (Department of Physics, 2009/2011). Teaching assistant of practical courses in Biochemistry (Department of Biochemistry, 2010). Supervision of one student trainee (Kathrin Stegmaier in 2011).

LANGUAGES

Mother tongue: **German**

Other languages: **English** (fluent).   General skills: excellent

Latin (good).   General skills: small Qualification

TECHNICAL SKILLS AND COMPETENCES

- Setup of EPR labs at MLU Halle in the group of Prof. Dr. D. Hinderberger.
- Practical experience in Mössbauer Spectroscopy and in general low-temperature setups.
- Authorized person for LASER protection since 2009.

Eidesstattliche Erklärung

Ich erkläre hiermit an Eides statt, dass ich die vorliegende Arbeit selbständig und ohne fremde Hilfe verfasst, keine anderen als die von mir angegebenen Quellen und Hilfsmittel benutzt und die den benutzten Werken wörtlich und inhaltlich entnommenen Stellen als solche kenntlich gemacht habe.

Weiterhin versichere ich, dass die vorliegende Arbeit keiner anderen Universität oder Hochschule vorgelegt wurde und ich mich zu keinem früheren Zeitpunkt um den Doktorgrad beworben habe.

Halle (Saale), im Juni 2018   Jörg Reichenwallner